รายงานวิจัยฉบับสมบูรณ์

พอลิเมอร์ที่นำและตอบสนองต่อไฟฟ้า

ศาสตราจารย์ ดร. อนุวัฒน์ ศิริวัฒน์

23 สิงหาคม 2558

สัญญาเลขที่ RTA 5580003

รายงานวิจัยฉบับสมบูรณ์

พอลิเมอร์ที่นำและตอบสนองต่อไฟฟ้า

ศาสตราจารย์ ดร. อนุวัฒน์ ศิริวัฒน์

วิทยาลัยปิโตรเลียมและปิโตรเคมี จุฬาลงกรณ์มหาวิทยาลัย

สนับสนุนโดยสำนักงานกองทุนสนับสนุนการวิจัย

(ความคิดเห็นในรายงานนี้เป็นของผู้วิจัย สกว. ไม่จำเป็นต้องเห็นด้วยเสมอไป)

ACKNOWLEDGEMENTS

The principle investigator would like to acknowledge the fundings provided by Thailand Research Fund through the Research Grant no. RTA 5580003, Conductive and Electroactive Polymers Research Unit, the Rachadapiseksompoch Fund of Chulalongkorn University.

Table of Contents

	Page
Acknowledgements	3
Table of Contents	4
Abstract	7
Introduction	8
Refereed Publications	11
Mechanical and electrical properties of alumina/natural rubber composites.	11
Poly(p-phenylene vilnylene)/zeolite Y composite as a ketone vapors sensor: effect of alkaline cation	32
Preparation and properties of calcium oxide from eggshells via calcinations	44
Polymer electrolyte membrane based on sulfonated poly(ether ketone ether sulfone) (S-PEKES) with low methanol permeability for direct methanol fuel cell application	54
Highly electroresponsive polymer blends of polyaniline nanoparticles and chloroprene Rubbers	64
Stress relaxation behavior of (Ala-Gly-Pro-Arg-Gly-Glu-4Hyp-Gly-Pro-) gelatin hydrogels under electric eld: Time-electric eld superposition	80
Sensitive and selective responses of poly(para-phenylene vinylene)/zeolite Y-based sensors toward ketone vapors	88
Electrostrictive properties of thermoplastic polyurethane elastomer: Effects of urethane type and soft-hard segment composition	95
Removal of water extractable proteins from concentrated natural rubber latex by eggshells	104
Development of polydiphenylamine/zeolite Y composite by dealumination process as a sensing material for halogenated solvents	121
Control of hematite nanoparticle size and shape by the chemical precipitation method	135
Ammonia sensing and electrical properties based on composite of poly(3-thiopheneacetic acid)	142

and zeolite Y

Effect of transition metal ion-exchanged into the zeolite Y on electrical conductivity and response of PEDOT-PSS/MY composites toward SO2 149

Polydiphenylamine/zeolite Yc and electrical conductivity responses toward halogenated hydrocarbons 155

Ceramic granules forming from calcium sodium aluminosilicate and carboxymethyl cellulose 165

Synthesis of poly(3,4-ethylenedioxythiophene) nanoparticles via chemical oxidation polymerization 174

Composite proton exchange membranes of sulfonated poly(ether ketone ether sulfone) (S-PEKES) and molecular sieve with high mechanical strength for direct methanol fuel cell 182

Thermo-electromechanical responses of 1-butyl-3-methylimidazolium chloride ionic liquid-cellulose gel 190

Lead zirconate (pbzro3) embedded in natural rubber as electroactive elastomer composites 199

High proton conductivity ZSM-5/sulfonated poly(ether ketone ether sulfone) (S-PEKES) composite proton exchange membrane for using in direct methanol fuel cell 206

Electrically controlled release of benzoic acid from poly(3,4 ethylenedioxythiophene)/ alginate matrix: Effect of conductive poly(3,4-ethylenedioxythiophene) morphology 212

Effect of electrolytes on electrochromic properties and morphology of poly(2,5-dimethoxy aniline) films 221

Synthesis of polydiphenylamine with tunable size and shape via emulsion polymerization 229

Electromechanical properties study of 1-butyl-3-methylimidazolium chloride/cellulosic gel blended with polydiphenylamine 237

Electromechanical properties of multi-walled carbon nanotube/gelatin hydrogel composites: Effects of aspect ratios, electric field, and temperature 250

Synthesis and characterization of sulfonated poly(aromatic imide-co-aliphatic imide) (S-coPI) Membrane for direct methanol fuel cells 259

Effect of transition metals on the electrical conductivity response of dPPV/zeolite Y composites toward ketone vapors 273

Effect of alumina particles embedded in natural rubber foams on cell morphology and 285

thermo-mechanical properties

Effect of alkaline and alkaline earth ion exchanged Y zeolites on electrical conductivity and response of PEDOT-PSS/Y zeolite composites toward SO2 294

Processing of kaolinite and alumina loaded in natural rubber composite foams 301

Outputs 311

Refereed Publications 311

Conference Proceedings 314

Oral Presentations 315

Poster Presentations 317

Organizing Annual Conferences 322

PhD Graduates 322

MS Graduates 323

Summary of Outputs 325

Conductive and Electroactive Polymers
Progress Report: RTA 5580003
Duration: 24 August 2012- 23 August 2015
PI: Anuvat Sirivat

Abstract

Conductive polymers (CPs) contain a conjugated system with **TT**-electrons delocalized along the polymer backbone, thus they possess the electrical and magnetic properties of metal, while retaining the mechanical properties of polymers. Conductive polymers offer distinct advantages: lightweight, flexibility, corrosion-resistivity, high chemical inertness, electrical insulation, the ease of processing and can be utilized at room temperature. In this proposal, the development of several conductive polymers (Ppy, Pani, Pth, Ppv, Pedot, pp, Pdpa, Paz) and the fabrication of polymeric matrices (elatomers, tri-block copolymers, cellulose, gelatin, alginate) with and without functional fillers (zeolites: A, X, Y, MCM41, ZSM-5, Beta, L, Modenite; carbon nanotubes, nanomagnetic particles) are systematically proposed. The polymeric blends and/or composites are tailored towards four main applications: a) the sensing materials for toxic gases and vapors at room temperature; b) the reversible actuation materials which can be precisely controlled by electric field; c) the drug delivery materials in which the delivery rates are programmable and activated by electric field, and d) the proton exchange membranes which are used in methanol and vanadium fuel cells.

Key Words: Conductive and Electroactive Polymers, Sensor and, Actuator, Drug Delivery, Proton Exchange Membrane

พอลิเมอร์นำไฟฟ้ามีโครงสร้างทางเคมีแบบไพคอนจูเกต ซึ่งสายโซ่หลักประกอบด้วยพันธะเดี่ยวสลับพันธะคู่ ส่งผลให้เกิดการเคลื่อนที่ของอิเล็กตรอนในโมเลกุล ดังนั้นพอลิเมอร์จึงมีสมบัติการนำไฟฟ้าคล้ายกับโลหะ แต่ยังคงสมบัติเชิงกลของพอลิเมอร์ ข้อดีของพอลิเมอร์นำไฟฟ้า คือ น้ำหนักเบา มีความยืดหยุ่นสูง ต้านทานการกัดกร่อน ทนต่อสารเคมี และสามารถสังเคราะห์ได้อุณหภูมิห้อง วัตถุประสงค์ของโครงการนี้ คือการพัฒนาพอลิเมอร์นำไฟฟ้าหลายชนิด เช่น พอลิพิโรล พอลิอะนิลีน พอลิไทโอฟีน และพอลิเอทธิลีนไดออกซีไทโอฟีน เป็นต้น นอกจากนี้ยังมีการพัฒนาเมทริกซ์จากพอลิเมอร์ เช่น อีลาสโตเมอร์ เซลลูโลส เจลลาติน และอัลจิเนต เป็นต้น ซึ่งเมทริกซ์ต่างๆถูกพัฒนาโดยการผสมกับสารเติมแต่ง เช่น ซีโอไลต์ ท่อคาร์บอนขนาดนาโนเมตร และอนุแม่เหล็กขนาดนาโนเมตร เป็นต้น เพื่อพัฒนาเมทริกซ์ให้มีสมบัติตามต้องการ โดยวัสดุผสมพอลิเมอร์นี้จะถูกนำไปประยุกต์ใช้ในงานด้านต่างๆ คือ 1) ใช้เป็นเซนเซอร์สำหรับตรวจวัดปริมาณก๊าซและไอระเหยต่างๆ ที่อุณหภูมิห้อง 2) ใช้เป็นวัสดุที่สามารถตอบสนองภายใต้กระแสไฟฟ้าในงานแอคทูเอเตอร์ 3) ใช้เป็นวัสดุในการบรรจุยาสำหรับควบคุมการปลดปล่อยปริมาณยาภายใต้กระแสไฟฟ้า และ 4) ใช้เป็นเยื่อแลกเปลี่ยนโปรตอนใน เซลล์เชื้อเพลิงชนิดเมทานอลและวานาเดียม

คำสำคัญ: พอลิเมอร์นำไฟฟ้าและพอลิเมอร์ตอบสนองต่อไฟฟ้า, เซนเซอร์และแอคทูเอเตอร์, การนำส่งยา, เยื่อแลกเปลี่ยนโปรตอน

Introduction

1. Problem Statements

Sensor

There are several types of gas sensors: electrochemical, infrared, catalytic bead, photoionization and solid-state. The most widely used gas sensor devices are produced from metallic oxides such as SnO2, ZnO, WO3, TiO3, In2O3, and etc. [A1-A5]. The electrical conductivity changes when gas molecules are adsorbed onto its surface. Even though its low selectivity has been improved, its operating temperature needs to be rather high: 300 – 400 oC [A6].

Conductive polymers contain a conjugated system with **TT**-electrons delocalized along the polymer backbone, thus they possess the electrical and magnetic properties of metal, while retaining the mechanical properties of polymers. Due to their unique electronic, chemical and physical properties, they are potentially suitable as sensing materials. Conductive polymers offer other advantages: lightweight, flexibility, corrosion-resistivity, high chemical inertness, electrical insulation, the ease of processing and can be operated at room temperature. Furthermore, conducting polymers can respond to a wide range of gases and in particular toxic gases. However, conducting polymers lack sensitivity and selectivity to particular gases at low concentrations [A7].

Zeolites are materials of interest as chemical sensors due to their nanometric sized channel system providing a size and shape-selective matrix for absorbed molecule while maintaining a high surface-to-mass ratio [A8]. The aluminum zeolite framework requires the necessary presence of cations. The selective adsorption mechanisms of zeolite can be summed up into two main mechanisms [A9]. First, the nanometric size of pores can be utilized to process the molecular sieve property. Second, the zeolite chemical composition, the Si/Al ratio, is the main factor controlling the hydrophilic/ hydrophobic properties of materials. The introduction of specific cations, by using the cation exchange method, can alter gas adsorption properties.

Actuator

Electroactive polymers (EAP) are the polymers that can convert electrical energy into mechanical energy [B1, B2]. They offer promising and novel characters as muscle-like actuators [B3]: lightweight, high energy density, and high flexibility. Actuators are the mechanical devices that can convert electrical energy into motion [B1, B2]. Actuators are used in many applications such as controllers, pumps, motors, robotic parts, artificial muscles, muscle/insect-like actuators, and MEM or NEM devices. EAPs can divided into 8 types [B1]: Piezoelectric polymers such as PVDF (polyvinylidine fluoride); Dielectric Elastomers such as polyurethane or PDMS; Electroactive Celluloses; Liquid Crystal Elastomers; Ionic Polymer Gels; Ionomeric Polymer-Metal Composites (IPMC); Conductive Polymers; and Carbon Nanotubes. Several research groups have attempted to blend two EAPs to improve the mechanical properties and processing conditions [B4, B5].
The remaining issues to be addressed are: responses at low electric field strength, temporal behaviors, and reversibility.

Drug Delivery

The goal of ideal drug delivery systems is to deliver medications intact to specifically targeted parts of the body through a medium that can control the therapy's administration. During the past decade, polymeric microspheres, polymer micelles, and hydrogel-type materials have all been shown to be effective in enhancing drug targeting specificity, lowering systemic drug toxicity, improving treatment absorption rates, and providing protection for pharmaceuticals against biochemical degradation [C1]. But these polymer microspheres, polymer micelles and hydrogel materials have slow rates of release limiting the ability to deliver the stimuli efficiently towards the target [C2]. Thus, the developments of materials capable of carrying out fast and controllable drug delivery at specified rates are required. A novel blend consisting of a conductive polymer and a hydrogel is thus expected to fulfill the important requirement of the ideal drug release device: the possibility of switching on/off and the precisely controlled release rate as a function of the applied electric potential [C4-C6].

Proton Exchange Membrane

A proton exchange membrane (PEM) is an electrolyte used in both polymer electrolyte membrane fuel cells (PEMFC) and direct methanol fuel cells (DMFCs) which allows protons to conduct from the anode to the cathode. It is expected to provide a barrier against electrons, methanol, and gas transporting through the membrane. The currently used PEM is Nafion which has been produced by Dupont since the 1960s. It is a perfluorinated polymer with sulfonic acid groups as pendant groups. Nafion has excellent ionic properties, the most important advantage of Nafion is its excellent proton conductivity in the fully hydrated condition. Furthermore, it has good physical, chemical, and mechanical stability. However, the main drawbacks are its high cost, high methanol permeability, and loss of proton conductivity at high temperature [D1]. Ideally, PEMs are expected to possess certain characteristics: high proton conductivity, low water and methanol permeability, excellent mechanical property, good thermal and chemical stabilities, high resistance to dehydration, low swelling, high resistance to oxidation, reduction, and hydrolysis, and low cost. Furthermore, the polymeric membrane must be an electron insulator to prevent the electron leakage, which leads to low efficiency. The Direct Methanol Fuel Cell (DMFC) is considered to be a highly promising power source for transportations and portable devices due to its several advantages e.g. no fuel processing unit, low temperature and pressure operation, high energy conversion efficiency, low emission, easy to design compact cell, quiet, clean and environmental friendly, and etc. The major problems are CO poison of catalyst, the high flux of fuel through the membrane or methanol crossover and the interface resistance between the electrode and the membrane. The selection of DMFC membrane is based on not only high proton conductivity but also good methanol barrier efficiency. A vanadium redox battery, or VRB, is a type of rechargeable flow battery used as an energy storage system. The VRB energy is stored chemically in different ionic forms of vanadium in a dilute sulfuric acid electrolyte. The function of a membrane is not only to prevent the cross mixing of the positive and negative electrolytes but also to allow the transport of ions to complete a circuit during the passage of current [D2]. For a VRB system, an ideal membrane should possess low permeability of vanadium ions, and low water transportability in order to obtain a higher Coulombic efficiency, longer life cycle, and higher proton conductivity to achieve higher voltage efficiency [D3].

2. ***Objectives***

Sensor

The present project proposes to develop reliable toxic gas sensing materials for CO, SO2, and toxic vapors which are inexpensive and easy to integrate into a system capable of detecting an individual gas in a gas mixture at a low concentration level and with a fast response.

Actuator

The present project proposes to develop actuation-reversible materials which can be precisely controlled by electric field. The actuation materials can be used in a variety of devices: robots, micro-motors, micromechanical devices, or even as artificial muscles for human or animals.

Drug Delivery

The present project proposes to develop conductive polymer/hydrogel blends and related materials in which the transdermal drug delivery can be precisely controlled by electric field. The drug delivery materials can be used in a variety of applications: the delivery of an anti-flammatory, drug-eluting membrane, and as a part of microchip laboratory.

Proton Exchange Membrane

The present project proposes to develop the proton exchange membranes from sulfonated poly(ether ketone ether sulfone), poly(ether ether ketone), and polyimide for using in direct methanol fuel cell (DMFC) and vanadium redox flow battery (VRB). The important properties are characterized and to be compared with the Nafion membrane which has several drawbacks such as high cost, high methanol permeability, and loss of proton conductivity at high temperature [D1].

Refereed Publications

Article

JOURNAL OF ELASTOMERS & PLASTICS

Journal of Elastomers & Plastics
44(1) 21–41
© The Author(s) 2011
Reprints and permissions:
sagepub.co.uk/journalsPermissions.nav
DOI: 10.1177/0095244311416579
jep.sagepub.com
SAGE

Mechanical and electrical properties of alumina/natural rubber composites

Nuchnapa Tangboriboon[1], Sarunya Chaisakrenon[1], Ancharee Banchong[1], Ruksapong Kunanuruksapong[2] and Anuvat Sirivat[2]

Abstract

The mechanical and electrical properties of natural rubber (STR 5L)/alumina (Al_2O_3) composites with dicumyl peroxide (DCP) functioning as the crosslinking agent and as the filler in the composites were investigated. SEM micrographs indicate that the alumina particles are moderately dispersed in the matrix and some thread-like structures form. Both dicumyl peroxide and the alumina particles act the bi-dispersed particles in the composites. The XRD patterns indicate that Al_2O_3 is of the β-phase polytype that possesses high ionic conductivity. The electrical conductivity of the composites with DCP loading increases by nearly two and three orders of magnitude, compared to those of the STR 5L/Al_2O_3 composite without DCP and the pristine natural rubber (STR 5L), respectively. The increase in the electrical conductivity originates from the strong C–C and the Al–O–C bonds, the ionic polarization of the alumina particles, and the induced dipole moments set up in the natural rubber matrix.

Keywords

electromechanical properties, crosslink agents, natural rubber STR 5L, crosslink density

[1]Department of Materials Engineering, Faculty of Engineering, Kasetsart University, Bangkok 10900, Thailand.
[2]The Petroleum and Petrochemical College, Chulalongkorn University, Bangkok 10330, Thailand.

Corresponding author:
Anuvat Sirivat, The Petroleum and Petrochemical College, Chulalongkorn University, Bangkok 10330, Thailand
Email: anuvat.s@chula.ac.th

Introduction

The backbone of natural rubber (NR), polyisoprene, is derived from the polyacetylene backbone through the saturation of every other double bond. Polyisoprene is a potential candidate for materials used in various devices: solar cells, LEDs, and FETs.[1,2] Raw elastomers, such as a natural rubber, generally have poor mechanical properties and needs to be reinforced. Reinforcement gives an improvement in the tear strength, the abrasion resistance, the stiffness, and the hardness. The solid particles, either as a reinforcing agent or filler, to a large extent, control the mechanical properties of the rubber matrix.[3] The reinforcement can be induced in principle by one of the three main mechanisms: (i) the stress transfer from the matrix to the non-isometric particles; (ii) the partial substitution of a soft matrix with a stiffer filler; and (iii) the segmental immobilization caused by the interaction between the polymer chains and the filler surface.[4] The stress transfer mechanism depends on the inclusion aspect ratio, its orientation to the applied load, the strength of adhesion, and thus it is considered to be a size–independent contribution in the case of sufficiently flexible matrix chains. The second mechanism is independent of particle size as well. On the other hand, the segmental immobilization mechanism contributes to the overall composite reinforcement where the extent is primarily affected by the size of the inclusions, becoming important for submicron particles with large surface-to-volume ratios.[4]

The chemical structure of natural rubber STR 5L is shown in Scheme I.

Natural rubber unlike many other polymers, is highly susceptible to degradation, due to the presence of double bonds in the main chain. Degradation of a natural rubber is accelerated mainly by heat, humidity, light, ozone, radiation, and other factors. Vinod et al.[5] and Jakubowickz[6] reported that alumina reduced heat, humidity, light, ozone and gamma radiation, flame resistance, and the crack growth in a natural rubber.

Alumina is a linear dielectric material with the ionic polarization and with potential uses as electrolytic capacitors, optical materials, and photoluminescents.[7] The most common form of a crystalline alumina is of the corundum phase, which has a rhombohedral Bravias lattice with a space group R-3c (Number 167 in the International Tables). Alumina also exists in other phases, namely

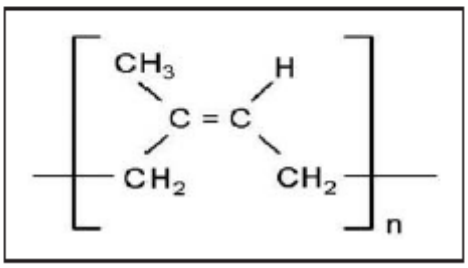

Scheme I. Standard Thai Rubber 5L (STR 5L) structure.

η, γ, θ, and δ theta alumina. All phases have a structure with a spinel-like Al–O network similar to that found in the β-alumina polytypes. Sutorik et al.[7] reported that β- and β"-alumina are high–temperature solid electrolytes that exhibit high ionic conductivity. These materials have been used in the energy storage, alkali–metal thermal-to-electric conversion (AMTEC) cells, and gas sensors[8]. The goal in working with β- and β"-alumina is to obtain the formation of β"-alumina (which has a higher ionic conductivity) over that of β-alumina. In general, the common properties of alumina (Al_2O_3) are low thermal-expansion, good thermal-shock fracture resistance, low density, high creep resistance, good chemical and thermal stability, a high melting point (1828°C ± 10°C), and excellent toughness and strength. Alumina (Al_2O_3) has been shown to be a potential candidate as the dispersed phase in the natural rubber matrix.[9,10] The structures of β- and β"-alumina are the closely related polytypes; both have the same general stacking pattern of Al–O spinel-like blocks separated by Na–O planes.[7,11]

Peroxide is the most widely used curing agent which may also acts as a filler or a dispersed phase within a rubber matrix. When peroxide is used together with an accelerator and an activator at elevated temperatures, thermally stable covalent bonds are formed between the elastomer chains as the carbon–carbon double bonds. Oh and Koenig[12] reported the preferred use of peroxide as the crosslinking agent for an elastomer. An important feature of peroxide as a curing agent is the superior strength of the C–C bond compared to the S–S or C–S bonds in the sulfur curing. The stronger bond strength results in superior heat and creep resistances at high temperatures compared to those of sulfur crosslinked systems. Bhowmick et al.[13] reported that the C–C crosslinking is more resistant to compression than the C–S crosslinking. The C–C crosslinking is induced by peroxides, which are basically divided into two types: peroxide with a carboxylic acid group, e.g., dibenzyol peroxide; and peroxide without a carboxylic acid group, e.g., dicumyl peroxide, di-*tert*-butyl peroxide, and etc. Peroxide without carboxylic groups has less sensitivity to acids, higher decomposition temperatures, and better compression properties. The overall advantages of a peroxide-based crosslinking elastomer are a high temperature resistance, a good elastic behavior with respect to compression, and no discoloration in the finished product.[14] The rate at which peroxide crosslinking takes place is dependent on the decomposition temperature, because the initial and rate–determining step in the crosslinking process is the first-order formation of free alkoxy radicals. The proper peroxide should be chosen based on its decomposition rate at the processing temperature. The chemical structure of DCP is shown in Scheme II.

Organic–inorganic composite materials are of great interest, as they are expected to have combined properties of both the inorganic particles (Al_2O_3) and the organic molecules (dicumyl peroxide, DCP) within the elastomeric matrix. When used as fillers, they can provide the mechanical strength and improved electrical properties through the inorganic particles, the crosslinking, the bridge bonding the interaction by the organic molecules, and the compatibility with the polymer matrix by the organic moiety. Within this composite, each phase may be spatially

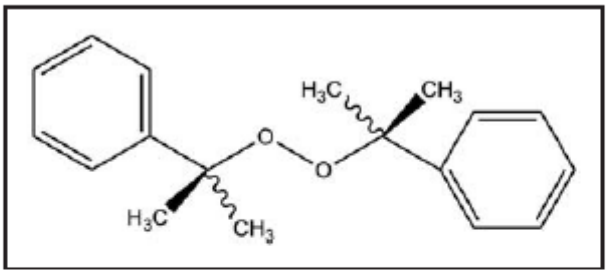

Scheme II. Dicumyl peroxide (DCP) structure.

self-connected in either one, two, or three dimensions. A common composite of bi-dispersed particles embedded in a matrix is designated as a 0–3 composite.[15] The preparation of 0–3 inorganic–organic composites involves a proper selection of the materials to be used. The inorganic or ceramic has to be transformed into a powder form from its usual block shape through pressing, curing, and firing stages. An organic or a polymer to be used determines the process in which the materials are to be mixed. In this case, it is a natural rubber, the mixing stage can be carried out with a two-roll mill at the vulcanization temperature. Technical problems to be faced in the mixing operation are a poor distribution of the organic polymer, the poor adhesion of component phases, the decomposition, and the crack formation. Inadequate distribution within the matrix commonly originates from an agglomeration of the ceramic grains. Decompositon of dicumyl peroxide requires choosing an appropriate vulcanization temperature and time. Crack formation in composites depends on the particle interaction as caused by both the inorganic (alumina) and the organic molecules (dicumyl peroxide) as the dispersed phases.

The purpose of the present work is to investigate the effects of dicumyl peroxide (DCP) and alumina particles as the dispersed phases or as the fillers on the interaction in the natural rubber (STR 5L) matrix. The amount of alumina (Al_2O_3) as the inorganic filler or a dispersed phase is fixed at the volume fraction of approximately 0.1230, the same amount used in a previous study.[16] Dicumyl peroxide is the other organic filler used as the crosslink agent as well as a filler to improve the mechanical and the electrical properties. This work involves the characterizations of related to the physical, thermal, and mechanical properties which will be reported here.

Experimental

Materials

Aluminum oxide (Al_2O_3) was purchased from Sigma-Aldrich Chemical Co., Ltd., USA (the specific gravity of the alumina powder was 3.90 g/cm^3). The starting natural rubber (STR 5L was supplied by Venus Technology Co., Ltd. (VTEC), Thailand. The STR 5L was a dried rubber type in an extra light color slab with a low dirt content, less than 0.04%. The specific gravity, the impurity content, the

Mooney viscosity, the initial plasticity, and the plasticity retention of the STR 5L were 0.92 g/cm^3, 0.02% by weight, 62.8, 32.0, and 81.3, respectively. STR 5L exhibits a high compounded gum tensile strength, and good hot tensile properties, and it possesses low level non-polymer constituents.[1,6,17] Dicumyl peroxide (DCP, $[C_6H_5C(CH_3)_2]_2O_2$), the crosslink agent, was purchased from Sigma-Aldrich Chemical Co., Ltd., USA. DCP is a white to light yellow in color and of 99.0% purity.

Instruments

Fourier transform infrared spectra (FTIR) were recorded on a spectrometer (Perkin Elmer, model Spectrum One) with a spectral resolution of 4 cm^{-1}. The samples were measured by single-crystal potassium bromide (KBr).

X-ray diffraction (XRD) data were taken and analyzed using an analyzer (Bruker, D8 Discover) with a VANTEC-1 detector and a double-crystal wide-angle goniometer. Scans were obtained from 10° to 80° 2θ at a scan speed of 5° 2θ/min in 0.05° or 0.03° 2θ increments using CuKα radiation (λ = 0.154 nm). Peak positions were compared with standard JCPDS files to identify the crystalline phases.

Simultaneous thermal analysis (Netzsch, model STA 490C) measurements were carried out. Thermal scans were performed from 27 to 600°C at a heating rate of 10°C/min under air atmosphere to determine the vulcanization behavior of the cured composites and the dicumyl peroxide (DCP). The heat of vulcanization was calculated by integrating the area under the exothermic signal.

SEM micrographs were obtained from a scanning electron microscope (SEM, model JEOL-5200). Samples of the natural rubber STR 5L, STR 5L/Al_2O_3 composites and alumina powder (Al_2O_3) were mounted on a stub using carbon paste and were sputter-coated with ~0.1 μm of gold to improve the conductivity. An acceleration voltage of 20 kV with magnifications of 100× and 2000× were used.

The electrical properties were obtained and measured using an impedance analyzer (HP, model 16451B) with an LCR meter (HP, model 4284A). The samples were prepared according to ASTM B263-94 for the electrical property measurement. Composite samples were prepared as thin discs having a diameter of 25 mm and a thickness of 0.50 mm. In our experiment, the electrical properties were measured at frequencies from 500 to 10^6 Hz with an AC current of 2 A. The measured electrical resistivity of the composite materials was converted to electrical conductivity as follows:[18]

$$\rho_{eff} = \frac{RA}{L} = \frac{1}{\sigma},$$

where ρ_{eff} is the effective resistivity (Ω.m), R is the resistance (Ω), A is the cross-section discs (m^2), and L is the thickness (m).

Cumulative and fractional distributions were measured by using a particle size analyzer (Mastersizer S, model Polydisperse 2.19). The samples were dispersed in a water medium and vibrated in an ultrasonic cleaner for 20 min.

The curing behavior was investigated at 160, 170, and 180°C using an oscillating disc rheometer (Techpro-Rheo Tech, ODR121105).

Crosslink density measurement was performed using the toluene-swelling method, as prescribed in ASTM D-6814-02. The vulcanized samples cured at 160, 170, and 180°C were cut into squares (1 cm wide and 3–5 mm thick) and weighed before being swollen in toluene until equilibrium, which normally took 72 h. The crosslink density was measured at room temperature and calculated by using the Flory–Rehner equation:

$$\nu_e = \frac{-\left[\ln(1 - V_r) + V_r + \chi_1 V_r^2\right]}{\left[V_1\left(V_r^{1/3} - (V_r)/2\right)\right]} \tag{1}$$

$$V_r = \frac{W_{Dryrubber}/density_{Dryrubber}}{\frac{W_{Dryrubber}}{D_{Dryrubber}} + \frac{W_{Absorbedsolvent}}{D_{Solvent}}} \tag{2}$$

where ν_e is the effective number of chains in real network per unit volume (mol/cm^3), V_r is the volume fraction of polymer in a swollen network in equilibrium with pure solvent; the dimensionless χ_1 is the Flory–Huggins interaction parameter (polymer–solvent interaction parameter; for toluene and Cis-polyisoprene it is 0.391 at 25°C, and V_1 is the molecular volume of solvent (toluene), $Mw/Density$ or 106.3 (cm^3/mol). The swelling ratio is calculated as

$$\text{Swelling ratio} = \frac{(w_2 - w_1)}{w_1}, \tag{3}$$

where w_1 is the weight of dry rubber (grams), and w_2 is the weight of swollen rubber (grams).

Tensile tests were carried out according to ISO 37 and ASTM D42 on type 1 dumbbell specimen in the tension mode using a Zwick tensile testing machine (model Instron 1011) at a constant cross-head speed of 500 mm/min (Scheme III). Compression molding and compression sets were tested according to ISO 815 on samples of 6 mm thickness and 13 mm diameter. The set-tests were conducted at temperature of 23°C and at 55% humidity.

Composite Sample Preparation

Composite samples of natural rubber (STR 5L) and alumina (Al_2O_3) with dicumyl peroxide (DCP) were prepared using a two-roll mill (Kodair Seisakusho, model R11-3FF). The dispersed phase (Al_2O_3) and the crosslink agent were added in

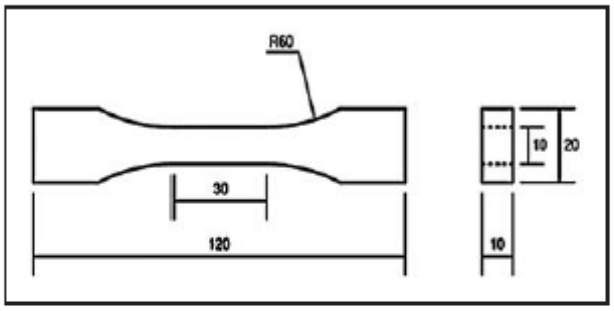

Scheme III. Dumbbell sample for tensile mode.

Table 1. Formulation of the composite samples

Samples	Weight of STR 5L (g)	Weight of alumina (Al_2O_3) (g)	Weight of dicumyl peroxide(DCP) (g)	Volume fraction of DCP, Φ
STR 5L_Al_1 DCP	100	60	1.000	0.0078
STR 5L_Al_3 DCP	100	60	3.000	0.0235
STR 5L_Al_5 DCP	100	60	5.000	0.0392

Density of STR 5L is 0.92 g/cm^3. Density of alumina is 3.90 g/cm^3. Density of dicumyl peroxide is 1.02 g/cm^3.

proper weights as calculated. The composites were vulcanized for periods in order to obtain a 90% cured reaction at t_{90}, as determined from the rheometer cure curves. Three curing conditions used in this work were the addition of 1 g (Φ = 0.0078), 3 g (Φ = 0.0235), and 5 g (Φ = 0.0392) DCP as the crosslink agent at 170°C. (The formulation of the composite samples is shown in Table 1.

Results and Discussion

Physical Characterizations

The particle size distribution of dicumyl peroxide (DCP) shows the cumulative particle fraction (CMPF) of 90% (d_{90}), 50% (d_{50}), and 10% (d_{10}) at the sizes of 1623.33, 963.33, and 311.85 microns, respectively. The average particle size of the DCP is 976.16 ± 22.26 microns. Alumina particle sizes corresponding to the cumulative particle fraction (CMPF) of 90% (d_{90}), 50% (d_{50}), and 10% (d_{10}), are 27.82, 0.16, and 0.06 microns, respectively. The average particle size of the alumina is 9.870 ± 0.023 microns. The chemical composition of the alumina powder, as measured by X-ray fluorescence, is 99.79% wt and contains 0.21% wt of other oxide contents.

Figure 1(a) and (b) shows the STA data of the uncured STR 5L/Al_2O_3 composite with dicumyl peroxide (DCP) and dicumyl peroxide particles, respectively. The STA

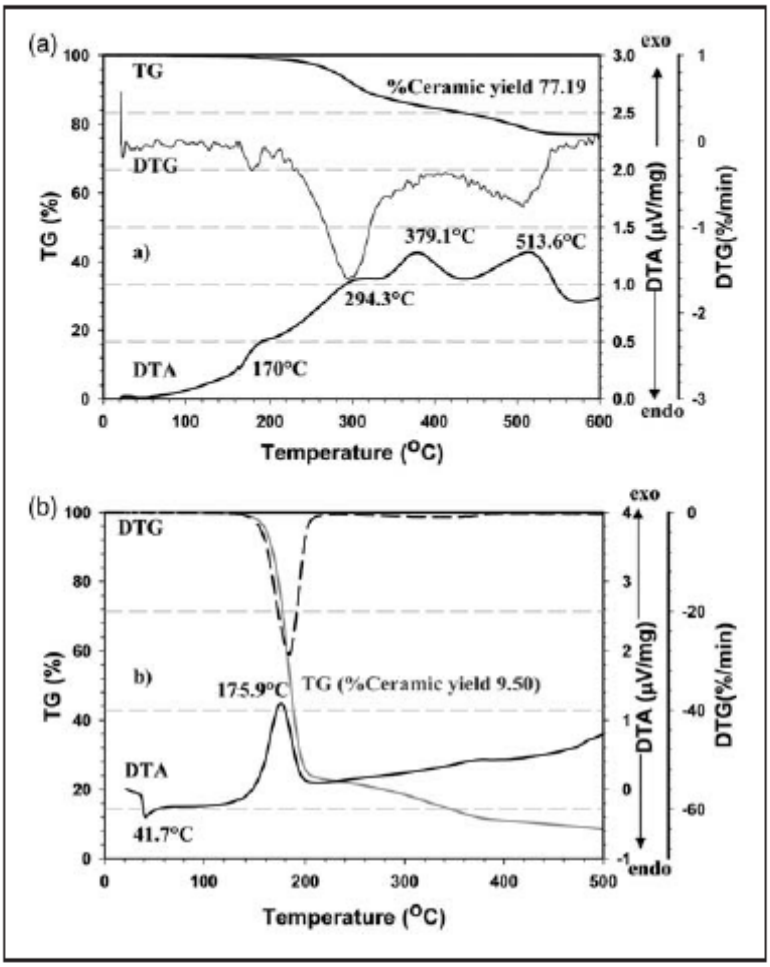

Figure 1. Simultaneous Thermal Analysis (STA) of: (a) the uncured STR 5L/Al_2O_3 with DCP composite and (b) dicumyl peroxide.

measurements were made under non-isothermal conditions in order to investigate the vulcanization behavior of the uncured composite sample. The DTA thermogram of the composite shows four peak positions at the reaction temperatures of 170, 294.3, 379.1, and 513.6°C under the exothermic signal. The DTA composite peak at 170°C corresponds to the exothermic reaction of dicumyl peroxide (Figure 2(b)) in which 175.9°C can be identified as the half life position of dicumyl peroxide. The percentage of the dicumyl peroxide remaining is equal to 9.50 at the crosslink decomposition temperature of 175.9°C. The three position peaks (294.3, 379.1, and 513.6°C) of the composite can be identified as the exothermic reactions caused by the effects of the alumina particle orientation and polarization within the STR 5L matrix. Dicumyl peroxide decomposes at high temperature over the curing temperature to become methane (0.91 mol/mol peroxide), acetophenone (0.91 mol/mol peroxide), 2-phenylpropanol-2 (1.06 mol/mol peroxide), α-methyl styrene (0.01 mol/mol peroxide), and water (0.01 mol/mol peroxide) molecules.[14] These small molecules can react

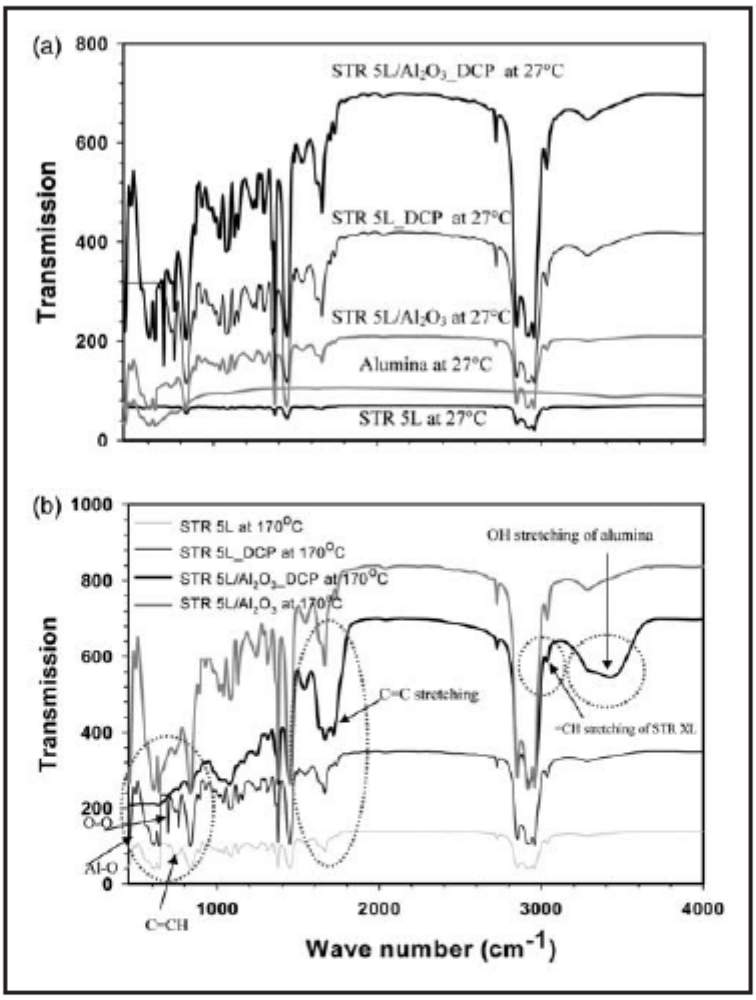

Figure 2. (a) FTIR spectra of STR 5L, alumina, and STR 5L/Al_2O_3 composites with/without DCP at 27°C. (b) FTIR spectra of STR 5L at 170°C, STR 5L with DCP at 170°C, the STR 5L/Al_2O_3 composite with DCP at 170°C, and the STR 5L/Al_2O_3 composite without DCP at 170°C.

with the alumina particles at high temperature to form Al–O, the CH_3 asymmetric deformation, and the O–H bonds as confirmed the FTIR results.

The FTIR spectra of natural rubber (STR 5L), alumina, and STR 5L/Al_2O_3 with/without DCP at 27°C and cured at 170°C are shown in Figure 2 and the data are tabulated in Table 3. The characteristic peaks of STR 5L/Al_2O_3 are at 3600–3200 cm^{-1} ν(O–H), 3000–2900 cm^{-1} ν(C-H) and (=CH), 2900–2800 cm^{-1} ν(CH_2), 1800–1600 cm^{-1} ν(C = C), 1500–1300 cm^{-1} (CH_3 asymmetric deformation), 1300–1100 cm^{-1} ν(C-O-C), 1100–740cm^{-1}(=CH bending), 640–580 cm^{-1} ν(Al-O). The FTIR spectra in both Figure 2(a) and (b) shows the peak differences especially at 3200–3400 cm^{-1} ν(C–H) and 1600–1800 cm^{-1} ν(C = C), as caused by the internal interaction of the STR 5L/Al_2O_3 composite cured with DCP. Our

Table 2. Curing times of STR 5L/Al_2O_3 composites with DCP cured at 170°C, measured at room temperature

Composite Samples	S_{max} (dNm)[a]	S_{min} (dNm)[b]	ΔS (dNm)[c]	TS_1 (min)	TS_2 (min)[d]	TS_{10} (min)	TS_{50} (min)	TS_{90} (min)[e]
STR 5L_Al 1 DCP	33.24	12.54	20.70	1.33	1.58	1.58	3.21	7.92
STR 5L_Al 3 DCP	56.15	12.65	43.50	0.88	1.04	1.33	3.17	7.67
STR 5L_Al 5 DCP	77.68	11.87	65.81	0.83	0.96	1.33	3.08	7.21

[a]Maximum rheometer torque.
[b]Minimum rheometer torque.
[c]Difference between the maximum and the minimum rheometer torques.
[d]Scorch time.
[e]Optimum curing time.
Vulcanized temperature = 170°C.

Table 3. FTIR spectra of natural rubber (STR 5L), alumina (Al), and STR 5L/Al_2O_3 composites

Wave number (cm^{-1})	Functional group
3281, 3467 (CAS7732-18-5); (CAS78-79-5)	OH stretching of Al_2O_3 added natural rubber, STR5L
2961, 3036 (CAS78-79-5)	-CH and = CH stretching vibration of isoprene
2851, 2918 (CAS78-79-5)	-CH_2 stretching vibration of C-CH_2CH_3
1663, 1710 (CAS78-79-4)	>C= C stretching for carbon double bonds
1449 (CAS78-79-5); (CAS110-54-3); (CAS73513-42-5)	-CH_3 asymmetric deformation
1376 (CAS78-79-5)	-CH_3 deformation of O-CH_2CH_3
1242, 1287 (CAS110-54-3)	asymmetric C-O-C stretching vibration
1128	R-CO-R symmetric stretching
740, 762, 1038, 1084 (CAS110-54-3)	skeletal vibration of hexane
572, 638	Al-O stretching

FTIR results are consistent with those reported by Ismail et al.[19] and Kansal et al.[20]

The cross-sectional microstructures of STR 5L and STR 5L/Al_2O_3 with 1, 3, and 5 g DCP cured at 170°C, obtained by SEM, are shown in Figure 3. Figure 3(a) shows the micrograph of pure STR 5L. Adding DCP and alumina particles into STR 5L generates the entanglement-bound rubber chains and the formation of a strong filler–rubber interaction. Both Figure 3(c) and (d) illustrate that the STR 5L/Al_2O_3 composites loaded with a high volume fraction of DCP possess increases in the mechanical strength and the crosslink density. However, it is noted that the

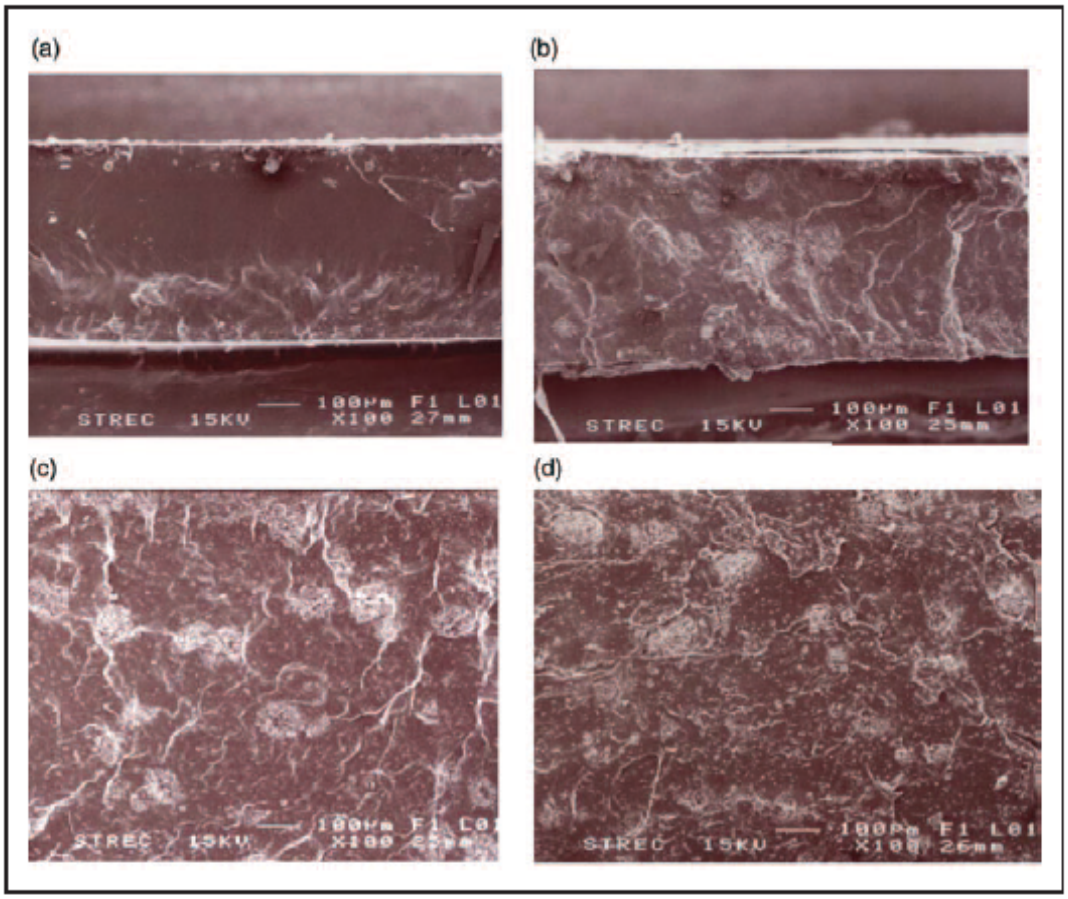

Figure 3. Cross-sectional SEM micrographs: (a) STR 5L; (b) the STR 5L/Al_2O_3 composite with 1 g DCP cured at 170°C; (c) the STR 5L/Al_2O_3 composite with 3 g DCP cured at 170°C; and (d) the STR 5L/Al_2O_3 composite with 5 g DCP cured at 170°C.

reinforcement and the crosslinking of dicumyl peroxide are restricted in a vicinity of the filler/elastomer interface. At low DCP loading, a vast surface area is unaffected, as can be seen in Figure 3(b).

Comparisons of the cross-sections (from a_1 to d_1) and the surfaces (from a_2 to d_2), from the SEM micrographs, at a magnification of 2000×, of STR5L, and the STR 5L/Al_2O_3 composites with 1, 3, and 5 g DCP cured at 170°C are shown in Figure 4. The cross-sectional microstructures of DCP added STR 5L/Al_2O_3 composites clearly illustrate the effect of DCP as the crosslinking agent and as the filler at the same time. At a higher amount of DCP, a higher crosslink density leads to the entangled natural rubber in the bulk. The rubber binding occurs in the transition zone between the highly immobilized rubber and the mobile natural rubber, leading to physical absorptions within the elastomer matrix, inducing higher tensile modulus, polarization, and electrical conductivity. The natural rubber chains are

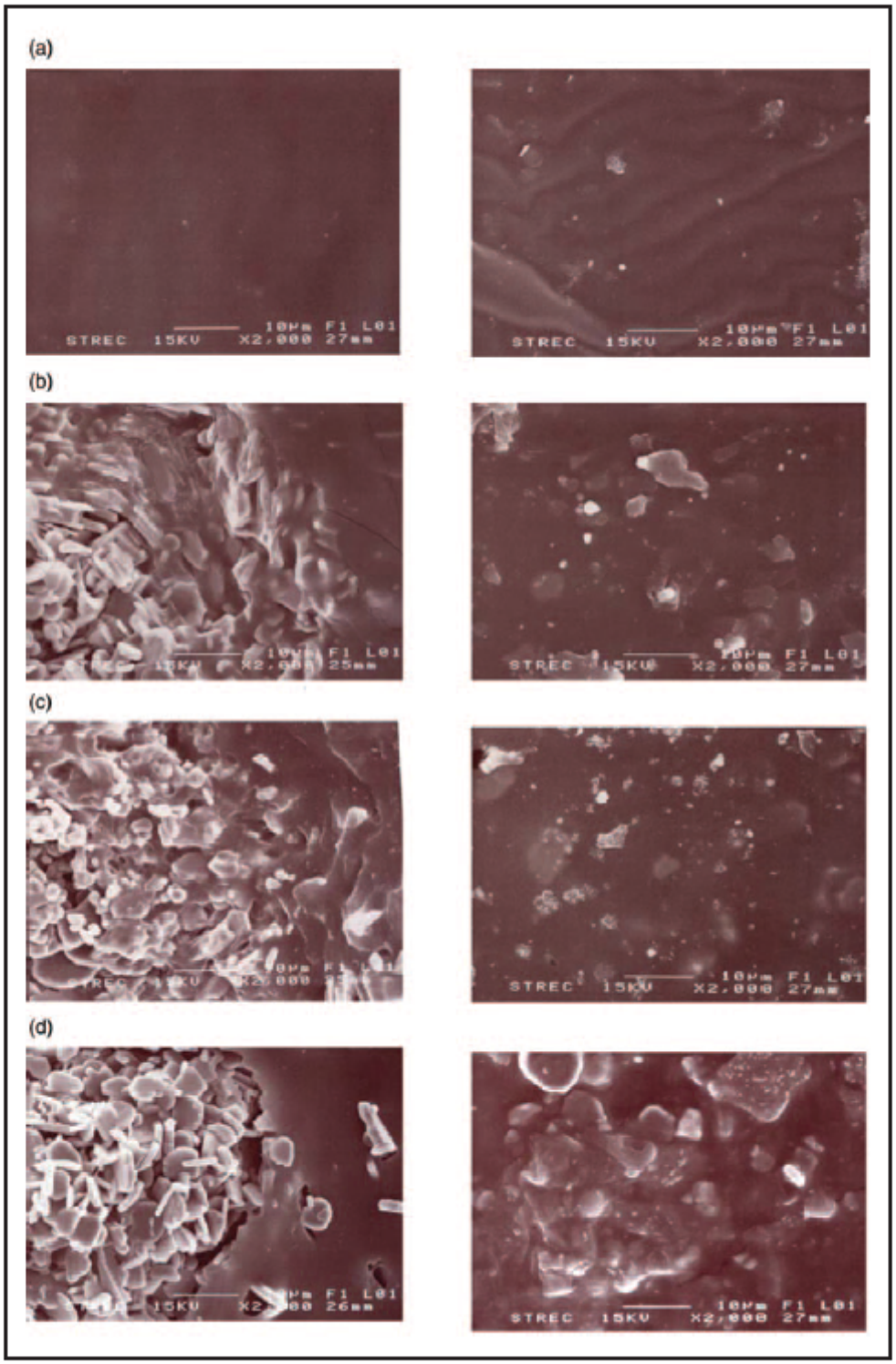

Figure 4. SEM micrographs (crosssection_1 and surface_2) of: (a) STR 5L; (b) the STR 5L/Al_2O_3 composite with 1 g DCP cured at 170°C; (c) the STR 5L/Al_2O_3 composite with 3 g DCP cured at 170°C; and (d) the STR 5L/Al_2O_3 composite with 5 g DCP cured at 170°C.

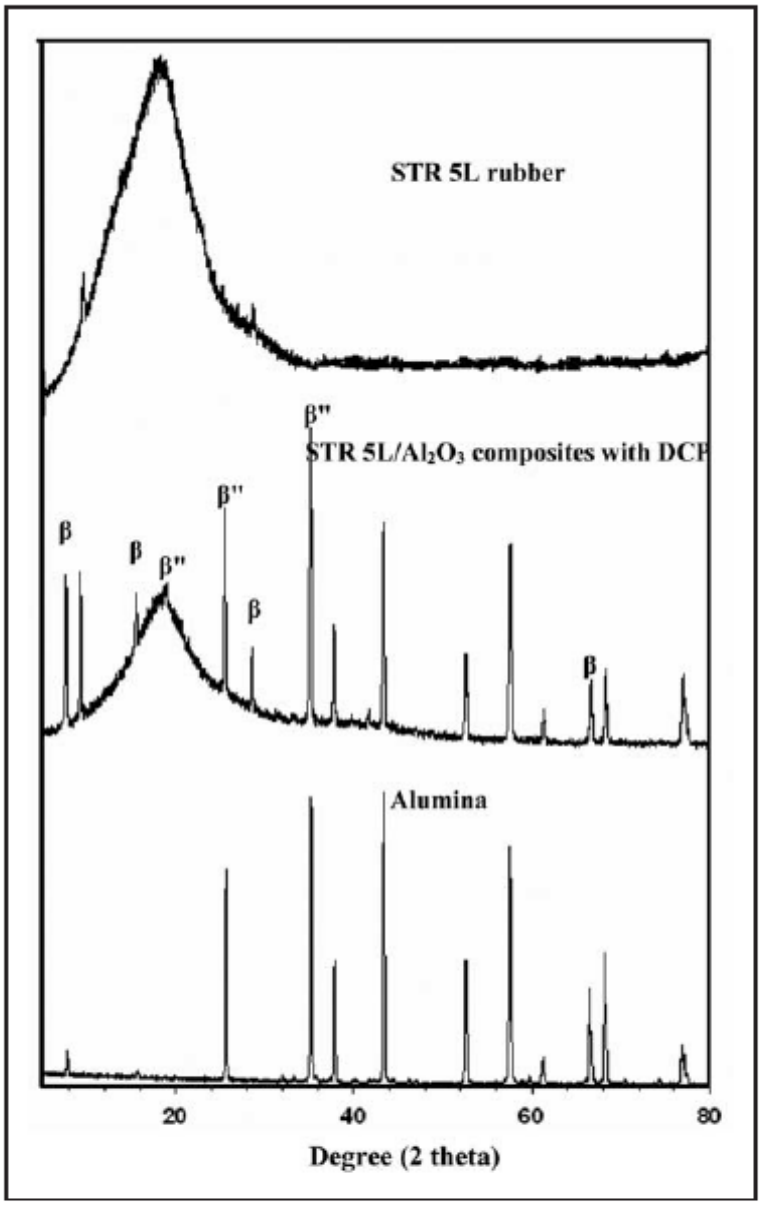

Figure 5. XRD peak patterns of natural rubber (STR 5L), alumina (Al_2O_3), and the STR 5L/Al_2O_3 composites with DCP cured at 170°C.

confined forming a highly ordered entangled structure as a result of the strong particle/elastomer interaction.

The XRD patterns of STR 5L, Al_2O_3, and STR 5L/Al_2O_3 composites with DCP cured at 170°C are shown in Figure 5. The XRD pattern of STR 5L shows an amorphous phase formation wheras the XRD pattern of alumina powder indicates a crystalline phase formation, resembling those recorded at the International Center for Diffraction Data (JCPDS number 00-042-1458).

The XRD peak pattern of STR 5L/Al_2O_3 composite with DCP cured at 170°C shows a mix between the amorphous and the crystalline phases, consistent with the JCPDS number 01-070-0384. The partially crystalline phase of STR 5L/Al_2O_3 composite with DCP cured at 170°C suggests the alumina phase transformation from the corundum phase to the hexagonal phase in the β- and β"-alumina forms. The β- and β"-alumina forms generally possess high ionic conductivity; impurity ions (K^+, Ca^{2+}, and Na^+) can migrate through a surplus of cationic sites in the crystal lattice.[5]

Curing Characteristics and Crosslink Density Measurement

The curing characteristics of STR 5L/Al_2O_3 with 1, 3, and 5 g DCP, at the vulcanization temperature of 170°C, are tabulated in Table 2. The data indicate that the curing time, as denoted by t_{90}, is approximately 8 min. To investigate the effect of DCP as the crosslinking agent on the curing characteristics, the optimum cure time and the maximum rheometer torque are the indicative parameters. Upon adding a percentage of DCP the vulcanization reaction of the cured STR 5L/Al_2O_3 composites increases, as indicated by the increases in the rheometer torque (more stiffness), the curing time, and the scorch time. This can be explained by the good interaction between the components of the cure system: the dispersed phase (Al_2O_3) and the natural rubber (STR 5L) matrix. Assuming that the rheometer torque is related to the crosslink density of the composites,[21] the STR 5L/Al_2O_3 composites with 1, 3, and 5 g DCP, at the vulcanization temperature of 170°C, show the highest crosslink density. To prove this hypothesis, the crosslink density and the swelling ratio measurements of the composites were carried out (Table 4). At low and the high vulcanization temperatures (e.g. 160 and 190°C), this effect is negligible owing to the vulcanization rate enhancement. This suggests under and over–curing reversion reactions, respectively, which undergo a bond linkage breakage.

Swelling Behavior

Figure 6 shows the swelling behavior, or the relationship between the crosslink density *vs.* the volume fraction of STR 5L/Al_2O_3 composites with 1, 3, and 5 g DCP, cured at 160, 170, 180, and 190°C, as determined in toluene according to D 6814-02, using the Flory–Rehner equation and the Flory–Huggins interaction parameter. The swelling ratio of the composites in equilibrium with toluene decreases with time from 1 to 5 g DCP when cured at 170°C. The highest crosslink density was obtained with the STR 5L/Al_2O_3 composite with 5 g DCP cured at 170°C, and the lowest crosslink density was obtained with the STR 5L/Al_2O_3 composites with 1, 3, and 5 g DCP cured at 190°C. The reinforcement and the network formation of the composites are temperature sensitive. Our results are consistent with the swelling behavior study of the recycled rubber powder-filled natural rubber compounds by Ismail.[19,22] In addition, the swelling ratio increases gradually at high vulcanization temperature over 190°C.

Table 4. Swelling ratio and crosslink density of STR 5L/Al_2O_3 composites with DCP cured at 170°C and measured at room temperature

Samples	Vulcanized Temperature (°C)	Swelling Ratio[a]	Crosslink Density, ν_e $\times 10^{-4}$ (mol/cm^3)[b]	M_c (g/mol)[c]	V_r [d]
STR5L _1 DCP	160	3.019	2.19	4203	0.24
	170	3.080	2.11	4360	0.23
	180	3.524	1.65	5581	0.21
	190	4.196	1.21	7695	0.18
STR5L_ 3 DCP	160	3.306	1.85	4965	0.22
	170	2.996	2.22	4146	0.24
	180	3.478	1.69	5450	0.21
	190	3.740	1.48	6228	0.20
STR5L_ 5 DCP	160	3.108	2.08	4432	0.23
	170	1.914	4.98	1845	0.33
	180	3.691	1.51	6079	0.20
	190	3.309	1.85	4974	0.22
STR5L__Al_2O_3_1 DCP	160	1.698	6.16	1493	0.36
	170	1.711	6.08	1514	0.36
	180	1.703	6.13	1500	0.36
	190	3.486	1.68	5471	0.21
STR5L_ Al_2O_3_3 DCP	160	2.212	3.85	2389	0.30
	170	1.606	6.79	1354	0.37
	180	2.006	4.59	2005	0.32
	190	3.850	1.40	6568	0.20
STR 5L_ Al_2O_3_5 DCP	160	1.826	5.42	1697	0.34
	170	1.215	10.92	1092	0.44
	180	2.395	3.34	2757	0.28
	190	2.804	2.51	3672	0.20

[a]Swelling ratio was calculated using the following equation: swelling ratio = $(w_2 - w_1)/w_1$, where w_1 and w_2 are the weights of the dry rubber and the swollen rubber, respectively.
[b]Crosslink density or effective number of chains in a real network per unit volume was calculated using the Flory–Rehner equation.
[c]Average molecular weight between the network crosslinks.
[d]Volume fraction of rubber in a swollen network in equilibrium with toluene.

Mechanical Properties of STR 5L/Al_2O_3 Composites Crosslinked by DCP at a Vulcanization Temperature 170°C

The mechanical properties in tensile mode of the STR 5L/Al_2O_3 composites with 1, 3, and 5 g DCP cured at 170°C are shown in Figure 7, and the data are tabulated in

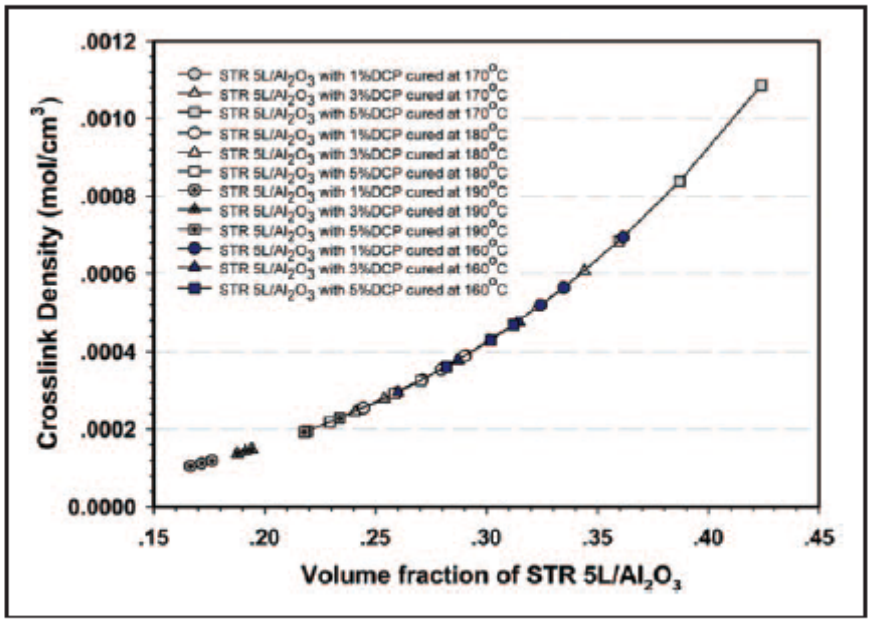

Figure 6. The Flory–Huggins interaction parameter between toluene and the STR 5L/Al_2O_3 composites with 1 ($\Phi = 0.0078$), 3 ($\Phi = 0.0235$), and 5 g ($\Phi = 0.0392$) DCP cured at 160, 170, 180, and 190°C.

Tables 5 and 6. Figure 7 shows the tensile stress–elongation at break curves of the cured composites at 170°C as a function of the percentage of DCP. Both the tensile stress and the elongation at break decrease but the elastic modulus increases with increasing amount of the crosslinking agent (DCP). The presences of the rigid alumina particles as the filler and the DCP particles as the filler and the curing agent thus result in the enhancement of the elastic modulus of STR 5L/Al_2O_3 composites with DCP relative to that of the pure STR 5L. There are three main causes for the elastic modulus enhancement: (i) the stress transfer from the matrix to the non-isometric particles; (ii) the partial substitution of the soft matrix with the stiffer filler, and (iii) the segmental immobilization caused by the interaction between polymer chains and the surface of the filler.

Grubbström et al.[23] studied the mechanical properties in tearing mode of silane crosslinked recycled low-density polyethylene wood composites. The flexural strength, the stiffness, the strain at break, and the energy absorbed at maximum load in all specimens increase with increasing silane crosslinking amount.[23]

Electrical Properties of Alumina Particles Embedded in Natural Rubber Composites (STR 5L/Al_2O_3) Crosslinked by DCP at the Vulcanization Temperature 170°C

Figure 8(a) and (b) show the electrical properties (electrical conductivity and dielectric constant) of the natural rubber (STR 5L), the alumina (Al_2O_3), and the STR

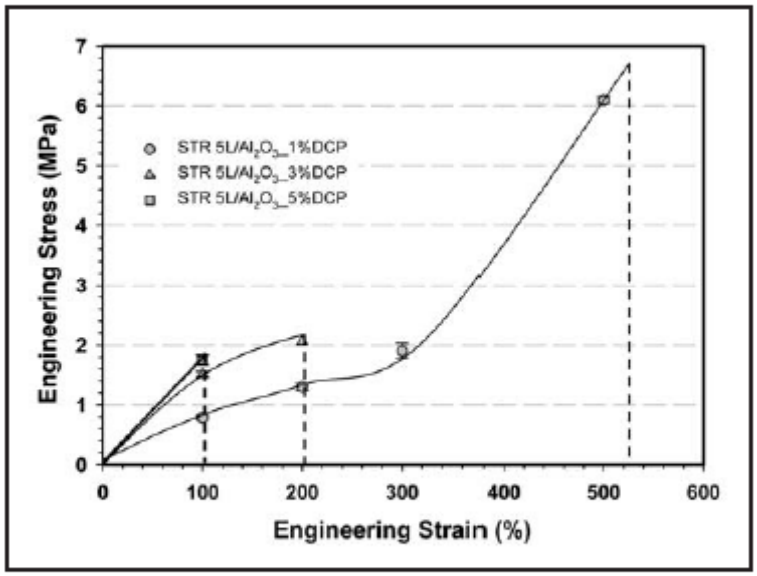

Figure 7. Modulus of elasticity of the STR 5L/Al_2O_3 composites with 1 ($\Phi = 0.0078$), 3 ($\Phi = 0.0235$), and 5 g ($\Phi = 0.0392$) DCP cured at 170°C.

Table 5. Mechanical properties of STR 5L/Al_2O_3 composites with DCP cured at 170°C and measured at room temperature

Samples	Load at Break, F (N)	Area (mm^2)	Tensile Stress, σ (MPa)	Tensile Strength, TS (MPa)	Elongation at Break, El (%)	Tensile Modulus of Elasticity, E (MPa)	Ductility (%El>5)
STR 5L_Al 1 DCP	88.01 ± 7.32	13.22	6.162 ± 0.353	4.93 ± 0.35	651.69 ± 27.86	0.477	√
STR 5L_Al 3 DCP	27.79 ± 3.07	12.36	2.095 ± 0.177	2.09 ± 0.22	162.13 ± 142.97	0.707	√
STR 5L_Al 5 DCP	20.08 ± 0.30	13.44	1.229 ± 0.029	1.23 ± 0.04	79.33 ± 6.19	–	√

– Not measured.

Table 6. Modulus of STR 5L/Al_2O_3 composites with DCP cured at 170°C and measured at room temperature

Samples	Load at Break (N)	Tensile Strength (MPa)	100% Modulus (MPa)	200% Modulus (MPa)	300% Modulus (MPa)	500% Modulus (MPa)
STR 5L_Al 1 DCP	88.01 ± 7.32	4.93 ± 0.35	0.41 ± 0.01	0.71 ± 0.01	1.03 ± 0.02	2.14 ± 0.11
STR 5L_Al 3 DCP	27.79 ± 3.07	2.09 ± 0.22	0.95 ± 0.04	1.66 ± 0.07	–	–
STR 5L_Al 5 DCP	20.08 ± 0.30	1.23 ± 0.04	–	–	–	–

– Not measured.

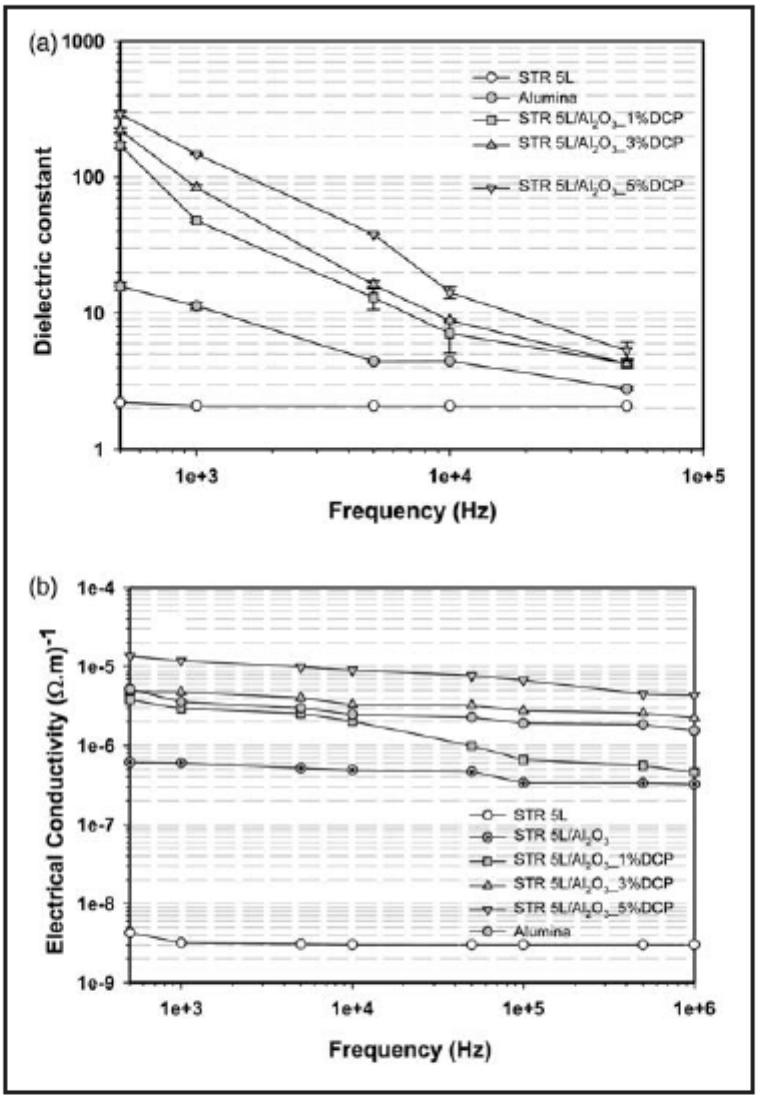

Figure 8. (a) Dielectric constant of natural rubber (STR 5L), alumina, and the STR 5L/Al_2O_3 composites with 1 ($\Phi = 0.0078$), 3 ($\Phi = 0.0235$), and 5 g ($\Phi = 0.0392$) DCP cured at 170°C vs. frequency from 500 Hz to 1 MHz measured at 27°C. (b) Electrical conductivity of natural rubber (STR 5L), alumina, and the STR 5L/Al_2O_3 composites with 1 ($\Phi = 0.0078$), 3 ($\Phi = 0.0235$), and 5 g ($\Phi = 0.0392$) DCP cured at 170°C vs. frequency from 500 Hz to 1 MHz measured at 27°C.

5L/Al_2O_3 composites with 1, 3, and 5 g DCP cured at 170°C versus the frequency from 500 Hz to 10^6 Hz, measured at room temperature. With increasing percentage of DCP, the electrical conductivity and the dielectric constant increases by an order of magnitude (data are tabulated in Table 7). The dielectric constant values are 1.542, 15.741, 171.575, 220.500, and 291.095 for STR 5L, Al_2O_3, and the STR 5L/

Table 7. Electrical properties of STR 5L/Al_2O_3 composites with DCP cured at 170°C and measured at room temperature, and at 500 Hz

Code	Mass of STR 5L (g)	Mass of Al_2O_3 (g)	Volume fraction of Al_2O_3 (Φ)	Dielectric constant ε' at 500 Hz	Dielectric loss factor ε'' at 500 Hz	Conductivity $(\Omega.m)^{-1}$, σ at 500 Hz
Al_2O_3	0.0000	1.0000	1.00000	15.741	7.662E-03	1.502E-07
Pure STR 5L	100.0000	0.0000	0.00000	1.542	6.841E-04	4.279E-09
STR 5L_Al	100.0000	60.0000	0.12302	126.095	3.640E-03	6.155E-07
STR 5L_Al 1 DCP	100.0000	60.0000	0.12302	171.575	7.692E-04	3.820E-06
STR 5L_Al 3 DCP	100.0000	60.0000	0.12302	220.500	5.482E-05	4.818E-06
STR 5L_Al 5 DCP	100.0000	60.0000	0.12302	291.095	9.866E-04	1.355E-05

Measured at 27°C. Density STR 5L is 0.92 g/cm^3. Density Al_2O_3 powder is 3.90 g/cm^3. STR 5L rubber has extra light color.

Al_2O_3 composites with 1, 3, and 5 g DCP, respectively, measured at room temperature at 500 Hz. The electrical conductivity values of STR 5L, Al_2O_3, and the STR 5L/Al_2O_3 composites with 1, 3, and 5 g DCP are 4.279×10^{-9}, 1.502×10^{-7}, 3.820×10^{-6}, 4.818×10^{-6}, and 1.355×10^{-5} $(\Omega.m)^{-1}$, respectively, measured at room temperature at 500 Hz. Alumina particles are a dielectric material which are expected to increase both the electrical conductivity and the dielectric constant of the composites without the presence of DCP. With a DCP loading, DCP molecules influence the alignment of the alumina particles into a more ordered arrangement and thus promote induced dipole moments within the composite matrix.

Conclusions

The experimental data show that the STR 5L/Al_2O_3 composite with 5 g (Φ = 0.0392) DCP as the crosslinking agent and as the filler at 170°C has the highest crosslink density, stiffness, tensile elastic modulus, and dielectric constant and electrical conductivity. The dielectric constant and the electrical conductivity of the STR 5L/Al_2O_3 composite with 1 g (Φ = 0.0078) DCP are 171.575 and 3.820×10^{-6} $(\Omega.m)^{-1}$, respectively, measured at room temperature and at 500 Hz. The electrical conductivity (σ) of the STR 5L/Al_2O_3 composite with 1 g (Φ = 0.0078) DCP increases by nearly two and three orders of magnitude as compared to the STR 5L/Al_2O_3 composite without DCP and pure natural rubber (STR 5L), respectively. A small amount of dicumyl peroxide (DCP) added as the crosslinking agent and as the filler induces a strong C–C bond crosslinking and the Al–O–C bonding within the natural rubber (STR 5L) matrix. Both bi-dispersed particles (alumina (Al_2O_3) and dicumyl peroxide (DCP) particles)_can be used as the fillers to alter the mechanical properties. The STR 5L/Al_2O_3 composite with 1 g (Φ = 0.0078) DCP appears to be a soft and flexible material and a potential

candidate as a novel, multi-functional soft-material, namely 'hybrid organic–inorganic composites', or for biomimetic actuators and/or artificial muscles.

Acknowledgements

The authors would like to thank the following: the Petroleum and Petrochemical College and the Scientific and Technological Research Equipment Centre, of Chulalongkorn University; the Rubber Technology Division, Rubber Research Institute of Thailand, Department of Agriculture; the Faculty of Engineering, Kasetsart University; and the Departments of Materials Engineering and Physics, at the Kasetsart University for the use of their analytical equipment. We are also grateful for the grant support from the Small Projects on Rubber (SPR) of the Thailand Research Fund. AS would like to acknowledge the funding from the Conductive and Electroactive Polymers Research Unit of the Chulalongkorn University, the Center of Petroleum, Petrochemicals and Advanced Materials, the Thailand Research Fund (TRF), and the Royal Thai Government (Budget of Fiscal Year 2552).

References

1. Najidha S, Saxena NS, Sreeja R, Unnithan CH and Predeep P. Optical and Electrical Characterization of $SbCl_5$ Doped cis-1,4-Polyisoprene. *Mat Lett* 2005; 59: 3431–3436.
2. Lowery, TH and Richardson, KS (1998). *Solvent, Mechanism and Theory in Organic Chemistry*, Harper Collins, p.181.
3. Ansarifar A, Azhar A, Ibrahim N, Shiah SF and Lawton JMD. The Use of a Silanised Silica Filler to Reinforce and Crosslink Natural Rubber. *Int J Adhes Adhes* 2005; 25: 77–86.
4. Kalfus J and Jancar J. Reinforcing Mechanism in Amorphoud Polymer Nano-Composites. *Compos Sci Technol* 2008; 68: 3444–3447.
5. Vinod VS, Varghese S and Kuriakose B. Degradation Behaviour of Natural Rubber-Aluminum Powder Composites: Effect of Heat, Ozone and High Energy Radiation. *Polym Degrad Stab* 2002; 75: 405–412.
6. Jakubowickz I. Evaluation of Degradability of Biodegradable Polyethylene (PE). *Polym Degrad Stab* 2003; 39–43.
7. Sutorik AC, Neo SS, Treadwell DR and Laine RM. Synthesis of Ultrafine β''-Alumina Powders Via Flame Spray Pyrolysis of Polymeric Precursors. *J Am Ceram Soc* 1998; 81(6): 1477–1486.
8. Kummer JT and Weber N. (1983). *Energy Conversion Device Comprising a Solid Crystalline Electrolyte and a Solid Reaction Zone Separator*, U.S. Pat.No.3: 404: 306.
9. Parthasarathy M and Klingenberg DJ. Electrorheology: Mechanisms And Models. *Mat Sci Eng* 1996; 17: 57–103.
10. Rob DFM. Taalman Isoprene: Background and Issues. *Toxicology* 1996; 113: 242–246.
11. Yamagushi G and Suzuki K. On the Structures of Alkalipolyaluminates. *Bull Chem Soc Jp* 1968; 41: 93–99.
12. Oh SJ and Koenig JL. Proton Spin-Spin Relaxation and n.m.r. Imaging Of Peroxide/Coagent Crosslinked *cis*-1, 4-Polyisoprene. *Polym* 1999; 40: 4703–4708.
13. Bhowmick AK, Hall M and Benarey HA. *Rubber Products Manufacturing Technology*. New York: Marcel Dekker, 1994, p. 55.

14. Thitithammawong A, Nakason C, Sahakaro K and Noordermeer JWM. Thermoplastic Vulcanizates Based on Epoxidized Natural Rubber/Polypropylene Blends: Selection of Optimal Peroxide Type and Concentration in Relation to Mixing Conditions. *Eur Polym J* 2007; 43: 4008–4018.
15. Dias CJ and Das-Gupta DK. Inorganic Ceramic/Polymer Ferroelectric Composite Electrets. *IEEE Trans Dielectr Electr Insul* 1996; 3(5): 706–734.
16. Tangboriboon N, Uttanawanit N, Longtong M, Wongpinthong P, Sirivat A and Kunanuraksapong R. Electrical and Electrorheological Properties of Alumina/Natural Rubber (STR XL) Composites. *Materials* 2010; 3(1): 656–671.
17. Tardif O, Nishiura M and Hou Z. Rare Earth Alkyl and Hydride Complexes Bearing Silylene-Linked Cyclopentadienyl-Phosphido Ligands. Synthesis, Structures, and Catalysis in Olefin Hydrosilylation and Ethylene Polymerization. *Tetrahedron* 2003; 59: 10525–10539.
18. Callister, WD. (2007). *Materials Science and Engineering an Introduction*, John Wiley & Sons, Inc. 7th edn, p. 806.
19. Ismail YA, Shin SR, Shin KM, Yoon SG, Shon K and Kim SI. Electrochemical Actuation in Chitosan/Polyaniline Microfibers for Artificial Muscles Fabricated Using an In Situ Polymerization. *Sen Actuators B* 2008; 129: 834–840.
20. Kansal P and Laine RM. A Processable Mullite Precursor Prepared by Reacting Silica and Aluminum Hydroxide with Triethanolamine in Ethylene Glycol: Structural Evolution on Pyrolysis. *J Am Ceram Soc* 1997; 80(10): 2597–2606.
21. Pojanavaraphan T and Magaraphan R. Prevulcanized Natural Rubber Latex/Clay Aerogel Nanocomposites. *Euro Polym J* 2008; 44: 1968–1977.
22. Ismail H, Nordin R and Noor AM. Cure Characteristics, Tensile Properties and Swelling Behavior of Recycled Rubber Powder-Filled Natural Rubber Compounds. *Polym Test* 2002; 21: 565–569.
23. Grubbström G, Holmgren A and Oksman K. Silane-crosslinking of Recycled Low-Density Polyethylene/Wood Composites. *Composites Part A* 2010; 41: 678–683.

J Polym Res (2012) 19:20
DOI 10.1007/s10965-012-0020-5

ORIGINAL PAPER

Poly(p-phenylene vilnylene)/zeolite Y composite as a ketone vapors sensor: effect of alkaline cation

Jirarat Kamonsawas · Anuvat Sirivat · Pimpa Hormnirun

Received: 20 July 2012 / Accepted: 29 October 2012
© Springer Science+Business Media Dordrecht 2012

Abstract This work is an attempt to improve the selectivity and sensitivity response of zeolite Y towards 3 different types of ketone vapors (acetone, MEK and MIBK) which are known to be toxic and flammable substances. The effects of cation type, cation concentration, ketone vapor type, and cyclic interval were investigated. Three different cations were exchanged in zeolite Y at 50 % mole: NaY, 50KNaY, 50MgNaY and 50CaNaY for the zeolite Y at a fixed Si/Al ratio of 5.1. 50KNaY sample exhibits the highest electrical conductivity sensitivity. This arises from the electrostatic interaction between the cation and the zeolite framework, which affects the adsorption properties of zeolite. The dPPV was mixed with 80KNaY matrix at 10 %v/v and was exposed to 3 different ketone vapors. The highest electrical conductivity sensitivity belongs to the acetone exposure, whereas the MIBK exposure shows the lowest value, as a result of the smaller acetone size. The sensitivity of the composite is higher than that of pure zeolite Y by an order magnitude. For the cyclic interval, the electrical conductivity response decreases with increasing number of the interval due to the interaction between the active site and ketone vapors. The response of samples is irreversible as evidenced by FTIR.

Keywords Poly (*p*-phenylene vinylene) · 2-propanone (acetone) · Butan-2-one (MEK) · 4-methylpentan-2-one (MIBK) · Zeolite Y

J. Kamonsawas · A. Sirivat (✉)
Conductive and Electroactive Polymer Research Unit,
The Petroleum and Petrochemical College,
Chulalongkorn University,
Bangkok 10330, Thailand
e-mail: anuvat.s@chula.ac.th

P. Hormnirun
Department of Chemistry, Faculty of Science,
Kasetsart University,
50 Phahonyothin Road, Ladyao, Chatuchak,
Bangkok 10900, Thailand

Published online: 20 November 2012

Introduction

The development of gas sensing materials with selectivity and reliability for volatile organic compounds (VOCs) detection has been of interest in many industrial process controls to control the pollution. Many industrial processes such as utilized ketone group solvents acetone (2-Propanone), MEK (Butan-2-one), MIBK (4-Methylpenta-2-one), xylene, toluene, alcohol (methanol, ethanol and propanol) which are known to be flammable, toxic, and harmful to human [1–6].

One of the possible sensor modes is the electrical conductivity response when exposed to volatile organic compounds vapors [1–13]. Various types of material are used as gas sensors: conductive polymers [2, 8, 9], porous materials [14, 15], and metal oxides [16, 17]. Zeolites are porous material which has been widely used as a gas sensing material such as Faujasite (zeolite x and zeolite Y), ZSM-5 and Mordernite. Zeolite has a high thermal stability, good chemical resistance, high porosity, high surface area, and good selective and adsorption properties towards particular gases and vapors. These characteristic properties of zeolite have been explored and utilized towards gas sensing [4, 18–21]. However, the electrical conductivity of zeolite is rather low. There have been several methods to improve the electrical conductivity and the electrical conductivity sensitivity properties of zeolite such as the ion exchange process, the reduction in the Al content in the zeolite structure, and the blending with other conductive polymers [4, 10–13]. The alkaline and alkaline earth cations are the one of the factors control the electrical conductivity and the adsorption properties. Recently, the exchange process and the mixing of a conductive polymer into a zeolite matrix has been attempted to improve of electrical conductivity of zeolite as a sensing materials to detect toxic gases [1–13, 22–24].

Poly(p-phenlene vinylene) (PPV) is the one of conductive polymers that has been widely used in gas sensing applications because it has high electrical conductivity after

doping with sulfuric acid, good mechanical properties, good chemical stability, and is easy to synthesize [25, 26]. Doped poly(p-phenlene vinylene) or dPPV may have a positive or negative response depending on the electrophilic or nucleophilic nature of the gases or chemical vapors. But PPV itself generally has poor selective and adsorption properties towards particular gases and chemical vapors. Therefore, combining the good characteristics of zeolite and the conductive polymer is expected to improve the selective, adsorptive, and electrical conductivity properties by mixing the conductive poly(p-phenlene vinylene) into the zeolite matrix [13, 23].

In this work, the effects of the cation type and the cation concentration of zeolite Y, at the fixed Si/Al ratio of 5.1, on the electrical conductivity sensitivity towards an acetone vapor are investigated. Then, the electrical conductivity response of the dPPV and zeolite Y composite towards the three different types of ketone vapor sensors (acetone, MEK, MIBK) are also investigated.

Experimental

Materials preparation

Synthesis of poly(p-phenylene vinylene) or PPV and doping process

Poly(p-phenylene vinylene) or PPV was chemically synthesized with α,α'-dichloro-p-xylene (Aldrich) and tetrahydrothiophene (Aldrich) to form a p-xylene-bis (tetrahydrothiophenium chloride) monomer. The base induced the polymerization of the p-xylene-bis(tetrahydrothiophenium chloride) monomer to form a precursor polymer and PPV was essentially obtained by heating the precursor polymer under vacuum at 180 °C for 6 h [26]. The doping process occurred after adding the 18 M sulfuric acid solution at the mole ratio 0f 1:100 (PPV repeating units and sulfuric acid) to the polymer powder. The process was monitored by observing the change of polymer color from bright yellow to black brown [25].

The cation exchange process

The zeolite Y (Si/Al = 5.1, Na^+) or NaY was purchased from Zeolyst. The NaY with different cation types were obtained by an ion exchange process. The solution of $MgCl_2$, $CaCal_2$ and KCl at 0.5 M was added in to 5 g of NaY and strired at 25 °C for 24 h to prepare zeolite Y (Si/Al = 5.1, 50 % mole of Na^+ and 50 % mole of Mg^{2+}) or 50MgNaY, zeolite Y (Si/Al = 5.1, 50 % mole of Na^+ and 50 % mole of Ca^{2+}) or 50CaNaY, zeolite Y (Si/Al = 5.1, 80 % mole of Na^+ and 30 % mole of K^+) or 30KNaY, zeolite Y (Si/Al = 5.1, 50 % mole of Na^+ and 50 % mole of K^+) or 50KNaY and zeolite Y (Si/Al = 5.1, 80 % mole of Na^+ and 20 % mole of K^+) or 80KNaY. Then zeolite samples were filtered and washed with DI-water for 5 times [21].

Preparation of dPPV_zeolilte Ypellet

The zeolite Y: NaY, NaMgY, NaCaY and KNaY at the same Si/Al ratio (5.1) were used as the matrices. The dPPV_Zeolite Y composites were prepared by a dry random mixing the zeolite Y with dPPV particles at 10 %v/v of dPPV. The composites were compressed into a disc form by using a hydraulic press at the pressure of 6 kN.

Characterization of PPV, dPPV and composite

An FT-IR spectrometer (Inclolet, model FRA 106/S) was used to characterize functional groups of PPV, dPPV and the interaction between the ketone vapors and the active site on

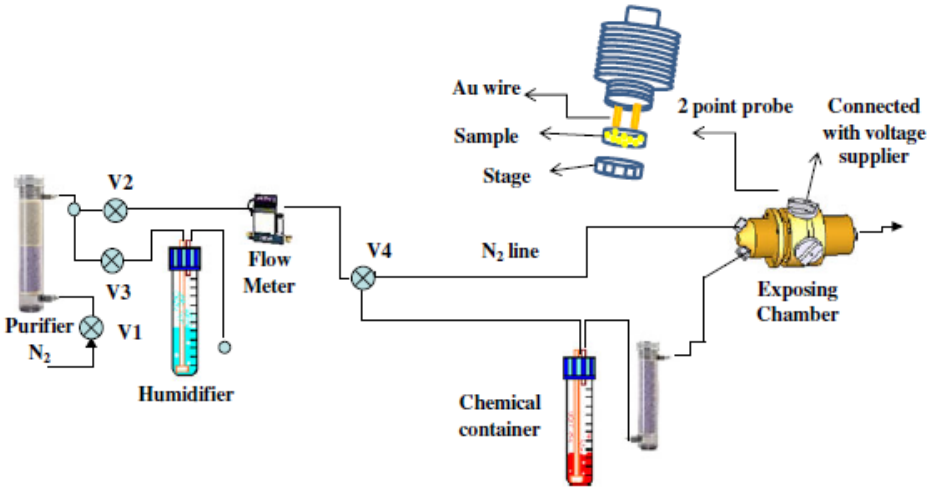

Fig. 1 Schematic diagram of detection system

the gas sensing materials. A scanning electron microscope (SEM, Hitachi, model S4800) was used to study the morphology of PPV, dPPV, Zeolite Y, the 10 %v/v of dPPV on the composites or dPPV_[90]80KNaY, and the dispersion of the conductive polymer particles in Zeolite Y, at the magnifications of 1000× and 5000× and at 5 and 10 kV. The surface area analysis (Sorptomatic-1990) was used to measure the pore sizes and the surface areas of the zeolite Y. The amount of cation was determined by an atomic adsorption spectrophotometer (Varian, Spectr A300). A custom made two-point probe with a linear geometric array and connected with a voltage supplier (Keithley, 6517A) was used to measure the specific electrical conductivity.

Electrical conductivity and chemical vapor detection

The electrical conductivity values of the gas sensing pellets under exposures to air, N_2 and chemical vapors were measured by using the custom made two-point probe, in the chemical chamber connected to a voltage supplier (Keithley, 6517A) in which its voltage was varied and the resultant of current was measured. The electrical conductivity was calculated by utilizing the Eq. 1.

$$\sigma = (I/KVt) \quad (1)$$

where I is the measured current (A), V is the applied voltage (V), t is the thickness, and K is the geometric correction factor of the two-point probe, as determined by calibrating the probe with a silicon wafer possessing a known resistivity value.

For the chemical vapor detection, the chemicals were used in this work were (Dimethyl Ketone or 2-Propanone (Acetone), Methyl Ethyl Ketone or Butan-2-one (MEK), Methyl Iso-Buthyl Methyl Ketone or 4-methylpentan-2-one (MIBK)) (Labscan, AR GRADE). All of ketone vapors were prepared through a flow system at the vapor concentration of 30,000 ppm (3 %v/v) in N_2. Nitrogen (N_2, TIG) was used as the surface cleaning gas and to vaporize the chemical solvents. All chemicals were used without further purifications. The detection system is as shown in Fig. 1. For the cyclic interval investigation, the measurement is 1,200 s for each cyclic interval. And each cyclic internal was evacuated of air and moisture by using a vacuum pump until steady state was obtained. N_2 gas was injected into the chamber and the steady state electrical conductivity was recorded as $\sigma_{N2,\text{before exposure}}$. Then chamber was evacuated before injecting the chemical vapor into the chamber. The ketone vapor was injected into the chamber and the steady state electrical conductivity was recorded as $\sigma_{\text{chemical vapor}}$. The ketone vapor was removed by the vacuum pump and N_2 was injected into the chamber, and the electrical conductivity was measured as $\sigma_{N2,\text{ after exposure}}$. The electrical conductivity response and sensitivity of the composites were determined by following the Eqs. 2 and 3.

Table 1 Structural, analytical data and electrical conductivity of dPPV, zeolite Y and dPPV_zeolite Y

Sample	Sample code	Zeolite content (%v/v)	% mole of cation	EN	Ionic radii (°A)	Median pore width (A°)	Surface area (m^2/g)	σ_{air} (S/cm)	σ_{N2} (S/cm)
Doped poly(p-phenylenevinylene)	dPPV	0	–	–	–	–	–	$1.25\times10^{1}\pm 7.30\times10^{-1}$	$2.21\times10^{-2}\pm 6.21\times10^{-4}$
Zeolite Y (Si/Al = 5.1, Na^+)	NaY	100	100 %Na^+	0.93(Na^+)	1.16(Na^+)	7.4875±0.34	617.0±7.0	$2.50\times10^{-3}\pm 2.51\times10^{-5}$	$8.38\times10^{-4}\pm 2.27\times10^{-5}$
Zeolite Y (Si/Al = 5.1, Na^+, Mg^{2+})	50MgNaY	100	53 %Mg^2, 47 %Na^+	0.93(Na^+), 1.31(Mg^{2+})	1.16(Na^+), 0.71(Mg^{2+})	8.0750±0.04	530.0±2.0	$1.72\times10^{-3}\pm 3.28\times10^{-5}$	$3.73\times10^{-4}\pm 3.71\times10^{-6}$
Zeolite Y (Si/Al = 5.1, Na^+, Ca^{2+})	50CaNaY	100	55 %Ca^{2+}, 45 %Na^+	0.93(Na^+), 1.00(Ca^{2+})	1.16(N a$^+$), 1.14(Ca^{2+})	8.0600±0.03	649.0±6.0	$2.19\times10^{-3}\pm 4.28\times10^{-5}$	$7.69\times10^{-4}\pm 3.70\times10^{-6}$
Zeolite Y (Si/Al = 5.1, Na^+, K^+)	50KNaY	100	56 %K^+, 44 %Na^+	0.93(Na^+), 0.82(K^+)	1.16(Na^+), 1.51(K^+)	7.7820±0.39	553.0±4.0	$5.55\times10^{-3}\pm 5.27\times10^{-4}$	$1.06\times10^{-3}\pm 2.27\times10^{-4}$
10 %v/v doped poly(p-phenylenevinylene)_Zeolite Y (Si/Al = 5.1, Na^+, K^+)	dPPV_[90] 80KNaY	90	81 %K+, 19 %Na+	0.93(Na^+), 0.82(K^+)	1.16(Na^+), 1.51(K^+)	–	–	$1.12\times10^{-1}\pm 3.58\times10^{-2}$	$5.86\times10^{-3}\pm 2.27\times10^{-3}$

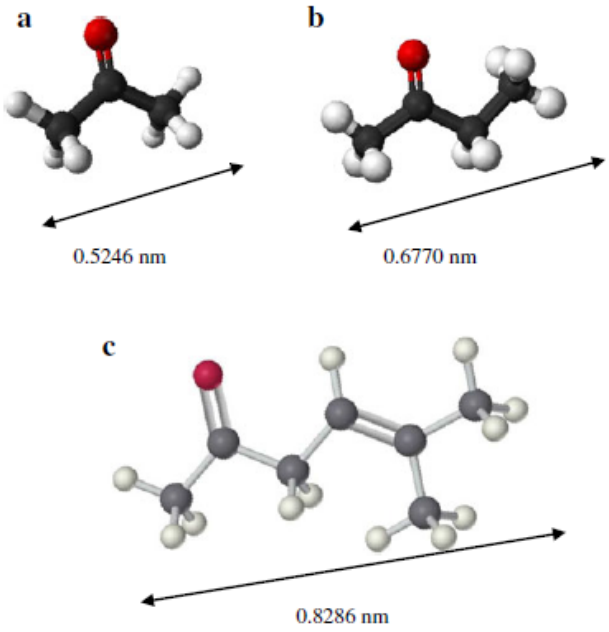

Fig. 2 The molecular structures of: a Propanone (acetone); b Buta-2-one (MEK); and c 4-Methylpentan-2-one (MIBK)

$$\Delta\sigma = \sigma_{\text{chemical vapor}} - \sigma_{\text{N2,before exposure}} \quad (2)$$

$$\text{Sensitivity} = \Delta\sigma/\sigma_{\text{N}_2\text{ before exposure}} \quad (3)$$

Δσ is the difference in the specific electrical conductivity (S/cm), where $\sigma_{\text{N2, before exposure}}$ is the specific electrical conductivity in N_2 before exposure (S/cm), and $\sigma_{\text{chemical vapor}}$ is the specific electrical conductivity under chemical vapor exposure (S/cm) [22–24].

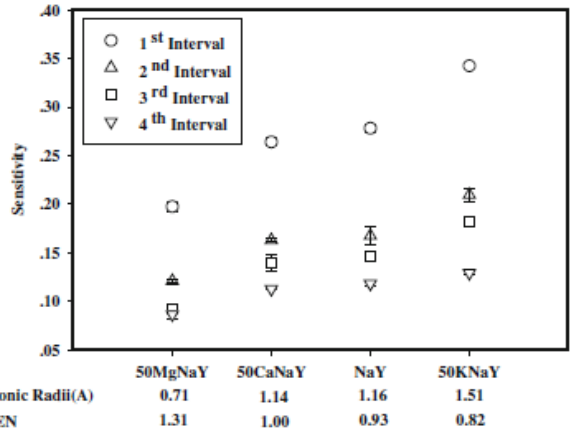

Fig. 4 Sensitivity of the NaY, 50MgNaY, 50CaNaY and 50KNaY in acetone exposure at 25 °C, 1 atm, at vapor concentration of 30,000 ppm (3 %v/v), and at the interval of 1,200 s

Results and discussion

Characterization of dPPV, zeolite Y and composites

The main analytical data and the electrical conductivity data in air and N_2 of dPPV, zeolite Y with different cations but

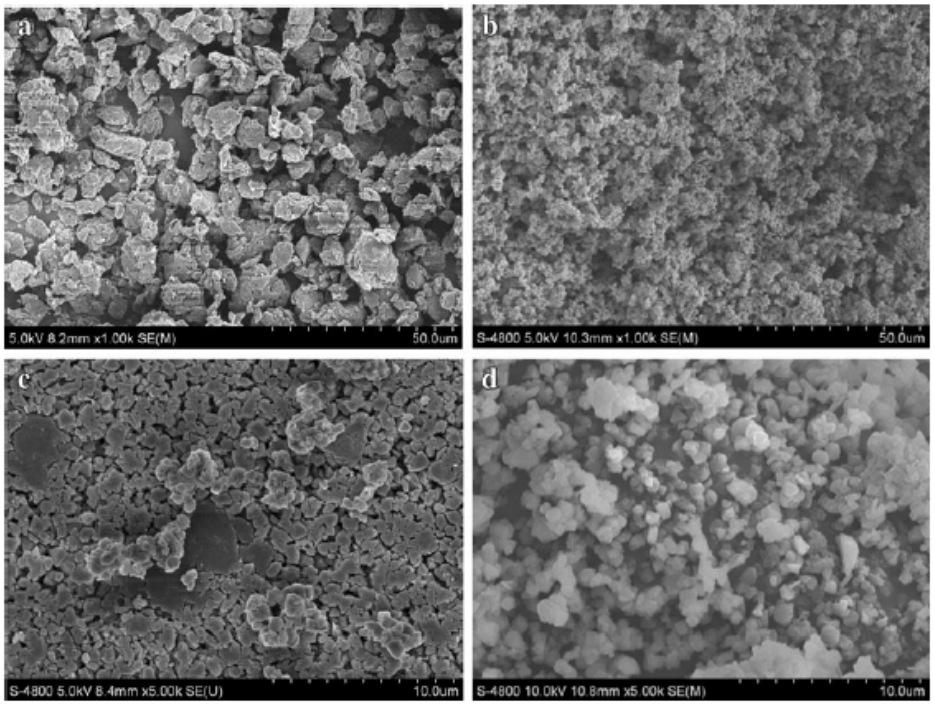

Fig. 3 The morphology of dPPV powder, KNaY powders and, dPPV_KNaY pellet and powder at 10 %v/v of dPPV: a dPPV at the magnification of 1000×; b KNaY at the magnification 1000×; c dPPV_KNaY pellet at the magnification of 51000×; and d dPPV_KNaY powder at the magnification of 5000×

Table 2 Electrical conductivity sensitivity of dPPV, zeolite Y and dPPV_zeolite Y exposed to Acetone, MEK and MIBK

Sample	Chemical vapor	1st interval			2nd interval			3rd interval			4th interval		
		Sensitivity	Induction time (min)	Recovery time (min)	Sensitivity	Induction time (min)	Recovery time (min)	Sensitivity	Induction time (min)	Recovery time (min)	Sensitivity	Induction time (min)	Recovery time (min)
dPPV	Acetone	$4.49\pm6.78\times10^{-01}$	35±0.2	20±1	$2.72\pm7.72\times10^{-01}$	14±1	12±1	$1.69\pm8.23\times10^{-02}$	14±1	12±1	$1.48\pm7.92\times10^{-02}$	11±0.3	11±0.5
NaY	Acetone	$2.68\times10^{-01}\pm1.99\times10^{-02}$	35±0.2	15±1	$1.68\times10^{-01}\pm9.41\times10^{-02}$	15±1	13±1	$1.46\times10^{-01}\pm2.75\times10^{-03}$	14±1	14±1	$1.18\times10^{-01}\pm2.78\times10^{-03}$	14±0.3	11±0.5
50MgNaY	Acetone	$1.97\times10^{-01}\pm5.06\times10^{-03}$	39±1	19±0.8	$1.21\times10^{-01}\pm5.74\times10^{-04}$	18±4	17±2	$9.12\times10^{-02}\pm1.72\times10^{-04}$	17±1	17±1	$8.64\times10^{-02}\pm4.22\times10^{-03}$	17±1	15±1
50CaNaY	Acetone	$2.57\times10^{-01}\pm2.40\times10^{-03}$	35±0.3	16±0.2	$1.63\times10^{-01}\pm1.37\times10^{-02}$	15±1	14±0.1	$1.40\times10^{-01}\pm8.21\times10^{-03}$	15±1	15±0.4	$1.12\times10^{-01}\pm9.82\times10^{-42}$	14±0.4	11±1
30KNaY	Acetone	$2.78\times10^{-01}\pm4.42\times10^{-03}$	33±0.5	14±0.2	$1.68\times10^{-01}\pm2.87\times10^{-03}$	14±0.9	11±0.4	$1.50\times10^{-01}\pm1.58\times10^{-03}$	13±0.2	11±1	$1.18\times10^{-01}\pm2.04\times10^{-03}$	11±1	11±0.8
50KNaY	Acetone	$3.42\times10^{-01}\pm4.67\times10^{-04}$	33±0.5	14±0.2	$2.09\times10^{-01}\pm6.27\times10^{-03}$	14±0.9	11±0.4	$1.81\times10^{-01}\pm6.12\times10^{-04}$	13±0.2	11±1	$1.28\times10^{-01}\pm0.00\times10^{0}$	11±1	11±0.8
80KNaY	Acetone	$4.26\times10^{-01}\pm1.25\times10^{-04}$	33±0.5	14±0.2	$2.92\times10^{-01}\pm8.28\times10^{-03}$	14±0.9	11±0.4	$2.30\times10^{-01}\pm4.40\times10^{-03}$	13±0.2	11±1	$1.30\times10^{-01}\pm1.63\times10^{-03}$	11±1	11±0.8
10dPPV_[90] 80KNaY	Acetone	$4.13\pm7.09\times10^{-02}$	22±0.2	14±0.1	$1.43\pm1.61\times10^{-02}$	14±0.1	11±0.5	$9.10\times10^{-01}\pm6.98\times10^{-03}$	12±0.2	11±0.2	$5.27\times10^{-01}\pm2.68\times10^{-05}$	11±0.3	11±0.1
10dPPV_[90] 80KNaY	MEK	$2.17\pm9.55\times10^{-02}$	17±0.3	14±0.2	$7.44\times10^{-01}\pm4.29\times10^{-02}$	12±0.1	11±0.1	$5.48\times10^{-01}\pm3.83\times10^{-02}$	12±0.1	11±0.1	$4.75\times10^{-01}\pm1.10\times10^{-02}$	11±0.1	11±0.1
10dPPV_[90] 80KNaY	MIBK	$1.01\pm1.03\times10^{-02}$	15±0.3	13±0.2	$5.71\times10^{-01}\pm2.98\times10^{-02}$	12±0.1	11±0.1	$3.89\times10^{-01}\pm1.82\times10^{-02}$	12±0.1	11±0.1	$2.44\times10^{-01}\pm3.16\times10^{-02}$	11±0.1	11±0.1

the same Si/Al ratio (5.1), and the composites are tabulated in Table 1. The molecular structures of acetone, MEK and MIBK are shown in Fig. 2. The SEM morphology of dPPV, KNaY and dPPV_KNaY are shown in Fig. 3.

The cage size of zeolite Y (Si/Al = 5.1, Na^+) or NaY is 1.3 nm and connected with a 0.74 nm window [21]. Figure 2 shows the molecular structure of 3 different types of ketone: acetone (2a), MEK (2b) and MIBK (2c) with length scales of 0.524 mn, 0.677 mn and 0.828 nm, respectively. It is anticipated that the acetone and MEK molecules can penetrate to the zeolite Y framework. However, the MIBK molecule is larger than the zeolite Y cage, and it is not expected to penetrate into the zeolite Y cage [21, 28].

The amounts of K^+, Mg^{2+} and Ca^{2+} ion exchanged with Na^+ in the zeolite Y were determined by an atomic adsorption spectrophotometer in terms of %mole of cation. The %mole of cation exchange is defined as the ratio of K^+, Mg^{2+} and Ca^{2+} divided by the sum of the moles of the cation and Na^+ multiplied by 100 [22]. For the NaY ion exchanged with K^+, the mole percentages are 30, 56 and 81 for the ion exchange times of 3 h, 12 h and 24 h, respectively. For the NaY exchanged with Mg^{2+} and Ca^{2+}, the mole percentages are 53 and 56 for the ion exchange time of 24 h, as listed in Table 1.

Figure 3a and b show the SEM monographs of dPPV or doped poly(p-phenylene vinylene), Zeolite Y (Si/Al = 5.1, K^+ and Na^+) or KNaY particles, at the magnification of 1000×, and at 5 kV; they appear to be moderately uniform in shape and sizes. A nearly uniform dispersion of dPPV particles within the zeolite Y matrix pellet and powder can be observed in Fig. 3c and d [12, 13, 22–24].

The electrical conductivity values of 50KNaY, NaY, 50CaNaY, 50MgNaY and under N_2 condition are $1.06\times10^{-03}\pm2.27\times10^{-04}$ S/cm, $8.38\times10^{-04}\pm3.76\times10^{-05}$ S/cm, $7.69\times10^{-04}\pm3.79\times10^{-04}$ S/cm and $3.73\times10^{-04}\pm3.70\times10^{-06}$ S/cm, respectively, as tabulated in Table 1. For the effect of cation type, the electrical conductivity of MgNaY is lower than NaY, CaNaY and KNaY, respectively. This is because of the EN of Mg^{2+} (1.31) is higher than Ca^{2+} (1.00), Na^+ (0.93) and K^+ (0.82). The large value of electronegativity and the small size of charge balancing ion lead to reduced proton mobility in the zeolite Y framework [20, 21, 27, 28]. The electrical conductivity of dPPV in N_2 condition is $2.21\times10^{-02}\pm6.21\times10^{-04}$ S/cm. When mixing dPPV in the KNaY matrix, the electrical conductivity increases up to $5.86\times10^{-03}\pm2.27\times10^{-03}$ S/cm. Thus, dPPV has been shown to improve the electrical conductivity of zeolite Y by an order of pure 80KNaY [13, 23]. The electrical conductivity sensitivity of dPPV, 50MgNaY, NaY, 50CaNaY, 50KNaY and dPPV_[90]80KNaY pellets exposed to 3 different types of ketone vapor is shown and discussed next.

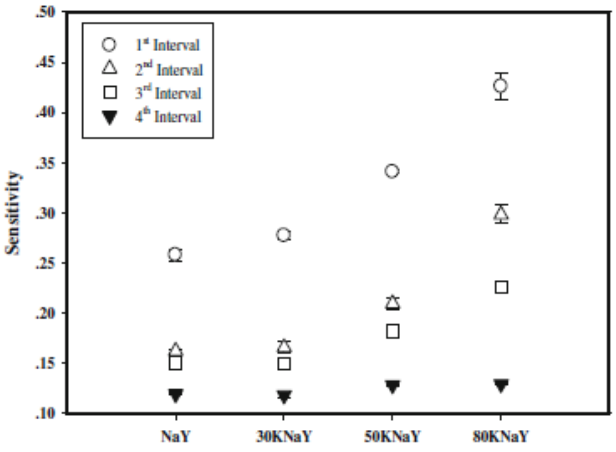

Fig. 5 Sensitivity of the NaY, 30KNaY, 50KNaY and 80KNaY in acetone exposure at 25 °C, 1 atm, at vapor concentration of 30,000 ppm (3 %v/v), and at the interval of 1,200 s

The response of zeolite Y at the cyclic interval of 1,200 s

The effect of cation type

Zeolite Y (Si/Al 5.1, Na^+) or NaY ion exchanged with Mg^{2+}, Ca^{2+} and K^+ cat 50 % mole are investigated for the effect of cation type and the cyclic response at the cyclic interval of 1,200 s towards the 3 %v/v acetone vapor in N_2. Figure 4 shows the plot of electrical conductivity sensitivity of 50MgNay, 50CaNaY, NaY and 50KNaY versus cation radius (°A) and electronegativity (EN) towards the acetone vapor at concentration of 3 %v/v in N_2. The electrical conductivity sensitivity values in the 1st interval of 50MgNaY, 50CaNaY, NaY

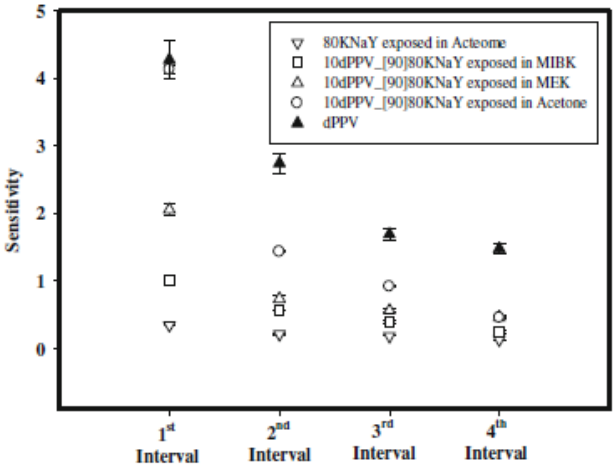

Fig. 6 Sensitivity of the 80KNaY, 10dPPV_[90]80KNaY and dPPV in acetone, MEK and MIBK exposure at 25 °C, 1 atm, at vapor concentration of 30,000 ppm (3 %v/v), and at the interval of 1,200 s

and 50KNaY are $1.97\times10^{-01}\pm5.06\times10^{-03}$, $2.57\times10^{-01}\pm2.40\times10^{-03}$, $2.68\times10^{-01}\pm1.99\times10^{-02}$ and $3.42\times10^{-01}\pm4.67\times10^{-04}$, respectively, as tabulated in Table 2. The electrical conductivity sensitivity increase with increasing of cationic radius and decreasing electronegativity (EN), because the large cationic radius corresponds to the reduced electrostatic interaction between the cation and the zeolite framework, resulting in the cation ability to transfer to another cage or the increase in proton mobility [20–22, 27, 28]. The cationic radius of K^+ (1.51 ˚A) is larger than Na^+ (1.16 ˚A), Ca^{2+} (1.14 ˚A) and Mg^{2+} (0.71 ˚A), respectively. Therefore, 50KNaY shows the highest electrical conductivity sensitivity value than those of NaY, 50CaNaY and MgNaY when exposed acetone vapor at a concentration of 3 %v/v in N_2.

The effect of cation concentration

The effect of the cation concentration in zeolite Y after ion exchanged with containing 0, 30, 50 and 80 % mole of K^+ on the electrical conductivity sensitivity towards the acetone vapor at 3 %v/v in N_2 is investigated and shown in Fig. 5. The electrical conductivity sensitivity values of NaY, 30KNaY, 50KNaY and 80KNaY in the 1st interval response are $2.68\times10^{-01}\pm1.99\times10^{-02}$, $2.78\times10^{-01}\pm4.42\times10^{-03}$, $3.42\times10^{-01}\pm4.67\times10^{-04}$ and $4.26\times10^{-01}\pm1.25\times10^{-04}$ as K^+ concentration in NaY increases from 0, 30, 50 and

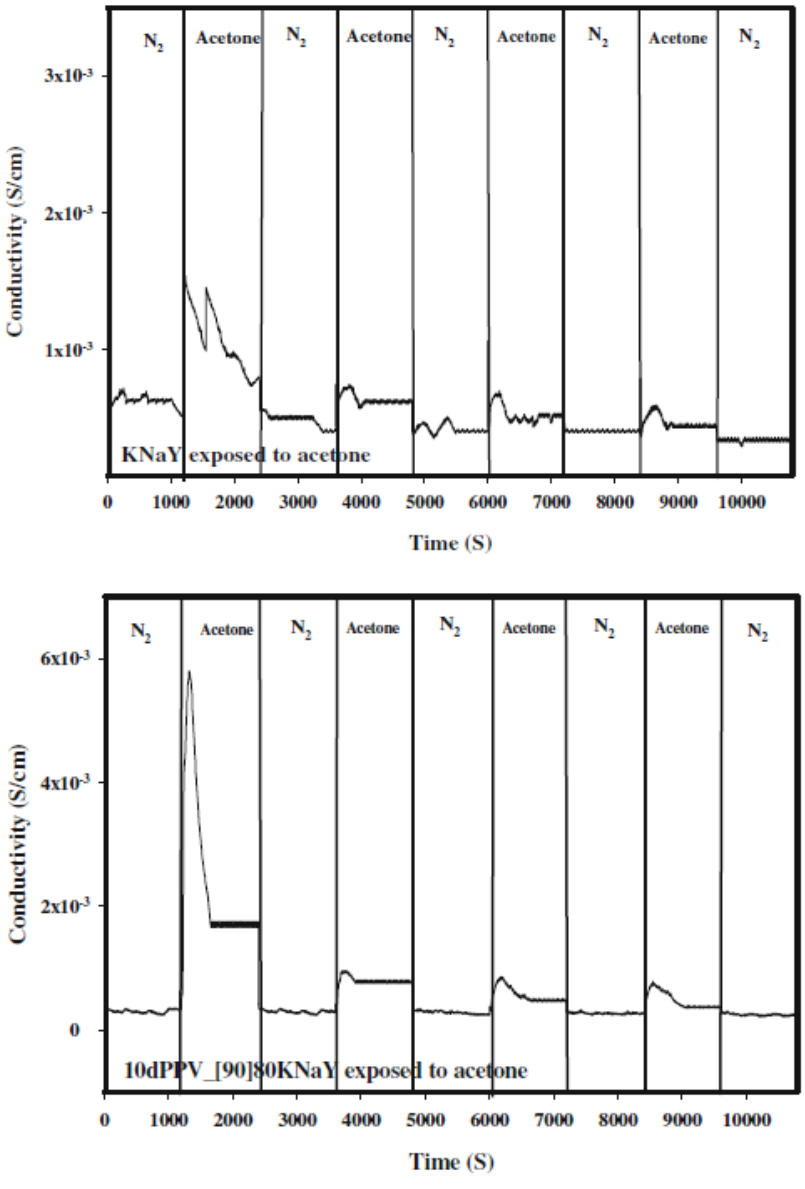

Fig. 7 The cyclic responses of KNaY: (*top*); and dPPV[90] 80KNaY (*bottom*) during acetone exposure at the vapor concentration of 30,000 ppm (3 %v/v), and at the interval of 1,200 s

80 % mole of K+, respectively. The electrical conductivity sensitivity value increases increasing percentage of K^+ in the NaY because of K^+ has a smaller electronegativity (EN) value than Na^+ which leads to the increase in the proton mobility and the ability to interact with acetone vapor more easier. Thus, increasing K^+ concentration in NaY and exposing to acetone vapor, results in the interaction between KNaY and acetone vapor to become more favorable. For the next interval, the electrical conductivity decreases because the interaction is not reversible and thus the reduced the proton mobility [20, 28–34]. In this present work, 80KNaY is used to study the effects of dPPV and solvent type next.

The response of dPPV_90[80]KNaY towards ketone vapors

Doped poly(p-phenylene vinylene) or dPPV was mixed into the KNaY at 80 % mole of K^+ cation making up the 80KNaY matrix with 10 %v/v of dPPV or dPPV_[90] 80KNaY. The electrical conductivity sensitivity values of the dPPV, dPPV_[90]80KNaY and 80KNaY towards the acetone vapor at 3 %v/v in the 1st cyclic interval are $4.49\pm6.78\times10^{-01}$, $4.13\pm7.09\times10^{-02}$ and $4.26\times10^{-01}\pm1.25\times10^{-04}$, respectively, as shown in Fig. 6 and Table 2. The highest electrical conductivity sensitivity toward the acetone vapor is dPPV because dPPV has a conjugated double bond which leads to induce the electron transfer

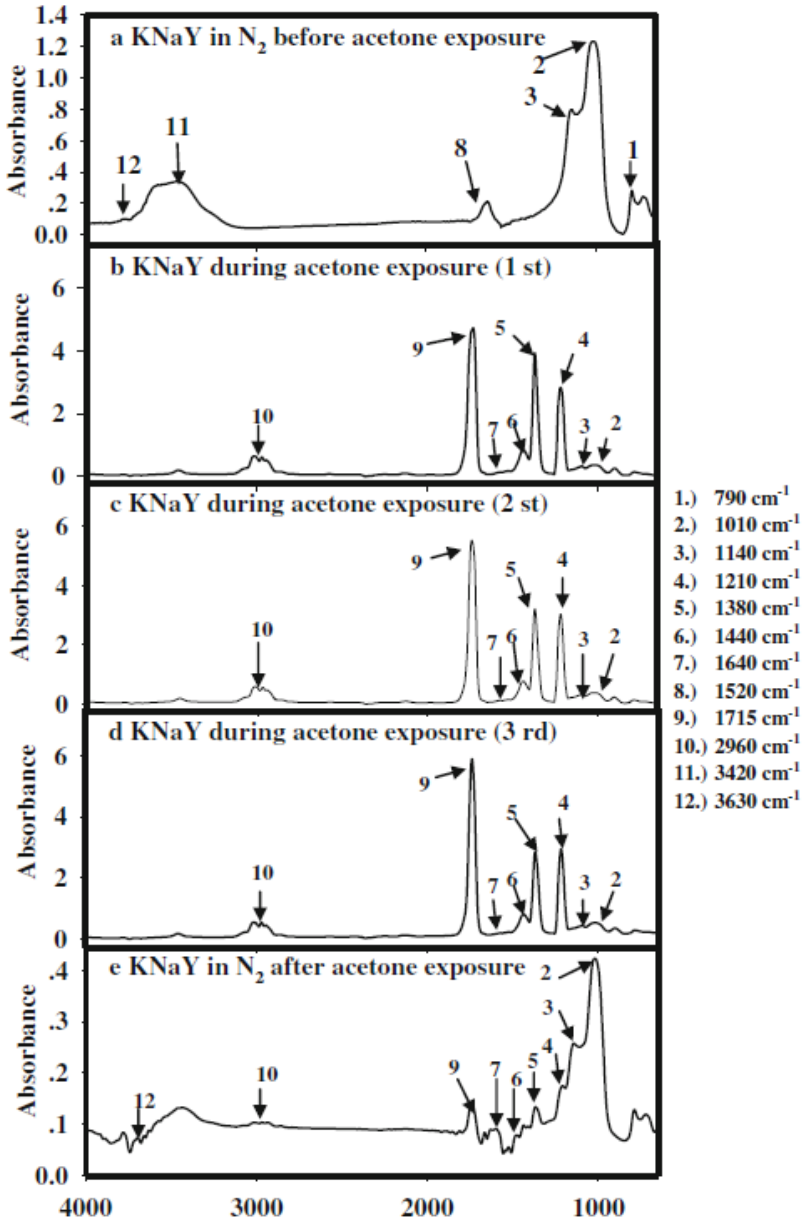

Fig. 8 IR spectra of KNaY: a before acetone exposure; b acetone exposure 1st interval; c acetone exposure 2nd interval; d acetone exposure 3rd; e after exposure at vapor concentration of 30,000 ppm (pressure at 1 atm and at T=25 °C)

along the conductive polymer molecule, resulting in the increase in the electrical conductivity sensitivity towards the acetone vapor [13, 23, 25]. However, KNaY can only transfer protons in the zeolite framework, resulting in lower electrical conductivity than dPPV or other conductive polymers [28–34]. Thus, mixing the dPPV in 80KNaY leads to an increase in the electrical conductivity sensitivity by an order magnitude of 80KNaY [13, 23]. The effect of ketone vapor type is shown and investigated next. Figure 6 shows the electrical conductivity response of dPPV_[90]80KNaY exposed to the acetone, MEK and MIBK vapors, respectively. The electrical conductivity of dPPV_[90]80KNaY in the 1st interval response increases significantly when exposed to acetone vapor in comparison with the exposures to the MEK and MIBK vapors. The electrical conductivity sensitivity of dPPV_ 90[80]KNaY towards acetone, MEK and MIBK are $4.13\pm7.09\times10^{-02}$, $2.17\pm9.55\times10^{-02}$, $1.01\pm1.03\times10^{-02}$, respectively, as shown in Fig. 6. The larger response in the 1st interval of dPPV_[90]80KNaY and higher sensitivity value occur towards acetone vapor than MEK and MIBK, respectively. The acetone (0.524 nm) is of a smaller molecular size than MEK (0.667 nm) and MIBK

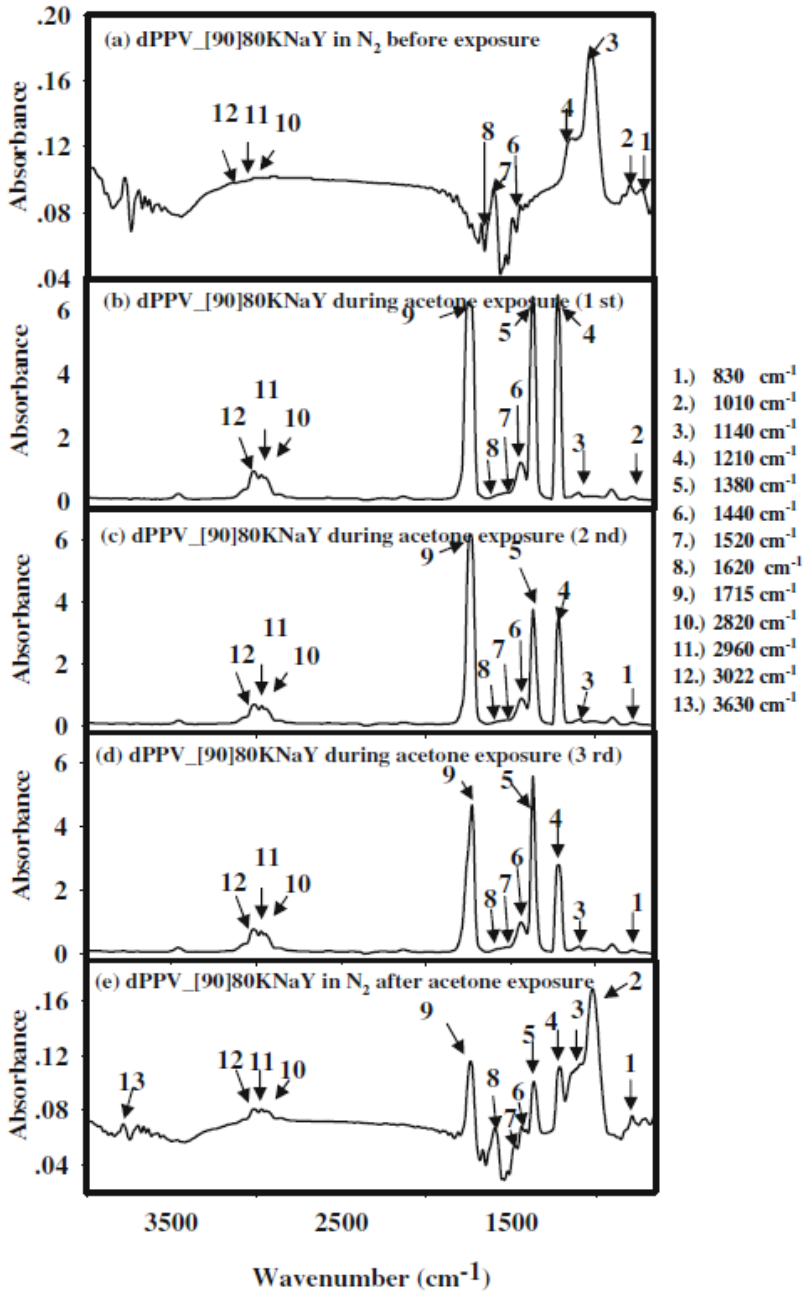

Fig. 9 IR spectra of dPPV_KNaY: **a** before acetone exposure; **b** acetone exposure 1st interval; **c** acetone exposure 2nd interval; **d** acetone exposure 3rd interval; **e** after exposure at vapor concentration of 30,000 ppm (pressure at 1 atm and at T=25 °C)

(0.828 nm), resulting in easier penetrate ion in the zeolite framework as compare to MEK and MIBK. Thus, the interaction between dPPV_[90]80KNaY is more favorable when exposed to acetone than in MEK and MIBK. Similar results are obtained in the following interval (2nd, 3rd and 4th interval), but the electrical conductivity is lower than the previous interval, as shown in Fig. 9 [12, 13, 20–24, 29, 30, 35].

The effect of cyclic interval

The 50KNaY, NaY, 50CaNaY and 50MgNaY samples are used to investigate the effect of cyclic interval time when exposed to acetone vapor at concentration of 3 %v/v in N_2. The electrical conductivity sensitivity values of 50KNaY in the 1st, 2nd, 3rd and 4th interval are $3.42\times10^{-01}\pm4.67\times10^{-04}$, $2.09\times10^{-01}\pm6.27\times10^{-04}$, $1.81\times10^{-01}\pm6.12\times10^{-04}$ and $1.28\times10^{-01}\pm9.12\times10^{-04}$, respectively, as shown in Fig. 7a (top) and tabulated in Table 2. The electrical conductivity sensitivity decreases with an increasing number of cyclic interval because of the interactions from the previous interval are not reversible leading to a reduced number of active sites and proton mobility with zeolite Y. Similar results are obtained in the other cations as well (NaY, 50CaNaY and 50MgNaY) [20, 28–30].

The cyclic interval of dPPV_[90]80KNaY towards 3 different ketone vapors (acetone, MEK and MIBK) at a concentration of 3 %v/v in N_2 is investigated next. The electrical conductivity sensitivity of dPPV_[90]80KNaY towards the acetone vapor at the 1st, 2nd, 3rd and 4th are $4.13\pm7.09\times10^{-02}$, $1.43\pm1.61\times10^{-02}$, $9.10\times10^{-01}\pm6.98\times10^{-03}$ and $5.27\times10^{-01}\pm2.68\times10^{-03}$, respectively, as shown in Fig. 7b (bottom) and listed in Table 2. The electrical conductivity sensitivity decreases with increasing numbers of cyclic intervals. The interaction is not completely reversible for 80KNaY, and the interaction between dPPV and acetone vapor is an irreversible one. Thus, mixing the 10 %v/v of dPPV in 80KNaY matrix leads to the irreversible interaction of the composite system and reduced active sites for the next interval [13, 20, 23]. Similar results are obtained in the MEK and MIBK exposures.

FTIR investigations of reactions of adsorbed acetone vapor

The interaction between zeolite Y and the ketone vapora is discussed from FTIR spectrum. The FTIR spectra of KNaY and dPPV_90[80]KNaY were taken in the 650–4,000 cm^{-1} regions (Figs. 8 and 9). The spectra were collected before (a), during exposure (1st interval)(b), during exposure (2nd interval)(c), during exposure (3rd interval)(d) and after the acetone exposure (e).

Figure 8 shows the FTIR spectra of KNaY before (8a), during acetone exposure 15 min interval (8b), and after the acetone exposure (8e). Before acetone exposure, the adsorption of the Si-OH group (ν=3,630 cm^{-1}) can be assigned to the zeolite characteristics [20, 21, 29, 30, 36]. The peaks at 790, 1,010, 1,140 cm^{-1} are the characteristics of the tetrahedral unit [30]. A peak at 1,640 cm^{-1} is the OH stretching which suggests the possibility of water in the zeolite structure [12, 20–22]. During acetone exposure, the spectrum shows new peaks at 3,420, 1,715 and 1,210 cm^{-1}; the former can be assigned to the carbonyl interaction between oxygen with the KNaY structure and the cation in the zeolite framework, as shown in Fig. 10a. The new peak at 1,210 cm^{-1} is assigned to the interaction between oxygen and the carbonyl group and hydrogen in the zeolite [20, 21, 29, 30, 35, 36]. After exposure to acetone in the 2nd and 3rd intervals, the interaction between the active sites and acetone molecule diminishes. Moreover, the responses in the 2nd and 3rd intervals are lower than the 1st interval, because the interaction is not reversible. This confirms that there are

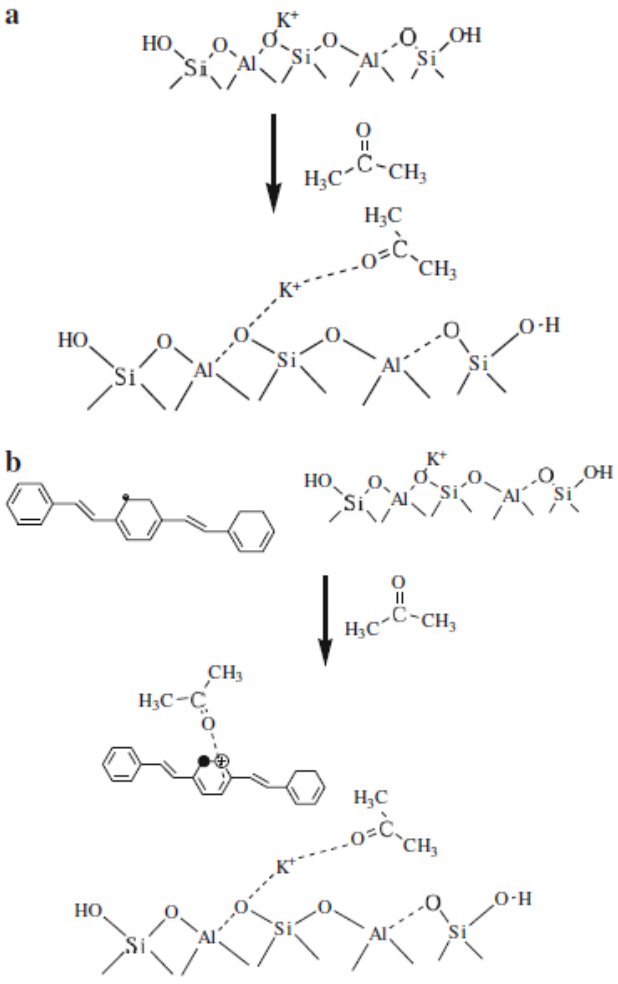

Fig. 10 Proposed mechanism for the interactions of: a KNaY-acetone; and b dPPV_KNaY-acetone

some residue interactions remaining between the acetone and KNaY from the previous interval, resulting in lower electrical conductivity response towards acetone in the next intervals. When replaced with nitrogen (8e), the IR spectrum peaks at 3,420 and 1,210 cm^{-1} evidently decrease; this also confirms that the interaction between acetone and the KNaY is not reversible, suggesting the irreversible responses to acetone under repeated exposures. [20–24].

Figure 9 shows the corresponding IR spectra of dPPV_[90]80KNaY. Before the acetone exposure, the adsorption peak of the quinoid structure, a characteristic of dPPV, appears at ν=1,140 cm^{-1}. The characteristics of phenylene are the peaks at 1,520, 2,960 and 3,022 cm^{-1} [13, 23, 26]. The peak at around 3,630 cm^{-1} is assigned to the Si-OH group [20, 21, 29, 30, 36]. During the acetone exposure, in the 1st cycle, the new peaks at 3,449 and 1,377 cm^{-1} are adsorption peaks of Si-O-C, suggesting an interaction between acetone and KNaY [20, 21, 29, 30, 36]. The new peak at 1,210 cm^{-1} indicates the bending of the OH group and the 3 °C-O; this also suggests an interaction between acetone and dPPV, as shown in Fig. 10b. The increase in the intensity at 1,140 cm^{-1} during the acetone exposure is caused by the increase in the number of the quinoid structure of dPPV [13, 23, 26]. After an evacuation and exposures to the acetone vapor in the 2nd and 3rd intervals, the interaction still remains, causing the lower electrical conductivity response than the previous interval, a similar result to KNaY . After the acetone exposure, the intensities at 3,022, 2,960 and 1,520 cm^{-1} decrease; these suggesting that acetone may act as a secondary dopant to increase the number of the quinoid structures in the dPPV chain [13, 23, 26]. The interaction is clearly irreversible.

Figure 10a shows the interaction of KNaY with acetone vapor. Acetone is an electron donating molecule which stabilizes the potassium cation in the KNaY structure. Thus, an electron from the acetone can move along the KNaY structure easily and thus the increase in the electrical conductivity when exposed to acetone vapor [20, 30, 33]. When dPPV is mixed with 80KNaY matrix at 10 %v/v and exposed to acetone vapor, acetone acts as an electron donating species for the KNaY and dPPV structures as shown in Fig. 10b. The lone pair electron from carbonyl of the acetone molecule stabilizes the cation on the dPPV chain resulting in greater negative charges along the dPPV molecule, and corresponding to higher electrical conductivity when exposed to acetone vapor [13, 23].

Conclusions

The NaY (Si/Al 5.1) is successfully ion exchanged into KNaY at 30, 50 and 80 % moles of the cation, MgNaY at 50 % mole of the cation, and CaNaY at 50 % mole of the cation. These ion exchanged zeolites are used to investigate the effects of cation type, cation concentration, solvent type, and the cyclic interval on the electrical conductivity response towards ketone vapors at 3 %v/v in N_2. The 50KNaY sample shows the highest electrical conductivity in comparison to NaY, 50CaNaY and 50MgNaY towards acetone vapor, due to the proton mobility in the zeolite framework. Increasing the cation size in the zeolite framework lead to the reduced electrostatic interaction between the zeolite framework and the cation, and to the ease in which a proton can transfer. For the effect of cation concentration, 80KNaY possesses the highest electrical conductivity, whereas 30KNaY shows the lowest value which is comparable in magnitude to that of NaY. dPPV is mixed into the 80KNaY matrix and exposed to 3 different ketone vapors (acetone, MEK and MIBK) at 3 % v/v in N_2. The acetone exposure provides the highest electrical conductivity sensitivity, whereas MIBK shows the lowest value which is due to the ability of the acetone molecule to penetrate into the zeolite framework. Thus, the electrical conductivity sensitivity is shown to be enhanced by mixing dPPV into the 80KNaY matrix. For the cyclic interval, the electrical conductivity response decreases with increasing number of cyclic intervals towards the acetone vapor, due to the irreversible interaction between the zeolite and the acetone vapor. The irreversible interactions between the active site and the ketone vapors are irreversible as evidenced by the FTIR spectrum.

Acknowledgments The authors would like to acknowledge the financial supports from the Conductive and Electroactive Polymers Research Unit of Chulalongkorn University, the Thailand Research Fund (TRF-BRG, TRF-RTA, PHD/0026/2553), and the Royal Thai Government.

References

1. Heeger AJ, Diaz-Gracia MA (1998) Semiconducting polymers as a material for photonic device. Curr Opin Solid State Mater Sci 3:16–22
2. Jung YS, Jung W, Tuller HL, Ross CA (2008) Nanowire conductive polymer gas sensor patterned using self assembled block copolymer lithography. Nano Lett 8:3777–3780
3. Vijaya JJ, Kenedy LJ, Sekaran G, Bayhan M, William M (2008) Preparation and VOC gas sensing properties of Sr(II)-added copper aluminate spinel composites. Sensors Actuators B Chem 134:604–612
4. Gao JF, Yan DX, Huang HD, Zeng XB, Zhang WQ, Li ZM (2011) Tunable positive liquid coefficient of an anisotropically conductive carbon nanotube-polymer composite. J Polym Res 18:2239–2243
5. Tang L, Li Y, Xu K, Hou X, Lv Y (2008) Sensitive and selective acetone sensor based on its cataluminescence from Nano-La_2O_3 surface. Sensors Actuators B Chem 132:243–249
6. Mori M, Nishimura H, Itagaki Y, Sadaoka Y (2009) Potentiometric VOC detection in air using 8YSZ-based oxygen sensor modified with $SmFeO_3$ catalytic layer. Sensors Actuators B Chem 142:141–146

7. Montserral V, Joaquin C, Albert C, Albert C, Ramon MJ, Jesus S (2007) Gas detection with SnO_2 sensors modified by zeolite films. Sensors Actuators B Chem 124:99–110
8. Benvenho ARV, Li RWC, Gruber J (2009) Polymeric electronic gas sensor for determining alcohol content in automotive fules. Sensors Actuators B Chem 136:173–176
9. Li RWC, Ventura L, Gruber J, Kawano Y, Carvalho LRF (2008) A selective conductive polymer–beasd sensor for volatile halogenated organic compounds (VHOC). Sensors Actuators B Chem 131:646–651
10. Ruangchuay L, Sirivat A, Schwank J (2004) Electrical conductivity response of polypyrrole to acetone vapor: effect of dopant anions and interaction mechanisms. Synth Met 140:15–21
11. Ruangchuay L, Sirivat A, Schwank J (2004) Selective conductivity response of polypyrrole-based sensor on flammable chemicals. React Funct Polym 6:11–22
12. Ruangchuay L, Sirivat A, Schwank J (2008) Polypyroole and its composites with 3A zeolite and polyamide 6 as sensors for four chemicals in lacquer thinner. React Funct Polym 68:1646–1651
13. Thongchai N, Kunanuruksapong R, Niamlang S, Wannatong L, Sirivat A, Wongkasenjit S (2009) Interactions between CO and poly(p-phenylene vinylene) as induced by ion-exchanged zeolites. Mater 2:2259–2275
14. Jalkane T, Tuura J, Makila E, Salonen J (2010) Electro-optical porous silicon gas sensor with enhance selectivity. Sensors Actuators B Chem 147:100–104
15. Chang CJ, Lin CK, Chen CC, Chen YC, Kuo EH (2011) Gas sensor with porous three dimensional framework using TiO_2/Polymer double shell hollow microsphere. Thin Solid Films 520:1546–1553
16. Hung ST, Chang CJ, Hsu CH, Chu BH, Lo CF, Hsu CC, Pearton SJ, Holzworth MR (2012) $Sn0_2$ functionalized AlGaN/GaNhigh electron mobility transistor for hydrogen sensing application. Int J Hydrogen Energy 37:13783–13788
17. Chang JC, Hung ST, Lin CK, Chen CY, Kuo EH (2010) Selective growth of ZnO nanorods for gas sensors using ink-jet printing and hydrothermal processes. Thin Solid Films 519:1693–1698
18. Yang P, Ye X, Lau C, Liu X, Lu J (2007) Design of efficient zeolite materials for n-Hexane. Anal Chem 79:1425–1432
19. Varsani P, Afonja A, Williams DE, Parkin IP, Binions R (2011) Zeolite-modified WO_3 gas sensors-enhanced detection of NO_2. Sensors Actuators B Chem 160:475–482
20. Yimlamai I, Niamlang S, Chanthaanont P, Kunanuruksapong R, Changkhamchom S, Sirivat A (2011) Electrical conductivity response and sensitivity of ZSM-5, Yand mordernite zeolite towards ethanol vapor. Ion 17:607–615
21. Li X, Dutta PK (2010) Interaction of dimethylmethylphosphonate with zeolite Y: impedance-based sensor for detecting nerve agent stimulus. J Phys Chem C 114:7986–7994
22. Soontornworajit B, Wannatong L, Hiamtup P, Niamlang S, Chotpattananont D, Sirivat A, Schwank J (2007) Induced interaction between polypyrrole and SO_2 via molecularsieve 13X. Mater Sci Eng B 15:78–86
23. Kamonsawas J, Sirivat A, Niamlang S, Hormnirun P, Prissanaroon-Ouijai W (2010) Electrical conductivity response of poly (phenylene vinylene)/zeolite composites exposed to ammonium nitrate. Sens 10:5590–5603
24. Thuwachaosoan K, Chottananont D, Sirivat A, Rujiravanit R, Schwank JW (2007) Electrical conductivity responses and interactions of poly(3-thiopheneacetic acid)/zeolites L, modernite, beta and H_2. Mater Sci Eng B 140:23–30
25. Ahlskog M, Reghu M, Noguchi T, Ohnishi T (1997) Doping and conductivity studies on poly (p-phenylene vinylene). Synth Met 89:11–15
26. Wessling RA, Zimmerman RG (1968) Polyelectrolytes from bis-sulfonium salts. U.S. Patent 3:401
27. McKeen JC, Davis ME (2009) Conductivity of Mo-and divalent cation in the microporous zincosilicate VPI9. J Phys Chem C 113:9870–9877
28. Scott MA, Katehleen AC, Dutta PK (2003) Handbook of zeolite science and technology. Marcel Dekker, New York
29. Florian J, Kubelkova L (1994) Proton transfer between H-Zeolite and adsorbed acetone or acetonitrile: quantum chemical and FTIR study. J Phy Chem 98:8734–8741
30. Panov AG, Fripiat JJ (1998) An infared study of acetone and mesityl oxide adsorption on acid catalyst. Langmuir 14:3788–3796
31. Biaglow AI, Gorte RJ, David W (1993) Molecular motions and 13C chemical shift anisotropy of acetone adsorbed inH-ZSM-5 zeolite. J Phys Chem 97:7135–7137
32. Martins AVG, Berlier G, Bisio C, Coluccia S, Pastore HO, Marchese L (2008) Quantification of bronsed sites in microporous catalysts by a combined FTIR and NH_3-TPD study. J Phys Chem C 112:7120–7139
33. Fameth WE, Gorte RJ (1995) Methods for characterizing zeolite acidicity. Chem Rev 95:615–635
34. Jian HZH, Ying W, Yuan C, Xiao SW (1998) Dispersion of potassium nitrate and the resulting basicity on alumina and zeolite NaY. J Chem Soc 94:1163–1169
35. Boekfa B, Pantu P, Prosbt M, Limtrakul J (2010) Adsorption and tautomerization reaction of acetone on acidic zeolites: the confinement effect in different types of zeolites. J Phys Chem C 114:15061–15067
36. Hoost TE, Laframboise KA, Otto K (1996) Infrared study of acetone and nitrogen oxides on Cu-ZSM-5. Catal Lett 37:153–156

art%3A10.2478%2Fs13536-012-0055-7.pdf http://download.springer.com/static/pdf/19/art%3A10.2478%2Fs13536...

Materials Science-Poland, 30(4), 2012, pp. 313-322
http://www.materialsscience.pwr.wroc.pl/
DOI: 10.2478/s13536-012-0055-7

VERSITA

Preparation and properties of calcium oxide from eggshells via calcination

N. TANGBORIBOON[1], R. KUNANURUKSAPONG[2], A. SIRIVAT[2*]

[1] Center for Advanced Studies in Industrial Technology and The Materials Engineering Department, Faculty of Engineering, Kasetsart University, Bangkok 10900, Thailand

[2] The Petroleum and Petrochemical College, Chulalongkorn University, Bangkok, 10330, Thailand

Duck eggs are one of the most versatile cooking ingredients in which residue eggshells are discarded. Raw duck eggshells were calcined at temperatures between 300 to 900 °C, for 1, 3, and 5 h. Both the raw and calcined duck eggshells were characterized by FTIR, STA, XRD, XRF, TEM, BET, a particle size analyzer, and an impedance analyzer. The proper calcination conditions are: 900 °C and 1 h, yielding calcium oxide with a purity of 99.06 % w/w. The calcium carbonate of the rhombohedral form ($CaCO_3$) transforms completely into the calcium oxide or lime of the face centered cubic form (CaO) at 900 °C, as shown by XRD diffraction patterns. The transmission electron microscopy (TEM) images of the calcium oxide reveal a moderately good dispersion of nearly uniform particles. The calcium oxide has a white color, a spherical shape, high porosity, and narrow particles size distribution. The percentage of ceramic yield of the calcium oxide is 53.53, as measured by STA (TG-DTA-DTG). The calcium oxide has a N_2 adsorption–desorption isotherm indicating the meso-porosity range. The dielectric constant and the electrical conductivity of the calcined calcium oxide are 35 and $1.0 \times 10^{-6}(\Omega \cdot m)^{-1}$, respectively, at the frequency of 500 Hz.

Keywords: *calcium oxide, pyrolysis, specific surface area, phase transformation*

© Wroclaw University of Technology.

1. Introduction

The egg and egg derivative consumption produce a great amount of residual shells which pose an environmental pollution as a result of microbial action. An important ingredient of an eggshell is calcium carbonate which can be potentially used in various material applications such as a filler in animal feed, pet food, printing ink, paper, glaze decoration, tiles, and as the source of calcium oxide or calcite. An eggshell waste primarily contains magnesium, calcium carbonate (limestone), and protein [1–3]. The calcium/magnesium contents in the shells can be converted into the calcium/magnesium oxide and the resultant burnt lime can be used as a liming agent. The calcium oxide obtained from calcined eggshells, whether from hen, duck, bird, goose, and partridge bird, can be potentially used in various applications: as filler in feed, fertilizer, paper, printing ink, pharmaceutical and cosmetic products, starting materials of dielectrics such as $CaSiO_3$, $CaTiO_3$, $CaAl_2O_4$, gypsum ($CaSO_4$), and as bio-catalysts [4–9]. Heung Jai *et al.*, (2007) studied heavy metals removal using a calcined waste eggshell in the treatment of synthetic wastewater containing heavy metals. A complete removal of Cd and a 99 % removal of Cr were observed within a period of 10 min [10]. An eggshell membrane generally contains about 10 % collagen, including the most common Type 1 collagen and the unusual Type 10 collagen. Collagen applications include: skin grafts, dental implants, angioplasty sleeves, cornea repair, plastic surgery, treatment of osteoporosis and pharmaceuticals, food castings, and film emulsions [11]. Other possibilities for utilizing eggshells include the production of biodegradable plastics from eggshell membrane proteins, altering the heat resistance of a food-borne bacterial pathogen with a bacteriolytic enzyme contained in an eggshell membrane, as a human dietary calcium supplement especially for post menopausal women. Eggshells also contain

*E-mail: anuvat.s@chula.ac.th

art%3A10.2478%2Fs13536-012-0055-7.pdf http://download.springer.com/static/pdf/19/art%3A10.2478%2Fs13536...

certain amounts of microelements such as strontium (Sr), fluorine (F) and selenium (Se); the membrane can be used as an adsorbent for the removal of reactive dyes from colored waste effluents as well as to eliminate heavy metal ions from a dilute waste solution [11].

Eggshells are a better source of calcium for calcium oxide (CaO), calcium carbonate ($CaCO_3$), calcium hydroxide ($Ca(OH)_2$), calcium phosphate, or hydroxyl apatite, in comparison to other sources such as carbonaceous rock, precipitated soil, teeth and bone, and crab or shrimp shells. The by-product of eggshell represents approximately 11 % w/w of the total weight (≈50–60) of a hen egg and 12.6 % w/w of the total weight (≈74.9–78) of a duck egg. The Agricultural Statistics of Thailand reported the quantities of egg production of approximately 9.8×10^9 hens' eggs and 1.5×10^9 ducks' eggs each year. Therefore, both hen and duck eggshells are approximately 60×10^6 metric tons per year in Thailand. Eggs can be produced in numerous countries in the world as an important nutrient source, and the world eggshells consumption amounts to millions metric tons per year. The by-product eggshells represent a significant amount of waste for the processors because they are traditionally useless. Most of the waste is commonly disposed of in a landfill without any pretreatment, causing odors from biodegradation, destroying microbial action, and changing the quality of soil. The advantages of eggshell waste utilization are to substitute the natural sources of calcium ($CaCO_3$, CaO, $Ca(OH)_2$), to reduce the waste problem in household, to conserve natural resources from rock and soil, to reduce the global climate warming, and to develop novelty of green ceramic materials and products: dielectrics, catalysts, biomaterials, fuel cell, and fillers.

In this work, we study the phase transformation and the electrical properties of the calcium oxide obtained by the calcination of the raw duck eggshells at the temperature range from a room temperature to 900 °C for 1, 3, and 5 h. Detailed investigations of the microstructure, chemical composition and organics (C/H/N) contents, functional groups, particle size distribution, density, specific surface area, phase transformation, and electrical properties (dielectric and electrical conductivity) are reported.

2. Experimental

2.1. Materials

Raw duck eggshells were collected from a local cafeteria. The eggshells were washed with tap water until the egg white was completely removed and dried at room temperature. After that the eggshells were broken into small pieces and crushed in a porcelain mortar into a fine powder, and kept in desiccators at a room temperature.

2.2. Instruments

A laboratory muffle furnace (Linn High Thermo GmbH, LM 412.27, model DC021032 with a thermocouple type K, NiCr-Ni) was used to calcine samples at temperatures from 27 °C to 1000 °C. Physical properties of the samples such as color, softness, and odor were studied. The samples were calcined in an alumina crucible for 1, 3, and 5 h at a heating rate of 10 °C/min.

Cumulative and fractional distributions were measured using a particle size analyzer (Mastersizer S long bed, model Polydisperse 2.19). The samples were dispersed in an aqueous medium and vibrated in an ultrasonic bath for 20 min.

Fourier transform infrared spectra (FTIR) were recorded on a spectrometer (Perkin Elmer, model Spectrum One) with a spectral resolution of 4 cm^{-1}, using a single-crystal potassium bromide mode.

Chemical compositions were obtained using an X-ray fluorescence (XRF) (Philips, model PW 2400) at a tube current of 1000 A with an acquisition lifetime of 30 s. The XRF diffraction pattern was used to determine the percentages of chemical compositions. The samples (raw duck eggshell and duck eggshell calcined at 900 °C for 1 h) were ground into powders and compressed into sample molds prior to testing. The elemental analysis (EA) was carried out on a C/H/N analyzer (Perkin Elmer, model PE 2400 series II). The elemental analysis was used to measure the organic C/H/N compositions.

X-ray diffraction (XRD) was taken and analyzed using a Bruker AXS analyzer (D8 Discover) with a VANTEC-1 Detector. Samples were analyzed using a double-crystal wide-angle goniometry with the 2θ scan from 10°–80° at a scan speed of 5° 2θ/min in

art%3A10.2478%2Fs13536-012-0055-7.pdf http://download.springer.com/static/pdf/19/art%3A10.2478%2Fs13536...

0.05° or 0.03° 2θ increments using CuKα radiation ($\lambda = 0.15406$ nm). The detected peak positions were compared with those of the International Center for Diffraction Data Standard (JCPDS) patterns to identify the crystalline phases.

Micrographs were obtained using a transmission electron microscope (TEM, JEM-2100) equipped with EDS for the X-ray microanalysis. The preparation of TEM samples of the raw material and the catalyst was carried out on a grid. An acceleration voltage of 80 to 200 kV with magnifications from 50 to 1.5 million times were used.

The thermal properties were measured using a differential scanning calorimeter (DSC, NETZSCH 409) and a simultaneous thermal analyzer (STA, NETZSCH 409). The samples were tested with a heating rate of 10 °C/min under air atmosphere.

True density of samples was measured with a gas pycnometer (Quantachrome, Ultra pycnometer 1000).

The specific surface area, the adsorption and/or desorption isotherms, the pore size, and the surface distributions were measured using an AUTOSORB-1 (QUANTACHROME), which measures the quantity of gas adsorbed onto or desorbed from the solid surface. The volume–pressure data were analyzed by the AUTOSORB-1 software to give the BET (Brunauer–Emmet–Teller) surface area (single and/or multipoint), the Langmuir surface area, the adsorption and/or desorption isotherms, the pore size and surface area distributions, the micropore volume, and the surface area. The determination of the surface area of solid materials involves the use of the BET equation as follows:

$$\frac{1}{W\left[(P_o/P)-1\right]} = \frac{1}{W_m C} + \frac{C-1}{W_m C}\left(\frac{P}{P_o}\right) \quad (1)$$

where W is the weight of gas adsorbed at a relative pressure, P/P_o, W_m is the weight of adsorbate constituting a monolayer of surface coverage, and C is a constant related to the energy of adsorption in the first adsorbed layer.

The specific surface area, S, of the solid was calculated from the total surface area and the sample weight, according to Eqs. (2) and (3) as follows:

$$S = S_t / W \quad (2)$$

$$S_t = \frac{W_m N A_{cs}}{M} \quad (3)$$

where S is the specific surface area of the solid, S_t is the total surface area, W is the sample weight, N is Avogadro's number (6.023×10^{23} molecules/mol), M is the molecular weight of the adsorbate, and A_{cs} is the area occupied by one adsorbate molecule (16.2×10^{-20} m^2 for N_2 and 19.5×10^{-20} m^2 for Kr) [13].

The electrical properties were measured using an impedance analyzer (HP, model 16451B) with an LCR meter (HP, model 4284A). The samples were prepared, according to ASTM B263-94, as thin discs with a diameter of 5.00 mm and a thickness of 0.50 mm. The electrical properties were measured at frequencies from 500 Hz to 106 Hz under an AC electrical field of 2 A.

2.3. Calcination process

Approximately 1.00 g of cleaned and crushed powder of raw duck eggshells was put into an alumina crucible and calcined in a muffle furnace under air atmosphere at various temperatures from 300 up to 900 °C, for 1, 3, and 5 h at a heating rate of 10 °C/min. After calcining, the sample crucibles were brought out from the muffle furnace and cooled down in air for a period of 10-20 min to avoid the hydrolysis, as shown in Eqs. (4) and (5). The raw duck eggshells and the calcined samples were subsequently characterized by STA, XRD, FTIR, TEM, BET, the particle size analyzer, and the impedance analyzer.

$$CaCO_3 \xrightarrow{\text{Calcination}} CaO + CO_2 \quad (4)$$

$$CaO + H_2O \xrightarrow{\text{Hydrolysis}} Ca^{2+} + 2OH \quad (5)$$

3. Results and discussion

3.1. Physical characterization of raw and calcined duck eggshells

Physical characterization data (color, odor, and softness) of raw duck eggshells and their calcined products from 300 °C to 1000 °C for 1, 3, and 5 h are tabulated in Table 1. A higher calcination temperature produces the samples which have a whiter

art%3A10.2478%2Fs13536-012-0055-7.pdf http://download.springer.com/static/pdf/19/art%3A10.2478%2Fs13536...

Table 1. Physical characterization of raw and calcined duck eggshells.

Number	Code	Physical characterization		
		Color	Odor	Softness
1.	000	White to light blue	Raw eggshell	Hard, Flake
2.	300_1	Gray brown	Stink	Hard, Flake
3.	300_3	Gray brown	Stink	Hard, Flake
4.	300_5	Dark gray brown	Stink	Hard, Flake
5.	500_1	Deep gray black	Stink	Hard, Flake
6.	500_3	Deep gray black	Stink	Hard, Flake
7.	500_5	Deep gray black	Stink	Hard, Flake
8.	700_1	Light gray	Slightly odor	Softer, Powder
9.	700_3	Light gray	Slightly odor	Softer, Powder
10.	700_5	Light gray	Slightly odor	Softer, Powder
11.	**900_1**	**White**	**Odorless**	**Softest, Powder**
12.	900_3	White	Odorless	Softest, Powder
13.	900_5	White	Odorless	Softest, Powder
14.	1000_1	White	Odorless	Softest, Powder
15.	1000_3	White	Odorless	Softest, Powder
16.	1000_5	White	Odorless	Softest, Powder

000 means ground raw duck eggshell at room temperature., 300_1 means calcined duck eggshell at 300 °C for 1 h., 300_3 means calcined duck eggshell at 300 °C for 3 h., 300_5 means calcined duck eggshell at 300 °C for 5 h., 500_1 means calcined duck eggshell at 500 °C for 1 h., 500_3 means calcined duck eggshell at 500 °C for 3 h., 500_5 means calcined duck eggshell at 500 °C for 5 h., 700_1 means calcined duck eggshell at 700 °C for 1 h., 700_3 means calcined duck eggshell at 700 °C for 3 h., 700_5 means calcined duck eggshell at 700 °C for 5 h., 900_1 means calcined duck eggshell at 900 °C for 1 h., 900_3 means calcined duck eggshell at 900 °C for 3 h., 900_5 means calcined duck eggshell at 900 °C for 5 h., 1000_1 means calcined duck eggshell at 1000 °C for 1 h., 1000_3 means calcined duck eggshell at 1000 °C for 3 h., 1000_5 means calcined duck eggshell at 1000 °C for 5 h.

Table 2. C/H/N contents in raw duck eggshells as measured with the elemental analyzer.

No.	% C	% H	% N
1.	13.43	0.57	0.57
2.	13.51	0.43	0.54
3.	13.99	0.47	0.78
Average	**13.64**	**0.49**	**0.63**

Table 3. Chemical compositions of samples as measured with the wavelength dispersive X-ray fluorescence spectrometer (XRF).

Composition (% w/w)	Raw duck eggshells	Duck eggshells calcined 900_1
Na_2O	<0.01	0.04
MgO	0.10	0.20
SiO_2	0.01	<0.01
P_2O_5	0.27	0.46
SO_3	0.16	0.12
K_2O	0.02	0.04
CaO	–	99.06
$CaCO_3$	96.35	–
SrO	0.02	0.05
ZrO_2	0.02	<0.01

color, are softer, and less odorous. A higher calcination temperature and time yield a higher percentage of calcium oxide content.

The organics contents (C/H/N composition) in the raw duck eggshells were investigated with the elemental analyzer and the data are tabulated in Table 2. The average percentages of carbon, hydrogen, and nitrogen contents are 13.64 %, 0.49 %, and 0.63 %, respectively.

Table 3 shows the chemical composition of the raw duck eggshells and duck eggshells calcined at 900 °C for 1 h, revealed by the X-ray fluorescence spectroscopy (XRF). Calcium oxide content in the raw duck eggshells is very small because

art%3A10.2478%2Fs13536-012-0055-7.pdf http://download.springer.com/static/pdf/19/art%3A10.2478%2Fs13536...

Table 4. True density of samples as measured by a gas pycnometer.

Samples	True density (g/cm^3)
Raw duck eggshells	2.25
Raw hen eggshells	2.20
Duck eggshells calcined 900_1	2.84
Hen eggshells calcined 900_1	2.16

calcium mostly exists in a form of calcium carbonate at the amount of 96.35 % w/w, other oxide compounds of 0.61 % w/w, and other organic matters of 3.04 % w/w. The calcium oxide content in the duck eggshells calcined at 900 °C for 1 h is approximately 99.06 % w/w, and the other oxide compounds amounts to only 0.94 % w/w. Thus the thermal treatment of raw duck eggshells transforms the chemical composition from calcium carbonate ($CaCO_3$) to calcium oxide (CaO) almost perfectly.

The true density of the samples was measured by a gas pycnometer and the data are tabulated in Table 4. The density values of the raw duck eggshells and the raw hen eggshells are 2.25 and 2.20 g/cm^3, respectively. The density values of the duck eggshells and the chicken eggshells calcined at 900 °C for 1 h are 2.84 and 2.16 g/cm^3, respectively; the differences are caused by the anatomy, the species, the breeding, and the feeding, which influences the deposition of calcium, phosphorus, amino acid, and other nutrients during the egg formation.

The particle size distribution and the cumulative mass percentage diameters (d_{10}, d_{50}, d_{90}, and mean diameter) of the raw duck eggshells, measured with a particle size analyzer, are 22.13, 415.22, 724.18, and 383.15 µm, respectively, as shown in Fig. 1a. The particle size distribution and the cumulative mass percentage diameters (d_{10}, d_{50}, d_{90}, and mean diameter) of the particles of duck eggshell calcined at 900 °C for 1 h (900_1) are 3.14, 12.12, 49.30, and 29.16 µm, respectively, as shown in Fig. 1b. The particle size distribution and the cumulative mass percentage diameters (d_{10}, d_{50}, d_{90}, and mean diameter) of the hen eggshells calcined at 900 °C for 1 h (900_1) are 15.91, 89.03, 538.55, and 193.54 µm, respectively. The cumulative mass percentage diam-

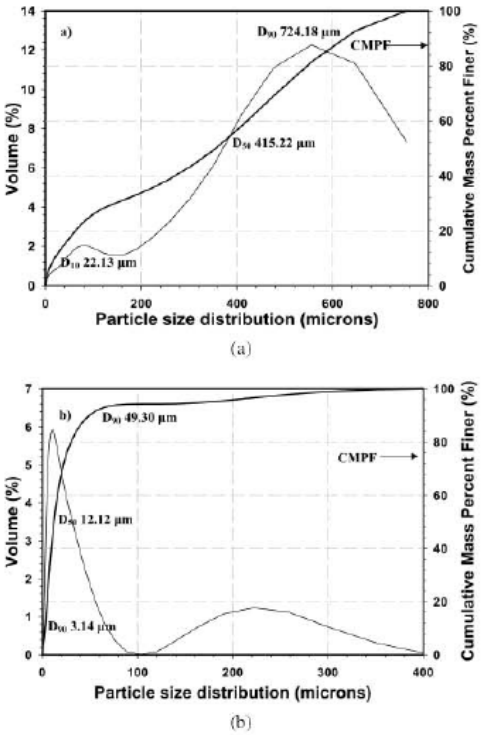

Fig. 1. Particle size distribution and fractional and cumulative distributions: a) raw duck eggshells; b) raw duck eggshells calcined at 900 °C for 1 h.

eters (CMPD) of calcined duck eggshells are smaller than those of calcined hen eggshells, in conformity with the true density values. The eggshells of both hen and duck are composed of three layers: a cuticle thin outer layer, a palisade thick middle layer, and an inner thin mammillary layer. However, the duck eggshells have a thicker shell layer, higher shell weight, more moisture and higher organic matter contents within the shell, more interactive bonding of the shell affecting the shell toughness, and higher true density than the hen eggshells.

The simultaneous thermal analysis (STA) plots from room temperature to 1200 °C, consisting of DTA, TG, and DTG spectra of the raw duck eggshells indicate two endothermic reactions (680 °C and 930.4 °C), as shown in Fig. 2. The DTA curve shows an onset at 861.5 °C. The first

art%3A10.2478%2Fs13536-012-0055-7.pdf http://download.springer.com/static/pdf/19/art%3A10.2478%2Fs13536...

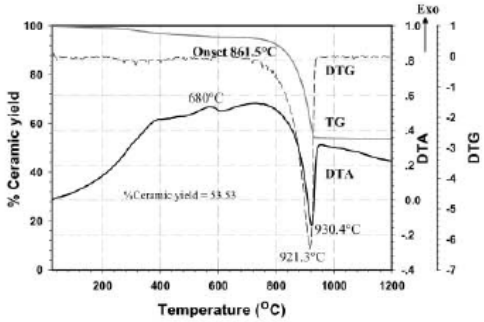

Fig. 2. Simultaneous Thermal Analysis (STA) of raw duck eggshells from 27 °C to 1200 °C at a heating rate of 10 °C/min.

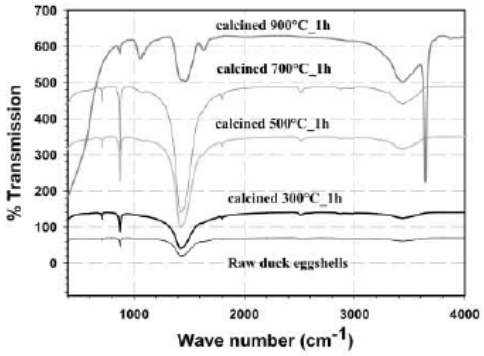

Fig. 3. FTIR spectra of raw duck eggshells and raw duck eggshells calcined at 300 °C, 500 °C, 700 °C, and 900 °C for 1 h.

stage of DTA plot expresses the moisture and the organic matter decomposition between room temperature and 680 °C, as well as the emission of CO_2 at 930.4 °C. The phase transformation from calcium carbonate ($CaCO_3$) to calcium oxide (CaO) occurs at 930.4 °C, which is consistent with the endothermic reaction. The thermogravimetric TG/DTG plot indicates the percentage of ceramic yield from room temperature to 1200 °C of the raw duck eggshells to be 53.53 % due to the single step carbon dioxide release.

FTIR spectra of the raw duck eggshells before and after the calcination are shown in Fig. 3. The characteristic peaks of the raw duck eggshells are consistent with the CAS [471-34-1] at the wavelengths from 400 to 4000 cm^{-1}. The bands at 875.08 and 1423.55 cm^{-1} are associated with the vibrations of the carbonate groups. The FTIR spectra of the duck eggshell samples calcined from 300 °C to 700 °C for 1 h reveal characteristic bands of the calcium carbonate structure at 713, 875, 1423, 1798, 2518, and 3435 cm^{-1}. The FTIR spectra of the duck eggshells calcined from 700 °C to 900 °C for 1 h show the bands at 3643 cm^{-1} strong ν(O–H), 3435 cm^{-1} ν(O–H), 1630 cm^{-1} strong ν(C=O), and 500–580 cm^{-1} ν(Ca–O).

TEM images of the raw duck eggshell samples before and after calcinations are shown in Figs. 4a and 4b at a magnification of 25000 X, and in Figs. 4a_1 and 4b_1 at a magnification of 12000 X, respectively. Before the calcination, the raw duck eggshells had a generally irregular crystal structure After the calcination at 900 °C for 1 h, as shown in Figs. 4b and 4b_1, the crystal structure changed into a porous structures; a small amount of agglomeration can be observed along with the decomposition of CO_2 as shown by STA. The formation of CO_2 can be assumed to follow an endothermic reaction as described in the reaction Eq. (4). Our TEM dispersion results resemble the SEM dispersion results reported by Heung Jai *et al.* [10].

3.2. Phase transformation of raw and claimed duck eggshells studied by XRD

X-ray diffraction patterns of the raw duck eggshell samples before and after calcinations are shown in Fig. 5. X-ray diffraction spectra of the samples were obtained with CuKα radiation (λ = 0.15406 nm) in a 2θ scan range of 5°–80°. The XRD peaks of the raw duck eggshells occur at 2θ equal to 29.399 (1 0 4), 35.981 (1 1 0), 39.417 (1 1 3), 43.171 (2 0 2), and 48.505 (1 1 6). The XRD peaks of the calcined duck eggshells can be seen at 2θ equal to 32.194 (1 1 1), 37.345 (2 0 0), and 53.843 (2 2 0). Comparing the XRD peaks in Fig. 5 with the standard peak patterns of JCPDS files, the raw duck eggshell peaks represents well the calcium carbonate or calcite ($CaCO_3$) of the rhombohedral form; R-3c; JCPDS No. 01-086-0174; the eggshell peaks calcined at 900 °C for 1, 3, and 5 h corre-

art%3A10.2478%2Fs13536-012-0055-7.pdf http://download.springer.com/static/pdf/19/art%3A10.2478%2Fs13536...

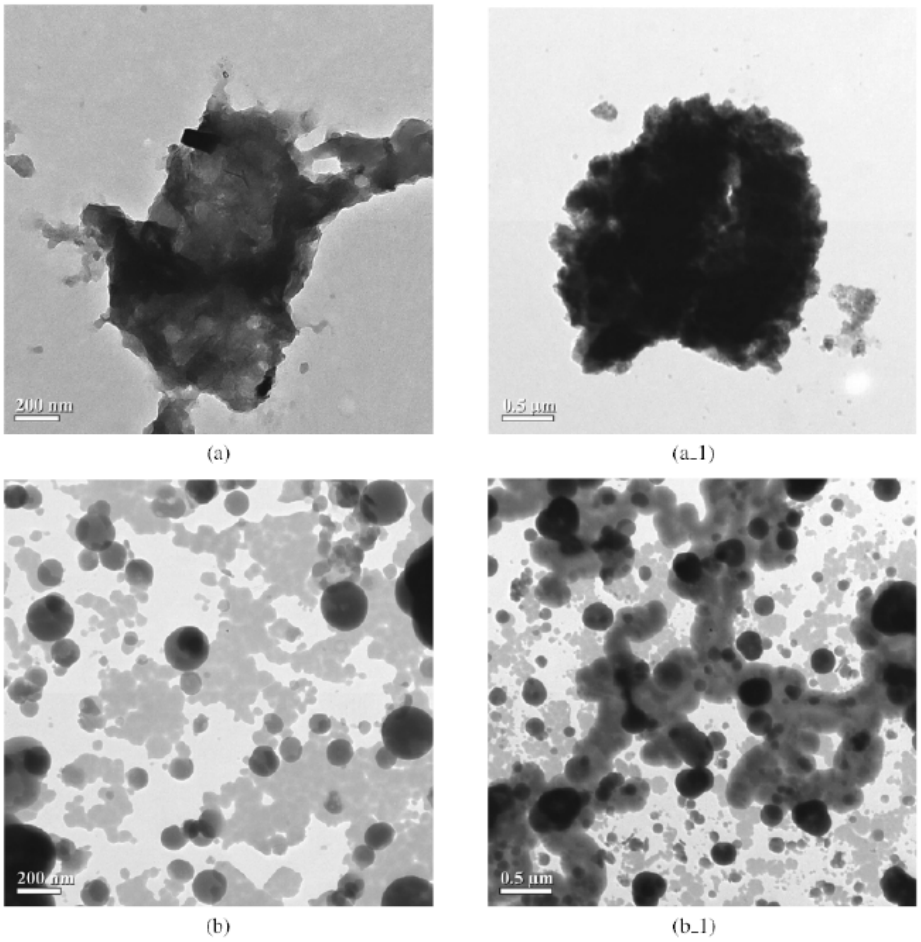

Fig. 4. TEM micrographs of raw duck eggshells and eggshells calcined at 900 °C for 1 h: a) raw duck eggshells at the magnification of 25000 X; and a_1) raw duck eggshells at the magnification of 12000 X; b) eggshells calcined at 900 °C for 1 h at the magnification of 25000 X; and b_1) eggshells calcined at 900 °C for 1 h, at the magnification of 12000 X.

spond to the calcium oxide (CaO) or the lime of the face-centered cubic form (Fm-3m; JCPDS No. 01-077-2010), with a small amount of calcium hydroxide ($Ca(OH)_2$ or portlandite) of the hexagonal form (P-3m1; JCPDS No. 01-087-0673) as a result of to the moisture absorption. The X-ray diffraction peaks of the samples calcined from 300 °C to 500 °C, for 1, 3, and 5 h, correspond to the calcium carbonate or calcite ($CaCO_3$). The XRD diffraction peaks of the raw duck eggshells calcined at 700 °C, for 1, 3, and 5 h, correspond to the lime or the calcium oxide (CaO) and the calcium carbonate or calcite ($CaCO_3$) in the meta-stable phase. A phase transformation from calcium carbonate to calcium oxide starts at 700 °C after 3 h processing. A longer calcination time at 700 °C, from 3 to 5 h, leads to a more complete phase transformation. The complete phase transformation yielding calcium oxide (CaO)

art%3A10.2478%2Fs13536-012-0055-7.pdf http://download.springer.com/static/pdf/19/art%3A10.2478%2Fs13536...

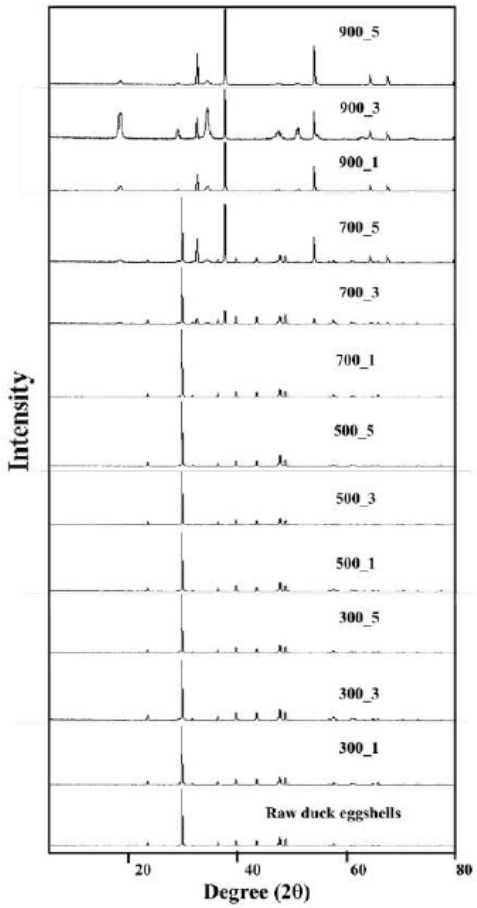

Fig. 5. XRD peak patterns and the phase transformation of raw duck eggshells and the eggshells calcined from 300 °C to 900 °C for 1, 3, and 5 h.

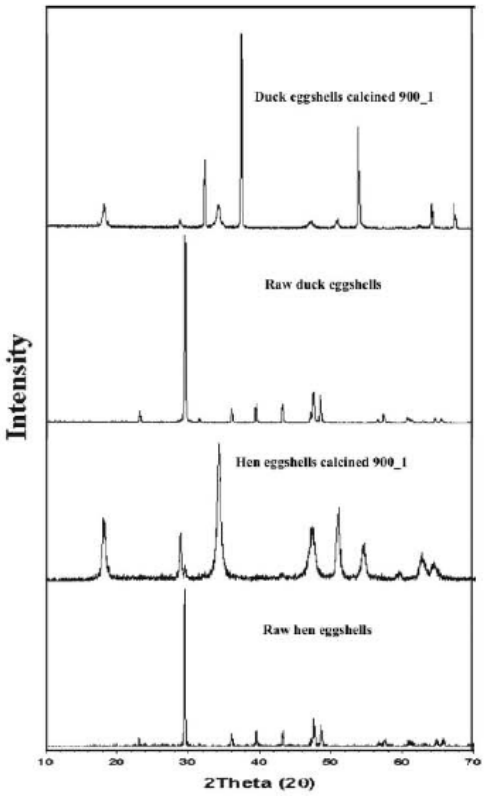

Fig. 6. Comparison XRD peak patterns between hen and duck eggshells before and after the calcination at 900 °C for 1 h.

occurs at 900 °C after 1 h calcination. Furthermore, the longer calcination time at 900 °C for 3 or 5 h yields a more calcium hydroxide ($Ca(OH)_2$) due to a reactive moisture adsorption. The phase transformation thus depends on a calcination temperature and time, which is consistent with the result obtained by the simultaneous thermal analysis (STA), as expressed by the endothermic peaks at 680 °C and 930.4 °C.

Fig. 6 shows the comparison of XRD spectra patterns between the hen and duck eggshells before and after calcinations at the same temperature of 900 °C for 1 h. The XRD results of the duck eggshells before and after calcinations are similar to the XRD results of the hen eggshells. The main peak of both raw eggshells (duck and hen) before calcination appears at 2θ = 29.399 indicating calcium carbonate ($CaCO_3$), calcite or a rhombohedral phase formation. Other peaks appear at 2θ = 35.981, 39.417, 43.171, 47.492, 48.505, 57.417, and 60.683.

The main XRD spectra patterns of the duck and hen eggshells, calcined at 900 °C for 1 h, are nearly the same. The main peak appears at 2θ = 37.345, *d*-value = 2.40600, and $(h\,k\,l) = (2\,0\,0)$. Other peaks appear at 2θ = 32.194, 53.843, 64.136, 67.357, 79.631, and 88.496. The peaks indicate calcium oxide or

art%3A10.2478%2Fs13536-012-0055-7.pdf http://download.springer.com/static/pdf/19/art%3A10.2478%2Fs13536...

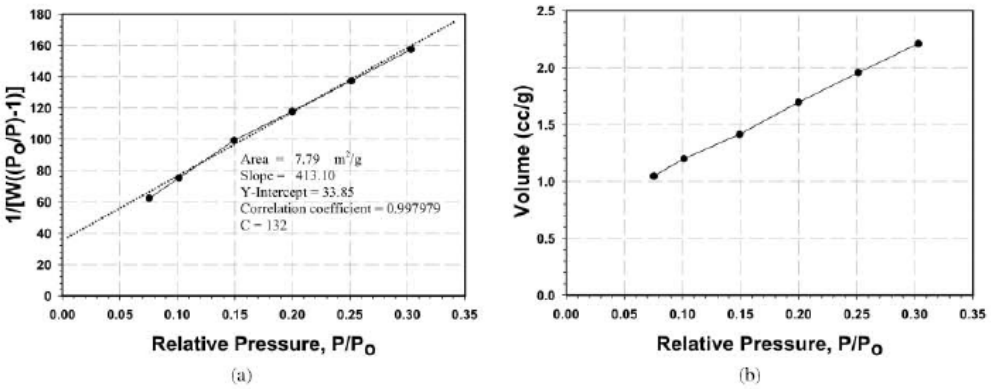

Fig. 7. a) Specific surface area of raw duck eggshells calcined at 900 °C for 1 h versus the relative pressure obtained by the BET method. b) Volume of nitrogen gas adsorption and desorption on raw duck eggshells calcined at 900 °C for 1 h at STP vs. the relative pressure obtained by the BET method.

lime (CaO), which is consistent with JCPDS No. 01-077-2010, with a small amount of calcium hydroxide ($Ca(OH)_2$ or portlandite) of the hexagonal form (P-3m1; JCPDS No. 01-087-0673), as a result of the moisture absorption. The XRD patterns of calcined hen eggshells 900_1 show only the calcium oxide phase formation, whereas the XRD peak patterns of calcined duck eggshells 900_1 show more small peaks belonging to calcium hydroxide ($Ca(OH_2)$ which are different from the XRD peak positions of the hen eggshells at $2\theta = 28.698$ (1 0 0) and 34.111 (1 0 1). However, both the eggshells undergo the identical phase transformation at the same calcination temperature and time which are 900 °C and 1 h, respectively. The duck eggshells are more prone to moisture adsorption than the hen eggshells because of different micro-organisms, weight and thickness of the eggshell, bridge bonding within the shell and particle size distribution effect on the duck shell toughness, amount of circular openings or pore effect on the reactive moisture adsorption within the shell microstructure, and true density.

3.3. Specific surface area of raw and calcined duck eggshells

The N_2 adsorption-desorption isotherms of CaO from the eggshells at room temperature (25 °C) are shown in Figs. 7a and 7b. The calcium oxide has the specific surface area, the total pore volume, and the average pore diameter of 7.79 m^2/g, 0.05, and 17.69 nm, respectively. The pore diameter of the calcium oxide is in the range of mesopore or in the range of 20 Å-500 Å (2–50 nm).

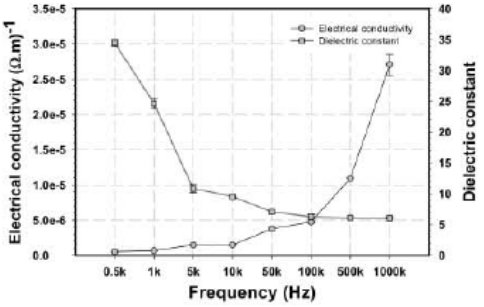

Fig. 8. Plots of the electrical conductivity and the dielectric constant versus frequencies from 500 Hz to 1 MHz, measured at room temperature.

3.4. Electrical properties of raw and calcined duck eggshells

The electrical properties (the dielectric constant and the electrical conductivity) of the duck eggshells calcined at 900 °C for 1 h measured at a room tem-

art%3A10.2478%2Fs13536-012-0055-7.pdf http://download.springer.com/static/pdf/19/art%3A10.2478%2Fs13536...

perature and at frequencies from 500 Hz to 1 MHz, are shown in Fig. 8. The electrical conductivity and the dielectric constant, measured at the frequency of 500 Hz, are 1.0×10^{-6} $(\Omega \cdot m)^{-1}$ and 35, respectively. Thus, the prepared calcium oxide is a potential material to be used as a dielectric material.

4. Conclusions

Raw duck eggshells or calcite ($CaCO_3$) of the rhombohedral form, transform completely into a face-centered cubic lime (CaO) after calcination at 900 °C for 1 h. The phase transformation from calcium carbonate ($CaCO_3$) to calcium oxide (CaO) depends on the calcination temperature and time. The higher calcination temperature and longer calcination time, the more complete phase transformation is obtained. The calcium oxide made from duck eggshells has a good dispersion, good electrical properties and high porosity, as evidenced by TEM, the impedance analyzer, and BET, respectively. The particle size distribution and the cumulative mass percentage diameters (d_{10}, d_{50}, d_{90}, and mean diameter) of calcium oxide particles, obtained from the egg shells calcined at 900 °C for 1 h, are 3.14, 12.12, 49.30, and 29.16 µm, respectively. The percentage of ceramic yield is 53.53 % with the purification of 99.06 % w/w. The calcium oxide has the specific surface area, the pore volume, and the average pore diameter of 7.79 m^2/g, 0.05, and 17.69 nm, respectively. The electrical conductivity and the dielectric constant, measured at the frequency of 500 Hz, are 1.0×10^{-6} $(\Omega \cdot m)^{-1}$ and 35, respectively. Furthermore, the eggshells of both hen and duck are composed of three layers: a cuticle thin outer layer, a palisade thick middle layer, and an inner thin mammillary layer. The suitable calcination temperature and the time of the phase transformation from $CaCO_3$ into CaO are the same for both the eggshells, namely – 900 °C and 1 h. However, the duck eggshells have a thicker shell layer, higher shell weight, more interactive bonding within the shells, and are of higher true density than the hen eggshells. Therefore, the physical and chemical properties of the calcium oxide derived from raw duck eggshells differ slightly from the properties derived from the raw hen eggshells. The calcium oxide derived from the raw duck eggshells is supposed to be a potential material used as a dielectric material, an absorbent, a filler in a variety of industries such as paper, printing ink, rubber, pharmaceutical and cosmetic, and as a starting material for sensors, insulators, and catalysts [14, 15].

Acknowledgements

The authors would like to thank the following institutions: The Petroleum and Petrochemical College, the Department of Geology, Faculty of Science, and the Scientific and Technological Research Equipment Centre, at Chulalongkorn University; the Departments of Materials Engineering and Physics at Kasetsart University for the use of their analytical equipment. We are also grateful for the financial supports from the Medium Projects on Rubber; MPR 52, No. RDG5250062 from the Thailand Research Fund, and the Center for Advanced Studies in Industrial Technology at Kasetsart University. Also, we would like to acknowledge the supports from the Conductive and Electroactive Polymers Research Unit, the Thailand Research Fund (TRF), the Royal Thai Government.

References

[1] THAPON J.L., BOURGEOIS C.M., *Lavousier Technique at Documentation*, L'Oeuf et les ovoproducts, 1994.
[2] RIVERA E.M. *et al.*, *Mater. Lett.*, 41 (1991), 128.
[3] ADEYEYE E.I., *Bull. Chem. Soc. Ethiop.*, 23 (2009), 159.
[4] FREIRE M.N., HOLAND J.N.F., *Cerâmica*, 52 (2006), 240.4.
[5] WAN X. *et al.*, *Mater. Sci. Eng.*, 25 (2005), 455.
[6] MEISZTERICS A., SINKO K., *Colloids Surf. A: Physicochem. Eng.*, 319 (2008), 143.
[7] CHRYSAFI R. *et al.*, *J. Eur. Ceram. Soc.*, 27 (2007), 1707.
[8] SOUTHAM D.C. *et al.*, *Curr. Appl Phys.*, 4 (2004), 355.
[9] RICHARDSON I.G., *Cem. Concr. Res.*, 38 (2008), 137.
[10] PARK H.J. *et al.*, *J. Environ. Sci.*, 19 (2007), 1436.
[11] JONES D., ADAS Consulting Ltd. UK Utilization of egg shell waste from UK egg processing and hatchery establishments, Pigs, Eggs and Poultry Division, DEFRA, Whitehall Place East, London, 2002 (`www.defra.gov.uk`).
[12] MURAKAMI F.S., RODRIGUES P.O., *Cienc. Technol. Aliment.*, 27 (2007), 658.
[13] LU G.Q., ZHAO X.S., *Nanoporous Materials Science and Engineering*, Imperial College Press, 4th editions, 2006.
[14] CHEN X.D. *et al.*, *Trans. I. ChemeE. part C*, 77 (1999), 40.
[15] SU B.L. *et al.*, Microporous Mesoporous Mater., 105 (2007), 49.

Received 2011-02-16
Accepted 2012-10-25

Polymer-Plastics Technology and Engineering, 52: 70–79, 2013
Copyright © Taylor & Francis Group, LLC
ISSN: 0360-2559 print/1525-6111 online
DOI: 10.1080/03602559.2012.721440

Taylor & Francis
Taylor & Francis Group

Polymer Electrolyte Membrane Based on Sulfonated Poly(Ether Ketone Ether Sulfone) (S-PEKES) with Low Methanol Permeability for Direct Methanol Fuel Cell Application

S. Changkhamchom[1,2] and A. Sirivat[1,2]

[1]*Conductive and Electroactive Polymers Research Unit, Chulalongkorn University, Bangkok, Thailand*

[2]*The Petroleum and Petrochemical College, Chulalongkorn University, Bangkok, Thailand*

Downloaded by [Chulalongkorn University] at 18:50 07 January 2013

Poly(ether ketone ether sulfone), (PEKES), was synthesized by the nucleophilic aromatic substitution polycondensation between bisphenol S and 4,4′-difluorobenzophenone (system A), and between bisphenol S and 4,4′-dichlorobenzophenone (system B). The oxidative stability was characterized by using a Fenton's reagent. S-PEKES membranes show a higher thermal stability than that of Nafion 117 and comparable to that of S-PEEK 150XF. The proton conductivity values of S-PEKES of the highest DS are comparable to those of Nafion 117 and S-PEEK. The methanol permeability of the synthesized and fabricated S-PEKES membrane is lower than that of Nafion 117 by at least an order of magnitude.

Keywords Degree of Sulfonation (DS); Proton conductivity; Proton Exchange Membrane (PEM); Sulfonated poly(ether ketone ether sulfone)

INTRODUCTION

A proton exchange membrane (PEM) is an electrolyte used in both polymer electrolyte membrane fuel cells (PEMFC) and direct methanol fuel cells (DMFCs), which transfers protons from anode to cathode and acts as a barrier to avoid the crossover of fuel.Currently, PEMs are mainly the commercially Nafion (DuPont) membranes, which is a perfluorinated polymer with sulfonic acid groups as pendant groups. It has excellent ionic properties, and the most important advantage of Nafion is its excellent proton conductivity in the fully hydrated condition. Furthermore, it has good physical, chemical, and mechanical stability. Even though Nafion membranes have demonstrated good performance in hydrogen fuel cells, the high cost and the high methanol permeability have limited their applications in direct methanol fuel cells (DMFCs)[1].

Address correspondence to A. Sirivat, The Petroleum and Petrochemical College, Chulalongkorn University, Bangkok 10330, Thailand. E-mail: anuvat.s@chula.ac.th

An ultimate aim in the PEM development is to find novel materials as alternatives to Nafion that are of low cost and can operate at a higher temperature. Presently, existing PEM materials are, for example, Nafion 117 (proton conductivity 90–120 $mS.cm^{-1}$ at 80°C and 34–100% RH), Nafion 115 (41 $mS.cm^{-1}$ at 25°C), sulfonated poly(ether ether ketone) (SPEEK) (0.9 $mS.cm^{-1}$ at 20°C), sulfonated poly(benzimidazole) (SPBI) (10–40 $mS.cm^{-1}$ at 130–180°C), sulfonated poly-(phosphazene) (40 $mS.cm^{-1}$ at 25°C), AMPS asymmetric-based acrylic (42 $mS.cm^{-1}$ at 90°C), poly(vinylidene fluoride) (PVDF) + styrene membrane (resistance 0.454 $\Omega.cm^2$), PVDF + SiO_2 or SiO_2 gel (70 $mS.cm^{-1}$ (SiO_2) and 200 $mS.cm^{-1}$ (gel) at 25°C), etc.[2].

The poly(arylene ether ketone) family is of particular interest because it is an engineering thermoplastic with excellent thermal and chemical stability, high mechanical strength, good insulating properties, and a relatively low cost compared to Nafion. The sulfonated poly (ether ether ketone) (S-PEEK) has good thermal stability and appropriate proton conductivity at a high degree of sulfonation (DS). Several articles have investigated and reported the sulfonation of PEEKs and their properties[3–15]. Synthesized derivatives of poly(ether ketone ether sulfone) have been reported using various starting monomers[16]. Sulfonated poly(arylene ether ketone) can dissolve in some organic solvents that allow it to be cast as a membrane. This solubility property offers a more convenient and less expensive process when compared with fabricating perfluorosulfonic acid membrane.

In this work, two synthesized S-PEKESs were investigated (System A and System B). System A and System B contain 4,4′-difluorobenzophenone and 4,4′-dichlorobenzophenone as the starting monomers, respectively. The synthesis and properties of System B have not been fully investigated and reported so far. In addition, the introduction of sulfone group (-SO_2-) in to the polymer backbone

Downloaded by [Chulalongkorn University] at 18:50 07 January 2013

leads to better solubility of PEKES in H_2SO_4 relative to that of PEEK 150XF, which results in higher sulfonation degrees.

Furthermore, the S-PEKESs backbones contain the aromatic rings, the carbonyl groups (-C = O), and the sulfone groups ($-SO_2-$), which promote the chain stiffness and thermal stability. The degree of sulfonation was varied by the reaction time. The synthesized polymers were characterized by TGA to identify the thermal properties. The methanol permeabilities (P) were measured by Gas Chromatography (GC). The storage modulus (G') of these membranes were investigated and measured by a melt rheometer (Rheometric Scientific, ARES). The oxidative stability was characterized by using a Fenton's reagent.

EXPERIMENTAL

Materials

Bisphenol S or 4,4′-sulfonyldiphenol, 4,4′-dichlorobenzophenone, and 4,4′-difluorobenzophenone (98–99%, Aldrich) were used as the monomers. Concentrated sulfuric acid (Merck, 98 wt%), sodium chloride (Univar, 99.9%), and sodium hydroxide (Univar, 97%) were used as received. Potassium carbonate (Riedel-de-Haen, 98–100%) and dimethyl sulfoxide (Riedel-de-Haen, 99.5%), and toluene (Fisher-Scientific 99.99%) were used as received. PEEK 150XF was purchased from Victrex. Nafion117 was purchased from Electrochem, Inc (USA).

Synthesis of Poly (Ether Ketone Ether Sulfone) (PEKES) and Sulfonated Poly(Ether Ketone Ether Sulfone) (S-PEKES)

Both PEKES and S-PEKES of various degrees of sulfonation (DS) were synthesized according to the previous work reported elsewhere[17]. The poly (ether ketone ether sulfone)s were synthesized via the nucleophilic aromatic substitution reaction by using these monomers: 4,4′-difluorobenzophenone (System A), 4,4′-dichlorobezophenone (System B), and bisphenol S. The monomer was mixed with potassium carbonate in DMSO toluene, in a 250-ml three-necked, round-bottom flask equipped with a Dean-Stark trap, a reflux condenser, a nitrogen inlet, and a thermostat.

The mixture was refluxed for 3 h at 150°C, and then the excess toluene was distilled off. Toluene was used to eliminate the water, which was a product in the reaction, and the solution was heated at 175°C for 20 h. The reaction mixture was then cooled to room temperature and poured into a mixture of methanol and distilled water (ratio 1:1). The crude product was then washed with water to remove any inorganic salt. The polymer was filtered and dried in a vacuum oven at 80°C for 48 h.

The synthesized PEKES and the commercial PEEK 150XF powder were dried in a vacuum oven at 100°C overnight. Then, 5.0 g of the polymer was dissolved in 50 ml concentrated sulfuric acid (98%), which was kept under a molecular sieve 4 A for 24 h, and vigorously stirred at 25 ± 2°C for durations of 12, 24, 36, 48, 60, 72, and 84 h. Then, the solution was gradually precipitated into ice-cold water under mechanical stirring. The polymer suspension was left overnight. Then, the precipitate was filtered, washed several times with distilled water until neutral a pH was obtained, and dried under vacuum at 60°C for 24 h. The chemical structures of S-PEKES-A, B, and S-PEEK 150XF are shown in Figure 1.

Membrane Preparation

Membranes were prepared by dissolving 1.0 g of polymer in 30 mL dimethyl sulfoxide (DMSO) with vigorous stirring for 12–18 h until the polymer solutions were homogeneous. Each solution was cast on a petri dish and kept at room temperature for 12 h, followed by drying at 80°C for 2 days under a vacuum.

Polymer Characterization

Thermal Behavior

A thermogravimetric analyzer (TGA) (Perkin Elmer/TGA7, USA) was used to investigate the thermal stability of the postsulfonated membranes. Between 5.0 and 10.0 mg samples were heated from 50–800°C at a rate of 10°C/min under N_2 atmosphere[14].

Proton Conductivity

The water uptake (%) of the membranes could be calculated from the method reported by Unnikrishnan et al.[18]. The proton conductivity values of the polymer membranes were measured by using an Agilent E4980A LCR meter at an AC potential of 1 V and in the frequency range of 20 Hz to 2 MHz, at 27 ± 1°C, 50%RH. The membranes were immersed in de-ionized water at various soaking times to obtain 10, 20, 30, 40, and 50% water content. The conductivity values (σ) of all samples were calculated from the

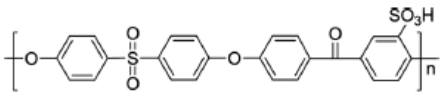

S-PEKES-A and S-PEKES-B

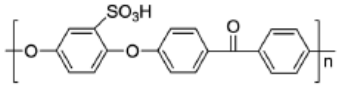

S-PEEK 150XF

FIG. 1. S-PEKES-A, S-PEKES-B, and S-PEEK 150XF.

Downloaded by [Chulalongkorn University] at 18:50 07 January 2013

impedance data, using the relation $\sigma = d/RS$ where σ is the proton conductivity (S/cm), d is the membrane thickness (cm), S is the membrane surface area (cm^2), and R is the resistance, which can be derived from the low intersect of the high frequency semicircle on a complex impedance plane with the Re(Z) axis[11]. The impedance of each sample was measured for 3 times to ensure data reproducibility.

Methanol Permeability

The methanol permeabilities of the membranes were determined by using the two compartments diffusion cell in Figure 2. One compartment (compartment A, $V_A =$ 250 ml) was filled with a solution of methanol (2.5 mol/L). The other compartment (compartment B, $V_B = 250$ ml) was filled with deionized water. The membrane was clamped between the two compartments. The solutions in the two compartments were magnetically stirred during the permeation experiments. Methanol flux was across the membrane due to the methanol concentration difference between the compartment A and the compartment B[19]. The methanol permeation in the receiving compartment as a function of time is given by:

$$P(\mathrm{cm}^2/\mathrm{s}) = \frac{kB \times VB \times L}{A \times (CA - CB)}, \quad (1)$$

where P is methanol permeability, C_A and C_B are the methanol concentrations in the compartment A and B, respectively, A and L are the area and the thickness of a membrane respectively, V_B is the volume of the solution in the compartment B, k_B is the slope of the methanol concentration profile in the compartment B. The methanol concentrations were measured by using a gas chromatography (Pr2100) fitted with athermal conductivity detector (TCD); ethanol was used as the internal standard.

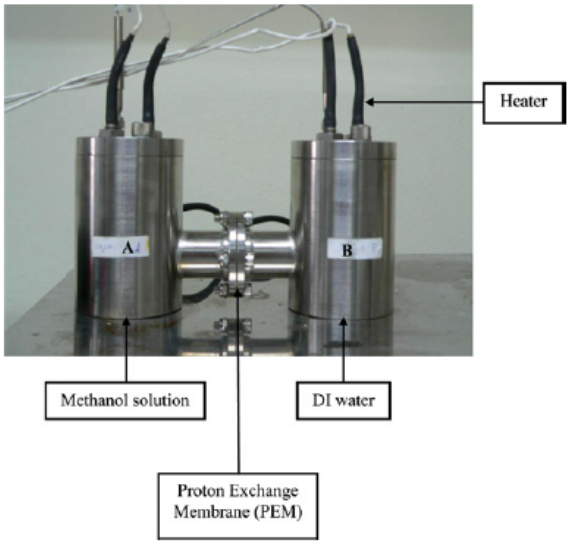

FIG. 2. Methanol diffusion cell. (Color figure available online.)

Storage Modulus

The dynamic mechanical properties of S-PEKES-A, S-PEKES-B, S-PEEK 150XF, and Nafion 117 were measured with a melt rheometer (Rheometric Scientific, ARES NJ, USA). The measurements were performed in the shear oscillatory mode using a parallel plate fixture (diameter of 25 mm). The range of angular frequency was from 0.04 to 100 rad/s at four different temperatures from 303, 323, 343, and 363 K. The strain amplitude of 0.1% was selected to be the suitable strain to measure dynamic moduli (G′ and G″) in the linear viscoelastic regime. The oscillatory shear strain was applied and the G′ and G″ were measured as functions of frequency and temperature.

Oxidative Stability

The oxidative stability was investigated by immersing the small pieces S-PEEK ($5 \times 5\,mm^2$) into a Fenton's reagent (3% H_2O_2 containing 2 ppm $FeSO_4$) at 80°C and recording the time in which the membranes began to break into pieces[20].

Mechanical Properties

Tensile properties of S-PEKES-A, S-PEKES-B, and S-PEEK 150XF membranes, equilibrated in water for 24 h at 27°C as strips (60 mm × 10 mm × 0.2 mm), were measured using a Lloyd UTM. Crosshead speed of 100 mm/min was maintained for all the samples. The gauge length is 30 mm. The measurements were run at an ambient condition (at 30°C and 50% RH). The samples for the dry state test were dried at 100°C in vacuum for 12 h before test. For each data point five samples were tested, and the average was recorded.

RESULTS AND DISCUSSION

Degree of Sulfonation (DS)

The synthesized PEKES-A, PEKES-B, and the commercial PEEK 150XF were sulfonated with 12–84 h reaction times. The DS of S-PEKES-A are 0.30, 0.50, and 0.67, of S-PEKES-B are 0.33, 0.51, and 0.67, and of S-PEEK 150XF are 0.25, 0.38, and 0.52, corresponding to the sulfonation times of 36, 60, and 84 h, respectively[17].

Thermogravimetric Analysis (TGA)

The S-PEKES-A, S-PEKES-B, and S-PEEK 150XF membranes with DS of 0.50, 0.51, and 0.52, respectively are shown in Figure 3. The thermograms of all membranes

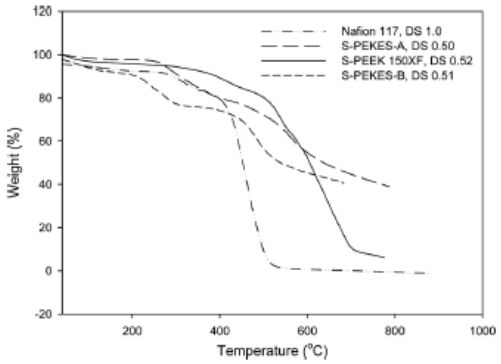

FIG. 3. Thermograms of Nafion® 117, S-PEKES-A, S-PEKES-B, and S-PEEK 150XF, with the sulfonation degrees of 1.0, 0.50, 0.51, and 0.52, respectively.

were compared with that of Nafion 117. The first step weight loss of the synthesized S-PEKES-A membrane starts at around 230–250°C, representing the splitting-off of the sulfonic acid group. The second step weight loss occurs at 430–450°C, representing the degradation temperatures of SPEKES-A main chain. For the synthesized S-PEKES-B membrane, its thermogram shows the first weight loss starting at 200–230°C and the second step weight loss occurs at 430–450°C.

The degradation of both S-PEKES-A and S-PEKES-B membranes are not complete because the char occurs and the remaining weights of the polymers are about 40%. The S-PEEK 150XF membrane shows the highest thermal stability, since its first slight weight loss occurs at around 400–450°C and the second step weight loss is at 580°C corresponding to the main PEEK chain decomposition; it is completely degraded and no char remains[4]. The poorest thermal stability belongs to Nafion 117 membrane, it shows the first degradation step at 250–280°C and the second step weight loss occurs at 400°C. In summary, all sulfonated polymers are thermally stable within the temperature range 25–120°C and are suitable for use in DMFC application.

Proton Conductivity (σ)

Table 1 shows the proton conductivities of all membranes of various water uptakes (%); 10, 20, 30, 40, 50%, at a room temperature (27°C) and 50% RH. The proton conductivity increase with increasing DS, which can be related to the number of acid sites increment that can enhance the proton transfer through the membrane[21]. The enhancement of the water uptake (%) within the hydrated membrane can also increase the DS. Figure 4 shows the effects of the degree of sulfonation and the water uptake (%) on the proton conductivities of S-PEKES-B membranes with the sulfonation degrees (DS) of 0.33,

TABLE 1
The proton conductivities of all membranes of various water uptakes (%) at a room temperature (27°C) and 50% RH

PEM	DS	Thickness (cm)	Water uptakes (%)	Proton conductivity (S/cm)	STD
Nafion 117	1	0.02	10	8.56E-07	7.39E-08
			50	1.09E-02	1.39E-03
S-PEKES-A	0.3	0.0353	10	5.51E-08	8.67E-09
			50	4.52E-03	1.35E-03
	0.5	0.0322	10	2.01E-07	4.17E-08
			50	6.25E-03	6.38E-04
	0.67	0.0423	10	4.73E-06	4.81E-07
			50	8.48E-03	9.00E-04
S-PEKES-B	0.33	0.0278	10	6.22E-08	7.79E-09
			50	6.07E-03	5.45E-04
	0.51	0.0252	10	2.08E-07	2.26E-08
			50	6.61E-03	2.50E-04
	0.66	0.0278	10	4.41E-06	4.84E-07
			50	8.45E-03	5.75E-04
S-PEEK 150XF	0.25	0.0446	10	1.81E-08	4.62E-09
			50	8.51E-04	8.83E-05
	0.38	0.0404	10	8.45E-08	7.30E-09
			50	7.10E-04	6.30E-05
	0.52	0.0423	10	3.36E-07	5.47E-08
			50	6.67E-03	2.45E-04

Downloaded by [Chulalongkorn University] at 18:50 07 January 2013

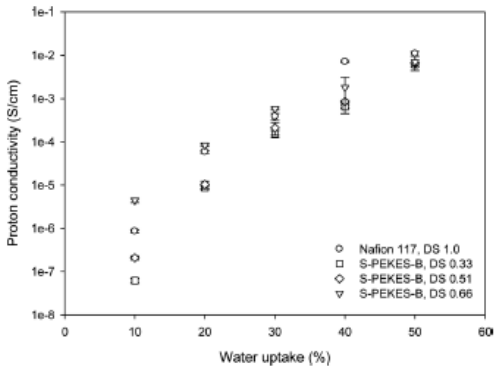

FIG. 4. The proton conductivities of S-PEKES-B membranes with the sulfonation degrees (DS) of 0.33, 0.51, and 0.66, respectively, and of the Nafion® 117, at a room temperature (27°C) and 50% RH.

0.51, and 0.66, respectively, and of Nafion 117 at a room temperature (27°C) and 50% RH.

For the S-PEKES-B membrane when the water uptake is varied between 10–50%, the proton conductivity increases from 6.22×10^{-8} to 6.07×10^{-3} S/cm at DS = 0.33, the proton conductivity increases from 2.08×10^{-7} to 6.61×10^{-3} S/cm at DS = 0.51, and the proton conductivity increases from 4.41×10^{-6} to 8.45×10^{-3} S/cm at DS = 0.66. These results confirm that the increments in DS and the water uptake (%) both enhance the proton conductivity.

Figure 5 shows the effect of PEM type on the proton conductivity. The proton conductivities of S-PEKES-A, S-PEKES-B, and S-PEEK 150XF membranes, at comparable degrees of sulfonation (DS) of 0.50, 0.51, and 0.52, respectively, are compared with that of Nafion® 117 at a

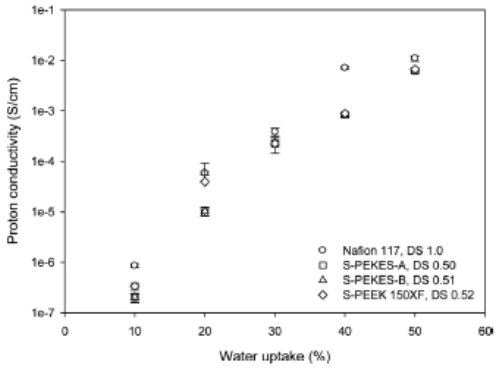

FIG. 5. The proton conductivities of S-PEKES-A, S-PEKES-B, and S-PEEK 150XF membranes with the sulfonation degrees (DS) of 0.50, 0.51, and 0.52, respectively, and of Nafion® 117 at a room temperature (27°C) and 50% RH.

room temperature (27°C) and 50% RH. For the S-PEKES-A membrane at DS = 0.50, the proton conductivity increases from 2.01×10^{-7} to 6.25×10^{-3} S/cm; for the S-PEKES-B membrane at DS = 0.51, the proton conductivity increases from 2.08×10^{-7} to 6.61×10^{-3} S/cm; for the S-PEEK 150XF membrane at DS = 0.52, the proton conductivity increases from 3.36×10^{-7} to 6.67×10^{-3} S/cm; when the water uptake value falls between 10–50%. The proton conductivities of the three PEM systems are comparable due to their comparable degrees of sulfonation. The proton conductivity of Nafion 117 increases from 8.56×10^{-7} to 1.09×10^{-2} S/cm, as the water uptake is varied between 10–50%.

In the work of Do and Kim[22], the room-temperature proton conductivity of the fully hydrated homogeneously S-PEEK membrane with a 68% degree of sulfonation was measured and compared with Nafion 117 (0.11 S/cm). The S-PEEK (DS = 0.68) has the IEC equal to 1.99 and the proton conductivity is 0.13 S/cm, which higher than that of Nafion 117 under the same experimental conditions. In the present study, the S-PEKES-A membrane (DS = 0.67, IEC = 1.34) has a proton conductivity equal to 0.00848 S/cm, the S-PEKES-B membrane (DS = 0.66, IEC = 1.36) has a proton conductivity equal to 0.00845 S/cm, and the S-PEEK 150XF (DS = 0.52, IEC = 1.01) has a proton conductivity equals to 0.00667 S/cm[17]; thus, these membranes have lower proton conductivity than that of Do's membrane due to the lower IEC and water uptake values.

In 2010, Fontananova et al.[23] studied the sulfonated derivative of amorphous polyetheretherketone, known as the SPEEK-WC membrane. The proton conductivity of the SPEEK-WC membrane with DS equal to 0.8 is 0.0007 S/cm, for S-PEEK-WC/PW12 with the same DS is 0.001 S/cm, for S-PEEK-WC/SiW12 with the same DS is 0.0015 S/cm, and for S-PEEK-WC/PMo12 with the same DS is 0.00125 S/cm. The proton conductivity measurements were carried out at 20 ± 1°C and with 100% relative humidity; all Do's and Kim's membranes have lower proton conductivities than those in the present work.

Methanol Permeability

The methanol permeability causes conversion losses in terms of lost fuel and depolarization losses at the cathode, resulting in overall poor fuel cell performance[1]. Nafion has been found out that over 40% of the methanol can be wasted in DMFCs through leaks across such membranes[24]. Table 2 represents the methanol permeability (P) of all membranes with various degree of sulfonation (DS) at 27°C, 50°C, and 70°C, respectively. Their methanol permeabilities increase with both the degree of sulfonation (DS) and temperature. The methanol permeability (P) was calculated from the slope (k_B) of the straight-line plot of

Downloaded by [Chulalongkorn University] at 18:50 07 January 2013

TABLE 2
Methanol permeability (P) of all membranes at the temperatures of 27°C, 50°C, and 70°C, respectively

PEM	DS	Thickness (cm)	Methanol Permeability, P (cm^2/s)		
			27°C	50°C	70°C
Nafion 117	1.00	0.0200	1.4147E-06	1.0725E-05	1.1689E-05
S-PEKES-A	0.30	0.0353	2.4970E-08	8.3209E-08	5.6916E-07
	0.50	0.0322	6.6964E-08	1.1506E-07	8.8552E-07
	0.67	0.0423	1.1968E-07	8.2516E-07	2.3142E-06
S-PEKES-B	0.33	0.0278	3.9329E-08	9.7941E-08	6.7276E-07
	0.51	0.0252	6.8702E-08	1.2144E-07	9.0517E-07
	0.66	0.0278	1.0347E-07	7.9574E-07	2.1358E-06
S-PEEK 150XF	0.25	0.0446	1.0679E-08	6.5961E-08	4.5703E-07
	0.38	0.0404	4.6316E-08	1.0252E-07	7.3455E-07
	0.52	0.0423	7.1140E-08	1.2850E-07	1.0583E-06

Downloaded by [Chulalongkorn University] at 18:50 07 January 2013

methanol concentration in the compartment B (C_B) vs. permeation time by using Eq. (1). The methanol permeability values of Nafion 117 are higher than those our synthesized S-PEKES-A and S-PEKES-B membranes by two orders of magnitude at a given temperature. The methanol permeability values of Nafion 117 at 27, 50, and 70°C are 1.42×10^{-6}, 1.07×10^{-5}, and 1.17×10^{-5} (cm^2/s), respectively.

Figure 6 shows the effects of the degree of sulfonation and the membrane type on the methanol permeability. The methanol concentrations (C_B) of all membranes increase linearly with permeation time. The slope (k_B) of these concentration profiles were used to calculate the methanol permeability (P). The S-PEKES-A membranes possess the methanol permeability values of 2.4970×10^{-8}, 6.6964×10^{-8}, and 1.1968×10^{-7} cm^2/s, at the DS values of 0.30, 0.50, and 0.67, respectively; the S-PEKES-B membranes possess the methanol permeability values of 3.9329×10^{-8}, 6.8702×10^{-8}, and 1.0347×10^{-7} cm^2/s, corresponding to the DS values of 0.33, 0.51, and 0.66, respectively; and the methanol permeability values of S-PEEK 150XF membranes are 1.0679×10^{-8}, 4.6316×10^{-8}, and $7.114\ 70 \times 10^{-8}$ cm^2/s, with the corresponding DS values of 0.25, 0.38, and 0.52, respectively.

These results indicate clearly that the methanol permeability of all membranes increases with increasing DS; the permeability values of S-PEKES-B membranes are higher than those of S-PEKES-A and S-PEEK 150XF, respectively. However, these values are in the same order of magnitude of 10^{-8}–10^{-9} cm^2/s and are lower than those of Nafion 117. Figure 7 shows the effect of temperature on methanol permeability, The methanol permeability of S-PEKES-B membrane increases with increasing temperature as the methanol molecules are more active to penetrate through the membrane[25]. For the highest DS (0.66) of S-PEKES-B, the methanol permeability values are 1.0347×10^{-7}, 7.9574×10^{-7}, and 3.1358×10^{-8} cm^2/s, corresponding to the temperatures of 27, 50, and 70°C, respectively.

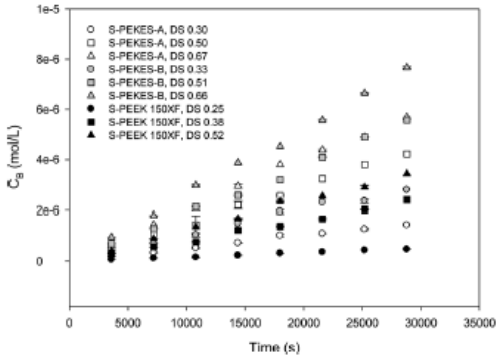

FIG. 6. Methanol concentration in compartment B (mol/L) vs. time (s) of membranes, with 2.5 mol/L initial feed composition and at a room temperature (27°C).

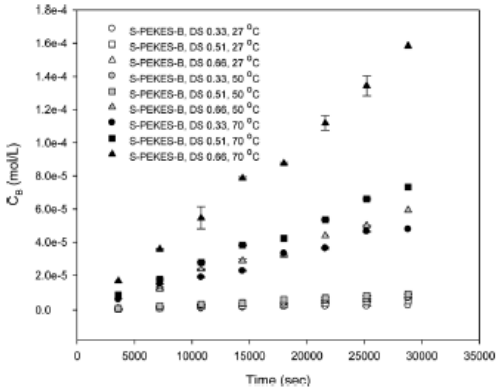

FIG. 7. Methanol concentration in compartment B vs. time of S-PEKES-B membranes, with 2.5 mol/L initial feed composition, at the temperatures of 27°C, 50°C, and 70°C.

Downloaded by [Chulalongkorn University] at 18:50 07 January 2013

In the work of Do and Kim[22], S-PEEK membrane methanol permeabilities were measured at a room temperature. The methanol permeabilities of the S-PEEK membranes are in the range of $0.10–0.35 \times 10^{-6}\,cm^2/s$ corresponding to the IEC values between 1.40–2.2, respectively, which are considerably higher than those in the present work. Li et al.[26] studied the methanol permeability of S-PEEK membranes; the pristine S-PEEK membrane has the methanol permeability in the range of $3.10–9.87 \times 10^{-7}\,cm^2/s$, which is one order of magnitude lower than that of the commercial Nafion 117. However, Li et al.'s membranes show higher methanol permeabilities than those of S-PEKES-A, S-PEKES-B, and S-PEEK 150XF in the present work.

Oxidative Stability

The hydrogen peroxide could be originated from the oxygen diffusion through the membrane and the incomplete reduction at the fuel cell anode, leading to a severe damage of PEM. The currently used membranes fail in the Fenton's tests, leading to low performances in actual fuel cell operations[27], their short life time, due to the occurring oxidative degradation. The accelerating oxidation measurement was taken by soaking the sulfonated membranes in Fenton's reagent (3% H_2O_2 containing 2 ppm $FeSO_4$) at 80°C[28]. To maintain the fuel cell performance during the operation, the oxidative stability of PEM should be sufficiently high.

As shown in Table 3, the oxidative stability decreases with increasing sulfonation degree. In our experiment, the oxidative degradation of our synthesized membranes; S-PEKES-A and S-PEKES-B, and commercial S-PEEK 150XF, were evaluated and are compared with that of Nafion 117. The time interval in which the membrane is broken into pieces is referred to as t_1. Whereas t_2 refers to the time in which the total membrane disappears or becomes fully dissolved in a Fenton's reagent. The Nafion 117 possesses the lowest oxidative stability when compared with those of other membranes; it takes 24 min before the membrane starts to break into small pieces and 56 min before it dissolves in the solution.

Whereas, the S-PEKES-A, S-PEKES-B, and S-PEEK 150XF membranes with the DS values of 0.66, 0.67, and 0.52, start to break at t_1 equal to 38, 35, and 43 min, respectively. They are totally dissolved in the Fenton's solution at t_2 equal to 76, 73, and 94 min, respectively. Therefore, the S-PEEK 150XF membrane shows the best oxidative stability, following with the S-PEKES-A, S-PEKES-B, and Nafion 117 membranes, respectively. All sulfonated membrane systems with DS range of 0.50–0.52, show comparable oxidative stability with the cross-linked sulfonated polysulfone membranes of Furtado Filho and Gomes[29], which can stay in the Fenton's reagent until 94 min before they are completely decomposed.

Storage Modulus

The storage moduli (G') of membranes with various sulfonation degrees (DS) at a room temperature (27°C) are shown in Figure 8.

The storage moduli (G') of the membranes are rather constant with respect to frequency at 27°C. The storage moduli (G') of S-PEKES-A, S-PEKES-B, and S-PEEK 150XF decrease with increasing DS, due to the reduction in the level of crystallinity. Generally, the structures of the nonsulfonated polymer; PEKES-A, PEKES-B, and PEEK 150XF are of linear chains which are able to pact tightly leading to high crystallinity. When the sulfonic acid groups are attached to the polymer backbones, they can act as the bulky groups and obstruct the packing between the adjacant chains. Thus, the steric effect increases with the degree of sulfonation. Figure 9 shows the effect of temperature on the storage modulus (G') of the S-PEKES-B

TABLE 3
Oxidative stabilities of the membranes immersed in Fenton's reagent at room temperature (27°C)

PEM	DS	Thickness (cm)	t_1 (min)	SD	t_2 (min)	SD
Nafion 117	1.00	0.0200	24.33	1.53	56.67	1.53
S-PEKES-A	0.30	0.0353	66.67	1.53	121.00	3.61
	0.50	0.0322	47.00	1.00	94.33	2.08
	0.67	0.0423	38.00	1.00	76.67	1.53
S-PEKES-B	0.33	0.0278	60.00	1.00	114.33	2.08
	0.51	0.0252	49.00	1.00	94.67	1.53
	0.66	0.0278	35.33	1.53	73.67	1.53
S-PEEK 150XF	0.25	0.0446	80.67	1.53	146.00	1.00
	0.38	0.0404	55.00	1.00	109.67	1.53
	0.52	0.0423	43.33	1.53	94.67	1.53

t_1, time of membrane breaking into pieces; t_2, time of membrane disappearing.

Downloaded by [Chulalongkorn University] at 18:50 07 January 2013

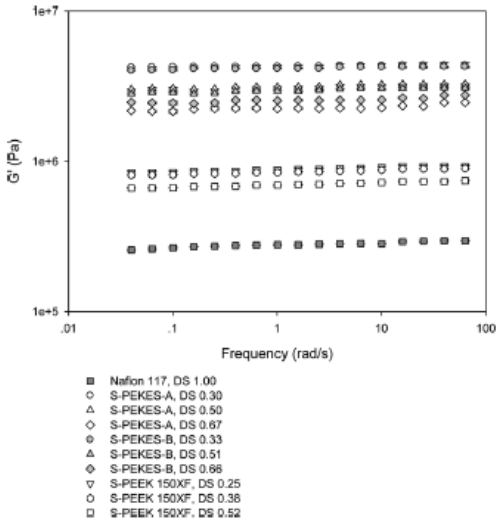

FIG. 8. The storage modulus (G′) of membranes of various sulfonation degrees (DS) at a room temperature (27°C).

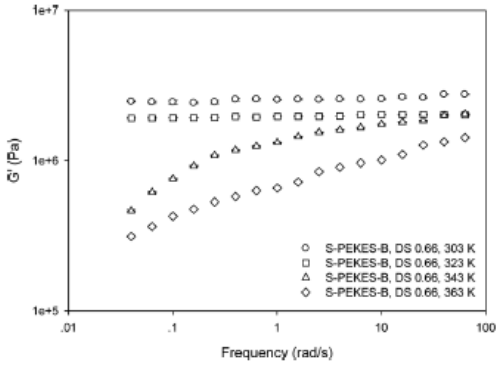

FIG. 9. Storage modulus (G′) vs. frequency of S-PEKES-B membranes with the DS of 0.66, at various temperatures.

membrane with DS of 0.66. The storage modulus (G′) of the membrane slightly decreases with increasing temperature, due to the increase of the free volume, which allows the easier chain movement at a high temperature[28].

Mechanical Properties

Good mechanical properties of the sulfonated polymer membranes, in the anhydrous or the hydrous state, are desirable for functional proton exchange membrane. The mechanical properties of the SPEES-A, S-PEKES-B, and FSPES-3 membranes are summarized in Table 4. The dry sulfonated membranes possess the tensile strength in the range of 17.8–53.3 MPa, Young's modulus of 459.9–34,382.74 MPa, and the elongation at break of 7.14–119.87%. The sulfonated membranes in the wet state possess good mechanical properties with the tensile strength of 7.75–31.55 MPa, the Young's modulus of 193.79–1,234.5 MPa, and the elongation at break of 137.88–538.44%.

In the hydrous or wet state, the tensile strength and the Young's modulus decrease with DS, while the elongation at break increases. The reason is that the sulfonic acid groups cause the steric hindrance and obstruct the polymer chains into a tight packing in which the crystallinity is reduced.

Water acts as an external plasticizer between polymer chains, leading to the ease in the chain movement and a decrease in the tensile strength. The mechanical strength in the hydrous state is thus lower than that in the anhydrous state. The sulfonated polymers which have DS value of around 0.3, are stronger than Nafion® 117[30–31].

In the work of Guhan and Sangeetha[32], the sulfonated poly(ether ether ketone) (SPEEK)/silicotungstic acid (SWA) composite membranes were prepared for use in fuel cell applications. The dry state tensile strength of all composite membrane systems are in the range of 7.5–15 MPa, which extremely lower than the sulfonated membranes prepared in our present work.

TABLE 4
Mechanical properties of sulfonated polymer at room temperature (27°C) and 50% RH

		Tensile strength (MPa)		Young's modulus (MPa)		Elongation at break (%)	
PEM	DS (%)	Dry	Wet	Dry	Wet	Dry	Wet
S-PEKES-A	0.30	53.33 ± 3.75	31.55 ± 1.43	34,382.74 ± 102.80	1,234.50 ± 34.36	7.14 ± 0.84	137.88 ± 11.63
	0.50	24.18 ± 1.79	13.69 ± 1.55	529.44 ± 22.18	453.98 ± 7.91	33.23 ± 2.04	184.80 ± 4.47
S-PEKES-B	0.33	40.05 ± 1.43	30.70 ± 1.40	17,681.38 ± 82.11	1,152.25 ± 32.92	7.52 ± 0.50	143.8 ± 11.08
	0.51	22.93 ± 0.61	8.63 ± 0.27	463.02 ± 36.75	338.84 ± 33.47	70.80 ± 13.01	214.07 ± 12.43
S-PEEK 150XF	0.38	32.19 ± 1.30	25.42 ± 1.26	16,523.57 ± 110.85	662.23 ± 21.09	7.71 ± 1.80	148.27 ± 12.85
	0.52	17.84 ± 1.53	7.75 ± 0.18	459.93 ± 6.86	193.79 ± 7.33	119.87 ± 0.85	538.44 ± 21.47
Nafion®117*	1.00	38.0	28.4	180	100	301.5	329.2

*The mechanical properties of Nafion® 117 are report in refs.[25,26].

Downloaded by [Chulalongkorn University] at 18:50 07 January 2013

CONCLUSIONS

The sulfonated poly(ether ketone ether sulfone)s show a high glass transition temperature and a higher heat resistance in the solid state. The S-PEKES membranes with the highest DS and water uptake (%) values possess comparable proton conductivity values but with lower methanol permeability than those of the Nafion 117 membrane. In particular, its methanol permeability, 1×10^{-7} cm^2 s^{-1}, is much lower than that of the Nafion 117 membrane, 1.4×10^{-6} cm^2 s^{-1}, at a room temperature. In addition, the oxidative stabilities and the storage moduli (G′) of all the S-PEKES and S-PEEK 150XF membranes are better than those of Nafion 117. These results show that the S-PEKES and S-PEEK 150XF membranes are potential candidates for the application in direct methanol fuel cells operating at medium temperatures. The S-PEKES-B membrane shows superior properties than those of the S-PEKES-A and S-PEEK 150XF membranes.

ACKNOWLEDGMENTS

The authors would like to acknowledge the financial supports from the Conductive and Electroactive Research Unit of Chulalongkorn University, the Thailand Research Fund (TRF-BRG, TRF-RTA, PHD/0081/2549), and the Royal Thai Government.

REFERENCES

1. Carette, L.; Friedrich, K.A.; Stimming, U. Fuel cells—Fundamentals and applications. Fuel Cells **2001**, *1*, 5–39.
2. Neburchilov, V.; Martin, J.; Wang, H.; Zhang, J. A review of polymer electrolyte membranes for direct methanol fuel cells. J. Power Sour. **2000**, *169*, 221–238.
3. Li, L.; Zhang, J.; Wang, Y. Sulfonated poly(ether ether ketone) membranes for direct methanol fuel cell. J. Membr. Sci. **2003**, *226*, 169–167.
4. Gil, M.; Ji, X.; Li, X.; Na, H.; Hampsey, J.E.; Lu, Y. Direct synthesis of sulfonated aromatic poly(ether ether ketone) proton exchange membranes for fuel cell applications. J. Membr. Sci. **2004**, *234*, 75–81.
5. Huang, R.Y.M.; Shao, P.; Burns, C.M.; Feng, X. Sulfonation of poly(ether ether ketone) (PEEK): kinetic study and characterization. J. Appl. Polym. Sci. **2001**, *82*, 2651–2660.
6. Javaid, Z.S.M. Preparation and characterization of composite membranes using blends of SPEEK/PBI with boron phosphate. Electrochim. Acta **2005**, *50*, 4771–4777.
7. Kaliaguine, S.; Mikhailenko, S.D.; Wang, K.P.; Xing, P.; Robertson, G.; Guiver, M. Properties of SPEEK based PEMs for fuel cell application. Catal. Today **2003**, *82*, 213–222.
8. Li, X.; Wang, Z.; Lu, H.; Zhao, C.; Na, H.; Zhao, C. Electrochemical properties of sulphonated PEEK used ion exchange membranes. J. Membr. Sci. **2005**, *254*, 147–155.
9. Li, X.; Zhao, C.; Lu, H.; Wang, Z.; Jiang, W.; Na, H. Preparation of a new type of ion-exchange membrane basec on sulfonated poly(eher ether ketone ketone)s. J. Appl. Polym. Sci. **2005**, *98*, 2481–2486.
10. Mikhailenko, S.D.; Robertson, G.P.; Guova, M.D.; Kaliaguine, S. Properties of PEMs based on cross-linked sulfonated poly(ether ether ketone). J. Membr. Sci. **2006**, *285*, 306–316.
11. Mikhailenko, S.D.; Wang, K.; Kaliaguine S.; Xing, P.; Robertson, G.P.; Guiver, M.D. Proton conducting membranes based on cross-linked sulfonated poly(ether ether ketone) (SPEEK). J. Membr. Sci. **2004**, *223*, 93–99.
12. Reyna-Valencia, A.; Kaliaguine, S.; Bousmina, M. Structural and mechanical characterization of poly(ether ether ketone) (PEEK) and sulfonated PEEK films: effects of thermal history, sulfonation, and preparation conditions. J. Appl. Polym. Sci. **2006**, *99*, 756–774.
13. Wang, F.; Li, J.; Chen, T.; Xu, J. Synthesis of poly(ether ether ketone) with high content of sodium sulfoante groups and its membrane characteristics. Polymer **2003**, *40*, 795–799.
14. Wang, Z.; Ni, H.; Zhao, C.; Li, X.; Fu, T.; Na, H. Investigation of sulfonated poly(ether ether ketone sulfone/Heteropolyacid composite membranes for high temperature fuel cell applications. J. Polym. Sci. Pol. Phys. **2006**, *44*, 1967–1978.
15. Xing, P.; Robertson, G.P.; Guiver, M.D.; Mikhailenko, S.D.; Wang, K.; Kaliaguine, S. Synthesis and characterization of sulfonated poly(ether ether ketone) for proton exchange membranes. J. Membr. Sci. **2004**, *229*, 95–106.
16. Rao, V.L.; Sabeena, P.U.; Ninan, K.N. Synthesis properties of polyetherketone and polyetherketonesulfone copolymers. Eur. Polym. J. **1998**, *34*, 567–570.
17. Changkhamchom, S.; Sirivat, A. Synthesis and properties of sulfonated poly(ether ketone ether sulfone) (S-PEKES) via bisphenol S: effect of sulfonation. Polym. Bull. **2010**, *65*, 265–281.
18. Unnikrishnan, L.; Nayak, S.K.; Mohanty, S.; Sarkhel, G. Polyethersulfone membranes: the effect of sulfonation on the properties. Polym.-Plast. Technol. Eng. **2010**, *49*, 1419–1427.
19. Mukomaa, P.; Joosteb, B.R.; Vosl, H.C.M. A comparison of methanol permeability in Chitosan and Nafion 117 membranes at high to medium methanol concentrations. J. Membr. Sci. **2004**, *243*, 293–299.
20. Shang, X.Y.; Shu, D.; Wang, S.J.; Xiao, M.; Meng, Y.Z. Fluorene-containing sulfonated poly(arylene ether 1,3,4-oxadiazole) as proton-exchange membrane for PEM fuel cell application. J. Membr. Sci. **2007**, *291*, 140–147.
21. Sengul, E.; Erdener, H.; Akay, R.G.; Yucel, H.; Bac, N.; Eroglu, I. Effects of sulfonated polyether-etherketone (SPEEK) and composite membranes on the proton exchange membrane fuel cell (PEMFC) performance. Int. J. Hydrogen Energ. **2009**, *34*, 4645–4652.
22. Do, K.T.N.; Kim, D. Comparison of homogeneously and heterogeneously sulfonated polyetheretherketone membranes in preparation, properties and cell performance. J. Power Sour. **2008**, *185*, 63–69.
23. Fontananova, E.; Trotta, F.; Jansen, J.C.; Drioli, E. Preparation and characterization of new non-fluorinated polymeric and composite membranes for PEMFCs. J Membrane Sci. **2010**, *348*, 326–336.
24. Beatie, P.D.; Orion, F.P.; Basura, V.I.; Zychowska, K.; Ding, J.; Chuy, C.; Scmeisser, J.; Holdcroft, S. Ionic conductivity of proton exchange membranes. J. Electroanal. Chem. **2001**, *503*, 45–56.
25. Xue, S.; Yin, G. Methanol permeability in sulfonated poly(etherether-ketone) membranes: A comparison with Nafion membranes. Eur. Polym. J. **2006**, *42*, 776–785.
26. Li, H.; Zhang, G.; Ma, W.; Zhao, C.; Zhang, Y.; Han, M.; Zhu, J.; Liu, Z.; Wu, J.; Na, H. Composite membranes based on a novel benzimidazole grafted PEEK and SPEEK for fuel cells. Int. J. Hydrogen Energ. **2010**, *35*, 11172–11179.
27. Zhong, S.; Fu, Z.; Dou, Z.; Zhao, C.; Na, H. Preparation and evaluation of proton exchange membrane based on cross-linkable sulfonated poly(ether ether ketone)s. J. Power Sour. **2006**, *162*, 51–57.
28. Pascual, A.M.D.; Martinez, G.; Gomez M.A. Synthesis and characterization of poly(ether ether ketone) derivatives obtained by carbonyl reduction. Macromolecules **2009**, *42*, 6885–6892.
29. Furtado Filho, A.A.M.; Gomes, A.D.S. Crosslinked sulfonated polysulfone-based polymer electrolyte membranes induced by gamma ray irradiation. Int. J. Polym. Mater. **2010**, *59*, 424–437.

30. Kim, D.S.; Robertson, G.P.; Kim, Y.S.; Guiver, M.D. Copoly(arylene ether)s containing pendant sulfonic acid groups as proton exchange membranes. Macromolecules **2009**, *42*, 957–963.
31. Liu, B.; Robertson, G.P.; Kim, D.; Guiver, M.D.; Hu, W.; Jiang, Z. Aromatic poly(ether ketone)s with pendant sulfonic acid phenyl groups prepared by a mild sulfonation method for proton exchange membranes. Macromolecules **2007**, *40*, 1934–1944.
32. Guhan, S.; Sangeetha, D. Evaluation of sulfonated poly(ether ether ketone) silicotungstic acid composite membranes for fuel cell applications. Int. J. Polym. Mater. **2009**, *58*, 87–98.

Downloaded by [Chulalongkorn University] at 18:50 07 January 2013

Highly Electroresponsive Polymer Blends of Polyaniline Nanoparticles and Chloroprene Rubbers

R. KUNANURUKSAPONG, A. SIRIVAT

The Petroleum and Petrochemical College, Chulalongkorn University, Bangkok, Thailand, 10330

Received: August 21, 2011
Accepted: June 27, 2012

ABSTRACT: Polymer blends between polyaniline (PANI) nano/large particles and chloroprene rubbers were fabricated and investigated as the electroresponsive materials. The effects of the chloroprene type, particle size, particle concentration, and electric field strength on the electrical properties, the storage modulus sensitivity, and the dielectrophoresis force were studied. Chloroprene W provides the highest storage modulus sensitivity at 55% and is chosen as the matrix. The electrical conductivity and the dielectric constant of the blends increase with an increasing concentration of PANI nano/large particles. The storage modulus of the blends (with and without the electric field) increases linearly with the PANI content. The maximum storage modulus sensitivities of the blends with PANI nano and large particles at $E = 2$ kV/mm are 73% at 0.01 vol% and 63% at 0.1 vol%, respectively. The dielectrophoresis force of all specimens increases monotonically with increasing electric field strength. The blends with PANI-nano and large particles at 0.01 vol% generate higher dielectrophoresis forces than those of the pure chloroprene W. For the 0.1 vol% of PANI nano and large particles, the resultant deflection angle and dielectrophoresis forces are lower than those of the 0.01 vol% systems and the pure chloroprene W, presumably due to the diminishing resultant dipole moments generated with increasing PANI concentration. © 2012 Wiley

Correspondence to: A. Sirivat; e-mail: anuvat.s@chula.ac.th.

Advances in Polymer Technology, Vol. 32, No. S1, E556–E571 (2013)
© 2012 Wiley Periodicals, Inc.

Periodicals, Inc. Adv Polym Techn 32: E556–E571, 2013; View this article online at wileyonlinelibrary.com. DOI 10.1002/adv.21301

KEY WORDS: Chloroprene rubbers, Dielectrophoresis force, Electroresponsive polymer, Polyaniline nanoparticles, Storage modulus sensitivity

Introduction

Electroresponsive polymeric materials are the new materials that can transform electrical energy directly into a mechanical response.[1,2] They provide promising and novel characteristics: lightweight, high mechanical efficiency and high flexibility. They have been continuously developed for a variety of applications such as muscle-/insect-like actuators, robotics, and drug releases. The most important type of electroresponsive material is the electroactive polymer,[3] which can be divided into the following eight types [1,4]: piezoelectric polymers such as PVDF (polyvinylidine fluoride); dielectric elastomers such as polyurethane or polydimethyl siloxane (PDMS); electroactive celluloses; liquid crystal elastomers; ionic polymer gels; ionomeric polymer–metal composites; conductive polymers; and carbon nanotubes.

Dielectric elastomers are electric field–activated polymers that are capable of producing large strains, fast response, and relatively high efficiency.[1] Examples of the dielectric elastomers are acrylic elastomers, silicone rubbers, polyurethane rubbers, and so on. In particular, chloroprene rubbers are one of the dielectric materials that have many advantages over other dielectric elastomers: high dielectric constants, good electrical properties, high chemical resistance, and ease of processing.[5,6] These properties are suitable for allowing large actuation strains when subjecting the material to an electric field.

Conductive polymers[7] are intrinsically conducting polymers without the presence of any conductive filler. Among many conductive polymers such as poly(*p*-phenylene), polythiophene, poly(*p*-phenylene vinylene), *polyaniline* (PANI) is the most well-known polymer that has many advantageous properties and is widely used in many applications.[8] Chuapradit et al.[9] prepared the composite materials between PANI and zeolite Linde Type A (LTA) for use as CO-sensing materials. Hiamtup et al.[10] prepared the electrorheological fluid from the PANI suspended in silicone medium under an applied electric field. Kaneto et al.[11] fabricated the electroresponsive film from doped PANI films coated on the metal electrode.

Recently, the synthesis of nanoconductive polymers has been of interest to generate new and novel materials. Kim et al.[12,13] synthesized a PANI nanoparticle using the micellar polymerization. The particle size varied between 60 and 80 nm. Zhang and Liu[14] synthesized PANI hollow nanoparticles from the γ-Fe_2O_3 template.[14]

Nowadays, the combination of conductive nanoparticle and elastomer matrices has been of interest for improving the overall properties of the blends such as the composites between styrene butadiene rubber filled with multiwall carbon nanotubes,[15] polystyrene–isoprene core–shell nanoparticles in styrene butadiene rubber,[16] silica nanoparticles embedded in polypropylene–polyethylene blends,[17] and the gold nanoparticle composites with electroactive cellulose.[18]

In our work, we fabricated the blends of PANI and chloroprene rubbers as electroresponsive materials. We investigated the effects of particle size, particle concentration, and electric field strength on electrical and electromechanical properties. For the effect of the particle size, we compared properties of the blends of PANI nanoparticles in chloroprene with the blends of PANI large particles in chloroprene. The electrical conductivity and dielectric constant of the conductive PANI particles are tailored in such a way to have nearly the same value.

Experimental

MATERIALS

An aniline solution (AR grade, Loba Chemie; Mumbai, India) was used as the monomer. Sodium lauryl sulfate (SDS), $C_{12}H_{25}NaO_4S$ (AR grade; Loba Chemie), was used as the surfactant. Ammonium

persulfate, $(NH_4)_2S_2O_8$ (AR grade, Rankem Chemical; Faridabad, India), was used as the initiator. Hydrochloric acid (AR grade; Lab-Scan) was used as the dopant. 1-Methyl-2-pyrrolidone (AR grade; Fluka Chemika) was used in dissolving PANI particles. Benzene (AR grade, Panreac Sintesis; Barcelona, Spain) was used as the solvent for casting films.

Chloroprene elastomers (Neoprene W: WM-1, WHV, and WRT) were provided by Chemical Innovation, Bangkok, Thailand. The silicone oil, poly(dimethylsiloxane) 200 fluid, was supplied by Dow Corning, Bangkok, Thailand. The oil had a kinematic viscosity of 100 cSt and was used as the medium in the deflection experiments.

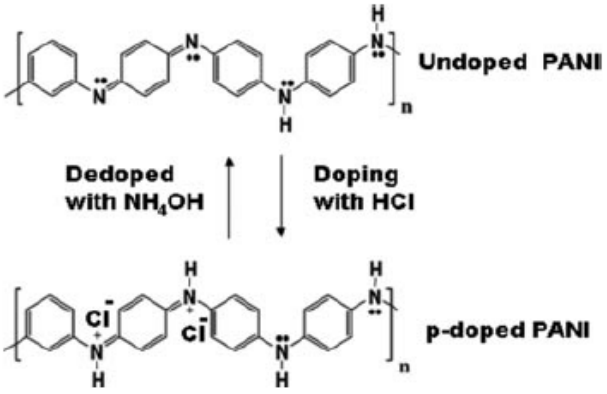

SCHEME 1. Chemical structure of undoped and p-doped PANI with HCl.

SYNTHESIS OF PANI NANO AND LARGE PARTICLES

In this work, the PANI nanoparticles were synthesized following the procedure of Kim et al.[12,13] using the aniline monomer, ammonium persulfate, and SDS. The reaction was carried out in an Erlenmeyer flask connected with a mechanical stirrer. The 0.1 M HCl solution was prepared from 10 M HCl (AR grade). 19.6 g of SDS was added into 100 mL of 0.1 M HCl solution with mechanical stirring at 500 rpm for 30 min, generating the micelles. After 30 min, 5.5 g of the aniline monomer was added into this mixture solution. 0.98 g of ammonium persulfate was dissolved with 10 mL of 0.1 M HCl solution and added dropwise at the rate of 1 mL/min into the previously obtained mixture solution. The reaction was performed at 20 ± 1°C with mechanical stirring at 500 rpm for 12 h.

After 12 h, an excess amount of methanol was added into the mixture to precipitate PANI nanoparticles by breaking the SDS micelles and to stop the reaction.[12] The precipitated powder was collected in a glass filter and washed two times each with methanol, acetone, and pure water until the washing solution became colorless.[12,13] Then, the PANI particles were dried in a vacuum oven for 48 h at 60°C.[12] The chemical structures of PANI are shown in Scheme 1.

The PANI large particles were synthesized following the procedures of Hiamtup et al.[7] and Cao et al.[19] using aniline as the monomer and ammonium persulfate as the initiator. 0.98 g of ammonium persulfate was dissolved into 10 mL of 0.1 M HCl solution and added dropwise at the rate of 1 mL/min into the mixture solution between 5.5 g of the aniline monomer and 100 mL of 0.1 M HCl. The reaction was performed at 0°C with mechanical stirring at 500 rpm for 12 h. Then the PANI powder was collected in a glass filter and washed two times each with methanol, acetone, and pure water until the washing solution became colorless.[7] Then, the PANI particles were dried in the vacuum oven for 48 h at 60°C.[7]

In this work, the specific electrical conductivities of conductive particles that were added into the chloroprene matrix remained the same. The PANI large particles were required to be dedoped with NH_4OH and then doped again with HCl to adjust the electrical conductivity. Dried PANI large particles were dedoped by suspending them in 100 mL of 0.1 M of NH_4OH at room temperature for 4 h.[7] After 4 h, the dedoped powders were filtered out by using a funnel and dried at 27°C under vacuum for 24 h.[7]

The dedoped PANI large particles were again doped by immersing in the HCl solution. The mixture was stirred at 0°C for 24 h.[9] The mole of HCl (N_{acid}) varied against the mole of monomer ($N_{monomer}$). The N_{acid}:$N_{monomer}$ was 150:1, 100:1, 80:1, 50:1, and 20:1. The doped PANI large particles were filtered out by using a funnel and dried at 27°C under vacuum for 24 h.[9] The chemical structures of the dedoped and doped PANI are shown in Scheme 1.

PREPARATION OF CHLOROPRENE FILMS AND POLYMER BLENDS

All specimens were fabricated through solution casting. Chloroprenes W, WHV, WRT and WM-1 were dissolved in benzene at 20% vol/vol. The solutions were cast onto a mold (diameter 25 mm,

thickness 1 mm), and the solvent was eliminated under a vacuum atmosphere at 300 K for 72 h.

The blends were prepared by the mechanical blending of PANI nano/large particles and chloroprene W. Chloroprene W was dissolved in 70 cm^3 of benzene and stirred for about 12 h. Then PANI particles were added and the mixture was stirred overnight. The dispersion of particles appeared to be homogeneous. Concentrations of the PANI nano/large particles in chloroprene W were 0.0001, 0.001, 0.01, 0.1, 1, 1, and 10% vol/vol. The films were cast in a mold and left in the vacuum oven to remove bubbles at 27°C for 24 h.

CHARACTERIZATION AND TESTING

The dedoped PANI large particles and doped PANI nano/large particles were characterized by a FT-IR spectrometer and UV–vis spectrometer to identify their functional groups. The FT-IR spectrometer (Thermo Nicolet, Nexus 670; Thermo Scientific, USA) was operated in the absorption mode with 32 scans and at a resolution of ±4 cm^{-1}, covering a wave number range between 400 and 4000 cm^{-1}, using a deuterated triglycine sulfate detector. Optical-grade KBr (Carlo Erba reagent) was used as the background material. The PANI powder was intimately mixed with dried KBr at a ratio of PANI:KBr = 1:20.

The UV–vis spectra of PANI nano/large particles were recorded with a UV–vis absorption spectrometer (Perkin-Elmer Lambda 10; Perkin-Elmer, Waltham, MA). Measurements were taken in the absorbance mode in the wavelength range of 200–700 nm. Synthesized PANI particles were grinded into a fine powder and dissolved in 1-methyl-2-pyyroridone. The scan speed was 50 mm/min, using a deuterium lamp as the light source.

The specific density (ρ_p) of the PANI nano and large particles was measured by using a glass pycnometer of 25 mL (Labor- und Messgerate GmbH Stutzerbach, Jena, Germany). The specific density (ρ_p) of chloroprene W, given in the product technical information sheet of Dupont Co. Ltd., is 1.23 g/cm^3.

The morphologies of PANI and blends were observed by a scanning electron microscope (SEM; Hitachi, S-4800). The scanning electron micrographs were obtained by using an acceleration voltage of 5–10 kV at various magnifications between 40,000× and 100,000×. The specimens were stacked onto stubs by using sticker carbon papers and were coated with platinum using an ion-coating machine (Hitachi, E-1010; Hitachi High-Technologies Corporation, Tokyo, Japan) at 90 s, for enhancing the electron conductivity. The photographs at the magnification of 100,000× were captured to measure the particle size of PANI nanoparticles in the W:PANI nano blends using Scion Image software (version 4.0.3).

The particle sizes of doped PANI large particles were determined by using a particle size analyzer (Malvern Instruments, Masterizer X version 2.15; Malvern Instruments Ltd., Malvern, UK). Forty-five mm diameter lenses were used in this experiment. The sample was placed in a sample cell across a laser beam. This instrument measures the average particle size and size distribution.

Volume electrical conductivities of the synthesized PANI were measured by a two-point probe-making contact with a surface of the sample. The probes were connected to a source meter (Keithley, model 6517A; Keithley Instruments Inc., Cleveland, OH) for a constant voltage source and for reading the current. The applied voltage and resultant current in the linear Ohmic regime were converted to the volume electrical conductivity of the polymer using Eq. (1)

$$\sigma_V = \frac{1}{\rho} = \frac{1}{R_s \times t} = \frac{I}{K \times V \times t} \tag{1}$$

where σ_V is the volume conductivity (S/cm), ρ is the specific resistivity (Ω·cm), R_s is the sheet resistivity (Ω), I is the measured current (A), K is the geometric correction factor, V is the applied voltage (voltage drop) (V), and t is the pellet thickness (cm).

The geometrical correction factor was taken into account for geometric effects, depending on the configuration and probe tip spacing and determined by using standard materials, silicon wafer chips (SiO_2), whose specific resistivities were known. In our case, the sheet resistivity was measured by using the two-point probe and the geometric correction factor was calculated by using Eq. (2)

$$K = \frac{\rho}{R \times t} = \frac{I \times \rho}{V \times t} \tag{2}$$

where K is the geometric correction factor, ρ is the known resistivity of the standard silicon wafer

(Ω·cm), t is the film thickness (cm), R is the film resistance (Ω), and I is the measured current (A).

Electrical conductivities of chloroprene rubbers and blend films were measured by a meter that consists of a resistivity test fixture (Keithley, Cleveland, model 8009). The probes were connected to a source meter (Keithley, model 6517A) for a constant voltage supply and for reading the current. The applied voltage and resultant current in the linear Ohmic regime were converted to the volume electrical conductivity of polymer using Eq. (3)

$$\sigma_V = \frac{t \times I}{22.9 \times V} \tag{3}$$

where 22.9 is the geometric correction factor of the test fixture.

The dielectric constants were measured by using an LCR meter (HP, model 4284A; Fotronic Corporation, Melrose, MA) connected to the rheometer (Rheometric Scientific, ARES; TA Instruments, New Castle, DE) with a 25-mm parallel plate fixture. The thickness of the specimens is typically 1 mm, and the diameter is about 25 mm. The top and bottom sides of the specimens were coated with silver adhesive to improve the electrical contact between the specimens and the electrodes. The measurements were carried out at a temperature of 300 K. The AC voltage applied was varied between 1 and 10 V, depending on the materials. The dielectric constant at a frequency of 20 Hz will be referred to as the dielectric constant of the materials.

A melt rheometer (Rheometric Scientific, ARES) was used to measure rheological properties. It was fitted with a custom-built copper parallel plate fixture (diameter of 25 mm). A DC voltage was applied with a DC power supply (Instek, GFG 8216A; GW Instek, Chino, CA), which can deliver an electric field strength of up to 2 kV/mm. In the experiments, the oscillatory shear strain was applied and the dynamic moduli (G' and G'') were measured as a function of the frequency and electric field strength. Strain sweep tests were first carried out to determine the suitable strain to measure G' and G'' in the linear viscoelastic regime. The appropriate strain was determined to be at 1.0% for all specimens. Then frequency sweep tests were carried out to measure the G' and G'' of each sample as a function of the frequency. The deformation frequency was varied from 0.1 to 100 rad/s. Experiments were carried out at the temperature of 300 K and repeated at least two or three times. The temporal response experiments were carried out at 1 and 2 kV/mm for pure

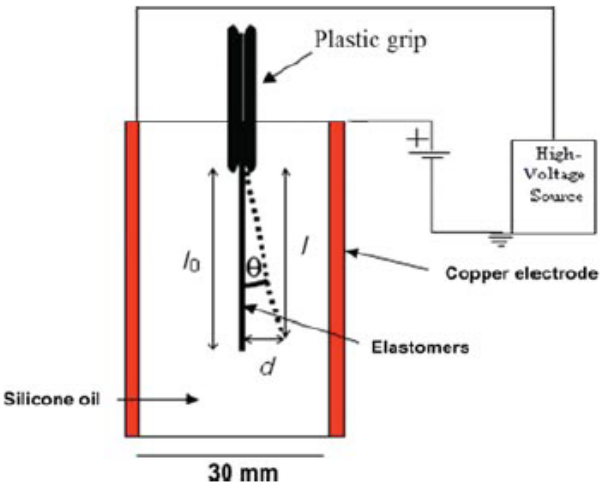

FIGURE 1. Experimental setup for the deflection measurement.

Chloropene W, and for the polymer blend PANI:W at 0.01 and 0.1 vol%.

The dielectrophoresis forces were determined by measuring the deflection distances of the elastomers in the vertical cantilever fixture under electric field. (The experimental setup is shown in Fig. 1.) The specimens were vertically immersed in the silicone oil (viscosity = 100 cSt) between parallel copper electrode plates (40 mm long, 30 mm wide, and 1 mm thick). The gap between the pair of electrodes was 30 mm. A DC voltage was applied with a DC power supply (Goldsun, GPS 3003B) connected to a high voltage power supply (Gamma High Voltage; model UC5-30P, Gamma High Voltage Research, Ormond Beach, FL), which can deliver an electric field of up to 25 kV. The output voltage from the high voltage power supply was calibrated using a Fluke 40 kV high voltage probe. A CCD video camera was used to record the movement during the experiment. Photographs were obtained from the video camera, and the deflection distances on x (d) and y axes (l) at the ends of the specimen were determined by using the Scion Image software (version 4.0.3). The electric field strength was varied between 0 and 600 V/mm at room temperature, 300 ± 1 K. We calculated the resisting elastic force of the specimens under the electric field using the nonlinear deflection theory of a cantilever,[20–24] which can be calculated from the standard curve between $F_e l_0^2 / E I$ and d/l_0, where l_0 is the initial length of specimens,[24] F_e is the elastic force, d is the deflection distance in the horizontal axis, l is the deflection distance in the vertical axis, E is the Young's modulus—which

is equal to $2G(1 + \nu)$, where G is the shear storage modulus taken to be G' ($\omega = 1$ rad/s, E) at various electric field strengths, ν is the Poisson's ratio (0.5 for an incompressible sample)—and I is the moment of inertia $1/12t^3w$, where t is the thickness of the film and w is the width of the film. The dielectrophoresis force can be calculated from the static horizontal force balance consisting of the elastic force and the corrective gravity force term ($mg \sin\theta$):

$$F_d = F_e + mg \sin\theta \tag{4}$$

where g is $= 9.8\ \mathrm{m \cdot s^{-2}}$, m is the mass of the specimen, and θ is the deflection angle.

Results and Discussion

CHARACTERIZATION OF PANI

FT-IR spectra of the PANI nano/large particles were taken to identify the characteristic absorption peaks.[25,26] The doped PANI nano/large particles show the same characteristic peaks at 3000–2800 cm^{-1}, which can be assigned to the stretching vibration of the C–H bond on the benzene ring; the peaks at 1570 and 1460 cm^{-1} represent the C–N stretching of the benzenoid and quinoid rings on the PANI backbone; the peak at 1293 cm^{-1} represents the C–N stretching of the secondary amine group; the peak at 1242 cm^{-1} is the characteristic peak of the PANI emeraldine salt; and the peak at 1120 cm^{-1} represents the vibration of C–H on the protonated quinoid ring.[15,25,26] After dedoping with NH_4OH, the characteristic peak at 1120 cm^{-1} is shifted to a higher wave number at 1160 cm^{-1} which can be referred to as the C–H stretching of a nonprotonated quinoid or dedoped form.[26]

UV–visible absorption spectra of dedoped PANI large particles show only one absorbance peak at 350 nm corresponding to the benzoid ring on the PANI backbone.[27] After the doping, PANI nano and large particles show the same absorbance peak of the π–π^* transition of the benzoid ring at 325 nm[27] and the absorbance peak at 630 nm representing the formation of the emeraldine salt structure (doped form) on the polymer chain.[27]

Morphology and particle sizes of specimens were observed using a SEM. The morphology of pure chloroprene W is shown in Fig. 2a. Figures 2b and 2c show the shapes of the PANI nanoparticles and the doped PANI large particles at N_{acid}:$N_{monomer} = 80{:}1$, respectively. The PANI nanoparticles are of a spherical shape, whereas the large particles are quite irregular in shape. The particle size of PANI nanoparticles measured using a SEM is 76.10 nm, with a standard deviation of 17.63 nm. The particle size of doped PANI-large particles measured using the particle size analyzer is 30.04 μm, with a standard deviation of 1.61 μm. Kim et al.[12,13] reported the

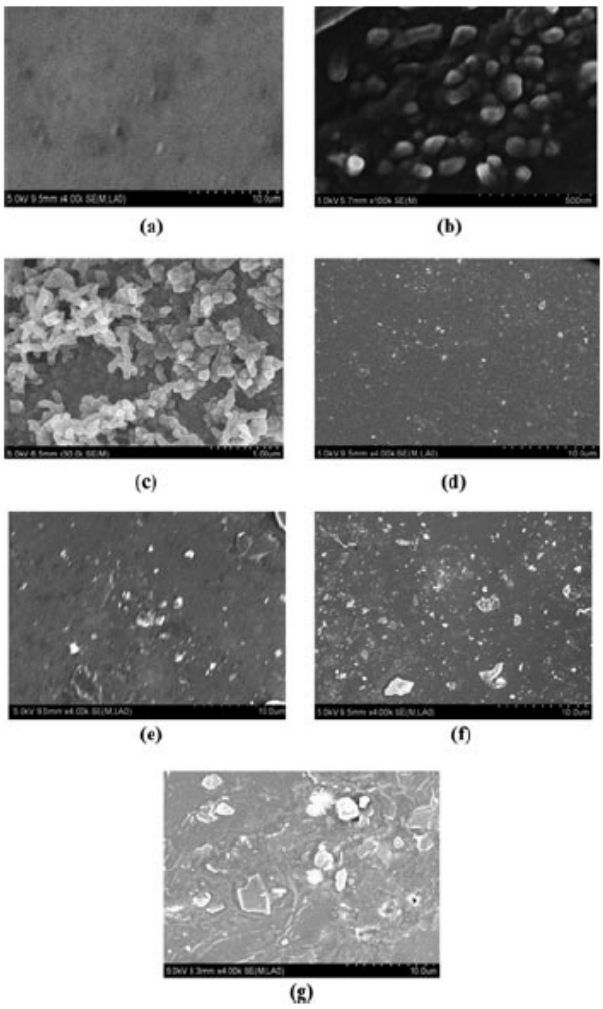

FIGURE 2. SEM images of specimens at 10 kV: (a) pure chloroprene W at a magnification of 4000×; (b) PANI nanoparticles at the magnification of 100,000×; (c) doped PANI large particles (N_{acid}:$N_{monomer} = 80{:}1$) at the magnification of 30,000×; (d) W:PANI nano 0.01 vol% at a magnification of 4000×; (e) W:PANI large particles 0.01 vol% at the magnification of 4000×; (f) W:PANI nano 10 vol% at the magnification of 4000×; and (g) W:PANI large 10 vol% at the magnification of 4000×.

average diameter of the synthesized PANI nanoparticles to be between 60 and 80 nm. Hiamtup et al.[10] reported the average diameter of the synthesized PANI large particles to be 23.5 μm, with a standard variation of 2.37 μm. Figures 2d–2g show the SEM images of the polymer blend between chloroprene W and PANI nano/large particles. At a low percentage concentration (0.01 vol%), the PANI particles are dispersed uniformly within the chloroprene matrix but at a high percentage concentration (10 vol%), the particles appear to be more aggregated. The particle sizes of PANI nanoparticles in the blends of 0.01 and 10 vol% were measured using the SEM images (Figs. 2d and 2f) and are 242 and 1380 nm, with a standard deviation of 52.41 and 430.57 nm, respectively. From the SEM images, the particle size of the dispersing PANI nanoparticles in the polymer blends is always less than that of the dispersing PANI large particles.

The specific densities of PANI nanoparticles and doped PANI-large particles (N_{acid}:$N_{monomer}$ = 80:1) are 1.36 and 1.34 g/cm^3, with a standard deviation of 0.02 and 0.03, respectively. The specific density of chloroprene W given by Dupont is 1.23 g/cm^3.[27]

The specific conductivity of PANI nanoparticles is 7.58 S/cm, with a standard deviation of 0.06. Zeng and Ko[26] found that the HCl solution acted as the dopant and on the doped PANI particles during the synthesis. The PANI nanoparticles were synthesized via the micellar polymerization in the HCl solution with the electrical conductivity varying between 4 and 10 S/cm.[12,28]

The synthesized PANI large particles were dedoped with NH_4OH[7] before the electrical conductivity measurement. The specific electrical conductivity of the dedoped PANI large particles is 5.28×10^{-6} S/cm, with a standard deviation of 4.24×10^{-4} S/cm. The specific conductivity of doped PANI large particles at N_{acid}:$N_{monomer}$ equaling to 150:1, 100:1, 80:1, 50:1 and 20:1 is 20.15, 12.74, 6.45, 0.92, and 8.77 $\times$ 10^{-2} S/cm, with a standard deviation of 0.18, 1.14, 0.09, 1.22 $\times$ $10^{-2,}$ and 1.58 $\times$ 10^{-3} S/cm, respectively. From these results, the doped PANI large particles at N_{acid}:$N_{monomer}$ = 80:1 were selected and used in comparison with the PANI nanoparticles.

The specific electrical conductivity of the four types of chloroprene rubbers (W, WRT, WM-1, and WHV) is 1.60×10^{-11}, 2.35×10^{-13}, 8.90×10^{-12}, and 3.58×10^{-12} S/cm, with the standard deviation of 3.53×10^{-13}, 9.07×10^{-15}, 2.13×10^{-14}, and 3.05×10^{-14} S/cm, respectively. The specific conductivities of all polymer blends are presented in Table I.

The dielectric constants of chloroprene W, WRT, WM-1, and WHV at T = 300 K and at frequency = 20 Hz are 6.40, 3.25, 6.21, and 5.65, respectively. Matsuo et al.[29] reported the dielectric constant of a polychloroprene to be 5.85 at f = 100 Hz, $T = -12$°C.[29] The dielectric constant of the dedoped PANI large particles, the doped PANI with N_{acid}:$N_{monomer}$ equaling to 80:1, and the doped PANI nanoparticles at T = 300 K and at frequency = 20 Hz, is 3.52, 60.77, and 61.30, respectively. In this work, the dielectric constants of the PANI nano and the large particles (N_{acid}:$N_{monomer}$ = 80:1) are nearly the same. Pant et al.[30] measured the dielectric constant of PANI. They reported that pure PANI doped by HCl had a dielectric constant equaling to 70 at 300 K and 100 Hz.[30] The dielectric constants and specific electrical conductivities of all polymer blends at various PANI concentrations are presented in Table I. From this table, the dielectric constants and the electrical conductivities of W:PANI nano and W:PANI large particles are nearly the same at a low volume percentage of PANI (below 0.1 vol%). But at a high volume percentage of PANI (more than 1 vol%), the electrical conductivities and dielectric constants of the blends with the PANI nano particles are higher than those of the blends with the PANI large particles. This finding might be due to the agglomeration of the PANI large particles in the chloroprene matrix. Peng et al.[31] studied the electrical properties of the epoxy/aluminum nitrate nanocomposites (AIN). They found that the dielectric constant and electrical conductivity of the nanocomposites between epoxy/surface treatments AIN are higher than those of the nanocomposites between epoxy/unsurface treatments AIN at a high volume fraction of AIN particles.[30] They reported the unsurface-treated AIN agglomerated in the epoxy matrix, whereas the surface-treated AIN were dispersed uniformly.[31] Agglomeration of the unsurface-treated AIN could introduce voids or air-trap cavities into the epoxy matrix, which could lead to the poorer electrical properties of composites.[31]

ELECTRORHEOLOGICAL PROPERTIES

Effect of Chloroprene Types

The effect of chloroprene type on the electromechanical properties was investigated at electric field strengths between 0 and 2 kV/mm, T = 300 K. The data are shown in Fig. 3 and presented in

TABLE I
Rheological Properties of Polymer Blends, Strain 1.0%, 27° C, Gap 0.4–0.8 mm

Sample	G'_0 (Pa)	$G'_{2kV/mm}$ (Pa)	$\Delta G'_{2kV/mm}$ (Pa)	$\Delta G'_{2kV/mm}/G'_0$	Specific Electrical Conductivity (S/cm)	ε'
Chloroprene W	11338	17573	6235	0.55	1.60×10^{-11}	6.40
Dedoped PANI large	N/A	N/A	N/A	N/A	4.24×10^{-04}	3.52
Doped PANI nano	N/A	N/A	N/A	N/A	6.45	61.30
Doped PANI large with $N_{acid} : N_{monomer} = 80{:}1$	N/A	N/A	N/A	N/A	7.58	60.77
W:PANI large 0.0001% v/v	13102	16001	2899	0.22	4.16×10^{-10}	6.41
W:PANI large 0.001% v/v	19387	24357	4970	0.26	8.63×10^{-10}	6.43
W:PANI large 0.01% v/v	38283	48109	9084	0.33	8.39×10^{-09}	6.52
W:PANI large 0.1% v/v	41533	60427	18264	0.63	6.54×10^{-08}	6.68
W:PANI large 1% v/v	54433	68151	14524	0.27	8.15×10^{-05}	6.99
W:PANI large 10% v/v	103730	114380	12694	0.12	5.44×10^{-04}	11.05
W:PANI nano 0.0001% v/v	15164	22073	6909	0.46	3.50×10^{-10}	6.43
W:PANI nano 0.001% v/v	38612	61430	22818	0.59	1.06×10^{-09}	6.44
W:PANI nano 0.01% v/v	55540	95920	40380	0.73	2.26×10^{-08}	6.67
W:PANI nano 0.1% v/v	87078	121530	34452	0.40	4.72×10^{-07}	6.80
W:PANI nano 1% v/v	138804	172413	33609	0.24	2.37×10^{-04}	7.12
W:PANI nano 10% v/v	351070	414670	63600	0.18	8.89×10^{-04}	11.86

All of materials were tested at frequency = 1 rad/s, strain 1.0% and, temperature = 27°C.
G'_0, and G''_0 are the storage and loss moduli without electric field.
$G'_{2kV/mm}$, and $G''_{2kV/mm}$ are the storage and loss moduli at 2 kV/mm.
$\Delta G'_{2kV/mm}$ is the storage modulus response defined as $G'_{2kV/mm} - G'_0$.
$\Delta G''_{2kV/mm}$ is the loss modulus response defined as $G''_{2kV/mm} - G''_0$.
$\Delta G'_{2kV/mm}/G'_0$ is the sensitivity of the storage modulus.
$\Delta G''_{2kV/mm}/G''_0$ is the sensitivity of the loss modulus.
ε' is the dielectric constant of polymer at f = 20 Hz.

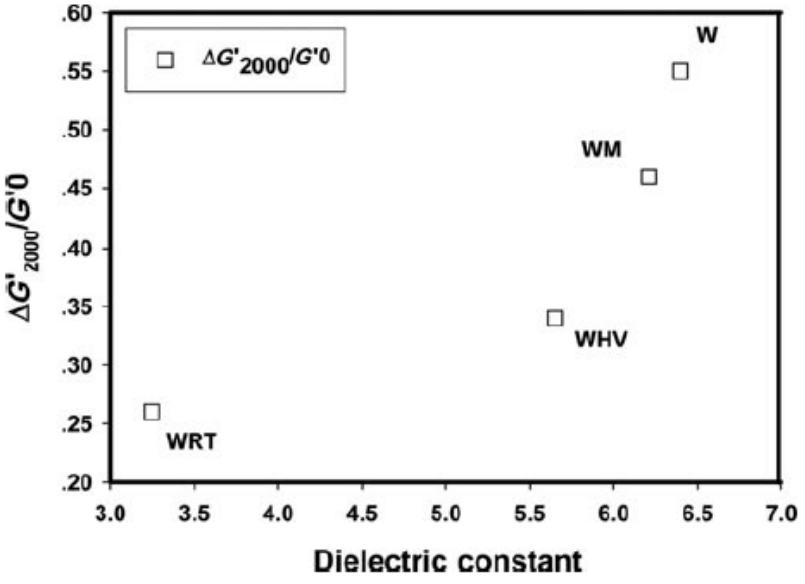

FIGURE 3. Storage modulus responses and sensitivities of four types of chloroprene rubber at E = 2 kV/mm vs. dielectric constant at f = 20 Hz.

TABLE II
Rheological Properties of Four Types of Chloroprene Rubber, Strain 1.0%, 27°C, Gap 0.5–0.8 mm

Sample	G'_0 (Pa)	$G'_{2kV/mm}$ (Pa)	$\Delta G'_{2kV/mm}$ (Pa)	$\Delta G'_{2kV/mm}/G'_0$	Specific Electrical Conductivity (S/cm)	ε'
Chloroprene WRT	54,329	68,708	14,379	0.26	2.35E–13	3.25
Chloroprene WHV	17,133	23,056	5923	0.34	3.58E–12	5.65
Chloroprene WM	35,933	52,522	16,529	0.46	8.90E–12	6.21
Chloroprene W	11,338	17,573	6235	0.55	1.60E–11	6.40

All of materials were tested at frequency = 1 rad/s, strain 1.0%, and temperature = 27°C.
G'_0, and G''_0 are the storage and loss moduli without the electric field.
$G'_{2kV/mm}$, and $G''_{2kV/mm}$ are the storage and loss moduli at 2 kV/mm. $\Delta G'_{2kV/mm}$ is the storage modulus response defined as $G'_{2kV/mm} - G'_0$.
$\Delta G''_{2kV/mm}$ is the loss modulus response defined as $G''_{2kV/mm} - G''_0$, $\Delta G'_{2kV/mm}/G'_0$ is the sensitivity of the storage modulus.
$\Delta G''_{2kV/mm}/G''_0$ is the sensitivity of the loss modulus.
ε' is the dielectric constant of polymer at f = 20 Hz.

Table II. The storage modulus sensitivities of all chloroprene rubbers increase with an increasing dielectric constant. The dielectric constant of chloroprene W is the highest (ε' = 6.40), and it provides the highest storage modulus sensitivity (55%), whereas chloroprene WRT has the lowest dielectric constant and possesses the lowest modulus sensitivity at 3.26% and 26%, respectively. From these results, chloroprene W was selected as the matrix for blending with PANI nano/large particles.

Time Dependence of the Electrorheological Response

The cyclic temporal responses of G' of the blends between pure chloroprene W and PANI nano/large particles at 0.01 vol% were measured by using the melt rheometer (Rheometric Scientific, ARES) under an oscillatory shear mode at E = 2 kV/mm, ω = 1 rad/s, T = 300 K, and strain% = 1.0. The data are shown in Fig. 4 and presented in Table III. In the case of pure chloroprene W, with the electric field turned

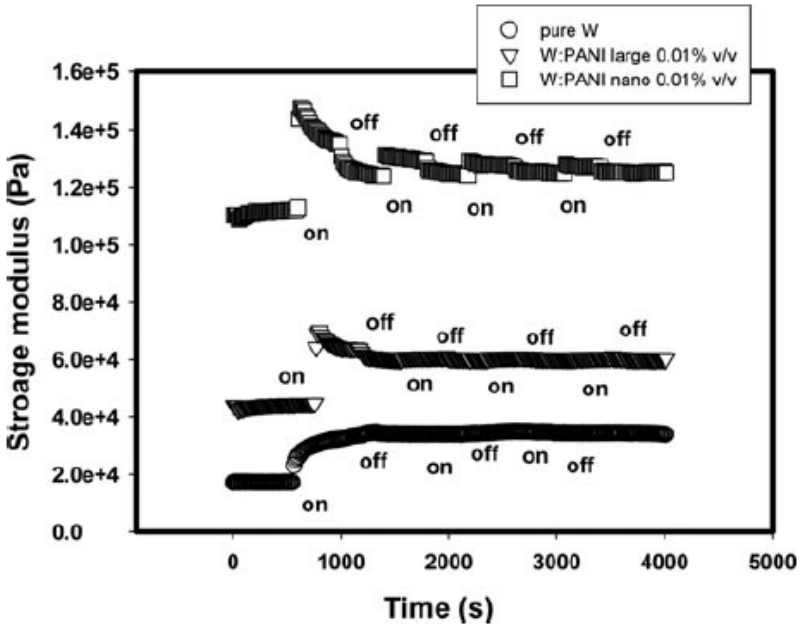

FIGURE 4. Temporal responses of polymer blends between chloroprene W and PANI nano and doped large particles (N_{acid}:$N_{monomer}$ = 80:1) at 0.01% v/v, E = 2 kV/mm, frequency 1.0 rad/s, strain 1.0%, gap 0.5–0.8 mm at 27°C.

TABLE III
Induction Time and Recovery Times of the Polymer Blends between Chloroprene W and PANI Nano and Doped Large Particles (N_{acid}:$N_{monomer}$ = 80:1) at 0.01 v/v%, E = 2 kV/mm, Frequency 1.0 rad/s, Strain 1.0%, Gap 0.5–0.8 mm at 27°C

Samples	Electric Field (kV/mm)	First Induction Time, τ_{ind} (s)	Saturated Induction Time, τ_{ind} (s)	First Recovery Time, τ_{rec} (s)	Saturated Recovery Time, τ_{rec} (s)	First $\Delta G'_{ind}$ (Pa·s)	Saturated $\Delta G'_{ind}$ (Pa·s)	First $\Delta G'_{rec}$ (Pa·s)	Saturated $\Delta G'_{rec}$ (Pa·s)
Pure chloroprene W	2	315	72	254	68	17,300	2,700	2,800	2,200
W:PANI nano 0.01%	2	394	195	247	161	24,200	4,200	10,800	4,100
W:PANI large 0.01%	2	321	105	202	144	21,900	3,800	5,100	3,700

on, the storage modulus increases monotonically toward its maximum value. This is due to the interactions between charges or the dipole moments within the elastomers.[7] As the electric field is removed, the interactions between charges almost vanish and the storage modulus decreases. In the first cycle, the response of chloroprene W is not completely reversible. With the electric field turned on and off periodically during the total experiment period of 4000 s, chloroprene W becomes a nearly reversible system. Chloroprene W has an induction time—the time at which the storage modulus increases and attains a steady-state value—of 72 s and a recovery time—the time at which the storage modulus decreases and reaches a steady-state value—of 68 s in the steady state. In the case of polymer blends with 0.01 vol% of PANI, the storage modulus increases suddenly after turning on the electric field, due to the interactions between the charges in the elastomers and conductive particles.[7] From Table III, the W:0.01% PANI nano system requires a longer induction time and longer recovery time than the W:0.01% PANI large system. The W:0.01% PANI nano system has an induction time of 195 s and a recovery time of 161 s, whereas the W:0.01% PANI large system has an induction time of 105 s and a recovery time of 144 s. The PANI nano particles have smaller sizes and higher surface areas. These facts presumably induce greater charge interactions and require a longer time for the dipole moments to vanish after turning off the electric field.

Effect of the Concentration and Particle Size

The effect of the concentration on the polymer blends between the chloroprene W and PANI nano/large particles is shown in Fig. 5 and presented in Table I. Figure 5a shows the storage moduli of the W:PANI nano system and W:PANI large system at various PANI concentrations without the electric field. Both moduli increase linearly with increasing PANI concentration. The PANI nano/large particles act as the fillers in the chloroprene matrix, leading to the increases in the storage modulus. But the storage modulus of the W:PANI nano system is always higher than the modulus of the W:PANI large particles, due to the better dispersion of the PANI nanoparticles. Meincke et al.[32] compared the mechanical properties of the composite materials between polyamide (PA), carbon nanotubes, and carbon black fillers. At the same volume fraction of fillers, the Young's modulus and the electrical conductivity of the composites between PA and carbon nanotubes were always higher than those of the composites between PA and carbon black fillers.[32]

Under the applied electric field at 2 kV/mm, the storage moduli of the W:PANI nano and the W:PANI large systems increase linearly with increasing electric field strength and volume percentage of particles as shown in Fig. 5b. With the applied electric field, the dipole moments between particles–particles and particles–matrices are generated. This leads to an increase in the material stiffness.[32,34] The storage modulus sensitivity at the electric field strength of 2 kV/mm is 55, 46, 59, 73, 40, 24, and 18% for the pure chloroprene W and the blends of 0.0001, 0.001, 0.01, 0.1, 1, and 10 vol% of PANI nanosystems, respectively. From Table I, the storage modulus sensitivity at the electric field strength of 2 kV/mm is 22, 26, 33, 63, 27, and 12% for the blends of 0.0001, 0.001, 0.01, 0.1, 1, and 10 vol% of the PANI large systems, respectively. The small storage modulus sensitivities at the low volume percentage of particles suggest that the fillers induce only additional free volume, the number of particles is too small, and the distances between particles are too large to create a significant particle interaction through the electric field–induced dipole moments.[33] However the storage modulus sensitivity of the

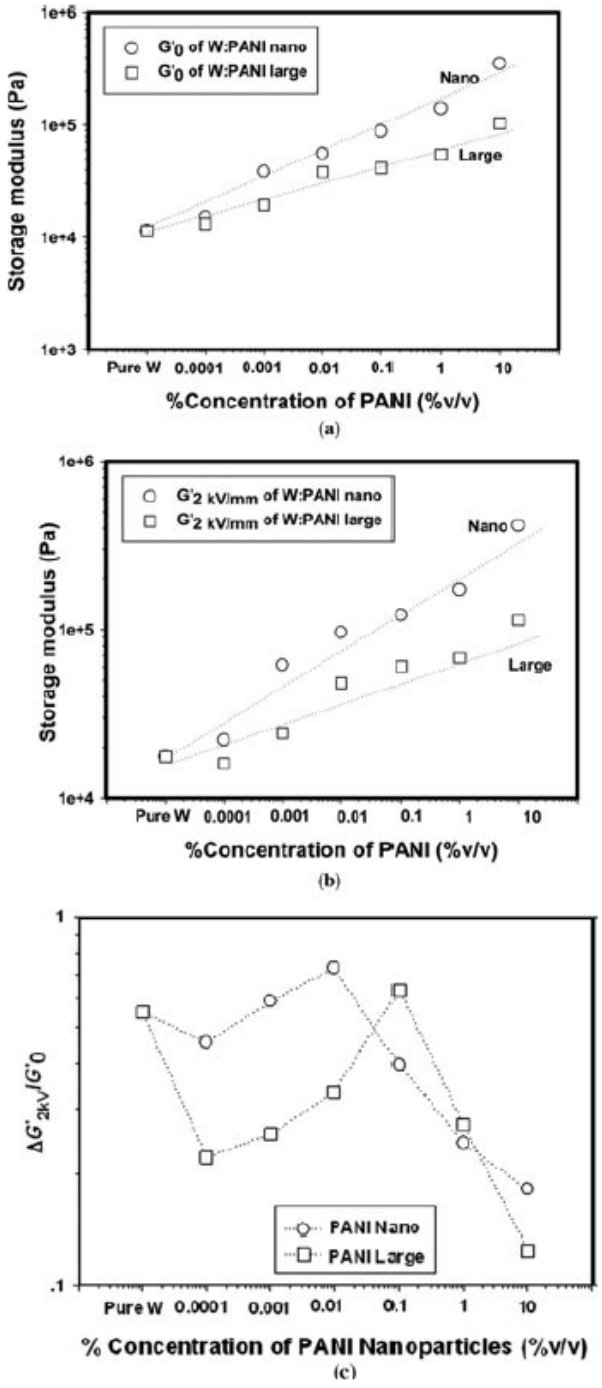

FIGURE 5. Effect of PANI concentrations on the (a) the storage modulus without the electric field; (b) the storage modulus with the electric field 2 kV/mm; (c) storage modulus sensitivities of W:PANI large particles and W:PANI nanoparticles, $E = 2$ kV/mm frequency 1.0 rad/s, strain 1.0%, gap 0.60–0.75 mm at 27°C. 2 kV/mm; (c) showing storage modulus sensitivities.

nanoparticles systems is always higher than those of the large particle systems. The PANI nanoparticles are of smaller sizes and have a better dispersion than that of the PANI large particle system. These lead to the higher sensitivity at low volume percentage of PANI.[32] At high PANI concentrations, the distances between particles–particles and particles–matrices become smaller and stronger as interparticle interactions are generated.[33]

From Fig. 5c, the storage modulus sensitivity of the W:PANI large systems attains the maximum at 0.1 vol%, whereas the storage modulus sensitivity of the W:PANI nanosystems reaches the maximum at 0.01 vol%; this is the effect of dispersion of the PANI nanoparticles.[32] After reaching the maximum point, the sensitivities of both systems decrease with an increasing PANI concentration. With an excess amount of particles, the effect of the electric field appears to diminish because the system is presumably hardened without the electric field applied and the phase separation may exist between the matrix and the particles and consequently a poor stress transfer; an additional increase in the storage modulus with the electric field is hampered.[32]

Kunanuruksapong and Sirivat[33] studied the storage modulus sensitivities of the blends between poly(*p*-phenylene) and acrylic elastomers. The modulus sensitivities increased with particle concentrations and attained maximum of 30 vol% at the $E = 2$ kV/mm.[33] Shiga[34] found the similar effect for the poly(*p*-phenylene) and silicone elastomer blend. The electroviscoelastic effect increased with increasing particle content.[34] Liu and Shaw[35] also reported a similar effect for a silicone/silica elastomer. The enhancement of the shear modulus was negligible below 8.0 vol%, but increased dramatically above this threshold concentration. At volume fraction above 55 vol%, the shear modulus decreased because the interparticle force decreased with the steric hindrance effect.[35]

Deflection of Pure Chloroprene W and Blends

The dimensions of specimens were fixed to neglect the effects of size and weight as presented in Table IV. The resisting elastic forces of the specimens were calculated under the electric field using the nonlinear deflection theory of a cantilever.[20–24] The effects of the DC electric field strength and particle concentration on the deflection angle and dielectrophoresis force were investigated under the

TABLE IV
Dimension and Electromechanical Responses of Specimens at Various DC Electric Field Strengths

Elastomers	Length (l_0) (mm)	Width (mm)	Thickness (mm)	Weight (g)	Electrical Yield Strength (V/mm)	Dielectric Constant (at $f = 20$ Hz)	Maximum Deflection Distance (mm)	Maximum Deflection angle (°)	Maximum F_d (mN)
Pure W	18.72	2.5	0.32	0.045	200	6.40	9.61	41.61	0.295
0.01% PANI nano:W	19.03	2.6	0.25	0.047	75	6.67	11.60	56.45	0.396
0.1% PANI nano:W	18.95	2.4	0.27	0.044	75	6.80	8.33	25.97	0.223
0.01% PANI large:W	18.98	2.9	0.30	0.052	125	6.52	11.50	55.74	0.379
0.1% PANI large:W	19.07	2.7	0.28	0.049	75	6.68	7.34	26.05	0.217

electric field strength between 0 and 600 V/mm at the temperature of 300 ± 1 K. (Photographs of our experiments are shown in Figs. 6a–6e). Initially, all of the specimens are straight at the center of the testing fixture without the electric field as shown in Fig. 1. After applying the DC electric field, the specimens start to deflect toward one of the electrodes. All of our specimens deflect toward the anode side (positive side). The deflection data are presented in Table IV and Fig. 7. The electrical yield strength—the electric field strength required for the materials to start to deflect—of the pure chloroprene W, the 0.01% W:PANI nanosystem, the 0.1% W:PANI nanosystem, the 0.01% W:PANI large system, and the 0.1% W:PANI large system is 200, 75, 75, 125, and 75 V/mm, respectively. These results suggest that the added particles improve the electrical yield strength; the materials require lower electrical energy to respond. From Figs. 7a and 7b, the deflection angle and dielectrophoresis force of all specimens increase with an increasing electric field. The dielectrophoresis force at $E = 600$ V/mm force of the pure chloroprene W, the 0.01% W:PANI nanosystem, the 0.1% W:PANI nanosystem, the 0.01% W:PANI large system, and the 0.1% W:PANI large system is 0.295, 0.396, 0.223, 0.379, and 0.217 mN, respectively. The blend with the PANI-nano/large particles system at 0.01 vol% provides the highest deflection angles and dielectrophoresis force relative to those of the pure chloroprene W.

For the 0.1 vol% of PANI nano/large particles systems, the deflection angles and dielectrophoresis forces are lower than that of the pure chloroprene W and the blends with 0.01 vol% of PANI nano/large particles systems. The storage modulus, stiffness, and rigidity of the polymer blends can be expected to increase with increasing particle concentrations as shown in Fig. 5a. However, above a certain threshold concentration (above 0.01 vol%), the resultant dipole moments generated are diminished, possibly due to the charge cancellations as the distances between the dipole moments are shorter, leading to the lower dielectrophoresis forces.

However, at the same volume percentage of PANI, the nanoparticle systems possess higher dielectrophoresis forces than those of large particle systems due to the better particle dispersion.

Metz et al.[36] investigated the bending behavior of the polymer blends of PVDF and PPy. The bending angle and the bending moment increased linearly with increasing electric field strength.[36] Hiamtup et al.[7] studied the deflection of blends between PANI large particles embedded in cross-linking poly(dimethyl siloxane). All of their specimens deflected toward the anode side.[7] Thongsak et al.[37] measured the deflection angles and dielectrophoresis forces of the pure styrene–isoprene–styrene triblock copolymers (SIS; D1114P) and the blends between SIS D1114P and polydiphenylamine (De_PDPA/D1114P). The De_PDPA/D1114P with 30 vol% of PDPA has a lower deflection angle and lower dielectrophoresis force relative to those of the 10 vol% PDPA blend and pure D1114P.[37]

The chemical structure of chloroprene rubber is shown in Scheme 2. In this case, the deflection direction depends on the internal dipole polarization of the chemical groups on the polymer chains.[36,38] The chemical structures of the chloroprene have many chloride groups attached to the polymer chains. This group can be polarized and store energy under the electric field, which leads to dimensional changes within the polymer.[38,39] In addition, the chloride groups are electrophiles; they can pull electrons from carbon atoms. Under the applied electric field, the polarities of this group become negative and generate the attractive force between unlike charges on the anode electrode and chloroprene rubbers leading to the bending toward the anode side (positive side).

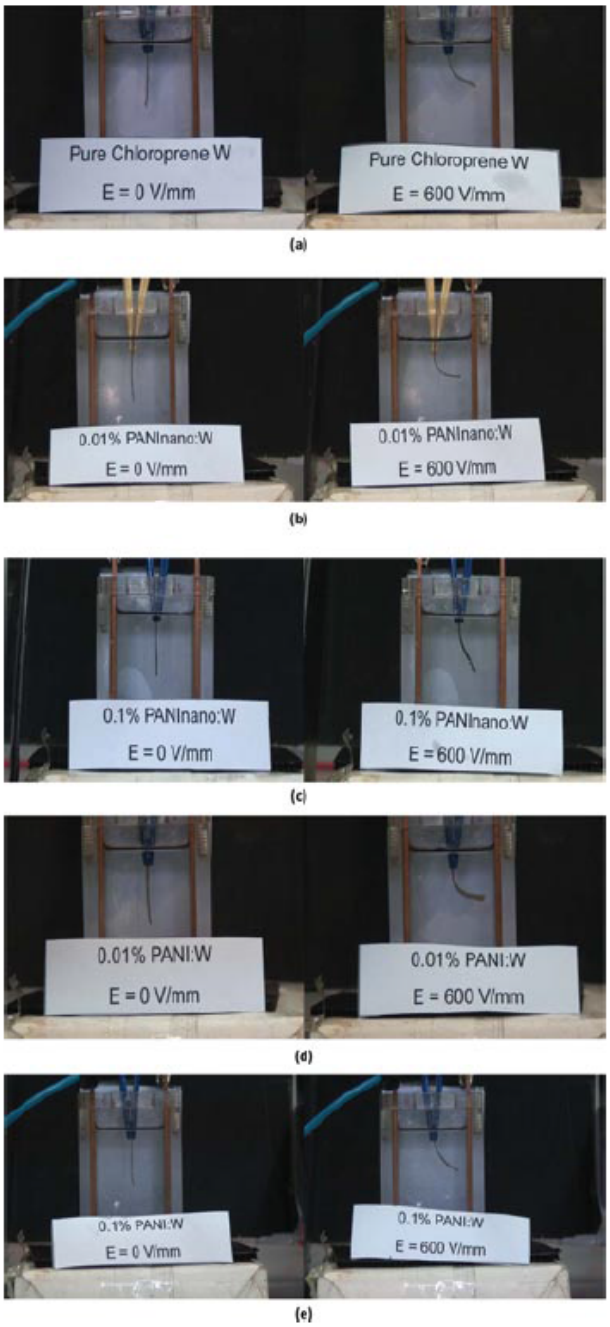

FIGURE 6. Deflection of specimens with and without the electric field: (a) pure Chloroprene W, (b) 0.01% PANI nano:W, (c) 0.1% PANI nano:W, (d) 0.01% PANI:W, and (e) 0.1% PANI:W.

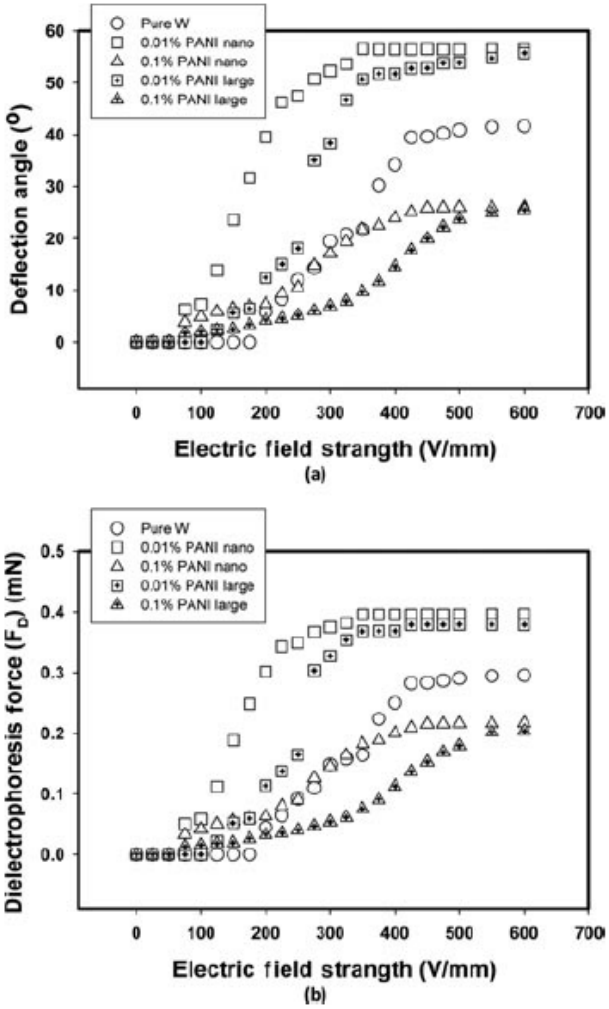

FIGURE 7. Electromechanical responses of specimens at various DC electric field strengths: (a) deflection angles and (b) dielectrophoresis forces (F_D).

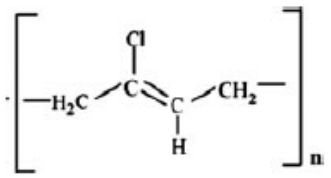

SCHEME 2. Chemical structure of chloroprene rubber.

The chemical structures of the undoped and the p-doped PANIs with HCl are shown in Scheme 1. After doping with HCl, the chemical structure of PANI changes from the emeraldine base (a neutral undoped form) to the emeraldine salt (a doped form), which has Cl^- counterions attached to the N^+ group.[40] Under the applied electric field, the dipole moments are generated and the chemical groups on the PANI chains are polarized.[38] The chloride

TABLE V
Dielectrophoresis Force of Dielectric Materials

Materials	DC Electric Field Strength (V/mm)	Dielectrophoresis Force (mN)	References
Acrylic elastomers (AR70)	600	0.367	Kunanuruksapong et al.[38]
Acrylic elastomers (AR71)	600	0.412	Kunanuruksapong et al.[38]
Acrylic elastomers (AR72)	600	0.318	Kunanuruksapong et al.[38]
Styrene-acrylic copolymers (SAR)	600	0.275	Kunanuruksapong et al.[38]
Styrene-butadiene rubbers (SBR)	600	0.157	Kunanuruksapong et al.[38]
Styrene-isoprene-styrene triblock copolymer (SIS D1112P)	600	0.071	Kunanuruksapong et al.[38]
Styrene-isoprene-styrene triblock copolymer (SIS D1114P)	600	0.033	Thongsak et al.[41]
Styrene-isoprene-styrene triblock copolymer (SIS D1161P)	600	0.013	Thongsak et al.[41]
Styrene-isoprene-styrene triblock copolymer (SIS D1114P) and 10% vol of polydiphenylamine blends	600	0.045	Thongsak et al.[37]
Styrene-isoprene-styrene triblock copolymer (SIS D1114P) and 30% vol of polydiphenylamine blends	600	0.022	Thongsak et al.[37]
Polypyrrole and Polyvinylidene composites	1 (V)	0.600	Alici et al.[43]
Polyvilny alcohol and poly 2-acrylamido-2-methyl-1-propanesulfonic acid blends	40	4.900	Dai et al.[44]
Electroactive cellulose	5 (V)	0.350	Kim et al.[22]
Poly dimethyl siloxane	500	0.256	Niamlang et al.[20]
10% Poly(*p*-phenylene vinylene) and Poly dimethyl siloxane blends	450	0.352	Niamlang et al.[21]
20% Poly(*p*-phenylene vinylene) and Poly dimethyl siloxane blends	450	0.190	Niamlang et al.[21]

counterion can be polarized to generate strong negative charges. In contrast, the N^+ group will become polarized and generate the positive charges. However, the effect of the negative charges (Cl^-) might be stronger than the positive charges (N^+) due to the higher electronegativity (E_n) of Cl atoms (3.16) over N atoms (3.04).[41] In addition, the benzene groups on the PANI chains can also pull electrons from the nitrogen atoms on the backbone. The polarity of the benzene group thus becomes negative.[38] Based on these reasons, the total net charges on our specimens are negative and generate the attractive force with the anode side, leading to the bending toward the anode electrode.[38] Trivedi[40] reported that the electrical and electromechanical properties of doped PANI were strongly influenced by the properties of counterion and type of dopants.[40]

DIELECTROPHORESIS FORCE COMPARISON

In this section, the dielectrophoresis force of our specimens is compared with those of other dielectric materials as presented in Table V.[37,41–44] The dielectrophoresis force of the pure chloroprene is 0.295 mN, which is higher than those of the styrene–isoprene–styrene triblock copolymer,[38,41] styrene–acrylic copolymer,[38] and polydimethyl siloxane.[20] But it is lower than that of the electroactive cellulose[22] and acrylic elastomer (AR70 and AR71).[38] In the case of polymer blends, the dielectrophoresis force of W:PANI nanoparticle at 0.01 vol% is 0.396 mN, which is higher than that of the blends between 10% vol of poly(*p*-phenylene vinylene) and poly(dimethyl siloxane)[21] and the blend between the styrene–isoprene–styrene triblock copolymer (SIS

D1114P) and 10 vol% of polydiphenylamines.[37] From these results, the blends between PANI nanoparticles and dielectric elastomers are potential candidates for electroresponsive materials.

Conclusions

In this work, the effects of the particle size, particle concentration of PANI, and electric field strength of the dielectric constant, electrical conductivity, storage modulus, storage modulus sensitivity, and dielectrophoresis force were investigated.

We selected chloroprene W, which has the highest dielectric constant and sensitivity among the four types of chloroprene as the matrix, and blended it with the PANI nano/large particles. The dielectric constant and electrical conductivity of the blends increase with an increasing volume percentage of PANI particles. At a high volume percentage of PANI, the blend systems with the PANI nanoparticles provide the higher electrical properties than the blends with the PANI large particles, due to higher dispersibility of the dispersed phase. The storage modulus with and without the electric field increases with an increasing volume percentage of the PANI particles. The blends with PANI-nano particles always give a higher storage modulus than those of the blends with the PANI-large particles due to the dispersion between the particles. The maximum storage modulus sensitivities of the blends with the PANI-nano particles and the PANI large particles are 73% at 0.01 vol% and 63% at 0.1 vol%, respectively. The dielectrophoresis forces of all specimens increase with an increasing electric field. The blends with the PANI-nano/large particles at 0.01 vol% provide a higher dielectrophoresis force than that of the pure chloroprene W, and they require lower electrical energy to respond. But for 0.1 vol% blends of PANI nano/large particles, the deflection angle and dielectrophoresis forces are lower than those of pure chloroprene and the blends with the PANI-nano/large particles at 0.01 vol%.

Acknowledgments

The authors would like to acknowledge financial support from the following: the Post Doctoral Fund from Graduate School, Conductive and Electroactive Polymers Research Unit, the Petroleum and Petrochemical College, all from Chulalongkorn University; the Petroleum, Petrochemical, and Advanced Materials Consortium; the Royal Thai Government; and the Thailand Research Fund (TRF). The material supports from the Innovation Group (Thailand) Co. Ltd., are also gratefully acknowledged.

References

1. Bar-Cohen, Y. SPIE Press, Electroactive Polymer (EAP) Actuators as Artificial Muscles: Reality, Potential, and Challenge; The International Society for Optical Engineering: Bellingham, WA, 2004.
2. Bar-Cohen, Y. Dielectric Elastomers as Electromechinacal Transducers: Fundamentals, Materials, Devices, Models and Applications of an Emerging Electroactive Polymer Technology, 1st ed.; Elsevier: Amsterdam, The Netherlands, 2004.
3. Krause, S.; Bohon, K. Macromolecules 2001, 34, 7179–7189.
4. Pelrine, R.; Kornbluh, R.; Pei, Q.; Joseph, J. G. Science 2000, 287, 836–839.
5. Ha-Anh, T.; Vu-Khanh, T. Polym Test 2008, 24, 775–780.
6. Pinho, M. S.; Dezotti, M.; Gorelova, M. M.; Soare, B. G. J Appl Polym Sci 1999, 71, 2329–2334.
7. Hiamtup, P.; Sirivat, A.; Jamieson, A. M. Mater Sci Eng C 2007, 15, 771–779.
8. Moon, D.; Ezuka, M.; Maruyama, T.; Osakada, K.; Yamamoto, T. Macromolecules 1993, 26, 364–369.
9. Chuapradit, C.; Ruangchuay Wannatong, L.; Chotpattananont, D.; Hiamtup, P.; Sirivat, A.; Schwank, J. Polymer 2005, 46, 947–953.
10. Hiamtup, P.; Sirivat, A.; Jamieson, A. M. J Colloid Interface Sci 2006, 295, 270–278.
11. Kaneto, K.; Kaneko, M.; Min, Y.; McDiarmid, A. G. Synth Met 1995, 71, 2211–2212.
12. Kim, B. J.; Oh, S. G.; Han, M. G.; Im, S. S. Synth Met 2001, 122, 297–304.
13. Kim, B. J.; Oh, S. G.; Han, M. G.; Im, S. S. Langmiur 2000, 16, 5841–5845.
14. Zhang, L.; Liu, P. Mater Lett 2010, 64, 1755–1757.
15. Lorenz, h.; Fritzshe, J.; Das, A.; Stockelhuber, K. W.; Jurk, R., Heinrich, G.; Klüppel, M. Compos Sci Technol 2009, 69, 2135–2143.
16. Lu, M.; He, B.; Wang, L.; Ge, W.; Lu, Q.; Liu, Y.; Zhang, L. Composites, Part B. 2012, 43, 50–56.
17. Elias, L.; Fenouillot, F.; Majeste, J. C.; Cassagnau, P. Polymer 2007, 48, 6029–6040.
18. Choi, K. Y.; Lim, h. G.; Yun, S. R.; Kim, K.; Kang, K. S. J Phys Chem C 2008, 112, 16204–160208.
19. Cao, Y.; Andreatta, A.; Heeger, A. J.; Smith, P. Polymer 1989, 30, 2305.

20. Niamlang, S.; Sirivat, A. Macromol Symp 2007, 264, 176–183.
21. Niamlang, S.; Sirivat, A. Smart Mater Struct 2008, 17, art. no. 035036.
22. Kim, J.; Kang, K.; Yun, S. Sens Actuators, A 2007, 133, 401–406.
23. Timoshenko, S. P.; Gere, J. M., Mechanics of Materials, 3rd ed.; Chapman & Hall, New York, USA.
24. Smith, T. S.; Seugling, R. M. Precision Eng 2006, 30, 245–264.
25. Han, M. G.; Cho, S. K.; Oh, S. G.; Im, S. S. Synth Met 2006, 126, 53–60.
26. Zeng, X.; Ko, T. Polymer 1998, 39: 1187–1195.
27. Dupont. Neoprene W; Product technical information, Rev. 5, July 2010.
28. Cherrak, Z.; Lagant, P.; Benharrats, N.; Semmoud, A.; Hamdache, F.; Vergoten, G. Spectrochim Acta, Part A 2005, 61, 1419–1429.
29. Matsuo, M.; Ishida, Y.; Yamafuji, K.; Takayanaki, Y.; Irie, F. Kolloid Z Z Polym 1965, 201, 89–93.
30. Pant, h. C.; Patra, M. K.; Negi, S. C.; Bhatia, A.; Vadrea, S. R.; Kumar, N. B. Mater Sci 2006, 29, 379–384.
31. Peng, W.; Huang, X.; Yu, J.; Jiang, P.; Liu, W. Composites, Part A 2010, 41, 1201–1209.
32. Meinckea, O.; Kaempfera, D.; Weickmanna, h.; Friedrich, C.; Vathauerb, M.; Warth, h. Polymer 2004, 45, 739–748.
33. Kunanuruksapong, R.; Sirivat, A. Mater Sci Eng, A 2007, 343–344, 454–461.
34. Shiga, T. Adv Polym Sci 1997, 134, 133–163.
35. Liu, B.; Shaw, T. M. J Rheol 2001, 45, 641–657.
36. Metz, P.; Alici, G.; Spinks, G. M. Sens Actuators A 2006, 130–131, 1–11.
37. Thongsak, K.; Kunanuruksapong, R.; Sirivat, A.; Lerdwijitjarud, W. Mater Sci Eng, C 2011, 31, 206–214.
38. Kunanuruksapong, R.; Sirivat, A. Curr Appl Phys, A 2011, 11, 393–401.
39. Uddin, Z.; Watanabe, M.; Shirai, h.; Hirai, T. J Polym Sci, Part B: Polym Lett 2003, 41 2, 119–2127.
40. Trivedi, D. C. B. Mater Sci 1999, 22, 447–455.
41. Bouma, J. J Chem Educ 1989, 66, 741–748.
42. Thongsak, K.; Kunanuruksapong, R.; Sirivat, A.; Lerdwijitjarud, W. Mater Sci Eng, A 2010, 527, 2504–2509.
43. Alici, G.; Mui, B.; Cook, C. Sens Actuator A 2007, 126, 396–404.
44. Dai, C. A.; Kao, A.; Chang, C.; Tsai, W.; Chen, W.; Liu, W.; Shih, W.; Ma, C. C. Sens Actuator A 2009, 155, 152–162.

Polymer 54 (2013) 2414–2421

Contents lists available at SciVerse ScienceDirect

Polymer

journal homepage: www.elsevier.com/locate/polymer

Stress relaxation behavior of (Ala-Gly-Pro-Arg-Gly-Glu-4Hyp-Gly-Pro-) gelatin hydrogels under electric field: Time-electric field superposition

Thawatchai Tungkavet [a], Anuvat Sirivat [a,*], Nispa Seetapan [b], Datchanee Pattavarakorn [c]

[a] The Petroleum and Petrochemical College, Chulalongkorn University, Bangkok 10330, Thailand
[b] National Metal and Materials Technology Center, Thailand Science Park, Pathumthani 12120, Thailand
[c] Department of Industrial Chemistry, Faculty of Science, Chiang Mai University, Chiangmai 50200, Thailand

ARTICLE INFO

Article history:
Received 20 December 2012
Received in revised form
21 February 2013
Accepted 26 February 2013
Available online 13 March 2013

Keywords:
Gelatin
Stress relaxation
Time-electric field superposition

ABSTRACT

An investigation has been conducted on stress relaxation functions and the corresponding relaxation time distribution functions of gelatin hydrogels for the effects of degree of crosslinking and the applied electric field strength. The experimental shift factors can be thus obtained from either the stress relaxation functions or the storage and loss moduli. Both approaches yield numerically the same shift factor values which successfully allow the time-electric field superposition of various related functions. The modified shift factors are obtained from the effective relaxation times and the material constant (C_τ). The material constant critically depends on the degree of crosslinking and weakly on the reference electric field strength used in the superposition. The relaxation time distribution clearly indicates two modes of relaxation under an electric field. The fast mode of relaxation, which occurs only under an electric field, can be attributed to the relaxation of protons present in the gelatin hydrogels.

© 2013 Elsevier Ltd. All rights reserved.

1. Introduction

Viscoelastic properties are often used to refer to the material chemical-microstructural relationship, as viscoelastics involve both solid-state and liquid-like behaviors [1]. Studies of viscoelastic materials include deformation, swelling, stability, and etc [2,3].

The present work focuses on the stress relaxation behavior, an important property for viscoelastic materials. Stress relaxation is the decrease in an internal stress when a material is held at a constant and finite strain. When an external strain is introduced to an elastic material, the applied strain causes a reversible deformation, and when the strain is removed, the residual stress rapidly relaxes to zero. Most materials are viscoelastic; when the material is subjected to an external strain, a stress is generated within the material and the generated stress relaxes through the process of stress relaxation [4]. The most simple law for the relaxation process of viscoelastic materials is described by the Maxwell model.

However, this model is not applicable towards real viscoelastic materials. Viscoelastic materials can exhibit many modes of relaxation processes. The relaxation processes can be divided into three stages: stage 1 is for the short time relaxation process (0–1 h); stage 2 is for the intermediate time relaxation (1–10^4 h); and stage 3 is for the long time relaxation process (>10^4 h) [4,5]. The Kohlrausch–Williams–Watts (KWW) equation is a well-known equation to describe the stage 1 of the stress relaxation process [4].

$$G(t) = G_\infty + G_0\left[e^{-\left(t/\tau\right)^n}\right] \quad (1)$$

where $G(t)$ is the stress relaxation function as obtained from the experiment, G_∞ is the equilibrium modulus or the long time value, t is the experimental time, τ is the effective relaxation time, and n ($0 < n \leq 1$) is the stretching parameter. Zhao et al. [6] studied the stress relaxation of alginate hydrogels with covalent crosslinks; the relaxation propagated through the network connectivity. Mao et al. [7] investigated the relaxation time of gelatin hydrogels at various degrees of crosslinking. The effective relaxation time shifted to a shorter amount of time as the degree of crosslinking increased.

Furthermore, the effect of temperature on viscoelastic materials has been studied through the stress relaxation due to temperature dependent molecular rearrangement processes occurring under applied stress. The relaxation process depends on the speed of the molecular motion in which temperature (T) is varied and the resultant viscoelastic functions of viscoelastic materials can be

* Corresponding author. Conductive and Electroactive Polymers Research Unit, The Petroleum and Petrochemical College, Chulalongkorn University, Bangkok 10330, Thailand. Tel.: +66 2 218 4131; fax: +66 2 611 7221.
E-mail address: anuvat.s@chula.ac.th (A. Sirivat).
URL: http://www.cepru.research.ac.th

0032-3861/$ – see front matter © 2013 Elsevier Ltd. All rights reserved.
http://dx.doi.org/10.1016/j.polymer.2013.02.045

expected to depend on temperature as well as time. Thus the relaxation function may be written as $G = G(t,T)$ [8,28].

If the relaxation times of all viscoelastic materials have the same temperature dependence, it is expected that it should be possible to superimpose linear viscoelastic data sets taken at different temperatures [9]. This is commonly known as the time–temperature superposition [10]. Stress relaxation function data at any temperature (T) can be superimposed onto the data taken at a reference temperature (T_o) using a time scale shift factor (a_T) as in the following equation [11,28].

$$a_T = \frac{\tau_i(T)}{\tau_i(T_o)} \tag{2}$$

where $\tau_i(T)$ and $\tau_i(T_o)$ are the characteristic time scales at T and T_o, respectively. The principle of the time–temperature superposition is based on the requirement that all time scales of the material system vary by the same factor or proportionality when temperature is varied from one to another.

There are many studies related to the time–temperature superposition in solid state materials, such as polyisobutylene [12], polybutadiene [13], polyethylene [14], polyurethane [15], and styrene-butadiene-styrene block copolymer [16]. Palade et al. [13] studied the time–temperature superposition and linear viscoelasticity of polybutadiene where the storage moduli and the stretching parameter depended on temperature. June et al. [17] studied the temperature effect on articular cartilage biomechanics; the stress relaxation proceeded faster and the stretching parameter decreased with increasing temperature. Chen et al. [18] investigated the time–temperature superposition of amorphous ethylene–styrene interpolymers in which the shift factor decreased as a function of temperature. Le et al. [19] studied the temperature dependent deformation behavior of different thermoplastic elastomers. Wortmann et al. [20] investigated the stress relaxation and the time–temperature superposition of polypropylene in which the characteristic relaxation time decreased with increasing temperature. Recently, the effects of electric field on viscoelastic properties and relaxation characteristic have been studied. The time-electric field relationship was investigated by Park et al. [21]. It was shown that the electric field reduced the time required to obtain the saturated storage modulus value of polypropylene/layered silicate nanocomposites.

In the present work, gelatin (Ala-Gly-Pro-Arg-Gly-Glu-4Hyp-Gly-Pro-) was used as the material to investigate stress relaxation behavior. Uncrosslinked and crosslinked gelatin hydrogels were prepared by adding a glutaraldehyde solution into a gelatin solution followed by a casting method. Stress relaxation functions of the uncrosslinked and crosslinked gelatin hydrogels were measured to study the effects of electric field strength and the crosslinking ratio. The horizontal shift factors ($a_{E,\exp}$) were experimentally obtained from both the stress relaxation function and the storage–loss moduli at various electric field strengths. These experimental shift factors ($a_{E,\exp}$) allow the time-electric field superpositions of the moduli and the stress relaxation function to be possible. Furthermore, it will be shown that $a_{E,\exp}$ could be calculated by the calculated shift factor ($a_{E,\mathrm{cal}}$), obtained from the ratio of the effective time scales incorporated with the material constant (c_τ).

2. Experimental

2.1. Materials

Gelatin powder (Type B, bovine skin, bloom strength 225, Sigma–Aldrich) has a typical structure of Ala-Gly-Pro-Arg-Gly-Glu-4Hyp-Gly-Pro, Glutaraldehyde (50% w/v GTA solution, AR grade, Fluka) were used as the starting materials for preparing gelatin hydrogels.

2.2. Preparation of gelatin hydrogels

Uncrosslinked gelatin hydrogels were prepared via the dissolution in the 10% v/v deionized water at 40 °C under continuous stirring for 40 min. Crosslinked gelatin hydrogels were prepared by adding a specific amount of glutaraldehyde solution into a 10% v/v gelatin solution; the glutaraldehyde concentration was varied at 3 and 7% v/v and the solution was stirred vigorously for 15 min at 40 °C to obtain a homogenous solution. Uncrosslinked and crosslinked gelatin solutions were poured into petri dishes. Hydrogels were obtained by solution casting at ambient temperature (30 °C) for 1 day and the crosslinked gelatin hydrogels were washed with deionized water 40 ml for 2 times. Finally, it was dried at room temperature to obtain approximately at 1 mm in thickness and 25 mm in diameter.

2.3. Characterization and testing of uncrosslinked and crosslinked gelatin hydrogels

Uncrosslinked and crosslinked gelatin hydrogels were identified for functional groups by a Fourier Transform Infrared Spectrometer (FTIR; Thermo Nicolet, Nexus 670, ATR) operated in the absorption mode with 32 scans and a resolution of ± 4 cm^{-1}, covering a wavenumber range of 3500 cm^{-1} to 500 cm^{-1}, with deuterated-triglycine sulfate as a detector.

Swelling measurement in deionized water was used to determine network crosslinking density of the hydrogel, the number-average molecular weight of the polymer chain segments between two consecutive segments (M_c) was calculated using the Flory–Rehner equation [22].

$$M_c = \frac{\rho V_1\left(\phi_g^{1/3} - 2\phi_g/f\right)}{\chi\phi_g^2 + \ln\left(1-\phi_g\right) + \phi_g} \tag{3}$$

where ρ is the density of the dry gelatin, which is studied by pycnometry, V_1 is the molar volume of the solvent, χ is the polymer–solvent interaction parameter ($\chi = 0.49 \pm 0.05$) [22], and φ_g is the volume fraction of the swollen gelatin, which was estimated from the following relation:

$$\phi_g = \frac{W_o\rho_w}{W\rho - W_o(\rho - \rho_w)} \tag{4}$$

where W_o is the initial weight of the sample, W is the weight of the swollen sample, ρ_w is the density of the water at room temperature, and ρ is the density of the dry uncrosslinked gelatin films.

Electrostatic force microscopy (EFM; XE100, Park System) images were taken with a scanning electron microscope to determine the surface morphology and phase of the gelatin hydrogels, using a scan rate of 0.3 Hz, a signal amplitude of 5 V, and a scan size of 3 μm × 3 μm. Each sample was scanned at two heights above the surface. In the first scan, the probe tip responded to the van der Waals force under the tapping mode and the surface morphology was recorded. The second scan was taken under the interleave mode to detect the electric field force.

A melt rheometer (Rheometric Scientific, ARES) was used to measure the stress relaxation properties of the gelatin hydrogels. The specimens were fitted with a custom-built copper parallel plate fixture (diameter of 25 mm). A DC voltage (Instek, GFG8216A) was applied through the specimen. A digital multimeter (Tektronic Incorporation, CDM250) was used to monitor the voltage input. In

these experiments, the $G(t)$ were measured as a function of time and electric field strength (0–800 V/mm). First, appropriate strains were determined for $G(t)$ to be in the linear viscoelastic regime. The suitable strain was measured to be 0.20% for both the uncrosslinked and crosslinked gelatin hydrogels. The measured stress relaxation data were then converted to the dynamic storage, loss moduli, and the relaxation time spectrum through the software program (TA Orchestrator version 6.60B1, TA Instruments Incorporation).

To quantify the long-time relaxation behavior of the samples, the stress relaxation function $G(t)$ was fitted to the phenomenological KWW equation. The effective relaxation time (τ) and the stretching parameter (n) were determined by fitting stress relaxation data to equation (1) through a software program (Polymath version 6.10, CACHE Corporation).

Where equation (1) is replaced to determine the relaxation time distribution by an integral [4].

$$G(t) = G_\infty + \int_0^\infty G(\tau)\left[e^{-\left(t/\tau\right)^n} d\tau\right] \tag{5}$$

where $G(t)$ is the stress relaxation function as obtained from the stress relaxation experiment, G_∞ is the equilibrium stress relaxation or the long time value, t is the experimental time, τ is the effective relaxation time, $G(\tau)$ is a continuous function over relaxation time, and n ($0 < n \leq 1$) is the stretching parameter. The effective relaxation time (τ) is presented on a logarithm scale. Thus, equation (5) can be written as:

$$G(t) = G_\infty + \int_{-\infty}^\infty H(\tau)\left[e^{-\left(t/\tau\right)^n} d\ln\tau\right] \tag{6}$$

where $H(\tau) = \tau G(\tau)$ is called the relaxation time distribution spectrum [4,23]. $H(\tau)$ was determined through the software program (TA Orchestrator version 6.60B1, TA Instruments Incorporation) using equation (6), where the mean relaxation time (τ_m) was determined from $H(\tau)$. The relaxation time distribution spectrum is a fundamental function of viscoelastic materials [24]. The stretching parameter (n) can be related to the width of the relaxation time distribution spectrum [25].

The dynamic moduli data can be obtained via a transformation of $G(t)$ in two steps. First, the stress relaxation data was converted into the relaxation time distribution spectrum, then the dynamic moduli were calculated from the relaxation time distribution spectrum by integration of the spectra as in equations (7) and (8) using the same software program (TA Orchestrator version 6.60B1, TA Instruments Incorporation) [26].

$$G'(\omega) = G_\infty + \int_0^\infty H(\tau)\frac{\omega^2\tau^2}{1+\omega^2\tau^2} d\tau \tag{7}$$

$$G''(\omega) = \int_0^\infty H(\tau)\frac{\omega^2\tau^2}{1+\omega^2\tau^2} d\tau \tag{8}$$

where $G'(\omega)$ and $G''(\omega)$ are the dynamic storage modulus and the dynamic loss modulus as functions of frequency (ω), respectively. G_∞ is the equilibrium stress relaxation function or the long time value, $H(\tau)$ is the relaxation time distribution spectrum, τ is the integrating relaxation time, and the stretching parameter n ($0 < n \leq 1$). From $G'(\omega)$ and $G''(\omega)$ data, the relaxation time of dynamic moduli data at the crossover (τ_c) was identified at the crossover point of ($G'(\omega)$) and ($G''(\omega)$) vs. frequency (ω); τ_c is reciprocal of the crossover frequency (ω_c) [26–28].

Horizontal shift factors of uncrosslinked and crosslinked gelatin hydrogels were determined to superimpose the G' and G'' data at different electric field strengths from 0 V/mm to 800 V/mm and identified as the experimental shift factor ($a_{E,\exp}$). By definition, the shift factor due to electric field can be generally calculated and expressed as:

$$a_{E,\mathrm{cal}} = \frac{\tau_i(E)}{\tau_i(E_o)} \tag{9}$$

where $\tau_{i(E)\ \text{and}\ \tau_{i(Eo)}}$ are the effective relaxation time scales of equation (1) taken from the stress relaxation measurement at the electric field strengths of E and E_o, respectively [11,29].

However, the calculated shift factors of uncrosslinked and crosslinked gelatin hydrogels as in equation (9) do not agree numerically with the experimental shift factors as they contain an intrinsic material dependence through a constant (C_τ) which is a strong function of the material and weakly dependent on the reference electric field strength between (0 and 800 V/mm). C_τ is defined here as the ratio of $a_{E,\exp}$ and $a_{E,\mathrm{cal}}$. Therefore, the calculated shift factor of equation (9) can be modified by a constant value of C_τ as shown in the following equation (10) and can be renamed as the modified shift factor ($a_{E,\mathrm{mod}}$).

$$a_{E,\mathrm{mod}} = C_\tau x a_{E,\mathrm{cal}} \tag{10}$$

where C_τ is the material constant which is weakly dependent on reference electric field strength, $\tau_{i(E)\ \text{and}\ \tau_{i(Eo)}}$ are the effective relaxation time scales at electric field strengths of E and E_o, respectively.

3. Results and discussion

3.1. Characterization of uncrosslinked and crosslinked gelatin hydrogels

The FTIR spectrum of uncrosslinked gelatin hydrogel shows characteristic peaks at 1250, 1550, 1630, 2922, and 3300 cm^{-1}. They correspond to the C–N stretching, the N–H bending, the C=O stretching vibration, the C–H stretching vibration, and the N–H stretching vibration, respectively. For the spectrum of the 7% v/v crosslinked gelatin hydrogel, additional peaks appear at 1641 cm^{-1} and 1450 cm^{-1}. These peaks represent the aldimine (CH=N) stretching vibration, indicating that the crosslinking between gelatin and glutaraldehyde occurred [30].

The glutaraldehyde crosslinking leads a significant reduction in swelling. Swelling measurements at longer times were prevented by the solubility of the hydrogel. The calculated average molecular weight between two neighboring crosslink points, M_c, decreases drastically with increasing of glutaraldehyde content, due to the formation of a packed network. The 3% v/v and 7% v/v crosslinked gelatin hydrogels show M_c of 1920 ± 296, and 320 ± 16 g/mol, respectively. The 7% v/v crosslinked gelatin hydrogel possesses the lowest degree of swelling. The amount of the crosslinking agent was higher than 7% v/v and did not induce any further change in the crosslinking density and the percentage of swelling of the crosslinked hydrogel. Fraga et al. [31] reported similar results by the termination of the reaction in the thermosetting systems of gelatin films.

3.2. Relaxation behavior of uncrosslinked and crosslinked gelatin hydrogels

The effects of crosslinking ratio and electric field strength on the $G(t)$, G' and G'' of the uncrosslinked and crosslinked gelatin

hydrogels were investigated at electric field strengths between 0 and 800 V/mm. Fig. 1(a) and (b) show $G(t)$ and the shifted stress relaxation of the uncrosslinked and 7% v/v crosslinked gelatin hydrogels in relation to time, respectively. The stress relaxation functions of the 7% v/v crosslinked gelatin hydrogel are shown in Fig. 1 as one of several crosslinked gelatin hydrogels investigated. Fig. 1(a) reveals the accelerated stress relaxation via the increases in crosslinking density and electric field. In other words, increasing molecular connectivity or increasing crosslinking ratio promotes the capability of the hydrogels to relax faster through available junctions connected with neighboring topological structures [32]. On the other hand, the electric field also induces polarization and dipole–dipole interaction that effectively produce electric field-induced connectivity which in turn enhances $G(t)$. Protsenko et al. [33] studied the stress relaxation of a porcine septal cartilage under applied electric field; they found that the specimen stress relaxation was accelerated under electric field. Konyali et al. [32] studied a similar effect on polyisoprene. The relaxation time scale of polyisoprene decreased with increasing degree of crosslinking, and the stress relaxation was distributed throughout the crosslinking molecular segments.

In Fig. 1(b), the experimental superimpositions of the stress relaxations ($G(t) - t/a_{E,\exp}$) of the uncrosslinked and 7% v/v crosslinked gelatin hydrogels are shown to produce master curves through the horizontal shifting of the stress relaxations at various electric field strengths towards the stress relaxation functions at the reference electric field (0 V/mm). The superimpositions of these $G(t) - t/a_{E,\exp}$ functions obviously produce two distinct superimposed master curves, one for the uncrosslinked and one for the 7% v/v crosslinked gelatin hydrogels. The experimental shift factors ($a_{E,\exp}$) of the uncrosslinked gelatin hydrogel at various electric field strengths (50, 100, 200, 400, and 800 V/mm) are 0.40, 0.36, 0.30, 0.23, and 0.16, respectively. While the value of $a_{E,\exp}$ of the 7% v/v crosslinked gelatin hydrogel are 0.92, 0.85, 0.70, 0.65, and 0.55. Effective relaxation times (τ) of the uncrosslinked and 7% v/v crosslinked gelatin hydrogels, obtained from fitting stress relaxation data with KWW equation (1), both decrease with increasing electric field strength, apparently due to the increase in the molecular connectivity under the applied electric field, as shown in Table 1. Park et al. [21] reported a similar effect of electric field strength on a time scale to reach equilibrium property of polypropylene nanocomposites. The electric field reduced the characteristic time of the polypropylene nanocomposites. Le et al. [19] found that the shift factor at different temperatures of polypropylene and nitrile rubber decreased with increasing network structure density.

Fig. 2(a) and (b) show the storage modulus (G') and experimentally shifted storage modulus vs. frequency (rad/s), where the G' of the uncrosslinked and crosslinked gelatin hydrogels were obtained from the transformation of $G(t)$ using equations (7) and (8) and the software program (TA Instruments Incorporation, TA Orchestrator version 6.60B1). In Fig. 2(a), G' of the gelatin hydrogels increases with increasing of frequency (rad/s) until reaching plateaus at high frequencies, a typical behavior of a gelatin structure [34]. Shiga et al. [35] found that G' increased gradually with frequency, whether an electric field was applied or not. Puvanatvattana et al. [36] reported that for the poly(3-thiophene acetic acid)/polyisoprene suspension G' increased with increasing frequency indicative of solid-like behavior. Wichiansee and Sirivat [37] reported a similar feature for the poly(dimethylsiloxane) and poly(3,4-ethylenedioxythiophene)/poly(styrene sulfonic acid)/ethylene glycol blends. For both uncrosslinked and crosslinked gelatin hydrogels, the G' at the electric field strength of 800 V/mm are higher than those of the electric field strength of 0 V/mm. As an electric field is applied, the gelatin structure responds by generating induced dipole moments, leading to intermolecular interactions and thus higher chain rigidity, as indicated by the resultant higher G' values [38].

In Fig. 2(b), the $a_{E,\exp}$ used for the shifting of the storage modulus ($G' - \omega a_{E,\exp}$ function) of these hydrogels are the same experimental shift factors used for the shifting of $G(t)$ as in Fig. 1(b).

Fig. 3(a) shows G'' of the uncrosslinked and 7% v/v crosslinked gelatin hydrogels in relation to frequency. The G'' of the uncrosslinked and 7% v/v crosslinked gelatin hydrogels also increase with increasing crosslinking ratio and applied electric field strength, apparently due to the higher induced intermolecular interaction [39]. Tangboriboon et al. [40] found that the G'' of lead zirconate-titanate/acrylic elastomer composites increased with electric field

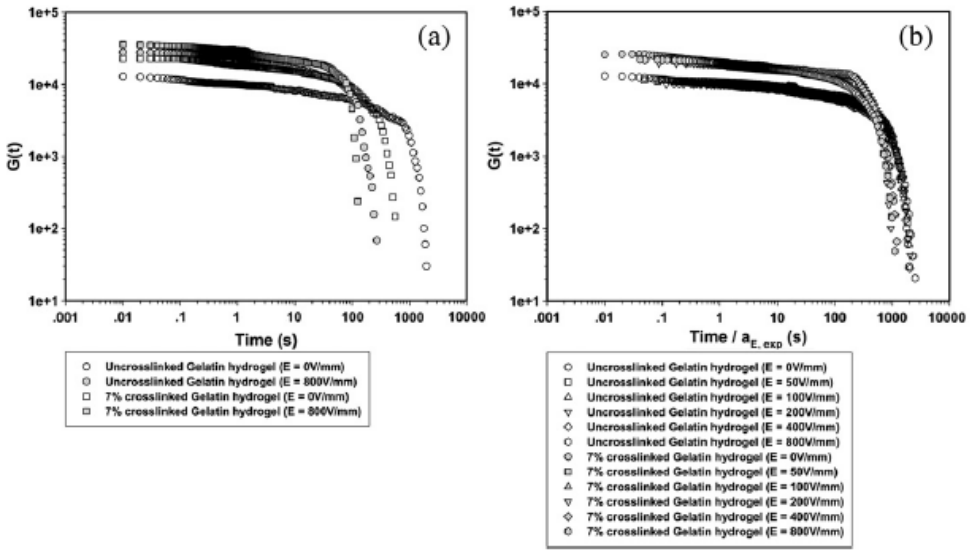

Fig. 1. (a) Stress relaxations of uncrosslinked and 7% v/v crosslinked gelatin hydrogels at 0 and 800 V/mm and (b) stress relaxation master curves of uncrosslinked and 7% v/v crosslinked gelatin hydrogels at electric field strengths between 0 and 800 V/mm (sample diameter 25 mm, gel thickness 0.988 mm, 25 °C, 0.20% strain).

Table 1
Relaxation parameters of uncrosslinked, 3% v/v crosslinked and 7% v/v crosslinked gelatin hydrogels at various electric field strengths, at 25 °C and 0.20% strain.

Materials	Electric field strength (V/mm)	Storage modulus crossover (G'_c) (Pa)	Time scale at dynamic crossover (τ_c)(s)	Effective relaxation time (τ) from fitting Eq. (1) (s)	n (stretching parameter : $0 < n < 1$)	R^2	Mean relaxation time from relaxation distribution functions (τ_m) (s)
Uncrosslinked gelatin hydrogel	0	2596 ± 166	160 ± 28	154 ± 44	0.284 ± 0.02	0.977	196
	50	3671 ± 170	90 ± 10	70 ± 15	0.373 ± 0.02	0.983	74
	100	4615 ± 196	68 ± 7	55 ± 10	0.399 ± 0.02	0.988	62
	200	5249 ± 194	54 ± 5	50 ± 8	0.419 ± 0.03	0.982	54
	400	6917 ± 179	45 ± 4	40 ± 5	0.464 ± 0.05	0.985	45
	800	8667 ± 165	38 ± 4	36 ± 4	0.475 ± 0.03	0.988	34
3% Crosslinked gelatin hydrogel	0	3813 ± 213	103 ± 21	123 ± 40	0.310 ± 0.02	0.968	128
	50	4682 ± 228	68 ± 7	60 ± 15	0.439 ± 0.02	0.981	63
	100	5685 ± 202	60 ± 6	50 ± 10	0.483 ± 0.02	0.983	53
	200	7840 ± 374	43 ± 4	44 ± 8	0.507 ± 0.02	0.984	42
	400	10,975 ± 310	41 ± 3	38 ± 6	0.510 ± 0.03	0.984	37
	800	11,849 ± 309	34 ± 4	30 ± 5	0.545 ± 0.03	0.984	28
7% Crosslinked gelatin hydrogel	0	4574 ± 233	60 ± 8	57 ± 22	0.437 ± 0.05	0.975	51
	50	5418 ± 236	50 ± 6	40 ± 18	0.449 ± 0.02	0.989	45
	100	8169 ± 164	45 ± 4	38 ± 10	0.495 ± 0.05	0.979	40
	200	8282 ± 196	39 ± 4	32 ± 6	0.537 ± 0.02	0.974	32
	400	12,207 ± 295	31 ± 3	28 ± 6	0.588 ± 0.04	0.979	30
	800	14,881 ± 252	26 ± 3	21 ± 4	0.622 ± 0.04	0.974	25

strength due to the effect of piezoelectric particles acting as a reinforcing filler. The time-electric field superimposition of the loss modulus ($G'' - \omega a_{E,\exp}$ function) of the uncrosslinked and 7% v/v crosslinked gelatin hydrogels are shown in Fig. 3(b). The same experimental shift factors for the shifting of $G(t)$ and the shifting of G' are used here resulting in two separate $G'' - \omega a_{E,\exp}$ functions.

Table 1 summarizes the relaxation times (τ) and the stretching parameter (n) of the uncrosslinked and crosslinked gelatin hydrogels as obtained by three different methods: τ from KWW; τ_c from the dynamic crossover between G' and G''; and τ_m from the relaxation time distribution spectrum. From these methods, the relaxation times of all gelatin hydrogels decrease with increasing electric field strength and crosslinking density, reaffirming the more rapid relaxation rate. The stretching parameter (n) is related to the width of the relaxation time distribution spectrum [24,25], in that n increases with increasing electric field strength and degree of crosslinking.

Fig. 4 shows the experimental shift factors ($a_{E,\exp}$) and the modified shift factors ($a_{E,\mathrm{mod}}$) obtained from the effective relaxation times (equation (1)) with C_τ according to equation (10), of the uncrosslinked and crosslinked gelatin hydrogels at various electric field strengths (50, 100, 200, 400, and 800 V/mm), at the reference electric field strength of 0 V/mm. Both shift factors of the uncrosslinked, 3% v/v crosslinked, and 7% v/v crosslinked gelatin hydrogels decrease with increasing electric field strength. The modified shift factors, as obtained from the adjustment of effective relaxation times with a material constant (C_τ); the chosen values are tabulated in Table 2. It can be concluded that the material constant is apparently dependent on the crosslinking density and weakly dependent on the reference electric field strength.

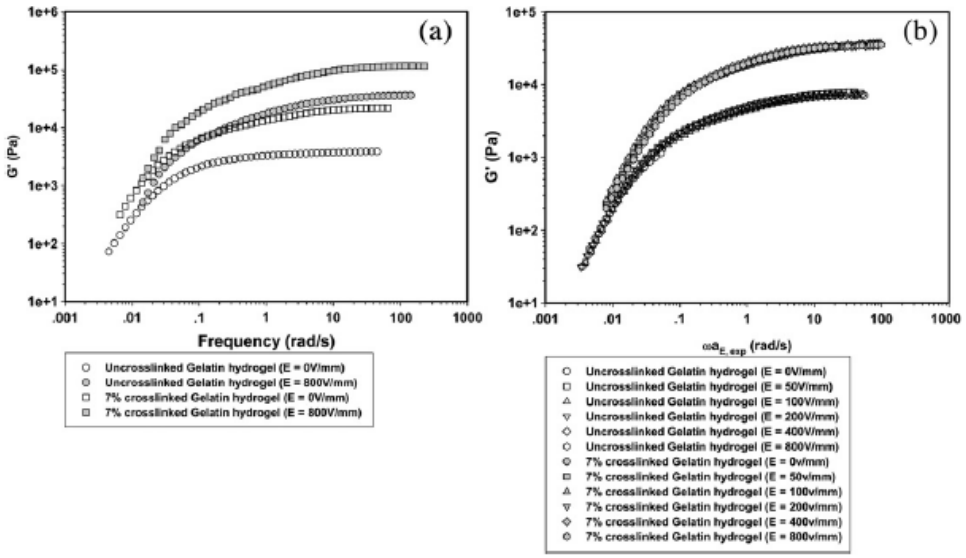

Fig. 2. (a) Storage modulus of uncrosslinked and 7% v/v crosslinked gelatin hydrogels at 0 and 800 V/mm and (b) storage modulus master curves of uncrosslinked and 7% v/v crosslinked gelatin hydrogels at electric field strengths between 0 and 800 V/mm (sample diameter 25 mm, gel thickness 0.988 mm, 25 °C, 0.20% strain).

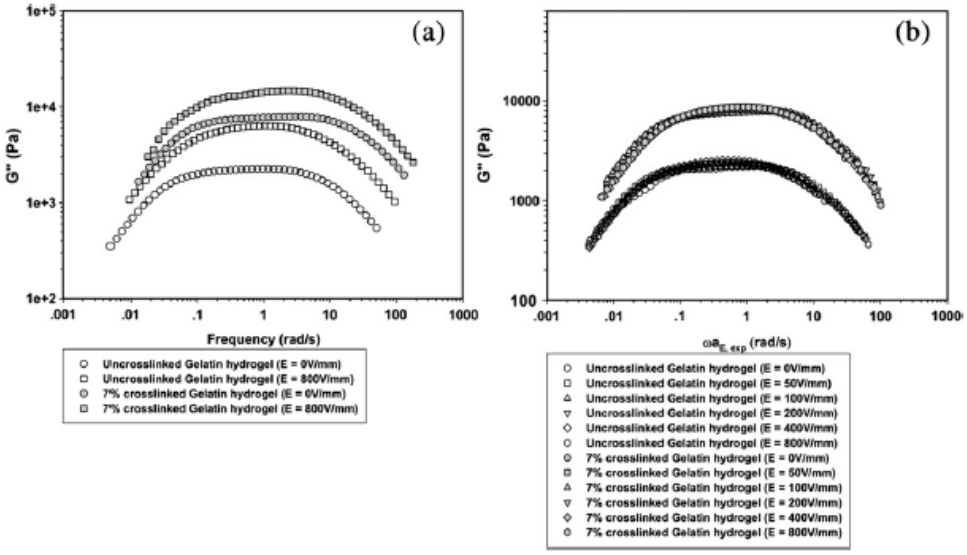

Fig. 3. (a) Loss modulus of uncrosslinked and 7% v/v crosslinked gelatin hydrogels at 0 and 800 V/mm and (b) loss modulus master curves of uncrosslinked and 7% v/v crosslinked gelatin hydrogels at electric field strength varied between 0 and 800 V/mm (sample diameter 25 mm, gel thickness 0.988 mm, 25 °C, 0.20% strain).

3.3. Effect of degree of crosslinking and electric field strength on relaxation time distribution spectrum

Relaxation time distributions of the uncrosslinked, 3% v/v and 7% v/v crosslinked gelatin hydrogels were investigated. The experimental shift factors ($a_{E,\exp}$) were applied to superimpose the relaxation time distributions of the hydrogels. In summary, the same a_E, in response to various electric field strengths, are successfully used in the shifting of the $G'(\omega)$, $G''(\omega)$, $G(t)$, and $H(\tau)$ functions. Superimposition of the relaxation time distributions of the uncrosslinked, 3% v/v crosslinked, and 7% v/v crosslinked gelatin hydrogels are shown in Fig. 5. From the distributions, the means of the relaxation time distributions (τ_m) can be calculated and they are tabulated in Table 1. The τ_m shifts towards the smaller values with increasing degree of crosslinking and electric field strength. In addition, the width of relaxation time distribution also decreases with increasing degrees of crosslinking and electric field strength, as the relaxation time and the width of relaxation time distribution corresponds with the elasticity of materials and the network connectivity of these hydrogels [24].

It may be noticed that the relaxation time distributions of the hydrogels are single peaked when the electric field is off. However, when the electric field is on, they become double peaked consisting of a fast relaxation mode and the slow relaxation mode, the latter always appears whether the electric field is on or off. The appearance of fast relaxation mode is related to a water proton ion present in the hydrogel while the slow relaxation mode responses to the structural relaxation of the hydrogel.

The relaxation times of a water proton ion in the uncrosslinked gelatin hydrogel are 1.14, 0.95, 0.97, 0.98, and 0.94 s at 50, 100, 200, 400, and 800 V/mm, respectively. The relaxation times of a water proton ion in the 3% v/v crosslinked gelatin hydrogel are 0.89, 0.95, 0.88, 0.81, and 0.77 s at 50, 100, 200, 400, and 800 V/mm, respectively. The relaxation times of a water proton ion in the 7% v/v crosslinked gelatin hydrogel are 0.83, 0.87, 0.87, 0.84, and 0.71 s at 50, 100, 200, 400, and 800 V/mm, respectively. The relaxation

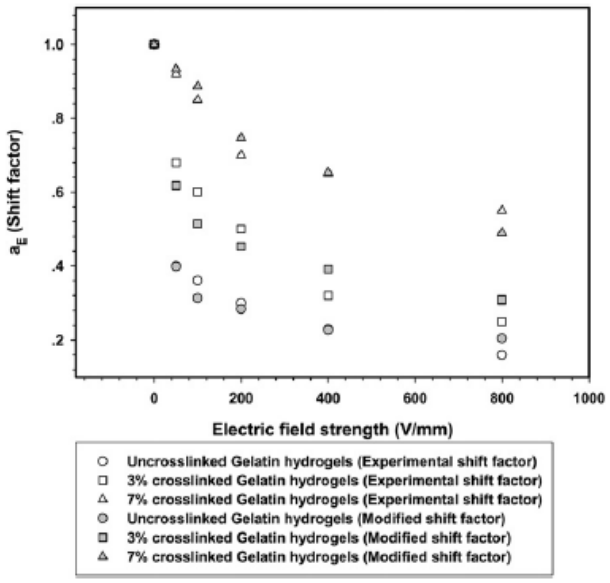

Fig. 4. The experimental and modified shift factors of uncrosslinked, 3% v/v crosslinked and 7% v/v crosslinked gelatin hydrogels vs. electric field at the reference electric field of 0 V/mm (sample diameter 25 mm, gel thickness 0.988 mm, 25 °C, 0.20% strain).

Table 2
Material constants (C_ε) of uncrosslinked, 3% v/v crosslinked and 7% v/v crosslinked gelatin hydrogels at various reference electric field strengths (V/mm).

Material constants (C_ε) of hydrogels	Reference electric field strength (V/mm)					
	0	50	100	200	400	800
Uncrosslinked gelatin hydrogels	0.88	0.85	0.80	0.78	0.73	0.70
3% crosslinked gelatin hydrogels	1.26	1.03	0.95	0.93	0.90	0.88
7% crosslinked gelatin hydrogels	1.33	1.20	1.19	1.19	1.18	1.14

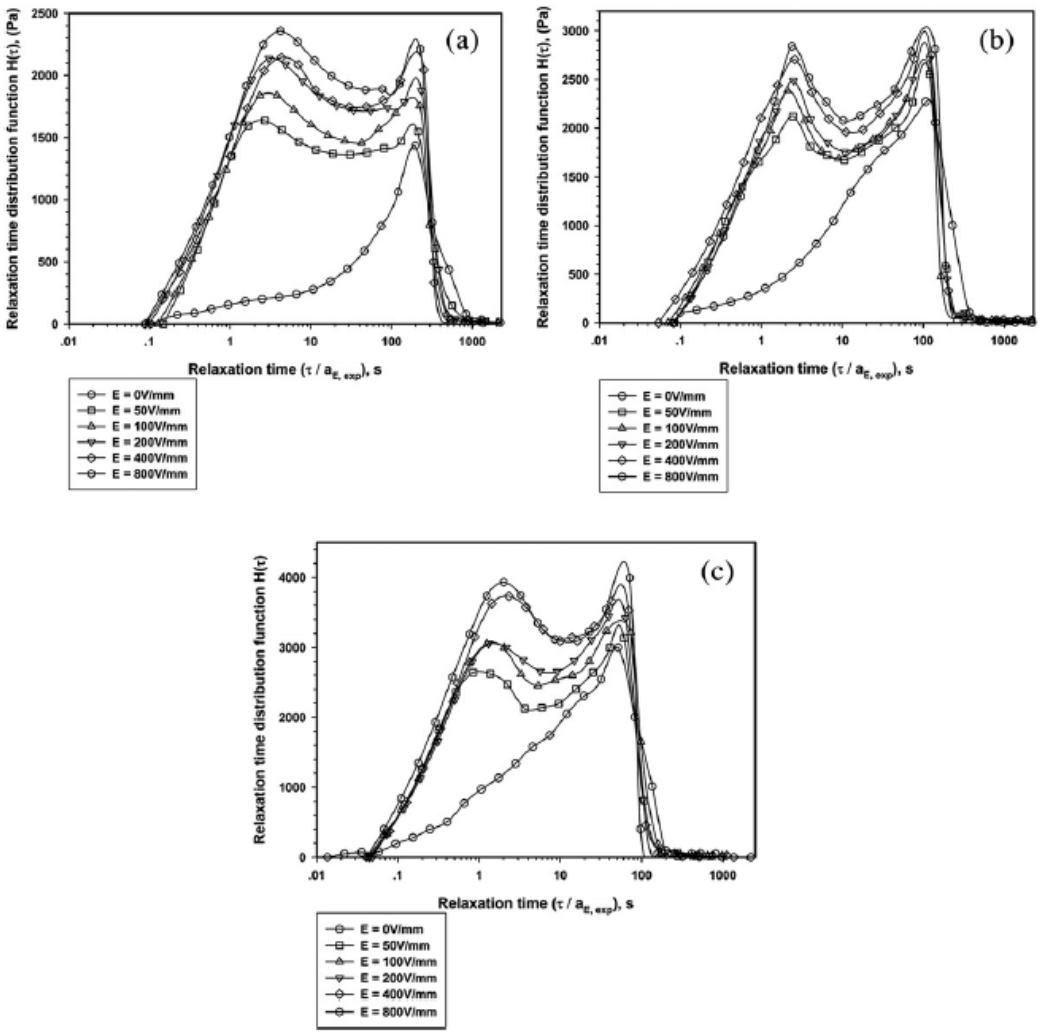

Fig. 5. Superimpositions of the relaxation time distribution functions $H(\tau)$ of the gelatin hydrogels at various electric field strengths: (a) uncrosslinked gelatin hydrogels; (b) 3% crosslinked gelatin hydrogels and; (c) 7% crosslinked gelatin hydrogels (0.20% strain, 25 °C, samples = 5).

times of water protons fall in the range of 0.71–1.14 s. Martron et al. [41] studied the relaxation time of a water proton, and they found the relaxation time of water protons was between 0.53 and 1.87 s. Thus it appears that the fast relaxation mode is due to the protonation of water molecules resulting proton ions in the hydrogels. Chatterjee and Bohidar [42] studied the effect of cations on properties of gelatin hydrogels in which the calcium ion (Ca^{2+}), sodium ion (Na^{+}), and potassium ion (K^{+}) were bound to the

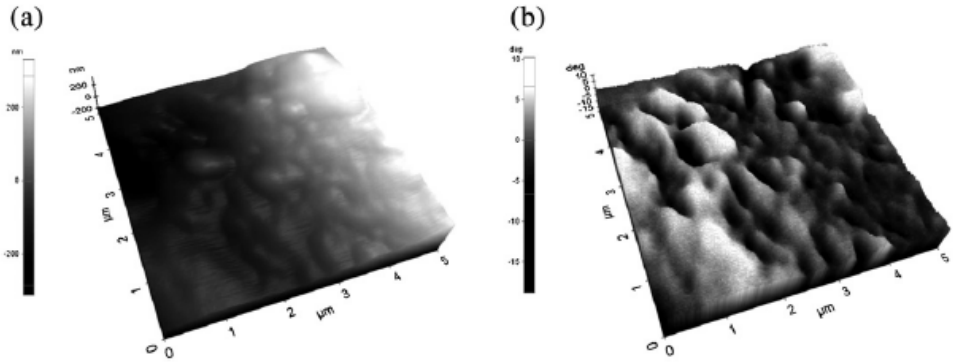

Fig. 6. (a) Topology image of uncrosslinked gelatin hydrogel and (b) EFM image under 5 V of voltage bias of uncrosslinked gelatin hydrogel at 300 K.

carboxyl groups of the amino acid on the backbone of the gelatin structure. Moreover the fast mode relaxation time was shifted to shorter time scales as the charge density and salt concentration were increased. However, the slow relaxation mode was less sensitive to additional salt concentration [42]. Richard [43] reported that the hydrogen ion (H^+) was bounded to the carboxyl group of gelatin.

Loeb et al. [44] studied the hydrogen ion binding to ribonuclease, where the carboxyl group was able to bind with the hydrogen ion. It has been known that the protons generated are capable of binding themselves with the carboxyl group of the gelatin structure [42,43], in which the decomposition of water molecules can be confirmed by the EFM phase measurement as shown in Fig. 6(a) and (b). Fig. 6(a) shows the topological surface of a gelatin hydrogel; it is far from being smooth at a nano scale. Fig. 6(b) shows the phase image of the same gelatin hydrogel. The image exhibits the charge distribution within the gelatin hydrogel; the light areas indicate the presence of the protons in our materials which are weakly bound with the gelatin chain structure, and therefore water proton ion are not associated with the slow relaxation mode. Mao et al. [7] studied the relaxation time distribution function of a gellan hydrogel in which the characteristic τ_m moved to a shorter time scale as Ca^{2+} concentration increased. Chatterjee and Bohidar [42] found that the $H(\tau)$ of a gelatin hydrogel exhibited two distinct peaks with increases in the Ca^{2+}, Na^+, and K^+ concentrations.

4. Conclusions

The relaxations of uncrosslinked and crosslinked gelatin hydrogels have been investigated under the effects of the degree of crosslinking and electric field strength. The characteristic relaxation time can be estimated by three methods; KWW; the dynamic crossover; and the relaxation time distribution spectrum $H(\tau)$. For the uncrosslinked, 3% v/v crosslinked and 7% v/v crosslinked gelatin hydrogels, the relaxation times decrease with increasing degrees of crosslinking and the applied electric field strengths. This is due to the increase in the molecular connectivity that promotes the capability of the stress relaxation process. The stress relaxation process of the uncrosslinked and crosslinked gelatin hydrogels shows two relaxation time modes under an applied electric field: fast relaxation mode and slow relaxation mode. The experimental shift factors ($a_{E,exp}$) of the uncrosslinked, 3% v/v crosslinked, and 7% v/v crosslinked gelatin hydrogels decrease with increasing electric field strength. The $a_{E,exp}$ characteristic is analogous to the time–temperature superposition. Thus, the existence of the time-electric field superposition is demonstrated here. Furthermore, $a_{E,exp}$ can be used on the shifting of $G'(\omega) - G''(\omega) - G(t) - H(\tau)$ functions. Effective relaxation times from stress relaxation experiment are used to determine the calculated shift factor, $a_{E,cal}$. The correlation between $a_{E,exp}$ and $a_{E,cal}$ is found to be dependent of the material constant and independent of the applied electric field.

Acknowledgments

The authors gratefully acknowledge the financial supports from the Conductive and Electroactive Polymers Research Unit of Chulalongkorn University; the Thailand Research Fund (TRF-RTA and MRG 5380100); the Royal Thai Government and the Doctoral Scholarship from the Thailand Graduate Institute of Science and Technology (TGIST) (TG-33-09-53-003D).

References

[1] Mayer M, Chawla KK. Mechanical behavior of materials. 2nd ed. New York: Cambridge University Press; 2009 [chapter 2].
[2] Kundu S, Crosby AJ. Soft Matter 2009;5:3963–8.
[3] Zhang Y, Matsumoto EA, Peter A, Lin PC, Kamien RD, Yang S. Nano Let 2008;8:1192–6.
[4] Matsuoka S. Relaxation phenomena in polymers. New York: Oxford University Press; 1992. [Chapter 1].
[5] Williams G, Watts DC. Trans Faraday Soc 1970;66:80–5.
[6] Zhao X, Huebsch N, Mooney DJ, Suo Z. J Appl Phys 2010;107:063509–5.
[7] Mao R, Tang J, Swanson BG. J Food Sci 2000;65:374–81.
[8] Lakes RS. Viscoelastic solids. Washington, D.C.: CRC Press; 1998 [chapter 8].
[9] Rubinstein M, Colby RH. Polymer physics. New York: Oxford University Press; 2003.
[10] Tobolsky AV. J Appl Phys 1956;27:673.
[11] Schwarzl F, Staverman AJ. J Appl Phys 1952;23:838–43.
[12] Ferry JD, Grandine LD, Fitzgerald ER. J Appl Phys 1953;24:911.
[13] Palade LL, Verney V, Attane P. Macromolecules 1995;28:7051–7.
[14] Onogi S, Asada T, Fukui Y, Fujisawa T. J Polym Sci A 1967;5:1067–78.
[15] Tobolsky AV. J Appl Polym Sci 1966;10:1837–44.
[16] Fileding-Russell GS, Fitzhugh RL. J Polym Sci A2 1972;10:1625–9.
[17] June RK, Fyhrie DP. J Exp Biol 2010;213:3934–40.
[18] Chen HY, Stepanov EV, Chum SP, Hiltner A, Bear E. Macromolecules 2000;33:8870–7.
[19] Le HH, Lupke T, Pham T, Radusch HJ. Polymer 2003;44:4589–97.
[20] Wortmann FJ, Schulz KV. Polymer 1995;36:315–21.
[21] Park JU, Choi YS, Cho KS, Kim DH, Ahn KH, Lee SJ. Polymer 2006;47:5145–53.
[22] Flory PJ, Rehner J. J Chem Phys 1943;11:521–6.
[23] Fried JR. Polymer science and technology. 2nd ed. Englewood Cliffs: Prentice Hall; 2003.
[24] Honerkamp J, Weese J. Rheol Acta 1993;32:65–73.
[25] Lindsey CP, Patterson GD. J Chem Phys 1980;73:3348.
[26] Schwarzl FR. Rheol Acta 1975;14:581–90.
[27] Belfiore LA. Physical properties of macromolecules. New Jersey: John Wiley & Sons, Inc; 2010 [chapter 10].
[28] Ferry JD. Viscoelastic properties of polymers. 3rd ed. New York: John Wiley & Sons, Inc; 1980 [chapter 1].
[29] Roland CM, Ngai KL. Macromolecules 1992;25:363–7.
[30] Nguyen TH, Lee BT. J Biomed Sci Eng 2010;3:1117–24.
[31] Fraga AN, Williams RJJ. Polymer 1985;26:113–8.
[32] Konyali H, Mencelogˇlu Y, Erman B. Polymer 2008;49:1056–65.
[33] Protsenko DS, Ho K, Wong BJF. Ann Biomed Eng 2006;34:455–64.
[34] Larson RG. The structure and rheology of complex fluids. New York: Oxford University Press; 1999.
[35] Shiga T, Ohta T, Hirose Y, Okada A, Kurauchi T. J Mater Sci 1993;28:1293–9.
[36] Puvanatvattana T, Chotpattananont D, Hiamtup P, Niamlang S, Kunanuruksapong R, Sirivat A, et al. Mat Sci Eng C 2008;28:119–28.
[37] Wichiansee W, Sirivat A. Mat Sci Eng C 2009;29:78–84.
[38] Tungkavet T, Pattavarakorn D, Sirivat A. J Polym Res 2012;19:9759.
[39] Hao T. Electrorheological fluids the non-aqueous suspensions. Amsterdam: Elsevier; 2005 [chapter 6].
[40] Tangboriboon N, Sirivat A, Kunanuruksapong R, Wongkasemjit S. Mat Sci Eng C 2009;29:1913–8.
[41] Martron A, Elvidge JA, Inczedy J. J Chromatogr 1980;201:79–84.
[42] Chatterjee S, Bohidar HB. Int J Biol Macromol 2005;35:81–8.
[43] Richard TW. J Am Chem Soc 1898;20:121–6.
[44] Loeb GI, Saroff HA. Biochemistry 1964;3:1819–26.

International Journal of Polymeric Materials and Polymeric Biomaterials, 62: 583–589
Copyright © 2013 Taylor & Francis Group, LLC
ISSN: 0091-4037 print/1563-535X online
DOI: 10.1080/00914037.2013.769162

Taylor & Francis
Taylor & Francis Group

Sensitive and Selective Responses of Poly(Para-Phenylene Vinylene)/Zeolite Y-Based Sensors Toward Ketone Vapors

JIRARAT KAMONSAWAS[1], ANUVAT SIRIVAT[1], and PIMPA HORMNIRUN[2]

[1]*Conductive and Electroactive Polymer Research Unit, The Petroleum and Petrochemical College, Chulalongkorn University, Bangkok, Thailand*
[2]*Department of Chemistry, Faculty of Science, Kasetsart University, Chatuchak, Bangkok, Thailand*

Received 14 March 2012, Accepted 26 December 2012

Downloaded by [Chulalongkorn University] at 21:25 19 May 2013

Poly (*p*-phenylene vinylene) doped with H_2SO_4 is mixed into zeolite Y matriced to improve the electrical conductivity responses toward ketone vapors. The effect of cation type, cation concentration, and ketone vapor type on the electrical conductivity response toward ketone vapors of dPPV_zeolite Y composites is investigated. The sensitivities of the composites increase linearly with increasing surface area and decreasing cationic radius of the cation in zeolite Y. The highest sensitivity is obtained with the dPPV_[90] NH_4^+Y when exposed to acetone, whereas in MIBK shows the lowest sensitivity The interactions between the ketone molecules and the composites are investigated though the FTIR.

Keywords: Conductive polymer, dimethyl ketone (acetone), gas sensor, MEK, methyl ethyl ketone, methyl iso-buthyl ketone, MIBK, poly (*p*-phenylene vinylene), zeolite Y

1. Introduction

Semiconductor gas sensors are widely used in domestic and industrial applications due to the favorable characteristics such as low cost and the ease of operation. The sensors still play an important role in the development and the improvement of public health through several aspects [1–7].

In the color industry, many solvents are utilized to prepare enamel paints: dimethyl ketone or propanone (acetone), methyl ethyl ketone or butan-2-one (MEK), methyl iso-buthyl ketone or 4-methylpentan-2-one (MIBK), and 1,4-dimethlybenzene (p-xylene). These solvents constitute flammable ingredients in the enamel paints, CED, and AED paints, car coating paints, and various ingredients used in chemical plants [8].

Several conductive polymers have been used as a gas sensing materials; polyaniline and polypyrrole have many common interesting features such as inexpensiveness, the ease in the syntheses, the high electrical conductivity, and the chemical stability. Another conductive polymer, poly(*p*-phenylene vinylene), is also a candidate. It has good mechanical properties, high electrical conductivity, and the chemical stability. Poly(*p*-phenylene vinylene) can be synthesized to yield a high molecular weight polymer. In the first step, the formation of the precursor is via the Wessling route, followed by the synthesis of the polymer from such precursor via the thermal reaction [9]. Recently, poly(*p*-phenylene vinylene) and its oligomers have been shown to be useful as active materials for gas sensors or for electronic noses [10,11].

Zeolites are polycrystalline, hydrated aluminosilicates of Group I and Group II elements, in particular, sodium, potassium, magnesium, calcium, strontium, and barium. Structurally, the zeolites are framework aluminosilicates, which are based on an infinitely extending three-dimensional network of $[AlO4]^{5-}$ and $[SiO4]^{4-}$ tetrahedrally linked to each other by sharing all of the oxygen. The framework contains channels and interconnected voids, which are occupied by the cations and water molecules. The cations are quite mobile and may be easily exchanged by other cations. Because of their unique structure, zeolites and related microporous materials posses the molecular sieving property, which is useful as catalysts, adsorbents, and in the ion exchanging. As a sensing material, zeolites are very advantageous: high thermal stability and chemical resistance. Characteristics of the molecular sieving property have been explored and utilized as chemical sensors [8,12]. Recently, composites consisting of the zeolite that is dispersed in a polymer matrix have been investigated as sensing materials to detect toxic gases [12–14].

Combining the advantages of the two materials, we propose to investigate the combination of a conductive polymer, poly(*p*-phenylene vinylene), and zeolite Y of various cations as ketone vapor sensors. The effects of dPPV concentration, cation type of zeolite Y, and the ketone solvent type on the electrical conductivity response of the composites will investigated and reported here.

Address correspondence to: A. Sirivat, Conductive and Electroactive Polymer Research Unit, The Petroleum and Petrochemical College, Chulalongkorn University, Bangkok 10330, Thailand. E-mail: anuvat.s@chula.ac.th

Downloaded by [Chulalongkorn University] at 21:25 19 May 2013

2. Experimental

2.1 Materials Preparation

2.1.1 Synthesis of Poly(p-phenylene vinylene) or PPV

The synthesis of the p-xylene-bis(tetrahydrothiophenium chloride) monomer was achieved by reacting α,α'-dichloro-p-xylene (Aldrich) with tetrahydrothiophene (Aldrich) [9]. The precursor sulfonium polyelectrolyte was prepared in an aqueous solution by the base induced polymerization of an appropriate *bis*-sulfonium monomer. The polymerization reaction was terminated by the addition of dilute aqueous hydrochloric acid to the reaction mixture, which was then dialyzed against water in order to separate the high molecular weight fraction from the monomeric and oligomeric residues as well as the sodium and chloride ions. Poly(p-phenylene vinylene) (PPV) was essentially obtained by heating poly(p-xylene-bis(tetrahydrothiophenium chloride) under vacuum at 180°C for 6 h [9,11].

2.1.2 Doping Process

The 18 M sulfuric acid was used as the dopant solution at the mole ratio between PPV repeating unit per sulfuric acid equal to 1:100. The doping process occurred after adding the dopant solution to the polymeric powder, and it was monitored by observing the color changes of the powder from bright yellow to black [15].

2.1.3 Preparation of dPPV_Zeolilte Y Pellet

Zeolite: CBV100 (Si/Al = 5.1, Na^+) (Zeolyst) or NaY, CVB300 (Si/Al = 5.1, NH_4^+) (Zeolyst), or NH_4^+Y, CVB 400 (Si/Al = 5.1, H^+) (Zeolyst) or HY were used as the adsorbents. dPPV_zeolite Y composites were prepared by dry mixing the doped PPV particles with the zeolite Y at 10% v/v. The composites were compressed into a disc form by using a hydraulic press at the pressure of 6 kN.

2.1.4 Materials Characterization

The FT-IR spectrometer (Bruker, model FRA 106/S) was used to characterize functional groups of PPV and the interaction between the chemical vapors and the composites. A scanning electron microscope (SEM; Hitachi, model S4800) was used to study the morphology of PPV or poly(p-phenylene vinylene), dPPV, or doped poly(*p*-phenylene vinylene), the zeolite Y, and the 10% v/v of dPPV_zeolite Y composites and the dispersion between the conductive polymer and the zeolite Y at the magnifications of 2000 and 5000 and at 5 and 10 kV. BET (Sorptomatic-1990) was used to measure the pore sizes and the surface areas of the zeolite Y. A custom made two-point probe with a linear geometric array was used to measure the specific electrical conductivity of samples.

2.1.5 Electrical Conductivity and Chemical Vapor Detection

The electrical conductivity of the PPV pellets under exposures to air, N_2, and chemical vapors were measured by using the custom made two-point probe, in the chemical chamber, connected to a voltage supplier (Keithley, 6517A) in which its voltage was varied and the resultant current was measured. The electrical conductivity was calculated by utilizing the equation: $\sigma = (I/KVt)$, where I is the measured current (A), V is the applied voltage (V), t is the thickness, and K is the geometric correction factor of the two-point probe determined by calibrating the probe with a silicon wafer possessing a known resistivity value. The chemicals used in this work were dimethyl ketone or propanone (acetone), methyl ethyl ketone or butan-2-one (MEK), methyl iso-buthyl ketone, or 4-methylpentan-2-one (MIBK) (Labscan, AR grade). All of ketone vapors were prepared through a flow system at the vapor concentration of 30000 ppm. Nitrogen (N_2, TIG) was used as the surface cleaning gas and to vaporize the chemical solvents. All chemicals were used without further purifications. The electrical conductivity response and sensitivity of the composites were determined by following the equations: $\Delta\sigma = \sigma_{\text{chemical vapor}} - \sigma_{\text{N2, before exposure}}$ and, respectively, where $\Delta\sigma$ is the difference in the specific electrical conductivity (S/cm), $\sigma_{\text{N2, before exposure}}$ is the specific electrical conductivity in N_2 before exposure (S/cm), and $\sigma_{\text{chemical vapor}}$ is the specific electrical conductivity under chemical vapor exposure (S/cm) [16–18].

3. Results and Discussion

3.1 Morphology of dPPV_zeolite Y

Figure 1 shows the SEM monographs of dPPV or doped poly(p-phenylene vinylene), zeolite Y (Si/Al = 5.1, NH_4^+), or NH_4^+Y, and dPPV_zeolite Y (Si/Al = 5.1, NH_4^+) or the dPPV_[90]NH_4^+Y composite at the dPPV volume fraction of 10% v/v. The dPPV particles are quite irregular in shape and size, as shown in Figure 1a. On the other hand, the zeolite Y appears to possess nearly uniform sizes and shapes, as shown in Figure 1b. However, a nearly uniform dispersion of dPPV particles within the NH_4^+Y matrix can be observed in Figures 1c and 1d [18].

3.2 Temporal Response of ZeoliteY and Composites When Exposed to Ketone Vapors

The temporal response of the composites is investigated next. The induction time is defined as the time required for the electrical conductivity to reach the equilibrium value when exposed to chemical vapors. The recovery time is defined as the time required for the electrical conductivity to attain the equilibrium value when chemical vapors are removed and replaced with nitrogen [18]. Table 1 lists the induction times and the recovery times of the zeolite Y and the composites. The induction times of NH_4^+ Y, NaY, and HY when exposed to acetone vapor at concentration of 30000 ppm in N_2 are 44 ± 1, 42 ± 2, and 29 ± 6 min, respectively. The recovery times of these samples are 15 ± 5, 27 ± 2, and 20 ± 2 min, respectively. The induction time of NH_4^+Y is the longest. This number is directly related to the specific surface area and the number of active sites in the zeolite Y framework. NH_4^+Y has the highest specific surface area ($766 \pm 3\,m^2/g$), whereas the NaY and HY surface areas are $731 \pm 12\,m^2/g$ and $648 \pm 2\,m^2/g$; thus, the acetone vapor can penetrate more easily into the NH_4^+Y structure and take the longer time than those of NaY and HY [19]. The recovery time of NaY is longer than HY because Na^+ has higher surface area than

Downloaded by [Chulalongkorn University] at 21:25 19 May 2013

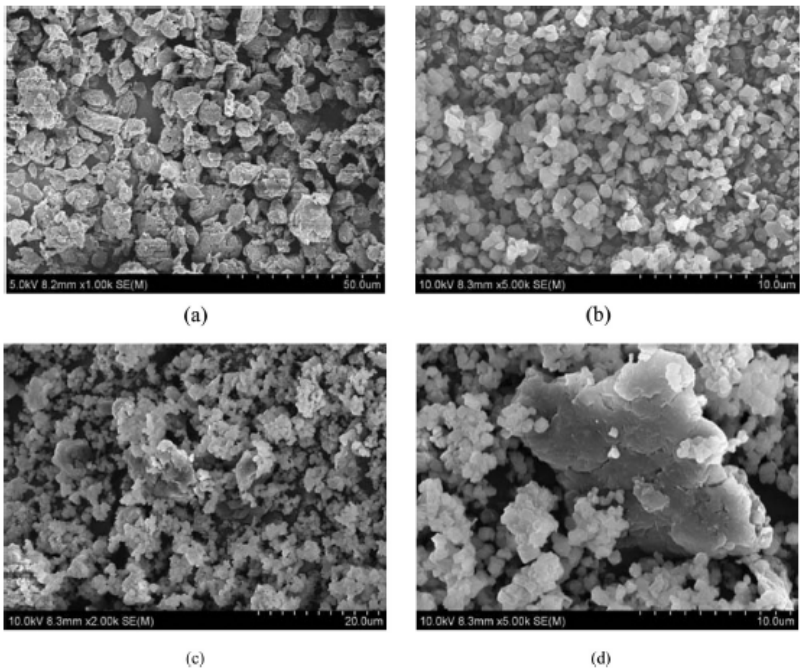

Fig. 1. The morphology of dPPV, NH_4^+Y powders, and dPPV_[90]NH_4^+Y composites at 10% v/v of dPPV: (a) dPPV at magnification of 1000×; (b) Zeolite Y at magnification 5000×; (c) dPPV_[90]NH_4^+Y at magnification of 2000×; and (d) dPPV_[90]NH_4^+Y at magnification of 5000×.

H^+ (electronegativity [EN] values of Na^+ and H^+ are 0.9 and 2.2, respectively); thus NaY has a stronger interaction with the acetone vapor than HY [18,19]. On the other hand, the recovery time of NH_4^+Y is 15 ± 5 min, the shortest, is due to the fact that NH_4^+ is a compound and thus interacts weakly with the acetone vapor. For the other ketone vapors (MEK and MIBK); the results are similar. We may note that the induction times of NH_4^+Y when exposed to acetone, MEK, and MIBK are 44 ± 1, 30 ± 2, and 22 ± 2 min, respectively; these values are higher than those NaY and HY due to the highest surface area of NH_4^+Y. The corresponding recovery times are 15 ± 5, 13 ± 1, and 12 ± 1 min, respectively; these values are lower than those NaY and HY due to the highest surface area of NH_4^+Y. These numbers can also directly related to the number of available active sites for the ketone vapor molecules. Since the size of acetone molecule is smaller than those of MEK and MIBK, it can penetrate further into the zeolite to interact with the available active sites and take the longer times than those of MEK and MIBK [19,20]. Adding 10% v/v of dPPV into NH_4^+Y matrix and exposing it to acetone, MEK and MIBK vapors at the concentration of 30000 ppm in N_2, the induction times decrease to 31 ± 3, 21 ± 1, and 11 ± 2 min, respectively. The presence of dPPV reduces the available active sites on the zeolite Y and therefore the time to reach equilibrium is shorter. For other cations (Na^+, H^+) in the composites, similar results are obtained as the dPPV_[90]NH_4^+ Y composite with respect to the ketone vapors [18,20]. In a previous work, the response time of the PS/PMMA/ABS blend to acetone vapor was shorter relative to those of the individual polymers [21].

3.3 Electrical Conductivity Sensitivity of Zeolite Y and dPPV_zeolite Y When Exposed to Ketone Vapors

Doped poly(*p*-phenylene vinylene) is mixed with NH_4^+Y at various dPPV contents: 0, 10, 20, 40, 60, 80, and 100% v/v. Figure 2 shows the electrical sensitivity of dPPV_NH_4^+Y when exposed to acetone vapor at the concentration of 30000 ppm in N_2. The electrical sensitivity of the composites with the dPPV contents between 0% and 40% v/v increases from $4.32 \times 10^{-01} \pm 1.30 \times 10^{-2}$ to $4.13 \pm 5.55 \times 10^{-02}$, an increase by nearly an order of magnitude. For the dPPV contents between 60% and 80% v/v, the electrical conductivity sensitivity decreases from $3.84 \pm 2.89 \times 10^{-02}$ to $3.77 \pm 7.09 \times 10^{-02}$. The initial increase in the electrical conductivity sensitivity between 0% v/v and 40% v/v of dPPV is due to the higher sensitivity of dPPV to acetone relative to that of NH_4^+Y, $4.49 \pm 6.78 \times 10^{-01}$ versus $4.32 \times 10^{-01} \pm 1.30 \times 10^{-02}$, a difference by an order of magnitude, as shown in Table 1. The decrease in the electrical conductivity sensitivity at the high content of dPPV is due to the reduced amount of the porous zeolite, which promotes the vapor molecules to interact with the available active sites of dPPV [16–19]. From this result, the composite with the 10% v/v

Downloaded by [Chulalongkorn University] at 21:25 19 May 2013

Table 1. PPV, dPPV, and 10%v/v dPPV_zeolite Y composites with the electrical conductivity responses, sensitivities and temporal responses to acetone, MEK, and MIBK (25°C, 1 atm, and the vapor concentration of 30000 ppm in N_2) and the specific surface areas

Sample	Sample code	BET surface area (m^2/g)	Sensitivity			Acetone		MEK		MIBK	
			Acetone	MEK	MIBK	Induction time (min)	Recovery time (min)	Induction time (min)	Recovery time (min)	Induction time (min)	Recovery time (min)
PPV	PPV	—	$1.61 \times 10^{-01} \pm 5.08 \times 10^{-02}$	$2.22 \times 10^{-02} \pm 8.50 \times 10^{-03}$	$1.33 \times 10^{-02} \pm 1.79 \times 10^{-03}$	51 ± 2	12 ± 1	19 ± 1	6 ± 3	17 ± 5	8 ± 1
100 dPPV	dPPV	—	$4.49 \pm 6.78 \times 10^{-01}$	$1.89 \pm 3.73 \times 10^{-01}$	$1.20 \pm 2.19 \times 10^{-01}$	35 ± 0.2	20 ± 1	32 ± 2	11 ± 5	12 ± 1	10 ± 4
zeolite Y ($Si/Al = 5.1$, Na^+)	NaY	731 ± 12	$2.68 \times 10^{-01} \pm 1.99 \times 10^{-02}$	$1.55 \times 10^{-01} \pm 4.76 \times 10^{-02}$	$1.47 \times 10^{-01} \pm 6.48 \times 10^{-02}$	42 ± 2	27 ± 2	19 ± 1	20 ± 3	17 ± 4	16 ± 3
zeolite Y ($Si/Al = 5.1$, NH_4^+)	NH_4^+ Y	766 ± 3	$4.32 \times 10^{-01} \pm 1.30 \times 10^{-02}$	$3.68 \times 10^{-01} \pm 3.23 \times 10^{-02}$	$2.14 \times 10^{-01} \pm 3.50 \times 10^{-01}$	44 ± 1	15 ± 5	30 ± 2	13 ± 1	22 ± 2	12 ± 1
zeolite Y ($Si/Al = 5.1$, H^+)	HY	648 ± 2	$1.52 \times 10^{-01} \pm 2.48 \times 10^{-02}$	$7.94 \times 10^{-02} \pm 6.59 \times 10^{-03}$	$4.01 \times 10^{-02} \pm 1.00 \times 10^{-03}$	29 ± 6	20 ± 2	17 ± 1	15 ± 4	16 ± 6	13 ± 1
100dPPV _[90]zeolite Y ($Si/Al = 5.1$, Na^+)	dPPV_ [90]NaY		$2.09 \pm 5.26 \times 10^{-02}$	$9.38 \times 10^{-01} \pm 1.51 \times 10^{-01}$	$5.43 \times 10^{-01} \pm 1.07 \times 10^{-01}$	20 ± 4	22 ± 2	20 ± 1	16 ± 2	13 ± 3	15 ± 5
100 dPPV _[90]zeolite Y ($Si/Al = 5.1$, NH_4^+)	dPPV_[90] NH_4^+ Y		$3.82 \pm 3.12 \times 10^{-02}$	$2.76 \pm 1.80 \times 10^{-01}$	$1.02 \pm 3.58 \times 10^{-01}$	31 ± 3	15 ± 4	21 ± 1	10 ± 1	11 ± 2	9 ± 2
100 dPPV_[90]zeolite Y ($Si/Al = 5.1$, H^+)	dPPV_[90]HY		$1.30 \pm 8.22 \times 10^{-02}$	$8.61 \times 10^{-01} \pm 4.59 \times 10^{-02}$	$2.20 \times 10^{-01} \pm 2.91 \times 10^{-02}$	16 ± 7	17 ± 3	17 ± 3	14 ± 1	15 ± 2	11 ± 4

Downloaded by [Chulalongkorn University] at 21:25 19 May 2013

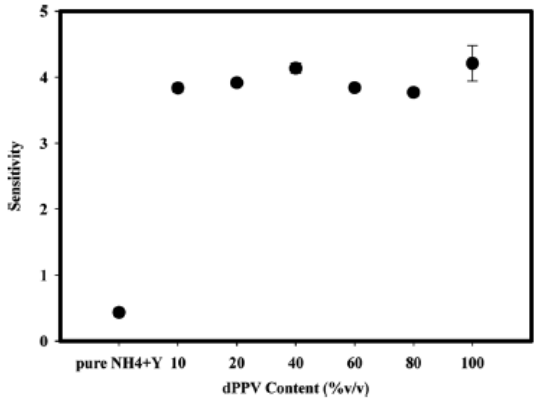

Fig. 2. Sensitivity of dPPV mixed with zeolite Y (Si/Al = 5.1, NH_4^+) or NH_4^+Y at various contents: 0, 10, 20, 40, 60, 80, and 100% (v/v) when exposed to acetone vapor concentration of 30000 ppm in N_2 (at 25°C, 1 atm).

of dPPV content is then chosen for further study on the electrical conductivity responses toward other ketone vapors since the sensitivity of the composite at 10% v/v of dPPV gives the sensitivity quite close to that of the pristine dPPV [16–18,20], as shown in Table 1.

The effect of cation type of the zeolite Y and the composites on the responses to the acetone vapor is investigated next. Table 1 lists the electrical conductivity responses and the sensitivity values of the zeolite Y and the composites of various cations. The electrical conductivity sensitivity values of zeolite Y with the cations of NH_4^+, Na^+, and H^+ when exposed to acetone vapor at the concentration of 30000 ppm in N_2 are $4.32 \times 10^{-01} \pm 1.30 \times 10^{-02}$, $2.68 \times 10^{-01} \pm 1.99 \times 10^{-03}$, and $1.52 \times 10^{-01} \pm 2.48 \times 10^{-02}$, respectively. Thus, NH_4^+Y possesses the highest sensitivity. Typically, the gas adsorption properties and the interactions are expected to depend on three factors: the specific surface area, the EN value, and the ionic radius (Å) The specific surface areas of zeolite Y with the cations of NH_4^+, Na^+, and H^+ are 766 ± 3, 731 ± 12, and $648 \pm 2\,m^2/g$, respectively. NH_4^+ Y have the highest specific surface area facilitating a larger amount of acetone vapor into the zeolite framework. In case of the cationic radii, NH_4^+ (1.43 Å) is larger than Na^+ (1.16 Å) and H^+ (0.37 Å), which reduced the electrostatic interaction with the anionic zeolite framework and cation, which led to the ease of interaction between cation in the zeolite Y framework and acetone [22]. For the 10% v/v of dPPV_zeolite Y composites with the three types of cation (NH_4^+, Na^+, and H^+), the sensitivity values to acetone increase to $3.82 \pm 3.12 \times 10^{-02}$, $2.09 \pm 5.26 \times 10^{-02}$, and $1.30 \pm 8.22 \times 10^{-02}$, respectively. These values are higher than those of the pristine zeolite Y by an order of magnitude, due to the presence of dPPV. The higher sensitivity values of the dPPV_zeolite Y composites than those of the pure zeolite Y are due to the available active sites along the dPPV chains. The positive increments in the sensitivity upon exposed to all of the ketone vapors imply that the solvent molecules act as a primary and a secondary dopant for PPV or doped PPV, resulting in a greater number of charges along the polymer backbone and correspondingly a larger sensitivity [23], as shown in Figure 3 and Table 1.

The effect of ketone vapor type on the electrical conductivity sensitivity is investigated next. The electrical conductivity sensitivity values of NH_4^+Y when exposed to acetone, MEK, and MIBK at the vapor concentration of 30000 ppm in N_2 are $4.32 \times 10^{-01} \pm 1.30 \times 10^{-02}$, $3.68 \times 10^{-01} \pm 3.23 \times 10^{-02}$, and $2.14 \times 10^{-01} \pm 3.50 \times 10^{-01}$, respectively, as shown in Table 1. These values are comparable in magnitude, and similar results are obtained for NaY and HY. On the other hand, for the dPPV_ [90]NH_4^+Y composites, the sensitivity values are $3.82 \pm 3.12 \times 10^{-02}$, $2.76 \pm 1.80 \times 10^{-01}$, and $1.02 \pm 3.58 \times 10^{-01}$, respectively. The molecular sizes are 5.246, 6.667, and 8.286 Å for acetone, MEK, and MIBK, respectively. The smaller size of the ketone vapor molecule leads to a better interaction between the vapor and the active sites [19,21–22,24].

3.4 FT-IR Investigations of Reactions of Adsorbed Ketone Vapor

The FT-IR spectra of NH_4^+Y and dPPV_[90]NH_4^+Y were taken in the 650–4000 cm^{-1} regions (Figures 4 and 5). The spectra are for before (a), during the 15-min interval (b), and after the acetone exposure (c) in order to study the interaction between the zeolite Y and acetone.

Figure 4 shows the FT-IR spectra of NH_4^+Y before (a), during the 15-m interval (b), and after the acetone exposure (c). Before the acetone exposure, the adsorption of the Si-OH group ($\nu = 3640\,cm^{-1}$) can be assigned to the zeolite characteristic [19,22,24–27] The peaks at 790, 1010, and 3640 cm^{-1} are the characteristic of tetrahedral unit [24]. The peaks at 1400 cm^{-1} are the stretching and bending of N-H bond in N_2 condition before acetone exposure [22,24]. A peak at 1600 cm^{-1} is the OH stretching, which suggests the possibility of the water in zeolite structure [19,22]. During the acetone

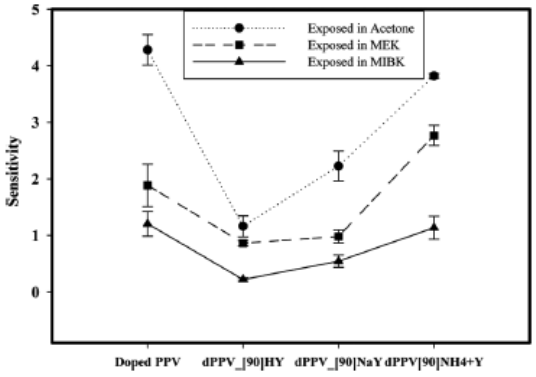

Fig. 3. Sensitivity values of dPPV, dPPV_[90]HY, dPPV_[90]NaY, and dPPV_[90]NH_4^+Y, when exposed to acetone, MEK and MIBK at 25°C, 1 atm, and at the solvent concentration of 30000 ppm in N_2.

Downloaded by [Chulalongkorn University] at 21:25 19 May 2013

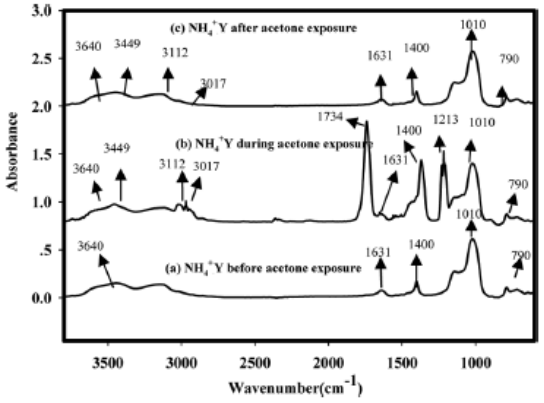

Fig. 4. FTIR Interaction between NH_4^+ Y and acetone at 25°C, 1 atm before, during, and after the exposure to acetone vapor at the concentration of 30000 ppm in N_2.

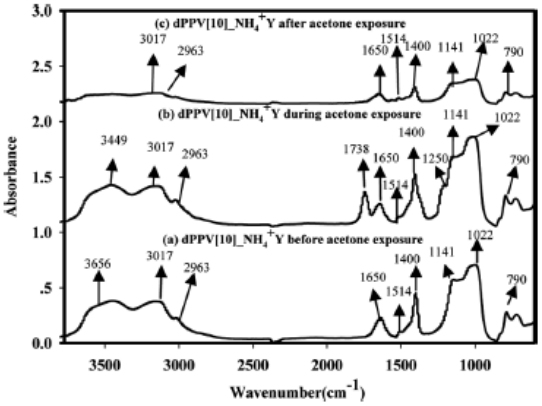

Fig. 6. FTIR Interaction between dPPV_[90]NH_4^+Y and acetone at 25°C, 1 atm before, during, and after the exposure to acetone vapor at the concentration of 30000 ppm in N_2.

exposure, the spectrum shows three new peaks at 3449, 1734, and 1213 cm^{-1}, the former can be assigned to the carbonyl interaction with oxygen on the zeolite structure and cation into zeolite framework, as shown in Figure 5. The new peak at 1213 cm^{-1} is assigned to the interaction between oxygen on to carbonyl group and hydrogen at the zeolite [22–27]. When acetone is removed and replaced with nitrogen, the IR spectrum peaks at 3449 and 1213 cm^{-1} evidently decrease; this confirms that there are some interactions remaining between acetone and the zeolite, suggesting the irreversible response to acetone [18].

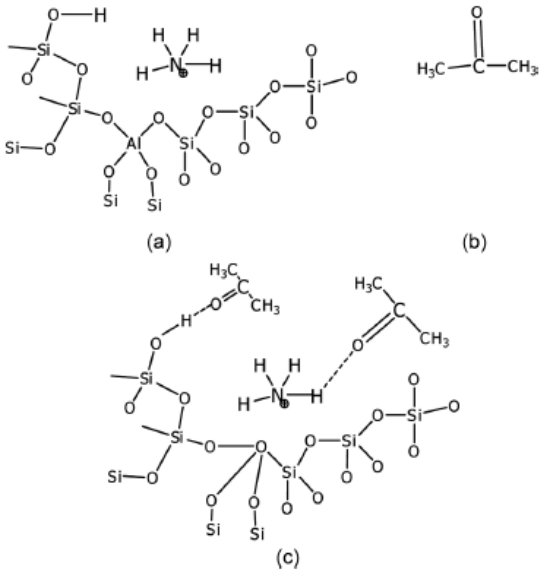

Fig. 5. Schematic of the proposed mechanism of the acetone-zeolite Y.

Figure 6 shows the corresponding IR spectra of dPPV_[90]NH_4^+Y. Before the acetone exposure, the adsorption peak of the quinoid structure, a characteristic of dPPV, appears at $\nu = 1141\ cm^{-1}$. The peaks at 1514, 2963, and 3017 cm^{-1} are the characteristics of phenylene [28–30]. The peak at around 3656 cm^{-1} can be assigned to the Si-OH group [24]. During the acetone exposure, the two new peaks at 3449 and 1250 cm^{-1} are the adsorption peaks of Si-O-C suggesting an interaction between acetone and the zeolite [24–27]. The

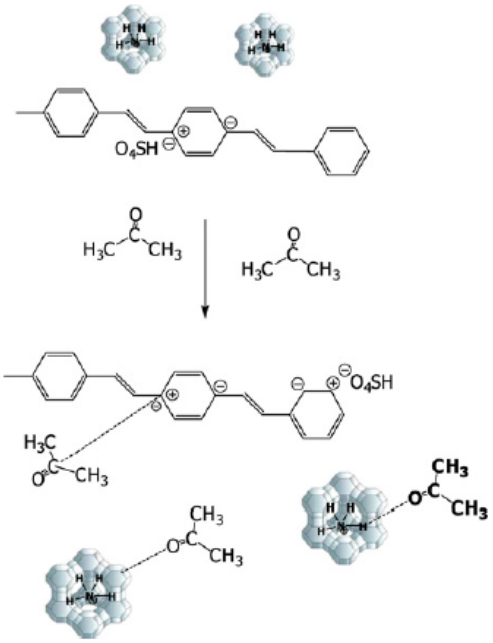

Fig. 7. Schematic of the proposed mechanism of the acetone-dPPV_[90]NH_4^+Y. (Figure is provided in color online.)

Downloaded by [Chulalongkorn University] at 21:25 19 May 2013

new peak at 1377 cm^{-1} indicates the C-O stretching; this also suggests an interaction between acetone and dPPV. The increase in the intensity at 1141 cm^{-1} during the exposure is caused by the increase in number of the quinoid structure of dPPV [28–30]. After the acetone exposure, the intensities at 3017, 2963, and 1514 cm^{-1} decrease; these suggest that acetone may act as a secondary dopant to increase the number of the quinoid structures in the dPPV chain [23,28–30]. The interaction between acetone with dPPV_[90]NH_4^+Y is proposed and shown in Figure 7. The interaction is clearly irreversible.

4. Conclusions

Zeolite Y with the three types of cation NH_4^+, Na^+, and H^+ are investigated and utilized as ketone vapors sensing materials. Electrical conductivity sensitivity of the zeolites toward ketone can be improved by introducing doped PPV into the zeolite Y matrices. The electrical conductivity sensitivity of zeolite Y and composites increases with increasing zeolite Y surface area and decreasing chemical vapor size. The electrical conductivity sensitivity of dPPV_[90]NH_4^+Y when exposed to acetone exhibits the highest value at $3.82 \pm 3.12 \times 10^{-02}$ since dPPV_[90]NH_4^+Y has the highest specific surface area and it can induce the more favorable acetone vapor adsorption in to the composite. The interaction is further investigates by the IR spectra and appears to be irreversible.

Acknowledgments

The authors would like to acknowledge the financial supports from the Conductive and Electroactive Polymers Research Unit of Chulalongkorn University, the Thailand Research Fund (TRF-BRG, TRF-RTA, PHD/0026/2553), and the Royal Thai Government Budget.

References

1. Vijayakumar, N.; Subramanian, E.; Padiyan, D. P. *Int. J. Polym. Mater.* **2012**, *61*, 847–863.
2. Alkskas, I. A.; Moosa, I. S. *Int. J. Polym.* **2011**, *61*, 1142–1153.
3. Luo, Y.; Yu, W.; Xu, F. *Polym.-Plast. Technol. Eng.* **2011**, *50*, 1084–1090.
4. Shukl, P.; Bhatia, V.; Gaur, V.; Jain, V. K. *Polym.-Plast. Technol. Eng.* **2011**, *50*, 1179–1184
5. Montserral, V.; Joaquin, C.; Albert, C.; Albert, C.; Ramon, M. J.; Jesus, S. *Sens. Actuators, B* **2007**, *124*, 99–110.
6. Heeger, A. J.; Diaz-Grazia, M. A. *Curr. Opin. Solid. State Mater. Sci.* **1998**, *3*, 16–22.
7. Luo, Y. L.; Miao, Y.; Xu, F.; Yao, Y. *Polym.-Plast. Technol. Eng.* **2012**, *51*, 290–297.
8. Mori, M.; Nishimura, H.; Itagaki, Y.; Sadaoka, Y. *Sens. Actuators, B* **2009**, *142*, 141–146.
9. Wessling, R. A.; Zimmerman, R. G. U.S Patent No. 3,401,152, 1968.
10. Das, T. K.; Prusty, S. *Polym.-Plast. Technol. Eng.* **2012**, *51*, 1487–1500.
11. Peres, L. O.; Jonas, G. *Mater. Sci. Eng., C* **2007**, *27*, 67–69.
12. Yang, J. C.; Dutta, P. K. *Sens. Actuators, B* **2007**, *125*, 30–39.
13. Sharma, A. L.; Kumar, P.; Deep, A. *Polym.-Plast. Technol. Eng.* **2012**, *51*, 1382–1387.
14. Mishira, I.; Akinyeye, R.; Baker, P.; Iwuoha, E. *Int. J. Polym. Mater.* **2011**, *50*, 469–489.
15. Ahlskog, M.; Reghu, M.; Noguch, I. T.; Ohnishi, T. *Synth. Met.* **1997**, *89*, 11–15.
16. Chuaypradit, C.; Wannathong, L.; Chotpattananont, D.; Hiamtupt, P.; Sirivatt, A.; Schwank, J. W. *Polym.* **2005**, *46*, 947–953.
17. Densakulprasert, N.; Wannathong, L.; Chotpattananont, D.; Hiamtup, P.; Sirivat, A.; Schwank, J. W. *Mater. Sci. Eng., B* **2005**, *117*, 276–282.
18. Thuwachaosoan, K.; Chotpattananont, D.; Sirivat, A.; Rujiravanit, R.; Schwank, J. W. *Mater. Sci. Eng., B* **2007**, *140*, 23–30.
19. Panov, A. G.; Fripiat, J. J. *Langmuir* **1998**, *14*, 3788–3796.
20. Ruangchuay, L.; Sirivat, A.; Schwank, J. W. *Talanta* **2003**, *60*, 25–30.
21. Ruangchuay, L.; Sirivat, A.; Schwank, J. W. *React. Funct. Polym.* **2003**, *61*, 11–22.
22. Yimlamai, I.; Niamlang, S.; Chantaanont, P.; Kunanuraksapong, R.; Changkhamchom, S.; Sirivat, A. *Ionics* **2011**, *17*, 607–615.
23. Kamonsawas, J.; Sirivat, A.; Niamlang, S.; Hormnirun, P.; Prissanarun, W. O. *Sens.* **2010**, *10*, 5590–5603.
24. Soontornworajit, B.; Wannathong, S.; Hiamtup, P.; Niamlang, S.; Chotpattananont, D.; Sirivat, A.; Schwank, J. W. *Mater. Sci. Eng., B* **2007**, *15*, 78–86.
25. Li, X.; Dutta, P. K. *J. Phys. Chem. C* **2010**, *4*, 7986–7994.
26. Gaare, K.; Akporiaye, D. *J. Phys. Chem. B* **1997**, *101*, 48–54
27. Hagen, G.; Dubbe, A.; Rettig, F.; Jerger, A.; Birkhofer, T.; Plog, C.; Moos, R. *Sens. Actuators, B* **2006**, *119*, 441–448.
28. Li, R. N. C.; Ventra, L.; Gruber, J.; Kawano, Y.; Carvalho, L. R. F. *Sens. Actuators, B* **2008**, *131*, 646–651.
29. Cirpan, A.; Kucukyavuz, Z.; Kucukyavuz, S. *Turk. J. Polym.* **2003**, *27*, 135–143.
30. Gagnon, D.; Capiston, J.; Karasz, F. E.; Lenz, R. W. *Polym.* **1987**, *28*, 567–573.

Current Applied Physics 13 (2013) 1119–1127

Contents lists available at SciVerse ScienceDirect

Current Applied Physics

journal homepage: www.elsevier.com/locate/cap

Electrostrictive properties of thermoplastic polyurethane elastomer: Effects of urethane type and soft–hard segment composition

K. Petcharoen, A. Sirivat*

Conductive and Electroactive Polymers Research Unit, The Petroleum and Petrochemical College, Chulalongkorn University, Bangkok 10330, Thailand

ARTICLE INFO

Article history:
Received 13 November 2012
Received in revised form
25 February 2013
Accepted 5 March 2013
Available online 21 March 2013

Keywords:
Polyurethane
Electromechanical properties
Flexible actuators
Electrostriction
Dielectrophoresis force

ABSTRACT

The electromechanical behavior of thermoplastic elastomer polyurethane (TPE-PU) is investigated under the effects of urethane type (ester and ether-types) and soft–hard segments at various electric field strengths and temperatures. The highest dielectric constant, electrical breakdown strength, and specific conductivity belong to the ester-type polyurethane (LPR matrix), while the lowest values are obtained from the ether-type polyurethane composing predominantly with the soft-segment (E 80A matrix). Under the electric field strength in the range between 0 and 2 kV/mm, the LPR matrix attains the storage modulus sensitivity ($\Delta G'/G'_0$) up to 2 at 2 kV/mm. For the temporal response, the polyurethanes behave with good reproductively (number of cycles $>10^5$ times) and with very good recoverability. The steady state behavior can be attained at the first actuation and at the electric field strength of 1 kV/mm. Furthermore, the storage modulus (G') shows linearly negative responses with increasing temperature. In the deflection experiments, the deflection distance and the dielectrophoresis force increase monotonically with increasing electric field strength. All of the TPE-PU possesses very fast response times for activation (<10 s.) and deactivation (<5 s.). TPE-PU material is systematically shown here to be a potentially good actuator material with high efficiency based on the electrostrictive performance data obtained.

© 2013 Elsevier B.V. All rights reserved.

1. Introduction

The smart materials generally tend to respond with any external stimuli such as pH [1], temperature [2], electric field [3] and etc, by changing shapes and or dimensions. Electroactive polymers (EAPs) belong to one sub-group of the smart materials in which the mechanical response can be induced by electric field [4]; as these materials can be utilized in the actuator and transducer applications [5]. There are many required properties: lightweight, good mechanical flexibility, high resilience, good processability and short response time [6–8]. Oshiki et al. (1975) reported that most EAPs are based on either the piezoelectric mechanism or the electrostrictive interaction in which can be described by following general equation:

$$T = G^E S + eE + \gamma E^2, \quad (1)$$

where T is the stress, G^E is the elastic coefficient, S is the strain, e is the piezoelectric stress coefficient, E is the electric field, and γ is the electrostriction coefficient [9]. The equation can be interpreted as the linear relation associated with the piezoelectricity and the quadratic response for the electrostriction behavior under an applied electric field. Thus, it is generally useful to classify a material and its behavior by using the stress response under electric field.

In the recent years, the EAPs such as poly(vinylidene fluoride) [10], acrylic elastomers [11], silicon [12], and urethane [13] are the most common smart materials providing high ability to convert electrical energy into strain response [14]. Nevertheless, high flexural endurance, high shape recoverability, and large deformation are attained only by the polyurethane [15,16]. Due to the polyurethane performances under an electric field, many attempts have been made to enhance the actuation behavior through electromechanical properties. Ueda et al. (1997) studied the actuation mechanism of polyurethane elastomers and they suggested that the deformation of the specimen under electric field was induced by the dipole orientation within the materials [17]. Guillot et al., (2003) investigated the electrostrictive properties in a polyurethane and found that up to 85% of the electromechanical activity came from the electrostrictive effect due to a phase separation in the polyurethane. The minor factor (less than 15%) was attributed to the Maxwell stress, due to the electrostatic

* Corresponding author. Tel.: +66 2 218 4131; fax: +66 2 611 7221.
E-mail address: anuvat.s@chula.ac.th (A. Sirivat).

1567-1739/$ – see front matter © 2013 Elsevier B.V. All rights reserved.
http://dx.doi.org/10.1016/j.cap.2013.03.005

attraction under applied electric field [18]. Generally, the effect of electrostriction on the strain response mainly depends on the chemical composition, the physical structure, the dielectric constant, the Young's elastic modulus, and the electrostrictive coefficient of material [19].

The thermoplastic elastomer polyurethane (TPE-PU) can be regarded as a linear block copolymer consisting of three segment structures: polyol, diisocyanate, and a chain extender. These segments can influence their properties over a wide range, such as elasticity due to the soft–hard segment composition [20]. The TPE-PU properties are directly related to their chemical structure (ether or ester types) and segmented flexibility which can dictate various electrostrictive behaviors under electric field [21].

The aim of our investigation is to determine the influence of the TPE-PU structure, in terms of the urethane type and the soft–hard segment composition on the electrostrictive behavior. In particular, the stress (storage modulus; G′) and the strain responses under the influence of an electric field strength and temperature are investigated, compared with others, and reported here.

2. Experimental

2.1. Materials

Thermoplastic Poly(ether-urethane), Elastollan® 1180A; (E80A) and 1195A; (E95A), BASF, and Thermoplastic Poly(ester-urethane), LPR®4525; (LPR), Behnmeyer were used as the electroactive polymers. The polyurethane consists of butanediol as the chain extender, diphenylmethane diisocyanate as the hard segment, and the different soft segment are tetramethylene glycol and adipate ester for the ether-type and ester-type polyurethanes, respectively, as shown in Fig. 1. All of the TPE-PU pellets were dried at 80 °C for 24 h prior to use for evaporation of moisture content. Poly(-dimethylsiloxane), (PDMS 100 cSt, Sigma–Aldrich), was used as a liquid medium in the bending experiment.

2.2. Preparation of the TPE-PU films

All TPE-PU films were prepared by using a compression molding technique (Wabash, Model 9354) at 225 °C for 10 min with a pressure of 15 tons. The compression mold was a spherical shape with a diameter of 25 mm and a thickness of 1 mm for electromechanical testing. For the bending experiment, the mold had a rectangular shape with a thickness of 0.2 mm.

2.3. Characterization and testing

2.3.1. Fourier transform infrared spectrometer

The TPE-PU films were first characterized for the functional groups by a FT-IR spectrometer (Thermo Nicolet, Nexus 670) in the absorption mode with 32 scans and a resolution of ±4 cm^{-1}, a wave-number range of 4000–400 cm^{-1} with a deuterated triglycine sulfate as a detector. For the ATR-FTIR technique, air was used as the background material.

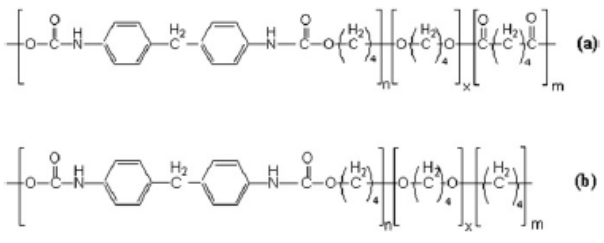

Fig. 1. TPE-PU structures: Ester-type (a); Ether-type (b).

2.3.2. Viscosity measurement

The average molecular weight was calculated from the Mark–Houwink equation:

$$[\eta] = KM^a, \tag{2}$$

where $[\eta]$ is the intrinsic viscosity, M is the viscosity-average molecular weight, the constant parameters K and a for polyurethane are $K = 6.80 \times 10^{-5}$ dL/g and $a = 0.86$. The intrinsic viscosity of polymer solutions in DMF was measured at 30 °C by using the Ubbelohde I capillary viscometer [22].

2.3.3. Thermal analysis

A thermogravimetric analyzer (Perkin Elmer, TGA7) was used to determine the degradation temperature of the TPE-PU. The experiment was carried out by weighting a sample of 5 mg and loaded into a platinum pan. The mass change under the temperature scan from 30 to 600 °C with a heating rate of 10 °C/min and under a nitrogen flow was monitored. A differential scanning calorimeter (Metter-Toledo, DSC-822e) was employed to obtain the melting temperature of the TPE-PU. The sample of about 5 mg was heated at a rate of 10 °C/min from 30 to 250 °C.

2.3.4. Electrical conductivity

The electrical conductivity measurement (Keithley, Model 8009) was performed at room temperature. The resistivity test fixture connected with the power source (Keithley, Model 6517A) to supply the voltage and to read the resultant current. The applied voltage and the current were used to determine the electrical conductivity by the following equation:

$$\sigma = \frac{1}{\rho} = \frac{t \times I}{22.9 \times V}, \tag{3}$$

where σ is the specific conductivity (S/cm), ρ is the specific resistivity (Ω cm), t is the specimen thickness (cm), I is the measured current (A), V is the applied voltage (V), and 22.9 is constant factor of the test fixture.

2.3.5. Electrical breakdown strength

The electric puncture tester (MFG Yaduda Seiki) was used to measure the electrical breakdown strength of the TPE-PU. The sample films were placed between the parallel electrodes and electric field was applied until it reached the breakdown voltage.

2.3.6. Dielectric constants

The LCR meter (HP, model 4284A) connected with the melt rheometer (Rheometric Scientific, ARES), parallel plate fixture with diameter of 25 mm, were used to measure the dielectric constants. The AC voltage of 10 V was applied through the specimens at temperature range of 300–360 K. Before testing, the specimens were coated with a silver paint.

2.3.7. Electromechanical behavior

The melt rheometer (Rheometric Scientific, ARES) was used to study the electromechanical properties of the films. The specimens were fitted with copper parallel plate fixture (diameter of 25 mm) and the DC voltage (Instek, GFG 8216A) was applied through the specimen. At first, the strain sweep test was carried out to

determine the suitable strain for measuring storage modulus (G') in the linear viscoelastic regime. The properly strain was used to investigate the G' behavior under the temporal sweep test and the frequency sweep test. In these experiments, the storage modulus, referred to the electrostrictive stress as above mentioned, was measured as functions of electric field strength (0–2 kV/mm) and temperature (300–360 K).

2.3.8. Bending actuation

The dielectrophoresis force and electrostrictive strain were determined by measuring the deflection of specimens which was carried out at room temperature under applied electric strengths. One end of the specimen was fixed and suspended vertically in a chamber containing PDMS (viscosity 100 cSt) between two parallel copper electrodes. The input electric field strength was generated by a DC power supply (Gold Sun 3000, GPS 3003D) connected to a high voltage power supply (Gamma High Voltage, UC5-30P). The bending distances of the specimens were measured along the x (d) and y (l) axes at the edges of the specimen using a Scion Image program (Beta 4.0.3).

The dielectrophoresis force (F_d) was calculated through the static horizontal force balance consisting of the elastic force, the gravity force, and the buoyancy force as shown in Eq. (4):

$$F_d = F_e + mg(\sin\theta) - \rho Vg(\sin\theta), \tag{4}$$

where m is the mass of the specimen, g is the gravity (9.8 m/s^2), θ is the deflection angle, ρ is the density of the fluid, and V is the volume of the displaced of fluid. The elastic force of the films was calculated through the non-linear deflection theory which obtained from the standard curve between $(F_e l_0^2)/(EI)$ and d/l_0; where F_e is the elastic force, l_0 is initial length of specimens, l is the deflection distance in the vertical axis, d is the deflection distance in the horizontal axis, and E is the Young's modulus which is equal to $2G'(1+\nu)$; where G' is the shear storage modulus taken to be $G'(\omega = 1$ rad/s) at various electric field strengths, and ν is the Poisson's ratio (0.5 for an incompressible sample).

The electrostrictive strain (S_E) was investigated through the Hooke's law which assumes that the strain at each point along the whole specimen is constant according to the following equation:

$$S_E = \frac{dt}{l_0^2}, \tag{5}$$

where d is the distance of bending, t is the thickness of the sample, and l_0 is the length of the sample.

2.3.9. Topology

The phase images of the specimens were obtained by using the atomic force microscope (AFM, Park System, XE-100) in air under ambient conditions. For the conventional AFM, the contact mode was operated with the cantilever (NSC36) tapping at scan rate of 0.2 Hz. The electrostatic force microscope (EFM) was performed at applied amplitude 5 V, a set point of 1200 nm and a scan rate of 0.4 Hz, and with the NSC36/Ti–Pt 10M cantilever probe tip. In the EFM mode, the sample was scanned twice. First, the tip scanned the surface to obtain the topography images in the non-contact AFM mode associated with the Van der Waals forces. The second scan was carried by the system measuring the tip-surface distance due to the electrostatic force of the material and the probe tip. The electric properties such as the surface potential and the surface charge distribution were obtained from the EFM technique.

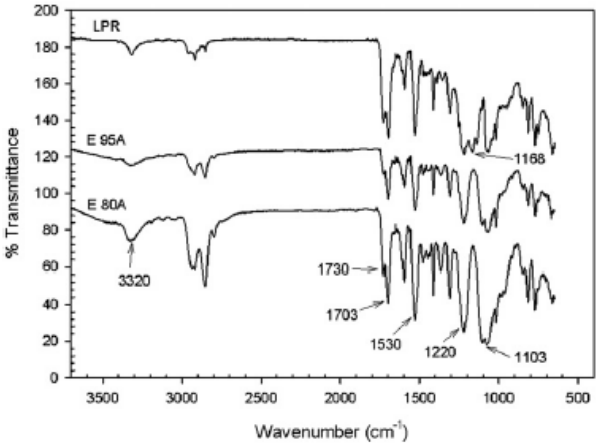

Fig. 2. FT-IR spectra of the TPE-PU.

3. Results and discussion

3.1. Characterizations of TPE-PU

The FT-IR spectra of the TPE-PU (LPR, E 95A and E 80A) are shown in Fig. 2. Generally, the chemical composition of the polyurethane is based on the hard segment (urethane group) crystalline domain and the soft segment (polyether or polyester) amorphous phase [23]. The presence of the urethane structure can be verified by the FT-IR peaks at 1530 cm^{-1}, 1703 cm^{-1} and 3320 cm^{-1}, which can be assigned to the NH bending, the carbonyl stretching and the NH stretching from the urethane linkage, respectively. In addition, the presence of the polyester (LPR) or polyether (E 95A and E 80A) group in the polymer can be identified by the band at 1103 cm^{-1} representing the ether (C–O–C) linkage [24] and the peak at 1220 cm^{-1} belonging to the ether group, whereas the band at 1168 cm^{-1} corresponds to the C–O stretching of ester linkage [25]. Furthermore, the increase in the hard segment content in the polyurethane chain can be identified by the increase in the peak intensity at 1703 cm^{-1}, while the peak at 1730 cm^{-1} is diminished [26]. These peaks correspond to the hydrogen-bonded carbonyl and the free carbonyl group, respectively. These can be attributed to the fact that the addition of the hard segment, or the higher amount of the amide group, leads to the increase of the hydrogen bonding between the NH groups and the soft-segment oxygen atom; the C=O group in polyester and the –COC– group in polyether.

The other characteristics of the TPE-PU, namely the viscosity–average molecular weight (M_v), the content of soft–hard segment, the melting temperatures (T_m), and the decomposition temperatures (T_d), are tabulated in Table 1. The quantities of the soft and hard segments are obtained from the TGA result based on the weight loss in their degradation stages. The melting and the degradation temperatures shift to lower values under the presence

Table 1
Viscosity–average molecular weight (M_v), content of soft–hard segment, melting temperatures (T_m), and decomposition temperatures (T_d) for the TPE-PU.

Samples	M_v	Segment contents (%)		T_m (°C)		T_d (°C)	
		Soft	Hard	Soft	Hard	Soft	Hard
LPR	568,334	44.4	56.8	26.3	181.8	393.2	314.4
E 95A	584,182	45.3	55.2	25.1	169.7	394.5	316.1
E 80A	638,226	58.9	42.4	24.6	142.6	395.1	316.6

Table 2
The specific electrical conductivity, the electrical breakdown strength and the dielectric constant at 20 Hz at 300 K.

Samples	Specific electrical conductivity (S/cm)	Electrical breakdown strength (kV/mm)	Dielectric constant at 300 K (20 Hz)	Dielectric constant at 380 K (20 Hz)
LPR	$1.12 \times 10^{-9} \pm 0.35 \times 10^{-9}$	8.92 ± 0.22	4.42 ± 0.02	15.81 ± 0.47
E 95A	$7.33 \times 10^{-10} \pm 0.67 \times 10^{-10}$	8.66 ± 0.16	4.31 ± 0.04	9.82 ± 0.12
E 80A	$2.49 \times 10^{-10} \pm 0.41 \times 10^{-10}$	8.23 ± 0.11	4.09 ± 0.03	9.08 ± 0.39

of larger soft segment due to the decrease in crystallinity. When TPE-PU is cooled from the molten stage, as in the DSC measurement, the hard segment is first crystallized and the soft segment is then solidified between hard domains. Thus, the soft domain movement is prohibited due to the hard segment formation. Furthermore, even if the material consists of greater physical interaction, such as Van der Waal and hydrogen bonding, it tends to form a higher crystallization.

3.2. The electrical properties

The specific conductivity, the electrical breakdown strength, and the dielectric constant at 20 Hz of LPR, E 95A and E 80A at temperature of 300 K are tabulated in Table 2. The data indicate that the best properties belong to the LPR matrix as a result of the ester functional group. The ester linkage provides a large polar group in the polymer chain which allows the electrons to transfer easily along the chain relative to the ether linkage (E 95A, E 80A). Moreover, changing of the chemical composition in the polymer chain also affects the electrical conductivity which is due to the charge-carrier mobility [27]. E 95A consists of a large amount of the aromatic ring (hard segment) relative to E 80A, thus the former provides a highly polarized group leading to the electron delocalization along the chain [28]. Additionally, both the electrical breakdown strength and the dielectric constant data can be similarly explained based on the diffusion of charges [29]. Generally, a material with ability to diffuse and store the charges often possesses a higher electrical breakdown strength and dielectric constant. Thus, the electrical properties of LPR are superior to those of E 95A and E 80A, respectively.

In Fig. 3, the dielectric constants (20 Hz) of all TPE-PU increase monotonically with increasing temperature due to the relaxation mechanism related to the migration and the existence of the soft–hard domain [30]. At a higher temperature, thermal energy induces a higher polymer chain mobility leading to a freer movement of the soft–hard segments and an easier orientation polarization of molecules [31]. Pissis et al. (1998) and Georgoussis et al., (1999) suggested that the Maxwell–Wagner–Sillars (MWS) interfacial polarization, meaning the dielectric polarization between the soft and hard domain, occurred above the glass transition temperature (T_g) [32,33]. At temperature of 380 K, the dielectric constant of LPR strongly increases up to 250%, while both E 95A and E 80A show the increases of the dielectric constants of about 120%. Thus, the major cause for the increases of the dielectric constants is the chemical group having an ability to polarize. Comparing with our previous works [31], the dielectric constant at 300 K of the elastomers namely the acrylic elastomer (AR70), the styrene–butadiene rubber (SBR), the styrene–isoprene–styrene copolymer (SIS), LPR, E 95A, and E 80A are 6.21, 2.87, 2.74, 4.42, 4.31, and 4.09, respectively. The corresponding dielectric constants at 350 K are 8.03, 3.41, 3.00, 7.47, 6.16, and 5.59, respectively. This implies that the dielectric constants of TPE-PU are highly temperature dependent (more than 35% increase in this temperature range) and they also reflect to the store-charge capability under a certain temperature. Furthermore, the dielectric loss of all TPE-PU also increases with increasing temperature due to the conductivity effect [34]. For the interfacial polarization, the ion migration occurs in the soft phase domain and creates an electrical current through this region at high temperature. For this reason, E 80A containing a larger soft segment provides a higher dielectric loss. The larger hard domains (LPR and E 95A) should impede the migrations. Nevertheless, the dielectric loss of all samples is too small over the temperature range they can be justified as good actuator materials with low energy dissipation.

3.3. Time dependence of the electromechanical response

The cyclic temporal response is investigated with an applied electric field switched on and off periodically at every 500 s, at 1 and 2 kV/mm. The temporal characteristics were measured in the linear viscoelastic regime at strain of 0.05% and frequency of 1 rad/s. Fig. 4 shows the storage modulus (G′) of the LPR matrix during the time sweep test under electric field. When the electric field is turned on at 1 kV/mm, G′ immediately increases and rapidly reaches a steady state as the electric field induces the dipole orientation within the urethane [17]. As the electric field is switched off, the interactions of dipolar domains diminish and G′ reduces close to its original value which can be referred to as a reversible material

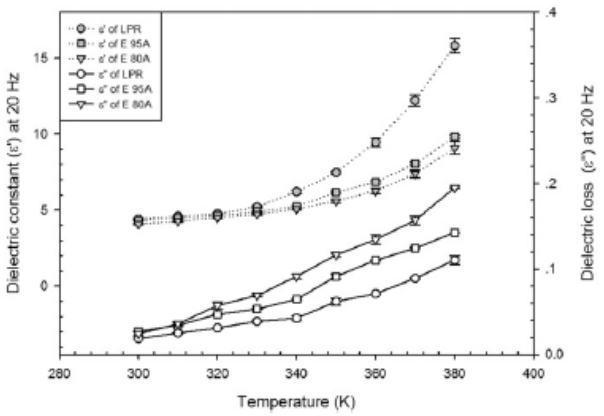

Fig. 3. The dielectric constant and dielectric loss (with silver coating at 10 V) of the TPE-PU at various temperatures.

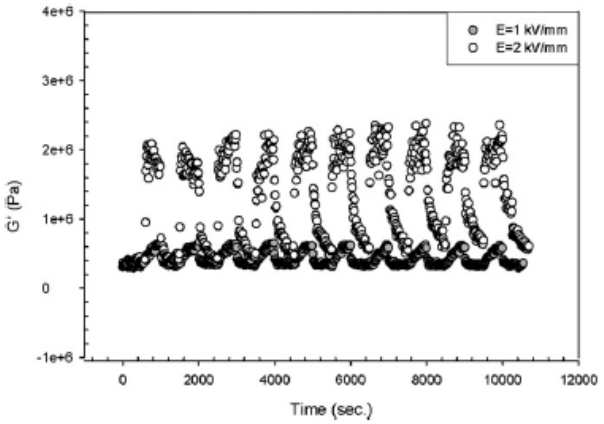

Fig. 4. Temporal response of storage modulus of LPR at electric field strength of 1 and 2 kV/mm ($\omega = 1$ rad/s and 300 K), strain 0.02%.

system. But for the electric field of 2 kV/mm, the response of G′ is dissimilar which can be divided into two regimes. In the first regime, or the initial regime, G′ does not reach the maximum value because some of the dipoles are not generated and cannot respond via orientation to the first applied electric field and they require some activation toward the equilibrium polarization. In the second regime, the steady state regime exhibits a reversible recovery as the electric field is turned off. Compared with the previous work, the temporal responses at the electric field strength of 1 kV/mm of the polyacrylate copolymer [21], the polythiophene/crosslinked polyisoprene blends [35], and the cellulose gel [36] require 7, 6, and 3 cycles to reach the steady states, respectively. Here, all TPE-PU reach the steady states within the first cycle under the applied electric field of 1 kV/mm.

Moreover, the time required for G′ to respond is also important to the electromechanical device [37]. Induction time (τ_{ind}) is the time required for G′ reach the steady state with the electric field turned on. Recovery time (τ_{rec}) is the time required for G′ to decay toward its steady state with the electric field switched off. As shown in Table 3, TPE-PU show the greater performance than other elastomers as they can respond to an electric field within 1 min and G′ increases more than 10^5 Pa which can be assigned to the stress generation within the material. Moreover, both of the τ_{ind} and τ_{rec} decrease with increasing electric field strength due to a higher activated energy. For the effect of polyurethane type, the ester-type requires higher τ_{ind} and τ_{rec} than those of the ether-type because of the highly polar group in the latter type. Furthermore, the softer material requires a shorter time to reach the steady state and the recovery toward its original state. As the E 80A take a shorter time than those of E 95A due to different elastic properties.

3.4. Effect of electric field strength on the electrostrictive stress

Generally, an elastomer is progressively stiffened by applied electric field strength. As an electric field is applied, some electrical dipole moments are generated and induce their intermolecular interactions between different segments within the matrix [38]. These intermolecular interactions cause the loss of free chain movements and induce a higher chain rigidity, as indicated by higher G′ values [39]. Fig. 5 shows the storage modulus response ($\Delta G' = G' - G'_0$) and the storage modulus sensitivity ($\Delta G'/G'_0$) of the TPE-PU under various electric field strengths (0.1–2 kV/mm). At a low electric field strength, E 95A has the lowest $\Delta G'$, while E 80A and LPR show higher responses. On the other hand, E 80A possesses the lowest $\Delta G'$ and $\Delta G'/G'_0$ at the highest electric field strength. The main reason is the chemical structure of E 80A; the soft matrix and the highly dipolar group require less energy to induce the stress response, and the soft structure cannot be further induced with higher electric field. Moreover, the highest sensitivity obtained from LPR is consistent with the dielectric constant result. It is thus shown that high efficiency of the electromechanical response may be achieved by improving the dielectric constant [40]. The molecular weight of polymer can have an impact on the response of a material under an

Table 3
Comparing of storage modulus response, induction time and recovery time (at steady state) with the others dielectric elastomers at electric field strength of 2 kV/mm ($\omega = 1$ rad/s and 300 K).

Samples	τ_{ind} (s)	τ_{rec} (s)	$\Delta G'_{ind}$ ($\times 10^5$ Pa)	$\Delta G'_{rec}$ ($\times 10^5$ Pa)	$\Delta G'_{2\ kV}/G'_0$	Ref.
LPR	67	49	13.0	7.40	2.08	–
E 95A	52	31	2.40	2.00	1.56	–
E 80A	43	28	1.50	1.10	1.13	–
AR 70	405	239	0.68	0.63	2.33	[28]
SAR	440	271	0.87	0.74	1.49	[28]

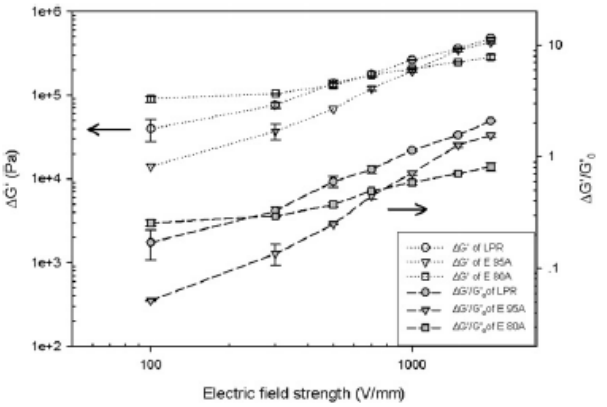

Fig. 5. Effect of electric field strength on the storage modulus response ($\Delta G'$) and the storage modulus sensitivity ($\Delta G'/G'_0$) at $\omega = 1$ rad/s and 300 K.

influence of electric field. Intanoo et al. (2011) reported that an increase in molecular weight creates a lower chain-end free volume and less intermolecular spacing. This causes a larger dipole interaction between dipole moments and thus the higher $\Delta G'/G'_0$ was obtained [41]. In contrast, the $\Delta G'/G'_0$ can be reduced when the material has a higher molecular weight due to a higher initial storage modulus (G'_0). However, in our work, different chemical structures and polar alignment ability should create larger impacts on their performances relative to the molecular weight.

In particular, the interpretation of piezoelectric and electrostrictive effects in the TPE-PU can be based on Eq. (1). As expected, when the specimen strain is fixed, the first term of Eq. (1) is neglected (strain; $S = 0$) and thus the electrostriction behavior can be expressed as:

$$T = \gamma E^2. \tag{6}$$

Notably, a material performing as the electrostrictive effect will generate the stress under the influence of quadratic electric field. In the present work, it can be inferred approximately from the data of Fig. 5 that $\Delta G'$ is dependent on an applied electric field (E) according to a power law; $\Delta G' \alpha E^m$. From the data, the scaling exponents of the power laws of LPR, E 95A, and E 80A are equal to 1.87, 1.78, and 1.82, respectively. This suggests strongly that the TPE-PU system could be categorized as the electrostrictive material group, as the scaling exponents are quite close to 2, and the major responsive deformation can be attributed to the orientation of the polar phase. Nevertheless, Su et al. (1999) reported that the electromechanical response of the polyurethane can be contributed by both of the electrostrictive (65%) and the Maxwell stress (35%) [42]. The Maxwell stress is responsible for the increase in G' which can be related to the effective pressure (P) based on the Maxwell stress equation:

$$P = \varepsilon_0 \varepsilon_r E^2, \tag{7}$$

where ε_0 is the permittivity of free space, ε_r is the relative permittivity of polymer, and E is the electric field strength. Whenever electric field is applied, the unlike charges will accumulate on the opposing surface of the material film, resulting in the deformation of the film in the thickness direction along with the resultant Maxwell stress generated [43]. In the present work, the Maxwell stress is zero as the electrodes were held fixed. Kim et al. (2011) demonstrated the non-contact strain measurement by applying insulated polyimide films onto electrodes in order to prevent charge accumulation on electrodes and to avoid the Maxwell stress

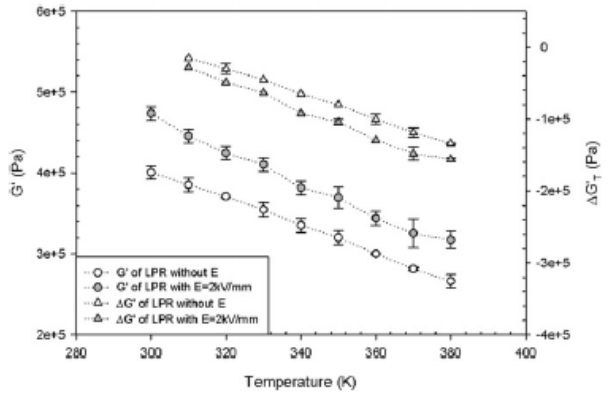

Fig. 6. Effect of temperature on the storage modulus and the storage modulus response ($\omega = 1$ rad/s) for LPR at $E = 0$ and 2 kV/mm.

effect. This experiment was used to evaluate the actuation response through the true electrostrictive effect only [44].

3.5. Effect of temperature on the electromechanical properties

The effect of temperature on the TPE-PU is investigated in the temperature range of 300–380 K under the electric field strength of 0 and 2 kV/mm. The results show that the storage modulus decreases with increasing temperature as shown in Fig. 6. With increasing temperature, the input heat will cause polymer chain softening from the hard segment, even though the soft segment of the TPE-PU is in the rubbery-state. As the temperature rises up (above T_g), the storage modulus is further reduced due to the behavior change from the rubbery-like to the plastic-like and it turns to the viscous-like when the temperature reaches to the T_m of material [45]. Generally, Van der Waal and hydrogen-bonded interactions are considered to hold the individual discrete domains of the rigid segments. As the temperature increases, the bonded-interaction could be destroyed allowing the free chain softening movement. Nevertheless, the storage modulus with electric field of 2 kV/mm is higher than those of without electric field at any temperature. This is because the dipole moment and the polarization are generated under electric field and they induce the intermolecular interaction between chain segments [27]. These interactions cause the physical crosslink sites in the hard segments which tend to restrict the free chain movement resulting in higher chain rigidity. For the storage modulus response ($\Delta G'_T$), it decreases with increasing temperature due to the loss of the interaction. As shown in Table 4, the E 80A matrix possesses the largest storage modulus sensitivity drop ($\Delta G'_T/G'_{300\ K}$) compared with those of others TPE-PU. This result can be referred to a large amount of the soft domains within their structure which are caused by the loss of segment interaction with increasing temperature. The LPR matrix is well sensitive to temperature and it still retains some residue dipolar interaction within the ester groups in the chain segments. Furthermore, the storage modulus response under effect of electric field ($\Delta G'_E$) at temperature of 380 K shows the consistent tendency for the $\Delta G'_T$ of the E 80A matrix to possess the best sensitivity under high temperature. However, the sensitivity of all TPE-PU at 380 K is obviously low comparing with temperature of 300 K because of the structure change as discussed above. Therefore, the TPE-PU is the most suitable to be used at room temperature as the best electroactive system.

3.6. The deflection response and the electrophoresis force of the TPE-PU

The bending behavior and the dielectrophoresis force of the TPE-PU are investigated at room temperature (300 K) under applied electric field strength between 0 and 550 V/mm, the experimental set-up is shown in Fig. 7(a). The specimen is aligned at the center of the PDMS chamber without applied electric field. The free end specimen bends toward the anode site (positive charge), as shown in Fig. 7(b), under the influence of an electric field due to the resultant dielectrophoresis force and the electrostriction effect [46]. The chemical structure of the TPE-PU containing the carbonyl group and the phenyl group in the hard segment tends to form the polar crystalline domains. When electric field is applied, these regions become polarized and create some deformations within the polymer matrix [47]. The polarization of the carbonyl and the phenyl group can be referred to the electrophilic behavior which can pull electrons from the carbon backbone and then generates the negative charges on their groups. Under an applied electric field, the attractive force between unlike charges is generated and induces the specimen to deflect toward the anode site. Moreover, the ester-type of TPE-PU seems to achieve a large bending angle and a high dielectrophoresis force relative to those of the ether-type because the ester-type contains the carbonyl group leading to an increase in the dipolar alignment ability which requires a lower electrical energy to respond under an electric field. As shown in Fig. 8, LPR starts to deflect at the electric field of 150 V/mm, while both E 95A and E 80A start to bend only after 200 V/mm. The higher applied electric field strength, the more severe bending angle is achieved. Nevertheless, the soft-segment or the amorphous phase in the polymer chain may also induce the specimen deflection due to the chain mobility [10]. For the E 80A matrix, the film is easily deflected under the electric field compared with E 95A. Furthermore, the dielectrophoresis forces, calculated through the Eq. (4), increase linearly with increasing electric field strength due to the increases in the dipole moments and polarization. At the electric field of 550 V/mm, LPR generates the highest dielectrophoresis force (43 μN). However, the dielectrophoresis force of the TPE-PU is relatively low compared with the previous works [38,43]. Interestingly, the TPE-PU does not reach the saturated bending angle and the saturated force within the electric field strength investigated; as higher electric field strength is required before they become saturated.

Table 4
The storage modulus response of the TPE-PU under the effects of temperature ($\Delta G'_T$) and electric field ($\Delta G'_E$) at $\omega = 1$ rad/s.

Samples	E (kV/mm)	G' at 300 K(Pa)	G' at 380 K (Pa)	$\Delta G'_T = G'_{380\ K} - G'_{300\ K}$ (Pa)	$\Delta G'_T/G'_{300\ K}$	$\Delta G'_{E\ (at 380\ K)} = G'_{2\ kV/mm} - G'_{0\ kV/mm}$ (Pa)	$\Delta G_E/G_{0\ kV/mm}$
LPR	0	406,340	271,960	−134,380	−0.33	52,940	0.19
	2	479,560	324,900	−154,660	−0.32		
E 95A	0	446,480	285,210	−161,270	−0.36	62,710	0.22
	2	586,270	347,920	−238,350	−0.41		
E 80A	0	303,700	172,449	−131,251	−0.43	46,251	0.27
	2	398,910	218,700	−180,210	−0.45		

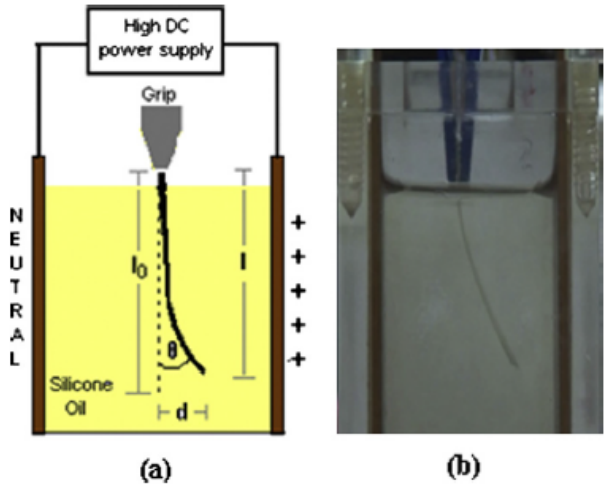

Fig. 7. The deflection experiment at 300 K: (a) experimental setup; and (b) deflection of LPR under electric field.

The induction time and the recovery time of bending response are investigated in Table 5. The induction time is the time required for the matrix bends toward the maximum distance under an electric field. At the electric field of 550 V/mm, the induction times of LPR, E 95A, and E 80A are 4, 10, and 6 s, respectively. The recovery time is the time required for the matrix to deflect back to its original position after switch off an electric field. The recovery times of the LPR, E 95A, and E 80A are 2, 5, and 3 s, respectively. In comparison with the others dielectric elastomer [43], all of the matrices investigated show fast bending responses, one of an important factor for the actuator applications. TPE-PU exhibits the fastest response under an electric field. It can be concluded that TPE-PU, especially for LPR, appears to provide a better electromechanical response over the other dielectric elastomers in term of the response times.

3.7. Effect of electric field strength on the electrostrictive strain

The strain responses are calculated through the Hooke's law (Eq. (5)) under the linear bending actuation. Fig. 9 reveals that the electromechanical behavior of the TPE-PU belongs to the electrostrictive type as the strains are linearly dependent on the electric field squared. E 80A shows a higher strain response than LPR

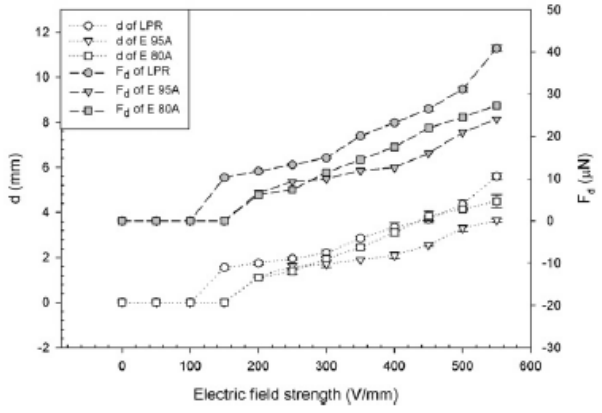

Fig. 8. Deflection distances measured along x-axis and dielectrophoretic forces of the TPE-PU at various electric field strengths calculated through the non-linear deflection theory (at 300 K).

Table 5
Comparison of the response time (at 550 V/mm) and the dielectrophoresis force with other dielectric elastomers for the deflection experiment.

Samples	LPR	E 95A	E 80A	AR70	AR71	AR72	SAR	SIS	SBR
Induction time (s)	4	10	6	7	3	5	9	10	15
Recovery time (s)	2	5	3	25	20	18	20	7	8

matrix. The main reason is due to flexibility of the material which can be related to the viscoelastic properties [48]. It may be noted that a large soft segment will promote an easily bending and strain response. Moreover, from the theory of electrostrictive effect [19], the strain response may be expressed as:

$$S_E = Q\varepsilon_0^2(\varepsilon_r - 1)^2E^2, \tag{8}$$

where S_E is the electrostrictive strain, Q is the electrostrictive coefficient, ε_0 is the permittivity of free space (8.85×10^{-12} F/m), ε_r is the dielectric constant of material, and E is the applied electric field. The slope of the strain straight line versus electric field squared can be used to determine the electrostrictive coefficient (Q) of material, as shown in Table 6. In comparison with the other materials such as polypropylene (PP), polyvinylidenefluoride (PVDF), polyvinylchloride (PVC), polyurethane (PU) and ceramic ($K_{0.95}Na_{0.05}Ta_{0.57}Ni_{0.43}O_3$), they have the electrostrictive coefficients equal to 4.2×10^6 [49], 2.4, 10.1, 850 [50], and 0.38 m^4/C^2 [51], respectively. While, the electrostrictive coefficients of our TPE-PU are much more than 10^6 m^4/C^2, an order of magnitude larger than that of the others. Thus, it can be emphasized that TPE-PU possesses very large electrostrictive coefficients exhibiting a superior actuator performance relative to others.

3.8. Topology and electrostatic behavior of the TPE-PU

AFM technique is used to study the morphological and structural behavior in nanoscale resolution. Fig. 10 shows that TPE-PU

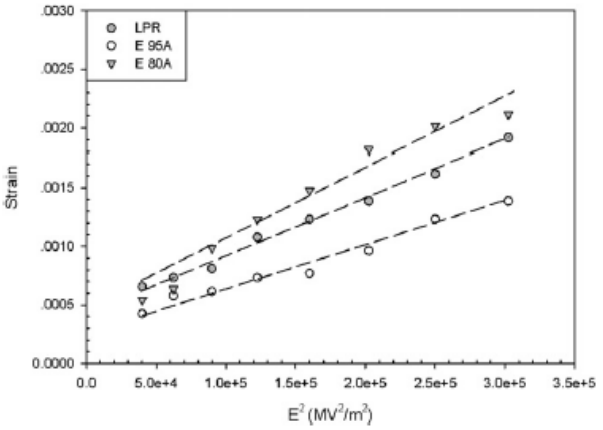

Fig. 9. The variation of strain as a function of squared electric field for the TPE-PU.

Table 6
The electrostrictive strain and the electrostrictive coefficient calculated from the experimental data.

Samples	Electrostrictive strain; S_E (at 550 V/mm)	Electrostrictive coefficient; Q (m^4/C^2)
LPR	1.92×10^{-3}	7.62×10^6
E 95A	1.39×10^{-3}	5.83×10^6
E 80A	2.11×10^{-3}	11.03×10^6

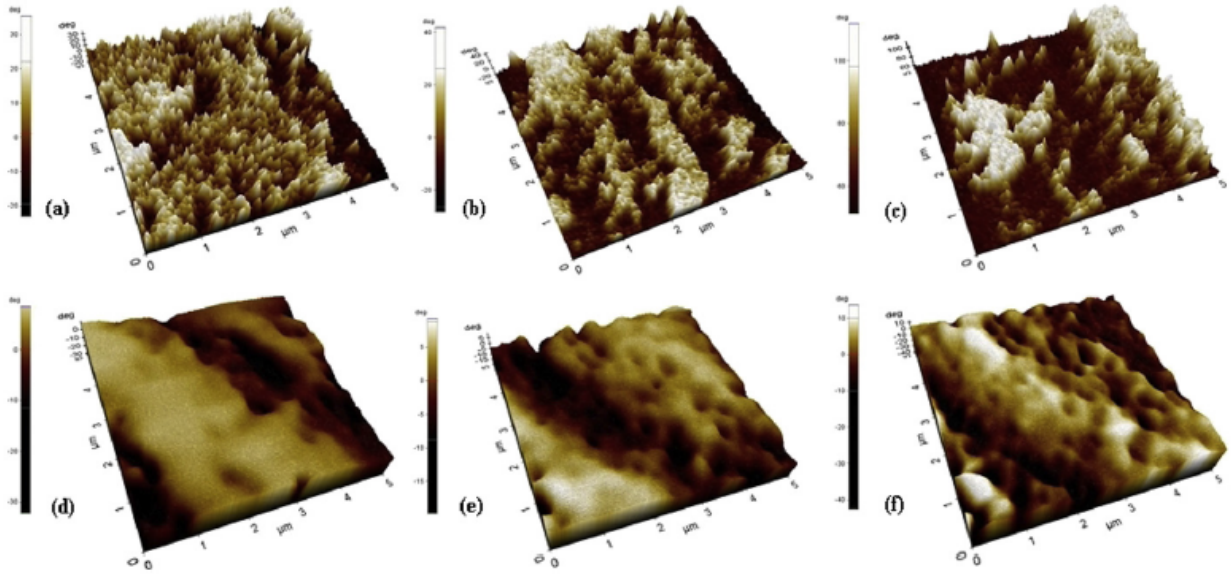

Fig. 10. AFM phase in tapping mode of LPR (a), E 95A (b), E 80A (c), and EFM phase with applied voltage bias of 5 V for LPR (d), E 95A (e), E 80A (f); scan size of 5 × 5 μm.

possesses the phase separation between the soft and hard segments, where the bright areas can be referred to the hard segments and the dark regions correspond to the soft segments. In contrast, an increase in the bright regions can be indirectly translated into the quantitative composition within material [52]. As can be seen in Fig. 10(a–c), the bright areas increase with the amount of hard segments. Aneja (2003) reported that the increase of a hard domain within the material promoted the connectivity of the hard phases toward an interlocking morphology at nanoscale [53]. However, these images do not reveal such evidence. Nevertheless, one way of studying the domain orientation behavior of material under an electric field is by testing in the EFM mode. As above mentioned, the hard segments comprise of the polar group which can respond to the electric field. Under applied electric field, the specimen charges and the polar group will be realigned and agglomerated and become progressively brighter with increasing hard segments as shown in Fig. 10(d–f). Moreover, it can be noted that some regions between the bright and the dark domains represent the space-charge trapping sites between their interfaces [18].

4. Conclusion

In this study, the dielectric constant, the storage modulus under the oscillatory shear mode and the bending measurement of the thermoplastic elastomer polyurethanes (TPE-PU) are investigated as functions of electric field and temperature. The dielectric constant increases with increasing temperature, and the ester-type polyurethane (LPR) shows the greatest dielectric constant at all temperatures investigated. The storage modulus response ($\Delta G'$) and the storage modulus sensitivity ($\Delta G'/G'_0$) increase with increasing electric field where LPR possesses the highest sensitivity, >2, at 2 kV/mm. Both G' and $\Delta G'$ values decrease with increasing temperature due to the softening of the polymers chain above the glass transition temperature due to the hard segments. From the deflection measurement, the deflection distance and the dielectrophoresis force of the matrices increase monotonically with increasing electric field strength. LPR shows the greatest deflection response. Furthermore, all TPE-PU performances indicate that TPE-PU as being the electrostrictive materials with the electrostrictive coefficients of order 10^6 m^4/C^2. From the present results, it can be suggested that TPE-PU, especially for LPR, is a potential candidate to be used as an electrostrictive material for various actuator applications with high electrostrictive stress, high stress response, and very good recoverability over existing dielectric elastomers.

Acknowledgments

The authors would like to acknowledge the financial supports from the Petroleum and Petrochemical College; the Conductive and Electroactive Polymers Research Unit of Chulalongkorn University; the Dusadee Pipat Fund of Chulalongkorn University; the Thailand Research Fund (TRF), and the Royal Thai Government. The material supports from BASF Polyurethane (Thailand) Ltd, and Behnmeyer Thai Co., Ltd., are gratefully acknowledged.

References

[1] C. Puig-Lleixa, C. Jimenez, E. Fabregas, J. Bartrolı, Potentiometric pH sensors based on urethane–acrylate photocurable polymer membranes, Sens. Actuators B. 49 (1998) 211–217.
[2] J.H. Kim, T.J. Kang, W.R. Yu, Thermo-mechanical constitutive modeling of shape memory polyurethanes using a phenomenological approach, Int. J. Plast. 26 (2010) 204–218.
[3] J.W. Kim, W. Jung, H.S. Kim, In-plane strain of electro-active paper under electric fields, Sens. Actuators A. 140 (2007) 225–231.
[4] Y.G. Ko, U.S. Choi, Y.J. Chun, Influence of particle size on shear behavior of amine-group-immobilized polyacrylonitrile dispersed suspension under electric field, J. Colloid Interface Sci. 335 (2009) 183–188.
[5] A. Nespoli, S. Besseghini, S. Pittaccio, E. Villa, S. Viscuso, The high potential of shape memory alloys in developing miniature mechanical devices: a review on shape memory alloy mini-actuators, Sens. Actuators A. 158 (2010) 149–160.
[6] M. Watanabe, M. Suzuki, Y. Hirako, H. Shirai, T. Hirai, Hysteresis in bending electrostriction of polyurethane films, J. Appl. Polym. Sci. 79 (2001) 1121–1126.
[7] L. Tian, L. Tevet-Deree, G. Botton, K. Bhattacharya, Dielectric elastomer composites, J. Mech. Phys. Solids 60 (2012) 181–198.
[8] J.Y. Li, Enhanced electromechanical properties in all-polymer percolative composites, Appl. Phys. Lett. 84 (2004) 3124–3126.
[9] M. Oshiki, E. Fukada, Inverse piezoelectric effect and electrostrictive effect in polarized poly(vinylidene fluoride) films, J. Mater. Sci. 10 (1975) 1–6.
[10] N. An, H. Liu, Y. Ding, M. Zhang, Y. Tang, Preparation and electroactive properties of a PVDF/nano-TiO_2 composite film, Appl. Surf. Sci. 257 (2011) 3831–3835.

[11] R. Palakodeti, M.R. Kessler, Influence of frequency and prestrain on the mechanical efficiency of dielectric electroactive polymer actuators, Mater. Lett. 60 (2006) 3437–3440.
[12] S.P. Lacour, S. Wagner, H. Prahlad, R. Pelrine, High voltage photoconductive switches of amorphous silicon for electroactive polymer actuators, J. Non-Cryst. Solids 338 (2004) 736–739.
[13] Y.C. Jung, H.J. Yoo, Y.A. Kim, J.W. Cho, M. Endo, Electroactive shape memory performance of polyurethane composite having homogeneously dispersed and covalently crosslinked carbon nanotubes, Carbon 48 (2010) 1598–1603.
[14] Y. Fujihara, T. Hanamoto, F. Dai, Fundamental research on polymer material as artificial muscle, Artif. Life Robot. 12 (2008) 232–235.
[15] Q. Meng, J. Hu, S. Mondal, Thermal sensitive shape recovery and mass transfer properties of polyurethane/modified MWNT composite membranes synthesized via in situ solution pre-polymerization, J. Membr. Sci. 319 (2008) 102–110.
[16] C. Huang, Q. Zhang, Fully functionalized high dielectric constant nanophase polymer with high electromechanical response, Adv. Mater. 17 (2005) 1153–1158.
[17] T. Ueda, T. Kasazaki, N. Kunitake, T. Hirai, J. Kyokane, K. Yoshino, Polyurethane elastomer actuator, Syn. Met. 85 (1997) 1415–1416.
[18] F.M. Guillot, E. Balizer, Electrostrictive effect in polyurethanes, J. Appl. Polym. Sci. 89 (2003) 399–404.
[19] I. Diaconu, D.O. Dorohoi, F. Topoliceanu, Electrostriction of a polyurethane elastomer-based polyester, IEEE Sens. J. 6 (2006) 876–880.
[20] D. De, R.J. Gaymans, Thermoplastic polyurethanes with TDI-based monodisperse hard segments, Macromol. Mater. Eng. 294 (2009) 405–413.
[21] P. Ludeelerd, S. Niamlang, R. Kunaruksapong, A. Sirivat, Effect of elastomer matrix type on electromechanical response of conductive polypyrrole/elastomer blends, J. Phys. Chem. Solids 71 (2010) 1243–1250.
[22] K. Gorna, S. Gogolewski, Molecular stability, mechanical properties, surface characteristics and sterility of biodegradable polyurethanes treated with low-temperature plasma, Polym. Degrad. Stab. 79 (2003) 475–485.
[23] G. Moroi, Preparation and characterization of polyesterurethane/copper metallopolymers, React. Funct. Polym. 68 (2008) 268–328.
[24] O. Mrad, J. Saunier, C.A. Chodur, V. Rosilio, F. Agnely, P. Aubert, J. Vigneron, A. Etcheberry, N. Yagoubi, A comparison of plasma and electron beam-sterilization of PU catheters, Radiat. Phys. Chem. 79 (2010) 93–103.
[25] B. Ravat, M. Grivet, Y. Grohens, A. Chambaudet, Electron irradiation of polyesterurethane: study of chemical and structural modifications using FTIR, UV spectroscopy and GPC, Radiat. Meas. 34 (2001) 31–36.
[26] Y. Xu, Z. Petrovic, S. Das, G.L. Wilkes, Morphology and properties of thermoplastic polyurethanes with dangling chains in ricinoleate-based soft segments, Polymer 49 (2008) 4248–4258.
[27] W. Wichiansee, A. Sirivat, Electrorheological properties of poly(-dimethylsiloxane) and poly(3,4-ethylenedioxythiophene)/poly(stylene sulfonic acid)/ethylene glycol blends, Mater. Sci. Eng. C 29 (2009) 78–84.
[28] N.J. Jo, D.H. Lim, G.M. Bark, H.H. Chun, I.W. Lee, H. Park, Polyurethane-based actuators with various polyols, J. Mater. Sci. Technol. 26 (2010) 763–768.
[29] J. Liebault, J. Vallayer, D. Goeuriot, D. Treheux, F. Thevenot, How the trapping of charges can explain the dielectric breakdown performance of alumina ceramics, J. Eur. Ceram. Soc. 21 (2001) 389–397.
[30] C. Tsonos, L. Apekis, K. Viras, L. Stepanenko, L. Karabanova, L. Sergeeva, Electrical and dielectric behavior in blends of polyurethane-based ionomers, Solid State Ionics 143 (2001) 229–249.
[31] R. Kunaruksapong, A. Sirivat, Electrical properties and electromechanical responses of acrylic elastomers and styrene copolymers: effect of temperature, Appl. Phys. A 92 (2008) 313–320.
[32] P. Pissis, A. Kanapitsas, Y.V. Savelyev, E.R. Akhranovich, E.G. Privalko, V.P. Privalko, Influence of chain extenders and chain end groups on properties of segmented polyurethanes II: dielectric study, Polymer 39 (1998) 3431–3435.
[33] G. Georgoussis, A. Kyritsis, P. Pissis, Y.V. Savelyev, E.R. Akhranovich, E.G. Privalko, V.P. Privalko, Dielectric studies of molecular mobility and microphase separation in segmented polyurethanes, Eur. Polym. J. 35 (1999) 2007–2017.
[34] C. Tsonos, L. Apekis, C. Zois, G. Tsonos, Microphase separation in ion-containing polyurethanes studied by dielectric measurements, Acta Mater. 52 (2004) 1319–1326.
[35] T. Puvanatvattana, D. Chotpattananont, P. Hiamtup, S. Niamlang, A. Sirivat, A.M. Jamieson, Electric field induced stress moduli in polythiophene/polyisoprene elastomer blends, React. Funct. Polym. 66 (2006) 1575–1588.
[36] W. Kunchornsup, A. Sirivat, Physically cross-linked cellulosic gel via 1-butyl-3-methylimidazolium chloride ionic liquid and its electromechanical responses, Sens. Actuators A 175 (2012) 155–164.
[37] R. Shankar, T.K. Ghosh, R.J. Spontak, Mechanical and actuation behavior of electroactive nanostructured polymers, Sens. Actuators A 151 (2009) 46–52.
[38] R.E. Pelrine, R.B. Kornbluh, J.P. Joseph, Electrostriction of polymer dielectrics with compliant electrodes as a means of actuation, Sens. Actuators A 64 (1998) 77–85.
[39] B. Liu, M.T. Shaw, Electrorheology of filled silicone elastomers, J. Rheol. 45 (2001) 641–657.
[40] R. Kunaruksapong, A. Sirivat, Effect of dielectric constant and electric field strength on dielectrophoresis force of acrylic elastomers and styrene copolymers, Curr. Appl. Phys. 11 (2011) 393–401.
[41] P. Intanoo, A. Sirivat, R. Kunaruksapong, W. Lerdwijitjarud, Electromechanical properties of ethylene propylene diene elastomers: effect of ethylene norbornene content, Mater. Sci. Appl. 2 (2011) 307–313.
[42] J. Su, J.S. Harrison, T.L. Clair, Y. Bar-Cohen, S. Leary, Electrostrictive graft elastomers and applications, MRS Symp. (1999), http://dx.doi.org/10.1557/PROC-600–131.
[43] S. Butkewitsch, J. Scheinbeim, Dielectric properties of a hydrated sulfonated poly(styrene–ethylene/butylenes–styrene) triblock copolymer, Appl. Surf. Sci. 252 (2006) 8277–8286.
[44] B. Kim, Y.D. Park, K. Min, J.H. Lee, S.S. Hwang, S.M. Hong, B.H. Kim, S.O. Kim, C.M. Koo, Electric actuation of nanostructured thermoplastic elastomer gels with ultralarge electrostriction coefficients, Adv. Funct. Mater. 21 (2011) 3242–3249.
[45] T. Sato, H. Watanabe, K. Osaki, Rheological and dielectric behavior of a styrene-isoprene-styrene triblock copolymer in n-tetradecane. 1. Rubbery-Plastic-Viscous transition, Macromolecules 29 (1996) 6231–6239.
[46] K. Wongtimnoi, B. Guiffard, A.B. Moortle, L. Seveyrat, C. Gauthier, J.Y. Cavaille, Improvement of electrostrictive properties of a polyether-based polyurethane elastomer filled with conductive carbon black, Comp. Sci. Technol. 71 (2011) 885–892.
[47] M.D.Z. Uddin, M. Watanabe, H. Shirai, T. Hirai, Effects of plasticizers on novel electromechanical actuations with different poly(vinyl chloride) gels, J. Polym. Sci. B 41 (2003) 2119–2127.
[48] M. Cianchetti, V. Mattoli, B. Mazzolai, C. Laschi, P. Dario, A new design methodology of electrostrictive actuators for bio-inspired robotics, Sens. Actuators B 142 (2009) 288–297.
[49] J.W. Zhang, L. Lebrun, B. Guiffard, J.P. Cottinet, R. Belouadah, D. Guyomar, L. Garbuio, Influence of corona poling on the electrostrictive behavior of cellular polypropylene films, Sens. Actuators A 175 (2012) 87–93.
[50] R.E. Newnham, V. Sundar, R. Yimnirun, J. Su, Q.M. Zhang, Electrostriction: nonlinear electromechanical coupling in solid dielectrics, J. Phys. Chem. B 101 (1997) 10141–10150.
[51] H. Tian, C. Hu, Q. Chen, Z. Zhou, High purely electrostrictive effect in cubic $K_{0.95}Na_{0.05}Ta_{1-x}Nb_xO_3$ lead-free single crystals, Mater. Lett. 68 (2012) 14–16.
[52] P. Schon, K. Bagdi, K. Molnar, P. Markus, B. Pukanszky, G.J. Vancso, Quantitative mapping of elastic moduli at the nanoscale in phase separated polyurethanes by AFM, Eur. Polym. J. 47 (2011) 692–698.
[53] A. Aneja, G.L. Wilkes, A systematic series of 'model' PTMO based segmented polyurethanes reinvestigated using atomic force microscopy, Polymer 44 (2003) 7221–7228.

Article

JOURNAL OF ELASTOMERS & PLASTICS

Journal of Elastomers & Plastics
45(3) 253–269
© The Author(s) 2012
Reprints and permissions:
sagepub.co.uk/journalsPermissions.nav
DOI: 10.1177/0095244312452273
jep.sagepub.com
SAGE

Removal of water extractable proteins from concentrated natural rubber latex by eggshells

Nuchnapa Tangboriboon[1,2], Prapaphan Phudkrachang[1,2], La-orngdow Mulsow[1,2], Wissawin Kunchornsup[3], and Anuvat Sirivat[3]

Abstract

The protein allergy caused by latex products has become an acute problem to human and animals; sweat removes proteins, which then comes in contact with the skin causing the sensitization or allergic reactions. Eggshells from chickens, ducks, and birds are potential starting materials to be used in reducing the water extractable proteins in concentrated natural rubber latex (NRL). The pyrolysis of eggshells at 900°C for 2 h transforms the crystal structure of calcium carbonate into calcium oxide with a high purity, creates a small and uniform particle size, a suitable specific surface area, and an average pore diameter that is suitable for reacting with hydrochloric acid to obtain calcium chloride ($CaCl_2$). The additions of $CaCl_2$ solution and sodium dodecyl sulphate into concentrated NRL are shown and reported here to extract effectively the proteins from the NRL film.

Keywords

Concentrate rubber latex, crude eggshells, extractable proteins, modified Lowry method

[1] Center for Advanced Studies in Industrial Technology, Faculty of Engineering, Kasetsart University, Chatuchak, Bangkok, Thailand
[2] Department of Materials Engineering, Faculty of Engineering, Kasetsart University, Chatuchak, Bangkok, Thailand
[3] The Petroleum and Petrochemical College, Chulalongkorn University, Phatumwan, Bangkok, Thailand

Corresponding author:
Anuvat Sirivat, The Petroleum and Petrochemical College, Chulalongkorn University, Soi Chula 12, Phayathai Road, Patumwan, Bangkok 10330, Thailand.
Email: anuvat.s@chula.ac.th

Downloaded from jep.sagepub.com at Chulalongkorn University on May 21, 2013

Introduction

Natural rubber latex (NRL) is one of the most important biosynthesized polymers displaying excellent chemical and physical properties that find a wide range of application in various areas.[1–3] NRL has been used in manufacturing medical products such as medical gloves, condoms, balloons, blood transfusion tubing, catheters, injector closures, and safety bags due to its excellent elasticity, flexibility, antivirus permeation, good formability, and biodegradability.[1,4] Rubber latex, from field collection, contains many natural substances including proteins and 33% polyisoprene. Ammonia is usually poured to the latex as a preservative to promote the alkalinity (pH) and to retard the microbial growth. The additional benefit from adding ammonia is the increase in the stability of NRL due to the increase in the negative surface charge of the rubber particles.[5] In addition, the alkaline conditions of ammoniated latex can denature some proteins. In addition, it may even partially hydrolyze others to smaller polypeptides. The resulting NRL is further processed to concentrate latex with approximate 60% rubber content. Nonrubber material contents such as proteins are removed during this processing step. NRL proteins are organic substances that consist of carbon, hydrogen, nitrogen, oxygen, and sulfur. There are naturally occurring polymer chains that may contain hundreds of individual amino acid residues connected together by peptide bonds. Some of these proteins are considered potential allergens based on their capacity to bind to immunoglobulin E antibodies from the sera of NRL-allergic people. It is generally believed that the potentially allergic protein components are those accompanied with the aqueous soluble serum fraction of NRL. These are the proteins that are dissolved in the latex serum and tend to concentrate during product manufacturing on the film surface.[5] Latex allergy symptoms are the result of a chain reaction that starts in the immune system. The immune system identifies what is typically harmless as an invader or allergen. The latex allergic reaction usually appears in the nose, lungs, throat, sinuses, ears, lining of the stomach, or on the skin. People with latex allergy may have symptoms such as urticaria or hives, itching or flushing, swelling, sneezing, runny nose, cough, wheeze, shortness of breath, chest tightness, nausea, dizziness, or lightheadedness, as shown in Figure 1.

There are many methods to reduce the protein content in NRL gloves: water leaching, chlorination, enzyme-treated NRL, and adding powder lubricants (i.e. silica, modified montmorillonite, starch, and ultra-fine calcium carbonate ($CaCO_3$)), as shown in Figure 2.

Water leaching removes hydrophilic components, reduces the formation of chemical blooming on the surface during heating and storage, reduces hydration and electrical conductivity, and reduces water-soluble components and proteins in NRL gloves; but it is not effective in leaching out larger proteins within the coagulated film. Chlorination is an effective means of reducing the extractable protein (EP) content on the glove surface, but the chlorination process is difficult to control and usually results in small fissures in the rubber film that can compromise the shelf-life and the barrier integrity of the glove.[6–8] Protease enzyme-treated NRL is usually used in the leather manufacturing and the NRL

Downloaded from jep.sagepub.com at Chulalongkorn University on May 21, 2013

Figure 1. Latex glove allergy (http://www.iacdworld.org).

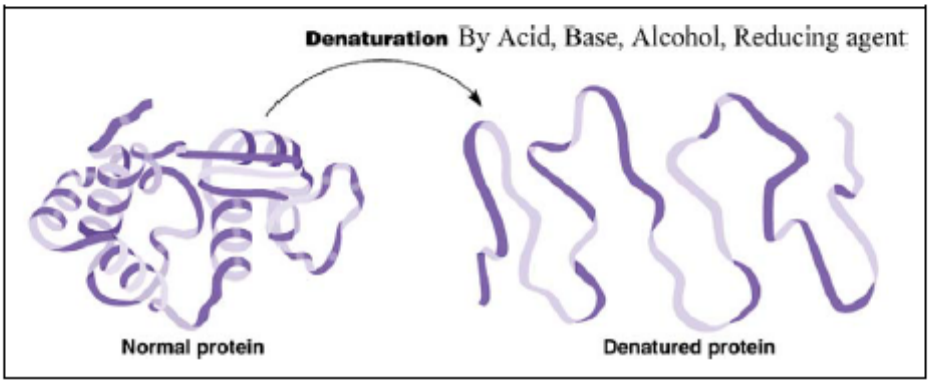

Figure 2. Protein denaturation.

device production.[9] There are several standard methods for measuring the proteins in the concentrated NRL, such as the American Society for Testing and Materials (ASTM) Standard Method D 5712 and the International Organization for Standardization 12243 (ISO 12243).[10]

The objective of this work is to extract or remove the water-soluble proteins or EPs from concentrated rubber latex compounds, in order to reduce the rubber latex allergic problem, by adding calcium chloride ($CaCl_2$) prepared from the pyrolysis of crude eggshells, such as chicken eggshells, duck eggshells, and bird eggshells. Eggshells were pyrolyzed at 900°C for 2 h to obtain calcium oxide (CaO) and then dissolved in 2 M hydrochloric acid (HCl) along with sodium dodecyl sulphate (SDS) as the stabilizer. The method used to determine the EPs is the modified Lowry method (ISO 12243). The amount of EPs, using $CaCl_2$ made from eggshells, was compared with the amount of EPs using $CaCl_2$ made of CaO and $CaCl_2$ (commercial grades) of the same weight (0.25 g) by the modified Lowry method. The rubber latex compounds and latex films were characterized by Fourier transform infrared (FTIR), near infrared (NIR), and x-ray diffraction (XRD) and are reported here.

Downloaded from jep.sagepub.com at Chulalongkorn University on May 21, 2013

Experimental

Materials

Concentrated NRL (60% dry rubber content (DRC) and concentrated high ammonia latex) was supplied by the Rubber Research Institute of Thailand (Bangkok, Thailand).

CaO from eggshells (chicken, duck, and bird) was prepared from pyrolysis of eggshells. The eggshells (chicken, duck, and bird) were collected from a local cafeteria. Crude eggshells were washed with tap water and dried at room temperature. The crude eggshells were crushed with a porcelain mortar. The CaO was successfully prepared by the pyrolysis technique at 900°C for 2 h, yielding a very high purity product of 97.41 wt% (bird), 98.15 wt% (chicken), and 99.00 wt% (duck), and then kept in a desiccator.

SDS (also NaDS or $C_{12}H_{25}SO_4Na$) is an anionic surfactant with a density, melting point, and molecular weight of 1.01 g cm^{-3}, 206°C, and 288.38 g mol^{-1}, respectively. The SDS compound activates in the mechanism of disrupting noncovalent bonds in the proteins, denaturing them, and causing the molecules to lose their native shape (conformation). Also, anions of SDS bind to the main peptide chains at a ratio of one SDS anion for every two amino acid residues. This effectively imparts a negative charge on the protein that is proportional to the mass of that protein (about 1.4 g SDS g^{-1} sprotein).[10] This obtained negative charge is significantly greater than the original charge of the proteins. The electrostatic repulsive interaction created by binding of SDS resulted in the proteins to unfold into a rod-like shape thereby eliminating differences in shape factor in the separation of the gel.[11]

$CaCl_2$ with a higher purity of 93.0–100.0 wt% and CaO of 96 wt% purity, water-insolubility <0.5 wt%, loss on ignition 8.79 wt%, oxalate 5 wt%, and other element impurities of <0.0043 wt% was supplied by Ajax Finechem Pty. Ltd (Australia). HCl (Analytical Reagent grade, AR) was purchased from Lab-Scan Co. Ltd (Thailand).

Instruments

Laboratory Muffle Furnace. Laboratory Muffle Furnace (Linn High Thermo GmbH, LM 412.27, model DC021032 with thermocouple type K, NiCr-Ni) was used to calcine eggshell samples from 27 to 900°C to obtain CaO. The raw eggshells were put in an alumina crucible in the muffle furnace and calcined at 900°C for 2 h with a heating rate of 10°C min^{-1}.

The elemental analysis. Elemental analysis was carried out on a C/H/N analyzer (Perkin Elmer, model PE 2400 series II). The gaseous samples were freed by the pyrolysis in high-purity oxygen and were chromatographically separated by the frontal analysis with quantities detected by a thermal conductivity detector.

Fourier transform infrared spectroscopy. FTIR was used to investigate functional groups by a PerkinElmer, model Spectrum One spectrometer with a spectral resolution of 4 cm^{-1}. The samples were measured by mode of the single-crystal potassium bromide, KBr.

Downloaded from jep.sagepub.com at Chulalongkorn University on May 21, 2013

Figure 3. Open cup of near infrared spectroscopy.

NIR spectroscopy. NIR spectroscopy (BRAN&LUEBBE, InfraAlyzer 500) was used to study the EP spectra of the concentrated latex compounds in the region of 1100–2500 nm or the wave number 12,500–4000 cm^{-1}. The samples were prepared within the open cup as shown in Figure 3.

The samples of the concentrated latex compounds were scanned in the reflectance mode with the NIR spectroscopy in the NIR region from 1100 to 2500 nm at 2 nm increment. The samples were packed in the standard open cup and each sample was repacked and scanned three times for the average value. The NIR absorbance spectra were stored for subsequent development of the calibration equation with the reference, that is, the EP data.

X-Ray fluorescence. XRF was used to determine the chemical compositions: Philips, model PW 2400 was used with the tube current of 1000 μA and an acquisition lifetime of 30s.

X-Ray diffraction. XRD was used to identify crystalline characteristics that were consistent with those of the International Center for Diffraction Data Standard (JCPDS) patterns. Bruker AXS analyzer (D8 Discover) was model used, which is incorporated with a Vantec-1 detector and a double-crystal wide-angle goniometry. Measurement of scanning was in the range of 5°–80° 2θ under 5° 2θ min^{-1} of scan speed in 0.05° or 0.03° 2θ increments, using CuK_α radiation ($\lambda = 0.15406$ nm).

Transmission electron microscope. TEM (JEM-2100) equipped with energy dispersive x-rays spectroscopy (EDS) for x-ray microanalysis and nano beam diffraction (NBD) was used to study microstructures. The TEM sample preparation of the crude eggshells and

Downloaded from jep.sagepub.com at Chulalongkorn University on May 21, 2013

calcined eggshells was done on a grid to investigate the morphology and microstructure. An acceleration voltage of 80–200 kV with the magnifications from 50 to 1.5 million times of TEM were used.

Gas pycnometer. Gas pycnometer (Quantachrome, Ultra pycnometer 1000) was used to determine the apparent density of samples.

Autosorb-1. Autosorb-1 (Quantachrome) was utilized to investigate the porosity characteristics in terms of the specific surface area, the adsorption and/or desorption isotherms, the pore size, and the surface distribution. The quantity of gas adsorbed onto or desorbed from the solid surface at some equilibrium vapor pressures was measured in the static volumetric method. The measured absorbed or desorbed volumes of nitrogen gas were investigated in the range of 10^{-6} to slightly below 1.0 of relative pressures using krypton and the micropore options. The Brunauer–Emmet–Teller (BET) surface area (single and/or multipoint), the Langmuir surface area, the adsorption and/or desorption isotherms, the pore size and surface area distributions, the micropore volume, and the surface area were calculated via Autosorb-1 software.

Preparation of $CaCl_2$ solution and concentrated latex film samples

$CaCl_2$ solution preparation. $CaCl_2$ solution was made of dissolving 4.71 g of CaO powders from the calcinations of the three kinds of crude eggshells (chicken, duck, and bird) at 900°C for 2 h in 2 M of HCl as shown in equation (1). After dissolving CaO powders in 2 M of HCl, a clear solution (pH ~ 2) was obtained.

$$CaO + 2HCl \rightarrow CaCl_2 + H_2O \quad (1)$$

Concentrated rubber latex films preparation. The formulae of concentrated rubber latex films are shown in Table 1. $CaCl_2$ of 0.25, 0.50, 0.75, 1.00, 1.25, 1.50, 1.75, and 2.00 g was used to prepare solutions according to CaCl2 Solution Preparation section according to equation (1), then mixed with 10 wt% SDS as a stabilizer, which was added into the concentrated latex. The concentrated latex compounds were stirred at 1300 r min^{-1} for 30 min. The concentrated NRL compounds were cast onto the plastic Petri dishes, dried at room temperature for 24 h, and kept in a dessicator. The other parts of concentrated latex compounds were poured into the sample cells of FTIR and NIR spectroscopy to determine the chemical functional groups including peptide and amino acid spectra of proteins.

Chemical analysis. The EPs of the concentrated latex compounds in the film samples were determined by the modified Lowry method (International Organization for Standardization 12243 (ISO 12243)). In general, the modified Lowry method was used for the determination of water EP in the medical gloves made from NRL. The measurement was repeated four times for each sample and the measured values were averaged. The precipitated protein was redissolved and quantified colorimetrically by the modified Lowry method using a protein standard.

Downloaded from jep.sagepub.com at Chulalongkorn University on May 21, 2013

Table 1. Formulation of concentrated natural rubber latex compounds for films preparation.

Compositions	Dry weight (g)	Wet weight (g)
Concentrated latex, 60% HAL	100	167
10% SDS[a]	20	200
4.71 g CaO in 2 M HCl	0.25	2.41
	0.50	4.83
	0.75	7.24
	1.00	9.66
	1.25	12.07
	1.50	14.49
	1.75	16.90
	2.00	19.32

[a]SDS is sodium dodecyl sulphate, an anionic surfactant.

NRL film samples preparation for the EP testing by the modified Lowry method. The cast film was cut into smaller and rectangular pieces and the mass of each sample (M_ρ) was recorded with an accuracy of approximately 1.5 ± 0.001 g.

Determination of the EPs by the modified Lowry method

Preparation of the pure protein concentration precipitate for the modified Lowry method. According to ISO 12243 (medical gloves made from NRL—determination of water EP using the modified Lowry method), the reagent A (alkaline copper citrate), the reagent B (dilute Folin reagent prepared by diluting 72 cm^3 of 2 N Folin reagent with 28 cm^3 of water), the reagent C (a solution of 6 g of sodium carbonate in 100 cm^3 of water), the reagent D (a solution containing 1.5 g of copper sulfate and 3 g of sodium citrate in 100 cm^3 of water), the sodium deoxycholate solution, and the trichloroacetic acid solution were prepared. The rubber latex films were cut in small pieces in a rectangular shape, and the mass (M_ρ) of each sample was determined. The rubber latex film sample was extracted at 25 ± 5°C for 120 min, followed by shaking for 15s. The extract was decated and removed of any particulate matters by centrifuging for 15 min. The extract was stored for 48 h at a temperature below 7°C, and the molecular weight (M_w) was measured. The protein concentration precipitate was divided and put into four sample tubes for testing by the ultraviolet (UV) spectrophotometer, which calculated and reported the average EP values.

According to the modified Lowry method, the cast film pieces were put into a conical flask, the distilled water of 20 ml was added, then the sample flasks in a water bath were shaken at 37°C for 5 min. The shaking water bath was set at the speed of 200 r min^{-1} for 1 h to extract the water soluble proteins. Water soluble proteins were poured out of the conical flask into a 50-ml plastic tube and the weight of water in the plastic tube (M_w) was measured. The plastic tube was put in a centrifuge with the high speed of 3000 r min^{-1} for 15 min. The protein concentration precipitate was divided into four

Downloaded from jep.sagepub.com at Chulalongkorn University on May 21, 2013

Table 2. Chemical composition analysis of crude eggshell.

Compounds	Raw chicken eggshells (wt%)	Raw duck eggshells (wt%)	Raw bird eggshells (wt%)
Na_2O	–	<0.1	0.23
MgO	–	0.10	1.12
SiO_2	–	0.01	0.04
P_2O_5	0.80	0.46	1.19
SO_3	1.79	0.96	0.98
Cl	–	–	0.06
ZrO_2	–	0.02	–
K_2O	0.21	0.20	0.11
SrO	779 ppm	0.02	0.02
$CaCO_3$	96.46	96.35	96.23

–: compounds that cannot be measured.

sample tubes for testing by a UV spectrophotometer that calculated and reported the average EP values.

Calculation of the extractable protein contents. The EP contents were determined from equation (2) as follows

$$\frac{C \times M_w}{M_\rho \times V} \tag{2}$$

where C is the absorbance from a UV spectrophotometer or the protein concentration in the redissolved protein solution, in micrograms per cubic centimeter ($\mu g\ cm^{-3}$), M_w is the mass in grams of the distilled water, M_ρ is the mass in grams of a rectangular piece of the cast film, and V is the volume of the extractant used, in cubic centimeters (cm^3).

Results and discussion

Physical and chemical characteristics of CaO made from chicken, duck, and bird eggshells

The chemical compositions of crude chicken, duck, and bird eggshells by XRF are tabulated in Table 2. Most of the crude eggshells contain approximately 96 wt% of $CaCO_3$ and the rest belonging to other oxide compounds: Na_2O, MgO, SiO_2, K_2O, SrO, and ZrO_2. Table 3 shows the organic compositions of the crude eggshells from chicken, duck, and bird as measured by the elemental analyzer. The data of specific surface area, the average pore diameter, the true density, and the average particle size of CaO are tabulated in Table 4. The specific surface area and average pore diameter values of CaO made from the chicken eggshells are 7.79 $m^2\ g^{-1}$ and 17 Å, respectively, which are close to the values of the duck eggshells of 7.70 $m^2\ g^{-1}$ and 17.69 Å, respectively. The specific surface area and average pore diameter of CaO from the bird eggshells are 3.47 $m^2\ g^{-1}$

Downloaded from jep.sagepub.com at Chulalongkorn University on May 21, 2013

Table 3. Organic composition of crude eggshells as measured by elemental analyzer (Perkin Elmer PE2400 SeriesII).

Element	Crude chicken eggshells (%wt)	Crude duck eggshells (%wt)	Crude bird eggshells (%wt)
C	14.001 ± 0.345	13.640 ± 0.230	14.270 ± 0110
H	0.097 ± 0.025	0.490 ± 0.050	0.850 ± 0.077
N	0.145 ± 0.031	0.630 ± 0.100	1.170 ± 0.023

Table 4. Physical characterization of calcium oxide made from eggshells calcined at 900°C for 2 h.

Raw materials	Specific surface area ($m^2\ g^{-1}$)	Average pore diameter (Å)	True density ($g\ cm^{-3}$)	Average particle size (micron)
CaO powder from chicken	7.79	17.00	2.16	2.00
CaO powder from duck	7.70	17.69	2.84	12.12
CaO powder from bird	3.47	82.99	2.88	12.44

and 82.99 Å, respectively. CaO here possesses the pore diameter in the range of mesopore: 20 Å-500 Å (2-50 nm). True density values of CaO of the chicken, duck, and bird eggshells are 2.16, 2.84, and 2.88 g cm^{-3}, respectively. The average particle size of CaO of the chicken, duck, and bird eggshells are 2.00, 12.12, and 12.44 μm, respectively. The particle size of CaO is very small, which is suitable for using as filler or dispersed phase in concentrated NRL.

TEM micrographs of CaO from chicken (Figure 4(a) and (a1)), duck (Figure 4(b) and (b1)), and bird (Figure 4(c) and (c1)) eggshells are shown in Figure 4 with the magnifications of 25,000× and 12,000×. The TEM micrographs show uniformly particle size distribution and an agglomeration due to fine particles, consistent with the results obtained from the particle size measurement.

FTIR spectra of CaO made from the crude chicken, duck, and bird eggshells show the same peak positions at 3643 cm^{-1} strong ν(O–H), 3435 cm^{-1} ν(O–H), 1630 cm^{-1} strong ν(C=O), and 500–580 cm^{-1} ν(Ca–O), as shown in Figure 5.

Properties of concentrated rubber latex

The properties of concentrated rubber latex are tabulated in Table 5, where the data were obtained following the ISO2004-1997. The properties of the concentrated latex compounds measured are the total solid content (ISO124); the DRC (ISO126); the nonrubber solids per rubber; the alkalinity content (ISO125); the volatile fatty acid number (ISO 506); the KOH number (ISO127); the pH values (ISO976); the specific gravity (ISO705); the mechanical stability (ISO35); and the apparent viscosity by the Brookfield test (ISO1652), according to the International Organization for Standardization.

Downloaded from jep.sagepub.com at Chulalongkorn University on May 21, 2013

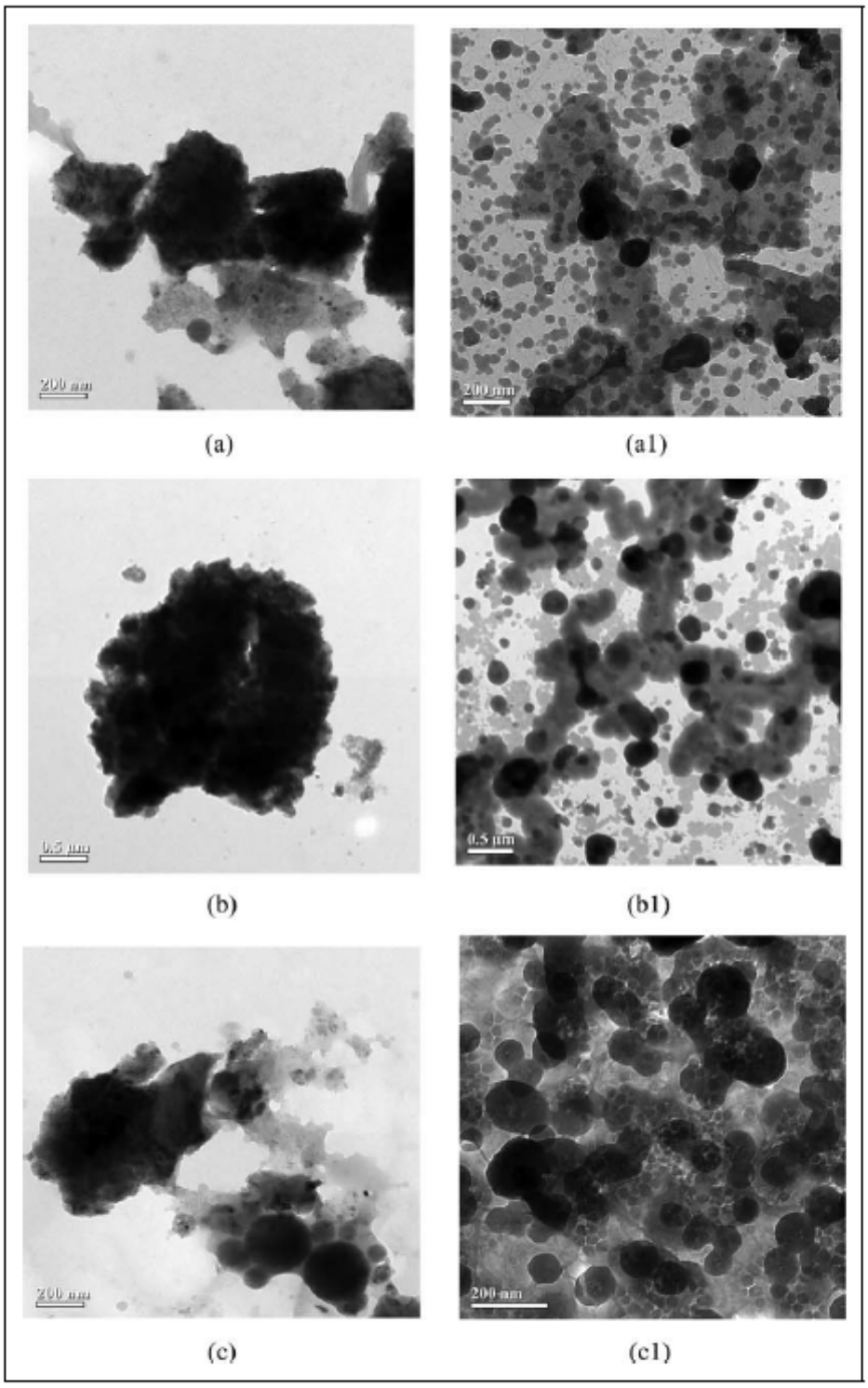

Figure 4. Transmission electron micrographs of eggshells with the magnifications of × 25,000 and ×12,000. (a) Crude chicken eggshells; (a1) chicken eggshells calcined at 900°C for 2 h; (b) crude duck eggshells; (b1) duck eggshells calcined at 900°C for 2 h; (c) crude bird eggshells; and (c1) bird eggshells calcined at 900°C for 2 h.

Downloaded from jep.sagepub.com at Chulalongkorn University on May 21, 2013

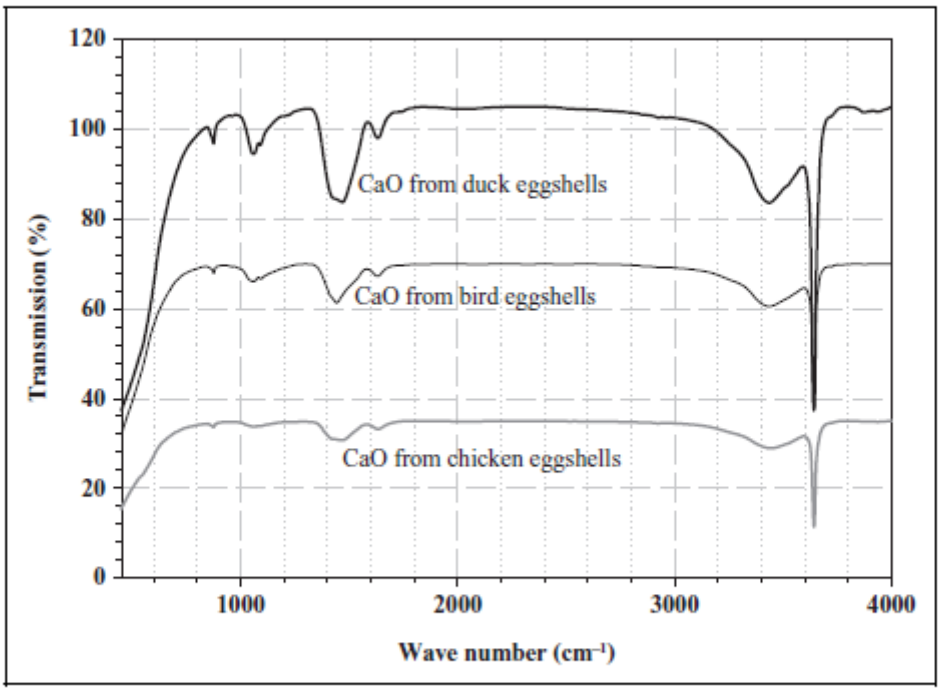

Figure 5. Fourier transformation infrared spectra of calcium oxide obtained from chicken, duck, and bird eggshells calcined at 900°C for 2 h.

Table 5. Properties of concentrated natural rubber latex compounds.

Properties	Concentrated latex	ISO 2004-1997	References
TSC per rubber weight (%)	61.86 ± 0.11	>61.50	ISO 124
DRC per rubber weight (wt%)	59.97 ± 0.10	>60.00	ISO 126
Non rubber solids per rubber weight (wt%)	1.89 ± 0.01	<2.00	–
NH_3 per rubber weight (wt%)	0.53 ± 0.08	>0.60	ISO 125
NH_3 per water weight (wt%)	1.38 ± 0.22	–	–
VFA number	0.050 ± 0.009	<0.20	ISO 506
KOH number	0.78	<1.00	ISO 127
pH	10.05 ± 0.09	–	ISO 976
Specific gravity	0.948 ± 0.001	–	ISO 705
MST (s)	852 ± 39	>650	ISO 35
Viscosity spindle no. 1		–	ISO 1652
Speed 6 r min^{-1} (cps)	186 ± 62		
Speed 30 r min^{-1} (cps)	111 ± 37		
Speed 60 r min^{-1} (cps)	90 ± 27		

TSC: total solid content; DRC: dry rubber content; VFA: volatile fatty acids; MST: mechanical stability time.

Downloaded from jep.sagepub.com at Chulalongkorn University on May 21, 2013

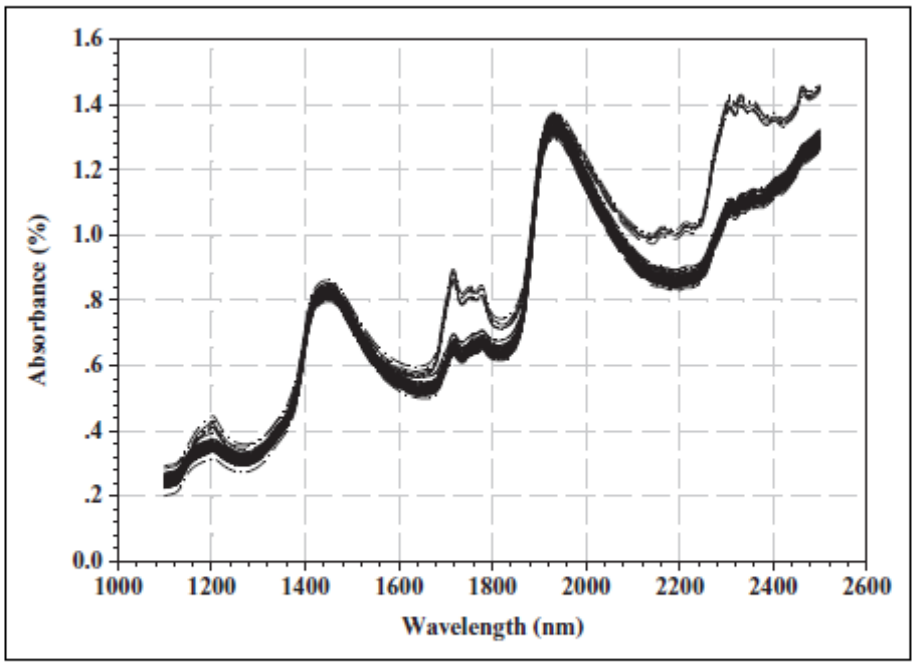

Figure 6. Near infrared spectroscopy spectra of natural rubber latex compounds added calcium chloride and sodium dodecyl sulphate.

Quality and quantity of EP removed from concentrated NRL surface films with the addition of $CaCl_2$ and SDS

NIR spectra of the concentrated latex compounds added with $CaCl_2$ solution and the stabilizer (SDS) in liquid state were measured in the region of 1100–2500 nm (12,500–4000 cm^{-1}), as shown in Figure 6. The characteristic peaks indicate the percentages of absorbances at the wavelengths of 1520 and 1980 nm, which are related to the EP contents in terms of peptide or amino acid of the first overtone N–H (υ_1N–H) and the asymmetric combination N-H, respectively, as previously reported by Osborne and Fearn[12] and Murray and William.[13] Furthermore, the absorbance peaks at the wavelengths of 1450 and 1920 nm indicate the first overtone of O–H (υ_1O–H) of the concentrated NRL compounds.

Concentrated NRL films were added with the $CaCl_2$ solution as obtained from the pyrolysis of the chicken, duck, and bird eggshells dissolved in HCl and SDS. The FTIR peaks in the range of 400–4000 cm^{-1} are shown in Figure 7. The FTIR spectra are encoded as: Latex film_chicken_05; Latex film_duck_05, and Latex film_bird_05; they show the same peak positions identifying the chemical functional groups at 2956 cm^{-1} ν(C–H of CH_3), 2919 cm^{-1} ν(C–H of CH_2), 2875 cm^{-1} ν(C=O) and δ(α-CH_3), 1468 cm^{-1} δ(CH_2), 1248 cm^{-1} ν(S–O of SO_4), 1221 cm^{-1} ν(C–O, C–O–C, and C–C–O), 1071 cm^{-1} ν(S–O of SO_4), 830 cm^{-1} ν(S–O–C), 722 cm^{-1} –$(CH_2)_n$-(n>3), and 633 and 587 cm^{-1} δ(SO_4). Furthermore, the FTIR spectra of concentrated rubber latex films added with $CaCl_2$ and SDS are compared with the FTIR spectra of CaO powder made from the calcined crude eggshells and the pure concentrated latex film. The FTIR spectrum of CaO

Downloaded from jep.sagepub.com at Chulalongkorn University on May 21, 2013

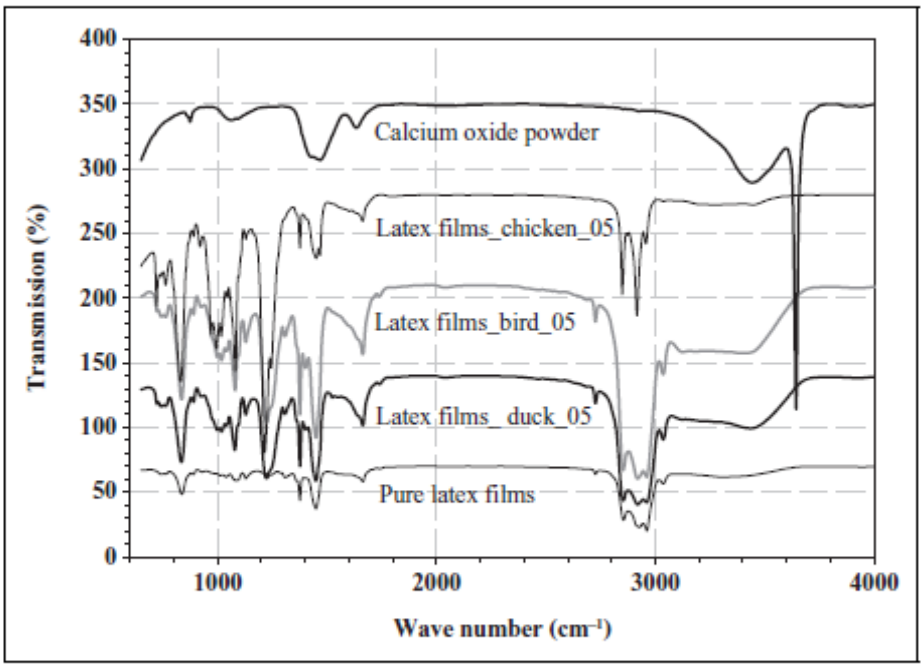

Figure 7. Comparison of Fourier transformation infrared spectra of natural rubber latex films added calcium chloride and sodium dodecyl sulphate.

shows peaks at 3600 cm^{-1} strong ν(O–H), 3450 cm^{-1} ν(O–H), 2800–2970 cm^{-1} δ(C–H), 1750 cm^{-1} ν(C=O), 1650 cm^{-1} strong ν(C=O), and 500–580 cm^{-1} ν(Ca–O). The characteristic peaks of the pure concentrated latex are at 3000–2900 cm^{-1} ν(C–H) and (=CH), 2900–2800 cm^{-1} ν(CH_2), 1800–1600 cm^{-1} ν(C=C), 1500–1300 cm^{-1}(CH_3 asymmetric deformation), 1300–1100 cm^{-1} ν(C–O–C), and 1100–740 cm^{-1} (=CH bending). All FTIR spectra encoded with Latex film_chicken, Latex film_bird, and Latex film_duck show the same peak positions, corresponding to the peak positions of pure latex films and the CaO powder, except for the peak positions at 3600 cm^{-1} strong ν(O–H) and 3450 cm^{-1} ν(O–H), which are due to dried latex films. These FTIR spectra assignments encoded Latex film_chicken, Latex film_bird, and Latex film_duck are of the same functional groups of the rubber latex as matrix phase and CaO as dispersed phase.

The XRD peak patterns of pure NRL films, latex films added with $CaCl_2$ and SDS, and CaO powder from eggshells are shown in Figure 8. The XRD peak pattern of pure NRL film shows an amorphous phase, whereas the XRD peak pattern of CaO powder indicates a crystalline phase of the lime face-centered cubic phase formation (Fm3m) which corresponding to CaO and consistent with JCPDS No.82-1690. Moreover, the XRD peak patterns of latex film added with $CaCl_2$ solution and SDS for all the three kinds of eggshells (chicken, duck, and bird) show a semicrystalline phase due to the amorphous phase and a small amount of crystalline phase. The crystalline phase found in the semicrystalline phase formation comes from adding SDS as the stabilizer and the $CaCl_2$ solution that contains ionic charge contents (Na^+, Ca^{2+}, O^{2-}, H^+, and Cl^-). The quantities of EPs, removed from concentrated NRL surface films added with $CaCl_2$

Downloaded from jep.sagepub.com at Chulalongkorn University on May 21, 2013

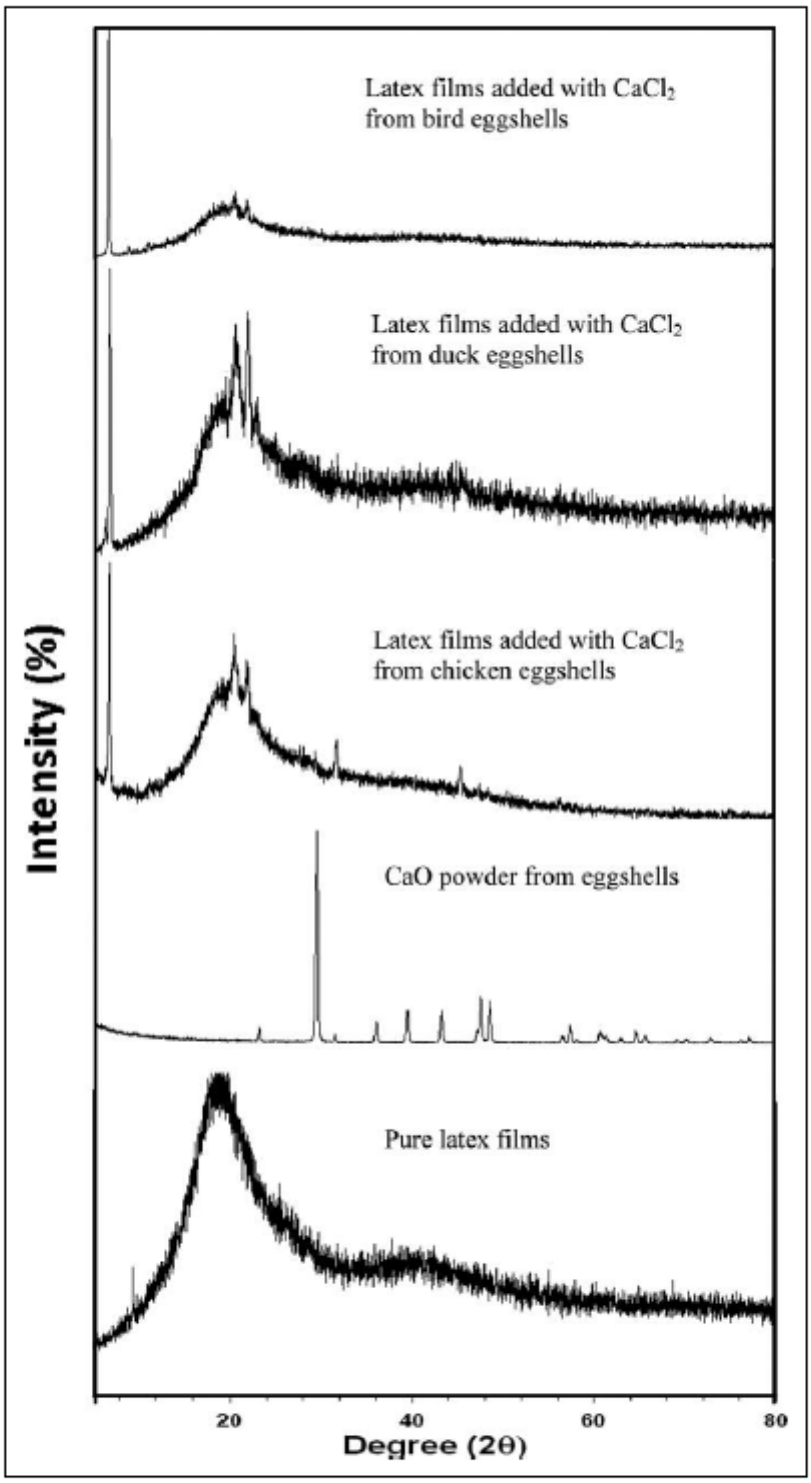

Figure 8. Comparison of x-ray diffraction patterns of pure concentrated natural rubber latex film, calcium oxide, rubber latex films added calcium chloride solution made from calcium oxide of eggshells dissolved in 2 M HCl.

Downloaded from jep.sagepub.com at Chulalongkorn University on May 21, 2013

solution and SDS, according to the formulation of Table 1, were determined four times for each sample. The water EP contents, as measured by the modified Lowry method, are shown in Table 6. The small amount of the EP of the pure NRL films is equal to 38.84 $\mu g\, g^{-1}$. The amount of EPs of Latex_01, Latex_02, and Latex_03 films added with only 2 M HCl (no CaO) are equal to 4515, 4360, and 6109 $\mu g\, g^{-1}$, respectively. Adding only HCl into the concentrated rubber latex can reduce the EP because HCl is a strong acid containing ionic charges of H^+ and Cl^-, which can form bonds with proteins, thus denaturing proteins and reducing the crosslink densities of concentrated rubber latex films. However, the comparison of the amount of EP values added with 0.5 and 1.0 g of 2 M HCl and encoded Latex_01, Latex_02, and Latex_03 are slightly lower than those of EPs with $CaCl_2$ as prepared from the CaO (chicken, bird, and duck eggshells) mixed with 2 M HCl to form a $CaCl_2$ solution. Latex films added with the $CaCl_2$ solution made from CaO of chicken, duck, and bird eggshells dissolved in 2 M HCl and mixed with SDS are encoded as Latex_chicken_(01-07), Latex_duck_(01-07), and Latex_bird_(01-07), respectively. Latex_chicken_05, Latex_duck_05, and Latex_bird_03 possess the highest values of the water EP contents: 7338, 5803, and 7008 $\mu g\, g^{-1}$, respectively. Especially, adding 0.75 g of $CaCl_2$ solution made from dissolving CaO bird eggshells in 2 M HCl is the most suitable for the extraction of proteins at the film surfaces. The higher amounts of $CaCl_2$ in the solutions, such as 1.75 and 2.00 g, yield lower water EPs contents than those of $CaCl_2$ in the range of 0.75–1.50 g $CaCl_2$. The amounts of water EPs from Latex_$CaCl_2$_01 and Latex_CaO_01 are lower than the latex added with $CaCl_2$ dissolved in 2 M HCl. It can be concluded that the $CaCl_2$ solution made from the eggshells is of a high purity, a high specific surface area, and containing more ionic specie contents (Ca^{2+}, H^+, Cl^-, and O^{2-}), suitable to denature proteins because CaO is a porous-solid material functioning as a heterogeneous catalyst. The different values of the obtained EPs are due the differing specific surface areas and pore diameters of CaO. The specific surface areas and the average pore diameters of CaO made from chicken and duck eggshells are nearly the same. They differ distinctly from the specific surface area and the pore diameter of CaO made from bird eggshells. The main advantage of a large average pore diameter of CaO from bird eggshells is the ability to trap the large and small molecular proteins from NRL more easily.

Conclusion

$CaCl_2$ made from CaO was produced by the pyrolysis of crude eggshells (chicken, duck, and bird) calcined at 900°C for 2 h and dissolved in 2 M HCl. The CaO made from eggshells are of high purity ($\sim$99 wt%), of small and uniform sizes (2–12 μm), of low true density, with high specific surface areas and average pore diameters, especially the bird eggshell with 3.47 $m^2\, g^{-1}$ and 82.99 Å, and possess more ionic specie contents (Ca^{2+}, O^{2-}, H^+, and Cl^-). CaO is a porous-solid material that can be used as a heterogeneous catalyst to absorb and denature proteins. The eggshells can be used as a starting material or the dispersed phase to extract the proteins from NRL. The proteins are known to cause latex-allergic problems to human skins. The effective way to prevent the allergic sensitization is to remove the EPs. Controlling the level of proteins on the finished products such as medical gloves, condoms, balloons, and medical/dental parts to a lower level is expected to reduce the sensitization of NRL product users.

Downloaded from jep.sagepub.com at Chulalongkorn University on May 21, 2013

Table 6. Water EP contents from the concentrated natural rubber latex films as measured by the modified Lowry method.[a]

Codes	Concentrated latex (g)	10 wt% SDS (g)	$CaCl_2$[b] solution or HCl[c] (g)	Water EP ($\mu g\ g^{-1}$)
Pure latex films	100	–	–	**38.84**
Latex_01[c]	100	20	0.50 g of 2 M HCl	4515
Latex_02[c]	100	20	1.00 g of 2 M HCl	4360
Latex_03[c]	100	20	2.00 g of 2 M HCl	6109
Latex_chicken_01	100	20	**0.25 g of $CaCl_2$**[b]	**3449**
Latex_chicken_02	100	20	0.50 g of $CaCl_2$[b]	4210
Latex_chicken_03	100	20	0.75 g of $CaCl_2$[b]	4212
Latex_chicken_04	100	20	1.00 g of $CaCl_2$[b]	4957
Latex_chicken_05	100	20	**1.50 g of $CaCl_2$**[b]	**7338**
Latex_chicken_06	100	20	1.75 g of $CaCl_2$[b]	6508
Latex_chicken_07	100	20	2.00 g of $CaCl_2$[b]	6517
Latex_bird_01	100	20	**0.25 g of $CaCl_2$**[b]	**6237**
Latex_bird_02	100	20	0.50 g of $CaCl_2$[b]	5588
Latex_bird_03	100	20	**0.75 g of $CaCl_2$**[b]	**7008**
Latex_bird_04	100	20	1.00 g of $CaCl_2$[b]	5512
Latex_bird_05	100	20	**1.50 g of $CaCl_2$**[b]	**5174**
Latex_bird_06	100	20	1.75 g of $CaCl_2$[b]	4169
Latex_bird_07	100	20	2.00 g of $CaCl_2$[b]	5129
Latex_duck_01	100	20	**0.25 g of $CaCl_2$**[b]	**3219**
Latex_duck_02	100	20	0.50 g of $CaCl_2$[b]	4834
Latex_duck_03	100	20	0.75 g of $CaCl_2$[b]	4731
Latex_duck_04	100	20	1.00 g of $CaCl_2$[b]	5639
Latex_duck_05	100	20	**1.50 g of $CaCl_2$**[b]	**5803**
Latex_duck_06	100	20	1.75 g of $CaCl_2$[b]	5706
Latex_duck_07	100	20	2.00 g of $CaCl_2$[b]	3965
Latex_$CaCl_2$_01	100	20	0.25 g of $CaCl_2$[d]	2830
Latex_CaO_01	100	20	0.25 g of $CaCl_2$[e]	1989

EP: extractable protein; SDS: sodium dodecylsulphate.

[a]All data are the average values from experimental testing three times per one sample, and data in the same evaluation.

[b]The weight of $CaCl_2$ solution obtained from CaO of chicken, bird, and duck eggshells dissolved in 2 M HCl as given in the below equations.

[c]Adding only 2 M HCl solution (not contain CaO) of 0.50 g (latex_01), 1.00 g (latex_02), and 2.00 g (latex_03) into the latex compound samples.

[d]The weight of $CaCl_2$ solution produced by dissolving $CaCl_2$ (commercial grade) with water.

[e]The weight of $CaCl_2$ solution produced by dissolving CaO (commercial grade) in 2 M HCl as given in the below equations

$$CaCO_3 \rightarrow CaO + CO_2$$

$$CaO + 2HCl \rightarrow CaCl_2$$

Downloaded from jep.sagepub.com at Chulalongkorn University on May 21, 2013

Acknowledgments

The authors thank the Petroleum and Petrochemical College and the Scientific and Technological Research Equipment Centre at Chulalongkorn University; the Departments of Materials Engineering at Kasetsart University for the use of analytical equipment; and the Rubber Research Institute of Thailand and the Kasetsart Agricultural and Agro-Industrial Product Improvement Institute, Kasetsart University for the concentrated latex testing.

Funding

This work was supported by the Medium Projects on Rubber (MPR 52 No. RDG5250062) of the Thailand Research Fund and Center for Advanced Studies in Industrial Technology, and also by the Conductive and Electroactive Polymers Research Unit of Chulalongkorn Univsersity, the Thailand Research Fund (TRF), and the Royal Thai Government.

References

1. Peng Z, Kong LX, Li SD, Chen Y, and Huang MF. Self-assembled natural rubber/silica nanocomposites: its preparation and characterization. *Compos Sci Technol* 2007; 67: 3130–3139.
2. Angellier H, Molina-Boisseau S, and Dufresne A. Mechanical properties of waxy maize starch nanocrystal reinforced natural rubber. *Macromolecules* 2005; 38: 9161–9170.
3. Sato S, Honda Y, Kuwahara M, Kishimoto H, Yagi N , and Muraoka K. Microbial scission of sulfide linkages in vulcanized natural rubber by a white rot basidiomycete, Ceriporiopsis subvermispora. *Biomacromolecules* 2004; 5: 511–515.
4. Rogero SO, Lugão AB, Yoshii F, and Makuuchi K. Extractable proteins from irradiated field natural rubber latex. *Radiat Phys Chem* 2003; 67: 501–503.
5. Perrella FW, and Gaspari AA. Natural rubber latex protein reduction with an emphasis on enzyme treatment. *Methods* 2007; 27: 77–86.
6. Truscott W. Sensitivity to latex in medical devices. In: *International latex conference, US Food and Drug Administration, CDRH*, Baltimore, MD, 5-7 Nov 1992.
7. Lai PF, and Ng KP. Production of high quality latex products: Malaysian efforts in meeting future requirements. In: *Latex: education symposium No. 36, Rubber Division, American Chemical Society Educational Symposium on Natural Rubber*, Philadelphia, 2 May 1995.
8. Aziz NAA. Chlorination of Gloves. In: *Latex Protein Workshop of the International Rubber Technology Conference (Rubber Research Institute of Malaysia)*, Kuala Lumpur, 14-16 June 1993.
9. Truscott W. The industry perspective on latex. *Immunology and Allergy Clinics of North America* 1995; 15: 89-115.
10. Marrakchi S, and Maibach HI. Sodium lauryl sulfate-induced irritation in the human face: regional and age-related differences. *Skin Pharmacol Physiol* 2006; 19(3): 177–180.
11. Mukerjee P, and Mysels KJ. *Critical micelle concentration of aqueous surfactant systems NSRDS-NBS 36*. Washington, DC: US Government Printing Office, 1971.
12. Osborne BG, and Fearn T. Theory of near infrared spectrophotometry. In: *Near infrared spectroscopy in food analysis*. England: Longman Scientific and Technical, Longman Group UK Limited, 1986, pp. 20–42.
13. Murray I , and Williams PC. Chemical principles of near infrared technology. In: Williams PC and Norris KH (eds) *Near infrared technology in agricultural and food industries*. St Paul, MI: American Association of Cereal Chemists Inc, 1990, pp. 17–31.

Downloaded from jep.sagepub.com at Chulalongkorn University on May 21, 2013

Polymer-Plastics Technology and Engineering, 52: 907–920, 2013
Copyright © Taylor & Francis Group, LLC
ISSN: 0360-2559 print/1525-6111 online
DOI: 10.1080/03602559.2013.763371

Taylor & Francis
Taylor & Francis Group

Development of Polydiphenylamine/Zeolite Y Composite by Dealumination Process as a Sensing Material for Halogenated Solvents

Tharaporn Permpool[1], Anuvat Sirivat[1], Darunee Aussawasathien[2], and Ladawan Wannatong[3]

[1]*The Petroleum and Petrochemical College, Chulalongkorn University, Bangkok, Thailand*
[2]*National Metal and Materials Technology Center, National Science and Technology Development Agency, Ministry of Science and Technology, Pathumthani, Thailand*
[3]*Faculty of Engineering, King Mongkut's University of Technology North Bangkok, Bangkok, Thailand*

Downloaded by [Chulalongkorn University] at 19:46 20 August 2013

Polydiphenylamine and zeolite Y composite were fabricated and tested for the ability to detect the halogenated solvent vapors; dichloromethane, 1,2-dichloroethane, and chloroform. To enhance the sensing properties of the composites, zeolite Y was modified by the dealumination process. The sensitivity of the composites towards the halogenated solvents was examined under the effects of acid treatment time, zeolite content, temporal response, and cyclic response. The resultant dealuminated zeolite Y showed a higher sensitivity when exposed to solvents than the pristine zeolite. An acid treatment time of 12 h provided the highest sensitivity. Sensitivity of the composites towards dichloromethane was higher than those of 1,2-dichloroethane, and chloroform, respectively. The optimal dealuminated zeolite content in the composites was 30 vol.%.

Keywords Conducting polymers; Dealumination process; Halogenated hydrocarbon; Polydiphenylamine; Sensors; Zeolites

INTRODUCTION

Halogenated hydrocarbons are widely used for many industrial purposes. They are used in the productions of herbicides, plastics, and solvents; solvent degreasing in the automotive and aerospace industries; dry-solvent cleaning; and solvent cleaning in the electronic field[1,2]. However, halogenated hydrocarbons impose several environmental problems, and exhibit high toxicity towards humans[3]. In order to reduce the risks of these problems, highly responsive chemical gas sensors are required to identify and detect toxic halogenated hydrocarbon vapors. Sensing materials previously investigated have been identified to contain a conductive polymer as a base material[4–6] and a porous material as a selective material[7].

Address correspondence to Anuvat Sirivat, The Petroleum and Petrochemical College, Chulalongkorn University, Bangkok, 10330, Thailand. E-mail: anuvat.s@chula.ac.th

Polydiphenylamine, PDPA, is a conductive polymer which is quite robust, high thermal and environmental stability, stable in a greater pH range than polyaniline, as well as and an inexpensive monomer[8]. Moreover, PDPA has been used as a material for many sensory systems such as methanol sensors[9], Fe^{3+} ion sensor[10], optical pH sensor[11], ascorbic acid sensor[12], ammonia sensor[13], and carbon monoxide sensors[14].

Zeolites are well known as a micro porous material and are widely used in many applications such as a catalyst for water purification[15], catalyst for ethylene oligomerization to liquid fuels[16], gas separation membrane for fuel cells[17,18], absorbent in refrigerators[19], and sensor applications[20–25]. Their unique properties are high surface area and porosity, shape selectivity, controllable acidity, adsorptivity, and presence of mobile ions[7,26–29]. These zeolite properties can be controlled by varying the Si/Al ratio. The dealumination method is a method to remove aluminum from the framework resulting in a higher Si/Al ratio, chemical and thermal stabililty, and zeolite hydrophobicity[16,30–32].

In this work, doped polydiphenylamine (D-PDPA) was used as a base material and zeolite Y (Si/Al = 80) as a selective material to make up the composites to be used as sensing materials for detecting the halogenated solvents dichloromethane (DCM), 1,2-dichloroethane (DCE), and chloroform. In order to improve the sensitivity of the composites towards these halogenated solvents, zeolie Y was modified by the acid treatment-dealumination process to increase the Si/Al ratio. The composition and structure characterization of dealuminated zeolite Y (D Y H) was investigated. The effects of acid treatment times, zeolite content, cyclic response, and chemical interaction of the composite were also investigated. As for PDPA, it is doped with a hydrochloric acid solution at the doping mole ratio of 100:1

Downloaded by [Chulalongkorn University] at 19:46 20 August 2013

($N_{HCl}/N_{monomer}$). The synthesis and characterization of D-PDPA follow the previous work[9].

EXPERIMENTAL PROCEDURE

Materials

Diphenylamine, DPA (reagent, Sigma Aldrich), ammonium persulfate, $(NH_4)_2S_2O_8$, (AR grade, Riedel-de Haën), 36.5–38.0 wt.% of hydrochloric acid at the mole ratio of 100:1 ($N_{HCl}/N_{monomer}$), HCl, (ACS reagent, J.T. Baker) were used for the D-PDPA synthesis. Zeolite Y (Zeolite International) with H^+ as a cation, possesses the Si/Al ratio of 80 (Y H 80) in powder form. Ammonium hydroxide, NH_4OH, (AR grade, Panreac), toluene (AR grade, Panreac), isopropyl alcohol (AR grade, Burdick & Jackson), and ethanol (AR grade, Lab Scan) were used without further purification.

Synthesis of Polydiphenylamine

The chemical oxidative polymerization was used to synthesize PDPA[33]. The DPA monomers in toluene were mixed with a 1 M HCl solution. The solution was stirred for 15 min. After that, the $(NH_4)_2S_2O_8$ solution was added and stirred continuously at 0°C for 4 h. The resultant green slurry of PDPA was washed with isopropanol and filtered. Then, PDPA was neutralized by immersing in NH_4OH at the ratio of 1:3 to get rid of an excess hydrochloric acid. After that, PDPA was doped with HCl at the ratio of 1:100 (N_{DPA} : N_{HCl}).

Dealumination of Zeolite Y

The pristine Y H 80 (supplied from Zeolyst International, with hydrogen cation) went through an acid treatment process[30]. The pristine Y H 80 was treated with 1 M HCl solution at 90°C by varying the acid treatment times (2, 4, 8, 10, 12, 18, and 24 h) to obtain various Si/Al ratios. In the dealumination process, all samples were filtered and washed with distilled water at least 3 times.

Preparation of D-PDPA/D Y H 80 Composites

The composites of D-PDPA and D Y H 80 were prepared as a circular pellet (1 cm in diameter) by a hydraulic press (GRASEBY SPECAC) at a pressure between 4 tons - 5 tons. The D-PDPA was mixed with D Y H 80 at various zeolite Y contents (0, 5, 10, 15, 20, 25, 30, 35, and 40 vol.%). A digital thickness gauge (PEAACOCK, model PDN-20) was used to measure the thickness of each composite.

Composition and Structure Characterization

The Fourier transform infrared (FT-IR) spectra of the samples were recorded with a Thermo Nicolet FT-IR spectrometer; model Nexus 670 in a wave number range of 1600–400 cm^{-1}, a resolution of 4 cm^{-1}, and a scan number of 64. The silicon and aluminum content were measured by an AXIOS, PW440, X-ray fluorescence (XRF). The morphology and crystal size of the samples were investigated by a HITACHI, S-4800 scanning electron microscope (SEM) with a magnification of 10,000x, operated at 10 kV. The Brunauer-Emmett-Teller (BET) surface area of the samples was measured by a Thermo Finnigan, Sorptomatic 1990 surface area analyzer (SAA). The samples were weighed and out gassed at 300°C for 12 h before determination of the adsorption and desorption isotherms with the He and N_2 gases. The temperature program of the sample was measured by a Perkin Elmer, TGA7, thermo gravimetric analyzer (TGA). The experiment was carried out by weighing a powder sample of 5 mg to 10 mg with a heating rate 10°C min^{-1} from 30°C–900°C.

The charges distribution along the composite backbone was measured by an electrostatic force microscopy (EFM) (Park System, XE-100) operating in the standard EFM mode with an NSC 14/Cr-Au tip, a scan size of 1 μm × 1 μm, and a scan rate of 0.1 Hz. The voltage was applied to the sample at 5 V. The EFM phase image exhibited brighter regions as the positively charges within the composite respond to the applied voltage. The EFM phase image exhibited darker regions as the negatively charges within the composite respond to the applied voltage.

Conductivity and Sensitivity Measurements

The conductivity and sensitivity of all samples towards the halogenated solvents were measured by the two-point probe method. The probes were connected to a Keithley 6517A conductivity meter and the current was measured in response to the applied voltage. The electrical conductivity of the samples was calculated by Eq. (1);

$$\sigma = (I/KVt) \tag{1}$$

where I is the measured current (A), V is the applied voltage (V), t is the thickness of samples, and K is the geometric correction factor that was calibrated by using standard silicon wafer sheets with known specific resistivity values. The change in conductivity of all samples ($\Delta\sigma/\sigma_{N2,\ initial}$) when exposed to a halogenated solvent divided by the conductivity in pure nitrogen is defined as the sensitivity. The difference in the specific electrical conductivity (S cm^{-1}) is $\Delta\sigma$ and it was calculated by Eq. (2);

$$\Delta\sigma = \sigma_{halogenated\ solvents} - \sigma_{N2,\ initial} \tag{2}$$

where $\sigma_{N2,\ initial}$ is the specific electrical conductivity in N_2 before the exposure (S cm^{-1}), and $\sigma_{halogenated\ solvent}$ is the specific electrical conductivity (S cm^{-1}) under the halogenated solvent exposure at various concentrations. All measurements were taken at 27 ± 1°C, at the atmospheric pressure using a 5 L min^{-1} air and N_2 flow rate.

Downloaded by [Chulalongkorn University] at 19:46 20 August 2013

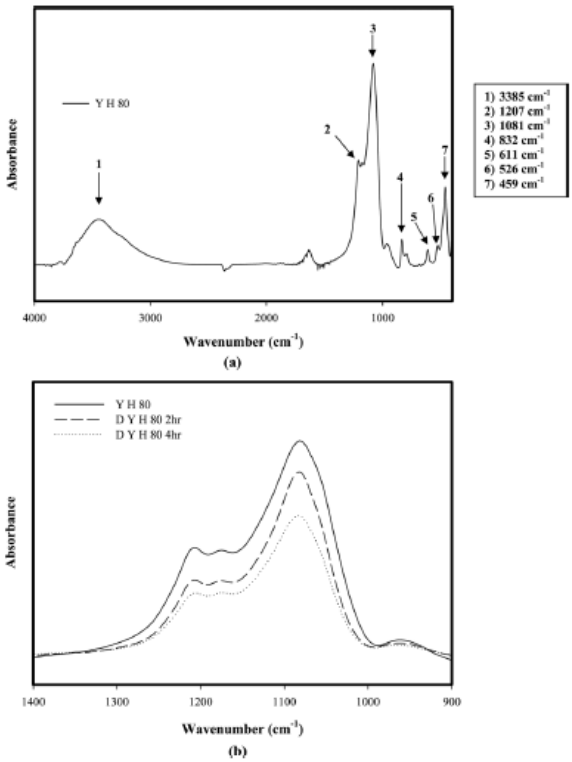

FIG. 1. FT-IR spectra of (a) Y H 80 and (b) D Y H 80.

RESULTS AND DISCUSSION

Composition and Structure of Dealuminated Zeolite Y

The FT-IR spectra of the Y H 80 are shown in Figure 1a. The absorption bands are at 3385 and 1207, 1081 cm^{-1} and can be assigned to the SiO_4, and AlO_4, vibrations, respectively[34]. The absorption bands at 832, 611, 526, and 459 cm^{-1} can be assigned to the vibrations of Si-O-Al bonds[34]. For the dealuminated zeolite Y (D Y H 80) through varying an acid treatment time, the intensity of the absorption band at 1081 cm^{-1} decreases with increasing acid treatment time[32]. This is due to the lower aluminum content within the zeolite framework[35]. Figure 1b shows an example of FT-IR spectra of D Y H 80 at 2 h and 4 h acid treatment times, and the areas under the bands were calculated by using a curve fitting technique[16].

The calculated band areas of the AlO_4 (1081 cm^{-1}) of the dealuminated samples were compared with the integrated band area of the vibrations of the Si-O-Al bonds (832 cm^{-1}) which do not change with the acid treatment time (internal standard). The resultant integrated band area decreases in the following order: $0 > 2 > 4 > 8 > 10 > 12$ h, as shown in Table 1. The actual Si/Al contents of D Y H 80 are also given in Table 1. The Si/Al ratio increases with increasing acid treatment time[35]; it increases from 61.58 to 263.34 when acid treatment time increases from 2 h to 12 h. For the increase in the acid treatment time from 18 h to 24 h, the Si/Al ratio decreases to 142.73. This is a result of the long dealumination process.

The zeolite framework is destroyed, a result which is in agreement with Triantafillidis and co-workers[32]. They modified zeolite Y using different dealumination processes to study the influence of the degree and type of dealumination on the structure and acidicity of zeolite Y. They found that after hydrothermal dealumination, agglomeration of the particles occurred. This was because the hydroxyl groups at the surface bonded with neighboring crystallites. The surface areas of the present samples are tabulated in Table 1.

The surface area increases with increasing acid treatment time[35], from 683.78 to 930.58 $m^2\ g^{-1}$ when acid treatment time increases from 2 h to 12 h, and decreases to 542.10 $m^2\ g^{-1}$ when the acid treatment time is between 18 h and 24 h. The morphology of D Y H 80 is the same as Y H 80 (Fig. 2), but the crystal size decreases with increasing acid treatment time in the range from 1.138 µm to 0.670 µm[35]. The TGA thermograms are shown in Figure 3.

TABLE 1
Properties of D Y H 8

Zeolite	Acid treatment time (hr)	Integrated band area (cm^{-1})	Si/Al ratio	Surface area ($m^2\ g^{-1}$)	Crystal size (µm)
Y H 80	0	164.32 ± 6.07	61.58 ± 1.95	683.78 ± 13.32	1.138 ± 0.178
D Y H 80 (2 h)	2	100.62 ± 0.40	131.98 ± 1.57	709.39 ± 9.65	1.029 ± 0.105
D Y H 80 (4 h)	4	43.17 ± 0.20	135.62 ± 1.97	749.85 ± 54.66	0.899 ± 0.088
D Y H 80 (8 h)	8	36.48 ± 0.16	137.48 ± 2.51	754.85 ± 54.66	0.788 ± 0.057
D Y H 80 (10 h)	10	20.68 ± 6.22	197.22 ± 3.84	837.20 ± 0.71	0.708 ± 0.068
D Y H 80 (12 h)	12	16.67 ± 0.77	263.34 ± 2.40	930.58 ± 0.03	0.670 ± 0.057
D Y H 80 (18 h)	18	17.26 ± 5.56	172.81 ± 4.12	580.90 ± 13.87	1.352 ± 0.189
D Y H 80 (24 h)	24	19.31 ± 1.09	142.73 ± 1.35	542.10 ± 26.73	1.486 ± 0.143

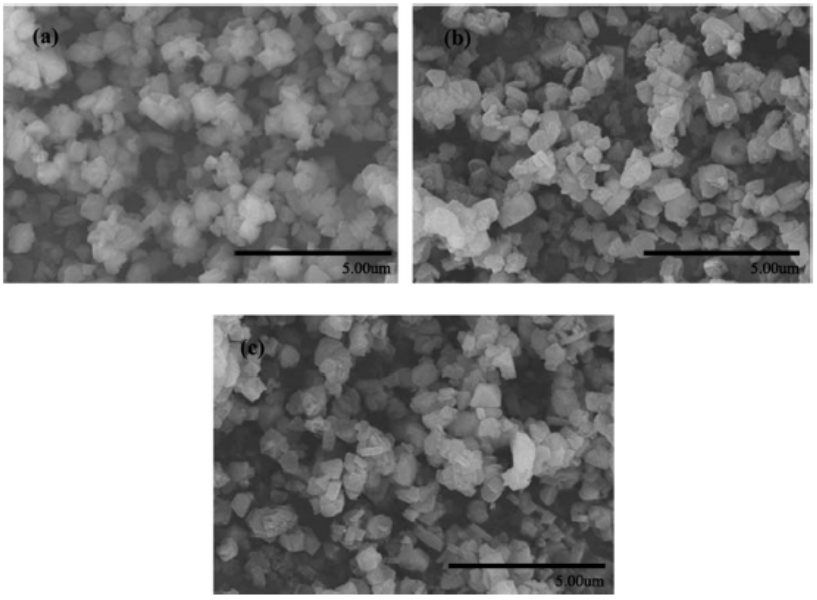

FIG. 2. Scanning electron micrographs of D Y H 80 with different acid treatment times: (a) 0 h; (b) 2 h; and (c) 4 h.

Downloaded by [Chulalongkorn University] at 19:46 20 August 2013

The weight loss, in the temperature range of 50–100°C can be attributed to the water loss and it decreases with increasing acid treatment time. This is due to the fact that a higher acid treatment time provides more hydrophobicity to D Y H 80. Therefore, the lower aluminum content in the zeolite structure, the lower water present in the zeolite structure. The weight loss between 500–700°C is due to the thermal dehydroxylation of hydroxyl nests site (Si-OH)

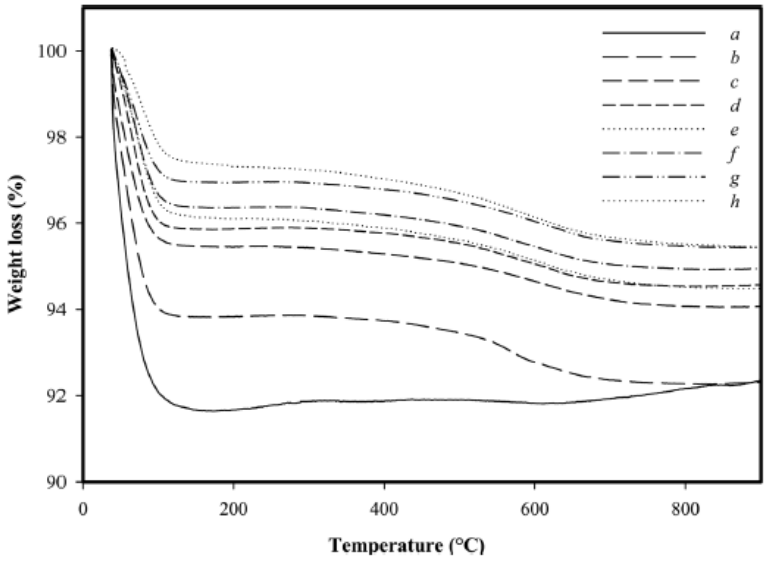

FIG. 3. TGA thermogram of D Y H 80 as various treatment times: (a) 0 h; (b) 2 h; (c) 4 h; (d) 8 h; (e) 10 h; (f) 12 h; (g) 18 h; and (h) 24 h.

Downloaded by [Chulalongkorn University] at 19:46 20 August 2013

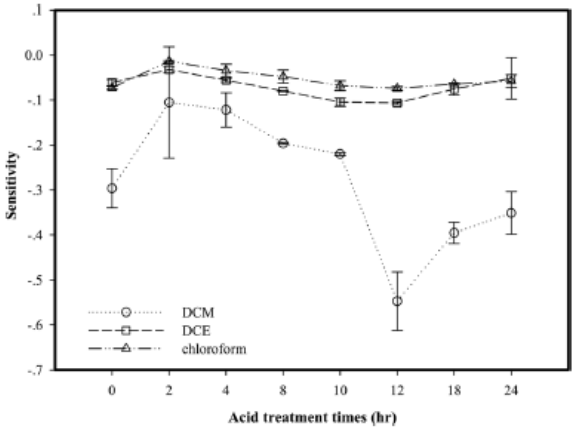

FIG. 4. Sensitivity of D Y H 80 at various acid treatment times towards DCM, DCE, chloroform.

of D Y H 80[36,37]. Hence, the water content in the structure of D Y H 80 at a high Si/Al ratio has a lower value than that at a low Si/Al ratio[35,38].

Effect of Acid Treatment Times on the Sensitivity Towards Halogenated Solvents

Figure 4 shows the sensitivity values of Y H 80 and D Y H 80 in relation to the acid treatment time under exposure to DCM, DCE, and chloroform. The sensitivity of Y H 80 is $(-3.03 \pm 0.44) \times 10^{-1}$, $(-6.27 \pm 0.71) \times 10^{-2}$, and $(-7.13 \pm 0.34) \times 10^{-2}$ for DCM, DCE, and chloroform, respectively. When the acid treatment time increases from 2 h to 12 h, the sensitivity of D Y H 80 increases from $(-1.21 \pm 0.90) \times 10^{-1}$ to $(-5.63 \pm 3.45) \times 10^{-1}$, from $(-3.30 \pm 0.75) \times 10^{-2}$ to $(-1.07 \pm 0.03) \times 10^{-1}$, and from $(-1.37 \pm 0.19) \times 10^{-2}$ to $(-7.29 \pm 0.44) \times 10^{-2}$ for DCM, DCE, and chloroform, respectively. When the acid treatment time increases from 18 h to 24 h, the sensitivity decreases to $(-3.62 \pm 0.48) \times 10^{-1}$, $(-6.41 \pm 4.59) \times 10^{-2}$, and $(-5.79 \pm 1.45) \times 10^{-2}$ for DCM, DCE, and chloroform, respectively (Table 2). The sensitivity of D Y H 80 is higher than the sensitivity of Y H 80 and increases with increasing acid treatment time from 2 h to 12 h.

The dealumination process removes aluminum from the zeolite framework causing more hydrogen atoms in the framework structure; the mechanism is shown in Scheme 1[39]. Hence, D Y H 80 has more hydrogen atoms available to induce hydrogen bonding with the solvent molecules than Y H 80[40–42]. Among the solvents, DCM has the highest sensitivity followed by DCE, then chloroform. The reason for this phenomenon is same as in the above discussion: the higher the hydrogen bonding with solvent molecules, the higher the sensitivity of the zeolite[43].

TABLE 2
The electrical response ($\Delta\sigma$), sensitivity ($\Delta\sigma/\sigma_i$) of Y H 80, and D Y H 80 when exposed to halogenated solvents (Measurements were made under chamber temperature of 27 ± 1°C at atmospheric pressure)

Materials	Response ($\Delta\sigma = \sigma_{halogenated\ solvent} - \sigma_{N2}$)			Sensitivity ($\Delta\sigma/\Delta\sigma_{N2}$)		
	DCM	DCE	Chloroform	DCM	DCE	Chloroform
Y H 80	$(-5.06 \pm 2.29) \times 10^{-6}$	$(-5.01 \pm 2.57) \times 10^{-7}$	$(-4.17 \pm 3.40) \times 10^{-7}$	$(-3.03 \pm 0.44) \times 10^{-1}$	$(-6.27 \pm 0.71) \times 10^{-2}$	$(-7.13 \pm 0.34) \times 10^{-2}$
D Y H 80 (2 h)	$(-5.75 \pm 4.96) \times 10^{-7}$	$(-2.12 \pm 1.92) \times 10^{-7}$	$(-9.12 \pm 5.45) \times 10^{-8}$	$(-1.21 \pm 0.90) \times 10^{-1}$	$(-3.30 \pm 0.75) \times 10^{-2}$	$(-1.37 \pm 0.19) \times 10^{-2}$
D Y H 80 (4 h)	$(-1.23 \pm 0.71) \times 10^{-6}$	$(-2.99 \pm 0.89) \times 10^{-8}$	$(-1.47 \pm 1.23) \times 10^{-7}$	$(-1.32 \pm 0.46) \times 10^{-1}$	$(-5.65 \pm 0.44) \times 10^{-2}$	$(-3.32 \pm 1.43) \times 10^{-2}$
D Y H 80 (8 h)	$(-1.94 \pm 0.06) \times 10^{-6}$	$(-5.96 \pm 2.57) \times 10^{-7}$	$(-2.74 \pm 1.45) \times 10^{-7}$	$(-1.96 \pm 0.01) \times 10^{-1}$	$(-8.02 \pm 0.09) \times 10^{-2}$	$(-4.96 \pm 1.47) \times 10^{-2}$
D Y H 80 (10 h)	$(-9.00 \pm 2.08) \times 10^{-7}$	$(-6.15 \pm 1.26) \times 10^{-7}$	$(-4.03 \pm 0.81) \times 10^{-7}$	$(-2.20 \pm 0.03) \times 10^{-1}$	$(-9.93 \pm 0.94) \times 10^{-2}$	$(-6.35 \pm 1.09) \times 10^{-2}$
D Y H 80 (12 h)	$(-7.82 \pm 3.20) \times 10^{-6}$	$(-6.95 \pm 0.17) \times 10^{-7}$	$(-7.11 \pm 0.55) \times 10^{-7}$	$(-5.63 \pm 3.45) \times 10^{-1}$	$(-1.07 \pm 0.03) \times 10^{-1}$	$(-7.29 \pm 0.44) \times 10^{-2}$
D Y H 80 (18 h)	$(-2.18 \pm 0.61) \times 10^{-6}$	$(-4.19 \pm 0.73) \times 10^{-7}$	$(-3.89 \pm 1.35) \times 10^{-7}$	$(-3.91 \pm 0.24) \times 10^{-1}$	$(-7.30 \pm 1.37) \times 10^{-2}$	$(-6.46 \pm 0.19) \times 10^{-2}$
D Y H 80 (24 h)	$(-4.09 \pm 2.25) \times 10^{-6}$	$(-7.97 \pm 9.04) \times 10^{-7}$	$(-3.27 \pm 0.83) \times 10^{-7}$	$(-3.62 \pm 0.48) \times 10^{-1}$	$(-6.41 \pm 4.59) \times 10^{-2}$	$(-5.79 \pm 1.45) \times 10^{-2}$

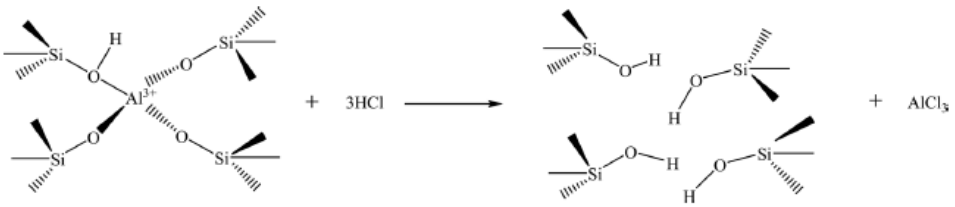

SCH. 1. Mechanism of silanols during dealumination in HCl medium.

Downloaded by [Chulalongkorn University] at 19:46 20 August 2013

DCM has two hydrogen atoms in its molecule; it can form two hydrogen bonds per molecule with D Y H 80. DCE has two hydrogen atoms in its molecule, the same as DCM, but DCE has a large molecule than DCM. So, the sensitivity of D Y H 80 toward DCE is lower than DCM due to the steric effect. The chloroform molecule has one hydrogen atom; it can form only one hydrogen bond with the zeolite structure. Therefore, the sensitivity of D Y H 80 toward chloroform is relatively low. Furthermore, the decrease in sensitivity of D Y H 80 with an increase of the acid treatment time from 18 h to 24 h could be related to the excessive dealumination time. The zeolite structure was destroyed[32]. The acid treatment time of 12 h thus provided the highest sensitivity towards all of the solvents. This condition was then used for fabrication of the composites between D-PDPA and D Y H 80 [D-PDPA-D Y H 80(12 h)].

Effect of Zeolite Content in the Composites on the Sensitivity Towards Halogenated Solvents

The effect of D Y H 80(12 h) content on the sensitivity of the composites towards the solvents is examined next. Figure 5 shows the sensitivity of D-PDPA-D Y H 80(12 h) composites towards DCM, DCE, and chloroform in relation to the D Y H 80 (12 h) content. The sensitivity of D-PDPA is $(-5.50 \pm 3.30) \times 10^{-2}$, $(-6.26 \pm 3.70) \times 10^{-2}$, and $(-1.22 \pm 0.16) \times 10^{-3}$ towards DCM, DCE, and chloroform, respectively. For the composites, as the zeolite content varies from 5 vol.% to 30 vol.%, the sensitivity of the composites increases from $(-1.51 \pm 0.12) \times 10^{-1}$ to $(-4.44 \pm 0.10) \times 10^{-1}$, from $(-4.87 \pm 0.65) \times 10^{-2}$ to $(-2.01 \pm 0.25) \times 10^{-1}$, and from $(-1.04 \pm 0.03) \times 10^{-2}$ to $(-9.07 \pm 3.95) \times 10^{-2}$ for DCM, DCE, and chloroform, respectively. When D Y H 80(12 h) content increases to 40 vol.%, it decreases to $(-2.04 \pm 0.18) \times 10^{-1}$, $(-8.64 \pm 3.88) \times 10^{-2}$, $(-7.58 \pm 2.98) \times 10^{-2}$ for DCM, DCE, and chloroform, respectively (Table 3).

The initial increase in sensitivity of the composite with increasing zeolite content is because the zeolite has a micro-porous structure which can trap solvent molecules. Thereby, the higher the zeolite content in the composite, the more the solvent molecules can be trapped[44]. However, when the zeolite content is between 30 vol.% and 40 vol.%, the sensitivity of the composites decreases because the active sites of the conductive polymer decreases[45]. The differences in the sensitivity of the composites can be traced back to the interaction between the composites and the vapors. The interaction between D-PDPA and the vapors is the dipole-dipole interaction of hydrogen atoms in the vapor molecule and the positive charges on the imine N_2 in the quinine ring, similar to the interaction between D-PDPA and N_2,; but the vapor interaction is stronger[46].

Due to the strong dipole-dipole interaction between D-PDPA and the vapors, electrons on the polymer chain tend to move slower. This results in a negative sensitivity response in the composites relative to those of N_2. The interaction between D Y H 80 and the vapors is the physical adsorption of the vapor molecules in the zeolite framework. The hydrogen atom can interact with –OH in the D Y H 80. With more –OH in the zeolite, the interaction between the vapors and the zeolite increases. This results in an increase in the sensitivity of the composites. It appears that the differences in the sensitivity values of the composites towards the solvents can be attributed to the change in the Si/Al ratio of the zeolite via the dealumination process.

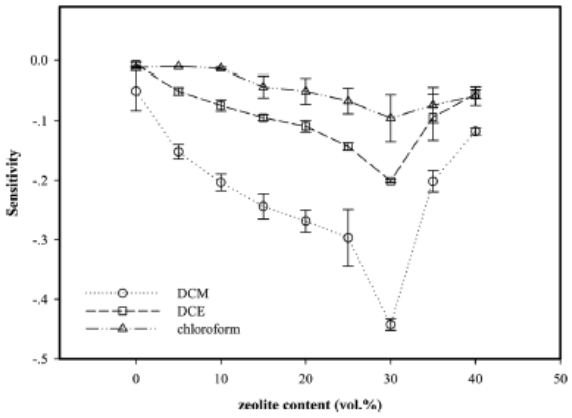

FIG. 5. Sensitivity of D-PDPA-D Y H 80(12h) composites at various zeolite contents towards DCM, DCE, chloroform.

Downloaded by [Chulalongkorn University] at 19:46 20 August 2013

TABLE 3
The electrical response $\Delta\sigma$), sensitivity ($\Delta\sigma/\sigma_i$) of D-PDPA and the composite when exposed to halogenated solvents (Measurements were made under chamber temperature of $27 \pm 1°C$ at atmospheric pressure)

Materials	Response ($\Delta\sigma = \sigma_{halogenated\ solvent} - \sigma_{N2}$)			Sensitivity ($\Delta\sigma/\Delta\sigma_{N2}$)		
	DCM	DCE	Chloroform	DCM	DCE	Chloroform
D-PDPA	$(-3.13 \pm 2.49) \times 10^{-7}$	$(-3.48 \pm 1.17) \times 10^{-8}$	$(-1.00 \pm 0.06) \times 10^{-7}$	$(-5.30 \pm 3.30) \times 10^{-2}$	$(-6.26 \pm 3.70) \times 10^{-2}$	$(-1.22 \pm 0.16) \times 10^{-3}$
D-PDPA-5% D Y H 80 (12 h)	$(-8.43 \pm 0.66) \times 10^{-7}$	$(-1.89 \pm 0.66) \times 10^{-7}$	$(-9.13 \pm 1.92) \times 10^{-8}$	$(-1.51 \pm 0.12) \times 10^{-1}$	$(-4.87 \pm 0.65) \times 10^{-2}$	$(-1.04 \pm 0.03) \times 10^{-2}$
D-PDPA-10% D Y H 80 (12 h)	$(-1.26 \pm 1.10) \times 10^{-6}$	$(-2.18 \pm 0.49) \times 10^{-7}$	$(-1.44 \pm 0.36) \times 10^{-7}$	$(-2.09 \pm 0.14) \times 10^{-1}$	$(-7.46 \pm 0.95) \times 10^{-2}$	$(-1.32 \pm 0.18) \times 10^{-2}$
D-PDPA-15% D Y H 80 (12 h)	$(-1.21 \pm 0.20) \times 10^{-6}$	$(-3.29 \pm 0.17) \times 10^{-7}$	$(-3.98 \pm 2.91) \times 10^{-7}$	$(-2.15 \pm 0.21) \times 10^{-1}$	$(-9.45 \pm 0.50) \times 10^{-2}$	$(-4.67 \pm 1.82) \times 10^{-2}$
D-PDPA-20% D Y H 80 (12 h)	$(-1.42 \pm 0.94) \times 10^{-6}$	$(-3.74 \pm 0.91) \times 10^{-7}$	$(-2.38 \pm 1.67) \times 10^{-7}$	$(-2.62 \pm 0.19) \times 10^{-1}$	$(-1.10 \pm 0.96) \times 10^{-1}$	$(-5.41 \pm 2.16) \times 10^{-2}$
D-PDPA-25% D Y H 80 (12 h)	$(-1.15 \pm 0.23) \times 10^{-6}$	$(-1.02 \pm 0.82) \times 10^{-6}$	$(-3.43 \pm 1.84) \times 10^{-7}$	$(-2.88 \pm 0.48) \times 10^{-1}$	$(-1.41 \pm 0.06) \times 10^{-1}$	$(-6.89 \pm 2.16) \times 10^{-2}$
D-PDPA-30% D Y H 80 (12 h)	$(-3.04 \pm 1.32) \times 10^{-6}$	$(-1.10 \pm 0.20) \times 10^{-6}$	$(-5.62 \pm 1.04) \times 10^{-7}$	$(-4.44 \pm 0.10) \times 10^{-1}$	$(-2.01 \pm 0.25) \times 10^{-1}$	$(-9.07 \pm 3.95) \times 10^{-2}$
D-PDPA-35% D Y H 80 (12 h)	$(-6.28 \pm 2.26) \times 10^{-7}$	$(-3.31 \pm 0.13) \times 10^{-7}$	$(-2.83 \pm 1.53) \times 10^{-7}$	$(-2.04 \pm 0.18) \times 10^{-1}$	$(-8.64 \pm 3.88) \times 10^{-2}$	$(-7.58 \pm 2.98) \times 10^{-2}$
D-PDPA-40% D Y H 80 (12 h)	$(-4.49 \pm 1.98) \times 10^{-7}$	$(-2.18 \pm 0.57) \times 10^{-7}$	$(-1.84 \pm 1.14) \times 10^{-7}$	$(-1.19 \pm 0.06) \times 10^{-1}$	$(-5.54 \pm 0.77) \times 10^{-2}$	$(-5.83 \pm 1.57) \times 10^{-2}$

Downloaded by [Chulalongkorn University] at 19:46 20 August 2013

TABLE 3
The electrical response $\Delta\sigma$), sensitivity ($\Delta\sigma/\sigma_i$) of D-PDPA and the composite when exposed to halogenated solvents (Measurements were made under chamber temperature of $27 \pm 1°C$ at atmospheric pressure)

Materials	Response ($\Delta\sigma = \sigma_{halogenated\ solvent} - \sigma_{N2}$)			Sensitivity ($\Delta\sigma/\Delta\sigma_{N2}$)		
	DCM	DCE	Chloroform	DCM	DCE	Chloroform
D-PDPA	$(-3.13 \pm 2.49) \times 10^{-7}$	$(-3.48 \pm 1.17) \times 10^{-8}$	$(-1.00 \pm 0.06) \times 10^{-7}$	$(-5.30 \pm 3.30) \times 10^{-2}$	$(-6.26 \pm 3.70) \times 10^{-2}$	$(-1.22 \pm 0.16) \times 10^{-3}$
D-PDPA-5% D Y H 80 (12 h)	$(-8.43 \pm 0.66) \times 10^{-7}$	$(-1.89 \pm 0.66) \times 10^{-7}$	$(-9.13 \pm 1.92) \times 10^{-8}$	$(-1.51 \pm 0.12) \times 10^{-1}$	$(-4.87 \pm 0.65) \times 10^{-2}$	$(-1.04 \pm 0.03) \times 10^{-2}$
D-PDPA-10% D Y H 80 (12 h)	$(-1.26 \pm 1.10) \times 10^{-6}$	$(-2.18 \pm 0.49) \times 10^{-7}$	$(-1.44 \pm 0.36) \times 10^{-7}$	$(-2.09 \pm 0.14) \times 10^{-1}$	$(-7.46 \pm 0.95) \times 10^{-2}$	$(-1.32 \pm 0.18) \times 10^{-2}$
D-PDPA-15% D Y H 80 (12 h)	$(-1.21 \pm 0.20) \times 10^{-6}$	$(-3.29 \pm 0.17) \times 10^{-7}$	$(-3.98 \pm 2.91) \times 10^{-7}$	$(-2.15 \pm 0.21) \times 10^{-1}$	$(-9.45 \pm 0.50) \times 10^{-2}$	$(-4.67 \pm 1.82) \times 10^{-2}$
D-PDPA-20% D Y H 80 (12 h)	$(-1.42 \pm 0.94) \times 10^{-6}$	$(-3.74 \pm 0.91) \times 10^{-7}$	$(-2.38 \pm 1.67) \times 10^{-7}$	$(-2.62 \pm 0.19) \times 10^{-1}$	$(-1.10 \pm 0.96) \times 10^{-1}$	$(-5.41 \pm 2.16) \times 10^{-2}$
D-PDPA-25% D Y H 80 (12 h)	$(-1.15 \pm 0.23) \times 10^{-6}$	$(-1.02 \pm 0.82) \times 10^{-6}$	$(-3.43 \pm 1.84) \times 10^{-7}$	$(-2.88 \pm 0.48) \times 10^{-1}$	$(-1.41 \pm 0.06) \times 10^{-1}$	$(-6.89 \pm 2.16) \times 10^{-2}$
D-PDPA-30% D Y H 80 (12 h)	$(-3.04 \pm 1.32) \times 10^{-6}$	$(-1.10 \pm 0.20) \times 10^{-6}$	$(-5.62 \pm 1.04) \times 10^{-7}$	$(-4.44 \pm 0.10) \times 10^{-1}$	$(-2.01 \pm 0.25) \times 10^{-1}$	$(-9.07 \pm 3.95) \times 10^{-2}$
D-PDPA-35% D Y H 80 (12 h)	$(-6.28 \pm 2.26) \times 10^{-7}$	$(-3.31 \pm 0.13) \times 10^{-7}$	$(-2.83 \pm 1.53) \times 10^{-7}$	$(-2.04 \pm 0.18) \times 10^{-1}$	$(-8.64 \pm 3.88) \times 10^{-2}$	$(-7.58 \pm 2.98) \times 10^{-2}$
D-PDPA-40% D Y H 80 (12 h)	$(-4.49 \pm 1.98) \times 10^{-7}$	$(-2.18 \pm 0.57) \times 10^{-7}$	$(-1.84 \pm 1.14) \times 10^{-7}$	$(-1.19 \pm 0.06) \times 10^{-1}$	$(-5.54 \pm 0.77) \times 10^{-2}$	$(-5.83 \pm 1.57) \times 10^{-2}$

TABLE 4
The induction time (t_i) and the recovery time (t_r) of D-PDPA, Y H 80, D-PDPA and D Y H 80 composites when exposed to halogenated solvents

Materials	t_i (min)			t_r (min)		
	DCM	DCE	Chloroform	DCM	DCE	Chloroform
Y H 80	15.42 ± 0.11	9.45 ± 0.14	6.45 ± 0.57	9.40 ± 0.07	8.69 ± 0.23	8.02 ± 0.46
D Y H 80 (2 h)	14.62 ± 0.23	9.35 ± 0.42	7.40 ± 0.21	7.59 ± 0.12	7.50 ± 0.37	8.46 ± 0.26
D Y H 80 (4 h)	14.93 ± 0.07	10.17 ± 0.07	8.03 ± 0.18	7.63 ± 0.18	8.11 ± 0.18	9.83 ± 0.40
D Y H 80 (8 h)	15.67 ± 0.04	10.29 ± 0.36	8.60 ± 0.53	8.44 ± 0.07	8.46 ± 0.30	10.05 ± 0.16
D Y H 80 (10 h)	15.77 ± 0.17	11.44 ± 0.45	9.01 ± 0.32	8.75 ± 0.07	9.82 ± 0.23	10.17 ± 0.23
D Y H 80 (12 h)	17.61 ± 0.09	12.51 ± 0.23	10.33 ± 0.46	8.88 ± 0.04	9.33 ± 0.48	11.24 ± 0.21
D Y H 80 (18 h)	15.54 ± 0.05	11.78 ± 0.18	10.17 ± 0.25	8.82 ± 0.23	9.23 ± 0.16	9.72 ± 0.30
D Y H 80 (24 h)	15.56 ± 0.01	11.25 ± 0.29	9.48 ± 0.25	9.03 ± 0.18	8.40 ± 0.23	9.40 ± 0.24
D-PDPA 100:1	11.35 ± 0.21	8.01 ± 0.63	7.74 ± 0.34	9.55 ± 0.14	6.83 ± 0.41	6.65 ± 0.28
D-PDPA-5% D Y H 80 (12 h)	12.48 ± 0.04	10.48 ± 0.25	10.17 ± 0.07	10.43 ± 0.04	10.87 ± 0.16	10.76 ± 0.16
D-PDPA-10% D Y H 80 (12 h)	12.56 ± 0.16	10.89 ± 0.15	10.60 ± 0.23	10.65 ± 0.14	11.15 ± 0.10	11.50 ± 0.16
D-PDPA-15% D Y H 80 (12 h)	13.51 ± 0.08	11.38 ± 0.04	11.55 ± 0.28	11.50 ± 0.07	11.50 ± 0.22	12.34 ± 0.23
D-PDPA-20% D Y H 80 (12 h)	13.56 ± 0.31	11.71 ± 0.23	12.50 ± 0.22	11.70 ± 0.07	11.72 ± 0.22	12.76 ± 0.16
D-PDPA-25% D Y H 80 (12 h)	14.80 ± 0.07	12.17 ± 0.21	13.38 ± 0.23	12.60 ± 0.71	12.02 ± 0.05	12.93 ± 0.52
D-PDPA-30% D Y H 80 (12 h)	15.50 ± 0.07	12.81 ± 0.23	13.66 ± 0.30	12.81 ± 0.08	12.39 ± 0.07	13.53 ± 0.07
D-PDPA-35% D Y H 80 (12 h)	14.75 ± 0.42	12.51 ± 0.23	13.44 ± 0.30	12.29 ± 0.23	12.66 ± 0.17	13.39 ± 0.52
D-PDPA-40% D Y H 80 (12 h)	14.45 ± 0.16	11.67 ± 0.16	12.77 ± 0.17	11.20 ± 0.23	12.82 ± 0.09	12.38 ± 0.07

Measurements were made under chamber temperature of 27 ± 1°C at atmospheric pressure.

Downloaded by [Chulalongkorn University] at 19:46 20 August 2013

The recovery times of all samples show the same trend as the induction time (Table 4). The recovery time of D Y H 80 increases with increasing zeolite content. For the composites, the recovery times of the composites are longer than that of D-PDPA and they also increase with increasing zeolite content. Furthermore, the recovery times of D-PDPA, the zeolite, and the composites towards DCM are higher than those of DCE and chloroform. This is because DCM has more hydrogen molecules to form hydrogen bonds with the active sites.

Effect of Vapor Concentration on the Electrical Sensitivity of the Composites Towards Halogenated Solvents

Figure 7 shows the sensitivity of D-PDPA-30% D Y H 80 (12 h) composite versus vapor concentration. When a composite [D-PDPA-30% D Y H 80 (12 h)] is exposed to DCM, the sensitivity of the composite increases from $(-3.61 \pm 3.34) \times 10^{-2}$ to $(-4.42 \pm 0.01) \times 10^{-1}$ as the DCM concentration increases from 7696 ppm to 153914 ppm, respectively. When the composite is exposed to DCE, the sensitivity of the composite increases from $(-1.57 \pm 0.02) \times 10^{-2}$ to $(-2.01 \pm 0.02) \times 10^{-1}$ as vapor concentration increases from 1015 ppm to 20299 ppm, respectively.

The data shows that the responses of the composite are nearly linear with respect to concentrations of the vapors. The slope of DCM vapor is greater than that of DCE vapor. This suggests that the selectivity of the composite toward DCM is higher than the selectivity toward DCE. A similar result was found in Ma and co-worker[47]. They studied the sensing properties of a triangular nano-sensor based on localized surface plasmon resonance towards ethanol, acetone, benzene, propanol, and hexane. They made the comparison of the peak wavelengths in response to the tested vapors. A good linear response was obtained. Ethanol showed the greatest slope among the tested vapors. It was concluded that the sensor has higher selectivity towards ethanol relative to other vapors.

In 2012, Luo and co-worker[48] developed the sensing properties of the composite film of polyurethane and multiwall carbonnanotubes towards benzene, cyclohexane, carbontetrachloride. The response of the composites film, with the benzene and cyclohexane concentrations varied from 1500 ppm to 7500 ppm, increased linearly with increasing vapor concentration.

The Cyclic Response and Chemical Reaction of D-PDPA-30% D Y H 80(12 h) Composites and the Vapors

Figure 8 shows the electrical conductivity of D-PDPA-30% D Y H 80(12 h) composite versus time toward DCM. The measurement spans 3 cycles, to determine the reversibility of the electrical conductivity. The composite

Downloaded by [Chulalongkorn University] at 19:46 20 August 2013

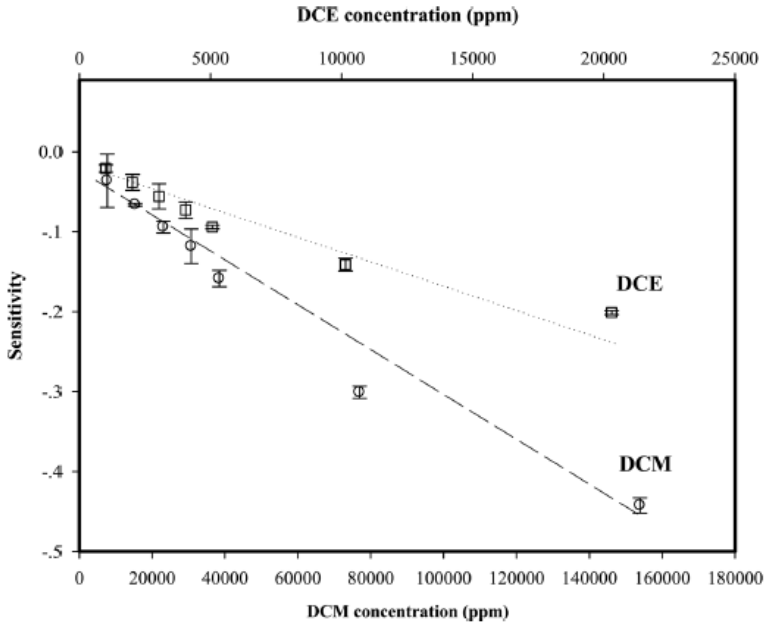

FIG. 7. The sensitivity of D-PDPA-30% D Y H 80 (12 h) composite toward DCM and DCE at different concentrations at 27 ± 1°C and 1 atm.

shows the negative cyclic response when exposed to DCM. The conductivity values of the composite of the 1st, 2nd, and 3rd cycles are 6.71×10^{-6}, 6.59×10^{-6}, and 6.54×10^{-6} S cm^{-1}, respectively. The conductivity values of the 2nd and 3rd cycle do not recover the conductivity value of the 1st cycle.

This suggests that the interaction between the composites and the vapors is not reversible. Moreover, the chemical interaction between the composites and the vapors can be confirmed by using a FT-IR spectrometer. The FT-IR spectra of the composite before, during, and after the exposure to DCM are shown in Figure 9. Before DCM exposure, the spectrum shows only the characteristic peaks of D-PDPA and D Y H 80 (12 h)[49–51]. During DCM exposure, the new peaks occur at 3009, 1275, and 750 cm^{-1} which can be assigned to the interaction between DCM and D-PDPA; CH_2 in DCM[52]; and the interaction between DCM and D Y H 80, respectively[53]. When DCM is removed and replaced with N_2, the absorption bands at 3009 cm^{-1} disappear, but the absorption bands at 1275 and 750 cm^{-1}, which are assigned to the interaction between DCM and D Y H 80, still remain. This indicates that the interaction between the composite and the vapor is irreversible. Figure 10 shows the proposed mechanism of the composite and DCM vapor. The chlorine atom of DCM is electron donating. It will stabilize the cation of the imines nitrogen in the composite.

The electron can move along the D-PDPA backbone. This results in an increase in the conductivity of D-PDPA. On the other hand, the hydrogen atom in the DCM molecule is electron withdrawing. It removes the electron from the active site in DY H 80 (–OH) and creates a hole on the D Y H 80 structure as a p type doping. The electron can move through π-bonds of the –OH, increasing the conductivity of the composite. This phenomenon is called the resonance effect[54].

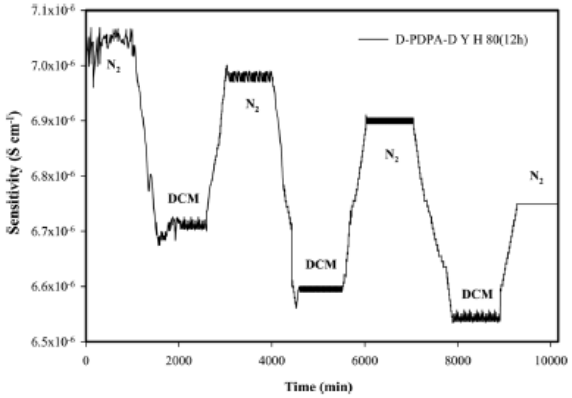

FIG. 8. Negative cyclic responses of D-PDPA-30% D Y H 80 (12 h) composite exposed to 50%v/v DCM vapor at 27°C, 70%RH.

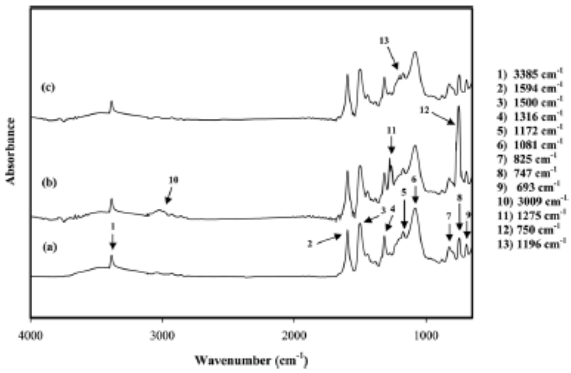

FIG. 9. FT-IR spectra of D-PDPA-30% D Y H 80 (12 h) composite exposed to 50 vol.% DCM vapors at 27°C, 70% RH: (a) before DCM exposure; (b) during DCM exposure; (c) after DCM exposure.

During the dealumination process, as more active sites (-OH) of the D Y H 80 are available, the greater resonance effect. Thus conductivity increases by adding D Y H 80. In addition, the charge distribution on the surface of the composite can be observed by EFM with external electric excitation of 5 volts. The EFM images (Fig. 11a and b) show the charges distributions on the surfaces of the composites before and after the exposure to DCM vapor. The image would appear as a bright contrast indicating the presence of positive charges; it would appear as a dark contrast when negatively charges are present[55]. Before the exposure to DCM (Fig. 11a), the image shows mainly brighter regions since the D-PDPA backbone has many holes or positively charges along the backbone due to p type doping process of D-PDPA.

During the exposure to DCM (Fig. 11b), the image shows darker regions as the vapors donate electrons to the polymer backbone. This result suggests that as the polymer is exposed to DCM, it attains more electrons along the backbone. After flushing out the DCM vapor out by N_2, the EFM image also shows darker regions, which implies that the polymer still retains some electrons. This clearly indicates that the interaction between the polymer and the vapor is irreversible. So, it can cause the interaction between the composite and the vapor is irreversible.

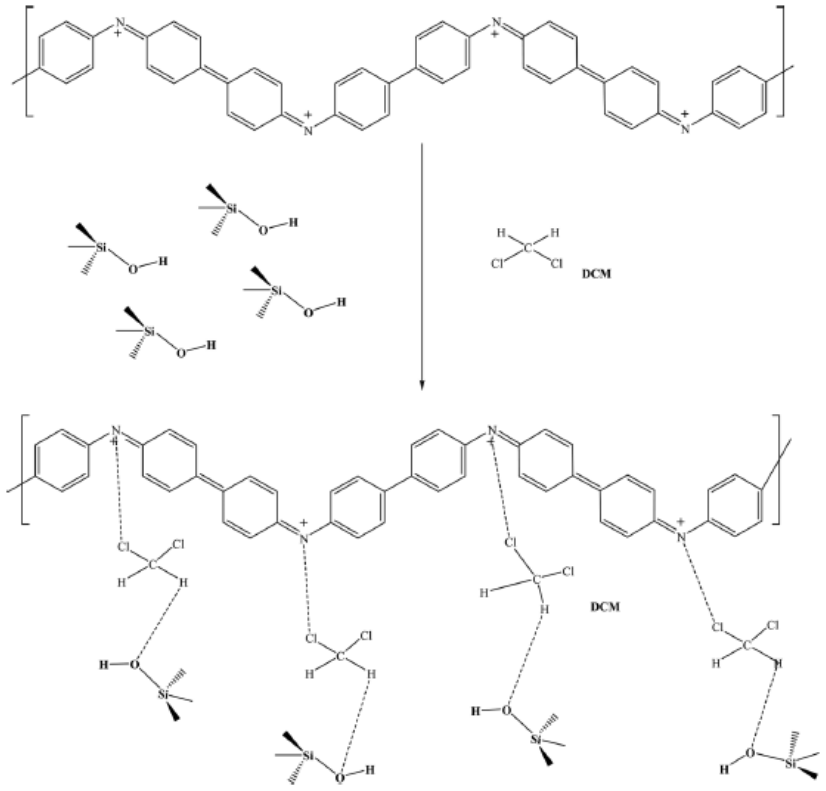

FIG. 10. Proposed mechanism for the interactions of D-PDPA-30% D Y H 80 (12 h) composite and DCM vapor.

Downloaded by [Chulalongkorn University] at 19:46 20 August 2013

Downloaded by [Chulalongkorn University] at 19:46 20 August 2013

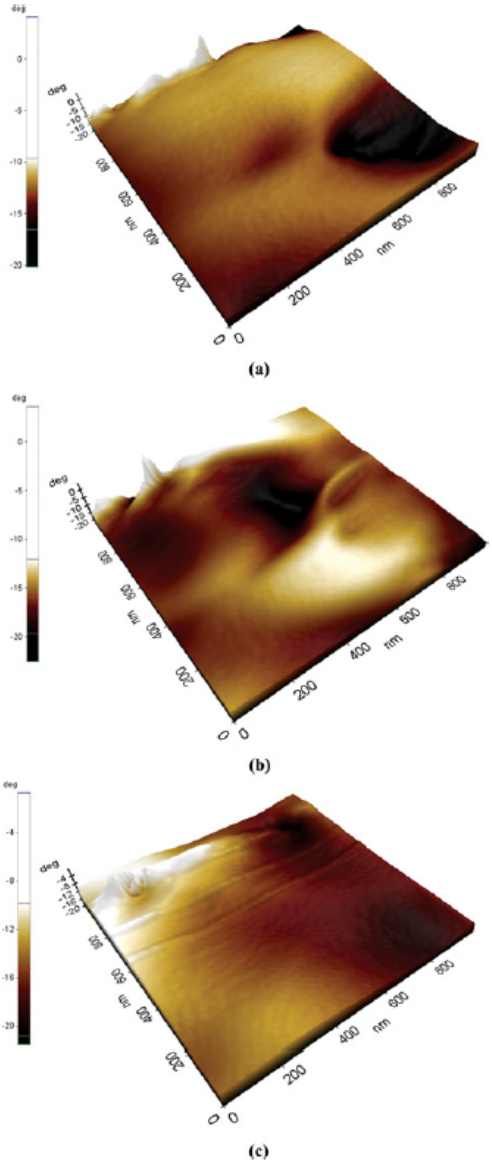

FIG. 11. EFM images of D-PDPA-30% D Y H 80 (12 h) composite (a) before and (b) during (c) after the exposure to DCM vapor. (Color figure available online.)

CONCLUSIONS

This work confirms a successful attempt to increase Si/Al ratios of zeolite Y by the dealumination method. The highest Si/Al ratio obtained is 263 at the acid treatment time of 12 h. The composites of D-PDPA and D Y H 80 were then used as a sensing material to investigate the electrical sensitivity towards three halogenated solvents; DCM, DCE, and chloroform. The composites with the dealuminated zeolite Y have a potential use as sensing materials for the halogenated solvents because they have a higher number of reactive sites in D Y H 80 to react with the vapors. The acid treatment of 12 h and 30 vol.% of zeolite provide the highest sensitivity towards the halogenated solvents. The results of the cyclic response show the interaction between the composite and the vapor is irreversible, as confirmed by FT-IR spectra and EFM images.

ACKNOWLEDGMENTS

The authors would like to acknowledge the financial support from: the Conductive and Electroactive Polymers Research Unit of Chulalongkorn University; the Thailand Research Fund (TRF-RTA); the Royal Thai Government; and the Thailand Graduate Institute of Science and Technology (TGIST) (TGIST-01-54-011).

REFERENCES

1. US EPA. Needs for Eleven TRI Organic Chemical Groups, Environmental Protection Agency, Pollution Prevention Research, Washington, DC, 1991.
2. Sidebottom, H.; Franklin, J. The atmospheric fate and impact of hydrochlorofluorocarbons and chlorinated solvents. Pure Appl. Chem. **1996**, *68*, 1757–1769.
3. Vallero, D.; Boubel, R.W.; Fox, D.L.; Turner, B.; Stern, A.C. Fundamentals of Air Pollution. 3rd Ed., Academic Press, San Diego, CA, 1994.
4. Bai, H.; Shi, G. Gas Sensors Based on Conducting Polymers. Sensors **2007**, *7*, 267–307.
5. Shamloo, A.; Vosoughi, M., Alemzadeh, I., Naeini, A.T., Darvish, M. Two Nano structured polymers: polyaniline nanofibers and new linear-dendritic matrix of poly(citric acid)-block-poly(ethylene glycol) copolymers for environmental monitoring in novel biosensors. Int. J. Polym. Mater. **2012**, *62* (7), 377–383.
6. Das, T.K.; Prusty, S. Review on conducting polymers and their applications. Polym. Plast. Tech. Eng. **2012**, *51*, 1487–1500.
7. Sahner, K.; Hagen, G.; Schönauer, D.; Reiß, S.; Moos, R. Zeolites — Versatile materials for gas sensors. Solid State Ionics **2008**, *179*, 2416–2423.
8. Agbor, N.E.; Petty, M.C.; Monkman, A.P. Polyaniline thin films for gas sensing. Sensor Actuat. B-Chem. **1995**, *28*, 173–179.
9. Permpool, T.; Supaphol, P.; Sirivat, A.; Wannatong, L. Polydiphenylamine–polyethylene oxide blends as methanol sensing materials. Adv. Polym. Tech. **2011**, *31*, 401–413.
10. Suganandam, K.; Santhosh, P.; Sankarasubramanian, M.; Gopalan, A.; Vasudevan, T.; Lee, K.-P. Fe^{3+} ion sensing characteristics of polydiphenylamine—electrochemical and spectroelectrochemical analysis. Sensor Actuat. B-Chem. **2005**, *105*, 223–231.
11. Tsai, Y.T.; Wen, T.C.; Gopalan, A. Tuning the optical sensing of pH by poly(diphenylamine). Sensor Actuat. B-Chem. **2003**, *96*, 646–657.
12. Ragupathy, D.; Gopalan, A.; Lee, K.P. Layer-by-layer electrochemical assembly of poly(diphenylamine)/phosphotungstic acid as ascorbic acid sensor. Microchim. Acta **2009**, *166*, 303–310.
13. Gopalan, A.I., Kwang, P.L., Manian, K.M.P., Santhosh, P., Kap, D.S., Duk, D.L. Fabrication of functional nanofibrous

Downloaded by [Chulalongkorn University] at 19:46 20 August 2013

ammonia sensor, Sixth IEEE Conference on Nanotechnology, June 17–20, 2006.

14. Santhosh, P.; Manesh, K.M.; Gopalan, A.; Lee, K.P. Novel amperometric carbon monoxide sensor based on multi-wall carbon nanotubes grafted with polydiphenylamine—Fabrication and performance. Sensor Actuat. B-Chem. **2007**, *125*, 92–99.
15. El-Shobaky, G.A.; Selim, M.M.; Ezzo, E.M. Effect of water treatment on the catalytic properties of decationated zeolite. The Research Institute for Catalysis, Hokkaido University, 1979.
16. Saidina, A.N.A.; Anggoro, D.D. Dealuminated ZSM-5 zeolite catalyst for ethylene oligomerization to liquid fuels. J. Nat. Gas Chem. **2002**, *11*, 79–86.
17. Adjemian, K.T.; Lee, S.J.; Srinivasan, S.; Benziger, J.; Bocarsly, A.B. Silicon oxide Nafion composite membranes for proton-exchange membrane fuel cell operation at 80–140 degrees C. J. Electrochem. Soc. **2002**, *149*, A256–A261.
18. Antonucci, P.L.; Aricò, A.S.; Cretí, P.; Ramunni, E.; Antonucci, V. Investigation of a direct methanol fuel cell based on a composite Nafion®-silica electrolyte for high temperature operation. Solid State Ionics **1999**, *125*, 431–437.
19. Miguel, R.L.E.; Manfred, J.H. Evaluation of Zeolite-Water Solar Adsorption Refrigerator, ISES Solar World Congress, Sweden, June 14–19, 2003.
20. Chuapradit, C.; Wannatong, L.R.; Chotpattananont, D.; Hiamtup, P.; Sirivat.A.; Schwank, J. Polyaniline/zeolite LTA composites and electrical conductivity response towards CO. J. Polym. **2005**, *46*, 947–953.
21. Densakulprasert, N.; Wannatong, L.; Chotpattananont, D.; Hiamtup, P.; Sirivat, A.; Schwank, J. Electrical conductivity of polyaniline/zeolite composites and synergetic interaction with CO. J. Mater. Sci. Eng. B **2005**, *117*, 276–282.
22. Kaneyasu, K.; Otsuka, K.; Setoguchi, Y.; Sonoda, S.; Nakahara, T.; Aso, I.; Nakagaichi, N. A carbon dioxide gas sensor based on solid electrolyte for air quality control. Sensor Actuat. B-Chem. **2000**, *66*, 56–58.
23. Meier, B.; Werner, T.; Klimant, I.; Wolfbeis, O.S. Novel oxygen sensor material based on a ruthenium bipyridyl complex encapsulated in zeolite Y: Dramatic differences in the efficiency of luminescence quenching by oxygen on going from surface-adsorbed to zeolite-encapsulated fluorophores. Sensor Actuat. B-Chem. **1995**, *29*, 240–245.
24. Payra, P.; Dutta, P.K. Development of a dissolved oxygen sensor using tris(bipyridyl) ruthenium (II) complexes entrapped in highly siliceous zeolites. Microporous Mesoporous Mater. **2003**, *64*, 109–118.
25. Xie, H.; Yang, Q.D.; Sun, X.; Yu, T.; Huang, J.Z.; Huang, Y. Gas sensors based on nanosized-zeolite films to identify dimethylmethylphosphonate. Sensor Mater. **2005**, *17*, 21–28.
26. Corma, A. Inorganic solid acids and their use in acid-catalyzed hydrocarbon reactions. Chem. Rev. **1995**, *95*, 559–614.
27. Dong, A.; Wang, Y.; Tang, Y.; Ren, N.; Zhang, Y.; Yue, Y.; Gao, Z. Zeolitic tissue through wood cell templating. Adv. Mater. **2002**, *14*, 926–929.
28. Maxwell, I.E.; Stork, W.H.J. In: Bekkum, H.V.; Flanigen, E.M.; Jacobs, P.A.; Jansen, J.C., eds. *Studies in Surface Science and Catalysis*, Elsevier, 2001; 747–819.
29. Valkenberg, M.H.; Holderich, W.F. Preparation and use of hybrid organic-inorganic catalysts. Catal. Rev. Sci. Eng. **2002**, *44*, 321–374.
30. Holmberg, B.A.; Wang, H.; Yan, Y. High silica zeolite Y nanocrystals by dealumination and direct synthesis. Microporous Mesoporous Mater. **2004**, *74*, 189–198.
31. Kumar, S.; Sinha, A.K.; Hegde, S.G.; Sivasanker, S. Influence of mild dealumination on physicochemical, acidic and catalytic properties of H-ZSM-5. J. Mol. Catal. A Chem. **2000**, *154*, 115–120.
32. Triantafillidis, CS.; Vlessidis, A.G.; Evmiridis, N.P. Dealuminated H-Y zeolites : Influence of the degree and the type of dealumination method on the structural and acidic characteristics of H-Y zeolites. Ind. Eng. Chem. Res. **2000**, *39*, 307–319.
33. Zhao, Y.; Chen, M.; Liu, X.; Xu, T.; Liu, W. Electrochemical synthesis of polydiphenylamine nanofibrils through AAO template. Mater. Chem. Phys. **2005**, *91*, 518–523.
34. Titova, T.I.; Kosheleva, L.S.K.; Zhdanov, S.P.; Shubaeva, M.A. IR spectroscopic study of structure-chemical aspects of the Na-Y zeolite dealumination with ethylene diamine tetraacetic acid. Pure Appl. Chem. **1993**, *65*, 2231–2236.
35. Shirazi, L.; Jamshidi, E.; Ghasemi, M.R. The effect of Si/Al ratio of ZSM-5 zeolite on its morphology, acidity and crystal size. Cryst. Res. Tech. **2008**, *43*, 1300–1306.
36. Beyer, H.K. Dealumination techniques for zeolites. Mol. Sieves **2002**, *3*, 204–255.
37. Shough, A.M. Quantum Chemistry Studies of Catalytic and Photocatalytic Materials: Transition Metal Substitution, Active Sites, Thermodynamics and Reaction Mechanisms. University of Delaware, 2008.
38. Xia, Y.; Liu, S.; Wang, X.; Han, Y.; Li, J.; Jian, X. The analysis of synergistic effects of zeolites applied in intumescent halogen-free flame-retardant ABS composites. Polym. Plast. Tech. Engin. **2008**, *47*, 613–618.
39. González, M.D.; Cesteros, Y.; Salagre, P. Comparison of dealumination of zeolites beta, mordenite and ZSM-5 by treatment with acid under microwave irradiation. Microporous Mesoporous Mater. **2011**, *144*, 162–170.
40. Ayad, M.M.; El-Hefnawey, G.; Torad, N.L. Quartz crystal microbalance sensor coated with polyaniline emeraldine base for determination of chlorinated aliphatic hydrocarbons. Sensor Actuat. B-Chem. **2008**, *134*, 887–894.
41. Shukla, P.; Bhatia, V.; Gaur, V.; Jain, V.K. Electrostatically functionalized multiwalled carbon nanotube/PMMA composite thin films for organic vapor detection. Polym. Plast. Tech. Eng. **2011**, *50*, 1179–1184.
42. Vijayakumar, N.; Subramanian, E.; Padiyan, D.P. Conducting polyaniline blends with the soft template poly(vinyl pyrrolidone) and their chemosensor application. Int. J. Polym. Mater. **2012**, *61*, 847–863.
43. Cangelosi, F.; Shaw, M.T. A review of hydrogen bonding in solid polymers: structural relationships, analysis, and importance. Polym. Plast. Tech. Eng. **1983**, *21*, 13–98.
44. Zheng, Y.; Li, X.; Dutta, P.K. Exploitation of Unique properties of zeolites in the development of gas sensors. Sensors **2012**, *12*, 5170–5194.
45. Phumman, P.; Niamlang, S.; Sirivat, A. Fabrication of poly(-p-phenylene)/zeolite composites and their responses towards ammonia. Sensors **2009**, *9*, 8031–8046.
46. Thuwachaowsoan, K.; Chotpattananont, D.; Sirivat, A.; Rujiravanit, R.; Schwank, J.W. Electrical conductivity responses and interactions of poly(3-thiopheneacetic acid)/zeolites L, mordenite, beta and H_2. Materials Sci Eng B **2007**, *140*, 23–30.
47. Ma, W.; Yang, H.; Wang, W.; Gao, P.; Yao, J. Ethanol vapor sensing properties of triangular silver nanostructures based on localized surface plasmon resonance. Sensors **2011**, *11*, 8643–8653.
48. Luo, Y.-L.; Miao, Y.; Xu, F.; Yao, Y. Novel HTPB/MWNTs-COOH PU conductive polymer composite films for detection of hazardous organic solvent Vapors. Polym.-Plast. Technol. Eng. **2012**, *51*, 290–297.
49. Santana, H.; Dias, F.C. Characterization and properties of polydiphenylamine electrochemically modified by iodide species. Mater. Chem. Phys. **2003**, *82*, 882–886.
50. Hua, F.; Ruckenstein, E. Water-soluble conducting poly(ethylene oxide)-grafted polydiphenylamine synthesis through a "graft onto" process. Macromole **2003**, *36*, 9971–9978.

51. Sathiyanarayanan, S.; Muthukrishnan, S.; Venkatachari, G. Synthesis and anticorrosion properties of polydiphenylamine blended vinyl coatings. Synth. Met. **2006**, *156*, 1208–1212.
52. Lambert, J.B.; Gronert, S.; Shurvell, H.F.; Lightner, D. Organic Structural Spectroscopy. Prentice Hall PTR, Englewood Cliffs, NJ, 2010.
53. Robert, M.; Silverstein, F.X.W.; David, K. *Spectrometric Identification of Organic Compounds*, 7th Ed., John Wiley & Sons, Inc.: New York, 2005.
54. Xu, L.; Hu, X.; Tze Lim, Y.; Subramanian, V.S. Organic vapor adsorption behavior of poly(3-butoxythiophene) LB films on quartz crystal microbalance. Thin Solid Films **2002**, *417*, 90–94.
55. Barisci, J.N.; Stella, R.; Spinks, G.M.; Wallace, G.G. Characterisation of the topography and surface potential of electrodeposited conducting polymer films using atomic force and electric force microscopies. Electrochim. Acta **2000**, *46*, 519–531.

Downloaded by [Chulalongkorn University] at 19:46 20 August 2013

Author's personal copy

Powder Technology 249 (2013) 353–359

Contents lists available at ScienceDirect

Powder Technology

journal homepage: www.elsevier.com/locate/powtec

Control of hematite nanoparticle size and shape by the chemical precipitation method

Kitibodee Supattarasakda [a], Karat Petcharoen [a], Tharaporn Permpool [a], Anuvat Sirivat [a,*], Wanchai Lerdwijitjarud [b]

[a] Conductive and Electroactive Polymers Research Unit, The Petroleum and Petrochemical College, Chulalongkorn University, Bangkok 10330, Thailand
[b] Department of Materials Science and Engineering, Faculty of Engineering and Industrial Technology, Silpakorn University, Nakhon Pathom 73000, Thailand

ARTICLE INFO

Article history:
Received 21 December 2012
Received in revised form 10 July 2013
Accepted 30 August 2013
Available online 9 September 2013

Keywords:
Magnetic nanoparticles
Size-controlled hematite
Chemical precipitation method
Electrical conductivity
Superparamagnetic behavior

ABSTRACT

Hematite (α-Fe_2O_3) nanoparticles were synthesized from the ferrihydrite precursor via a simple chemical precipitation method with trace amounts of Fe(II) as the catalyst under nitrogen atmosphere. The characteristic of the synthesized hematite particles were evaluated by XRD, FT-IR, and FE-SEM. The magnetic and electrical properties were studied by a vibrating sample magnetometer (VSM) and an electrometer, respectively. The synthesized products were of a single phase of the hexagonal structure hematite without any other impurities. The physical morphology of the synthesized hematite appears to be composed of a large number of very small particles appearing as the "raspberry shape". The particle size of the synthesized hematite can be successfully controlled at 50–150 nm, appearing as three different morphologies: the spherical-like, the cubic-like, and the ellipsoidal shape, through adjusting the synthesis conditions. The smallest particle possesses the highest electrical conductivity of 5.2×10^{-3} s/cm. On the other hand, the largest particle exhibits weak ferromagnetism and the highest saturation magnetization (M_s) of 1.94 emu/g, is higher than that of the smaller particle, which possesses the super-paramagnetic behavior. Furthermore, the different particle shapes are shown here to critically affect the electrical and magnetic properties of the nanoparticles.

Crown Copyright © 2013 Published by Elsevier B.V. All rights reserved.

1. Introduction

Magnetic nanoparticles can exhibit many unique properties such as chemical, electrical, and magnetic properties which are advantageous towards a variety of the applications. There are many types of magnetic particles, and one of the most important groups is iron oxides generally existing in the forms of hematite (α-Fe_2O_3), maghemite (γ-Fe_2O_3), and magnetite (Fe_3O_4) all can be utilized for different specific applications [1]. Hematite, which is the most stable form at the ambient conditions, has an attention in the nano-innovation because of their advantages in inorganic pigments [2], catalysts [3], gas and humidity sensors [4,5], photoanode for photo-electrochemical cells [6], photoelectrolysis reactors [7], water treatment [8], and lithium ion batteries [9].

The preparation method is a key factor in determining the particle size, the morphology, the particle size distribution, the surface chemistry, and therefore the properties of the final products. Up to now, various methods have been reported in the literatures on the preparation of hematite nanoparticles, such as the hydrolysis method [10,11], the hydrothermal treatment [12–14], the chemical precipitation method [15,16], the solvothermal process [17], the facile solution route [18], and the microemulsion method [19,20]. In comparison to all methods, the chemical precipitation method is probably the simplest and the most effective as well as of a relatively low cost without any requirement of the special equipment or any additives. Recently, the chemical precipitation system through the catalytic phase transformation has been successfully synthesized hematite nanoparticles [16]. The experimental results revealed that this method has several advantages, such as using a high reactant concentration, a very short reaction time as well as a low reaction temperature, and high purity hematite nanoparticles.

Controlling of the particle size and morphology is considerably important in the preparation of hematite nanoparticles, because their properties of the ultrafine particles depend on the morphology, particle size, and dispersion of the products [21]. Until now, several researches have focused on the study of the factors affecting the particle size and shape of the synthesized hematite nanoparticles. These factors have been reported in the literatures, such as the reactant concentration, the solution pH, the solution mixture, the reaction time and temperature, the ionic strength, the anions, the surfactant, and the nature of iron salts [22–27]. However, in some cases such as using surfactants or anions, the additional steps of the removal of the excessive amounts of chemicals used are required and the products obtained may have the lower properties compared to using the simple method.

In this work, a simple chemical precipitation method has been employed to directly synthesize hematite nanoparticles, with trace amounts of Fe(II) as the catalyst, under nitrogen atmosphere. The influences of the synthesis conditions, consisting of the precursor concentration (C), the

* Corresponding author. Tel.: +66 2 218 4131; fax: +66 2 611 7221.
E-mail address: anuvat.s@chula.ac.th (A. Sirivat).

0032-5910/$ – see front matter. Crown Copyright © 2013 Published by Elsevier B.V. All rights reserved.
http://dx.doi.org/10.1016/j.powtec.2013.08.042

Author's personal copy

solution pH, the amount of catalyst ($n_{Fe(II)}/n_{Fe(III)}$), the ionic strength (I), the reaction time and temperature on particle size and morphology of the synthesized hematite are systematically investigated. Moreover, the magnetic properties and the electrical conductivity depending on the particle size and shape of the synthesized hematite are also reported here.

2. Experimental

Hematite nanoparticles were synthesized via the chemical precipitation method as described by Liu et al., with some alterations [28,29]. All chemicals were analytical reagent grades and used without further purification. In a typical preparation, sodium hydroxide (NaOH) solution (6.0 M) was added into a ferric chloride solution (Fe(III), 1.0 M, 50 ml) until pH 7 was obtained under vigorous stirring at room temperature. In the mixed solution, brown precipitate precursor ($Fe(OH)_3$) formed and were confirmed to be 2-line ferrihydrite by XRD. The agitation was performed for an additional 10 min, followed by adding trace amounts of ferrous chloride (Fe(II)), ($n_{Fe(II)}/n_{Fe(III)} = 0.02$) into the system. The desired pH 7 was once again readjusted with a dilute NaOH solution (1.0 M) and the total volume was adjusted to 100 ml so that the total concentration (C) of the precursor reached 0.5 M. The suspension was heated up to the boiling point and kept refluxing for 1 h under vigorous stirring. All stages of the experiment were carried out under pure N_2 gas to avoid the oxidation of Fe(II). The final product was filtered off, washed with distilled water, and dried at about 70–80 °C. In addition, the preparation conditions were adjusted to study various effects while holding the other parameters constant.

The crystal structure and the characteristic functional groups of the synthesized hematite particles were characterized by an X-ray powder diffractometer (Bruker AXS, D8 Advance) and a Fourier transform infrared spectrometer (Thermo Nicolet, Nexus 670), with a deuterated triglycine sulfate detector, respectively. The morphology of the synthesized hematite particles was evaluated by the field-emission scanning electron microscope (Hitachi, S4800). The particle size of the hematite was determined by an analytical software of SemAfore over 2–3 FE-SEM images by the quantitative statistical method. A surface area analyzer (Thermo finnigan, Sorptomatic 1990) was used to determine the specific surface area of the synthesized hematite particles. More details about the electrical conductivity and the magnetization of the synthesized hematite particles were observed at room temperature by an electrometer (Keithley, 6517A), with a custom-built two-point probe, and a vibrating sample magnetometer (LakeShore, 7404), with a 4-inch electromagnet, respectively.

3. Results and discussion

3.1. Characterization of the synthesized hematite nanoparticles

The purity and crystallinity of the precursor and the synthesized products were examined by the XRD diffraction, as shown in Fig. 1. The precursor exhibits two extremely board peaks at 2θ about 36.0° and 62.5° which can be attributed to the poorly crystalline phase of 2-line ferrihydrite [30]. This poorly ordered compound is metastable which can be further transformed to hematite at the appropriate physico-chemical conditions. From the XRD pattern of the synthesized product, all of the peaks can be assigned to the hexagonal structure of hematite (space group: $R\bar{3}c$), with lattice constants of a = 0.5034 nm and c = 1.375 nm [1], which are in good agreement with the literature result (JCPDS card no. 33-0664). The narrow sharp peaks indicate that the hematite products are highly crystalline [31]; implying that the high purity of the synthesized hematite particles is obtained by using this synthesis method.

The functional groups of the ferrihydrite precursor and the synthesized hematite particles were characterized by the FT-IR spectroscopy, as shown in Fig. 2. From the FT-IR spectrum of the ferrihydrite precursor, the very broad band appearing at 3384 cm^{-1} and the peak at

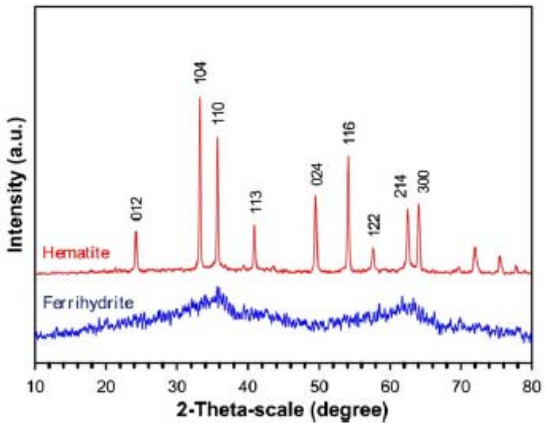

Fig. 1. XRD patterns of the 2-lineferrihydriteprecursor ($C = 0.3$ M, pH 7) and the synthesized hematite nanoparticles ($C = 0.3$ M, $n_{Fe(II)}/n_{Fe(III)} = 0.02$, pH 7, 100 °C, and 1 h).

1622 cm^{-1} can be observed and attributed to the superposition of stretching vibrations of the hydroxyl (OH) groups and water molecules. The strong and broad band with peaks at 431 and 578 cm^{-1} is typical for the low crystalline ferrihydrite [32]. For the hematite product, the strong absorption peaks at 475 and 560 cm^{-1} can be attributed to the Fe – O bond vibrations [16,33]. The very broad absorption band centered at 3449 and peak at 1632 cm^{-1} is assigned to the stretching and bending vibrations of the hydroxyl groups and/or water molecules, respectively. The result indicates the presence of a small amount of adsorbed water on the surface of the product and the structural hydroxyl groups in the product as the products were prepared in the aqueous solution. Both XRD and FT-IR results indicate that no any other by-products are present in the synthesized products.

3.2. Particle sizes of the synthesized hematite nanoparticles

The average particle sizes of the synthesized hematite particles under the effects of various preparation conditions are shown in Fig. 3. For the effect of the precursor concentration (Fig. 3(a)), the average particle diameter of hematite decreases from 139.5 nm to 49.3 nm (factor of 2.8) with decreasing precursor concentration from 0.5 M to 0.1 M. The reason is that the ferrihydrite precursor aggregation creates the nuclei of hematite and the Fe content in this aggregation limits the size of the hematite particles [23]. However, the precursor concentration cannot be further decreased because a low concentration of precursor (e.g., $C = 0.05$ M) requires longer time to reach the saturation

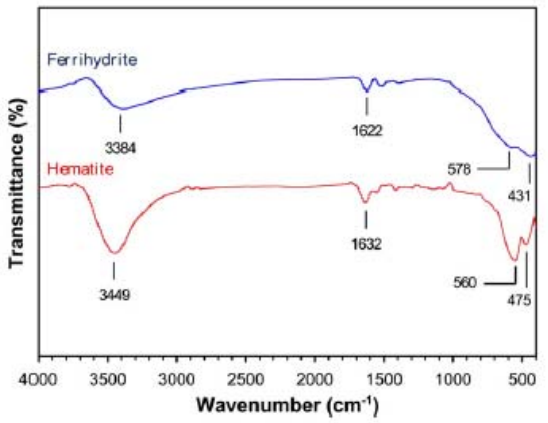

Fig. 2. FT-IR spectra of the 2-lineferrihydrite precursor ($C = 0.3$ M, pH 7) and the synthesized hematite nanoparticles ($C = 0.3$ M, $n_{Fe(II)}/n_{Fe(III)} = 0.02$, pH 7, 100 °C, and 1 h).

Author's personal copy

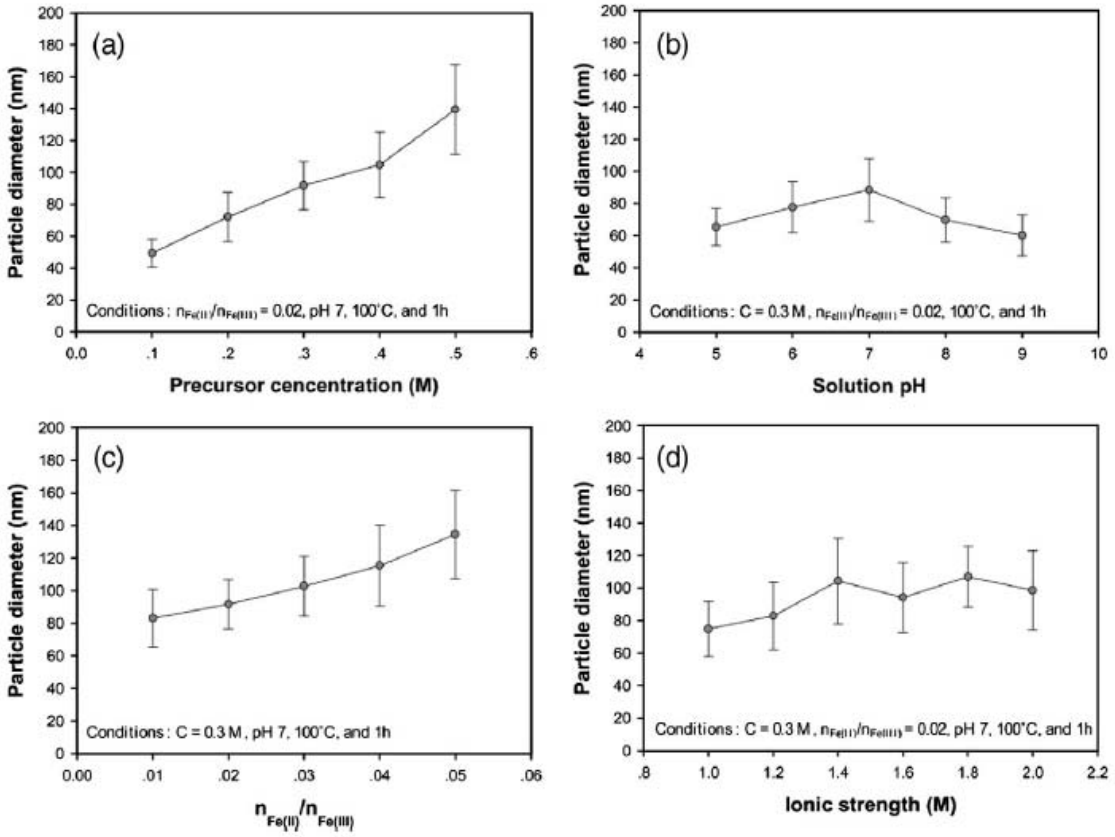

Fig. 3. Average particle sizes of the synthesized hematite nanoparticles under the effect of various preparation conditions: (a) the precursor concentration; (b) the solution pH; (c) the amount of Fe(II); and (d) the ionic strength.

concentration to obtain the hematite formation [30] and it also gives a very low yield percentage about 36% compared to 61% of hematite when using $C = 0.1$ M.

In order to study the effect of solution pH, the precursor concentration $C = 0.3$ M which possesses the moderate particle size was chosen to use in our further study. The effect of the solution pH on the particle size of the products was studied when other preparation conditions were held constant. Fig. 3(b) shows that the average particle size of the products increases as the solution pH increases from pH 5 until reaching the pH 7, and then the particle size decreases as the solution pH further increases up to pH 9 which is consistent with the result of Liu et al. [16]. This can be explained by the different species of Fe(II) ions formed at the different pH values; at the pH range from 5 to 9, Fe(II) ions exist in the form of Fe^{2+}, $FeOH^{+}$, $Fe(OH)_2$, and $Fe(OH)_3^-$. The predominated species of Fe(II) ions at pH 7 ($FeOH^{+}$) and at pH 9 ($Fe(OH)_2$) are proposed to catalyze the dissolution/reprecipitation mechanism (growth step) and the solid-state transformation (nucleation step), respectively [15]. Therefore, at pH 7 the crystal growth rate is very high resulting in the larger particle size; while at pH 9, the nucleation is predominant leading to the smaller particle size.

The effect of the amount of Fe(II), used as the catalyst, was investigated, as shown in Fig. 3(c). In the presence of Fe(II), not only the solid-state transformation (nucleation step) from ferrihydrite is accelerated, but also the dissolution of ferrihydrite, resulting in the rapid formation of hematite via the dissolution/reprecipitation mechanism (growth step) [15]. In this part, the solution pH was controlled at pH 7 to study the effect of Fe(II) in the crystal growth step of the phase transformation process. The result clearly demonstrates that the average particle size of hematite decreases from 134.5 nm to 83.1 nm (about 1.6 times) with decreasing molar ratio of Fe(II) to Fe(III) ($n_{Fe(II)}/n_{Fe(III)}$) from 0.05 to 0.01, because Fe(II) acts as a catalyst to induce the phase transformation from 2-line ferrihydrite into hematite; the lower the amount Fe(II) is used, the smaller the particle size of hematite is achieved.

The effect of the ionic strength on the particle size of hematite was investigated by adding certain amounts of NaCl solution (5.0 M) into the suspension to control the ionic strength of the solution in the range of 1.0 to 2.0. Based on the literature data, the high ionic strength can lower the aggregation and retard the dissolution of the ferrihydrite precursor [22]. However, our result as shown in Fig. 3(d) demonstrates that there is no significant effect of ionic strength on the particle size of hematite in the range of ionic strength values used in the present preparation. This may suggest the finding that the rapid growth rate of hematite particles as catalyzed by Fe(II) may overcome the effect of the ionic strength.

The effects of the reaction temperature and reaction time on the particle size of the products were also studied in the range of 60–100 °C and 10–120 min which are the appropriate conditions to synthesize the hematite. These results show that the reaction temperature and reaction time do not significantly affect the particle size of the synthesized hematite. However, according to the literature data [34], the reaction temperature and the reaction time are very important in the transformation process from ferrihydrite to various iron (hydr)oxides, such as goethite (α-FeOOH), lepidocrocite (γ-FeOOH), magnetite (Fe_3O_4), and also hematite (α-Fe_2O_3).

Author's personal copy

3.3. Particle morphologies of the synthesized hematite nanoparticles

The spherical-like hematite nanoparticles are successfully prepared by using a typical synthesis condition, as shown in Fig. 4. The FE-SEM image in Fig. 4(a) shows the morphology of the ferrihydrite precursor which is of a very small sphere with the average diameter of 11.5 nm. The synthesized hematite particles prepared by varying the initial precursor concentrations are shown in Fig. 4(b–d). It can be clearly seen that the lower the precursor concentration used, the smaller the particle size of hematite is obtained. The average sizes of the hematite particles are about 50–140 nm, which are higher than that of the particle sizes obtained by Liu et al. [16]. However, the ferrihydrite precursor and hematite particles prepared have a normal size distribution as shown in the *inset plots* of Fig. 4(a–d).

The synthesized hematite particles with the different morphologies are also successfully prepared, as shown in Fig. 5. The spherical-like (Fig. 5(a, b)), the cubic-like (Fig. 5(c)), and the ellipsoidal hematite particles (Fig. 5(d)) can be obtained by preparing with a typical ratio of $n_{Fe(II)}/n_{Fe(III)}$, ($n_{Fe(II)}/n_{Fe(III)} = 0.02$), with a very small ratio of $n_{Fe(II)}/n_{Fe(III)}$, ($n_{Fe(II)}/n_{Fe(III)} = 0.001$), and with NH_4OH instead of NaOH used in a typical synthesis, respectively. This result can be used to explain the difference of the formation mechanism occurred. In a typical synthesis condition, the hematite particles are proposed to form through the "nucleation–aggregation–dissolution–recrystallization–Oswald ripening" mechanism; while in the system with a very small amount of Fe(II) used, the products are proposed to form via the "nucleation–aggregation–recrystallization–Oswald ripening" mechanism [35]. For the ellipsoidal particles, the formation may occur via the anisotropic growth mechanism by the adsorption of ions on the surface planes parallel to the basal [001] plane of the hematite nuclei [36]. This can prevent the growth of hematite in those directions and allow only the recrystalization along the c-axis which produces the final ellipsoidal particles [37]. The high magnification FE-SEM image of hematite particles clearly reveals that the surfaces of hematite particles are not smooth (Fig. 5(b)). The whole hematite particle consisted of a large number of small nanoparticles of ferrihydrite precursor (*inset* of Fig. 5(b)) which can be called the "raspberry shape" [38]. Moreover, this surface structure is composed of a larger specific surface area compared to the smooth surface particle, which is the favorable condition in the catalyst and gas sensor applications [3,5]. In comparison, the specific surface area of our smallest hematite particles (average diameter of 49.3 nm) is 55.4 m^2/g which is higher than that of the value reported by Liu et al. [16] which was 31.83 m^2/g for the particle size about 60–80 nm.

3.4. Electrical conductivity of the synthesized hematite nanoparticles

The specific conductivities (σ) of the synthesized hematite particles with different particle sizes and shapes were measured by using electrical conductivity measurement, as shown in Fig. 6. The smallest hematite particles possess the highest electrical conductivity of 5.2×10^{-3} s/cm which is in the range of the semiconducting materials (σ is about 10^3–10^{-8} s/cm). In comparison to our previous work [39], the specific conductivity of the hematite particles is higher than that of the highest value of the magnetite particles (1.3×10^{-3} s/cm) about 4 times. In addition, the result shows that the particle size of hematite critically affects their electrical conductivity which increases about 5.4 times when decreasing the particle size from about 140 nm to 50 nm. The reason is that the smaller particles provide a tighter aggregation resulting in a better packing efficiency of the smaller particles; therefore, more contact area for electron transfer between particles is available [40]. Another reason is based on the adsorption of water on the surface of hematite where the water molecules can react reversibly

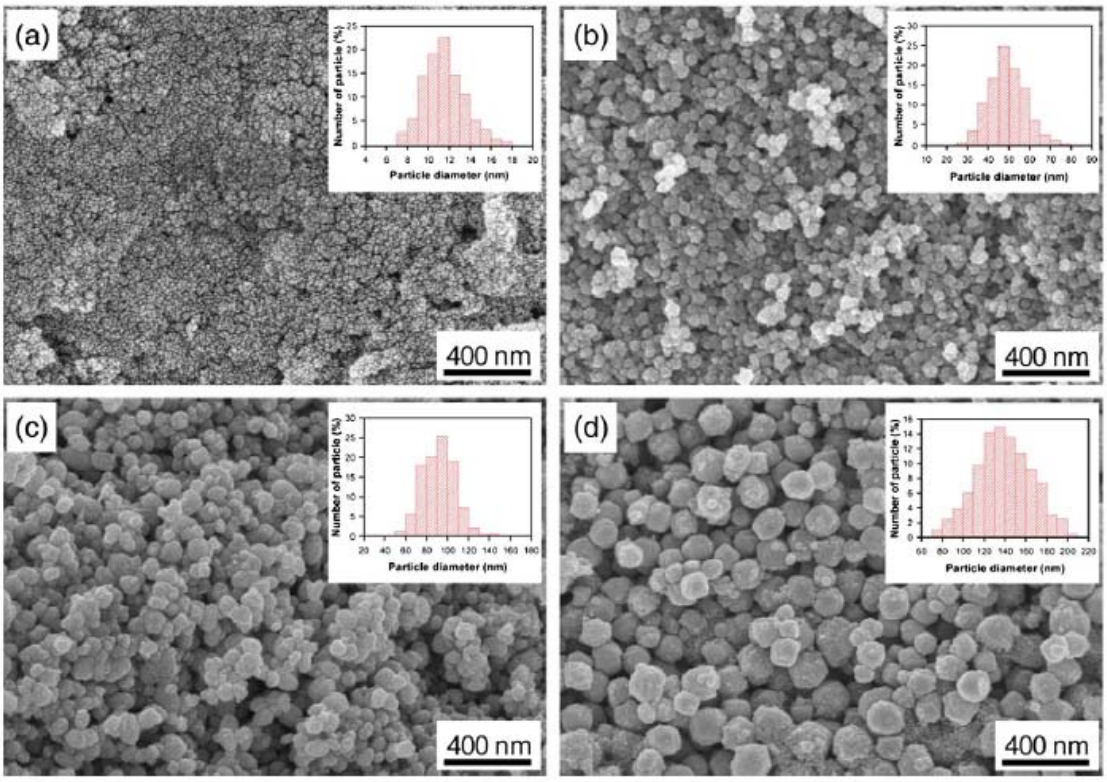

Fig. 4. FE-SEM images of: (a) the 2-line ferrihydrite precursor($C = 0.3$ M, pH 7); and the synthesized hematite nanoparticles ($n_{Fe(II)}/n_{Fe(III)} = 0.02$, pH 7, 100 °C, and 1 h); (b) hematite $C = 0.1$ M; (c) hematite $C = 0.3$ M; and (d) hematite $C = 0.5$ M (Note: *Inset plots* demonstrate the particle size distribution from the corresponding FE-SEM images).

Author's personal copy

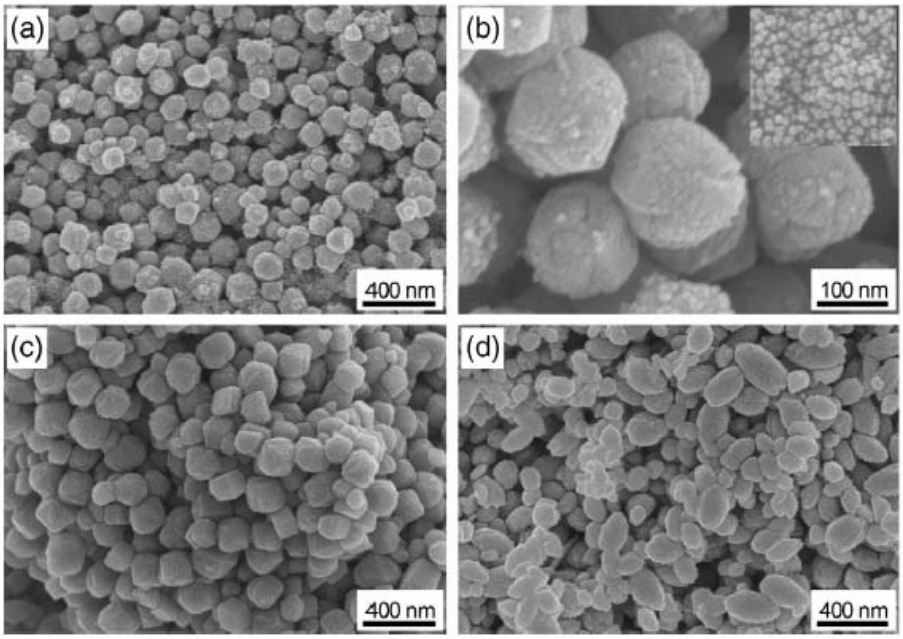

Fig. 5. FE-SEM images of the synthesized hematite nanoparticles with different morphologies: (a, b) the spherical-like particles at low and high magnifications; (c) the cubic-like particles; and (d) the ellipsoidal particles (Note: *inset* in (b) represents the magnified view of the particle surface).

with the lattice iron (Fe) to produce free electrons leading to the increase in the electrical conductivity. Consequently, a decrease in the particle size leads to a higher surface area, thus providing more active iron sites available for adsorbing water [4]. The latter reason is confirmed by the specific surface area measurement which shows that the specific surface area increases from 18.5 m^2/g to 55.4 m^2/g (factor of 3.0), when the particle size decreases from about 140 nm to 50 nm. For hematite particles with different sizes and shapes, the cubic-like particles (130 nm; *square* in Fig. 6) have the specific conductivity value of about 1.0×10^{-3} s/cm which is close to the value of the largest spherical-like particles (9.7×10^{-4} s/cm), but the ellipsoidal particles (120 nm; *triangle* in Fig. 6) have a lower conductivity value of about 3.2×10^{-4} s/cm because the ellipsoidal particles are more difficult to pack together compared to the spherical-like particles.

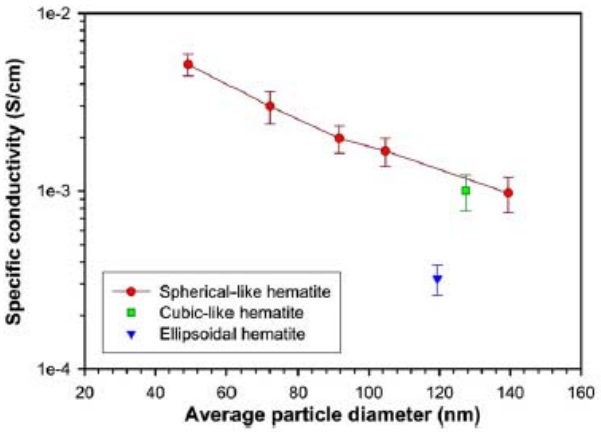

Fig. 6. Specific conductivities of the synthesized hematite nanoparticles with different particle sizes and morphologies.

3.5. Magnetic properties of the synthesized hematite nanoparticles

The magnetic properties of the synthesized hematite particles were studied by using a VSM measurement at room temperature. The magnetization curves of the synthesized hematite particles with different particle sizes and different morphologies are shown in Fig. 7(a) and (b), respectively.

It is clearly seen that the largest hematite particle (*dashed line* in Fig. 7(a)) exhibits a large hysteresis loop, and the hysteresis loop decreases with decreasing particle size (*dotted line* in Fig. 7(a)). The smallest hematite particle (*solid line* in Fig. 7(a)) has no remanent magnetization (M_r) at zero magnetic field strength and has a very low coercive force (H_c) (*inset plot* of Fig. 7(a)), which is an indication of the superparamagnetism. When the magnetic particle size decreases, the multidomain of particles change into a single domain because the formation of domain walls becomes energetically unfavorable [41]. Whether the single domain particles are small enough, the fluctuation of magnetic moment direction occurs and leads to the superparamagnetism due to their thermal agitation [14]. The smallest hematite particles obtained (49.3 nm) show the single-domain particles and superparamagnetism. The magnetic domain of these particles is approximately 50 nm, which is in agreement with the largest size of 41 nm as reported by Raming et al. [10]. The magnetic parameters consisting of H_c, M_r, M_s, and M_r/M_s of the synthesized hematite particles with different particle sizes are summarized in Table 1, where H_c is the coercive force; M_r is the remanent magnetization (at $H = 0$ Oe); and M_s is the saturation (maximum) magnetization. The H_c and M_r/M_s values are both measured for the amount of ferromagnetic behavior present in the samples. It is clearly seen that the ferromagnetic behavior decreases with the particle size (Fig. 7(a) and Table 1), because the anisotropic energy of magnetic moments depend on the particle volume [10]. It is noted that the saturation magnetization (M_s) also decreases from 1.94 emu/g to 0.80 emu/g with decreasing of particle size from 140 nm to 50 nm because of the increase in surface to volume ratio of the smaller particles. This can result in the higher disordered spin configuration leading to the reduction of the net magnetic moment of the hematite particles which is known as the surface effect [42,43].

Author's personal copy

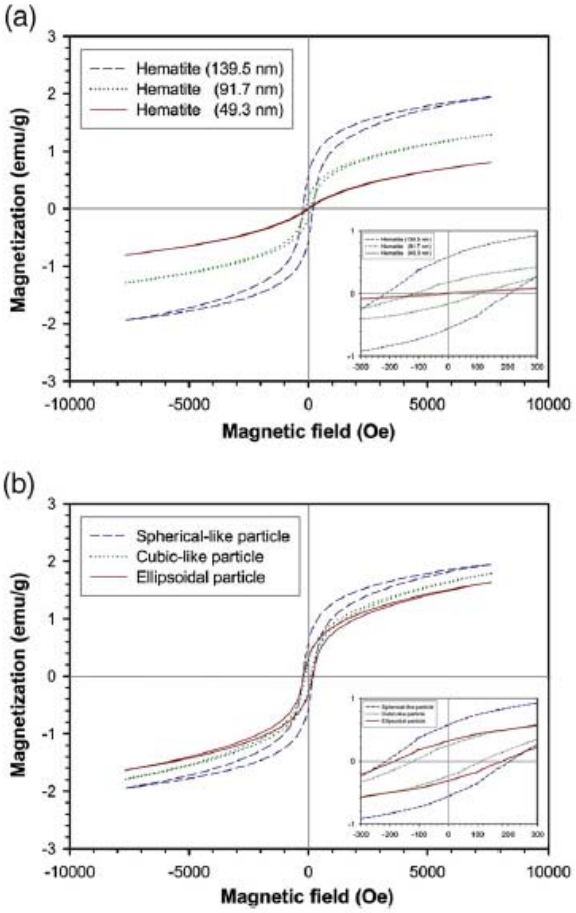

Fig. 7. Room temperature magnetization curves of the synthesized hematite nanoparticles with: (a) different particle sizes; and (b) different morphologies (Note: *dash line* is the same line as represented in (a); and *inset plots* illustrate the magnified view of the corresponding magnetization curves).

The magnetic hysteresis loops were obtained for all samples (particle sizes are about 120–140 nm) of different morphologies, as shown in Fig. 7(b). The hysteresis loops show that the hematite nanostructures are weak in ferromagnetic behavior at room temperature. The magnetic parameters consisting of H_c, M_r, M_s, and M_r/M_s of the synthesized hematite particles with different morphologies are also summarized in Table 1. Generally, the difference in the remanent magnetization (M_r) is related to the particle morphology and the magnitude of coercive force (H_c) is proportional to the particle size [44,45]. In fact, the hematite particles prepared in various preparation conditions are both different in morphology and particle size, as shown in the FE-SEM images (Fig. 5). In addition, the particle size of the spherical-like hematite is about 140 nm and that of the cubic-like and ellipsoidal hematite are about 130 and 120 nm, respectively. As can be seen from Table 1, the saturation magnetization (M_s) value of the spherical-like particles (1.94 emu/g) is higher than that of the cubic-like particles (1.78 emu/g), and the ellipsoidal particles (1.63 emu/g), which may be referred to the increase of surface effect with decreasing particle size as described previously. It is suggested that the higher M_r and H_c values of the ellipsoidal hematite compared to the cubic-like hematite (*inset plot* of Fig. 7(b) and Table 1) may be depend on their aspect ratio, because the shape anisotropy can prevent the magnetization except along the easy magnetic axes resulting in more difficult magnetization and demagnetization [46]. This shape anisotropy critically influences the magnetic properties, such as lower saturation magnetization (M_s), as well as increases the remanent magnetization (M_r) and coercive force (H_c) [47]. In comparison, our hematite particles have a moderate M_s value compared to that of the value reported in the literatures using the other methods which are in the range from low value as 0.03 emu/g [14] to high value as 5.1 emu/g [48]. This may be explained by the fact that the different synthesis methods usually provide the different particle sizes, morphologies and also surface structures which critically affect to the magnetic properties of the products as already discussed.

Table 1
Summary of the magnetic parameters of the synthesized hematite nanoparticles with different particle sizes and morphologies.

Sample		Magnetic parameters			
Particle shape	Particle size (nm) ($\bar{X} \pm$ SD)	H_c (Oe)	M_r (emu/g)	M_s (emu/g)	M_r/M_s
Sphere	49.3 ± 8.8	30.2	0.009	0.802	0.012
Sphere	91.7 ± 15.1	115.3	0.171	1.287	0.133
Sphere	139.5 ± 28.2	211.5	0.565	1.943	0.291
Cube	127.5 ± 24.3	120.2	0.245	1.786	0137
Ellipsoid	119.4 ± 44.3	185.2	0.312	1.633	0.191

Hc is the coercive force; *Mr* is the remanent magnetization (at $H = 0$ Oe); and *Ms* is the saturation (maximum) magnetization.

4. Conclusions

The synthesized particles fabricated at pH 5–9 and at temperatures between 60 and 100 °C for 1 h are confirmed to be the single phase hexagonal structure and highly crystalline hematite. The physical morphology of the synthesized hematite seems to be composed of a large number of very small particles with the highest specific surface area of 55.4 m^2/g and consisted of hydroxyl surface structure. The particle size of the synthesized hematite decreases with decreasing precursor concentration and the amount of catalyst. The solution pH provides the maximum particle size at the neutral pH, which is preferred for the growth step by dissolution/reprecipitation process. The effect of the transformation mechanism from ferrihydrite to hematite can overcome the effect of the ionic strength of the reaction system. The reaction time and the reaction temperature have no significant effect on the hematite particle size. The synthesized hematite particles can be successfully controlled at 50–150 nm possessing three different morphologies: the spherical-like, the cubic-like, and the ellipsoidal shapes. The particle size and shape of the synthesized hematite critically affect their electrical and magnetic properties. The specific conductivity increases with decreasing hematite particle size and the smallest particle possesses the highest conductivity of 5.2×10^{-3} s/cm. The large hematite particles exhibit hysteresis loops indicating the weak ferromagnetic behavior at room temperature with the highest M_s of 1.94 emu/g, and change from multidomain to single domain exhibited the superparamagnetism as the particle size further decreases. Moreover, the different shape hematite also shows varying magnitudes of the magnetic parameters in the hysteresis loops. The advantage of various structures and size of the synthesized hematite nanoparticles is the wide range of applications: the size of adsorbed gas for gas sensor device, or the reactivity of a catalyst for catalytic application.

Acknowledgments

The authors are grateful for the financial supports from the Petroleum and Petrochemical College; the Conductive and Electroactive Polymers Research Unit of Chulalongkorn University; the Thailand Research Fund (TRF); and the Royal Thai Government.

Author's personal copy

References

[1] A.S. Teja, P.Y. Koh, Synthesis, properties, and applications of magnetic iron oxide nanoparticles, Prog. Cryst. Growth 55 (2009) 22–45.
[2] M. Hosseini-Zori, F. Bondioli, T. Manfredini, E. Taheri-Nassaj, Effect of synthesis parameters on a hematite-silica red pigment obtained using a coprecipitation route, Dyes Pigment. 77 (2008) 53–58.
[3] A.S.C. Brown, J.S.J. Hargreaves, B. Rijniersce, A study of the structural and catalytic effects of sulfation on iron oxide catalysts prepared from goethite and ferrihydrite precursors for methane oxidation, Catal. Lett. 53 (1998) 7–13.
[4] P. Chauhan, S. Annapoorni, S.K. Trikha, Humidity-sensing properties of nano-crystalline haematite thin films prepared by sol–gel processing, Thin Solid Films 346 (1999) 266–268.
[5] L. Huo, W. Li, L. Lu, H. Cui, S. Xi, J. Wang, B. Zhao, Y. Shen, Z. Lu, Preparation structure and properties of three-dimensional ordered α-Fe_2O_3 nanoparticulate film, Chem. Mater. 12 (2000) 790–794.
[6] A. Watanabe, H. Kozuka, Photoanodic properties of sol–gel-derived Fe_2O_3 thin films containing dispersed gold and silver particles, J. Phys. Chem. B 107 (2003) 12713–12720.
[7] A. Kay, I. Cesar, M. Gratzel, New benchmark for water photooxidation by nanostructured α-Fe_2O_3 films, J. Am. Chem. Soc. 128 (2006) 15714–15721.
[8] S. Cao, Y. Zhu, Hierarchically nanostructured α-Fe_2O_3 hollow spheres: preparation, growth mechanism, photocatalytic property, and application in water treatment, J. Phys. Chem. C 112 (2008) 6253–6257.
[9] Z. Wu, K. Yu, S. Zhang, Y. Xie, Hematite hollow spheres with a mesoporous shell: controlled synthesis and applications in gas sensor and lithium ion batteries, J. Phys. Chem. C 112 (2008) 11307–11313.
[10] T.P. Raming, A.J.A. Winnubst, C.M. Kats, A.P. Philipse, The synthesis and magnetic properties of nanosized hematite (α-Fe_2O_3) particles, J. Colloid Interface Sci. 249 (2002) 346–350.
[11] S. Music, S. Krehula, S. Popovic, Z. Skoko, Some factors influencing forced hydrolysis of $FeCl_3$ solutions, Mater. Lett. 57 (2003) 1096–1102.
[12] S. Lian, E. Wang, Z. Kang, Y. Bai, L. Gao, M. Jiang, C. Hu, L. Xu, Synthesis of magnetite nanorods and porous hematite nanorods, Solid State Commun. 129 (2004) 485–490.
[13] Q. Sun, X. Lu, G. Liang, Controlled template-free hydrothermal synthesis of hematite nanoplatelets, Mater. Lett. 64 (2010) 2006–2008.
[14] Y.C. Zhang, J.Y. Tang, X.Y. Hu, Controllable synthesis and magnetic properties of pure hematite and maghemite nanocrystals from a molecular precursor, J. Alloys Compd. 462 (2008) 24–28.
[15] H. Liu, Y. Wei, Y. Sun, The formation of hematite from ferrihydrite using Fe(II) as a catalyst, J. Mol. Catal. A Chem. 226 (2005) 135–140.
[16] H. Liu, Y. Wei, P. Li, Y. Zhang, Y. Sun, Catalytic synthesis of nanosized hematite particles in solution, Mater. Chem. Phys. 102 (2007) 1–6.
[17] J. Lu, D. Chen, X. Jiao, Fabrication characterization and formation mechanism of hollow spindle-like hematite via a solvothermal process, J. Colloid Interface Sci. 303 (2006) 437–443.
[18] C. Min, Y. Huang, L. Liu, High-yield synthesis and magnetic property of hematite nanorhombohedras through a facile solution route, Mater. Lett. 61 (2007) 4756–4758.
[19] A. Bumajdad, J. Eastoe, M.I. Zaki, R.K. Heenan, L. Pasupulety, Generation of metal oxide nanoparticles in optimised microemulsions, J. Colloid Interface Sci. 312 (2007) 68–75.
[20] L.H. Han, H. Liu, Y. Wei, In situ synthesis of hematite nanoparticles using a low-temperature microemulsion method, Powder Technol. 207 (2011) 42–46.
[21] L. Diamandescu, D.M. Tarabasanu, N.P. Pogrion, A. Totovina, I. Bibicu, Hydrothermal synthesis and characterization of some polycrystalline α-iron oxides, Ceram. Int. 25 (1999) 689–692.
[22] R.M. Cornell, R. Giovanoli, Effect of solution conditions on the proportion and morphology of goethite formed from ferrihydrite, Clay Miner. 33 (1985) 424–432.
[23] U. Schwertmann, J. Friedl, H. Stanjek, From Fe(III) ions to ferrihydrite and then to hematite, J. Colloid Interface Sci. 209 (1999) 215–223.
[24] K. Kandori, S. Ohnishi, M. Fukusumi, Y. Morisada, Effects of anions on the morphology and structure of hematite particles produced from forced hydrolysis of $Fe(NO_3)_3$–HNO_3, Colloids Surf. A 331 (2008) 232–238.
[25] N.K. Ilona, R. Aleksander, P. Mihaly, Novel methods for the synthesis of magnetite nanoparticles with special morphologies and textured assemblages, J. Nanopart. Res. 14 (2012) 1150–1159.
[26] M. Ming, Z. Yu, G. Zhirui, G. Ning, Facile synthesis of ultrathin magnetic iron oxide nanoplates by Schikorr reaction, Nanoscale Res. Lett. 8 (2013) 16–22.
[27] A. Ibrahim, A.B. Abubakar, Some wet routes for synthesis of hematite nanostructures, Afr. J. Pure Appl. Chem. 7 (2013) 114–121.
[28] L. Hui, W. Yu, S. Yuhan, The formation of hematite from ferrihydrite using Fe(II) as a catalyst, J. Mol. Catal. A Chem. 226 (2005) 135–140.
[29] L. Hui, W. Yu, L. Ping, Z. Yanfeng, S. Yuhan, Catalytic synthesis of nanosized hematite particles in solution, Mater. Chem. Phys. 102 (2007) 1–6.
[30] R.M. Cornell, U. Schwertmann, The Iron Oxides: Structure Properties Reaction Occurrences and Uses, second ed. Wiley-VCH, Weinheim, 2003.
[31] C. Su, H. Wang, X. Liu, Controllable fabrication and growth mechanism of hematite cubes, Cryst. Res. Technol. 46 (2011) 209–214.
[32] M. Ristic, E.D. Grave, S. Music, S. Popovic, Z. Orehovec, Transformation of low crystalline ferrihydrite to α-Fe_2O_3 in the solid state, J. Mol. Struct. 834 (2007) 454–460.
[33] Z. Jing, S. Wu, Synthesis and characterization of monodisperse hematite nanoparticles modified by surfactants via hydrothermal approach, Mater. Lett. 58 (2004) 3637–3640.
[34] H. Liu, M. Ma, M. Qin, L. Yang, Y. Wei, Studies on the controllable transformation of ferrihydrite, J. Solid State Chem. 183 (2010) 2045–2050.
[35] J. Lian, X. Duan, J. Ma, P. Peng, T. Kim, W. Zheng, Hematite (α-Fe_2O_3) with various morphologies: ionic liquid-assisted synthesis formation mechanism and properties, ACS Nano 3 (2009) 3749–3761.
[36] X. Hu, J.C. Yu, Continuous aspect-ratio tuning and fine shape control of monodisperse α-Fe_2O_3 nanocrystals by a programmed microwave-hydrothermal method, Adv. Funct. Mater. 18 (2008) 880–887.
[37] M. Ocana, M.P. Morales, C.J. Cerna, The growth mechanism of α-Fe_2O_3 ellipsoidal particles in solution, J. Colloid Interface Sci. 171 (1995) 85–91.
[38] M.G. Han, S.P. Armes, Synthesis of poly(3,4-ethylenedioxythiophene)/silica colloidal nanocomposites, Langmuir 19 (2003) 4523–4526.
[39] K. Petcharoen, A. Sirivat, Synthesis and characterization of magnetite nanoparticles via the chemical co-precipitation method, Mater. Sci. Eng. B Solid 177 (2012) 421–427.
[40] S. Chunhui, P. Mu, Y. Runzhang, The effect of particle size gradation of conductive fillers on the conductivity and the flexural strength of composite bipolar plate, Int. J. Hydrogen Energy 33 (2008) 1035–1039.
[41] L.L. Vatta, R.D. Sanderson, K.R. Koch, Magnetic nanoparticles: properties and potential applications, Pure Appl. Chem. 78 (2006) 1793–1801.
[42] Z. Huang, Q. Feng, Z. Chen, S. Chen, Y. Du, Surface and size effects of magnetic properties in ferromagnetic nanoparticles, Microelectron. Eng. 66 (2003) 128–135.
[43] R.D. Zysler, M. Mansilla, D. Fiorani, Surface effects in α-Fe_2O_3 nanoparticles, Eur. Phys. J. B 41 (2004) 171–175.
[44] X. Cao, R. Prozorov, Y. Koltypin, G. Kataby, I. Felner, A. Gedanken, Synthesis of pure amorphous Fe_2O_3, J. Mater. Res. 12 (1997) 402–406.
[45] L. Li, G. Li, R.L. Smith, H. Inomata, Microstructural evolution and magnetic properties of $NiFe_2O_4$ nanocrystals dispersed in amorphous silica, Chem. Mater. 12 (2000) 3705–3714.
[46] B. Tang, G. Wang, L. Zhuo, J. Ge, L. Cui, Facile route to α-FeOOH and α-Fe_2O_3 nanorods and magnetic property of α-Fe_2O_3 nanorods, Inorg. Chem. 45 (2006) 5196–5200.
[47] D. Wang, C. Cao, S. Xue, H. Zhu, γ-Fe_2O_3 oriented growth by surfactant molecules in microemulsion, J. Cryst. Growth 277 (2005) 238–245.
[48] P.P. Sarangi, S.R. Vadera, M.K. Patra, C. Prakash, N.N. Ghosh, DC electrical resistivity and magnetic property of single-phase α-Fe_2O_3 nanopowder synthesized by a simple chemical method, J. Am. Ceram. Soc. 92 (2009) 2425–2428.

Ammonia sensing and electrical properties based on composite of poly(3-thiopheneacetic acid) and zeolite Y

S. Konkayan[1], P. Chanthaanont[1], W. Prissanaroon[2], P. Hormnirun[3] and A. Sirivat*[1]

Poly(3-thiopheneacetic acid) (Pth) was synthesised and doped with perchloric acid. The electrical conductivity sensitivity towards ammonia is further improved by introducing Y zeolites into the doped Pth matrix. For the effect of zeolite content, the composite with 10% (v/v) of the Y zeolite gives the highest electrical conductivity sensitivity ($\Delta\sigma/\sigma_{N2}$) values when exposed to NH_3. The electrical conductivity sensitivity ($\Delta\sigma/\sigma_{N2}$) monotonically increases with increasing Si/Al ratio. The highest electrical conductivity sensitivity of all composites investigated is obtained with the doped Pth/zeolite Y (Si/Al=80) at the value of $(7{\cdot}46 \pm 3{\cdot}56) \times 10^2$. The interaction between NH_3 and the doped Pth is shown to be reversible based on the Fourier transform infrared spectra.

Keywords: Conductive polymer, Polythiophene, Polymer composites, Ammonia sensors, Gas sensor, Zeolite Y

Introduction

Ammonia gas has been known to be hazardous to both humans and the environment. Due to its high toxicity, even low concentrations (ppm) can pose a serious health threat. The industrial processes, including fertiliser manufacturing, chemical manufacturing, livestock farms, and refrigeration involve the use of an ammonia gas. Existing ammonia gas sensing devices show low selectivity and sensitivity. A new approach is desirable to increase the sensor selectivity and sensitivity towards ammonia gas.[1]

One method for dealing with low selectivity and sensitivity is the use of conductive polymers as gas sensing materials. In comparison with most commercially available sensors, based usually on metal oxides, which are operated at high temperatures, the sensors made of conducting polymers have several favourable characteristics. They have high sensitivities and moderately short response times; these features can operate at room temperature. Conducting polymers are ease of synthesis via chemical or electrochemical medthods, and their molecular chain structure can be altered conveniently by copolymerisation or structural derivations. Furthermore, conducting polymers have moderately good mechanical properties, which allow a facile fabrication of sensors.[2] Polythiophene has several advantages over other semiconducting polymer particles; it can be easily polymerised by an oxidative polymerisation at a relatively low temperature to giving a high yield, and it can be doped from an insulating state to a conducting state by using simple protonic acids.[3] A polythiophene film can be expected to show a highly sensitive response to ammonia and that the response can be easily recovered with N_2. Furthermore, with the proven reproducibility, it can be developed into electronic noses.[4] The aim of this work is to explore the possibility of using poly(3-thiopheneacetic acid) (Pth) as a NH_3 gas sensor material.

Zeolites are naturally and synthetically occurring aluminosilicate minerals with three-dimensional structure based on $[SiO_4]^{4-}$ and $[AlO_4]^{4-}$ polyhedral.[5] Owing to the size and shape selectivity of zeolite crystals, zeolites of type Y are utilised to promote or to demote one species of gas interaction via the size selection and the cationic interaction.[5]

The objectives of this work are to investigate the effects of zeolite contents and Si/Al mole ratios on the electrical conductivity response of Pth/zeolite Y composites. The scope of this research covers the followings: the synthesis a conductive polymer, polythiophene, and the fabrication of composite sensing materials with commercial zeolites of type Y, and use as a selective NH_3 gas sensor. The electrical conductivity sensitivity of Pth/zeolite Y composites when exposed to NH_3 gas are investigated and compared with previous work.

Experimental

Materials

3-thiopheneacetic acid (3TAA, AR grade; Fluka) was used as the monomer and anhydrous ferric chloride, $FeCl_3$ (AR grade) was used as the oxidant as received. Chloroform, $CHCl_3$ (AR grade; Lab-Scan), methanol, CH_3OH (AR grade; Lab-Scan), and dimethyl sulphoxide, DMSO (AR grade; Lab-Scan) was dried over

[1]The Petroleum and Petrochemical College, Chulalongkorn University, Bangkok 10330 Thailand
[2]Department of Industrial Chemistry, Faculty of Applied Science, KMITNB, 1518 Pibulsongkram Road, Bangsue, Bangkok 10800, Thailand
[3]Department of Chemistry, Faculty of Science, Kasetsart University, 50 Phahonyothin Road, Ladyao, Chatuchak, Bangkok 10900, Thailand

*Corresponding author, email anuvat.s@chula.ac.th

© 2013 W. S. Maney & Son Ltd.
Received 14 November 2012; accepted 20 January 2013
DOI 10.1179/1753555713Y.0000000065

Materials Technology mte171.3d 6/2/13 14:14:27
The Charlesworth Group, Wakefield +44(0)1924 369598 - Rev 7.51n/W (Jan 20 2003)

CaH_2 for 24 h under the nitrogen atmosphere and then distilled, before be used as solvents. Hydrochloric acid, HCl (AR grade; Lab-Scan), was used to neutralise and to precipitate the synthesised polymer. Sulphuric acid, H_2SO_4 was used to protect the oxidative decomposition of the monomer. Diethyl ether, $C_4H_{10}O$ and distilled water were used to extract and to wash materials. Sodium hydroxide, NaOH, was used as the hydrolysing agent. Perchloric acid, $HClO_4$ (AR grade; Panreac Quimica) was used as received and as the dopant.

Zeolite of type Y with different Si/Al ratios were purchased from Zeolyst International (USA).

Nitrogen (99%; Linde Thailand) was used as the carrier gas for ammonia (99·99%; Linde Thailand).

Synthesis of Pth

The reaction was by the oxidative coupling polymerisation according to the method of Kim *et al.*[6] Poly(3-thiopheneacetic acid) was prepared by a reflux of 10·0 g 3TAA in 50 mL dry methanol with one drop of concentrated H_2SO_4 for 24 h. Then, methanol was evaporated and the residue was extracted with diethyl ether. The extract was washed with distilled water, dried with anhydrous $MgSO_4$, and filtered. The 3-thiophene methyl acetate was recovered after diethyl ether was evaporated.

The prepared monomer, 3-thiophene methyl acetate, of 10 mmol was dissolved in 20 mL chloroform and then added dropwise to a solution of 40 mmol ferric chloride in 30 mL chloroform under nitrogen atmosphere. The reaction was carefully maintained at $0\pm0{\cdot}5$°C for 24 h. The mixture was precipitated by pouring the solution in an excess amount of methanol. The precipitate was washed with methanol and distilled water. Finally, poly(3-thiophenemethyl acetate) was obtained.

Poly(3-thiophenemethyl acetate) was hydrolysed by heating 0·5 g precipitate in 50 mL of 2·0M NaOH solution for 24 h at 100°C. Poly(3-thiopheneacetic acid) was obtained by the neutralisation and precipitation in a dilute HCl solution. Poly(3-thiopheneacetic acid) was repeatedly washed with distilled water before vacuum drying at room temperature for 2 days.

Preparation of doped Pth

Particles of Pth were stirred in 2·0M $HClO_4$ at room temperature for 3 days. The doping ratio of $HClO_4$/3TAA was varied from 1 : 1 to 300 : 1. Doped Pth was filtered and then vacuum dried.[7]

Preparation of Pth/zeolite composites

Before mechanical mixing, Pth was grinded and sieved with mesh size of 38 µm. Then, a zeolite was grinded and dried before mixing with Pth grinding. The mixtures were compressed into a pellet form by a hydraulic machine.

Characterisation methods

Undoped and doped Pth powders were investigated for their functional groups by a Fourier transform infrared (FTIR) spectrometer (Thermo Nicolet, Nexus 670) operated in the absorption mode with 32 scans and a resolution of ±4 cm^{-1}, covering a wavenumber range of 4000–400 cm^{-1}. Optical grade KBr was used as the background material, and the polymers were mixed with dried KBr at a ratio 1 : 20. In order to investigate the spectrum of Pth_10 : 1 and the Y zeolites before, under and after exposure with NH_3 gas, a gas cell with a ZnSe window was used.

A thermal gravimetric analyser (Perkin Elmer) was used to characterise the thermal property of the undoped and the doped Pth at 10 : 1 mole ratio between the dopant and the monomer unit. Measurements were carried out with the temperature scan from 30 to 800°C and a heating rate of 10°C min^{-1}. The samples were weighed in the range of 5–20 mg and loaded into a platinum pan, and then it was heated under N_2 flow.

The average particle size of Pth and the zeolites were determined by a particle size analyser (Malvern, Mastersizer X version 2.15). The samples were grounded and sieved with a mesh size of 38 µm before measurements were taken. An X-ray diffractometer (XRD) (D/MAX 2200) was used to identify the crystallinity and the structure of Pth and the zeolites. Powders of polymer and the zeolites were packed onto a glass plate, and data were collected after X-ray passing though the samples.

Morphology of undoped and doped Pth, the zeolites and the composites were observed by the scanning electron microscopy (SEM, JEOL, JSM-5410LV). Surface area and pore size of zeolite Y were measured by using a surface area analyser (Physisorption, Quantachrome, Autosorb-1MP). Zeolite powder was weighed and out gassed at 300°C over night before the adsorption and the desorption with He and N_2 gases. During the operation, zeolite powder was cooled by liquid N_2. A custom built two-point probe with a linear geometric array (Keithley, model 6517A) was used to measure the specific conductivity of each sample. Current used was in the linear Ohmic regime.

Electrical conductivity measurement

The specific electrical conductivity values σ (S cm^{-1}) of the Pth and the composites were measured by using a custom built two-point probe. The specific electrical conductivity was calculated from

$$\sigma=(1/Rt)(1/K) \quad (1)$$

where t is the pellet thickness and K is the geometric correction factor which is equal to the ratio w/l (where w and l are the width and the length of probe respectively). The value of K was determined by calibrating the two-point probe with semiconducting silicon sheet of known resistivity value.

A custom built two-point probe consists of two chambers of equal volume. All measurements were taken at 26 ± 1°C and 1·1 atm in the linear Ohmic regime. The procedure was as follows. Initially, the sample was measured the specific electrical conductivity in air. Then the chambers were evacuated of air and moisture by using a vacuum pump and the steady state electrical conductivity value in vacuum was measured. Nitrogen gas was injected until the pressure reached 1·1 atm and the steady state electrical conductivity value was measured as $\sigma_{N_2\text{initial}}$. Then the chambers were re-evacuated. Ammonia gas was injected until the pressure reached 1·1 atm and the steady state electrical conductivity σ_{NH_3} was measured. Finally ammonia gas was evacuated then nitrogen gas was injected and the steady state electrical conductivity value was remeasured as $\sigma_{N_2\text{final}}$. From the measurement procedure, the electrical conductivity response can be calculated from

Materials Technology mte171.3d 6/2/13 14:14:33
The Charlesworth Group, Wakefield +44(0)1924 369598 - Rev 7.51n/W (Jan 20 2003)

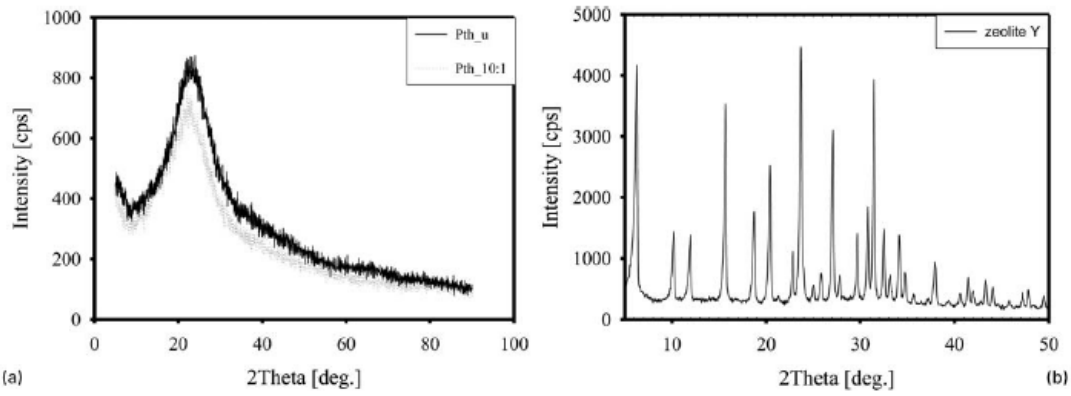

1 X-ray diffraction patterns of *a* undoped and doped Pth with $HClO_4$ and *b* zeolite Y 3

$$\Delta\sigma = \sigma_{NH_2} - \sigma_{N_2 initial} \quad (2)$$

and the sensitivity $\Delta\sigma/\sigma_{N_2 initial}$ of Pth and its composites were calculated.

Results and discussion

Characterisation of Pth and zeolite

From the FTIR spectrum of Pth, a characteristic peak appears at 3200–3000 cm^{-1} which can be assigned to the stretching vibration of the C-H bond on the thiophene ring; peaks between 3000 and 2800 cm^{-1} represent the aliphatic C-H bonds; a peak at 1700 cm^{-1} represents the C=O stretching vibration; a peak at 1400 cm^{-1} represents the thiophene ring stretching vibration; and peaks between 1300 and 1200 cm^{-1} represent the C-O stretching vibration. The important feature peak is the extremely broad O-H absorption occurring in the region from 3400 to 2400 cm^{-1}, which can be attributed to the strong hydrogen bonding of the dimer. After doping with perchloric acid, some characteristic peaks of acid appear on FTIR spectra: a lower absorbance at 3400–2400 cm^{-1} and a sharp peak at 1200 cm^{-1}.

2 The thermal gravimetric analysis thermogram of synthesised Pth shows two transitions at 219 and 474·7°C. The first transition can be referred to as the side chain degradation. The other transition can be referred to as the backbone degradation.[8] The doped Pth with perchloric acid has lower thermal stability than pristine polymer; its degradation temperature is 120·7°C.

The mean particle diameter of undoped and doped Pth is $39{\cdot}28 \pm 0{\cdot}26$ and $39{\cdot}53 \pm 0{\cdot}41$ μm respectively. These were obtained by grounding and sieving through a mesh of size 38 μm. The mean particle diameter of the Y zeolite is $30{\cdot}07 \pm 1{\cdot}16$ μm.

The X-ray diffraction pattern of synthesised undoped and doped Pth shows broad peaks at 2θ equal to 23·30 and 22·15° respectively. This can be identified as the amorphous part and attributed to the stacking distance between successive thiophene rings of two polymers, as shown in Fig. 1*a*.[9] The structure of zeolite can be considered from the position of each peak as shown in Fig. 1*b*.[10] The density values of undoped Pth and zeolite Y are equal to 1·5974 and 1·7931 g cm^{-3} respectively.

The morphology of undoped and doped Pth, zeolite Y, and the composites was observed and investigated using SEM. Both undoped and doped Pth particles were quite irregular in shape. The zeolite is uniform in both size and shape. Figures 2 and 3 show SEM monographs of undoped Pth, doped Pth_10:1, zeolite Y, Pth_10:1/Y_10% and Pth_10:1/Y_20% composites in which a non-uniform distribution of zeolite particles within the matrix can be observed.

Electrical conductivity in air and N_2

The specific electrical conductivity values of the undoped and doped Pth 10::1 are $(1{\cdot}16 \pm 0{\cdot}14) \times 10^{-4}$ and $(10{\cdot}31 \pm 2{\cdot}61) \times 10^{0}$ S cm^{-1} respectively. Since the doped Pth has the repulsive force between the positive charges of the counter anions (ClO_4^-) along back bone, so the extended chain conformations are obtained. The specific conductivity of undoped and doped Pth with different mole ratios of $HClO_4$ to monomer unit is shown in Fig. 4. The specific electrical conductivity of the doped Pth 10:1 is higher than that of the undoped Pth, because the electrons can move easily along the extended polymer chain. The electrical conductivity values of zeolite NaY, NH_4Y and HY are $(3{\cdot}48 \pm 2{\cdot}34) \times 10^{-4}$, $(1{\cdot}30 \pm 0{\cdot}73) \times 10^{-4}$ and $(3{\cdot}55 \pm 4{\cdot}45) \times 10^{-4}$ S cm^{-1} respectively. The electrical conductivity of Pth_10:1 in N_2 decreases to $(3{\cdot}68 \pm 0{\cdot}12) \times 10^{-9}$ S cm^{-1}, as shown in Table 1. The greater electrical conductivity values in air can be attributed to the interaction of moisture and O_2 with the polaron and the bipolaron species.[5]

Electrical conductivity sensitivity of doped Pth and composites in NH_3: effect of zeolite content

The electrical conductivity sensitivities of the composites versus zeolite content are shown in Fig. 5. Zeolite NaY was mixed into Pth_10:1 at various contents: 0, 10, 20, 30, 40 and 50% (v/v). For the zeolite content between 0 and 10% (v/v), the electrical conductivity sensitivity increases from $(1{\cdot}97 \pm 0{\cdot}01) \times 10^{2}$ to $(8{\cdot}53 \pm 0{\cdot}64) \times 10^{2}$ S cm^{-1}. For the zeolite content from 20 to 50% (v/v), the electrical conductivity sensitivity decreases from $(4{\cdot}68 \pm 0{\cdot}27) \times 10^{2}$ to $(1{\cdot}16 \pm 0{\cdot}79) \times 10^{2}$ S cm^{-1}, as shown in Fig. 5. The highest electrical conductivity sensitivity is obtained with the 10% (v/v) composite. The addition of a mesoporous material into a conductive polymer allows more NH_3 molecules to adsorb and diffuse into the composite thus promoting the NH_3–dPth interaction.[7] The decrease in the electrical conductivity sensitivity at higher zeolite contents (20–50%, v/v) is due to the reduction in the number of available active sites on the polymer chains for NH_3 to

Materials Technology mte171.3d 6/2/13 14:14:35
The Charlesworth Group, Wakefield +44(0)1924 369598 - Rev 7.51n/W (Jan 20 2003)

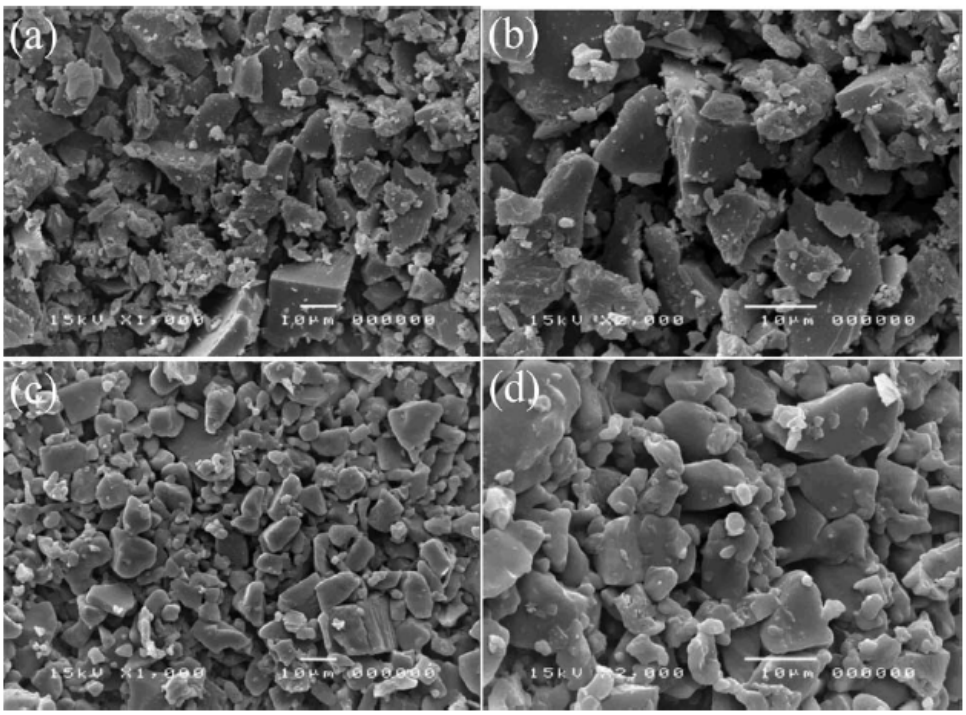

2 Images (SEM) of undoped Pth at magnifications of *a* ×1000 and *b* ×2000 and doped Pth_10:1 at magnifications of *c* ×1000 and *d* ×2000

interact.[15] Various poly(p-phenylene)/zeolite composites were studied by Phumman.[11] The sensitivity increased initially with increasing zeolite content from 0 to 30 vol.-%. Beyond the volume fraction of 40 vol.-% zeolite, the sensitivities decreased as the mechanically mixed systems contained the lesser number of active sites available on

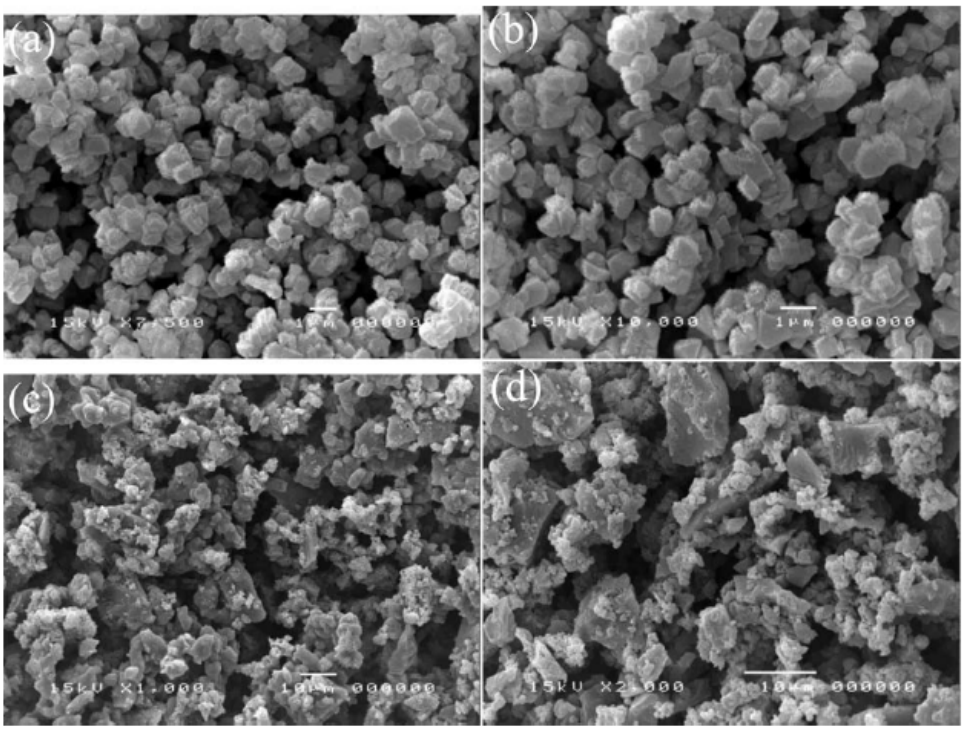

3 Images (SEM) of zeolite Y at magnifications of *a* ×7500 and *b* ×10 000 and Pth_10:1/Y_10% at magnifications of *c* ×1000 and *d* ×2000

Materials Technology mte171.3d 6/2/13 14:15:03
The Charlesworth Group, Wakefield +44(0)1924 369598 - Rev 7.51n/W (Jan 20 2003)

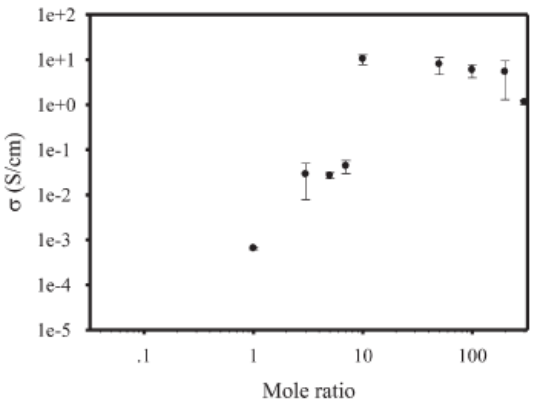

4 Specific conductivity (S cm^{-1}) of undoped and doped Pth with different mole ratios between $HClO_4$ and monomer unit

dPPP to interact with the target gas as zeolite content increased. The effect of zeolite content were measured by Yahiro.[12] The conductivities of zeolite/poly(tetrafluoroethylene) composite membranes increased with increasing zeolite content up to 80 wt-%. However, a further increase in zeolite content resulted in a decrease in electrical conductivity.

Electrical conductivity sensitivity of doped Pth and composites in NH_3: effect of Si/Al ratio

The electrical conductivity sensitivity of doped Pth is the interaction of doped Pth with ammonia molecules. Owing to the wider range of Si/Al ratio, H^+ form of zeolite Y was chosen to study the effect of Si/Al ratio on the electrical conductivity sensitivity and response. The zeolite HY at the Si/Al ratios of 5·1, 30, 60 and 80 were used to investigate the effect of Si/Al ratio on the electrical conductivity sensitivity towards NH_3. The 10% (v/v) zeolite content was used in all composites, since it is the optimum concentration for the highest response. The electrical conductivity sensitivities of the composites versus Si/Al ratio are shown in Fig 6. For Si/Al ratio between 5·1 and 80, the electrical conductivity sensitivity increases from $(4{\cdot}88 \pm 0{\cdot}94) \times 10^0$ to $(7{\cdot}46 \pm 3{\cdot}56) \times 10^2$ S cm^{-1}. The highest electrical conductivity sensitivity is obtained with Si/Al 80 of $(7{\cdot}46 \pm 3{\cdot}56) \times 10^2$ S cm^{-1}. This is due to the increase in the number of Si in the zeolite Y structure that facilitates the electrostatic interaction between oxygen of the SiO_2 molecule in the Zeolite Y and NH_3. The increasing electrostatic interaction between target gas and zeolite has been shown to improve the electrical conductivity sensitivity of the Pth/zeolite Y composites.[13] From the specific surface areas of the zeolites in Table 2, the Y zeolite with Si/Al 80 has the highest surface area. The higher surface area favourably induces the target gas to reside within the cavity, and the electrical conductivity sensitivity thus increases with increasing surface area.[13] The effect of Si/Al ratio of ZSM-5 zeolite were measured by Shirazi.[14] ZSM-5 zeolites with different molar ratios of Si/Al in the range of 10–50 were synthesised. The surface areas of the H-ZSM-5 were measured using BET method and their results showed that the surface area increased with increasing the Si/Al molar ratio. Table 1 shows

Table 1 Electrical conductivity responses $\Delta\sigma$ and electrical conductivity sensitivities $\Delta\sigma/\sigma_{N2}$ in NH_3 at 26±1°C and 1·1 atm: data shown are average values taken from at least two samples*

Sample	t_r/min	t_r/min	σ/S cm^{-1} Air	N_2	NH_3	$\Delta\sigma$/S cm^{-1}	$\Delta\sigma/\sigma_{N2}$	$\Delta\sigma_r$/S cm^{-1}
Pth_10 : 1	30	13	$(1{\cdot}31 \pm 0{\cdot}55) \times 10^{-4}$	$(3{\cdot}68 \pm 0{\cdot}12) \times 10^{-9}$	$(7{\cdot}28 \pm 0{\cdot}23) \times 10^{-7}$	$(7{\cdot}24 \pm 0{\cdot}23) \times 10^{-7}$	$(1{\cdot}97 \pm 0{\cdot}01) \times 10^{2}$	$(-7{\cdot}24 \pm 0{\cdot}23) \times 10^{-7}$
Pth_10 : 1/Y_Na_10	19	16	$(1{\cdot}32 \pm 1{\cdot}06) \times 10^{-6}$	$(4{\cdot}59 \pm 1{\cdot}42) \times 10^{-9}$	$(3{\cdot}23 \pm 0{\cdot}01) \times 10^{-6}$	$(3{\cdot}23 \pm 0{\cdot}01) \times 10^{-6}$	$(8{\cdot}53 \pm 0{\cdot}64) \times 10^{2}$	$(-3{\cdot}23 \pm 0{\cdot}01) \times 10^{-6}$
Pth_10 : 1/Y_Na_20	15	15	$(2{\cdot}39 \pm 1{\cdot}21) \times 10^{-8}$	$(3{\cdot}70 \pm 0{\cdot}004) \times 10^{-9}$	$(1{\cdot}73 \pm 0{\cdot}10) \times 10^{-6}$	$(1{\cdot}73 \pm 0{\cdot}10) \times 10^{-6}$	$(4{\cdot}68 \pm 0{\cdot}27) \times 10^{2}$	$(-1{\cdot}73 \pm 0{\cdot}10) \times 10^{-6}$
Pth_10 : 1/Y_Na_30	20	14	$(6{\cdot}33 \pm 0{\cdot}14) \times 10^{-7}$	$(3{\cdot}83 \pm 0{\cdot}12) \times 10^{-9}$	$(6{\cdot}40 \pm 1{\cdot}80) \times 10^{-7}$	$(6{\cdot}36 \pm 1{\cdot}80) \times 10^{-7}$	$(1{\cdot}66 \pm 0{\cdot}42) \times 10^{2}$	$(-6{\cdot}36 \pm 1{\cdot}80) \times 10^{-7}$
Pth_10 : 1/Y_Na_40	25	23	$(1{\cdot}51 \pm 0{\cdot}14) \times 10^{-6}$	$(4{\cdot}42 \pm 0{\cdot}27) \times 10^{-9}$	$(7{\cdot}77 \pm 3{\cdot}86) \times 10^{-7}$	$(7{\cdot}72 \pm 3{\cdot}86) \times 10^{-7}$	$(1{\cdot}72 \pm 0{\cdot}77) \times 10^{2}$	$(-7{\cdot}72 \pm 3{\cdot}87) \times 10^{-7}$
Pth_10 : 1/Y_Na_50	41	26	$(6{\cdot}78 \pm 2{\cdot}79) \times 10^{-6}$	$(5{\cdot}59 \pm 0{\cdot}85) \times 10^{-9}$	$(6{\cdot}23 \pm 3{\cdot}44) \times 10^{-7}$	$(6{\cdot}17 \pm 3{\cdot}45) \times 10^{-7}$	$(1{\cdot}16 \pm 0{\cdot}79) \times 10^{2}$	$(-6{\cdot}14 \pm 3{\cdot}42) \times 10^{-7}$
Pth_10 : 1/Y_H(5·1)_10	27	13	$(1{\cdot}02 \pm 0{\cdot}72) \times 10^{-8}$	$(3{\cdot}85 \pm 0{\cdot}09) \times 10^{-9}$	$(2{\cdot}26 \pm 0{\cdot}31) \times 10^{-8}$	$(1{\cdot}88 \pm 0{\cdot}32) \times 10^{-8}$	$(4{\cdot}88 \pm 0{\cdot}94) \times 10^{0}$	$(-1{\cdot}91 \pm 0{\cdot}31) \times 10^{-8}$
Pth_10 : 1/Y_H(30)_10	20	13	$(3{\cdot}02 \pm 0{\cdot}21) \times 10^{-8}$	$(4{\cdot}91 \pm 0{\cdot}47) \times 10^{-9}$	$(1{\cdot}60 \pm 0{\cdot}35) \times 10^{-8}$	$(1{\cdot}11 \pm 0{\cdot}40) \times 10^{-8}$	$(2{\cdot}31 \pm 1{\cdot}03) \times 10^{0}$	$(-2{\cdot}25 \pm 1{\cdot}78) \times 10^{-8}$
Pth_10 : 1/Y_H(60)_10	17	10	$(2{\cdot}67 \pm 0{\cdot}28) \times 10^{-8}$	$(3{\cdot}74 \pm 0{\cdot}14) \times 10^{-9}$	$(2{\cdot}64 \pm 1{\cdot}29) \times 10^{-8}$	$(2{\cdot}27 \pm 1{\cdot}31) \times 10^{-8}$	$(6{\cdot}13 \pm 3{\cdot}72) \times 10^{0}$	$(-2{\cdot}28 \pm 1{\cdot}30) \times 10^{-8}$
Pth_10 : 1/Y_H(80)_10	13	12	$(3{\cdot}81 \pm 0{\cdot}50) \times 10^{-7}$	$(3{\cdot}48 \pm 0{\cdot}14) \times 10^{-9}$	$(2{\cdot}59 \pm 1{\cdot}22) \times 10^{-6}$	$(2{\cdot}59 \pm 1{\cdot}22) \times 10^{-6}$	$(7{\cdot}46 \pm 3{\cdot}56) \times 10^{2}$	$(-2{\cdot}59 \pm 1{\cdot}22) \times 10^{-6}$

*t_r=induction time, t_r=the recovery time, σ=the electrical conductivity in air, N_2 and NH_3 and the electrical response ($\Delta\sigma$), the electrical conductivity recovery ($\Delta\sigma_r = \sigma_{N2\ final} - \sigma_{NH3}$), electrical conductivity sensitivity ($\Delta\sigma/\sigma_{N2\ initial}$)

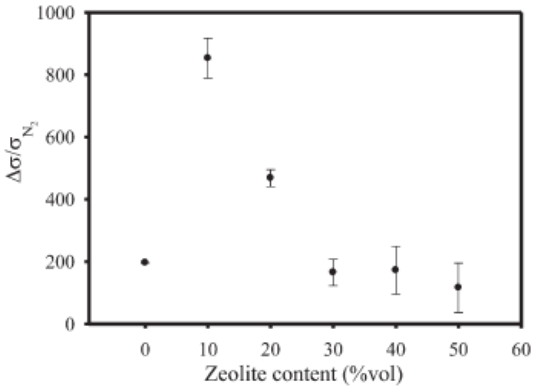

5 Electrical conductivity sensitivity ($\Delta\sigma/\sigma_{N2}$) versus zeolite content (vol.-%) of 10:1 dPth/NaY composites when exposed to NH_3 at 26±1°C and at 1·1 atm: data shown were obtained from at least two samples

the temporal response times of the composites studied: Pth_10: 1/Y_H(5·1)_10, Pth_10: 1/Y_H(30)_10, Pth_10: 1/Y_H(60)_10 and Pth_10: 1/Y_H(80)_10. Their temporal response times are 27, 20, 17 and 13 min respectively. This indicates that a zeolite with more Si can interact with and trap NH_3 molecules more effectively through the dipole–dipole interaction resulting in a shorter response time.[16] The recovery times of the composites are in the same range (10–13 min), suggesting that the Si/Al does not plays an important role during the gas desorption.

Investigations of interactions of adsorbed NH_3 by FTIR

The interaction of the active sites of Pth_10:1 and zeolite NaY with NH_3 were investigated by FTIR spectroscopy at 26±1°C and under pressure 1·1 atm. FTIR spectra were taken by the KBr pellet technique. The sample pellet was placed on a sample holder and put it into the gas cell. The spectrums of samples were recorded, before NH_3 exposure, when exposed to NH_3, and after the NH_3 exposure, in order to study the interaction between these samples and NH_3, as shown in Figs. 6 and 7.

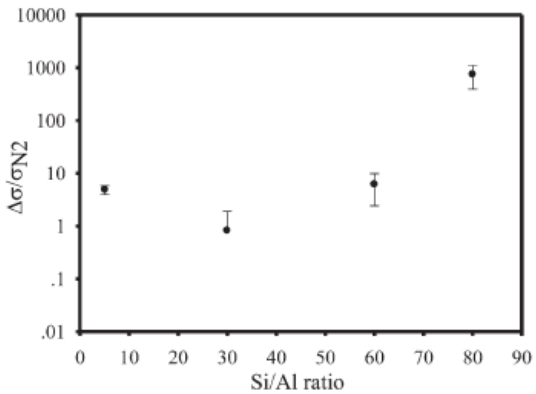

6 Electrical conductivity sensitivity ($\Delta\sigma/\sigma_{N2}$) versus Si/Al ratios of 10:1 dPth/HY composites when exposed to NH_3 at 26±1°C and at 1·1 atm: data shown were obtained from at least two samples

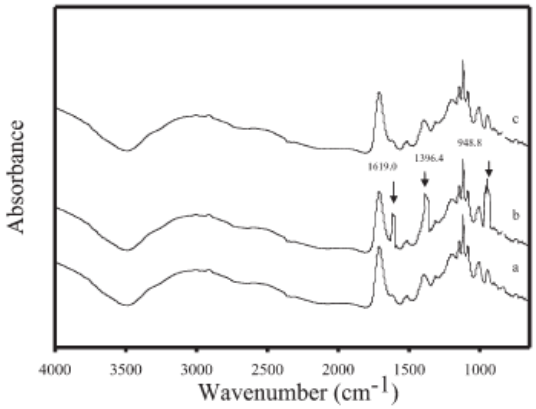

7 Spectra (FTIR) of Pth_10:1 *a* before, *b* during and *c* after exposure to NH_3

When exposed to NH_3, FTIR spectra were taken every 5 min for 45 min, each FTIR spectrum has the same patterns but with different intensities evolving in time. Peaks at 948·8 and 1619·0 cm^{-1} can be assigned to the vibrations of NH_3 molecules, and a peak at 1396·5 cm^{-1} belongs to the vibration of NH_4^+ molecules.[17] After NH_3 is replaced with N_2, the bands at 948·8, 1396·5 and 1619·0 cm^{-1} disappear from the FTIR spectra. Therefore, the interaction of NH_3 and doped Pth is reversible, as shown in Fig. 7.

From the FTIR spectra of NaY zeolite before, during and after the NH_3 exposure. The bands at 963·2 cm^{-1} appear when the exposed to NH_3, but disappear when NH_3 is replaced by N_2. This peak shift from 968·09 cm^{-1} represents the Lewis sites of NH_3 molecules.[11] The IR spectrum shows a new peak at 3332 cm^{-1} which can be assigned to NH_4^+ interacting with oxygen on the Y zeolite.[18] Figure 8 shows that there is no significant difference in the band patterns before and after exposure to NH_3, therefore the interaction between NH_3 and the NaY zeolite is reversible based on the FTIR spectrum. The sensitivity of polyaniline (PANI) films to ammonia has been investigated. When PANI is interacting with ammonia, ammonia molecules take up protons from PANI, forming ammonium, NH_4^+. However, in air, ammonium decomposes into ammonia and protons which restores the initial level of doping. In such a way, reversibility of the ammonia effect on PANI layers occurs.[15]

Conclusions

The effects of acid dopant ratio, zeolite content and Si/Al ratio on the electrical conductivity response of Pth

Table 2 Surface areas of zeolite Y

		Surface area/m^2 g^{-1}		
Cation type	Si/Al ratios	1	2	AVG
Na^+	5·1	611·0	640·0	625·5±20·5
NH_4^+	5·1	594·3	583·2	588·8±7·8
H^+	5·1	601·2	633·3	617·3±22·7
H^+	30	634·9	742·6	688·8±76·1
H^+	60	713·9	748·1	731·0±24·2
H^+	80	768·4	763·8	766·1±3·2

Materials Technology mte171.3d 6/2/13 14:15:49
The Charlesworth Group, Wakefield +44(0)1924 369598 - Rev 7.51n/W (Jan 20 2003)

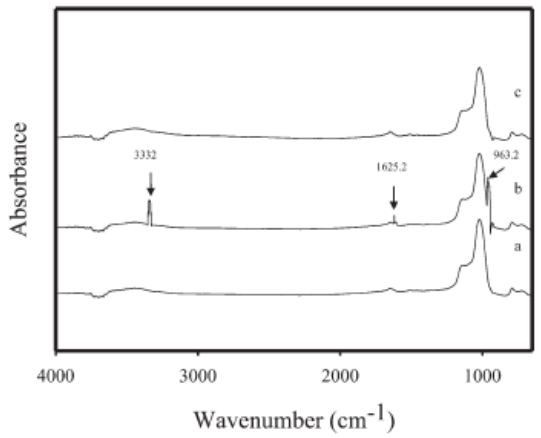

8 Spectra (FTIR) of zeolite NaY *a* before, *b* during and *c* after exposure to NH_3

and composites, when exposed to NH_3 were investigated. Doped Pth at 10:1 has the highest electrical conductivity. The electrical conductivity sensitivity of the composites towards NH_3 is improved with the addition of the Y zeolite up to 10% (v/v). From 20 to 50% (v/v) of zeolite Y, the electrical conductivity sensitivity decreases due to the diminishing of the active sites that available for the interaction between NH_3 and the polaron or the bipolaron species. The electrical conductivity sensitivity ($\Delta\sigma/\sigma_{N2}$) increases linearly with increasing Si/Al ratio. The larger number of Si in the Y zeolite structure facilitates the electrostatic interaction between oxygen on the Si molecule in the zeolite Y and NH_3. The interaction between NH_3 and the doped Pth is reversible based on the FTIR spectra. The zeolite concentration and the Si/Al ratios of zeolite can affect the electrical conductivity response of the composites toward ammonia. These results demonstrate an improvement of the electrical conductivity response of the composites which can be used as a high performance sensing material.

Acknowledgements

The first author is grateful for the scholarship and the funding of the work by the Petroleum and Petrochemical College. The authors acknowledge the financial supports from the Thailand Research Fund (TRF-RTA), the Conductive and Electroactive Research Unit of Chulalongkorn University, and the Royal Thai Government.

References

1. B. Brantley: 'Characterization of nanocomposite materials for ammonia gas sensor application', University of South Florida, Tampa, FL, USA, 2004.
2. H. Bai and G. Shi: *Sensors*, 2007, **7**, 267–307.
3. T. Puvanatvattana, D. Chotpattananont, P. Hiamtup, S. Niamlang, R. Kunanuruksapong, A. Sirivat and A.M. Jamieson: *Mater. Sci. Eng. C*, 2008, **C28**, 119–128.
4. X. F. Ma, G. Li, H. Xu, M. Wang and H. Chen: *Thin Solid Films*, 2006, **515**, 2700–2704.
5. C. Chuapradit, R. Wannatong, D. Chotpattananont, P. Hiamtup, A. Sirivat and J. Schwank: *Polymer*, 2005, **46**, 947–953.
6. B. S. Kim, L. Chen, J. Gong and Y. Osada: *Macromolecules*, 1999, **32**, 3964–3969.
7. K. Thuwachaowsoan, D. Chotpattananont, A. Sirivat, R. Rujiravanit and J. W. Schwank: *Mater. Sci. Eng. B*, 2007, **B140**, 23–30.
8. D. Chotpattananont, A. Sirivat and A. M. Jamieson: *Colloid Polym. Sci.*, 2004, **282**, 357–365.
9. T. A. Chen, X. Wu and R. D. Rieke: *J. Am. Chem. Soc.*, 1995, **117**, 233–244.
10. B. C. Norma and P. K. Dutta: *J. Phys. Chem. B*, 2001, **105B**, 1537–1542.
11. P. Phumman, S. Niamlang and A. Sirivat: *Sensors*, 2009, **9**, 8031–8046.
12. H. Yahiro, Y. Konda and G. Okada: *Phys. Chem. Chem. Phys.*, 2003, **5**, 620–623.
13. B. Soontornworajit, L. Wannatong, P. Hiamtup, S. Niamlang, D. Chotpattananont, A. Sirivat and J. Schwank: *Mater. Sci. Eng. B*, 2007, **136B**, 78–86.
14. L. Shirazi, E. Jamshidi and M. R. Ghasemi: *Cryst. Res. Technol.*, 2008, **43**, 1300–1306.
15. A. Zecchina, L. Marchese, S. Bordig, C. Paze and E. Gianotti: *J. Phys. Chem. B*, 1997, **101B**, 10128–10135.
16. N. Densakulprasert, L. Wannatong, D. Chotpattananont, P. Hiamtup, A. Sirivat and J. Schwank: *Mater. Sci. Eng. B*, 2005, **117B**, 276–282.
17. F. Yin, L. Blumenfeld, V. Gruver and J. J. Fripait: *J. Phys. Chem. B*, 1997, **101B**, 1824–1830.
18. A. Zecchina, F. Geobaldo, C. Lamberti, G. Ricchiard, S. Bord and P. G. Turnes Palomino: *J. Phys. Chem.*, 1996, **100**, 18883.

Materials Technology mte171.3d 6/2/13 14:15:56
The Charlesworth Group, Wakefield +44(0)1924 369598 - Rev 7.51n/W (Jan 20 2003)

Effect of Transition Metal Ion-Exchanged into the Zeolite Y on Electrical Conductivity and Response of PEDOT-PSS/MY Composites toward SO_2

POJJAWAN CHANTHAANONT, ANUVAT SIRIVAT

Conductive and Electroactive Polymers Research Unit, The Petroleum and Petrochemical College, Chulalongkorn University, Bangkok 10330, Thailand

Correspondence to: Anuvat Sirivat; email: anuvat.s@chula.ac.th.

Received: February 11, 2013
Accepted: May 29, 2013

ABSTRACT: This study aims to investigate and compare the effects of different divalent transition metal cations (M^{2+}: Mn^{2+}, Fe^{2+}, Co^{2+}, Ni^{2+}, Cu^{2+}, and Zn^{2+}) exchanged into the hydrated zeolite Y on the electrical conductivity and sensitivity response of Poly(3,4-ethylenedioxythiophene) doped with poly(styrene sulfonic acid), PEDOT-PSS/MY composites, when exposed to sulfur dioxide. All composites show higher electrical sensitivity values and significantly longer response times than the pristine conductive polymer matrix. The results obtained can be attributed to the electronegativity of the transition metal cations exchanged into the zeolite Y micropores, which critically affects the adsorption properties of the zeolite Y, and which in turn influences the electrical sensitivity of the composites. The highest electrical conductivity response and sensitivity pertain to the PEDOT-PSS/MnY composite. All composites investigated show nearly reversible responses toward sulfur dioxide. © 2013 Wiley Periodicals, Inc. Adv Polym Technol 2013, 32, 21367; View this article online at wileyonlinelibrary.com. DOI 10.1002/adv.21367

KEY WORDS: Conducting polymers, Gas sensors, Poly (3, 4-ethylenedioxythiophene), Sulfur dioxide, Zeolite Y

Introduction

The main purposes of improving gas sensors are faster response, higher sensitivity, reproducibility, and superior long-term stability. One of the possible directions is to combine two or more materials that have distinct but collaborative properties[1–3]. An advantage of this approach is the unique property obtained from the fabricated composite materials. Gas-sensing materials using conductive polymers with or without modifiers are promising as they can be fine-tuned for the electrical conductivity response towards particular gases or vapors. The fillers employed may include several metals or metal oxides[4,5], carbon nanotubes[6], graphene[7], insulating polymers[8], clays[9], and zeolites[10–13]. Polymer/zeolites composites with improved sensor responses have been reported for gas detections[10–13]. Sensitivity response and interaction mechanisms between polypyrrole/ zeolite 13X composites and CO_2, CO, and SO_2 were investigated[10]. Zeolite 13 X has been shown to promote the interaction between SO_2 and polypyrrole[10].

Contract grant sponsor: Conductive and Electroactive Polymers Research Unit of Chulalongkorn University Ratchadaphiseksomphot Endowment Fund. Contract grant sponsor: Thailand Research Fund, The Royal Thai Government. Contract grant number: TRF-RTA and PhD/0082/2550.

The aim of this study is to investigate the gas-sensing properties and the sensitivity improvement of conductive polymer/zeolite composites as gas-sensing materials for sulfur dioxide detection. PEDOT-PSS was utilized as the semiconductor since its electrical conductivity response can be altered and is measurable when exposed to various gases[12]. Zeolite Y microporous material was chosen to improve the sensitivity to sulfur dioxide. Zeolite Y with its exchangeable cations possesses more weak bonds to the adjacent atoms than the framework ions, thus enhancing their mobility. Their electrical conductivity is influentially affected by the mobility of existing cations in zeolite micropores[14,15]. The conductivity of zeolite strongly depends on the content of water into the channels[16]. Moreover, ionic conduction of zeolite could be considerably enhanced at high-pressure treatment in water medium, and subsequent isolation to preserve the overhydrated structure[17].

In the present work, ion-exchanged zeolite NaY, with various transition metal cations, was obtained through the ion-exchange process. PEDOT-PSS/ zeolite Y composites with different transition-metal ions were fabricated. The electrical conductivity and sensitivity values of PEDOT-PSS, zeolite Y, and their composites under exposure to sulfur dioxide were measured, analyzed, and compared. Experimental results and discussion are presented here concerning the effects of zeolite content (v/v %) and cation type of zeolite Y on electrical conductivity and sensitivity response of PEDOT-PSS/zeolite Y composites,

© 2013 Wiley Periodicals, Inc.

when exposed to sulfur dioxide. The gas-sensing mechanisms of the composites with sulfur dioxide are proposed.

Experimental

MATERIALS

The 3,4-ethylenedioxythiophene, EDOT (AR grade, Aldrich), was used as the monomer. Poly (styrene sulfonic acid), PSS, was used as the dopant. Sodium persulfate, $Na_2S_2O_8$ (AR grade, Aldrich, Singapore) was used as the oxidant. Zeolite Y samples (NaY with Si/Al = 5.1, hydrated form) in a powder form were purchased from Zeolyst (Kansas City, MO). Sulfur dioxide (Thai Industrial Gas Public Co., Ltd., Bangkok, Thailand; 1000 ppm in N_2) and Nitrogen (TIG, 99% purity) were used as the target gases.

POLYMERIZATION OF POLY(3,4-ETHYLENEDIOXYTHIOPHENE)

The chemical polymerization of PEDOT-PSS was followed from the procedures as reported previously[18]. PEDOT-PSS at 1:1 mole ratio of EDOT:PSS was prepared by adding EDOT monomers to an aqueous solution of PSS and $Na_2S_2O_8$. After an initial stirring at room temperature for 10 min, $Fe_2(SO_4)_3$ was added and the mixture was stirred vigorously for 24 h. The obtained dark aqueous PEDOT-PSS mixture was purified by the ion exchanging with ion-exchange resins (Lewatit, M600 and S100), resulting in a dark blue aqueous PEDOT-PSS solution. The PEDOT-PSS film was obtained by casting the aqueous PEDOT-PSS solution at 100°C for 24 h in a vacuum oven.

PREPARATION OF ION-EXCHANGE ZEOLITES

The M^{2+} zeolites studied in this work are zeolite Y (Zeolyst, Si/Al = 5.1, hydrated form) with different compensating cations (Mn^{2+}, Fe^{2+}, Co^{2+}, Ni^{2+}, Cu^{2+}, and Zn^{2+}). The Mn^{2+}, Fe^{2+}, Co^{2+}, Ni^{2+}, Cu^{2+}, and Zn^{2+}-exchanged zeolite Y were carried out using the conventional ion-exchange procedures[19]. Zeolites NaY was used as the starting material for the ion exchange. For ion-exchanged zeolites, 1 g of the zeolite NaY was added to 25 mL of 0.1 M metal chloride solution at room temperature and stirred for 24 h. The modified zeolite was filtered and washed with distilled water to remove Cl^- ions followed by drying at 100°C in air for 24 h.

COMPOSITE PREPARATION

PEDOT-PSS powder was ground, sieved with a 38-μm sieve, and then dried at 100°C prior to being mechanically mixed with dried zeolite Y powders at various zeolite amounts (v/v %). The v/v % means the percentage of the zeolite Y volume over that of the PEDOT-PSS polymer. The weights of the zeolite Y and the PEDOT-PSS were measured before fabrication. The mixtures were obtained by compressing with a hydraulic press machine at a pressure of 6 kN into a thin disc with a diameter of 10 mm and a nominal thickness of 1 mm.

CHARACTERIZATION

A Fourier transform infrared spectrometer (FT-IR Nicolet, Nexus 670) with a resolution of 4 cm^{-1} and 32 scans was used to characterize functional groups. The thermal stability of PEDOT-PSS was investigated by using a thermogravimetric analyzer (Dupont, TGA 2950) with a heating rate of 10°C/min under O_2 atmosphere. A scanning electron microscope (SEM JEOL, JSM 5200) was used to observe the morphology of PEDOT-PSS, zeolites, and PEDOT-PSS/zeolite composites in a powder form. An X-ray diffractometer (XRD Phillips, Rigaku) was used to examine the degree of crystallinity of PEDOT-PSS and the crystal order of the zeolites. The surface area, the pore width, and the pore volume of zeolite Y were measured using a surface area analyzer (Sorptomatic-1990). The percentage of ion exchange was measured for each zeolite Y sample by the inductively coupled plasma technique (Perkin-Elmer/ Optima 4300DV).

ELECTRICAL CONDUCTIVITY MEASUREMENT AND GAS DETECTION

The electrical conductivity values of PEDOT-PSS, zeolite Y, and their composites under exposure to air, N_2, and SO_2 were measured in a special gas cell. It consisted of two stainless steel chambers connected in series. The first and the second chamber were called the mixing and measurement chambers, respectively. The temperature controllers, connecting to both chambers, were used to monitor and control the temperature within the gas chambers. The second chamber contained two custom-built two-point probe meters connected to a voltage supplier (Keithley, 6517A) for applying a constant voltage source and recording a resultant current. The specific conductivity σ (S/cm) values of the pellets were obtained by measuring the bulk pellet resistance R (Ω). The relation $\sigma = (1/Rt)(1/K) = (I/Vt)(1/K)$ was used to calculate the specific electrical conductivity, where t is the pellet thickness (cm), I is the resultant current (A), V is the applied voltage (V), and K is the geometric correction factor which is equal to the ratio w/l, where w and l are the probe width and the length, respectively. The geometrical correction factor (K) was determined by calibrating the custom-built two-point probe with semiconducting silicon sheets of known resistivity values. Electrical conductivity values of several samples were first measured at various applied DC voltages to identify their linear Ohmic regimes. The electrical conductivity response ($\Delta\sigma$) and sensitivity (S) of the composites are defined by the following equation $\Delta\sigma = \sigma_{SO_2} - \sigma_{N_2}$ and $S = \Delta\sigma/\sigma_{N_2}$, respectively. σ_{N_2} and σ_{SO_2} are the electrical conductivities of the composite in N_2 and the target gas SO_2, respectively.

Results and Discussion

CHARACTERIZATION OF PEDOT-PSS, Y ZEOLITE, AND COMPOSITES

PEDOT-PSS was synthesized by the polymerization of EDOT in an aqueous solution of PSS using $S_2O_8^{2-}$ as the oxidant. From the FT-IR spectrum of PEDOT-PSS, the peaks at 1520 and

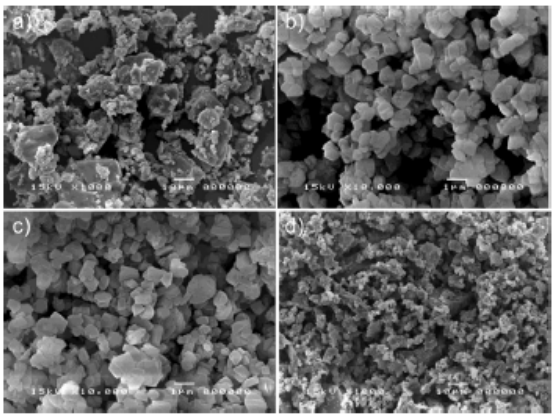

FIGURE 1. Morphology of PEDOT-PSS particles, Zeolite Y powders, and PEDOT-PSS/Zeolite Y composites: a) PEDOT-PSS at 1000×; b) Zeolite MnY at 10,000×; c) Zeolite CuY at 10,000×; and d) PEDOT-PSS/MnY at 1000×.

1339 cm^{-1} can be assigned to the C=C and the C–C stretchings of the thiophene ring[20–23] and the peaks at 929 and 834 cm^{-1} correspond to the symmetric vibration of C–S bond in the thiophene ring[20,21,23]. The peaks at 1127 and 1039 cm^{-1} are assigned to the stretching mode of the ethylenedioxy group[20,21,23] and the peaks at 1198 and 929 cm^{-1} correspond to the $-SO_3^-$ and the S–OH stretchings of the PSS molecule[20,23,24]. The vibration of the bending mode of the C–H bond in EDOT monomer (~892 cm^{-1}) is not present[20,23]. This result confirms the formation of PEDOT molecular chains. The absorption peak at 1645 cm^{-1} can be assigned to the oxidation state of PEDOT, which indicates the successful doping of PEDOT polymer with PSS. In summary, the FT-IR spectrum data indicate the successful formation of PEDOT molecular chains doped with the PSS counterion. Four transitions can be observed in the PEDOT-PSS thermograms: 30°C–110°C, 160°C–380°C, 380°C–550°C, and 560°C–900°C; they can be referred to as the loss of water, the side chain degradation, and the polymer backbone degradations of PSS and PEDOT, respectively[18,23]. From XRD patterns of PEDOT-PSS, no characteristic peak is observed by X-ray diffraction; the broad scattering background indicates the amorphous nature of the materials[23,25]. The mean particle diameter of PEDOT-PSS_1:1 was determined to be approximately 34 ± 0.22 μm. The micrograph in Fig. 1 of PEDOT-PSS particles shows rough surfaces and irregular shapes; they are moderately dispersed. The density of PEDOT-PSS_1:1 is 1.4750 ± 0.0003 g/cm^3. The electrical conductivity of PEDOT-PSS in air and nitrogen atmosphere is (1.169 ± 0.003) × 10^1 S/cm and (1.123 ± 0.001) × 10^1 S/cm, respectively.

Zeolite Y was modified by the ion-exchanged process with various divalent transition metal cations (Mn^{2+}, Fe^{2+}, Co^{2+}, Ni^{2+}, Cu^{2+}, and Zn^{2+}) with approximately 80% exchanged (Table I). Observation of the SEM of pure zeolite Y and the modified zeolite Y indicates that the morphology of modified zeolite Y has not changed after the modification process. The transition metal cation exchange does not markedly affect the main structure of zeolite Y[26,27]. Zeolite Y particles possess irregular crystal shapes and expose themselves to be inhomogeneously dispersed in the conductive polymer matrix of the composites (Fig. 1).

The X-ray diffractogram of all zeolite Y samples exhibits the characteristic peaks of the zeolite Y framework, that it is highly crystalline in the range of 5° to 60°. Comparison of X-ray diffraction patterns of the transition metal cation exchanged zeolite Y to the starting zeolite NaY shows no notable alterations in the crystalline structure of the zeolite during the modification process (Fig. 2). Due to the low content and high dispersion of transition metal cations exchanged, there is no significant change of diffraction lines observed after modification[28,29]. The mean particle diameters of Mn^{2+}, Fe^{2+}, Co^{2+}, Ni^{2+}, Cu^{2+}, and Zn^{2+}-exchanged zeolite Y (Si/Al mole ratios equal to 5.1) are 500 nm approximately.

The specific surface areas, the pore width, and the pore volume of zeolite Y (Si/Al = 5.1) of MnY, FeY, CoY, NiY, CuY, and ZnY are tabulated in Table I. Comparison with the starting zeolite NaY shows that the trasition metal cation exchanged zeolite exhibits a greater pore volume. The Brunauer, Emmett and Teller (BET) surface area and pore volume are exactly consistent with the cationic size, that is, in the order of MnY > FeY > CoY > ZnY > NiY > CuY. The BET surface area and pore volume increase as the transition metal cation size decreases. This result suggests that the smaller ion occupies less pore space, resulting in more available adsorbing sites.

The electrical conductivity data in N_2, for the Y zeolites with different cation types, are tabulated in Table I. The CuY zeolite has the smallest charge-balancing cation (0.69 Å) exhibiting the

TABLE I
Physicochemical Properties of Zeolite Y

Zeolite structure	NaY[a] FAU	MnY FAU	FeY FAU	CoY FAU	NiY FAU	CuY FAU	ZnY FAU
Pore size[b] (nm)	0.74 × 0.74	0.74 × 0.74	0.74 × 0.74	0.74 × 0.74	0.74 × 0.74	0.74 × 0.74	0.74 × 0.74
Surface area (m^2/g)	800	811	833	819	836	867	842
Pore volume (cm^3/g)	0.2476	0.2645	0.2694	0.2689	0.2706	0.2856	0.2761
Cation exchange (%)	–	84	85	83	84	85	86
Cation ionic radius (Å)	0.97	0.91	0.83	0.82	0.78	0.69	0.74
EN of cation (Pauling)	0.93	1.55	1.83	1.88	1.91	1.90	1.65
Atomic number	11	25	26	27	28	29	30
σ (10^{-3} S/cm)[c]	2.69 ± 0.417	2.30 ± 0.428	2.18± 0.378	2.01 ± 0.765	1.77 ± 0.567	1.59 ± 0.146	1.83 ± 0.186

[a]Zeolite based for cation exchange process.
[b]Data from Zeolyst.
[c]DC electrical conductivity (σ) calculated from two-point probe measurement.

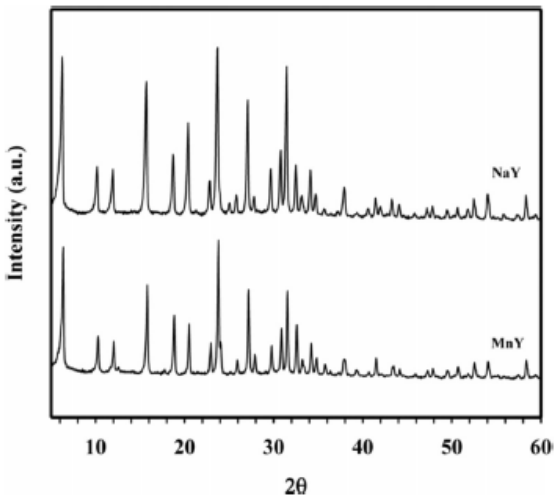

FIGURE 2. X-ray diffraction patterns of zeolites NaY and MnY.

lowest electrical conductivity. Inversely, the MnY zeolite has the highest electrical conductivity due to the larger cation radius (0.91 Å) which induces the reduction of electrostatic interaction with the anionic framework sites and the ease in which a cation can move from one site to another[14,15]. Although, the transition metal cation exchanged zeolite Y has a greater pore volume than starting zeolite NaY (EN = 0.93). The higher elecrtronegativity of transition metal cations (EN = 1.55–1.91) significantly affects the electrical conductivity of the modified zeolite Y, and the lower the electrical conductivity can be observed.

ELECTRICAL CONDUCTIVITY RESPONSE TO SO_2

Effect of Zeolite Content

The electrical sensitivity values of PEDOT-PSS_1:1 and its composites with the zeolite Y when exposed to air, N_2, and SO_2 were measured under chamber temperature of 27 ±1°C, and at 1 atm. The electrical conductivity sensitivity values of the PEDOT-PSS/NaY composites in 1000 ppm SO_2/N_2 versus Y zeolite content is shown in Fig. 3. All composites exhibit negative responses to SO_2. The sensitivity value of PEDOT-PSS/NaY increases as zeolite NaY content increases from 0% to 20%, an obvious evidence for the induced interaction. Beyond this volume fraction, the sensitivity value decreases as the zeolite NaY content increases from 20% and 50%, respectively. As more zeolite NaY is added, its presence also prohibits the direct contact area between SO_2 and PEDOT, and consequently a lower response or sensitivity. This result suggests that the composite with a proper zeolite content can be applied as an enhanced sensor material. The addition of a zeolite to a pure polymer at an optimal combination can promote the electrical conductivity response of the composites[10–13].

Effect of Cation Type

The electrical conductivity sensitivity values of PEDOT-PSS/MY composites in 1000 ppm SO_2/N_2 versus zeolite Y content are shown in Fig. 4. In the present work, it is shown that the cation type in the zeolite Y influences the gas-adsorption characteristics of the composites and can alter the electrical conductivity and sensitivity response of the composites toward SO_2. Ion-exchanged transition metal cations in the zeolite Y do not affect the main structure of the zeolite Y framework[14,15]. The presence of the exchanged transition metal cations increases the adsorbing sites in zeolite micropores. Hence, target gases have more available active sites resulting in more adsorbed target gas molecules to interact with the polymer matrix[10–13]. The electrical sensitivity of PEDOT-PSS/MY can be observed to be consistent with the ionic radii of the transition metal cations on zeolite Y in the order of MnY > FeY > CoY > NiY > CuY < ZnY (the order of transition metals in the sequence is the same as in the periodic table). Thus, the PEDOT-PSS/MnY has the highest electrical sensitivity due to their lesser interaction with SO_2. These results suggest that the electrostatic interaction exists between the transition metal cations and the target gases and it should be correlated with the ionic potential[14,15]. The exchanged

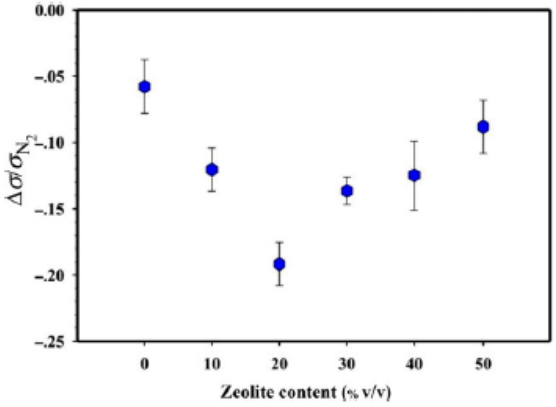

FIGURE 3. The electrical conductivity sensitivity of PEDOT-PSS_1:1 and PEDOT-PSS_1:1/Zeolite NaY composites at various contents: 0%, 10%, 20%, 30%, 40%, and 50% (v/v) when exposed to SO_2 at 27±1°C and 1 atm.

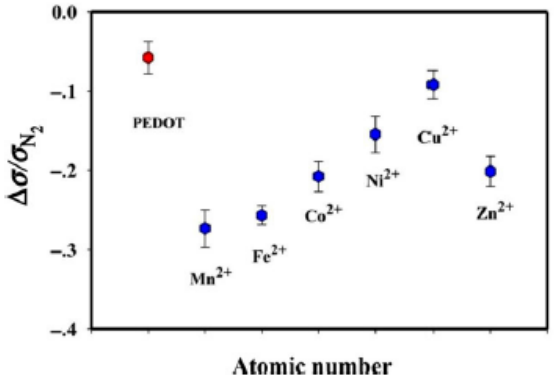

FIGURE 4. The electrical conductivity sensitivity of PEDOT-PSS and PEDOT-PSS/Zeolite Y composites with various transition metal cation type: Mn^{2+}, Fe^{2+}, Co^{2+}, Ni^{2+}, Cu^{2+}, and Zn^{2+} (20% v/v) when exposed to SO_2 at 27 ± 1°C and 1 atm.

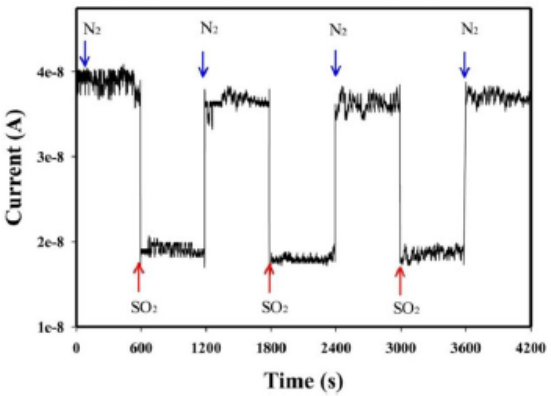

FIGURE 5. Responses of PEDOT-PSS/MnY composite when exposed to N_2 (recovery) and SO_2 (sensing) at 27 ± 1°C and 1 atm.

transition metal cation with a radius, the lesser metal–SO_2 interactions, and then the target gas can move more easily and consequently a greater interaction between SO_2 and the active sites on the PEDOT polymer chain. PEDOT-PSS/ZnY composites have a higher electrical sensitivity than PEDOT-PSS/NiY and PEDOT-PSS/CuY composites, but lower than that of the other composites. This consequence is not consistent with the sequence in the periodic table. This should be due to the lower electronegativity of Zn^{2+}, Ni^{2+}, and Cu^{2+}, respectively. The out-of-line position of the electrical sensitivity of PEDOT-PSS/CuY is a consequence of the fact that Cu^{2+} often forms a very strong interaction with others molecules due to its smallest size, and with a high electronegativity value (ionic radius = 0.69 Å and EN = 1.90)][30,31].

The temporal response time is the time required for the electrical conductivity value to rise from its initial value in N_2 towards the equilibrium value when exposed to SO_2[1]. The recovery time is the time required for the electrical conductivity value return to initial value after the step removal of SO_2. By adding the zeolite Y, a longer response time and recovery time are observed, and the response time and recovery time increase with the decreasing cation size of the zeolite Y. The response time of PEDOT-PSS/CuY is longer than that of PEDOT-PSS and those of the other composites (14.1 min), corresponding to the higher density of the adsorption sites available for SO_2 molecules and the greater ion–quadrupole interactions with SO_2. The shortest temporal response and recovery time is obtained from PEDOT-PSS/MnY due to the weaker interaction between SO_2 molecules and the MnY zeolite (8.2 min), which allows SO_2 molecules to diffuse away from the composites. The addition of the Y zeolite is thus shown to enhance the interaction between PEDOT-PSS and SO_2 molecules; the zeolite improves the sensitivity of the pristine PEDOT-PSS but at the expense of a longer response time[10–13].

The PEDOT-PSS/MY composite is examined in three sensing cycles by repeating the sensing and recovery process to examine the reversibility and reproducibility of the composite responses. The conductivity of the PEDOT-PSS/MnY composite, possessing the highest sensitivity for SO_2 gas, is shown in Fig. 5 as a function of time when exposed to three cycles of a sequence of the SO_2 exposure (sensing), evacuation, and under the N_2 atmosphere (recovery). During the recovery process, the conductivity of the composites nearly recovers the initial value; this suggests that the sensing characteristics are quite reproducible.

THE PROPOSED MECHANISM OF SO_2 ADSORPTION IN PEDOT-PSS AND Y ZEOLITES

An observed electrical conductivity decrease can be attributed to the charge transfer due to the chemical nature of SO_2 gas. The conductivity of the conductive polymer is known to be due to the product between the charge-carrier concentration and the charge-carrier mobility along the polymer backbone. The reduction in the charge-carrier concentration on the backbone of *p*-type PEDOT polymer occurs upon the electron transfer from SO_2 to the positive-charged sulfur site on the polymer backbone. Therefore, the charge-carrier concentration along the polymer backbone decreases resulting in the electrical-conductivity decrease (Fig. 6). The electrical conductivity of all composites return almost completely to their baselines after SO_2 is evacuated and replaced by N_2. This result suggests that the interaction that occurs between SO_2 and the composites is weak. This also

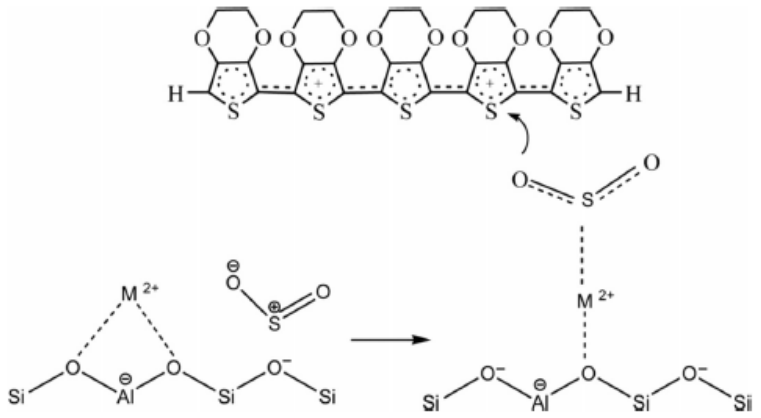

FIGURE 6. A schematic diagram indicating the possibility of electrostatic interactions between SO_2, Zeolite Y, and PEDOT-PSS.

suggests that the interaction between SO_2 and MnY is not permanent. Most importantly, the interaction between SO_2 and the zeolite Y takes place through the basic oxygen centers of the Si–O–Al fragment. An oxygen atom can form a bond with the sulfur atom of an SO_2 molecule via the donor–acceptor interaction. In addition to the charges on oxygen, other zeolite sites also interact with SO_2, namely the bridging metal center via the ion–dipole interaction[32].

CONCLUSIONS

An adjusted combination of the composite between PEDOT-PSS and zeolite Y produces some remarkable changes in the composite electrical conductivity response. The composite at 20% (v/v) of the zeolite Y content provides the highest sensitivity to SO_2. The results suggest that the addition of the zeolite Y to the pristine polymer PEDOT-PSS at the optimized combination can promote the electrical sensitivity response of the composites to SO_2 gas. The metal cation in the zeolite Y intimately induces a synergism to adsorb SO_2, but at the expense of the longer response and recovery time. The highest electrical sensitivity response pertains to the PEDOT-PSS/MnY composite. The exchange of transition metal cations can enlarge the pore volume of zeolites. Therefore, the target gas SO_2 can further introduce to interact with PEDOT-PSS polymer. In the presence of the transition metal cations, with respect to the zeolite micropores, the cations can influence the adsorption properties of the system. The electrical sensitivity of the composite can be correlated with the electronegativity of the transition metal cations of the cation-exchanged zeolite Y. The reproducibility of the composite response can be observed and the response is nearly reversible at room temperature.

References

1. Bai, H.; Shi, G. Sensors 2007, 7, 267.
2. Adhikari, B.; Majumdar, S. Prog Polym Sci 2004, 29, 699–766.
3. Rajesh; Ahuja, T.; Kumar, D. Sens Actuators, B 2009, 136, 275–286.
4. Galdikas, A.; Kancleris, Ž.; Senulien, D.; Šetkus, A. Sens Actuators, B 2003, 95, 244–251.
5. Ram, M.K.; Yavuz, Ö.; Lahsangah, V.; Aldissi, M. Sens Actuators, B 2005, 106, 750–757.
6. Chen, Y.; Li, Y.; Wang, H.; Yang, M. Carbon 2007, 45, 357–363.
7. Hu, N.; Wang, Y.; Chai, J.; Gao, R.; Yang, Z.; Kong, E.S.W.; Zhang, Y. Sens Actuators, B 2012, 163, 107–114.
8. Matsuguchi, M.; Io, J.; Sugiyama, G.; Sakai, Y. Synth Met 2002, 128, 15–19.
9. Cosnier, S.; Da Silva, S.; Shan, D.; Gorgy, K. Bioelectrochemistry 2008, 74, 47–51.
10. Soontornworajit, B.; Wannatong, L.; Hiamtup, P.; Niamlang, S.; Chotpattananont, D.; Sirivat, A.; Schwank, J. Mater Sci Eng, B 2007, 136, 78–86.
11. Thuwachaowsoan, K.; Chotpattananont, D.; Sirivat, A.; Rujiravanit, R.; Schwank J.W. Mater Sci Eng, B 2007, 140, 23–30.
12. Chuapradit, C.; Wannatong, L.R.; Chotpattananont, D.; Hiamtup, P.; Sirivat, A.; Schwank, J. Polymer 2005, 46, 947–953.
13. Densakulprasert, N.; Wannatong, L.; Chotpattananont, D.; Hiamtup, P.; Sirivat, A.; Schwank, J. Mater Sci Eng, B 2005, 117, 276–282.
14. Izni, E.; Izni, A. Turk J Chem 2007, 31, 523–530.
15. Franke, M.E.; Simon, U. Solid State Ionics 1999, 118, 311–316.
16. Goryainov, S.V.; Secco, R.A.; Huang, Y.; Liu, H. Physica B 2007, 390, 356–365.
17. Goryainov, S.V.; Secco, R.A.; Huang, Y.; Likhacheva, A.Y. Microporous Mesoporous Mater 2013, 171, 125–130.
18. Louwet, F.; Groenendaal, L.; Dhaen, J.; Manca, J.; Van Luppen, J.; Verdonck, E.; Leenders, L. Synth Met 2003, 135–136, 115–117.
19. Thomas, B.; Sugunan, S. Microporous Mesoporous Mater 2004, 72, 227–238.
20. Han, D.; Yang, G.; Song, J.; Niu, L.; Ivaska, A. J Electroanal Chem 2007, 602, 24–28.
21. Garreau, S.; Louarn, G.; Buisson, J. P.; Froyer, G.; Lefrant, S. Macromolecules 1999, 32, 6807–6812.
22. Li, C.; Imae, T. Macromolecules 2004, 37, 2411–2416.
23. Chanthaanont, P.; Sirivat, A. e-Polym, 2012, 10, 1–11.
24. Martin, B.D.; Nikolov, N.; Pollack, S.K.; Saprigin, A.; Shashidhar, R.; Zhang, F.; Heiney, P.A. Synth Met 2004, 142, 187–193.
25. Wichiansee, W.; Sirivat, A. Mater Sci Eng, C 2009, 29, 78–84.
26. Bendenia, S.; Marouf-Khelifa, K.; Batonneau-Gener, I.; Derriche, Z.; Khelifa, A. Adsorption 2001, 17, 361–370.
27. Maurin, G.; Llewellyn, P.L.; Poyet, T.; Kuchta, B. Microporous Mesoporous Mater 2005, 79, 53–59.
28. Nam, S.S.; Kim, H.; Kishan, G.; Choi, M.J.; Lee, K.W. Appl Catal, A 1999, 179, 155–163.
29. Castaldi, P.; Santona, L.; Enzo, S.; Melis, P. J Hazard Mater 2008, 156, 428–434.
30. Mews, R.; Lork, E.; Watson, P.G.; Görtler, B. Coord Chem Rev 2000, 197, 277–320.
31. Matsuguchi, M.; Tamai, K.; Sakai, Y. Sens Actuators, B 2001, 77, 363–367.
32. Nasluzov, V.A.; Shor, A.M.; Nörtemann, F.; Staufer, M.; Yudanov, I.V.; Rösch, N. J Mol Struct Theochem 1999, 466, 235–244.

Materials Research. 2013; 16(5): 1020-1029
DOI: 10.1590/S1516-14392013005000092

© 2013

Polydiphenylamine/Zeolite Y Composites and Electrical Conductivity Responses toward Halogenated Hydrocarbons

***Tharaporn Permpool*[a], *Anuvat Sirivat*[a]*, *Darunee Aussawasathien*[b], *Ladawan Wannatong*[c]**

[a]*The Petroleum and Petrochemical College, Chulalongkorn University, Bangkok, 10330, Thailand*
[b]*National Metal and Materials Technology center, National Science and Technology Development Agency, Ministry of Science and Technology, Pathumthani, 12120, Thailand*
[c]*Faculty of Engineering, King Mongkut's University of Technology North Bangkok, Bangkok, 10800, Thailand*

Received: November 8, 2012; Revised: February 8, 2013

Composites of polydiphenylamine (D-PDPA) and zeolite Y with H^+ as the cation (Y_H^+) have been fabricated to be used as a sensing material towards non-halogenated and halogenated solvents (hexane, dichloromethane, 1, 2-dichloroethane, chloroform). These composites are toxic towards human and environment and are widely used as solvents in various industries. Polydiphenylamine, zeolite Y, and their composites are characterized by Fourier transform infrared spectroscopy, scanning electron microscopy, particle size analysis, surface area, and pore size analysis. The effects of the Si/Al ratio, zeolite content, and vapor concentrations are investigated. The electrical conductivity sensitivity of the composites towards the solvents is higher than the pristine D-PDPA by ~1 order of magnitude. The composites can discriminate a non-halogenated solvent from halogenated solvents. They possess maximum electrical conductivity sensitivity values towards dichloromethane, but the composites do not respond to hexane. Generally, the sensitivity of the composites increases with increasing zeolite content and vapor concentration. The interactions between the composites and the vapors are investigated by FT-IR spectroscopy and UV-Vis spectroscopy. A mechanism for the interaction between the composites and the solvents is proposed.

Keywords: *Conductive polymer, electrical conductivity, polydiphenylamine, Zeolite Y, halogenated hydrocarbon*

1. Introduction

Volatile organic compounds (VOCs) are organic compounds that easily evaporate at normal pressure and room temperature. The VOCs are widely used in daily products and used as solvents in various industries[1]. Nevertheless, the toxicity of these chemical vapors causes serious environmental and human health concerns. The VOCs are divided into two groups; non-halogenated hydrocarbons, and halogenated hydrocarbons. Non-halogenated hydrocarbons are volatile hydrocarbons that do not contain a chlorine atom within the molecule. Normally, this group is found in daily life products such as plastics, cleaning solvents, and paints, and it can affect human health through the respiratory system. Examples of non-halogenated hydrocarbons are aliphatic hydrocarbons, aromatic hydrocarbons, alcohol, aldehyde, and ketones. The other type of VOCs is halogenated hydrocarbons which consist of a chlorine atom within the molecule. They are used in dry cleaning, metal cleaning, furniture making, thermoplastics production, degreasing, printing, paper and textile production, and paint removal[1]. They are clear liquids, and vaporize at room temperature[2-4]. Examples of halogenated solvents are trichloroethylene, perchloroethylene, methylene chloride, ethylene chloride, carbon tetrachloride, chloroform, and methyl chloroform. The toxicity of these chemical vapors is more severe to human health than non-halogenated hydrocarbons. The solvents pose a major source of environmental problems such as stratospheric ozone depletion, smog formation, acid rain production, and global warming. Health problems caused by exposing humans to these solvents are systemic, immunological, neurological, reproductive, developmental, and genotoxic and carcinogenic in nature; which can lead to death[5]. The severity of the chemicals on human health depends on the concentration and exposure levels. The National Institute of Occupational Safety and Health (NIOSH) defined the limit for personal exposure to the chemical that cause to death or immediate or delayed permanent adverse health effects as the immediately dangerous to life or health concentrations (IDLHs)[6]. For instance, the exposure level of chloroform that leads to death in humans is ~40,000 ppm[7]. The level of chloroform that leads to human loss of responsiveness, loss of skeleton muscle reflex, and decreased stress response is less than 22,500 ppm[5,8]. The deadly inhalation concentration for methylene chloride, or dichloromethane (DCM), in a study of animals, was ~3,000 ppm[9]. Hence, effective sensory systems are required to identify the presence of these

*e-mail: anuvat.s@chula.ac.th

solvents. One development of sensing materials has focused on conductive polymers due to their unique properties. They are: light weight, easy to synthesize, possess high sensitivity and short response time, and have good mechanical properties over metal oxides[10-12]. Polydiphenylamine (PDPA) is an N-aryl substituted derivative of polyaniline and it shows better mechanical strength, electrochemical, conductivity, and electro chromic properties than polyaniline[13-16]. Additionally, PDPA has been used as a sensing material for many sensory systems: pH sensors, CO sensors, and glucose biosensors[17-19]. Another group of materials that can also be used as sensing materials are zeolites. Zeolites are aluminosilicate minerals that have micro porous cages within their crystal structures. Due to their unique structures, zeolites can act as molecular sieves to separate different types of molecules. Thus, zeolites can be used as a catalyst support, an absorbent for moisture and toxic gases, and for ion exchange. Recently, there have been several studies on conductive polymer/zeolite composites as gas or vapor sensing materials[20-22].

This work is aimed at fabricating the composites between D-PDPA and zeolite Y with H^+ as a cation (Y_H^+) to discriminate between the non-halogenated and halogenated hydrocarbon solvents, based on the electrical conductivity response when exposed to halogenated vapors. The influences of the Si/Al ratio, zeolite Y content, and vapor concentration of the halogenated solvents—dichloromethane (DCM), 1,2-dichloroethane (DCE), and chloroform—on the electrical conductivity response of D-PDPA/zeolite Y composites (D-PDPA/Y_H^+) are investigated. The physical adsorption of the halogenated solvents on the composites is examined by FT-IR and UV-Vis spectroscopy.

2. Experimental

2.1. *Materials*

Diphenylamine, DPA (reagent, Sigma Aldrich), Ammonium persulfate, $(NH_4)_2S_2O_8$, (AR grade, Riedel-de Haën), and 37 %v/v of hydrochloric acid, HCl (ACS reagent, J T Baker), were used at a mole ratio of 100:1 ($N_{HCl}/N_{monomer}$). Zeolite Y (Zeolite International) with H^+ as a cation (Y_H^+), having Si/Al ratios of 5.1 (Y_H^+[5.1]), 30 (Y_H^+[30]), 60 (Y_H^+[60]), and 80 (Y_H^+[80]) were used in powder form. Ammonium hydroxide, NH_4OH (AR grade, Panreac), toluene (AR grade, Panreac), isopropyl alcohol (AR grade, Burdick & Jackson), and ethanol (AR grade, Lab Scan) were used without further purification.

2.2. *Chemical vapor detection*

Dichloromethane, DCM (AR grade, Lab Scan), 1,2-dichloroethane, DCE (AR grade, Lab Scan), chloroform (AR grade, Lab Scan), and hexane (AR grade, Lab Scan) were used as the chemical vapors in this work.

2.3. *Synthesis of PDPA and doping process*

Polydiphenylamine (PDPA) was synthesized via chemical oxidative polymerization[23,24]. A DPA solution in toluene was mixed with $(NH_4)_2S_2O_8$ solution in distilled water. The solution mixture was stirred by using an overhead stirrer, cooled to 0 °C for 15 minutes, then a HCl solution in distilled water was added to the mixture. The reaction mixture was continuously stirred at 0 °C for 4 hr; next the green slurry of PDPA was precipitated. The precipitate was washed with isopropyl alcohol at least 3 times. Then the HCl-doped PDPA was dedoped in a mixture of ethanol and ammonium hydroxide solution (1:4 v/v) for 24 hours. The neutralized PDPA was doped with 5M HCl solution at a mole ratio of 100:1 ($N_{HCl}/N_{monomer}$) and stirred at room temperature for 24 hours. The resultant doped PDPA, D-PDPA, was filtered and dried in a vacuum oven at room temperature for 24 hr to remove excess HCl.

2.4. *Preparation of D-PDPA pellets and D-PDPA/Y_H⁺ composites*

The D-PDPA powder was ground with the Y_H^+ powder at various Y_H^+ concentrations (0, 5, 10, 20, and 30 %v/v). The D-PDPA powder and D-PDPA/Y_H^+ composites were compressed into pellets for the electrical conductivity and sensitivity measurements with a hydraulic press machine (GRASEBY SPECAC) under a 4-5 ton load. Pellets were produced in disc form using a 1 cm stainless steel die. The thickness of each pellet was between 0.03-0.04 cm as measured by a digital thickness gauge (PEAACOCK, dial stand type model PDN-20).

2.5. *Characterization*

Fourier transform infrared (FT-IR) spectra of D-PDPA were recorded with a Thermo Nicolet, Nexus 670 FT-IR spectrometer using a resolution of 2 cm^{-1}, a scan number of 32, and a wavenumber range of 400-4000 cm^{-1}. Scanning electron micrographs of D-PDPA, Y_H^+, and D-PDPA/Y_H^+ were taken using a HITACHI, S-4800 scanning electron microscope (SEM) with a magnification of 10 000x, operating at 10 kV. The particle sizes of D-PDPA and Y_H^+ were measured by using a Mastersizer X particle size analyzer. The surface area and pore size of Y_H^+ were measured with a Physisorption, Quantachrome, Autosorb-1MP surface area analyzer. Zeolite powder was weighed and out gassed at 300 °C over night before adsorption and desorption with He and N_2 gases. During the operation, the zeolite powder was cooled by liquid N_2. The specific density of the D-PDPA and Y_H^+ were measured with a pycnometer. The optical properties of the D-PDPA and Y_H^+ when exposed to DCM were taken by a UV-Vis spectrophotometer (SHIMADZU, UV 1800) in the wavelength number of 200 nm to 500 nm at room temperature.

2.6. *Conductivity and sensitivity measurements*

The conductivity and the sensitivity of D-PDPA, Y_H^+, and D-PDPA/Y_H^+ towards halogenated solvents were measured by a custom built two-point probe connected with a conductivity meter (KEITHLEY 6517A) which applied voltage; the resultant current was measured. The electrical conductivity was calculated by the equation $\sigma = (I/KVt)$, where I is the measured current (A), V is the applied voltage (V), t is the thickness (cm), and K is the geometric correction factor of the two-point probe as calibrated by standard silicon wafer sheets with known specific resistivity values. All measurements were taken at 27 ± 1 °C and at

atmospheric pressure. The electrical conductivity responses and sensitivities under exposure to air, N_2, and halogenated solvents were determined by the equation $\Delta\sigma = \sigma_{\text{halogenated solvents}} - \sigma_{N2,\text{ initial}}$ and $\Delta\sigma/\sigma_{N2,\text{ initial}}$, respectively, where $\Delta\sigma$ is the difference in the specific electrical conductivity (S cm^{-1}), $\sigma_{N2,\text{ initial}}$ is the specific electrical conductivity in N_2 before exposure (S cm^{-1}), and $\sigma_{\text{halogenated solvent}}$ is the specific electrical conductivity (S cm^{-1}) under halogenated solvent exposure. The effect of the halogenated solvent concentration was determined at concentrations of 5, 10, 15, 20, 25, 30, 35, and 50 %v/v in N_2.

3. Results and Discussion

3.1. *Characterization of PDPA and Y_H⁺*

The FT-IR spectra of D-PDPA showed absorption peaks at 3388, 3053, 1594, 1505, 1318, 1173, 821, 748, and 748-694 cm^{-1}. These peaks can be assigned to: N-H stretching, C-H in the aromatic ring, quinoid ring stretching, phenyl hydrogen, benzenoid ring stretching, vibration band of N_2 in quinone, C-H out of plane aromatic, 1, 4 substituted on aromatic rings, and C-H out of plane bending vibration, respectively[15,24-26]. The FT-IR spectra of Y_H⁺ show major absorption peaks at 1213, 1080, 836, and 459 cm^{-1}. These peaks can be assigned to the asymmetric stretch of the internal tetrahedral, the asymmetric stretch of the external linkage, the symmetric stretch of the external linkage, and the T-O bend of the internal tetrahedral, respectively[27, 28]. The average particle size of D-PDPA and Y_H⁺ was 125.96 ± 5.51 µm and 20.66 ± 0.58 µm, respectively. The surface area, pore size, and pore volume of Y_H⁺ are comparable at various Si/Al ratios (Table 1). The specific density of D-PDPA and Y_H⁺ is 0.85 ± 0.01 g cm^{-3} and 1.61 ± 0.35 g cm^{-3}, respectively. The micrographs shown in Figure 1 reveal that the shapes of Y_H⁺ are square shaped (Figure 1a) and the shape of the D-PDPA particles (Figure 1b) is irregular. Nevertheless, the Y_H⁺ particles are dispersed uniformly within the D-PDPA matrix (Figure 1c).

Table 1. Physical characteristics of Y_H⁺

Si/Al ratio	Surface area ($m^2\ g^{-1}$)	Pore size (Å)	Pore volume ($cm^3\ g^{-1}$)
5.1	617.3 ± 2.27	3.665 ± 0.01	0.403 ± 0.01
30	731.0 ± 2.42	3.670 ± 0.02	0.569 ± 0.01
60	688.8 ± 7.62	3.675 ± 0.04	0.608 ± 0.03
80	766.1 ± 3.25	3.691 ± 0.01	0.555 ± 0.08

3.2. *Sensitivity of D-PDPA and Y_H⁺ towards halogenated solvents*

The electrical conductivity sensitivity of D-PDPA, Y_H⁺ towards the four solvents is shown in Figure 2. The D-PDPA and Y_H⁺ exhibit negative responses towards all four solvents. Table 2 shows the initial electrical conductivity values of D-PDPA, Y_H⁺, D-PDPA/Y_H⁺[80] when exposed to halogenated solvents. The sensitivity values of D-PDPA, Y_H⁺ towards the four solvents, shown in Table 3, show that D-PDPA and Y_H⁺ possess maximum sensitivity responses towards DCM followed by DCE and chloroform, but they hardly respond to hexane. This is presumably due to the differences in the molecular structure, the strength of the electrostatic interaction, the dipole moment, and the dielectric constant[29] (Table 4). The interaction between D-PDPA and the vapors occurs at the N-H⁺ site and the Cl⁻ atom. Since, the dipole moment of DCM (1.80) is higher than that of DCE (1.60) and chloroform (1.10), the dipole-dipole interaction between the Cl⁻ atom of the DCM molecule and the N-H⁺ site of D-PDPA is stronger than those of DCE and chloroform[30]. Therefore, the sensitivity of D-PDPA toward DCM is higher than those of other vapors. Because the hexane structure is an aliphatic hydrocarbon chain and it has no dipole moment, the interaction between D-PDPA and

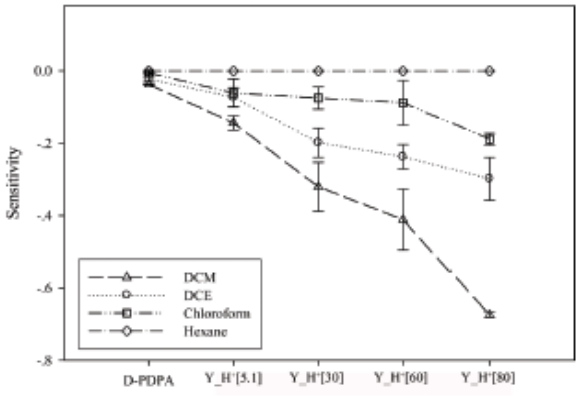

Figure 2. The sensitivity of D-PDPA, Y_H⁺ at various Si/Al ratios when exposed to halogenated solvents at 27±1°C and 1 atm.

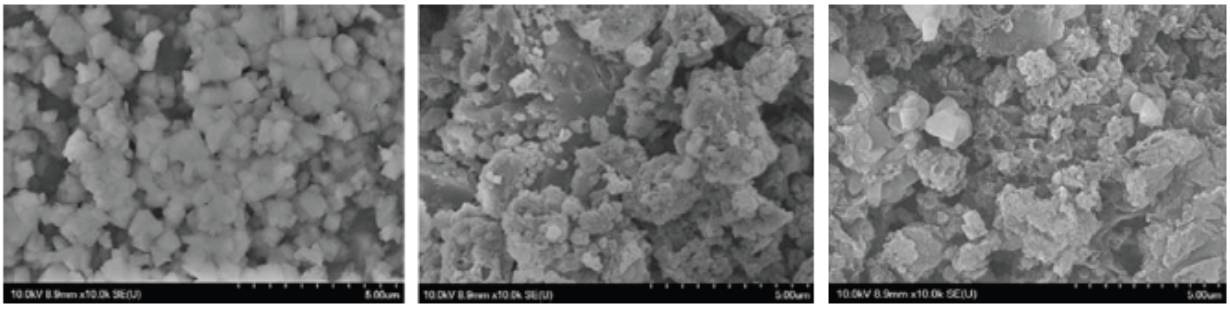

(a) (b) (c)

Figure 1. SEM micrographs at 10000x of: (a) Y_H⁺; (b) D-PDPA; and (c) D-PDPA/Y_H⁺.

Table 2. The initial electrical conductivity of D-PDPA, Y_H+, D-PDPA/Y_H+[80] in N_2 before exposed to halogenated solvents at 27±1°C and 1 atm.

Solvent Vapor	Initial conductivity in N_2 before exposed to the solvents, σ_{N2} (S cm^{-1})				
	D-PDPA	Y_H+[5.1]	Y_H+[30]	Y_H+[60]	Y_H+[80]
DCM	(2.29±0.91)×10^{-4}	(6.49±2.46)×10^{-5}	(7.87±3.45)×10^{-5}	(1.31±0.26)×10^{-4}	(2.64±0.39)×10^{-4}
DCE	(1.83±0.45)×10^{-4}	(6.41±0.76)×10^{-5}	(6.98±0.66)×10^{-5}	(7.49±1.63)×10^{-5}	(9.34±1.05)×10^{-5}
Chloroform	(1.34±0.01)×10^{-4}	(9.69±1.15)×10^{-5}	(8.92±0.39)×10^{-5}	(9.26±0.05)×10^{-5}	(1.44±0.68)×10^{-4}
Hexane	(1.42±0.16)×10^{-4}	(6.86±0.03)×10^{-5}	(8.66±0.81)×10^{-5}	(1.04±0.06)×10^{-4}	(1.75±0.02)×10^{-4}
Solvent Vapor	**D-PDPA/5% Y_H+[80]**	**D-PDPA/10% Y_H+[80]**	**D-PDPA/20% Y_H+[80]**	**D-PDPA/30% Y_H+[80]**	
DCM	(1.60±0.35)×10^{-4}	(1.39±0.07)×10^{-4}	(1.97±0.22)×10^{-4}	(2.24±0.04)×10^{-4}	
DCE	(2.15±0.31)×10^{-4}	(2.26±0.24)×10^{-4}	(1.95±0.25)×10^{-4}	(1.90±0.10)×10^{-4}	
Chloroform	(1.70±0.01)×10^{-4}	(1.75±0.14)×10^{-4}	(3.08±1.88)×10^{-4}	(2.11±1.03)×10^{-4}	
Hexane	(1.61±0.02)×10^{-4}	(1.41±0.15)×10^{-4}	(1.73±0.07)×10^{-4}	(1.34±0.29)×10^{-4}	

Table 3. Electrical conductivity sensitivity of D-PDPA, Y_H+, D-PDPA/Y_H+[80] when exposed to halogenated and non-halogenated solvents at 27±1°C and 1 atm.

Material	Response ($\Delta\sigma$ = σhalogenated solvent-σ_{N2})[a]			
	DCM	DCE	chlroform	hexane
D-PDPA	(–8.77±3.82)×10^{-6}	(–1.79±0.73)×10^{-5}	(–8.07±4.05)×10^{-7}	(–5.11±3.25)×10^{-8}
Y_H+[5.1]	(–9.60±4.81)×10^{-6}	(–4.81±2.25)×10^{-6}	(–5.76±3.09)×10^{-6}	(–4.30±0.56)×10^{-8}
Y_H+[30]	(–2.10±2.41)×10^{-5}	(–1.32±0.52)×10^{-5}	(–6.80±3.01)×10^{-6}	(–5.75±2.70)×10^{-8}
Y_H+[60]	(–5.28±0.03)×10^{-5}	(–1.78±0.09)×10^{-5}	(–8.20±5.77)×10^{-6}	(–6.61±2.27)×10^{-8}
Y_H+[80]	(–1.78±0.25)×10^{-4}	(–2.39±1.48)×10^{-5}	(–3.74±2.87)×10^{-5}	(–1.35±0.35)×10^{-7}
D-PDPA/5% Y_H+[80]	(–1.86±0.28)×10^{-5}	(–5.96±7.78)×10^{-6}	(–1.58±0.02)×10^{-6}	(–5.94±5.92)×10^{-8}
D-PDPA/10% Y_H+[80]	(–2.32±0.11)×10^{-5}	(–7.83±5.74)×10^{-6}	(–9.36±2.31)×10^{-7}	(–4.86±0.88)×10^{-8}
D-PDPA/20% Y_H+[80]	(–3.63±2.35)×10^{-5}	(–9.66±9.04)×10^{-6}	(–8.90±1.84)×10^{-6}	(–6.07±2.91)×10^{-8}
D-PDPA/30% Y_H+[80]	(–7.78±3.79)×10^{-5}	(–3.37±0.26)×10^{-5}	(–8.32±0.62)×10^{-6}	(–5.10±0.50)×10^{-8}
Material	**Sensitivity ($\Delta\sigma/\sigma_{N2}$)[b]**			
	DCM	DCE	chlroform	hexane
D-PDPA	(–3.83±0.15)×10^{-2}	(–2.42±0.73)×10^{-2}	(–6.01±3.02)×10^{-3}	(–3.60±2.70)×10^{-4}
Y_H+[5.1]	(–1.48±0.19)×10^{-1}	(–7.50±2.64)×10^{-2}	(–5.94±3.92)×10^{-2}	(–6.27±0.79)×10^{-4}
Y_H+[30]	(–2.67±2.09)×10^{-1}	(–1.89±0.06)×10^{-1}	(–7.63±3.04)×10^{-2}	(–6.63±2.50)×10^{-4}
Y_H+[60]	(–4.03±0.84)×10^{-1}	(–2.34±0.03)×10^{-1}	(–8.86±6.18)×10^{-2}	(–6.35±2.54)×10^{-4}
Y_H+[80]	(–6.74±0.06)×10^{-1}	(–2.56±1.30)×10^{-1}	(–2.60±0.87)×10^{-1}	(–7.76±1.90)×10^{-4}
D-PDPA/5% Y_H+[80]	(–1.16±0.08)×10^{-1}	(–2.90±0.03)×10^{-2}	(–9.27±0.77)×10^{-3}	(–3.69±3.68)×10^{-4}
D-PDPA/10% Y_H+[80]	(–1.67±0.16)×10^{-1}	(–3.50±0.03)×10^{-2}	(–5.36±1.28)×10^{-3}	(–3.44±0.99)×10^{-4}
D-PDPA/20% Y_H+[80]	(–1.85±0.99)×10^{-1}	(–5.00±4.03)×10^{-2}	(–2.89±1.43)×10^{-2}	(–3.51±0.25)×10^{-4}
D-PDPA/30% Y_H+[80]	(–3.48±1.64)×10^{-1}	(–1.77±0.04)×10^{-1}	(–3.95±1.86)×10^{-2}	(–3.79±0.44)×10^{-4}

[a]$\Delta\sigma$ = the electrical response; [b]$\Delta\sigma/\sigma_{N2}$ = electrical conductivity sensitivity.

hexane vapor is suspected to be physical adsorption on the matrix surface without the dipole-dipole interaction, unlike the other chlorinated hydrocarbon molecules[31-33]. Therefore, the sensitivity of D-PDPA towards hexane is low. For zeolite, the interaction between Y_H+ and the vapors is the hydrogen bonding at the Si-O$^-$ or Al-O$^-$ site and the –H atom of the vapor molecules. The sensitivity of Y_H+ towards DCM is also higher than those of DCE (–50%) and chloroform (–60%). For DCM, there are two hydrogen atoms that form the hydrogen bond with D-PDPA and Y_H+. For DCE, a lower sensitivity than DCM occurs due to the larger chemical structure of DCE over DCM, known as the steric effect. For chloroform, since there is only one hydrogen atom in the chemical structure, and the dipole moment and dielectric constant are also very low, the strength of the hydrogen bonding between Y_H+ and chloroform is lower than the strength of the hydrogen bonding between Y_H+ and DCM and Y_H+ and DCE[30]. Moreover, the sensitivity of Y_H+ increases with increasing Si/Al ratio. This occurs because the hydrophobicity of zeolite increases with the Si/Al ratio[34]. Hence, the halogenated solvents, which are non-polar solvents, produce more favorable responses towards the zeolites Y_H+ with higher Si/Al ratios. Therefore, the zeolite Y_H+[80] was chosen to form composites with D-PDPA, in order to further improve the sensitivity of D-PDPA towards the halogenated solvents.

3.3. *Sensitivity of D-PDPA/Y_H⁺[80] composites toward halogenated solvents: Effect of zeolite Y contents*

The effect of Y_H⁺[80] content on the sensitivity of D-PDPA/Y_H⁺[80] towards the halogenated solvents was investigated. The composites show negative sensitivity towards the solvents (Table 3). According to the doping theory[35], D-PDPA is doped via the p type doping process. When it is exposed to the vapors, which are electron-donating groups, the vapors will give up an electron to fill the hole on the D-PDPA backbone. Thus, the electron mobility along the D-PDPA backbone is more difficult, resulting in a decrease in conductivity, which is why the composites show negative sensitivity towards the solvents. It appears that the sensitivities of the composites are higher than those of pure D-PDPA by about 1 order of magnitude towards DCM and DCE; the sensitivity increases with increasing Y_H⁺[80] content (Figure 3). With a higher zeolite content, a greater interaction results between the micro-porous structure and the target vapor. With a Y_H⁺[80] content of –30 %v/v, the composite shows the highest sensitivity. The sensitivity of chloroform is quite constant with respect to the Y_H⁺[80] content because it has no dipole moment and very low dielectric constants[36]. The composite does not respond to hexane, even when the zeolite content increases to 30 %v/v, because the interaction between the composite and hexane is only physical absorption. The selectivity of the composite towards the three halogenated solvents is in this order: DCM>DCE>chloroform. Therefore, it can be concluded that the addition of zeolites can improve the sensitivity of D-PDPA and it can discriminate a non-halogenated solvent from halogenated solvents.

Table 4. Values of dielectric constant (ε), dipole moment (μ) of the solvent tested[29].

Solvents	Dipole moment	Dielectric constant
Dichloromethane	1.80	9.10
1,2 dichloroethane	1.60	10.45
chloroform	1.10	4.80
hexane	0.00	1.88

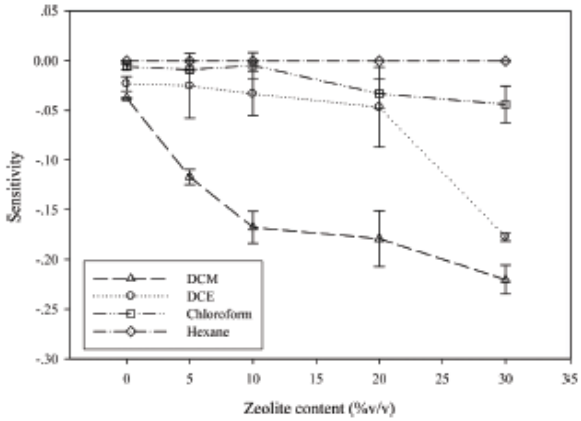

Figure 3. The sensitivity of D-PDPA/Y_H⁺[80] at various zeolite concentrations when exposed to halogenated solvents at 27±1°C and 1 atm.

3.4. *Sensitivity of D-PDPA/Y_H⁺[80] composites toward halogenated solvents: Effect of vapor concentration*

The composite consisting of 30 %v/v of Y_H⁺[80] with D-PDPA (D-PDPA/30% Y_H⁺[80]) was next investigated with respect to DCM and DCE at various vapor concentrations. The sensitivity of the composite, which is exposed to DCM, increases from $(-1.23 \pm 0.004) \times 10^{-2}$ to $(-3.47 \pm 1.64) \times 10^{-1}$ as the vapor concentration increases from 7,696 ppm to 153,914 ppm, respectively (Figure 4). When the composite is exposed to DCE, the sensitivity increases from $(-1.09 \pm 0.96) \times 10^{-1}$ to $(-1.77 \pm 0.04) \times 10^{-1}$ as the vapor concentration increases from 1,015 ppm to 20,299 ppm, respectively. When the composites are exposed to both of DCM and DCE, they exhibit linear relationships between the sensitivity and vapor concentration. As the vapor concentration increases, the sensitivity of D-PDPA/30% Y_H⁺[80] increases. A similar result has been also found by Jiang et al.[37]. They prepared a polypyrrole and polyvinylalcohol composite via in situ vapor state polymerization to detect methanol vapors. The composite showed a linear relationship between sensitivity and gas concentration in the gas range of 50-1059 ppm. The minimum concentrations of DCM and DCE that the composite can detect are 7696 ppm and 1015 ppm, respectively; these values are equivalent to the IDLHs[30,38,39]. The chemical interactions between DCM and the composites were investigated by FT-IR spectroscopy and UV-VIS spectroscopy. Figure 5 shows the FT-IR spectra of the vapors. Before exposure to DCM, the absorption peaks at 1594, 1505, 1318, 1213, 1080, 836, and 748 cm^{-1} can be assigned to the quinoid ring stretching of D-PDPA[25], the phenyl hydrogen of D-PDPA[15], the benzenoid ring stretching of D-PDPA, the asymmetric stretch of the internal tetrahedral in Y_H⁺[80], the asymmetric stretch of the external linkage, the symmetric stretch of external linkage[27,28], and the 1, 4 substituted on aromatic rings[24], respectively. During exposure to DCM, new peaks occur at 3097, 1285, and 752 cm^{-1} which can be assigned to the hydrogen bonding between the oxygen atom of Y_H⁺ and the hydrogen atom

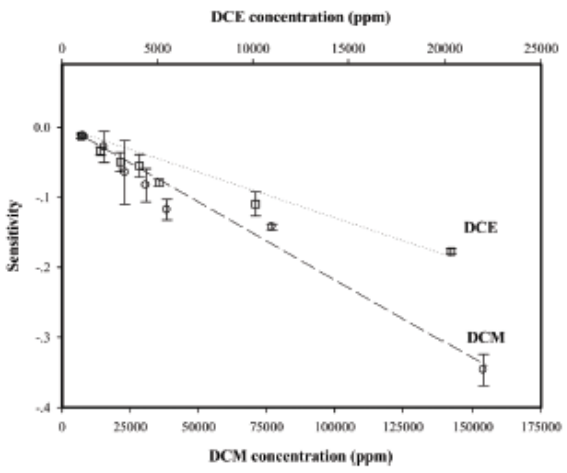

Figure 4. The sensitivity of D-PDPA/30%Y_H⁺[80] toward DCM and DCE at different concentrations at 27±1°C and 1 atm.

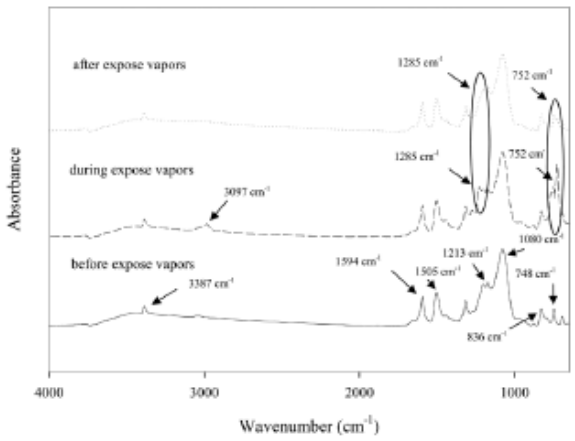

Figure 5. FT-IR spectra of D-PDPA/30% Y_H+[80] when exposed to DCM and DCE vapors at 27±1°C and 1 atm.

of DCM molecule[40], CH_2 in CH_2-Cl[41], and the interaction of the chlorine atom of DCM and the nitrogen atom of D-PDPA backbone[42], respectively. After exposure to DCM, the peaks at 3097, 1285, and 752 cm^{-1} disappear. This indicates that no interaction occurs between the composite and DCM molecules. The proposed mechanism is shown in Figure 6. From the proposed mechanism, the FT-IR absorption band of D-PDPA cannot be clearly discerned when exposed to DCM, thus the second derivative of the spectrum is used instead. During exposure to DCM, the absorption bands at 1596 and 1318 cm^{-1} corresponding to the quinoid ring stretching and the benzenoid ring stretching, respectively shift from the original positions before exposed to DCM by 4 cm^{-1} for thequinoid ring stretching and by 7 cm^{-1} for the benzenoid ring stretching as shown in Figure 7. Anitha and Subramanian[43] have also observed that the FT-IR absorption band of polyaniline when exposed to DCM shifted by 3 cm^{-1} due to the electron displacement from chlorine atom of DCM to the polyaniline backbone.

The UV-Vis spectra are used to confirm the interaction between DCM and the composite. The spectrum of the D-PDPA is shown in Figure 8a. There are two absorption bands, one at 282 nm which corresponds to the characteristic absorption bands of DCM, and the other at 342 nm which corresponds to the n-π* transition at –N+= of the D-PDPA backbone[44]. It is clear from Figure 8a that the absorption band is blue shifted from 342 nm to 334 nm and the absorbance intensity decreases with increasing DCM concentration from 5%v/v to 25 %v/v. This indicates that the shift in the absorption band is due to DCM giving up an electron to fill hole on D-PDPA back bone. Thus, the electron mobility along the D-PDPA backbone becomes more difficult, and the band gap of D-PDPA increases. It needs more energy to accelerate the electron to a higher conduction band, resulting in the shift of the electronic band of D-PDPA to a higher energy or a lower wavelength[16,45]. The absorption band observed at 271 nm corresponds to the $–Si-O_4^{2-}$ site on the Y_H+ framework[46] (Figure 8b). The absorption band is red shifted from 271 nm to 277 nm and the absorbance intensity decreases with increasing DCM concentration from 5%v/v to 25 %v/v because the electron

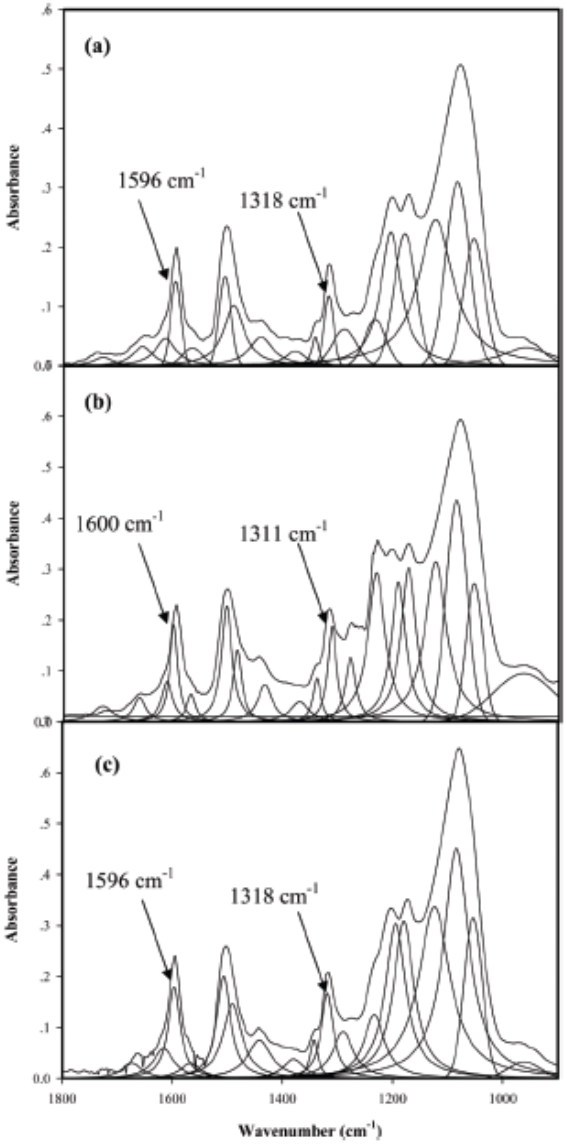

Figure 6. FT-IR second derivative of D-PDPA/30%Y_H+[80] composite when exposed to DCM.

donor and acceptor interact between the $–Si-O_4^{2-}$ site of the Y_H+ framework and the –H atom of the DCM molecule. For D-PDPA/30% Y_H+[80] composite (Figure 8c), they are also two absorption bands at –340 nm and –265 nm which correspond to the n-π* transition at –N+= of the D-PDPA backbone and the $–Si-O_4^{2-}$ site on the Y_H+ framework, respectively. The absorption band at 342 nm is blue shifted from 340 nm to 336 nm. The absorption band at 262 nm is red shifted to 275 nm. This occurs similarly to D-PDPA and Y_H+[80]. It can be concluded that the interaction between the composite of D-PDPA/30% Y_H+[80] and DCM occurs as shown in the proposed mechanism (Figure 7). Choi and co-worker[47] studied iodine absorption on various zeolites. The absorption band was gradually red shifted when the iodine molecules increasingly absorbed on the zeolite Y framework. They attributed the phenomenon to $–Si-O_4^{2-}$ donating an electron to the adsorbed iodine molecules.

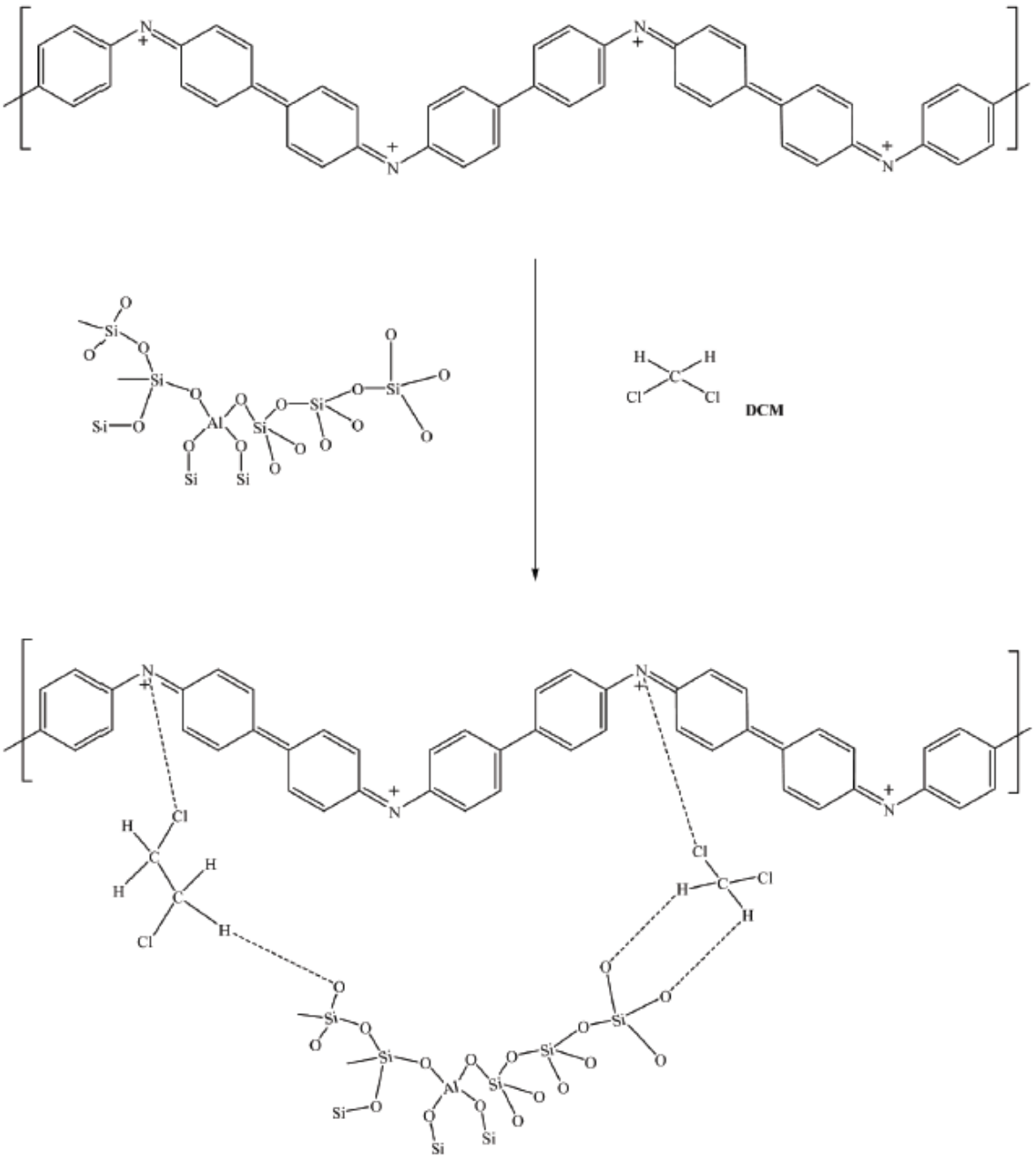

Figure 7. Proposed mechanism of adsorbed DCM, and DCE on D-PDPA/30% Y_H⁺[80].

3.5. *The temporal response D-PDPA/Y_H⁺[80] composites*

The induction time of the D-PDPA when exposed to DCM, DCE, and chloroform was around 13.50 ± 2.12, 8.56 ± 1.25, 15.00 ± 1.41 min, respectively. For the D-PDPA/30% Y_H⁺[80] composite, the induction time was about 18.50 ± 0.71 min for DCM, 17.65 ± 0.43 min for DCE, 15.95 ± 1.34 min for chloroform. The results showed that the induction time of the composite was higher than D-PDPA. This suggests that the presence of zeolite, a micro porous structure, introduces more active sites for the vapors to absorb. D-PDPA showed a reduction time when exposed to DCM, DCE, and chloroform of 9.50 ± 4.86, 6.35 ± 1.57, and 13.75 ± 7.84 min, respectively. The reduction times of the composite when exposed to DCM, DCE, and chloroform were 6.00 ± 3.04, 6.10 ± 0.49, and 7.05 ± 2.87 min, respectively. The reduction time of the D-PDPA/30% Y_H⁺[80] composite was also higher than the D-PDPA due to the micro porous structure of the zeolite. A similar result was also found by Thuwachaowsoan and co-worker[48]. They fabricated a composites of poly(3-thiopheneacetic acid) (Pth) with zeolites L, mordenite (MOR), and beta (BETA) as H_2 gas sensors. They found that the induction time of the Pth 200:1/BETA

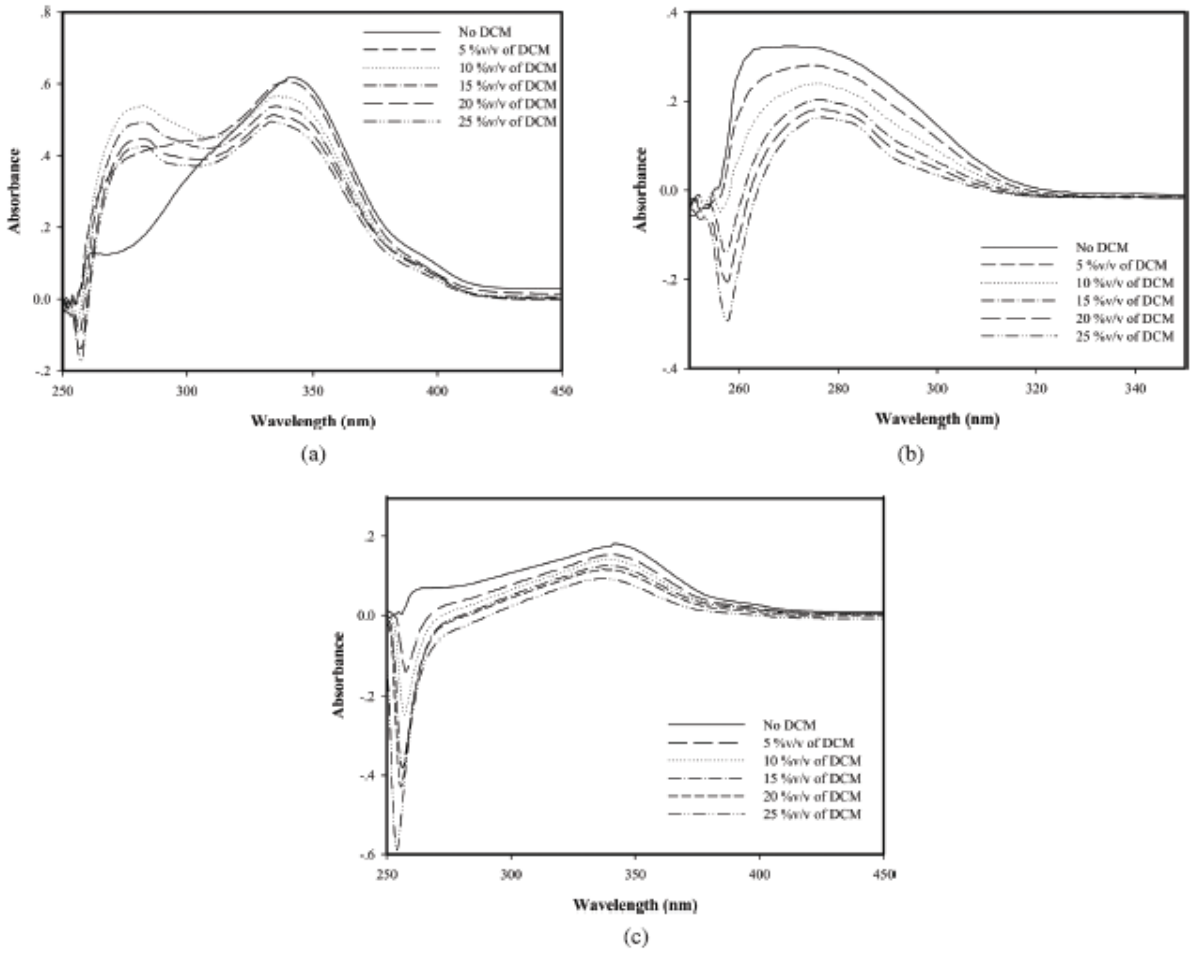

Figure 8. UV-Vis spectra of: a) D-PDPA; b) Y_H$^+$ when exposed to DCM; and c) D-PDPA/30%Y_H$^+$[80] composite at various concentrations.

20 was longer than that of the polymer and other composites. They concluded that the presence of zeolite introduces more reactive sites to interact with the H_2 molecules.

Conclusions

D-PDPA was fabricated into a composite with Y_H$^+$ to detect the toxic halogenated solvent vapors DCM, DCE, chloroform, and hexane. The composites show improved sensitivity responses towards DCM, DCE, and chloroform than hexane, because of the differences in the chemical structures of the dipole moment, and the dielectric constants of the target vapors. The sensitivities of the composites increase with increasing Si/Al ratio, zeolite content, and vapor concentration due to greater interactions between the zeolite and target vapors. For the temporal response, the induction and recovery times of the composite were higher than those of the pristine D-PDPA due to more active sites being available for the vapor molecules. The UV-Vis spectra show that the interaction between the composite and DCM does exist; the UV absorption band of D-PDPA and Y_H$^+$ is shifted by the delocalization of the Cl^- atom. The electron donor, acceptor interaction occurs between Y_H+ and the –H atom when exposed to DCM. It may be concluded that the fabricated composites possess a potential use as a sensing material for discriminating non-halogenated solvents from halogenated hydrocarbon solvents.

Acknowledgements

The authors would like to acknowledge the financial support from: the Conductive and Electroactive Polymers Research Unit of Chulalongkorn University; the Thailand Research Fund (TRF-RTA); the Royal Thai Government; and the Thailand Graduate Institute of Science and Technology (TGIST) (TGIST-01-54-011).

References

1. Sidebottom H and Franklin J. The atmospheric fate and impact of hydrochlorofluorocarbons and chlorinated solvents. *Pure and Apply Chemical*. 1996; 68(9):1757-69. http://dx.doi.org/10.1351/pac199668091757
2. Penza M and Cassano G. Application of principal component analysis and artificial neural networks to recognize the individual VOCs of methanol/2-propanol in a binary mixture by SAW multi-sensor array. *Sensors and Actuators B: Chemical*. 2003; 89(3):269-84. http://dx.doi.org/10.1016/S0925-4005(03)00002-9
3. Kukla AL, Pavluchenko AS, Shirshov YM, Konoshchuk NV and Posudievsky OY. Application of sensor arrays based on thin films of conducting polymers for chemical recognition of volatile organic solvents. *Sensors and Actuators B: Chemical*. 2009; 135(2):541-51. http://dx.doi.org/10.1016/j.snb.2008.09.027
4. Feng J and MacDiarmid AG. Sensors using octaaniline for volatile organic compounds. *Synthetic Metals*. 1999; 102(1-3):1304-5. http://dx.doi.org/10.1016/S0379-6779(98)00989-8
5. Whitaker AM and Jones CS. Report of 1500 Chloroform Anesthetics Administered With a Precision Vaporizer*. *Anesthesia & Analgesia*. 1965; 44(1):60-5. http://dx.doi.org/10.1213/00000539-196501000-00016
6. NOAA's Office of Response and Restoration (OR&R). Immediately Dangerous to Life and Health Limits (IDLHs). Available from: <http://response.restoration.noaa.gov/idlhs>.
7. Featherstone HW. Chloroform. *Anesthesiology*. 1947; 8(4):362-71. http://dx.doi.org/10.1097/00000542-194707000-00004
8. Anesthesia. Available from: <http://en.wikipedia.org/w/index.php?title=Anesthesia&oldid=515002047>.
9. Williams PL, James RC and Roberts SM. *Principles of Toxicology*: Environmental and Industrial Applications. Wiley; 2000.
10. Bailey ALPS, Pisanelli AM and Persaud KC. Development of conducting polymer sensor arrays for wound monitoring. *Sensors and Actuators B*: Chemical. 2008; 131(1):5-9. http://dx.doi.org/10.1016/j.snb.2007.12.035
11. Bai H and Shi G. Gas Sensors Based on Conducting Polymers. *Sensors*. 2007; 7(3):267-307. http://dx.doi.org/10.3390/s7030267
12. Albert KJ, Lewis NS, Schauer CL, Sotzing GA, Stitzel SE, Vaid TP et al. Cross-Reactive Chemical Sensor Arrays. *Chemical Reviews*. 2000; 100(7):2595-626. http://dx.doi.org/10.1021/cr980102w
13. Li CY, Wen TC, Guo TF and Hou SS. A facile synthesis of sulfonated poly(diphenylamine) and the application as a novel hole injection layer in polymer light emitting diodes. *Polymer*. 2008; 49(4):957-64. http://dx.doi.org/10.1016/j.polymer.2007.12.031
14. Hua F and Ruckenstein E. Hyperbranched Sulfonated Polydiphenylamine as a Novel Self-Doped Conducting Polymer and Its pH Response. *Macromolecules*. 2005; 38(3):888-98. http://dx.doi.org/10.1021/ma047756t
15. Hua F and Ruckenstein E. Water-Soluble Conducting Poly(ethylene oxide)-Grafted Polydiphenylamine Synthesis through a "Graft Onto" Process. *Macromolecules*. 2003; 36(26):9971-8. http://dx.doi.org/10.1021/ma030431c
16. Chung CY, Wen TC and Gopalan A. Identification of electrochromic sites in poly(diphenylamine) using a novel absorbance-potential-wavelength profile. *Electrochimica Acta*. 2001; 47(3):423-31. http://dx.doi.org/10.1016/S0013-4686(01)00742-3
17. Santhosh P, Manesh KM, Uthayakumar S, Gopalan AI and Lee KP. Hollow spherical nanostructured polydiphenylamine for direct electrochemistry and glucose biosensor. *Biosensors and Bioelectronics*. 2009; 24(7):2008-14. http://dx.doi.org/10.1016/j.bios.2008.10.004
18. Santhosh P, Manesh KM, Gopalan A and Lee KP. Novel amperometric carbon monoxide sensor based on multi-wall carbon nanotubes grafted with polydiphenylamine - Fabrication and performance. *Sensors and Actuators B:* Chemical. 2007; 125(1):92-9. http://dx.doi.org/10.1016/j.snb.2007.01.044
19. Rodríguez Presa MJ, Posadas D and Florit MI. Conditioning treatment to improve the potentiometric pH response of polydiphenylamine modified electrodes. *Sensors and Actuators B*: Chemical. 2007; 123(1):142-7. http://dx.doi.org/10.1016/j.snb.2006.08.002
20. Hugon O, Sauvan M, Benech P, Pijolat C and Lefebvre F. Gas separation with a zeolite filter, application to the selectivity enhancement of chemical sensors. *Sensors and Actuators B*: Chemical. 2000; 67(3):235-43. http://dx.doi.org/10.1016/S0925-4005(00)00514-1
21. Wu JY, Liu QL, Xiong Y, Zhu AM and Chen Y. Molecular Simulation of Water/Alcohol Mixtures' Adsorption and Diffusion in Zeolite 4A Membranes. *The Journal of Physical Chemistry B*. 2009; 113(13):4267-74. http://dx.doi.org/10.1021/jp805923k
22. Xu X, Wang J and Long Y. Zeolite-based Materials for Gas Sensors. *Sensors*. 2006; 6(12):1751-64. http://dx.doi.org/10.3390/s6121751
23. Orlov A, Ozkan S and Karpacheva G. Oxidative polymerization of diphenylamine: A mechanistic study. *Polymer Science Series B*. 2006; 48(1):11-7. http://dx.doi.org/10.1134/S1560090406010039
24. Sathiyanarayanan S, Muthukrishnan S and Venkatachari G. Synthesis and anticorrosion properties of polydiphenylamine blended vinyl coatings. *Synthetic Metals*. 2006; 156(18-20):1208-12. http://dx.doi.org/10.1016/j.synthmet.2006.08.008
25. Athawale AA, Deore BA and Chabukswar VV. Studies on poly(diphenylamine) synthesized electrochemically in nonaqueous media. *Materials Chemistry and Physics*. 1999; 58(1):94-100. http://dx.doi.org/10.1016/S0254-0584(98)00258-2
26. De Santana H and Dias FC. Characterization and properties of polydiphenylamine electrochemically modified by iodide species. *Materials Chemistry and Physics*. 2003; 82(3):882. http://dx.doi.org/10.1016/j.matchemphys.2003.07.005
27. George E and Christidis HP. Synthesis of FAU Type Zeolite Y from Natural Raw Materials: Hydrothermal SiO2Sinter and Perlite Glass. *The Open Mineralogy Journal*. 2008; 2(1):1-5. http://dx.doi.org/10.2174/1874456700802010001
28. Kondru AK, Pradeep K and Shri C. Catalytic wet peroxide oxidation of azo dye (Congo red) using modified Y zeolite as catalyst. *Journal of Hazardous Materials*. 2009; 166(1):342-7. http://dx.doi.org/10.1016/j.jhazmat.2008.11.042
29. Archer M, Christophersen M and Fauchet PM. Electrical porous silicon chemical sensor for detection of organic solvents. *Sensors and Actuators B*: Chemical. 2005; 106(1):347-57. http://dx.doi.org/10.1016/j.snb.2004.08.016
30. Smallwood IM. *Handbook of organic solvent properties*. New York: John Wiley & Sons, Inc.; 1996.
31. Lu L, Xie G, Jiang Y, Du X and Sun P. Organic vapor adsorption behavior of poly (3-henxylthiophene) films on quartz crystal microbalance. *Proceeding of International Conference on Optical Instruments and Technology:Advanced Sensor*

Technologies and Applications. 2009; 7508(1). http://dx.doi.org/10.1117/12.837934

32. Xu L, Hu X, Tze Lim Y and Subramanian VS. Organic vapor adsorption behavior of poly(3-butoxythiophene) LB films on quartz crystal microbalance. *Thin Solid Films*. 2002; 417(1-2):90-4. http://dx.doi.org/10.1016/S0040-6090(02)00634-X
33. Jose KA, Biju P, Ashwin W, Vijay KV and Reddy CC. A compact wireless gas sensor using a carbon nanotube/PMMA thin film chemiresistor. *Smart Materials and Structures*. 2004; 13(5):1045. http://dx.doi.org/10.1088/0964-1726/13/5/010
34. Auerbach SM, Carrado KA and Dutta PK. *Handbook of Zeolite Science and Technology*. M. Dekker; 2003. http://dx.doi.org/10.1201/9780203911167
35. Freund MS, Deore B. *Self-doped conducting polymers*. Wiley; 2007. http://dx.doi.org/10.1002/9780470061725
36. Ayad MM, El-Hefnawey G and Torad NL. Quartz crystal microbalance sensor coated with polyaniline emeraldine base for determination of chlorinated aliphatic hydrocarbons. *Sensors and Actuators B*: Chemical. 2008; 134(2):887-94. http://dx.doi.org/10.1016/j.snb.2008.06.058
37. Jiang L, Jun H-K, Hoh Y-S, Lim J-O, Lee D-D and Huh J-S. Sensing characteristics of polypyrrole-poly(vinyl alcohol) methanol sensors prepared by in situ vapor state polymerization. *Sensors and Actuators B*: Chemical. 2005; 105(2):132-7. http://dx.doi.org/10.1016/j.snb.2003.12.077
38. Tukker A and Simons ILP. *Dichloromethane*: Advantages and drawbacks of possible market restrictions in the EU. 1999. TNO Report STB – 99-53 Final.
39. Satcher D. *Immediately Dangerous To Life or Health (IDLH)*. Centers for Disease Control and Prevention; 1994 . Available from: <http://www.cdc.gov/niosh/idlh/intridl4.html>.
40. Silverstein RM, Webster FX and Kiemle D. *Spectrometric Identification of Organic Compounds*. New York: John Willey & Sons, Inc.; 2005.
41. Lambert JB, Gronert S, Shurvell HF and Lightner D. *Organic Structural Spectroscopy*. Prentice Hall PTR; 2010.
42. Martin HP, Muller E, Richter R, Roewer G and Brendler E. Conversion process of chlorine containing polysilanes into silicon carbide: Part I Synthesis and crosslinking of poly(chloromethyl)silanes-carbosilanes and their transformation into inorganic amorphous silicon carbide. *Journal of Materials Science*. 1997; 32(5):1381-7. http://dx.doi.org/10.1023/A:1018577111536
43. Anitha G and Subramanian E. Recognition and exposition of intermolecular interaction between CH_2Cl_2 and $CHCl_3$ by conducting polyaniline materials. *Sensors and Actuators B*: Chemical. 2005; 107:605-15. http://dx.doi.org/10.1016/j.snb.2004.11.027
44. Vivekanandan JPV, Mahudeswaran A and Vijayanand PS. Synthesis, characterization and conductivity study of polyaniline prepared by chemical oxidative and electrochemical methods. *Archives of Applied Science Research*. 2011; 3(6):147.
45. De Santana H and Temperini MLA. The Spectroscopic Charactarization of Polydiphenylamine and one of its Oligomeric Fraction. *Journal of Brazilian Chemical Society*. 1996; 7(6):485-90. http://dx.doi.org/10.5935/0103-5053.19960087
46. Bennur TH, Srinivas D and Sivasanker S. Oxidation of ethylbenzene over "neat" and zeolite-Y-encapsulated copper tri- and tetraaza macrocyclic complexes. *Journal of Molecular Catalysis A*: Chemical. 2004; 207(2):163-71. http://dx.doi.org/10.1016/S1381-1169(03)00502-8
47. Choi SY, Park YS, Hong SB and Yoon KB. Iodine as a Visible Probe for the Evaluation of Zeolite Donor Strength. *Journal of the American Chemical Society*. 1996; 118(39):9377-86. http://dx.doi.org/10.1021/ja952112+
48. Thuwachaowsoan K, Chotpattananont D, Sirivat A, Rujiravanit R and Schwank JW. Electrical conductivity responses and interactions of poly(3-thiopheneacetic acid)/zeolites L, mordenite, beta and H_2. *Materials Science and Engineering*: B. 2007; 140(1-2):23-30. http://dx.doi.org/10.1016/j.mseb.2007.03.005

Journal of Ceramic Processing Research. Vol. 14, No. 6, pp. 658~666 (2013)

J O U R N A L O F
Ceramic
Processing Research

Ceramic granules forming from calcium sodium aluminosilicate and carboxymethyl cellulose

Nuchnapa Tangboriboon[a], La-orngdow Mulsow[a], Wissawin Kunchornsup[b] and Anuvat Sirivat[b,*]
[a]*The Materials Engineering Department, Faculty of Engineering, Kasetsart University, Bangkok 10900, Thailand*
[b]*The Petroleum and Petrochemical College, Chulalongkorn University, Bangkok 10330, Thailand*

Calcium sodium aluminosilicate with a molar ratio of 1 : 1 : 2 : 8 of $CaO : Al_2O_3 : Na_2O : SiO_2$, was successfully synthesized, by a sol-gel process using chicken eggshell powder as the starting material, through the calcination at 300 °C for 1 hr. Carboxymethyl cellulose was used as an organic binder to produce the granulation of the ceramic powder without altering any ceramic powder properties. The calcium sodium aluminosilicate granules possess the specific surface area of 38.89 $m^2 g^{-1}$, the pore volume of 0.37 cm^3, the average pore diameter of 38.34 nm, and the true density of 1.96 g cm^{-3}. The obtained ceramic granule is of a very fine particle and it is white in color. The obtained ceramic granules possess good flowing ability and uniform granule size. Fourier transformation infrared spectra (FTIR), X-ray diffraction patterns (XRD), scanning electron micrographs (SEM), transmission electron micrographs (TEM), and physical properties are reported to confirm the existence of the ceramic granules.

Key words: Wet granulation, Ceramic-polymer composite, Carboxymethyl cellulose, Ceramic flow property, Calcination, Zeolite.

Introduction

The egg and egg derivative consumptions produce a great amount of residue shells which pose an environmental pollution through microbial actions. The Agricultural Statistics of Thailand reported the egg production of approximately 9.8×10^9 hens' eggs in 2011 and the number tends to increase indefinitely. The by-product eggshell represents approximately 11% w/w of the total weight (about 50-60 g) of a hen egg. Therefore, the hen eggshells yield approximately 60×10^6 metric tons of the by-product per year in Thailand alone. The eggshells such as from hen, duck, bird, goose, partridge bird are important sources for calcium carbonate, calcium oxide, and calcium hydroxide potentially used in various applications: filler in feed, fertilizer, paper, printing ink, pharmaceutical and cosmetic products, starting materials of dielectrics such as $CaSiO_3$, $CaTiO_3$, $CaAl_2O_4$, gypsum ($CaSO_4$), bio-catalysts for bio-diesel and bio-gasoline [1-10]. Most of eggshell by-products are commonly disposed of by land filling without any pretreatment. This causes odors from biodegradation, microbial actions, and a change in the quality of soil. Eggshells are generally composed of three layers: a thin cuticle outer layer, a thick palisade middle layer, and a thin mammillary inner layer. In particular, the thick palisade middle layer has many large pores. Therefore, it is possible for the eggshell to enhance the catalytic activity per unit mass using the porous palisade layer with a higher fraction.

The porous-solid ceramic namely calcium sodium aluminosilicate with the mole ratioof 1 : 1 : 2 : 8 of $CaO : Al_2O_3 : Na_2O : SiO_2$, was previously obtained from eggshells via the sol-gel process through the calcination at 300 °C for 1 hr, as very fine powder [10-15]. Calcium sodium aluminosilicate is a kind of heterogeneous solid catalysts that is implemented in the environmental protection and in the waste treatment. However, fine particles having low dispersion may affect several operations in the powder processing; flow, storage, mixing, fluidization, moisture absorption, and pressing.. There are several methods to solve the poor particle dispersion, in order to reduce packaging problem, to reduce chemical usage, to comply with air pollution regulation, and to decrease energy consumption. The dispersion can be controlled by modifying the characteristics of the particles or by changing the properties of a dispersed medium, at the same time avoiding any characteristics change of the powders. Small particles are modified for free flowing, poor cohesive forces, and with no caking problem. Two kinds of industrial processes mostly used are the wet granulation and the spray drying; they normally lead to spherical final products [16].

Granulation, also known as agglomeration, pelletisation or balling, is the process of agglomerating fine particles together into larger, semi-permanent aggregates (granules) in which the original particles can still be distinguished.

*Corresponding author:
Tel : +66-2-218-4131
Fax: +66-2-611-7221
E-mail: anuvat.s@chula.ac.th

It consists of a combination of three rate processes (wetting and nucleation, consolidation and growth, and attrition and breakage) [17]. The obtained granules can be used as an adsorbent or a catalyst because of high packing density with minimum air entrapment. On the other hand, a narrow size distribution is preferred in fixed bed reactors to reduce the pressure drop. Wet granulation is the process of bringing material together, by combining smaller particles into larger agglomerates and granules, with a binding agent to enhance flow property and dusting behavior [18]. In the wet granulation process, the capillary and viscous forces from the binder tend to agglomerate particles. The organic liquid binds the particles together until more permanent bonds are established, leading to the granule formation. Overall, the organic binder induces the appropriate cohesive strength and free flowing properties [17, 19-20].

Carboxymethyl cellulose (CMC) is microcrystalline organic colloidal particle; it is a non-toxic binder and the most important commercial cellulose functioning as an organic binder in the granulation process. Applications of CMC based on its rheological properties are: fillers, extenders, glues, hydrophilic colloid thickeners in detergents, oil drilling mud, and wall paper glues. High purity CMC grade is found in pharmaceuticals, toothpaste, and in medical and food industries [21-26].

The obtained calcium sodium aluminosilicate particles are of a fine powder and high specific surface area, therefore, it is potential to apply as catalyst and adsorbent. However, the flow ability problem of calcium sodium aluminosilicate is not suitable for using as column packed bed, storage, or compression. Therefore, the objective of this work is to fabricate ceramic granules of calcium sodium aluminosilicate, with improve flow properties for use, storage, and modified applications. This was carried out by mixing the ceramic powder with sodium carboxymethylcellulose (CMC) which acts as a binder, a lubricant, a stabilizer, a thickener, a gelling agent, and a wet tack with long lasting adhesion. The calcium sodium aluminosilicate ceramic granule detailed characteristics such as bulk density, microstructures, X-ray diffraction patterns (XRD), the particle size distribution, FTIR, the specific surface area, the isotherm plot, and the true density are investigated and reported here.

Experimental

Materials and methods

Calcium oxide (CaO) was prepared from the pyrolysis of chicken eggshells collected from a cafeteria at Kasetsart University, Bangkok, Thailand. Hydrophilic fumed silica (SiO_2, 99.8% pure, the specific surface areas of 206 m^2 g^{-1}, the pH value of 3.9, and the average particle size of 40 microns) was obtained from WACKER Chemie AG, Germany. Precipitated sodium aluminosilicate (82% silica, 10% alumina, 6% sodium oxide, and 0.04% iron oxide), was obtained from United Silica (Siam) Ltd., Thailand. Sodium hydroxide pellets (98% pure) were obtained from Molecule Co., Ltd., Thailand. Hydrochloric acid (Analytical Reagent grade, AR) was purchased from Lab-Scan Co. Ltd., Thailand. Carboxymethyl cellulose (CMC 10000) or a cellulose gum powder, as supplied by Amarin Ceramics Corp., Ltd., Thailand, was used as the binder in the granule preparation. CMC 10000 is highly purified sodium carboxymethyl cellulose. The sodium content (dry basis), the moisture content, the degree of substitution, the pH value, and the viscosity (Brookfield LVF 60 rpm) of CMC 10000 are 99.5% min, 8%, 0.60-0.95, 6-8, 700-1500 mPas (25 °C, 1%), respectively.

Instruments

A laboratory muffle furnace (Linn High Thermo GmbH, LM 412.27, model DC021032 with the thermocouple of type K, NiCr-Ni) was used to prepare the CaO samples from eggshells. The calcination was carried out in an alumina crucible under the heating rate of 10 °C/min.

Cumulative and fractional distributions were measured using a particle size analyzer (Mastersizer S long bed, model Polydisperse 2.19). The samples were dispersed in a water medium and vibrated in an ultrasonic cleaner for 20 min. Cumulative and fractional distributions were measured by using a particle size analyzer (Mastersizer S, Model Polydisperse 2.19).

Fourier transform infrared spectra (FTIR) were recorded (PerkinElmer, model Spectrum One spectrometer) with a spectral resolution of 4 cm^{-1} using transparent KBr pellets obtained by mixing 0.001 g of a sample with 0.06 g of KBr and hydraulically pressed.

X-ray diffraction patterns (XRD) were analyzed using an X-ray diffractometer (Bruker AXS analyzer (D8 Discover) with a VANTEC-1 Detector) consisting of CuKα radiation ($\lambda = 0.154$ nm). The double-crystal wide-angle goniometry was used to analyze the samples. Scanning was operated from 5 ° to 80 ° 2θ at a scan speed of 5 ° 2θ min^{-1} in 0.05 ° or 0.03 °.

Micrographs were obtained using a transmission electron microscope (TEM, JEM-2100) equipped with EDX for the X-ray microanalysis and for the nano beam diffraction (NBD). Ceramic granule samples were cut to obtain a thin foil for the beam to penetrate to investigate the morphology and microstructure.

Scanning electron (SEM) micrographs were obtained from a scanning electron microscope (JEOL, Model 5200). The ceramic granules were immobilized on stubs using a carbon paste and were sputter-coated to ~ 0.1 μm with gold to improve electrical conductivity and quality of the SEM images.

True density of the samples was measured by a gas pycnometer (Quantachrome, Ultra pycnometer 1000). Bulk density of granules was measured on the basis of its mass (m) and volume (V) according to ASTM E727/E727M-08 in equation (1);

$$\rho_b = \frac{m}{v} \quad (1)$$

where ρ_b is the bulk density of granulation (g cm^{-3}), m is the mass (g), and V is the volume (cm^3).

The specific surface area, the adsorption and/or desorption isotherms, the pore size and the surface distributions were measured using an AUTOSORB-1 (Quantachrome) based on the BET (Brunauer-Emmet-Teller) equation:

$$\frac{1}{W((P_O/P)-1)} = \frac{1}{W_m C} + \frac{C-1}{W_m C}\left(\frac{P}{P_O}\right) \quad (2)$$

where W is the weight of gas adsorbed at a relative pressure, P/P_o, W_m is the weight of adsorbate constituting of a monolayer of surface coverage; and C is the constant related to the energy of adsorption in the first adsorbed layer and consequently its value is thus an indication of the magnitude of the adsorbent/adsorbate interactions.

The specific surface area, S, of the solid can be calculated from the total surface area and the sample weight, according to equations (2) and (3):

$$S = S_t/W \quad (3)$$

$$S_t = \frac{W_m N A_{cs}}{M} \quad (4)$$

where S is the specific surface area of the solid, S_t is the total surface area, W is the sample weight, N is Avogadro's number (6.023×10^{23} molecules mol^{-1}), M is the molecular weight of the adsorbate, and A_{cs} is the area occupied by one adsorbate molecule (16.2×10^{-20} m^2 for N_2 and 19.5×10^{-20} m^2 for Kr). There are three types of porosity classifications by gas adsorption: (i) pores with openings exceeding 500 Å in diameter are called "macropores"; (ii) "micropores", which can be identified with pores of diameters less than 20 Å; and (iii) pores of intermediate sizes between the above pores are called "mesopores".

Calcium sodium aluminosilicate ceramic powder preparation by sol-gel process [15]

Calcium chloride solution preparation: calcium oxide (CaO) was prepared from eggshells by the pyrolysis. The eggshells were cleaned and crushed in an alumina crucible, calcined with the muffle furnace under an air atmosphere at 900 °C, for 1 hr at a 10 °C min^{-1} of heating rate, and then cooled in air. Calcium oxide (0.5 g) was dissolved in 20 ml of 1M HCl to obtain a solution.

Mixture of sodium aluminosilicate solution preparation: The mixture was obtained by mixing fumed silica (SiO_2) powder 0 to 0.5 g, precipitated sodium aluminosilicate, and 1.0 g of sodium hydroxide (NaOH) with 20 ml of distilled water.

Calcium sodium aluminosilicate preparation: The mixture solution of 2.3.1 and the mixture solution of 2.3.2 were mixed, and the solution of the mixtures changed into a gel within 5 hrs. The samples were allowed to age to obtain the particle growth for a duration of 24 hrs at room temperature. The molar ratios of the $CaO : Al_2O_3 : Na_2O : SiO_2$ were 1 : 1 : 2 : 8 by the sol-gel process at room temperature (25 °C). The gel samples were dried at 110 °C for 24 hrs and then calcined at 300 °C for 1 hr. All dried white powder samples were obtained.

Calcium sodium aluminosilicate ceramic granules preparation and classification

Calcium sodium aluminosilicate ceramic powder granules were produced directly from fine ceramic powders (10 g) premixed with a small percentage (0.20 g) of carboxymethyl cellulose (CMC) in 10 ml warm water (approximately temperature 60-70 °C) as a binder solution at room temperature. The mixture of calcium sodium aluminosilicate ceramic powder and the CMC binder solution was stirred for approximately 5 to 10 min. After few minutes, an agglomeration called a granule or seed formed initially. The growth of ceramic granules occurred by layering and by the

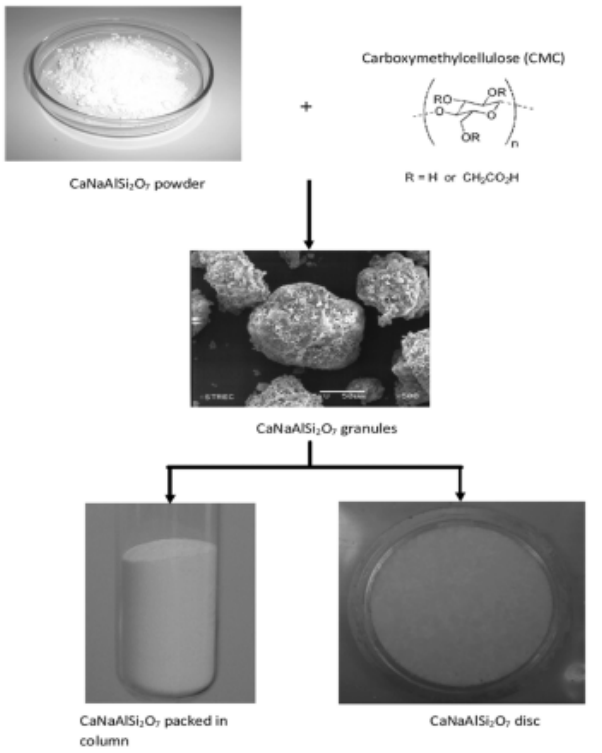

Fig. 1. Flowchart of calcium sodium aluminosilicate ceramic granules and disc formation.

agglomeration of particles. The growth of granules depends on the ratio between CMC and water (solution viscosity), temperature, and the effective adsorption of liquid into the agglomerate. The ceramic granules were put on the top tray and the stack of sieves was vibrated circularly by hand for 30 min. Granules were classified by the gravitation force during the sieving for 30 min. The obtained ceramic granule sizes were classified by passing them through the U.S. Standard sieves of the International Standards Organization (ISO). The sieves were arranged in a stack from the coarsest to the finest (65 mesh (212 μm), 100 mesh (150 μm), 150 mesh (106 μm), and 200 mesh (75 μm), respectively. The percentage of ceramic granules remaining was calculated for each sieve size. The obtained granules are with good flow ability, and of round shapes. The obtained ceramic granules can be packed into a column or pressed under pressure to measure the bulk density and to form ceramic discs, as shown in Fig. 1.

Results and Discussion

Characterizations of raw materials for porous-solid ceramic powder

Calcium oxide (CaO) was prepared from the pyrolysis of chicken eggshells. Raw eggshells were cleaned with tap water and dried at a room temperature. Then they were crushed by a porcelain mortar and kept in a desiccator until further use. The calcium oxide was successfully extracted by the pyrolysis technique at 900 °C for 1 hr, which produced the yield with a very high purity of 98.15%. The FTIR spectra 900_1 exhibit strong ν(O-H) and ν(Ca-O) vibrations. The broad peaks indicate the O-H stretching vibration ν(O-H) of the calcium oxide (CaO), fumed silica (SiO_2), and aluminosilicate at 3,643 and 3,443 cm^{-1}, 3434 cm^{-1}, and 3435 cm^{-1}, respectively. They can be assigned to the water absorbed on the surface of the products. The band at 1630-1633 cm^{-1} can be attributed the O-H bending δ(O-H) of CaO, SiO_2 and aluminosilicate. The characteristic peaks of the amorphous SiO_2, CaO, and aluminosilicate correspond to ν(Si-O-Si), ν(Ca-O), and ν(Al-O-Si) at 1108 and 810 cm^{-1}, 874 cm^{-1}, and 1079 and 791 cm^{-1}, respectively.

A phase transformation was investigated by XRD patterns which reveal that the rhombohedral form of the calcium carbonate (calcite, $CaCO_3$), the main composition of eggshell, transforms into the hexagonal form of calcium oxide and hydroxide. The ceramic yield of calcium oxide content is equal to 74.42%, as characterized by STA [15]. The data suggests that calcium carbonate ($CaCO_3$) was converted to calcium oxide (CaO) with high purification. Both fumed silica (SiO_2) and aluminosilicate show amorphous phases in the XRD patterns. Therefore, all raw materials (CaO, SiO_2, and aluminosilicate) for the ceramic compound preparation are of high purity suitable to prepare a porous-solid ceramic powder.

The specific surface area, the total pore volume, the average pore diameter, and true density of calcium oxide (CaO) values are 7.79 $m^2\ g^{-1}$, 0.0072 $cm^3\ g^{-1}$, 17.00 Å, and 2.16 g cm^{-3}, respectively. The specific surface area, the percentage of loss on drying, the pH value, the bulk density, true density, and the particle size of sodium aluminosilicate are 75 $m^2\ g^{-1}$, 5.2, 10.0, 200 kg m^{-3}, 2.04 g cm^{-3}, and 45 microns, respectively [15].

Characterizations of calcium sodium aluminosilicate ceramic granules

The physical properties data of CaO, fumed silica, aluminosilicate, and calcium sodium aluminosilicate ceramic granules are tabulated in Table 1. The specific surface areas of CaO made from eggshells, fumed silica (SiO_2), aluminosilicate, and the calcium sodium aluminosilicate granules are 7.79, 206, 75, and 38.89 m^2g^{-1}, respectively. The specific surface area of the calcium sodium aluminosilicate ceramic granules suggests it is in the range of mesoporous particles. True densities of CaO made from eggshells, fumed silica (SiO_2), aluminosilicate, and the calcium sodium aluminosilicate ceramic granule are 2.16, 2.12, 2.04, and 1.96 g cm^{-3}, respectively. The average pore diam-eter of the calcium sodium aluminosilicate ceramic granules is equal to 38.34 nm.

The particle size distribution of the ceramic powder is shown in Fig. 2. The d_{10}, d_{50}, d_{90}, and d_{avg} of the calcium sodium aluminosilicate ceramic powder are 2.67, 9.88, 29.10, and 13.27 μm, respectively.

FTIR spectra of the CaO made from eggshells, fumed silica, aluminosilicate, and the calcium sodium

Table 1. Physical properties of CaO, fumed silica, aluminosilicate, and calcium sodium aluminosilicate ceramic granules.

Samples	Specific surface area BET (m^2/g)	Total pore volume (cm^3/g)	Average pore diameter (Å)	True density (g/cm^3)
CaO	7.79	0.0072	17.00	2.16
Fumed silica (SiO_2)	206.00	–	–	2.12
Aluminosilicate	75.00	–	–	2.04
Calcium sodium aluminosilicate granules	38.89	0.3728	383.40	1.96

"–" means not measured.

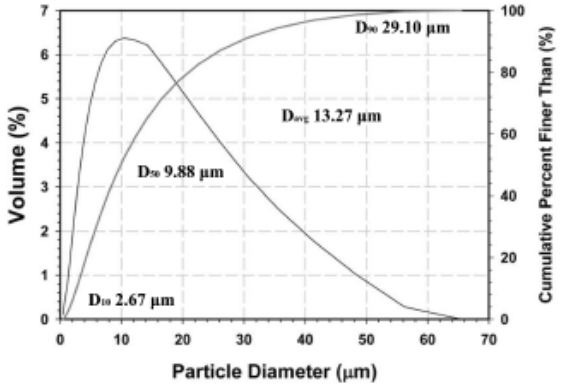

Fig. 2. Particle size distribution of calcium sodium aluminosilicate ceramic powder.

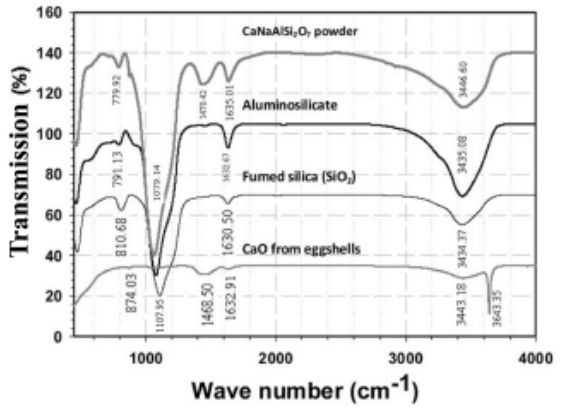

Fig. 3. FTIR spectra of CaO, fumed silica (SiO_2), aluminosilicate, and calcium sodium aluminosilicate ceramic powder.

aluminosilicate powder are shown in Fig. 3. The FTIR spectrum of the calcium oxide (CaO) exhibits peaks at 3600 cm^{-1} due to strong (O-H), 3450 cm^{-1} due to ν(O-H), 2800-2970 cm^{-1} due to δ(C-H), 1750 cm^{-1} of ν(C = O), 1650 cm^{-1} due to strong ν(C = O), and 500-580 cm^{-1} due to ν(Ca-O). The FTIR spectra of the aluminosilicate and the fumed silica show a broad peak at 3450 cm^{-1} due to strong ν(O-H), and at 540 cm^{-1} due to ν(Al-O-C), ν(Si-O-Al), ν(Si-O), and ν(Si-O-Si). The FTIR spectra of the calcium sodium aluminosilicate powder differ from the FTIR spectra of the raw materials (CaO, SiO_2, and aluminosilicate); the peaks are at 1470 cm^{-1} due to strong ν(C = O), 640-580 cm^{-1} due to ν(Al-O), and nearly 500-550 cm^{-1} due to ν(Al-O-C), ν(Si-O-Al), ν(Si-O), and ν(Si-O-Si).

FTIR spectra of the calcium sodium aluminosilicate ceramic powder, CMC as the binder, and the calcium sodium aluminosilicate ceramic granules in the range of 4000 to 400 cm^{-1} are shown in Fig. 4. The FTIR spectrum of the calcium sodium aluminosilicate ceramic granules and CMC show peaks at 3433 cm^{-1} due to strong ν(O-H) and 3436 cm^{-1} due to ν(O-H), corresponding to the hydroxyl group of anhydroglucose units of cellulose molecule. Furthermore, the FTIR spectra of the calcium sodium aluminosilicate ceramic

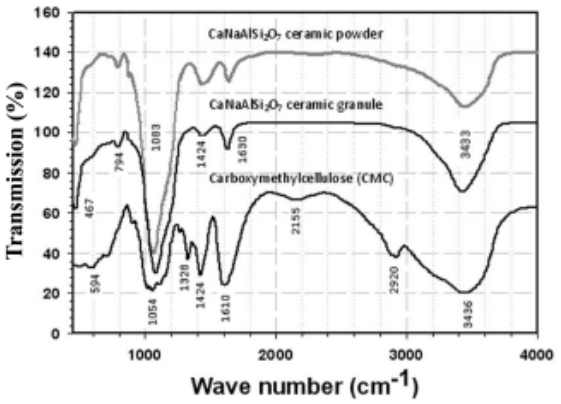

Fig. 4. FTIR spectra of carboxymethyl cellulose, calcium sodium aluminosilicate powder, and calcium sodium aluminosilicate ceramic granules.

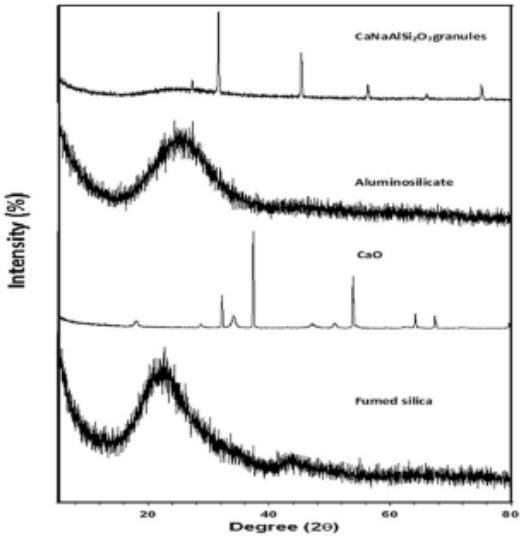

Fig. 5. XRD patterns of CaO, fumed silica (SiO_2), aluminosilicate, and calcium sodium aluminosilicate ceramic granules.

granules and carboxymethyl cellulose show peaks at 2920 cm^{-1} due to δ(C-H) of CH_2, 1610 cm^{-1} due to ν(C = O) of the ketone group, 1424 cm^{-1} and 1328 cm^{-1} due to δ(C-H) of CH_2, 1054 cm^{-1} and 1083 cm^{-1} due to ν(CH_2-OH) and ν(C-O), and 594 cm^{-1} due to δ(= C-H).

XRD patterns of the fumed silica (SiO_2), CaO made from eggshells, the aluminosilicate, and the calcium sodium aluminosilicate ceramic granules are shown in Fig. 5. The XRD patterns of the fumed silica and the aluminosilicate exhibit an amorphous phase formation. The XRD pattern of the CaO made from eggshells shows a crystalline phase formation, corresponding to those assigned at the International Center for Diffraction Data (JCPDS) patterns, with numbers 85-1108 and 72-1651. With the peaks 2θ equal to 29.466, 36.039, 39.489, 47.625, and 48.615, they correspond to the rhombohedral form of calcium carbonate (calcite, $CaCO_3$). The X-ray characteristic peaks and patterns of the calcium sodium aluminosilicat ceramic granules are

consistent with JCPDS numbers 71-2066, 77-2064, and 76-479. With the peaks at 2θ and (hkl) equal to 31.605 (211), 45.432 (220), 56.452 (222), 29.310 (201), 68.714 (521), and 75.263 (420), they correspond to the tetragonal form of calcium sodium aluminosilicate. The crystal structure of the calcium sodium aluminosilicate granule corresponds to the crystal structure shown in Fig. 5. The crystal structure of calcium sodium aluminosilicate suggests it is possible to express ion exchange in the general formula of sodium aluminosilicate. Ca^{2+} can be substituted for Na^{+} at the site of monovalent. Furthermore, calcium sodium aluminosilicate is one kind of catalyst structures that are ion exchangers whose cations are catalytically active as shown in the equation (5).

$$M_2O.Al_2O_3.xSiO_2.yH_2O = xSiO_2\ (AlO_2^-, M^+).yH_2O \quad (5)$$

Specific surface area and isotherm of calcium sodium aluminosilicate ceramic granules

The specific surface area and the N_2 adsorption-desorption isotherms of CaO from eggshells and the as-synthesized calcium sodium aluminosilicate granule, are shown in Fig. 6a and 6b. The specific surface area, the total pore volume, and the average porosity diameter of calcium sodium aluminosilicate granules are 38.89 $m^2\ g^{-1}$, 0.3728, and 38.34 nm, respectively. The pore size distribution vs. pore diameter of the calcium sodium aluminosilicate shows the pore diameter in the range of 20 Å to 500 Å, which can be called a mesoporous structure through its hysteresis loop, following the Kelvin equation. It is widely accepted that the desorption isotherm is more appropriate than the adsorption isotherm for investigating the pore size distribution of an adsorbent. The desorption branch of the isotherm, for the same volume of gas, shows a lower relative pressure, causing a lower free energy state. Thus, the desorption isotherm is close to the thermodynamic equilibrium. The high specific surface area and porosity of solid-porous particles are the most important properties required for removing pollutants, reagents separation, and products purification,

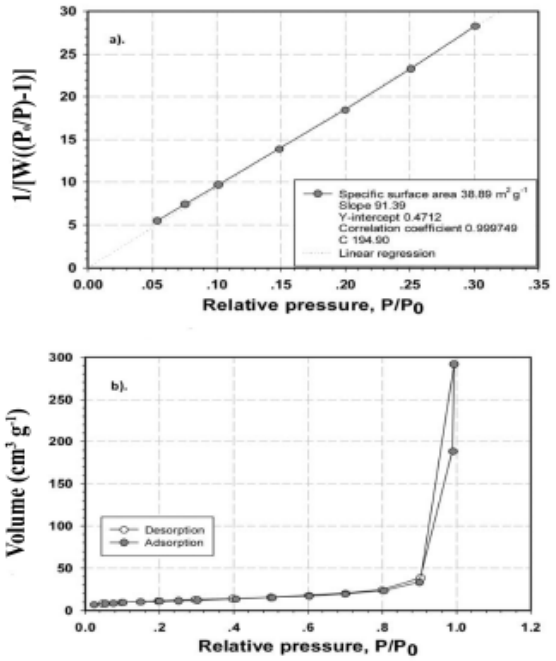

Fig. 6. (a) Specific surface area of calcium sodium aluminosilicate ceramic granules versus the relative pressure and (b) Isotherm plot of adsorption and desorption of calcium sodium aluminosilicate ceramic granules versus the relative pressure.

by acting as a heterogeneous catalysis; however its catalytic activity should be verified further. Calcium sodium aluminosilicate is one kind of porous-solid types whose pores arise from the intrinsic crystalline structure containing Al, Si, Ca, Na, and O. Al-O, and Si-O tetrahedral units cannot occupy the space perfectly, and therefore they produce cavities which are suitable for pollutant trapping or ion exchange.

Bulk density and micrographs of ceramic granules

Bulk density values of the calcium sodium aluminosilicate granules are data tabulated in Table 2. The bulk density values of the calcium sodium aluminosilicate ceramic granules of sizes 75, 106, 150, and 212 µm are 0.0329 ± 0.0124, 0.0369 ± 0.0263, 0.0381 ± 0.0304, 0.0415 ± 0.0258 g cm^{-3}, respectively.

Table 2. Bulk density of calcium sodium aluminosilicate ceramic granules.

Sieve size[a*] (mesh)	Average diameter of granules (µm)	Bulk density granules with pores (g/cm^3)	Amount granules with pores[b*] (%)
200	75	0.0329 ± 0.0124	72.61
150	106	0.0369 ± 0.0263	12.74
100	150	0.0381 ± 0.0304	8.28
65	212	0.0415 ± 0.0258	6.36

[a*] U.S.A Standard Sieve Series-ASTM Specification E11-70.
[b*] mean amount granules with pores in unit of percent when granules classified by standard screens arranged in a stack from the coarsest to the finest (65, 100, 150, 200, and solid tray, respectively) with a pan below the bottom sieve to collect the fines. The calcium sodium aluminosilicate ceramic granules are introduced on the top screen and the stack of sieves is vibrated such that the ceramic granules will stratify by particle size through the sieves.

The percentages of granules or agglomeration on each sieve size were classified by passing them through the standard screens arranged in a stack from the coarsest to the finest 65 mesh (212 μm), 100 mesh (150 μm), 150 μmesh (106 μm), and 200 mesh (75 μm), respectively, are 6.36%, 8.28%, 12.74%, and 72.61%, respectively. Aulton and Banks (1979) reported that as the wettability of the powder mixture increased, the mean granule size decreased [20]. Wetting and spreading can also be described using surface free energies. The spreading coefficient (λ) is a measure of the tendency of a liquid and a solid to spread over each other and is related to the works of adhesion and cohesion [17]:

$$\text{Work of cohesion for a solid: } W_{CS} = 2\gamma_{SV} \quad (6)$$

$$\text{Work of cohesion for a liquid: } W_{CL} = 2\gamma_{LV} \quad (7)$$

$$\text{Work of adhesion for an interface: } W_A = \gamma_{SV} + \gamma_{LV} + \gamma_{SL} + \gamma_{LV}(\cos\theta + 1) \quad (8)$$

where γ_{SV}, γ_{SL}, and γ_{LV} are the effective interfacial tensions between two phases, λ is the spreading coefficient for each phase which can be calculated using the following relationships [27]:

$$\lambda_{LS} = W_A\text{-}W_{CL} \quad (9)$$

$$\text{and } \lambda_{SL} = W_A\text{-}W_{CS} \quad (10)$$

The SEM micrographs with a magnification of 100X of calcium sodium aluminosilicate ceramic granules were classified by the sieve analysis, as shown in Fig.7. The granule sizes of calcium sodium aluminosilicate (75, 106, 150, and 212 μm) are uniform; the granules are of good flow property, with a dense and smooth surface. Wet granulation is used to improve flow, compressibility, bio-availability, homogeneity, electrostatic properties, and stability of solid dosage forms. There are many factors affecting the wet granulation: agglomeration, mixing, wet massing, porosity of powder, liquid bridges, coalescence, electrostatic force, chemical bonding, and etc. Other important factors of a porous-solid granule are specific surface area, moisture content, particle size distribution, particle shape, intra-granular porosity, heating, evaporation, mean granule size, apparent viscosity including gravity force during granulation process, and surface tension [22].

Comparison of TEM micrographs of calcium sodium aluminosilicate ceramic granules between the granule with the size of 75 μm with magnifications of 80,000X, 40,000X, and 25,000X (a1, a2, and a3) and the granule with the size of 212 μm with magnifications of 80,000X, 40,000X, and 25,000X (b1, b2, and b3), respectively are shown in Fig. 8. Fig. 8(b1, b2, b3) belong to the granule with the size of 212 μm showing

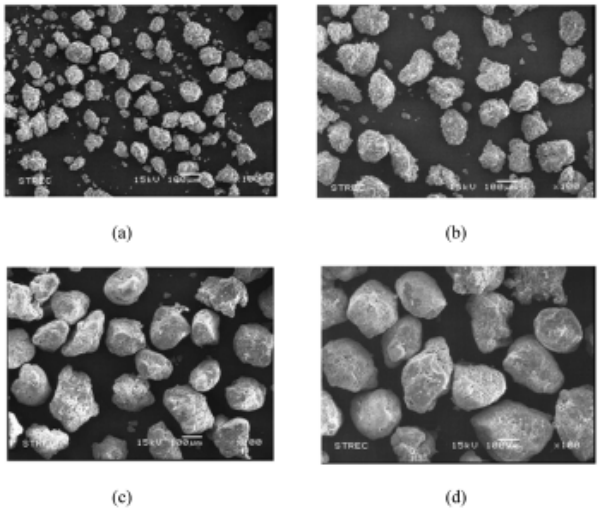

Fig. 7. SEM micrographs of calcium sodium aluminosilicate ceramic granules; (a) 75 μm, (b) 106 μm, (c) 150 μm, and (d) 212 μm.

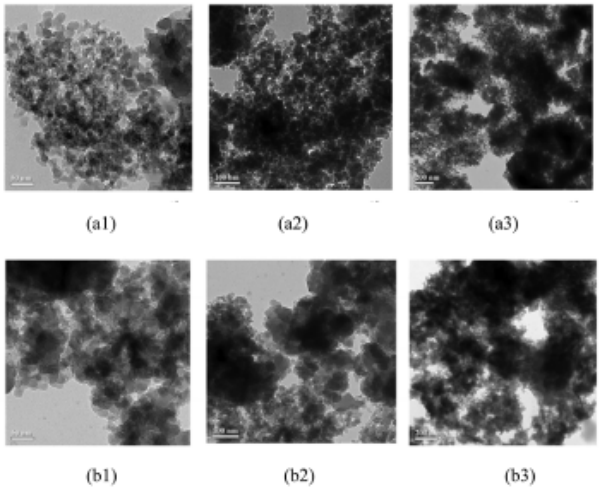

Fig. 8. TEM micrographs of calcium sodium aluminosilicate ceramic granules with the diameters; (a1) 75 μm with the magnification of 80000X, (a2) 75 μm with the magnification of 40000X, (a3) 75 μm with the magnification of 25000X, (b1) 212 μm with the magnification of 80000X, (b2) 212 μm with the magnification of 40000X, and (b3) 212 μm with the magnification of 25000X.

larger granules size than those of Fig. 8(a1, a2, a3) (75 μm). Porous-solid materials have a cohesive structure which depends on the interaction between the primary particles. The cohesive structure causes a void space which is not occupied by atoms, ions, and fine particles. However, the porous-solid materials have the inter-particle forces which are different depending on chemical bonding, van der Waal force, covalent bond, hydrogen bond, magnetic force, electrostatic force, and surface tension of the thick adsorbed layer on the particle surface. Therefore, pores within solids are classified into the intra-particle pores (called intrinsic and extrinsic intra-particle pores), the inter-particle pores called agglomeration (rigid inter-particle pore), and aggregation (flexible inter-particle pore) [28]. The

porous-solid ceramic granules obtained possess stable agglomerates. Thus, inter-particle pores have influences on stability, capacity, shape, and size according to packing of primary particles. The stability depends on the surrounding conditions, such as temperature, moisture, air velocity, pressure. Almost all inter-particle pores in agglomerates are rigid, whereas those in aggregates are flexible. Almost all sintered or calcined porous-solid materials have rigid pores due to strong chemical bonding among the particles. Therefore, the ceramic granulation prepared by the porous-solid ceramic yields mesoporosity (between 2 nm-50 nm), with sodium carboxymethyl cellulose (CMC) as secondary particles and potential utilizations as adsorbents [22, 29].

Conclusion

Sodium carboxymethyl cellulose (CMC) was used successfully as a binder or a dispersion medium, thickenner, gelling agent, long-lasting adhesion, and wet attack in a solution to form calcium sodium aluminosilicate ceramic granules without any change in the ceramic powder property. CMC is non toxic, anionic, moisture absorption, and it is a colloidal binder. The obtained solid ceramic granules (calcium sodium aluminosilicate) were fabricated from biomaterials. The obtained calcium sodium alu-minosilicate granules are potential candidates to be used as an adsorbent in a variety of chemical industries due to non corrosiveness, chemical stability, non toxicity, and low cost. The advantages of calcium sodium aluminosilicate ceramic granules are of good flow ability, suitable for compression, of uniform granule size, non-contaminated, and easy for phase separation. The calcium sodium aluminosilicate ceramic granule sizes depend on a variety of important parameters: the type of binder (the DS value), the binder solution concentration, the granule formation temperature, the surface preparation of ceramic particles, the particle size and shape of particles, the specific surface area and the pore size distribution of particles, the particle discharge on surface (polar and non-polar), the adhesion-cohesion force of wet ag-glomeration, including attractive-repulsive force between particles.

Acknowledgments

The authors would like to thank the following: The Petroleum and Petrochemical College, and the Scientific and Technological Research Equipment Centre, at Chulalongkorn University, Thailand; the Department of Materials Engineering, at Kasetsart University for the use of their analytical equipment. We are also grateful for the grant support from Center for Advanced Studies in Industrial Technology and the Kasetsart University Research and Development of the fiscal year 2010. We also would like to acknowledge the financial supports from the Conductive and Electroactive Polymers Research Unit of Chulalongkorn University, the Thailand Research Fund (TRF), and the Royal Thai Government.

References

1. J.L. Thapon, C.M. Bourgeois, in "L'Oeuf et les ovoproduits", Paris: Lavousier Technique at Documentation (1994) 344.
2. E.M. Rivera, M. Araiza, W. Brostow, V.M. Castano, J.R. Díaz-Estrada, R. Hernández, and J.R. Rodríguez, Mater. Lett. 41 (1999) 128-134.
3. E.I. Adeyeye, Bull. Chem. Soc. Ethiop. 23 (2009) 159-166.
4. M.N. Freire, J.N.F. Holand, Cerâmica. 52 (2006) 240-244.
5. X. Wan, C. Chang, D. Mao, L. Jiang, and M. Li, Mater. Sci. Eng. 25 (2005) 455-461.
6. A. Meiszterics, K. Sinkó, Colloids Surf. A: Physicochem. Eng. 319 (2008) 143-148.
7. R. Chrysafi, T. Perraki, and G. Kakali, J. Eur. Ceram. Soc. 27 (2007) 1707-1710.
8. D.C. Southam, T.W. Lewis, A.J. McFarlane, and J.H. Johnston, Curr. Appl Phys. 4 (2004) 355-358.
9. I.G. Richardso, Cem. Concr. Res. 38 (2008) 137-158.
10. Y.B. Cho, G. Seo, Bioresour. Technol. 101 (2010) 8515-8519.
11. J.W. Kim, D.J. Kim, J.U. Han, M. Kang, J.M. Kim, and J.E. Yie, Catal. Today. 87 (2003) 195-203.
12. R.L. Virta, in "Zeolites. In: United States Geological Survey. compiler. Minerals Yearbook: Volume 1 - Metals and Minerals.", United States Department of the Interior (2004) 83.1-83.4.
13. G.K. Reynolds, J.S. Fu, Y.S. Cheong, M.J. Hounslow, and A.D. Salman, Chem. Eng. Sci. 60 (2005) 3969-3992.
14. T. Gluba, A. Obraniak, and E. Gawot-Mlynarczyk, Physicochem Probl Mi. 38 (2004) 177-186.
15. N. Tangboriboon, S. Wongkasemjit, R. Kunanuruksapong, and A. Sirivat, J. Inorg. Organomet. Polym. Mater. 21 (2011) 50-60.
16. C. Pagnoux, N. Tessier-Doyen, A. Pringuet, M. Cerbelaud, and P. Garcia-Perez, J. Eur. Ceram. Soc. 29 (2009) 1379-1385.
17. S.M. Iveson, J.D. Litster, K. Hapgood, and B.J. Ennis, Powder Technol. 117 (2001) 3-39.
18. R.P.J. Sochon, S.K. Dorvlo, A.I. Rudd, I. Hayati, M. Hounslow, and A.D. Salman, Chem. Eng. Res. Des. 83 [A11] (2005) 1325-1330.
19. B.J. Ennis, J.D. Lister, in "Particle size enlargement, Perr's Chemical Engineers' Handbook, 7th ed", McGraw-Hill, New York (1997).
20. M.E. Aulton, M. Bank, in Proceedings of the International Conference on Powder Technology in Pharmacy, Basel, Switzerland, 1979, edited by Powder Advisory Center.
21. J.S. Reed, in "Introduction to the Principles of Ceramic Processing", John Wiley & Sons Inc (1988) 486.
22. E.M. Holt, Powder Technol. 140 (2004) 194-202.
23. A. Latif, T. Anwar, and S. Noor, Jour. Chem. Soc. Pak. 29 [2] (2007) 143-150.
24. R. J. Maile, U.S. Patent, 4,917,823 (1990).
25. A.M. Adel, H. Abou-Youssef, A.A. El-Gendy, and A.M. Nada, Nat. Sci. 8 [8] (2010) 244-256.
26. C.B. Hollabaugh, L.H. Burt, and A.P. Walsh, Ind. Eng. Chem. (1945) 943-947.

27. A. Trujillo-vazquez, H. Metiver-pignon, L. Tiruta-barna, and P. Piantone, Waste manage. 29 [2] (2009) 530-538.
28. P. York, R.C. Rowe, in Proceedings of the First International Particle Technology Forum, Denver, USA (1994).
29. K. Kaneko, J. Membr. Sci., Review. 96 (1994) 59-89.

Research Article

Received: 29 January 2013 Revised: 22 March 2013 Accepted: 25 March 2013 Published online in Wiley Online Library: 20 May 2013

(wileyonlinelibrary.com) DOI 10.1002/pi.4538

Synthesis of poly(3,4-ethylenedioxythiophene) nanoparticles via chemical oxidation polymerization

Nophawan Paradee and Anuvat Sirivat*

Abstract

Poly(3,4-ethylenedioxythiophene) (PEDOT) nanoparticles were synthesized via chemical oxidation polymerization using 3,4-ethylenedioxythiophene as the starting monomer and ammonium peroxydisulfate (APS) as the oxidant. The effects of APS concentration, surfactant concentration and type of surfactant, namely dodecylbenzenesulfonic acid and sodium dodecylsulfate, were investigated. Distinct particle shapes were obtained: irregular, raspberry agglomerate, coralliform, orange-peel, globular and plum shapes. The particle sizes and the electrical conductivity are in the ranges 60 to 900 nm and <1 to 153 S cm^{-1}, respectively, depending on the polymerization conditions. PEDOT synthesis in the absence of a surfactant yields a smaller particle size because a larger amount of initiator induces lower molecular weights and smaller PEDOT particles. The smaller PEDOT particles correspond to higher electrical conductivity because of the larger surface areas for electron transfer and a smaller amount of obstructing surfactant aliphatic segments. Moreover, particle size and shape can be varied, depending on surfactant type and concentration which dictate the micellar shapes in the polymerization reaction. This work is focused on the tailor-made PEDOT shape and property relationship under synthesis conditions where several shapes have not been previously seen.
© 2013 Society of Chemical Industry

Keywords: nanoparticle synthesis; poly(3,4-ethylenedioxythiophene); chemical oxidation polymerization; electrical conductivity

INTRODUCTION

A nanoparticle refers to a body in which at least one dimension of its structure is below 100 nm; it is fabricated to improve optical, electrical, mechanical and chemical properties.[1] A well-controlled conducting polymer nanostructure is one of the targets in nanotechnology towards many advanced applications. Poly(3,4-ethylenedioxythiophene) (PEDOT), consisting of 3,4-disubstituted thiophene rings, is one type of conducting polymer, previously developed by Bayer AG in the 1980s.[1–3] PEDOT has been widely implemented in many applications: sensors,[2,4] electrochromics,[5,6] light-emitting diodes[7] and solar cells.[8] It has been widely used because it shows promising electrical conductivity with a low band gap, transparency, and thermal and environmental stability.[3,9–11]

Normally, PEDOT can be prepared by chemical oxidation polymerization or electrochemical polymerization. Electrochemical polymerization is preferred for PEDOT in thin-film form; however, its yield is quite low. On the other hand, the synthesis of PEDOT by chemical oxidation polymerization utilizes oxidizing agents to produce a higher PEDOT yield.[1,9,12]

In general, several kinds of oxidants can be used in chemical oxidation polymerization depending on the reaction conditions. Corradi and Armes[13] prepared PEDOT via a chemical synthesis route. They used $FeCl_3$, $Ce(SO_4)_2$ and $(NH_4)Ce(NO_3)_6$ as the oxidants. The electrical conductivity of PEDOT varied from 6.80×10^{-4} to 5.30 S cm^{-1}, depending on the oxidant type, reaction temperature and reaction time. Choi *et al.*[10] studied PEDOT nanoparticle preparation by using a surfactant to produce emulsion polymerization. Dodecylbenzenesulfonic acid (DBSA) was used to act as a surfactant to form micelles. $FeCl_3$ and ammonium peroxide were used as the oxidants. The PEDOT nanoparticles obtained were spherical and their diameter varied from 35 to 120 nm and the electrical conductivity was between 1 and 50 S cm^{-1}. Huajing *et al.*[2] prepared PEDOT nanoparticles by a reverse micelle method. Sodium bis(2-ethylhexyl)sulfosuccinate mixed with $FeCl_3$ was used to create an oxidant active point at the interface of the reversed micelle. The PEDOT nanoparticles obtained possessed particle sizes between 30 and 100 nm and electrical conductivity between 16.7 and 33.7 S cm^{-1}. However, the PEDOT particle size also depends on other parameters in the synthesis: reaction temperature, reaction time and oxidant concentration. The PEDOT particle size obtained directly influences the electrical conductivity.

In the work reported here, PEDOT nanoparticles were prepared through chemical oxidation polymerization. Different particle sizes, particle shapes and corresponding electrical conductivity values of the obtained PEDOT are reported here under the effects of oxidant concentration and type and concentration of surfactant. PEDOT characterization was also carried out via Fourier transform infrared (FTIR) spectroscopy and XRD to investigate the functional groups and crystallography, respectively. In addition, TGA was

* *Correspondence to: Anuvat Sirivat, Conductive and Electroactive Polymer Research Unit, Petroleum and Petrochemical College, Chulalongkorn University, Bangkok, 10330 Thailand. E-mail: anuvat.s@chula.ac.th*

Conductive and Electroactive Polymer Research Unit, Petroleum and Petrochemical College, Chulalongkorn University, Bangkok 10330, Thailand

used to investigate the thermal properties and stability of PEDOT as a function of aging time.

EXPERIMENTAL

Materials

3,4-Ethylenedioxythiophene (EDOT) was used as the monomer and DBSA, a sodium salt, and sodium dodecylsulfate (SDS) as the surfactants (purchased from Sigma-Aldrich). The oxidant, ammonium peroxydisulfate (APS; AR grade), was purchased from Qrec. Acetone and methanol were purchased from Labscan. Distilled water was used as the solvent.

Synthesis of PEDOT nanoparticles

Nanoparticles of PEDOT were prepared by dropping 1.6 mL of EDOT into 100 mL of APS solution, and the solution was stirred for 72 h.[14] To study the effects of the type and concentration of surfactant, 100 mL of surfactant solution was prepared by stirring the surfactant in distilled water for 2 h. Then 1.6 mL of EDOT was added dropwise into the surfactant solution, and then the solution was stirred for 2 h before adding APS.[3,10] The solution was then stirred for 72 h. During this time, the mixture solution colour changed from yellow to green and then blue to dark blue. The product in the solution was centrifuged and washed with an acetone and methanol solution (acetone/methanol = 3:20).[14] Finally the polymer product was dried in a vacuum oven at 60 °C for 24 h.

Characterization of PEDOT nanoparticles

A FTIR spectrometer (Thermo Nicolet, Nexus670) was used to identify the PEDOT nanoparticle functional groups. Samples were prepared using the KBr pellet technique, with KBr as the background material. The spectrometer was operated in absorption mode with spectra being obtained with 32 scans with a resolution of 4 cm^{-1} covering the wavenumber range 400–4000 cm^{-1}.

A wide-angle X-ray diffractometer (Bruker AXS, D8 Advance) was used to determine the crystalline structure of the nanoparticles. The Cu Kα radiation source was operated at 40 kV/30 mA. The interference peak was eliminated by a K-beta filter. Divergence slit and scattering slit of 0.5° together with a 0.3 mm receiving slit were used. The nanoparticles were mounted on a sample holder and a measurement was continuously run. The experiment was run by monitoring the diffraction pattern appearing in the 2θ range of 5° to 40°, with a scan speed of 1° min^{-1} and a scan step of 0.02°.

The thermal behaviour of the nanoparticles was investigated using a thermogravimetric analyser (PerkinElmer, TGA7). Samples, which weighed 5 to 10 mg, were loaded into an aluminium pan. The mass change was scanned from 30 to 900 °C at a heating rate of 10 °C min^{-1}, under nitrogen flow.

The morphology of the nanoparticles was studied using SEM (Hitachi, S4800). Samples were placed on the holder with adhesive tape and coated with a thin layer of platinum. SEM images were obtained using an acceleration voltage of 5 kV with magnification in the range ×25 to ×200 000.

Electrical conductivity was measured using a two-point probe (Keithley, model 8009). These probes were connected to a source meter (Keithley, model 6517A) which provided the applied voltage and the resultant current was recorded. The applied voltage was plotted as a function of the current to determine the linear ohmic regime for each sample based on the van der Pauw method. The applied voltage and the current change in the linear ohmic regime were converted to the electrical conductivity of PEDOT using the following equation:

$$\sigma = \frac{1}{\rho} = \frac{1}{R_s \times t} = \frac{I}{K \times V \times t} \quad (1)$$

where σ is the specific conductivity (S cm^{-1}), ρ is the specific resistivity (Ω cm), R_s is the sheet resistivity (Ω), I is the measured current (A), K is the geometric correction factor (3.22×10^{-3}), V is the applied voltage (V) and t is the pellet thickness (cm).

RESULTS AND DISCUSSION

Structural characterization of PEDOT nanoparticles

FTIR analysis

The structures of PEDOT obtained using different synthesis conditions were investigated using FTIR spectroscopy. The peaks at 1520 and 1360 cm^{-1} originate from the C–C or C=C stretching of the quinoidal structure of the thiophene ring and the stretching of the thiophene ring, respectively. The peaks at 1206, 1143 and 1099 cm^{-1} correspond to the stretching vibration of the C–O–C bond in the ethylenedioxy group. The bands of the C–S bond in the thiophene ring are seen at 982, 845 and 693 cm^{-1}. The absorption peak at 1650 cm^{-1} indicates the doping level of the polymer; this peak shifts to a lower wavelength due to the over-oxidant side reaction. The PEDOT particles, as obtained when using a surfactant, show smaller peaks at 2800 to 3000 cm^{-1} which can be assigned to the aliphatic C–H stretching mode depending on the long alkyl tail of the surfactant.[4,9,10]

XRD patterns

XRD patterns of PEDOT particles obtained using various APS concentrations with and without surfactant are shown in Figs 1(a) and (b), respectively. PEDOT nanoparticle diffraction peaks appear at 2θ = 6.6°, 12.6° and 17.5°, which can be referred to a structurally similar system where the interchain packing is along a pseudo-orthorhombic a axis, while the diffraction peak at 2θ = 25.7° can be referred to as the interchain planar ring-stacking distance.[15] Figure 1(a) shows that the intensity of the peaks at 6.6° and 12.6° increases, and the peak at 25.7° shifts to higher angle as the APS concentration changes from 0.15 to 0.30 mol L^{-1}. This phenomenon suggests that increasing the doping level with increasing APS concentration induces a higher order in the PEDOT nanoparticle structure.[2,10,11] When the APS concentration is 0.45 mol L^{-1}, it is in the over-oxidation state, and the intensity of the peaks at 6.6° and 12.6° decreases. Furthermore, the intensity of the diffraction peak at 17.5° increases with increasing APS concentration; this can be ascribed to the change in PEDOT particle shapes: irregular, raspberry and coralliform.

Figure 1(b) shows the effect of DBSA and SDS surfactants on the PEDOT structure. The intensity of the peaks at 6.6° and 12.6° decreases, and the peak at 25.7° shifts to a lower angle with addition of surfactants. This indicates that the degree of crystallinity decreases after adding the surfactants. The diffraction peak of PEDOT synthesized using SDS is sharper than that of PEDOT synthesized using DBSA. This is because the DBSA consists of a bulky benzene ring structure leading to a more amorphous structure for PEDOT.[12,16,17]

 © 2013 Society of Chemical Industry

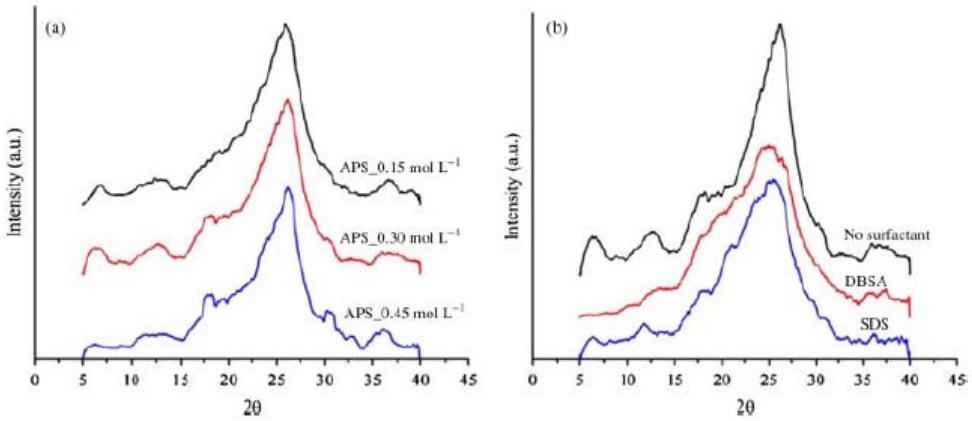

Figure 1. XRD patterns of PEDOT nanoparticles: (a) various APS concentrations; (b) various types of surfactant.

Morphology

The SEM images in Figs 2, 3 and 4 show different PEDOT particle sizes and shapes depending on the polymerization conditions. Figure 2 shows the morphology of the PEDOT particles under the effect of APS concentration without a surfactant. The particle size varies from 70 to 212 nm and the shape changes from irregular (Fig. 2(a)), to raspberry agglomerate (Fig. 2(b)), and to coralliform (Fig. 2(c)). Thus, the particle size decreases and the particle shape changes from irregular to coralliform with increasing APS concentration. APS acts as oxidant and initiator, as shown in Fig. 5, creating an EDOT cation radical in the first step. Then, the PEDOT polymeric chain is generated from the EDOT cation radicals to become a protonated dimer which subsequently gets deprotonated. Finally, the PEDOT polymer is doped by sulfate ion residues in which they can act as a counter ion.[4,18,19] Because APS is an initiator, the APS concentration affects the polymerization rate and amount of PEDOT polymeric cation radicals in the first step. A larger amount of PEDOT polymeric cation radicals can generate a greater electro-repulsive force between the PEDOT polymeric cation radicals during the polymerization in the second step. The greater electro-repulsive force between PEDOT polymeric cation radicals and the faster rate of polymerization lead to a smaller particle size because there are more active sites of the EDOT cations. On the other hand, a greater APS concentration can simultaneously increase the amount of sulfate counter anions, which in turn screens the electro-repulsive force between PEDOT polymeric cations, the so-called screening effect of the electro-repulsive force. This causes particle agglomeration resulting in a larger particle size. At an APS concentration lower than 0.30 mol L^{-1}, the largest PEDOT particle size (*ca* 212 nm) is obtained with particles of irregular shape (Fig. 2(a)). This is because a lower APS concentration creates a smaller amount of PEDOT polymeric cation chains, a weaker electro-repulsive force between the PEDOT polymeric cations and a lower polymerization rate, thus leading to a larger PEDOT particle size. At an APS concentration of 0.30 mol L^{-1}, the PEDOT particle size is the smallest (*ca* 70 nm), appearing as a raspberry shape, as shown in Fig. 2(b). Thus, it appears that this amount of APS is suitable for balancing the number of polymeric cation chains and the electro-repulsive force to yield the smallest PEDOT particle size. Nevertheless, the smallest PEDOT particles can easily become agglomerated and create a larger particle size as in the raspberry agglomerate. For higher APS concentrations (higher than 0.30 mol L^{-1}), the electro-repulsive force between PEDOT polymeric cations is screened by sulfate anions as the counter ion, inducing the fusion of the polymerizing PEDOT particles, and eventually transforming them to the coralliform shape, as shown in Fig. 2(c).

The particle size under the effect of DBSA concentration varies from 63 to 396 nm and the particle shape changes from the orange-peel shape (Fig. 3(a)), to the raspberry agglomerate (Fig. 3(b)) and to the fused globular agglomerate (Fig. 3(c)) at 0.25 $\times$ 10^{-2}, 0.05 and 0.10 mol L^{-1} DBSA concentration, respectively. At 0.25 $\times$ 10^{-2} mol L^{-1} DBSA concentration, the particles are the largest (*ca* 396 nm) appearing as the orange-peel shape, as shown in Fig. 3(a). This DBSA concentration is lower than the critical micelle concentration (CMC, which is 0.29 $\times$ 10^{-2} mol L^{-1}), and there are no micelles formed during polymerization. Above the CMC, the increase in surfactant concentration produces more micelles.[3,20,21] Figure 3(b) shows the smallest particle size (*ca* 63 nm) as the raspberry agglomerate shape as obtained from 0.05 mol L^{-1} DBSA concentration. At a concentration greater than the CMC, polymerization occurs within the micelle core, causing smaller PEDOT particles.[22] On the other hand, with a further increase in DBSA concentration to

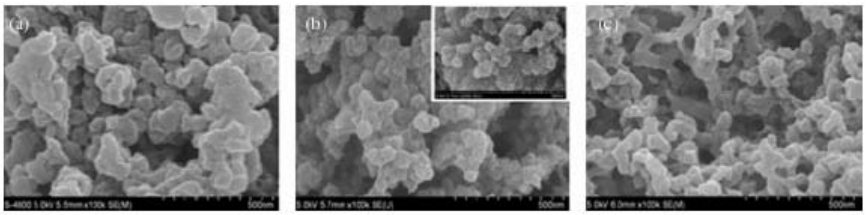

Figure 2. Morphologies of PEDOT nanoparticles prepared using various APS concentrations: (a) 0.15 mol L^{-1}; (b) 0.30 mol L^{-1}; (c) 0.45 mol L^{-1}.

© 2013 Society of Chemical Industry

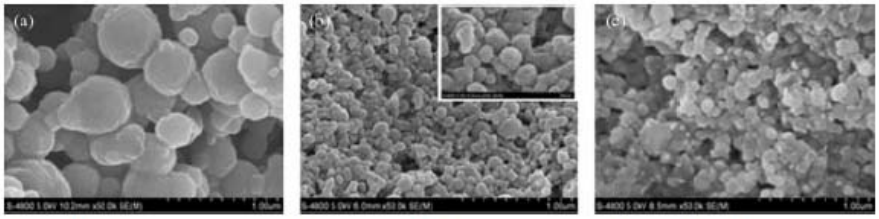

Figure 3. Morphologies of PEDOT nanoparticles prepared using various DBSA concentrations: (a) 0.25 × 10^{-2} mol L^{-1}; (b) 0.05 mol L^{-1}; (c) 0.10 mol L^{-1}.

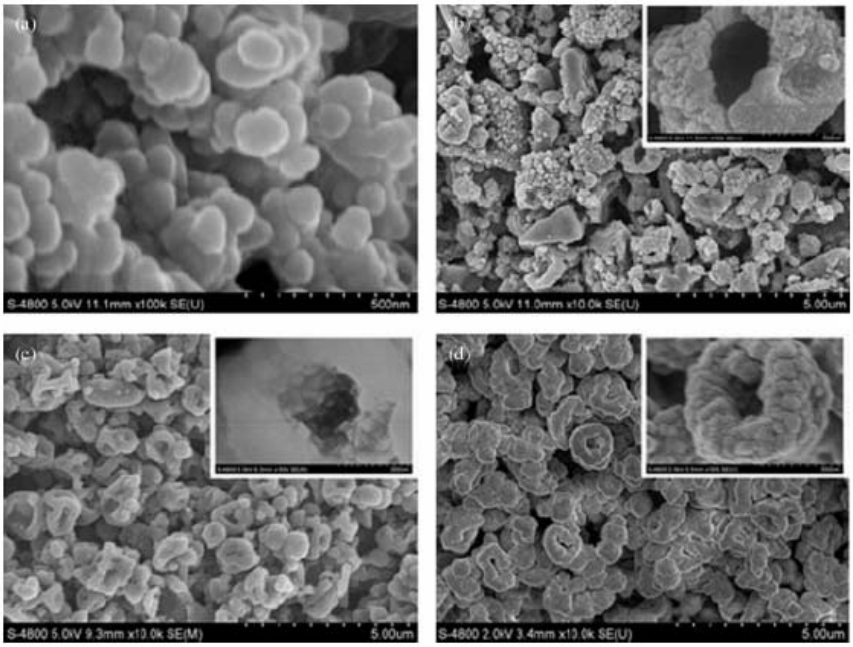

Figure 4. Morphologies of PEDOT nanoparticles prepared using various SDS concentrations: (a) 0.25 × 10^{-2} mol L^{-1}; (b) 0.25 × 10^{-1} mol L^{-1}; (c) 0.05 mol L^{-1}; (d) 0.10 mol L^{-1}.

0.10 mol L^{-1}, an agglomeration of PEDOT particles occurs as the micelles undergo micelle fusion, resulting in larger PEDOT particle sizes in the globular agglomerate shape,[21] as shown in Fig. 3(c).

The particle size of the PEDOT particles under the effect of SDS concentration varies between 147 and 938 nm and the particle shape changes from a globular shape (Fig. 4(a)) to various plum shapes (Figs 4(b)–(d)) at 0.25 × 10^{-2}, 0.25 × 10^{-1}, 0.05 and 0.10 mol L^{-1} SDS concentrations, respectively. Normally, the presence of SDS can lead to micelles in a unilamellar vesicle form, consisting of closed lamellar bilayers. The packing parameter, $V_H/l_c a_0$, is close to 1 (V_H is the volume occupied by the hydrophobic groups in the micellar core, l_c is the length of the hydrophobic groups in the core and a_0 is the cross-sectional area occupied by the hydrophilic groups). There are critical geometric and flexibility requirements for their formation.[21] At 0.25 × 10^{-2} mol L^{-1} SDS concentration, it is not possible to create a unilamellar vesicle micelle, even though the concentration is above the CMC. Due to the lack of unilamellar vesicle micelles, the PEDOT particle size is larger appearing in the globular form (Fig. 4(a)). With a further increase in SDS concentration from 0.25 × 10^{-1} to 0.10 mol L^{-1}, the PEDOT particles form a larger particle agglomerate (*ca* 896 to 938 nm) in the plum shape, as shown in Figs 4(b)–(d). However, these PEDOT plum particle sizes are approximately the same as the SDS concentration increases from 0.25 × 10^{-1} to 0.10 mol L^{-1}, because unilamellar vesicle micelle formation is limited at these surfactant concentrations.

Electrical conductivity

The electrical conductivity increases and the particle size decreases with increasing APS concentration up to 0.30 mol L^{-1}, where the smallest particle size and the highest electrical conductivity are obtained (Fig. 6). The smallest particle size corresponds to the highest surface area for electron transfer; this concentration also corresponds to the optimized doping level along with the highest electrical conductivity.[4] At APS concentrations above 0.30 mol L^{-1}, the electrical conductivity decreases and the particle size increases with increasing APS concentration. There are two reasons for the decrease in electrical conductivity: (i) aggregation of PEDOT particles occurs, changing the particle shape into the coralliform, which provides a lower surface area for electron transfer due to greater free space, thus reducing electron mobility; and (ii) over-oxidation occurs due to excessive APS concentrations, resulting in lower electrical conductivity, as confirmed by the FTIR spectrum[4,10] and the XRD pattern.[10,11]

 © 2013 Society of Chemical Industry

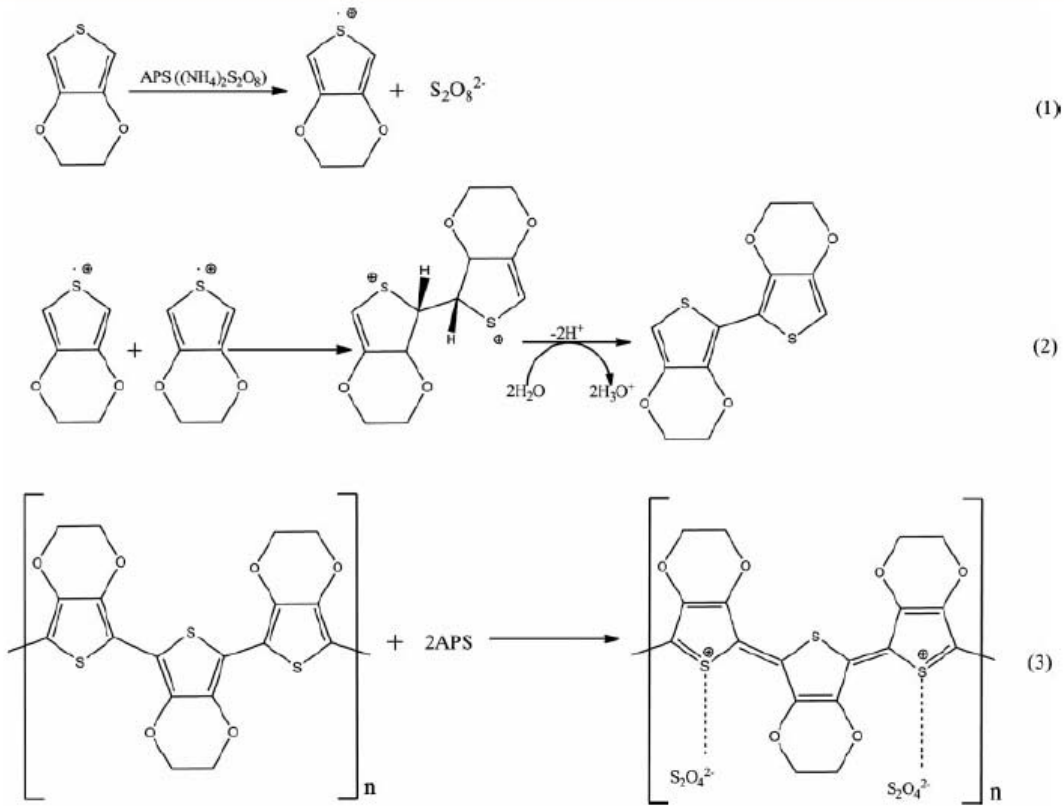

Figure 5. Proposed polymerization mechanism of PEDOT: (1) EDOT as a monomer is oxidized by APS to a cation radical; (2) EDOT cation radicals form dimers that subsequently get deprotonated; and (3) PEDOT polymer is doped and sulfate ion acts as counter ion.[18]

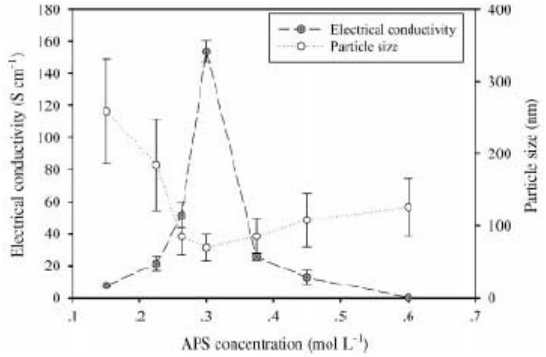

Figure 6. Electrical conductivity and particle size of PEDOT nanoparticles as a function of APS concentration.

Table 1 compares the PEDOT particle sizes, particle shapes and electrical conductivity with and without DBSA and SDS surfactants. The results without the surfactants are shown in Fig. 6. PEDOT was synthesized at various APS concentrations, APS acting as the oxidant. The molar ratio between the monomer (EDOT) and oxidant (APS) without surfactant (1:1 to 1:4 molar ratio) was varied by increasing the APS concentration. The particle size decreases with increasing APS concentration (decreasing molar ratio) until the APS concentration reaches 0.30 mol L^{-1} (1:2 molar ratio) resulting in the smallest particle size of 70 nm. APS acts more as an initiator and oxidant in the polymerization process.[13,14] At an APS concentration higher than 0.30 mol L^{-1}, the particle size becomes larger in the coralliform shape due to the screening effect from the counter ions (sulfate anions). Electrical conductivity increases with increasing APS concentration (0.15 to 0.30 mol L^{-1}) until it reaches the highest value of 153 S cm^{-1} at 0.30 mol L^{-1} APS concentration. The smaller particle size corresponds to the highest surface area for electrons to transfer[4] and the highest doping level due to the amount of APS dopant used.[14,23] As the APS concentration is increased to greater than 0.30 mol L^{-1}, the electrical conductivity decreases because the PEDOT particle shape changes to a corralliform shape and over-oxidation occurs for this greater APS concentration. The optimal APS concentration is 0.30 mol L^{-1} (1:2 molar ratio) and was further investigated.

DBSA and SDS were used to study the effect of surfactant concentration, reported in terms of molar ratio between the monomer (EDOT) and surfactant, as shown in Table 1. The PEDOT particle size at 0.25 × 10^{-2} mol L^{-1} DBSA concentration is the largest (*ca* 396 nm) in the orange-peel shape because this DBSA concentration is lower than the CMC. Above the CMC, the PEDOT particle size decreases with increasing DBSA concentration (decreasing molar ratio) up to 0.05 mol L^{-1} DBSA (3:1 molar ratio), where the PEDOT particle size is the smallest. The smaller PEDOT particles are polymerized within the micelle cores.[22] When the

 © 2013 Society of Chemical Industry

Table 1. Comparison of particle size, particle shape and electrical conductivity of PEDOT obtained under various synthesis conditions

Synthesis method	Particle size (nm)	Shape	Electrical conductivity (S cm^{-1})	Remarks[a]
Chemical oxidation polymerization	212 ± 72	Irregular	7.65 ± 1.00	EDOT:APS = 1:1 (0.15 mol L^{-1} APS)
	179 ± 65	Irregular agglomerate	21.16 ± 4.57	EDOT:APS = 1:1.5 (0.23 mol L^{-1} APS)
	85 ± 26	Irregular	51.53 ± 7.59	EDOT:APS = 1:1.75 (0.26 mol L^{-1} APS)
	70 ± 19	Raspberry agglomerate	153.72 ± 6.52	EDOT:APS = 1:2 (0.30 mol L^{-1} APS)
	85 ± 25	Irregular	25.44 ± 2.03	EDOT:APS = 1:2.5 (0.38 mol L^{-1} APS)
	108 ± 37	Coralliform	11.49 ± 5.75	EDOT:APS = 1:3 (0.45 mol L^{-1} APS)
	125 ± 40	Coralliform	0.29 ± 0.67	EDOT:APS = 1:4 (0.60 mol L^{-1} APS)
Emulsion polymerization (DBSA as surfactant)	396 ± 140	Orange-peel	3.96 × 10^{-4} ± 0.03	EDOT:DBSA = 3:0.05 (0.25 × 10^{-2} mol L^{-1} DBSA)
	96 ± 26	Globular	3.73 × 10^{-2} ± 0.08	EDOT:DBSA = 3:0.50 (0.25 × 10^{-1} mol L^{-1} DBSA)
	63 ± 14	Raspberry agglomerate	4.85 × 10^{-2} ± 0.02	EDOT:DBSA = 3:1 (0.05 mol L^{-1} DBSA)
	90 ± 25	Semi-fused globular agglomerate	1.31 × 10^{-2} ± 0.02	EDOT:DBSA = 3:2 (0.10 mol L^{-1} DBSA)
	118 ± 37	Fused globular agglomerate	7.27 × 10^{-3} ± 0.08	EDOT:DBSA = 3:3 (0.15 mol L^{-1} DBSA)
	146 ± 50	Fused globular agglomerate	2.23 × 10^{-3} ± 0.01	EDOT:DBSA = 3:5 (0.25 mol L^{-1} DBSA)
Emulsion polymerization (SDS as surfactant)	147 ± 37	Globular	4.29 × 10^{-2} ± 0.04	EDOT:SDS = 3:0.05 (0.25 × 10^{-2} mol L^{-1} SDS)
	920 ± 385	Plum	4.72 × 10^{-3} ± 0.02	EDOT:SDS = 3:0.50 (0.25 × 10^{-1} mol L^{-1} SDS)
	896 ± 229	Plum	5.22 × 10^{-2} ± 0.07	EDOT:SDS = 3:1 (0.05 mol L^{-1} SDS)
	938 ± 223	Plum	1.52 × 10^{-2} ± 0.06	EDOT:SDS = 3:2 (0.10 mol L^{-1} SDS)
Chemical oxidation polymerization[13]	—	—	4.30	$FeCl_3$ as oxidant, 25 °C
	—	—	1.80	$FeCl_3$ as oxidant, 50 °C
	—	—	5.00 × 10^{-3}	$FeCl_3$ as oxidant, 95 °C
	—	—	0.50	$Ce(SO_4)_2$ as oxidant, 25 °C
	—	—	5.07 × 10^{-2}	$(NH_4)_2Ce(NO_3)_6$ as oxidant, 25 °C
Emulsion polymerization[3,10]	35–60	Spherical	<1.00	DBSA–APS as surfactant–oxidant
	60–120	Spherical	50.00	DBSA–$FeCl_3$ as surfactant–oxidant
Reverse micelle polymerization[2]	30–40	Irregular	33.70	$FeCl_3$–toluenesulfonic acid as oxidant
	50–60	Irregular	28.30	$FeCl_3$–toluenesulfonic acid as oxidant
	80–100	Irregular	16.70	$FeCl_3$–toluenesulfonic acid as oxidant

[a] Ratios given are molar ratios.

DBSA concentration is higher than 0.05 mol L^{-1} (3:1 molar ratio), the particle size increases with increasing DBSA concentration due to micelle fusion and the permissible connection between the PEDOT particles.[21] When SDS acts as a surfactant, it can create unilamellar vesicle micelles for the polymerization with the areas of the tail groups facing each other, and eventually a plum shape is created[21] at SDS concentration higher than 0.25 × 10^{-1} mol L^{-1} (3:0.05 molar ratio). At 0.25 × 10^{-2} mol L^{-1} SDS concentration, the smallest particle size results in a globular shape because the SDS content is not sufficient to form unilamellar vesicle micelles. Electrical conductivity increases with increasing surfactant concentration until the electrical conductivity approaches the highest value of 4.85 × 10^{-2} and 5.22 × 10^{-2} S cm^{-1} at 0.05 mol L^{-1} DBSA and SDS, respectively, due to the greater surface area of the particles. In addition, both surfactants also act as dopants, which can be correlated with the increase in the doping level with increasing surfactant concentration.[24,25] In contrast, electrical conductivity decreases with increasing surfactant concentrations higher than 0.05 mol L^{-1} because of the lower surface area for electrons to transfer due to larger particle sizes. One reason for the decrease in electrical conductivity with increasing surfactant content is the self-screening on polymerizing and the doping process via excessive dodecylbenzenesulfate anions of DBSA and dodecylsulfate anions of SDS.[24,25]

The PEDOT particle size when the reaction is carried out without a surfactant is the smallest because surfactant molecules can form micelles during polymerization allowing larger PEDOT particle sizes and a more globular shape. However, the smaller PEDOT particles obtained without a surfactant can still undergo particle aggregation. Electrical conductivity of PEDOT particles formed without a surfactant is highest because the structure of the surfactant consists of an aliphatic chain, which cannot effectively transfer electrons resulting in lower electrical conductivity.[21] The particle size when using SDS is larger than when using DBSA because SDS can form unilamellar vesicles leading to a larger particle size.[21] Generally, the surfactant concentration significantly affects the particle shape. The micellar shape changes from a sphere to cylinder, to hexagonal, and to lamellar structures with increasing surfactant concentration.[24] Electrical conductivity, with SDS as a surfactant, is higher than when using DBSA. The surfactant leads to the incorporation of the dopant anion, which is the dodecylbenzenesulfate anion of DBSA and the dodecylsulfate anion of SDS, onto the PEDOT backbones. The DBSA dopant consists of a bulky benzene ring which contributes to a steric barrier for electron transfer in the PEDOT chain resulting in lower electrical conductivity.[25]

Corradi and Armes[13] synthesized PEDOT particles via chemical oxidation polymerization. $FeCl_3$, $Ce(SO_4)_2$ and $(NH_4)_2Ce(NO_3)_6$ were used as oxidants and the effect of temperature was

 © 2013 Society of Chemical Industry

investigated. At 25 °C, using $FeCl_3$ as an oxidant gave the highest electrical conductivity compared to using $Ce(SO_4)_2$ and $(NH_4)_2Ce(NO_3)_6$. Thus the electrical conductivity significantly depended on the type of anion in the oxidant structure acting as a dopant. When using $FeCl_3$ as an oxidant, electrical conductivity decreased with increasing temperature because the increasing polymerization rate led to more aggregation of the PEDOT particles, resulting in decreased electrical conductivity. Oh and Im[3] and Choi *et al.*[10] studied PEDOT synthesis using DBSA as a surfactant, and APS and $FeCl_3$ as oxidants. The PEDOT particles showed a spherical shape with sizes of 30–60 nm and 60–90 nm and electrical conductivity values <1.00 and 50.00 S cm^{-1} for APS and $FeCl_3$, respectively. It was claimed that, because different complexes of oxidant–anionic surfactant formed, electrical conductivity was strongly affected. The existence of a complex between the oxidant and the anionic surfactant ($FeCl_3$–DBSA) in aqueous solution caused an insoluble complex between the iron(III) species and dodecylbenzenesulfonate anion which contributed to a greater attractive force and a higher doping level on the PEDOT particles. Huajing *et al.*[2] synthesized PEDOT particles using various amounts of $FeCl_3$–toluenesulfonic acid as the oxidant. An irregular shape of PEDOT particles was obtained and the particle size varied between 30 and 100 nm. Electrical conductivity decreased with increasing PEDOT particle size. They explained that the increase of toluenesulfonic acid concentration could promote the ordering of the PEDOT particle monocubic chain and hence lead to smaller particles.

We can observe from the results in Table 1 that electrical conductivity increases with decreasing particle size. This phenomenon can be explained by the quantum size effect.[2] The particle size and shape of synthesized PEDOT significantly depend on the synthesis conditions: oxidant type and concentration, surfactant type and concentration, and synthesis temperature.

Thermal stability of PEDOT nanoparticles

The thermal stability of the PEDOT particles was investigated using TGA to give the onset decomposition temperature ($T_{d,onset}$) of PEDOT particles as shown in Fig. 7. The data indicate that $T_{d,onset}$ decreases with decreasing particle size because a smaller particle size has a higher surface area for heat transfer resulting in more efficient material decomposition.[26] $T_{d,onset}$ with a surfactant is lower than without a surfactant because the decomposition temperature of the surfactant is lower than that of the PEDOT polymer.[10,27] $T_{d,onset}$ with SDS as the surfactant is lower than that with DBSA as the surfactant. This is because the amount of carbon in the SDS structure is less than that in the DBSA structure, and the decomposition temperature of SDS is lower than that of DBSA. The char yield of the PEDOT particles is consistent with the $T_{d,onset}$ data (Table 2). The char yield increases with decreasing $T_{d,onset}$ because the lower $T_{d,onset}$ provides much more time for particle decomposition and char formation.[26] However, the char yield when using SDS as the surfactant is lower than that when using DBSA because of the lower $T_{d,onset}$, and amount of carbon in the SDS structure.

PEDOT stability (aging property)

PEDOT particles were studied for the effect of aging time reported in terms of electrical conductivity. Figure 8 shows the electrical conductivity of PEDOT particles synthesized using 0.30 mol L^{-1} APS concentration without a surfactant. The electrical conductivity

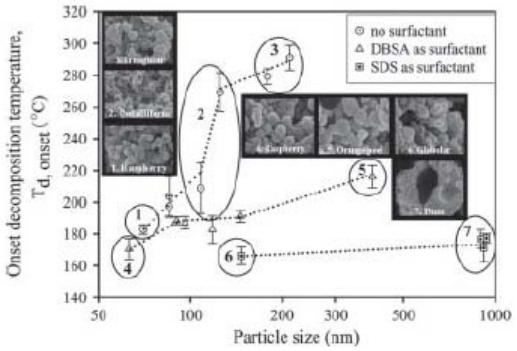

Figure 7. Onset decomposition temperature of PEDOT nanoparticles as a function of particle size.

Table 2. Char yield of PEDOT nanoparticles

PEDOT synthesis conditions[a]	Particle size (nm)	$T_{d,onset}$ (°C)	Char yield (%)
No surfactant			
EDOT:APS = 1:1	212 ± 72	291.06 ± 7.85	16.45 ± 1.11
EDOT:APS = 1:1.5	179 ± 65	279.35 ± 4.92	17.27 ± 0.56
EDOT:APS = 1:1.75	85 ± 26	203.67 ± 12.26	19.70 ± 0.78
EDOT:APS = 1:2	70 ± 19	182.88 ± 2.99	25.50 ± 0.63
EDOT:APS = 1:2.5	85 ± 25	197.34 ± 6.90	20.38 ± 0.87
EDOT:APS = 1:3	108 ± 37	188.80 ± 12.33	18.79 ± 2.43
EDOT:APS = 1:4	125 ± 40	269.33 ± 12.36	17.42 ± 2.16
Surfactant addition			
EDOT:DBSA = 3:0.05	396 ± 140	216.10 ± 7.39	13.21 ± 2.05
EDOT:DBSA = 3:0.50	96 ± 26	187.05 ± 4.01	22.69 ± 1.66
EDOT:DBSA = 3:1	63 ± 14	170.56 ± 7.53	32.55 ± 2.53
EDOT:DBSA = 3:2	90 ± 25	188.36 ± 2.40	32.57 ± 0.67
EDOT:DBSA = 3:3	118 ± 37	182.74 ± 8.64	28.60 ± 2.60
EDOT:DBSA = 3:5	146 ± 50	190.96 ± 3.60	20.15 ± 1.59
Surfactant addition			
EDOT:SDS = 3:0.05	147 ± 37	166.21 ± 5.48	10.36 ± 2.72
EDOT:SDS = 3:0.50	920 ± 385	171.14 ± 9.02	18.02 ± 2.40
EDOT:SDS = 3:1	896 ± 229	176.81 ± 5.77	16.64 ± 1.09
EDOT:SDS = 3:2	938 ± 223	177.37 ± 2.79	14.06 ± 0.75

[a] Ratios given are molar ratios.

increases to a maximum when PEDOT particles are kept at room temperature for 14 days and at 50% relative humidity. The electrical conductivity also remains approximately constant after 14 days. This is because the PEDOT particles can absorb moisture from the air creating a pathway for proton hopping through the water channel. The phenomenon of moisture absorption by the PEDOT particles can be confirmed using TGA, which shows the decomposition of water at 80 to 100 °C (Fig. 9). The weight (%) at a temperature of *ca* 100 °C decreases with increasing aging time. This implies an increase in the water absorption of the PEDOT particles with aging time.

CONCLUSIONS

This work focused on the tailor-made PEDOT shape and property relationship under various synthesis conditions. PEDOT

© 2013 Society of Chemical Industry

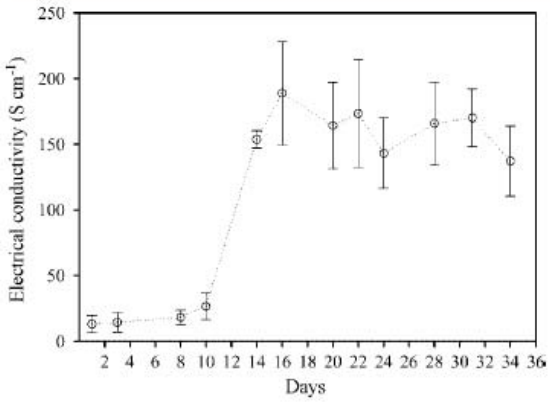

Figure 8. Electrical conductivity of PEDOT nanoparticles as a function of aging time.

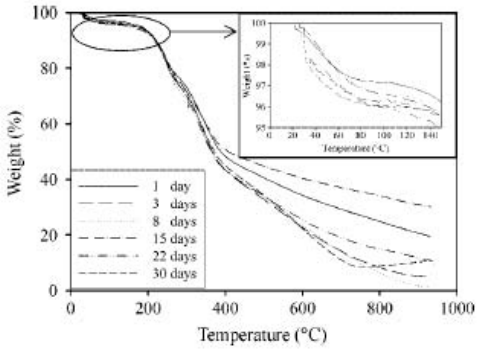

Figure 9. Weight loss of PEDOT nanoparticles over time.

nanoparticles were synthesized via the chemical oxidation polymerization of EDOT using APS as the oxidant, with and without a surfactant. DBSA and SDS were chosen as the surfactants at various concentrations. The PEDOT particle size varies between 60 and 900 nm, the particles having various shapes: irregular, raspberry agglomerate, coralliform, orange-peel, globular and plum shapes. In addition, the electrical conductivity varies between <1.00 and 153.72 S cm^{-1}, depending on the polymerization conditions. The PEDOT nanoparticles synthesized without a surfactant show the smallest particle size and the highest electrical conductivity. The presence of the surfactants was shown to affect the particle shape because the surfactants can form different micellar shapes depending on the type of surfactant: DBSA leads to spherical micelles while SDS leads to unilamellar vesicles during the PEDOT polymerization reaction. Synthesis with SDS provides a plum shape which is directly determined by the SDS micellar shape. The plum-shape of the PEDOT particles is a porous-like cage which can accommodate structural modifications for many applications such as controlled drug release.

ACKNOWLEDGEMENTS

The authors are grateful for the financial support provided by the Thailand Research Fund (TRF-RTA, RGJ PHD/0285/2551), the Conductive and Electroactive Polymer Research Unit, the Royal Thai Government and the Petroleum and Petrochemical College of Chulalongkorn University.

REFERENCES

1 Jang J, *Adv Polym Sci* **199**:189–259 (2006).
2 Huajing Z, Yadong J, Jianhua X and Yajie Y, *Sci China Technol Sci* **53**:2355–2362 (2010).
3 Oh SG and Im SS, *Curr Appl Phys* **2**:273–277 (2002).
4 Yang Y, Jiang Y, Xu J and Yu J, *Polymer* **48**:4459–4465 (2007).
5 Rauh RD, Wang F, Reynolds JR and Meeker DL, *Electrochim Acta* **46**:2023–2029 (2001).
6 Lock JP, Lutkenhaus LL, Zacharia NS, Im SG, Hammond PT and Gleason KK, *Synth Met* **17**:894–898 (2007).
7 Wu S, Han S, Zheng Y, Zheng H, Liu N, Wang L et al., *Org Electron* **12**:504–508 (2011).
8 Kim Y, Ballantyne AM, Nelson J and Bradley DD, *Org Electron* **10**:205–209 (2009).
9 Wu CH, Don TM and Chiu WY, *Polymer* **52**:1375–1384 (2011).
10 Choi JW, Han MG, Kim SY, Oh SG and Im SS, *Synth Met* **141**:293–299 (2004).
11 Li Y, Feng Y and Feng W, *Synth Met* **162**:781–787 (2012).
12 Kasisomayajula SV, Qi X, Vetter C, Croes K, Pavlacky D and Gelling VJ, *Coat Technol Res* **7**:145–158 (2010).
13 Corradi R and Armes SP, *Synth Met* **84**:453–454 (1997).
14 Chiu WW, Travas-Sejdic J, Cooney RP and Bowmaker GA, *Synth Met* **155**:80–88 (2005).
15 Han MG and Foulger SH, *Small* **2**:1164–1169 (2006).
16 Xing S, Chu Y, Sui X and Wu ZJ, *Mater Sci* **40**:215–218 (2005).
17 Chen CF, Lei IA and Chiu WY, *J Appl Polym Sci* **126**:195–205 (2012).
18 Mueller M, Fabretto M, Evans D, Hojati-Talemi P, Gruber C and Murphy P, *Polymer* **53**:2146–2151 (2012).
19 Chattopadhyay D, Chakraborty M and Mamdal BM, *Polym Int* **50**:538–544 (2001).
20 Monteiro MJ and Barbeyrac JD, *Macromolecules* **34**:4416–4423 (2001).
21 Rosen MJ, *Surfactant and Interfacial Phenomena*, 3rd edition. Wiley-Interscience, New York (2004).
22 Odiam G, *Principles of Plymerization*, 3rd edition. Wiley-Interscience, New York (2004).
23 Wan M, *Adv Mater* **20**:2926–2932 (2008).
24 Han MG, Cho SK, Oh SG and Im SS, *Synth Met* **126**:53–60 (2002).
25 Reung-U-Rai A, Prom-Jun A, Prissanaroon-Ouajai W and Ouajai SJ, *Metals Mater Mineral* **18**:27–31 (2008).
26 Lyon RE, *Polym Degrad Stab* **61**:201–210 (1998).
27 Han YG, Kusunose T and Sekino T, *Synth Met* **159**:123–131 (2009).

 © 2013 Society of Chemical Industry

International Journal of Polymeric Materials and Polymeric Biomaterials, 63: 315–322
Copyright © 2014 Taylor & Francis Group, LLC
ISSN: 0091-4037 print/1563-535X online
DOI: 10.1080/00914037.2013.845185

Taylor & Francis
Taylor & Francis Group

Composite Proton Exchange Membranes of Sulfonated Poly(ether ketone ether sulfone) (S-PEKES) and Molecular Sieve With High Mechanical Strength for Direct Methanol Fuel Cell

S. CHANGKHAMCHOM and A. SIRIVAT

Conductive and Electroactive Polymers Research Unit, The Petroleum and Petrochemical College, Chulalongkorn University, Bangkok, Thailand

Received 11 February 2013, Accepted 12 September 2013

Downloaded by [Chulalongkorn University] at 22:58 21 January 2014

Composite proton exchange membranes are prepared by solvent casting via the incorporation of molecular sieves 3A, 4A, and 5A into the sulfonated poly(ether ketone ether sulfone) (S-PEKES) at the sulfonation degree of 0.66, with varying the ratio at of 3%, 6%, 9%, and 12% v/v. The influences of type and amount of the molecular sieves on the proton conductivity, methanol permeability, structural, thermal, and mechanical stabilities of the membranes are investigated. The composite membranes are characterized by FTIR, TGA, LCR meter, and GC techniques. All properties of the composite membrane are compared with the pristine S-PEKES and Nafion 117 membrane.

Keywords: Molecular sieve, proton conductivity, proton exchange membrane (PEM), sulfonated poly(ether ketone ether sulfone)

1. Introduction

Direct methanol fuel cell (DMFC) has attracted substantial interest as an alternative energy source for applications in various portable devices such as mobile phone, laptop, and etc. A proton exchange membrane (PEM) is a solid polymer electrolyte membrane used in both polymer electrolyte membrane fuel cells (PEMFCs) and direct methanol fuel cells (DMFCs). It allows protons to pass through from the anode to the cathode and acts as a barrier to prevent the methanol crossover. Currently, Nafion membrane is mainly used as PEM due to its excellent proton conductivity in the fully hydrated condition. However, Nafion still has high methanol permeability and cannot be used at high temperature. Furthermore, its cost is very high. The challenge of PEM development with high proton conductivity and thermal stability, low cost and methanol permeability is of interest [1].

In recent years, there are many types PEM developed: perfluorinated, partially fluorinated, nonfluorinated acid-base blends, and other supported composite membranes [2]. Nonfluorinated polymer membranes are based on the aromatic main chain such as the modified sulfonated poly(arylene ether ketone) series, considered as a novel and excellent proton exchange membrane material. They are composed thermoplastics with excellent chemical and thermal stabilities, good insulator, high mechanical strength, and a relatively low cost compared to Nafion membrane. These sulfonated polymer membranes have good thermal stability and high proton conductivity at a high sulfonation degree. Several articles have reported the sulfonation of these membranes and their properties [3–10].

In order to improve the functioning of PEM, it is possible to modify the membrane composition by adding other materials to form different type of membrane: adding plasticizers and/or crosslinking agent to the polymer matrix, polymer blended membrane, and inorganic/polymer composite membrane. The latter is of interest toward the increase in proton conductivity, the maintenance of water at high temperatures, and the increased mechanical support [11]. In this context, the incorporation of inorganic additives, such as molecular sieves, into the polymer matrix, has been developed to form composite membranes. The incorporation of a molecular sieve, within an appropriate polymer matrix, can offer several advantages: proper mixing of inorganic and polymer at a molecular level provides good mechanical stability compared with a pure polymer membrane; since proton conductivity is the effect of proton transporting on the surface of the proton conductor particles, an increase in surface area is expected to increase the proton conductivity obtained for a composite membrane [2]. In the previous work, the sulfonated

Address correspondence to: A. Sirivat, Conductive and Electroactive Polymers Research Unit, The Petroleum and Petrochemical College, Chulalongkorn University, Soi Chula 12, Phyathai Road, Pathumwan, Bangkok 10330, Thailand. E-mail: anuvat.s@chula.ac.th

Downloaded by [Chulalongkorn University] at 22:58 21 January 2014

bisphenol-A-polysulfone (SPSF) with the degrees of sulfonation between 46% and 83% could be used as PEM [12]. The proton conductivity of the composite membrane of zeolite beta filled sulfonated poly(ether ether ketone) (SPEEK) increased to 0.13 $S \cdot cm^{-1}$ from the 0.06 $S \cdot cm^{-1}$ of the pristine SPEEK [13]. Krivobokov et al. [14] incorporated tetrapropylammonium (TPA) and tetrabutylammonium (TBA) to a Nafion membrane, thus lowering its methanol permeability and higher selectivity compared to Nafion. The SPEEK/silicotungstic acid (SWA) composite membrane was fabricated; the proton conductivity was found to be in the order of 10^{-3} $S \cdot cm^{-1}$ [15]. The proton conducting composite membranes comprising sulfonated poly(1,4-phenylene sulfide) and zeolite molecular sieve 3A were prepared [16], and they possessed higher thermal stability than the pristine polymer membrane by reason of the strong specific interaction between the molecular sieve 3A particles and the sulfonic acid group of polymer matrix. The Nafion-Faujasite composite membranes were fabricated by Zhang et al. [17], and the Faujasite zeolite addition increased the water uptake and mobility due to the hydrogen bonding between the Si-OH and SO_3H groups, leading to the increase in proton conductivity. The HZSM-5 zeolite with a higher aluminum content exhibits a higher proton conductivity due to its high water retention, and improves the thermomechanical properties [18]. The composite polymer membranes comprising of P(VDF-*co*-CTFE)-*g*-PSSA graft polymer and a zeolite showed high thermal stability up to 300°C suitable for the DMFC application [19]. Incorporating Cloisite 30B (C30B) in a sulfonated polysulfone matrix was shown to increase the proton conductivity of the composite membrane [20].

In this work, the effect of a molecular sieve zeolite was investigated. The synthesized sulfonated poly(ether ketone ether sulfone) (S-PEKES) were used as the polymer matrix, where 4,4′-difluorobenzophenone and 4,4′-dichlorobenzophenone are the starting monomers [21]. The S-PEKES with a sulfonation degree of 0.66 was chosen to prepare the composite membranes. Molecular sieves 3A, 4A, and 5A were used as the inorganic fillers at various volume percentages. The composite membranes were fabricated by solvent casting. The influence of the molecular sieves on the structural, thermal, and mechanical properties; proton conductivity; and methanol permeability of the membranes were characterized and compared with those of the pristine S-PEKES and Nafion 117 membranes. The addition of the molecular sieve zeolite into the S-PEKES improves drastically the mechanical and thermal stabilities, and the proton conductivity relative to the pristine S-PEKES membrane. In particular, the proton conductivity of the highest ratio of molecular sieve/S-PEKES composite membrane is close to that of the commercial Nafion 117 membrane.

2. Experimental

2.1 Materials

Bisphenol S or 4,4′-sulfonyldiphenol and 4,4′-dichlorobenzophenone (98–99%, Aldrich) were used as the monomers. Sodium chloride (Univar, 99.9%), concentrated sulfuric acid (Merck, 98 wt%), and sodium hydroxide (Univar, 97%) were used as received. Toluene (Fisher-Scientific 99.99%), dimethyl sulfoxide (Riedel-de-Haen, 99.5%), and potassium carbonate (Riedel-de-Haen, 98–100%) were used as received. Dimethyl sulfoxide was purchased from RCI Labscan Limited. Molecular sieves 3A, 4A, and 5A as the inorganic fillers were purchased from Aldrich. Nafion 117 was purchased from Electrochem, Inc.

2.2 Synthesis of Poly(ether ketone ether sulfone) (PEKES) and Sulfonated Poly(ether ketone ether sulfone) (S-PEKES)

Both PEKES and S-PEKES at the 0.66 degree of sulfonation (DS) were synthesized according to the previous work reported elsewhere [21]. S-PEKES was synthesized by using these monomers: 4,4′-dichlorobezophenone and bisphenol S via the nucleophilic aromatic substitution reaction. The two monomers were mixed with DMSO and toluene, K_2CO_3 as catalyst, in a 250 mL three-necked round-bottom flask equipped with a Dean-Stark trap, a nitrogen inlet, a reflux condenser, and a thermostat. The mixture was refluxed for 3 h at 150°C, and excess toluene was distilled off during the reflux process. Toluene was used to remove the water byproduct, and the solution was heated at 175°C for 20 h. The mixture was cooled to room temperature and poured into a solution of methanol and distilled water (50% v/v). The crude product was then washed with water to remove any inorganic salt, filtered, and dried in a vacuum oven at 80°C for 48 h.

Then, 5.0 g of the PEKES powder was dissolved in 50 mL concentrated H_2SO_4 (98%) and vigorously stirred at 25 ± 2°C for 84 h. The solution was precipitated on crushed ice. The suspension was left for 12 h at room temperature. Then, the precipitate was filtered, washed with deionized water several times until neutral pH was obtained, and dried under vacuum to get the S-PEKES powder at 60°C for 24 h. The chemical structure of S-PEKES is shown in Figure 1.

2.3 Membrane Preparation

One gram of mixture was dissolved in 30 mL dimethyl sulfoxide (DMSO) with vigorous stirring for 12–18 h until the polymer solutions were homogeneous and the molecular sieve was dispersed evenly. Composite proton exchange membranes were prepared by solvent casting via the incorporation of 3%, 6%, 9%, and 12% v/v of molecular sieves 3A, 4A, and 5A into the solution of the S-PEKES at the sulfonation degree of 0.66. Each solution was cast on a Petri dish and kept at room temperature for 12 h, followed by drying at 80°C for two days under a vacuum.

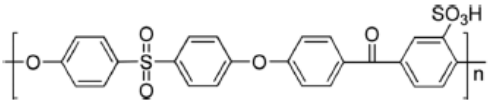

Fig. 1. Sulfonated poly(ether ketone ether sulfone) (S-PEKES).

Downloaded by [Chulalongkorn University] at 22:58 21 January 2014

2.4 Polymer Characterizations

2.4.1 *Fourier Transform Infrared Spectroscopy (FTIR)*

The FTIR spectra of molecular sieves 3A, 4A, and 5A/S-PEKES composite membranes with 12% v/v were taken, using a Thermo Nicolet/Nexus 670 FTIR spectrometer, and the background material was spectronic-grade KBr. The operation condition covered the wavenumber range of 4000–400 cm^{-1} under the absorption mode with 32 scans at a resolution of $\pm 4\,cm^{-1}$.

2.4.2 *Thermal Behavior*

A thermogravimetric analyzer (TGA; Perkin Elmer/TGA7) was used to investigate the degradation temperature of all composite proton exchange membranes: the pristine S-PEKES; molecular sieves 3A, 4A, and 5A/S-PEKES; and Nafion 117 membranes. Between 5.0 and 10.0 mg samples were heated from 50 to 800°C at a rate of 10°C/min under N_2 atmosphere [22].

2.4.3 *Proton Conductivity*

The proton conductivity values of the composite proton exchange membranes were measured by an Agilent E4980A LCR meter at a AC potential of 1 V and in the frequency range between 20 Hz to 2 MHz, at 27 ± 1°C, and at 50% RH. The composite membranes were immersed in deionized water at various soaking times to obtain 10% and 50% water contents. The water uptake (%) of the membranes was calculated from the method previously reported [23]. The conductivity values (σ) of all samples were calculated from the impedance data, using the relation $\sigma = d/RS$ where σ is the proton conductivity (S/cm), S is the membrane surface area (cm^2), d is the membrane thickness (cm), and R is the resistance which can be derived from the low intersect of the high-frequency semicircle on a complex impedance plane with the Re(Z) or Z' axis [24,25]. The impedance of each sample was measured three times to ensure data reproducibility. The proton conductivity values of all composite membranes were compared with the pristine S-PEKES and Nafion 117 membrane.

2.4.4 *Methanol Permeability*

The methanol permeability of the membranes was determined by using the two compartments diffusion cell as previously reported [26]. The compartment A ($V_A = 250$ mL) was filled with a solution of methanol (2.5 mol/L). The compartment B ($V_B = 250$ mL) was filled with deionized water. The membrane was clamped between the two compartments. The solutions in the two compartments were mechanically stirred during the permeation periods. Methanol diffused across the membrane due to the methanol concentration difference between the compartment A and the compartment B [27]. The methanol permeation in the receiving compartment as a function of time was calculated by:

$$P\,(cm^2/s) = \frac{k_B \times V_B \times L}{A \times (C_A - C_B)}, \qquad (1)$$

where P is the methanol permeability, C_A and C_B are the methanol concentrations in the compartments A and B, respectively; k_B is the slope of the methanol concentration gradient in the compartment B; V_B is the volume of the solution in the compartment B; and A and L are the area and the thickness of a membrane, respectively. The methanol concentrations were measured by using a gas chromatography (Pr2100) fitted with a thermal conductivity detector (TCD); ethanol was used as an internal standard.

2.4.5 *Mechanical Properties*

Mechanical properties such as Young's modulus, tensile strength, and elongation at break were measured (Lloyd, UTM) for all proton exchange membranes: the pristine S-PEKES; molecular sieves 3A, 4A, and 5A/S-PEKES; and Nafion 117 membranes. They were previously equilibrated in water for 24 h and at 27°C as strips (60 mm × 10 mm × 0.2 mm). A crosshead speed of 100 mm/min was used. And the gauge length was 30 mm. The measurements were run at 27°C and at 50% RH. The samples for the dry state test were dried at 100°C in vacuum for 12 h before each test. For each reported data point, five samples were tested, and the average value was calculated and reported.

3. Results and Discussion

3.1 Fourier Transform Infrared Spectroscopy (FTIR)

The FTIR spectra of the composite proton exchange membrane, incorporated with 12% v/v molecular sieves with the highest degree of sulfonation S-PEKES (DS 0.66), are shown in Figure 2. The absorbance peaks at around 1585 and 1655 cm^{-1} represent the stretching of the carbonyl group, and the peaks at 1242 and 1149 cm^{-1} represent the stretching of the sulfone group [28]. The absorption band at 1243 cm^{-1} represents the asymmetric stretching of the sulfone group, the bands at 1013, 1070, and 1030 cm^{-1} correspond to the symmetric stretching of the -SO_2- of the sulfonic acid group

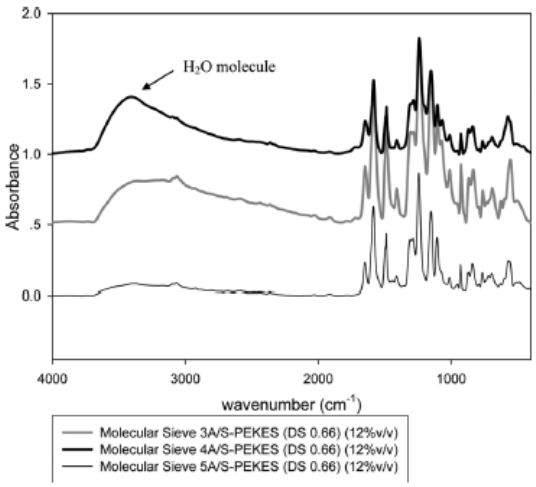

Fig. 2. FTIR spectra of composite proton exchange membrane incorporated with 12% v/v molecular sieves with the highest degree of sulfonation S-PEKES (DS 0.66).

Downloaded by [Chulalongkorn University] at 22:58 21 January 2014

[29]. The broad band of all composite membranes appear in the wavenumber range 3700–3100 cm^{-1}, which can be assigned to the hydroxyl group. The FTIR spectra, in the wavenumber range 1800–400 cm^{-1}, indicate various characteristic peaks of S-PEKES functional groups as in our previous work [21].

The hydroxyl characteristic peak of the molecular sieve 4A/S-PEKES composite proton exchange membrane has higher intensity than those of the 3A and 5A composite membranes. The pore size of molecular sieve 4A is more suitable than those of the molecular sieves 3A and 5A for water molecules to penetrate and adsorb. This is because the 4A pore size is close to that the water molecule, significantly affecting the amount of water trapped inside the composite membrane. Typically, the sulfonic acid group of S-PEKES is very hydrophilic and has high affinity toward water molecules. Water molecules are absorbed on the sulfonic group along the S-PEKES backbone and trapped inside the molecular sieve pore. The higher amount of water trapped inside the composite membrane can be related to the broad band of the hydroxyl group. The presence of water molecules in the membrane is indicated by the enlargement and increased intensity of the band. Thus, the addition of the molecular sieves facilitates and improves the hygroscopic property of the composite membrane [22].

3.2 *Thermogravimetric Analysis (TGA)*

Thermograms of the molecular sieve 4A/S-PEKES composite proton exchange membranes (3%, 9%, and 12% v/v) are shown in Figure 3. The first step weight loss of the S-PEKES membrane starts above 300°C, representing the splitting off of the sulfonic acid group. The second step weight loss occurs at 420–450°C, representing the degradation temperatures of S-PEKES backbone. Nafion 117 membrane, on the other hand, possess the most inferior thermal stability, its first degradation step occurs around 250–280°C and the second step weight loss is at 400°C. The composite membrane thermograms are compared with those of the pristine S-PEKES and Nafion 117 membranes. The molecular sieve 4A/S-PEKES composite membranes (3%, 9%, and 12% v/v) possess the thermal degradation temperature in the same range as the pristine S-PEKES, although the composite membranes cannot degrade completely. The remaining weights or chars of the composite membranes are about 8%, 50%, and 50%, for the composite membranes at 3%, 9%, and 12% v/v molecular sieve, respectively [28]. Furthermore, the composite membranes show highly thermal stability than Nafion 117 membrane. The molecular sieve 4A itself has extremely high thermal stability and cannot be degraded in this temperature range [30]. In summary, all molecular sieve/S-PEKES composite membranes have high thermal stability within the temperature range 25–120°C, and thus are suitable for use in DMFC application.

3.3 *Water Uptake*

Water uptake (%) of the molecular sieves 3A, 4A, and 5A/S-PEKES composite proton exchange membranes at room temperature (27°C) with various amount of molecular sieve (% v/v) are shown in Figure 4. The water uptake (%) values of the pristine S-PEKES membranes at 0.66 DS are $20.44 \pm 1.90\%$. After adding the molecular sieve 3A to form the composite membranes at 3%, 6%, 9%, and 12% v/v, the water uptake (%) increases to $34.03 \pm 1.53\%$, $37.22 \pm 1.51\%$, $40.98 \pm 1.55\%$, and $44.60 \pm 0.87\%$, respectively. The water uptake (%) values of the molecular sieve S-PEKES membranes 4A/S-PEKES composite membranes are $37.00 \pm 1.57\%$, $40.62 \pm 1.20\%$, $43.00 \pm 1.79\%$, and $47.45 \pm 0.73\%$, corresponding to 3%, 6%, 9%, and 12% v/v, respectively,

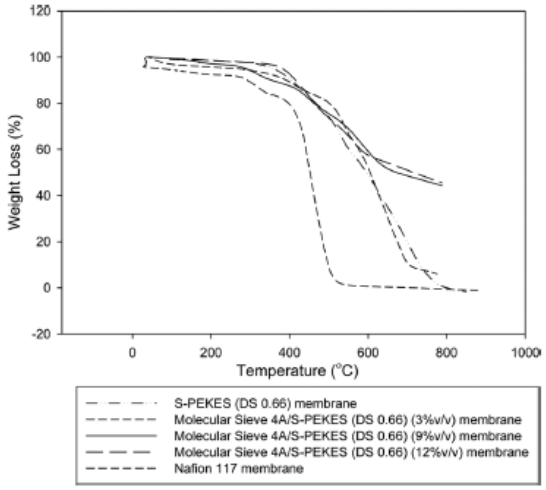

Fig. 3. Thermograms of the pristine S-PEKES membrane, molecular sieve 4A/S-PEKES composite membranes (3%, 9%, and 12% v/v, respectively), and Nafion 117 membrane.

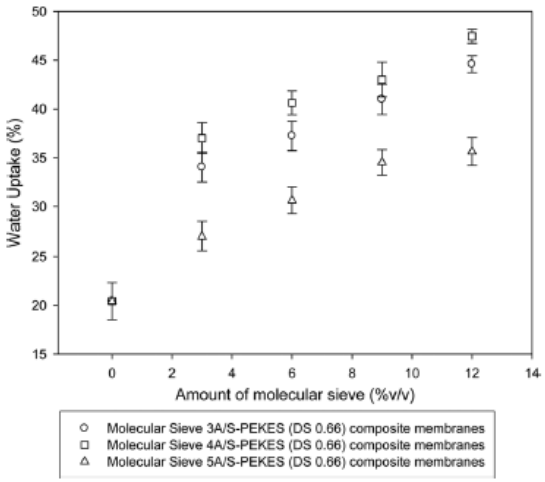

Fig. 4. The water uptake (%) of the molecular sieve 3A, 4A, and 5A/S-PEKES composite proton exchange membranes at room temperature (27°C).

Downloaded by [Chulalongkorn University] at 22:58 21 January 2014

of molecular sieve 4A. The molecular sieve 5A/S-PEKES composite membranes show the lowest water uptake (%), which is $27.05 \pm 1.44\%$, $30.62 \pm 1.37\%$, $34.51 \pm 1.31\%$, and $35.63 \pm 1.43\%$, corresponding to 3%, 6%, 9%, and 12% v/v, respectively, of molecular sieve 5A. The molecular sieve 4A/S-PEKES composite membrane has the highest water uptake (%) among three types of composite membranes, consistent with the TGA results, which indicate its high ability to adsorb water molecules. The molecular sieve has the hydrophilic property, which promotes the composite membrane to adsorb more water apart from the sulfonic acid group. The water cluster can be trapped in the molecular sieve pore, consistent with the work previous reported [31].

3.4 Ion Exchange Capacity (IEC)

Figure 5 represents the ion exchange capacities (IECs) of molecular sieves 3A, 4A, and 5A/S-PEKES composite proton exchange membranes at room temperature (27°C). The IEC values of the pristine S-PEKES membranes at 0.66 DS is $0.64 \pm 0.05\,\text{meq} \cdot \text{g}^{-1}$. The highest IEC belongs to the molecular sieve 4A/S-PEKES composite membrane, which shows the values of 1.16 ± 0.10 to $1.36 \pm 0.04\,\text{meq} \cdot \text{g}^{-1}$, corresponding to 3–12% v/v of molecular sieve 4A. Molecular sieve 3A and 5A/S-PEKES composite membranes possess lower IEC values than that of 4A. The IEC values of all composite membrane systems increase with increasing amount of molecular sieve (%v/v). The IEC increase is in the same trend with the water uptake (%).

The increment in both water uptake (%) and IEC, of the molecular sieve/S-PEKES membrane when compared with the pristine S-PEKES membrane, can be related to the proton conductivity enhancement, as reported in a previous work [26].

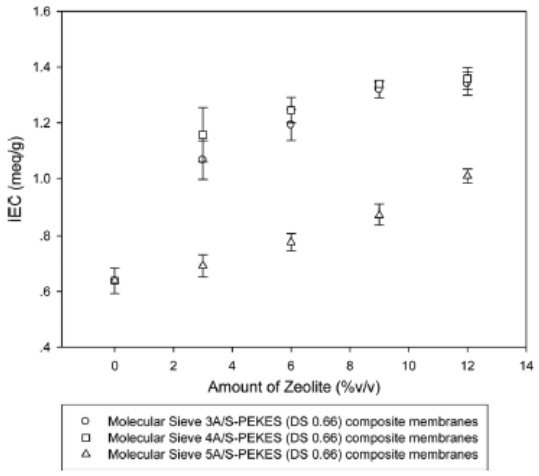

Fig. 5. The ion exchange capacities (IECs) of the molecular sieve 3A, 4A, and 5A/S-PEKES composite proton exchange membranes at room temperature (27°C).

3.5 Proton Conductivity (σ)

The proton conductivity (σ) is the most important property of the proton exchange membrane, indicating the performance of the PEMFC or DMFC. The effects of molecular sieve amount (v/v%) and water uptake (%) within the composite proton exchange membranes on the proton conductivity are investigated next. The calculated proton conductivities of all membranes with 10 and 50% water uptakes at a room temperature (27°C) and 50% RH are shown in Table 1. The pristine S-PEKES membranes (DS 0.66) attain the proton conductivity enhancement from $4.41 \times 10^{-6} \pm 4.84 \times 10^{-7}$ to $8.45 \times 10^{-3} \pm 5.74 \times 10^{-7}\ \text{S} \cdot \text{cm}^{-1}$, as water uptake is varied from 10% to 50%. The molecular sieve 3A/S-PEKES composite membranes (6%v/v) with various water uptake (%) from 10% to 50% possess the proton conductivity varying from $6.89 \times 10^{-08} \pm 1.08 \times 10^{-08}$ to $5.65 \times 10^{-03} \pm 1.69 \times 10^{-03}\ \text{S} \cdot \text{cm}^{-1}$.

At 50% water uptake, the molecular sieve 3A/S-PEKES composite membranes possess proton conductivities of $5.65 \times 10^{-3} \pm 1.69 \times 10^{-3}$, $7.81 \times 10^{-3} \pm 7.97 \times 10^{-4}$, and $1.06 \times 10^{-2} \pm 1.13 \times 10^{-3}\ \text{S} \cdot \text{cm}^{-1}$, corresponding to 6%, 9%, and 12% v/v of molecular sieve 3A, respectively. Furthermore, at 50% water uptake, the molecular sieve 4A/S-PEKES composite membranes possess proton conductivities of $7.59 \times 10^{-3} \pm 6.82 \times 10^{-4}$, $8.26 \times 10^{-3} \pm 3.13 \times 10^{-4}$, and $1.06 \times 10^{-2} \pm 7.19 \times 10^{-4}\ \text{S} \cdot \text{cm}^{-1}$, corresponding to 6%, 9%, and 12% v/v of molecular sieve 4A, respectively. The molecular sieve 5A/S-PEKES composite membranes show the proton conductivities in the range of $1.06 \times 10^{-3} \pm 1.10 \times 10^{-4}$ to $8.36 \times 10^{-3} \pm 3.07 \times 10^{-4}\ \text{S} \cdot \text{cm}^{-1}$, corresponding to 6% to 12% v/v molecular sieve 5A.

The highest proton conductivity of molecular sieve 4A/S-PEKES composite membrane (12% v/v) at 50% water uptake is nearly the same as that of Nafion 117 membrane, which has the value of $1.09 \times 10^{-2} \pm 1.39 \times 10^{-3}\ \text{S} \cdot \text{cm}^{-1}$ at the same condition. From these results, the proton conductivities of all proton exchange membranes increase with increasing water uptake (%). The type of molecular sieve can affect the proton conductivity; the molecular sieve 4A/S-PEKES composite membrane has the highest proton conductivity, followed by the 3A and 5A composite membranes, respectively. Auimviriyavat et al. [32], prepared the Ferrierite zeolite/SPEEK composite membranes with various % v/v of Ferrierite zeolite (5%, 10%, 15%, 17%, 20%v/v). They confirmed that the inorganic filler enhanced the proton motion by the sieve water retention characteristics [13]. Thus, the addition of molecular sieve into the S-PEKES matrix promotes the increase in the proton conductivity of the membrane.

The mechanism of proton transport within the composite membrane can occur via two pathways: first, the transport mechanism by water, where there is the formation of water channels. The combination of protons and water molecules generates a set of hydronium ions (H_3O^+), which can transport the protons of water through the channels [33,34]. In this case, the molecular sieve provides additional water channels within the composite membrane. The second mechanism, called Grotthuss mechanism, occurs in the electrostatic

Table 1. The proton conductivities of all membranes with 10 and 50% water uptakes at a room temperature (27°C) and 50% RH

PEM	DS	Amount of molecular sieve (v/v)	Thickness (cm)	Water uptake (%)	Proton conductivity (S/cm)
Nafion 117	1.0	0	0.0200	10	$8.56\times10^{-07}\pm7.39\times10^{-08}$
				50	$1.09\times10^{-02}\pm1.39\times10^{-03}$
S-PEKES	0.66	0	0.0278	10	$4.41\times10^{-06}\pm4.84\times10^{-07}$
				50	$8.45\times10^{-03}\pm5.75\times10^{-04}$
Molecular sieve 3A/S-PEKES	0.66	6	0.0220	10	$6.89\times10^{-08}\pm1.08\times10^{-08}$
				50	$5.65\times10^{-03}\pm1.69\times10^{-03}$
		9	0.235	10	$2.51\times10^{-07}\pm5.22\times10^{-08}$
				50	$7.81\times10^{-03}\pm7.97\times10^{-04}$
		12	0.0208	10	$5.91\times10^{-06}\pm6.01\times10^{-07}$
				50	$1.06\times10^{-02}\pm1.13\times10^{-03}$
Molecular sieve 4A/S-PEKES	0.66	6	0.0214	10	$7.78\times10^{-08}\pm9.74\times10^{-09}$
				50	$7.59\times10^{-03}\pm6.82\times10^{-04}$
		9	0.0205	10	$2.60\times10^{-07}\pm2.83\times10^{-08}$
				50	$8.26\times10^{-03}\pm3.13\times10^{-04}$
		12	0.0255	10	$5.51\times10^{-06}\pm6.06\times10^{-07}$
				50	$1.06\times10^{-02}\pm7.19\times10^{-04}$
Molecular sieve 5A/S-PEKES	0.66	6	0.0248	10	$2.27\times10^{-08}\pm5.77\times10^{-09}$
				50	$1.06\times10^{-03}\pm1.11\times10^{-04}$
		9	0.0239	10	$1.06\times10^{-07}\pm9.12\times10^{-09}$
				50	$8.88\times10^{-04}\pm7.88\times10^{-05}$
		12	0.0210	10	$4.20\times10^{-07}\pm6.84\times10^{-08}$
				50	$8.34\times10^{-03}\pm3.07\times10^{-04}$

interactions. For this mechanism, protons are transferred along the chain via ionic interactions and the hydrogen bonding "jumping" from a functional group to another. In this case, the sulfonic acid group (-SO_2-) reduces the energy barrier for the proton transport [11,35].

3.6 Methanol Permeability (P)

Methanol crossover is always a problem to the DMFC; methanol permeates easily through the electrolyte membrane from the anode to the cathode side of the DMFC. As a consequence, excessive methanol crossover of any PEM not only wastes the methanol fuel but also decrease the efficiency in fuel cell performance [1]. It is known that 40% of the methanol can be wasted in DMFCs via methanol crossover through the membranes [36]. Table 2 represents the methanol permeability (P) of all proton exchange membranes investigated here at the temperatures of 27°C, 50°C, and 70°C, respectively. The methanol permeability values of Nafion 117 at 27, 50, and 70°C are 1.42×10^{-6}, 1.07×10^{-5}, and $1.17\times10^{-5}\,cm^2\cdot s$, respectively [18]. Between 6% and 12% v/v, the methanol permeability of the molecular sieve 3A/S-PEKES composite membranes increases from 1.12×10^{-7} to $7.47\times10^{-7}\,cm^2\cdot s^{-1}$ at 27°C. The same results occur for molecular sieve 4A and 5A composite membranes. The molecular sieve 5A/S-PEKES composite membranes have the highest methanol permeability over the molecular sieve 4A and 3A composite membrane, respectively. At 27°C and 6% v/v composite membrane, the methanol permeabilities are 1.1213×10^{-7}, 2.6219×10^{-7}, and $4.1295\times10^{-7}\,cm^2\cdot s^{-1}$ for molecular sieves 3A, 4A, and 5A/S-PEKES composite membranes, respectively.

The methanol permeability values of Nafion 117 are the highest among all proton exchange membranes by two orders of magnitude at a given temperature. For the effect of temperature, the methanol permeabilities of all membranes increase with increasing temperature, as methanol molecules are more active to penetrate through the membrane [37]. The type of the molecular sieve seems to have an influence on the methanol permeability. The molecular sieve 5A/S-PEKES composite membrane has the highest methanol permeability over the molecular sieve 4A and 3A composite membrane, respectively, due to the largest pore size of the molecular sieve 5A in which the water molecule can pass trough more easily. However, the methanol permeabilities of all composite membranes are significantly lower than that of Nafion 117 membrane.

Sulfonated poly(ether sulfone ether ketone ketone)/sulfonated poly(ether sulfone) blend membranes were prepared by Zeng et al. [38]; the methanol permeability of all the blend membranes are in the range of $0.58–2.18\times10^{-6}$ $cm^2\cdot s^{-1}$, which are higher than our composite membranes by an order of magnitude.

3.7 Mechanical Properties

Mechanical properties of all proton exchange membranes at room temperature (27°C) and 50% RH are shown in Table 3. The mechanical properties of all membranes were evaluated by means of the standard tensile test in the same method with the previous work [26]. The tensile strength, elongation at break, and Young's modulus were measured and are

Downloaded by [Chulalongkorn University] at 22:58 21 January 2014

Table 2. Methanol permeability (P) of all proton exchange membranes at the temperatures of 27°C, 50°C, and 70°C

PEM	DS	Amount of zeolite (% v/v)	Thickness (cm)	Methanol permeability (P) (cm^2/s)		
				27°C	50°C	70°C
Nafion 117 [16]	1	0	0.0200	1.4147E-06	1.0725E-05	1.1689E-05
S-PEKES-B	0.66	0	0.0278	1.0347E-07	7.9574E-07	2.1358E-06
S-PEKES-B/molecular sieve 3A	0.66	6	0.0220	1.1213E-07	6.9259E-07	4.7988E-06
	0.66	9	0.0235	4.8632E-07	1.0765E-06	7.7128E-06
	0.66	12	0.0208	7.4697E-07	1.3493E-06	1.1112E-05
S-PEKES-B/molecular sieve 4A	0.66	6	0.0214	2.6219E-07	8.7369E-07	5.9762E-06
	0.66	9	0.0205	7.0312E-07	1.2081E-06	9.2980E-06
	0.66	12	0.0255	1.2566E-06	8.6642E-06	2.4299E-05
S-PEKES-B/molecular sieve 5A	0.66	6	0.0248	4.1295E-07	1.0284E-06	7.0640E-06
	0.66	9	0.0239	7.2137E-07	1.2751E-06	9.5043E-06
	0.66	12	0.0210	1.0864E-06	8.3553E-06	2.2426E-05

Table 3. Mechanical properties of all proton exchange membranes at room temperature (27°C) and 50% RH

PEM	DS (%)	Amount of zeolite % (v/v)	Tensile strength (MPa)		Young's modulus (MPa)		Elongation at break (%)	
			Dry	Wet	Dry	Wet	Dry	Wet
S-PEKES-B/ molecular sieve 3A	0.66	6	212.73 ± 14.95	33.99 ± 3.85	2296.18 ± 63.91	498.09 ± 49.20	60.04 ± 11.03	6.86 ± 1.60
	0.66	12	159.78 ± 5.69	79.90 ± 3.22	2143.18 ± 61.24	973.47 ± 31.00	28.18 ± 1.73	190.52 ± 11.06
S-PEKES-B/ molecular sieve 4A	0.66	6	71.17 ± 6.09	19.24 ± 0.45	861.22 ± 68.36	24289.65 ± 162.95	101.65 ± 0.72	6.36 ± 0.75
	0.66	12	122.44 ± 5.57	21.42 ± 0.67	360.46 ± 13.63	25991.62 ± 120.70	456.60 ± 18.20	6.69 ± 0.45
S-PEKES-B/ molecular sieve 5A	0.66	6	96.45 ± 7.15	56.90 ± 1.52	984.75 ± 41.25	50542.63 ± 151.12	116.92 ± 9.86	164.47 ± 3.97
	0.66	12	101.42 ± 5.04	78.31 ± 3.54	844.40 ± 14.72	679.09 ± 10.09	121.94 ± 9.39	131.96 ± 11.44
S-PEKES-B	0.66	0	28.24 ± 1.28	7.94 ± 0.25	178.29 ± 6.74	16266.87 ± 75.54	495.37 ± 19.75	6.91 ± 0.46
Nafion117	1.00	0	38.0	28.4	180	100	301.5	329.2

Downloaded by [Chulalongkorn University] at 22:58 21 January 2014

reported here. The tensile strengths, of the composite membranes at 12% v/v, for 3A, 4A, and 5A/S-PEKES composite membranes, are higher than the value of the pristine S-PEKES membrane by factors of 5, 4, and 3 times, respectively. In the previous work of Zeng et al. [38], the sulfonated poly(ether sulfone ether ketone ketone)/sulfonated poly(ether sulfone) blend membranes showed a lower tensile strength than our present work; their membranes exhibited the tensile strength only in the range of 47.8–71.9 MPa. All molecular sieve/S-PEKES composite membranes show much higher tensile strengths and the lower elongations at break than those of the pristine S-PEKES and Nafion 117 membrane, especially in the dry state. In the hydrous state, water acts as an external plasticizer between polymer chains, leading to the ease in the chain movement and a decrease in the tensile strength. The mechanical strength in the hydrous state is thus lower than that in the anhydrous state [26]. The composite membranes in all systems are thus strong and flexible enough to be used as polymer electrolytes in a fuel cell. Thus, the addition of the molecular sieve significantly improves the mechanical strength of the PEM.

4. Conclusions

The composite membranes show high thermal stability because the degradation temperature start at above 250°C indicates that the composite membranes can be safely operated for DMFC at normal condition [39] and can be used in PEMFC as well [15]. The water uptake (%), IEC, and proton conductivity of the molecular sieve composites membranes are found to be higher than that of the pure S-PEKES membrane and they increase with increasing content of molecular sieve. Especially, the mechanical strength of composite membrane is the property, which shows the most significant improvement. Although, the methanol permeability of composite membrane increases from the pristine one, the value is still much lower than that of Nafion 117 membrane. From the overall results, the molecular sieve 3A/S-PEKES composite membrane at 12% v/v is selected to be the PEM candidate for DMFC, due to its higher proton conductivity, lower methanol permeability, and much higher tensile strength, when compared with the two other composite membranes.

Funding

The authors would like to acknowledge the financial supports from the 90th Anniversary of Chulalongkorn University Fund (Ratchadaphiseksomphot Endowment Fund), the Conductive and Electroactive Research Unit of Chulalongkorn University, the Thailand Research Fund (TRF-RTA, PHD/0081/2549), and the Royal Thai Government.

References

1. Carette, L.; Friedrich, K. A.; Stimming, U. *Fuel Cells* **2001**, *1*, 5–39.
2. Smitha, B.; Sridhar, S.; Khan, A. A. *J. Membr. Sci.* **2005**, *259*, 10–26.
3. Zhang, H.; Pang, J. H.; Wang, D.; Li, A.; Li, X.; Jiang, Z. *J. Membr. Sci.* **2005**, *264*, 56–64.
4. Zhao, C.; Lin, H.; Han, M.; Na, H. *J. Membr. Sci.* **2010**, *353*, 10–16.
5. Lin, H.; Zhao, C.; Cui, Z.; Ma, W.; Fu, T.; Na, H.; Xing, W. *J Power Sources* **2009**, *193*, 507–514.
6. Fu, L.; Xiao, G.; Yan, D. *J. Membr. Sci.* **2010**, *362*, 509–516.
7. Zhao, C.; Lin, H.; Zhang, Q.; Na, H. *Int. J. Hydrogen Energy* **2010**, *35*, 10482–10488.
8. Gasa, J. V.; Boob, S.; Weiss, R. A.; Shaw, M. T. *J. Membr. Sci.* **2006**, *269*, 177–186.
9. Chen, Y.; Guo, R.; Lee, C. H.; Lee, M.; McGrath, J. E. *Int. J. Hydrogen Energy* **2012**, *37*, 6132–6139.
10. Wang, C.; Shin, D. W.; Lee, S. Y.; Kang, N. R.; Lee, Y. M.; Guiver, M. D. *J. Membr. Sci.* **2012**, *405–406*, 68–78.
11. Ramírez-Salgado, J. *Electrochim. Acta* **2007**, *52*, 3766–3778.
12. Filho Furtado, A. A. M.; Gomes, A. S. *Int. J. Polym. Mater.* **2010**, *59*, 424–437.
13. Sengul, E.; Erdener, H.; Akay, R. G.; Yucel, H.; Bac, N.; Eroglu, I. *Int. Hydrogen Energy* **2009**, *34*, 4645–4652.
14. Krivobokov, I. M.; Gribov, E. N.; Okunev, A. G.; Spoto, G.; Parmon, V. N. *Solid State Ionics* **2010**, *180*, 1694–1701.
15. Guhan, S.; Sangeetha, D. *Int. J. Polym. Mater.* **2009**, *58*, 87–98.
16. Choi, J. M.; Patel, R.; Han, J. Y. *Ionics* **2010**, *16*, 403–408.
17. Zhang, Z.; Desilets, F.; Felice, V.; Mecheri, B.; Licoccia, S.; Tavares, A. C. *J. Power Sources* **2011**, *196*, 9176–9187.
18. Han, W.; Kwan, S. M.; Yeung, K. L. *Chem. Eng. J.* **2012**, *187*, 367–371.
19. Patel, R.; Park, J. T.; Lee, W. S.; Kim, J. H.; Min, B. R. *Polym. Adv. Technol.* **2009**, *20*, 1146–1151.
20. Unnikrishnan, L.; Madamana, P.; Mohanty, S.; Nayak, S. K. *Polym.-Plast. Technol. Eng.* **2012**, *51*, 568–577.
21. Changkhamchom, S.; Sirivat, A. *Polym. Bull.* **2010**, *65*, 265–281.
22. Wang, Z.; Ni, H.; Zhao, C.; Li, X.; Fu, T.; Na, H. *J. Polym. Sci. Polym. Phys.* **2006**, *44*, 1967–1978.
23. Unnikrishnan, L.; Nayak, S. K.; Mohanty, S.; Sarkhel, G. *Polym.-Plast. Technol. Eng.* **2010**, *49*, 1419–1427.
24. Mikhailenko, S. D.; Wang, K.; Kaliaguine, S.; Xing, P.; Robertson, G. P.; Guiver, M. D. *J. Membr. Sci.* **2004**, *223*, 93–99.
25. Shashidhara, G. M.; Kumar, K. N. *Polym.-Plast. Technol. Eng.* **2010**, *49*, 796–806.
26. Changkhamchom, S.; Sirivat, A. *Polym.-Plast. Technol. Eng.* **2013**, *52*, 70–79.
27. Mukoma, P.; Joosteb, B. R.; Vosl, H. C. M. *J. Membr. Sci.* **2004**, *243*, 293–299.
28. Gil, M.; Ji, X.; Li, X.; Na, H.; Hampsey, J. E.; Lu, Y. *J. Membr. Sci.* **2004**, *234*, 75–81.
29. Xiao, G.; Sun, G.; Yan, D. *Polym. Bull.* **2002**, *48*, 309–315.
30. Osterholm, H.; Kumar, N.; Lindblad, M.; Tiitta, M.; Salmi, T.; Murzin, D. *Microporous Mesoporous Mater.* **2012**, *154*, 124–132.
31. Coma, A. *Chem. Rev.* **1997**, *97*, 2373–2419.
32. Auimviriyavat, J.; Changkhamchom, S.; Sirivat, A. *Ind. Eng. Chem. Res.* **2011**, *50*, 12527–12533.
33. Jiang, Z.; Zheng, X.; Hong, Wu H.; Wang, J.; Wang, Y. *J. Power Sources* **2008**, *180*, 143–153.
34. Cui, Z.; Xing, W.; Liu, C.; Liao, J.; Zhang, H. *J. Power Sources* **2008**, *188*, 24–29.
35. Wang, J.; Zheng, X.; Wu, H.; Zheng, B.; Jiang, Z.; Xiaopeng, X.; Wang, B. *J. Power Sources* **2008**, *178*, 9–19.
36. Beatie, P. D.; Orion, F. P.; Basura, V. I.; Zychowska, K.; Ding, J.; Chuy, C.; Scmeisser, J.; Holdcroft, S. *J. Electroanal. Chem.* **2001**, *503*, 45–56.
37. Xue, S.; Yin, G. *Eur. Polym. J.* **2006**, *42*, 776–785.
38. Zeng, R.; Xiao, S.; Chen, L.; Chen, Y. *High Perform. Polym.* **2012**, *24*, 153–160.
39. Sangeetha, D. *Int. J. Polym. Mater.* **2007**, *56*, 535–548.

Downloaded by [Chulalongkorn University] at 22:58 21 January 2014

J Polym Res (2014) 21:369
DOI 10.1007/s10965-014-0369-8

ORIGINAL PAPER

Thermo-electromechanical responses of 1-butyl-3-methylimidazolium chloride ionic liquid-cellulose gel

Wissawin Kunchornsup · Anuvat Sirivat

Received: 10 October 2013 / Accepted: 22 January 2014
© Springer Science+Business Media Dordrecht 2014

Abstract 1-butyl-3-methylimidazolium chloride ($BMIM^+Cl^-$) is an ionic liquid utilized as an effective cellulose gelling agent for the fabrication of $BMIM^+Cl^-$ cellulose gel, called CelGel. The little-known transient thermo-electromechanical responses are investigated via an oscillatory shear experiment, under absence and presence of an electric field at equilibrium and non-equilibrium between 30 °C and 60 °C. In the equilibrium state with no electric field, the shear storage modulus (G′) increases with increasing temperature due to the stronger interaction between the cellulosic hydroxyl group and the chloride anion. In the equilibrium state with an electric field of strength 1 kV/mm , G′ continuously decreases with increasing temperature as chloride anions move out of crosslinking positions to become polarized under the electric field. The heating rate effect in the absence of an electric field is investigated between 0.5 and 20.0 °C/min. In the temperature-increasing step, G′ significantly increases because of the stronger interaction, along with cellulose chain expansion. In the temperature-decreasing step, G′ remains at its higher value, as it needs a longer time to relax. The heating rate effect in the presence of an electric field is also investigated. In the temperature-increasing step, G′ increases with a slower rate because of a shorter time scale required for the $BMIM^+$ polarization. In the temperature-decreasing step, a recrystallization occurs at a lower temperature because the shorter time scale obstructs the recrystallization process. Thus, transient thermo-electromechanical properties of CelGel have been systematically investigated here for the first time under the thermal equilibrium and non-equilibrium states.

W. Kunchornsup · A. Sirivat (✉)
The Petroleum and Petrochemical College,
Chulalongkorn University, Bangkok 10330, Thailand
e-mail: anuvat.s@chula.ac.th

Published online: 13 February 2014

Keywords Thermo-electromechanical responses · Cellulose · 1-butyl-3-methylimidazolium chloride ($BMIM^+Cl^-$) · Ionic liquid · Actuator

Introduction

Cellulose consists of β-(1→4)-linked glucose repeating units [1].The non-centrosymmetry refers to its internal rotation of polar atomic groups associated with asymmetric carbon atoms which contribute to the piezoelectric properties of cellulose [2]. However, the strong inter-molecular and intra-molecular hydrogen bondings of the cellulosic hydroxyl group in the dissolution process are well known to be the main obstacle in utilizing cellulose. Kim and coworkers investigated cellulose as a smart material, termed electroactive paper (EAPap), via the xanthate reaction system in 2006. They prepared films which demonstrated drastic actuation performances based on two actuation mechanisms: the dipolar orientation of the hydroxyl group of cellulose and the water-bound Na^+ cation motion [3]. In addition, EAPap is ultra-lightweight, inexpensive, and biodegradable.

Some of the well-known cellulose solvents are the ionic liquids or the ionic compounds which exist as liquids at low temperature [4, 5]. Their interesting properties are high stability, suitable polarity, high ionic conductivity, and easy recyclability [6]. Nafion™ swollen in 1-ethyl-3-methylimidazolium bis(triflouromethyl- sulfonyl)imide (EMI-IM) has been studied by Bennett and coworkers in 2006 [7]. They showed that the actuation speed and the ionic conductivity could be increased by increasing counterion size and increasing content of the ionic liquid, with the counterions acting as the primary charge carriers [7]. The use of EMI-IM was then demonstrated as a solvent for Nafion™ polymer actuators and sensors. The Nafion™ polymer actuators solvated with this ionic liquid possessed improved stability when

operated in air in comparison to the same materials solvated with water [8].

1-Butyl-3-methylimidazolium chloride ($BMIM^+Cl^-$), a well-known ionic liquid, was utilized in the previous work as the gelling agent for a microcrystalline cellulose [9–11], named CelGel. Kadokawa et al. [2008] reported a dissolution of 13 % cellulose via 87 % $BMIM^+Cl^-$ at 100 °C [9]. Furthermore, N, N-dimethylacetamide (DMAc) was added as a physical gelling agent to plasticize the viscous solution [10, 11]. The electromechanical properties of the cellulose gels were investigated under the oscillatory shear mode at electric field strengths between 0 and 1 kV/mm, and as functions of temperature. The shear storage modulus (G′) increased linearly with temperature up to 60 °C at 1 rad/s in the absence of an electric field. G′ also increased linearly with temperature up to 40 °C at 1 rad/s in the presence of 1 kV/mm of electric field strength and decreased above 40 °C, consistent with the behavior of dielectric permittivity (ε′). In the deflection experiments under an applied DC electric field, the deflection distances of the gels linearly increased with increasing electric field strength along with the dielectrophoresis forces above the electrical yield strength of 100 V/mm [10, 11]. In addition, it was known that temperature in an actuator system can be increased via a heat build-up process under high electrical frequency, electric field strength, and strain amplitude [12–14]. The temperature factor has been of remarkably concern for materials used in actuator applications.

Putz and Burghelea [2009] studied the temperature effect between 5 °C and 20 °C on solid–fluid transition of Carbopol® 940, or sodium polyacrylate, in the polyanion family [15]. The solid–fluid transition in terms of dynamic elastic modulus was strongly influenced by temperature through competition between destruction and reformation of the gel. A microscopic scale scenario for the competition between break-up and recombination of solid structure elements and the mediating role of temperature was explained in two regimes. In the low temperature regime, free polymer chains explored a limited number of possible configurations because of weak Brownian motion. Thus, the probability for different chains to come into an effective binding range was small, and over long enough periods of time, the shear-induced destruction of soft structural units dominated. An increase in temperature reversed the effect. The Brownian motion of free polymer chains was strong enough to bring free molecules into an interacting range; thus, the recombination of the network became probabilistically plausible [15]. Ruan and coworkers [2008] studied different gelling behaviors of cellulose solution dissolved in aqueous NaOH/thiourea between −5 °C and 40 °C [16]. The time dependence of G′ and G″ for 5 wt% cellulose solution under different temperatures at ω=1 rad/s was investigated. The solution was able to remain as a viscous liquid at 0 °C without gelling. Interestingly, the gelation of the cellulose solution took place easily at 30 °C. It was suggested that the rheological properties of the cellulose solution were strongly sensitive to temperature. In the cellulose solution system, the inclusion complex (IC) structure was formed through hydrogen-bonding networks. With an increase in temperature, the hydrogen-bonding network structure of IC could be destroyed and self-associated to form a gel. However, the IC became less stable and produced a lower equilibrium modulus when gelation temperature increased [16]. The temperature could also influence electrical conductivity of poly(tetrahydrofuran) when the tetrahydrofuran-repeating unit was partially decomposed upon thermal cycling, resulting in a self-plasticizing effect [17]. This suggested a novel processing strategy that could combine the conductivity performance of gel with the processing advantage of polymers. Moreover, the decomposed tetrahydrofuran was further susceptible to the formation of explosive peroxides that were likely to have limited application [17].

Li and coworkers [2007] studied temperature effect on the high amplitude vibration of piezoelectric bending actuators [14]. Temperature was increased with increasing frequency, electric field, and vibration amplitude due to higher mechanical and electrical losses. The uneven stress distribution had resulted in a high-to-low gradient temperature rise from the clamped end to the free end of the actuator [14]. Time-temperature profiles of multi-layer soft lead zirconate titanate actuators were investigated by Pritchard and coworkers [2004] [12]. The investigation of temperature rise of actuators as a function of operation conditions (frequency, electric field magnitude and polarity, actuator mounting, and material properties) was important in accelerated lifetime testing of these devices. The temperature rise was found to be approximately proportional to the frequency, while the total loss of the actuator per cycle increased with applied field and frequency. The rise of temperature can lead to overheating, thermal degradation, depolarization, and electrode delamination due to loss mechanisms contributing to heat generation [12]. Yoon [2012] studied the effect of temperature on the actuation performance of electro-fluid-thermal-compliant (ETC.) actuators [13]. The electric potential caused built-up temperature in the actuator and produced more actuation displacement. When rising heat was dissipated via surrounding media with high thermal and electrical conductivities, actuation displacement was decreased [13].

Both cellulose and ionic liquids are interesting for use as electroactive materials due to the piezoelectric [3] and ionic polarizations [11], respectively. The cellulose is used for polarizable scaffolding to trap ionic liquid and exhibits mixed electronic-ionic polarization effects for electroactive applications. Both materials could be mixed and fabricated by sol–gel processes [10]. In the present work, we are interested in investigating the transient thermo-electromechanical responses of $BMIM^+Cl^-$cellulose gel, named CelGel, via oscillatory shear experiment. The thermo-electromechanical

responses under absence and presence of an electric field at equilibrium and non-equilibrium are reported here. In addition, thermo-chemical properties at equilibrium and thermal properties at non-equilibrium under absence of an electric field are investigated via Fourier transform infrared spectroscopy (FTIR) and differential scanning calorimetric (DSC), and shall be reported here.

Experimental

Materials

Cellulose microcrystalline powder (AR grade, Sigma-Aldrich), 1-butyl-3-methylimidazolium chloride ($BMIM^+Cl^-$) (HPLC grade, Sigma-Aldrich), and N,Ndimethylacetamide (DMAc) were used as received without further purification.

Preparation of 1-butyl-3-methylimidazolium chloride ionic liquid-cellulose gel (CelGel)

$BMIM^+Cl^-$ and the dried cellulose were mixed at a composition of 87 % w/w of $BMIM^+Cl^-$ (2.15 g) and 13 % w/w of cellulose (0.323 g) , equivalent to a 6.19:1 molar ratio of $BMIM^+Cl^-$: glucose [9], as this molar ratio allows the maximum dissolution of cellulose in $BMIM^+Cl^-$ at 100 °C. The cellulose was dissolved in $BMIM^+Cl^-$ at 100 °C for 15 minutes. The obtained viscous solution was filled with 1.5 ml of N, N-dimethylacetamide (DMAc) as a plasticizer and a co-solvent, and was stirred for 60 minutes. The solution was degassed and cast into a mold having a diameter of 25 mm and a thickness of 1 mm, and kept under a vacuum for 12 hours. The 1-butyl-3-methylimidazolium chloride ionic liquid-cellulose gel (CelGel) was obtained after curing at ambient conditions for 24 hours [10]. The CelGel was then characterized for thermo-electromechanical responses under absence and presence of an electric field.

Characterization of prepared CelGel

To investigate the chemical structure of the CelGel at different temperatures, FTIR was used (Thermo Nicolet, Nexus 670), using a ZnSe (zinc selenide) crystal, a resolution of 4.0 cm^{-1}, a scan number of 64, and a wavenumber range of 750–4000 cm^{-1}. The CelGel was pasted on the ZnSe and measured with increasing and decreasing temperature between 30 °C and 60 °C.

To investigate the thermal properties of the CelGel at different heating rates, the differential scanning calorimetric (DSC) curve was measured under N_2 atmosphere, corresponding with a programmed temperature profile via a simultaneous thermal analyzer (STA), Netzch STA 449 F3. The procedure of temperature programming was: holding at 30 °C for 5 min; increasing from 30 °C to 60 °C with a certain heating rate; holding at 60 °C for 5 min; decreasing from 60 °C to 30 °C with a certain heating rate; and holding at 30 °C for 15 min.

The thermo-electromechanical properties were measured by a rheometer (Rheometric Scientific, ARES) fitted with a parallel plate fixture (diameter 25 mm). DC voltage was applied with a DC power supply (Instek, GFG 8216A), which can deliver an electric field up to 4 kV. A digital multimeter (Tektronix, CDM 250) was used to monitor the voltage input. The samples were prepared in the configuration of a Polyimide/CelGel/Polyimide sandwich to prevent the shortening of the circuit. The Polyimide (PI), ®Kapton TH-012 (12 micron) was produced by and obtained from ©2006 Saint Gobain Performance Plastic Corporation. The PI film represents an excellent insulator up to 7 kV/mm for preventing a voltage breakdown; with a dielectric constant value of 3.3, and a volume resistivity >10 $^{16}\Omega$-cm. In these experiments, an oscillatory shear strain was applied. Strain sweep tests were first carried out to determine the suitable strains to measure G′ in the linear viscoelastic regime[11]. The appropriate strain was determined to be 0.25 % for the CelGel study. To determine relaxation time (τ_r) at 60 °C under absence and presence of an electric field, the stress relaxation (G′(t) vs t) of CelGel was measured. It was transformed to the relaxation spectrum ($H(\lambda)$ vs λ) and the storage moduli crossover (G′ and G″ vs frequency). τ_r, the relaxation time, was determined as the reciprocal of the crossover frequency [18]. The thermo-electromechanical response at equilibrium was investigated in the time sweep test mode between 30 °C and 60 °C with 100 rad/s and 0.25 % strain under absence and presence of an electric field. The steady G′ of certain temperature and electric field strength was plotted in terms of G′ vs. temperature. The thermo-electromechanical response at non-equilibrium was investigated in the mode of temperature sweep test mode with 100 rad/s and 0.25 % strain. The procedure for the temperature sweep test is: holding at 30 °C for 5 min; increasing from 30 °C to 60 °C with a certain heating rate (0.5 or 20.0 °C/min); holding at 60 °C for 5 min; decreasing from 60 °C to 30 °C with a certain heating rate; and holding at 30 °C for 15 min, respectively.

As shown in Table 1, the criteria for non-equilibrium is $\tau_m << \tau_e << \tau_r$; they are the measuring, experimental, and relaxation time scales, respectively. The measuring time scale (τ_m) refers to the reciprocal of ω of the measured G′(ω), which is 10^{-2} s at ω=100 rad/s of frequency. The experimental time scale (τ_e) was ∞, 120, and 3 s, corresponding to 0, 0.5, and 20.0 °C/min of heating rates, respectively. The relaxation time scale (τ_r) was determined from the reciprocal of the crossover frequency at 60 °C, which is 2.84×10^3 s and 2.75×10^3 s at the electric field strengths of 0 and 1 kV/mm, respectively. The data suggeststhat the cellulose chain in CelGel dominates the relaxation behavior in all conditions with a long time scale. The criteria for equilibrium is $\tau_m << \tau_e >> \tau_r$, in which τ_e is

Table 1 Measuring time scale (τ_m), experimental time scale (τ_e), and relaxation time scale (τ_r) of CelGel at different electric field strengths and heating rates

Electric field strength (kV/mm)	Heating rate (°C/min)	τ_m (s)	Comparison	τ_e (s)	Comparison	τ_r (s)	State
0	0.0	10^{-2}	<<	∞	>>	2.84E+03	equilibrium
	0.5	10^{-2}	<<	120	<<	2.84E+03	non-equilibrium
	20.0	10^{-2}	<<	3	<<	2.84E+03	non-equilibrium
1.0	0.0	10^{-2}	<<	∞	>>	2.75E+03	equilibrium
	0.5	10^{-2}	<<	120	<<	2.75E+03	non-equilibrium
	20.0	10^{-2}	<<	3	<<	2.75E+03	non-equilibrium

Note: The τ_m is determined by the reciprocal of 100 rad/s, which is equal to 10^{-2} s. The τ_e is determined by reciprocal of the certain heating rate. The τ_r is determined by the reciprocal of dynamic crossover frequency, $G'(\omega)=G''(\omega)$ at 60 °C, which is transformed from stress relaxation ($G'(t)$ vs t) and relaxation spectrum ($H(\lambda)$ vs λ), respectively.

infinitely large as the condition of 0 °C/min is obtained via the time sweep test. In short, the three time scales determine whether the experiment is in equilibrium or non-equilibrium. If the relaxation process has a shorter relaxation time scale compared to τ_m and τ_e, the equilibrium condition is satisfied. On the other hand, non-equilibrium is satisfied when the relaxation process timescale is longer than τ_m and τ_e.

Results and discussion

Thermo-electromechanical responses in the absence and presence of electric field at equilibrium

Figure 1 shows the thermo-electromechanical responses in the absence of an electric field at equilibrium. The shear storage modulus (G') at 100 rad/s increases from 1.9×10^5 to 3.3×10^5 Pa with continuously increasing temperature from 30 °C to 50 °C. This is due to the fact that an increase in temperature promotes a stronger interaction between the cellulosic hydroxyl group and the ionic liquid chloride anion, as evidenced from the FTIR spectra, with a lower absorbance peak at 3402 cm^{-1}[19]. However, G' decreases to 2.9×10^5 Pa when temperature is further increased to 60 °C; this is because temperature approaches the melting temperature of $BMIM^+Cl^-$ (60 °C) [20] where the OH-OH cellulose interaction diminishes and induces a lower G' [21]. In other words, a stronger cellulosic hydroxyl group-chloride anion interaction dominates from 30 °C to 50 °C and the melting process of $BMIM^+Cl^-$ dominates from 50 °C to 60 °C, as confirmed by the absorbance depletion of 3094 cm^{-1}. In decreasing temperatures from 60 °C to 30 °C, the thermo-electromechanical response in the absence of an electric field exhibits nearly the same values relative to the increasing temperature path due to being in the equilibrium state. Figure 2 shows the thermo-electromechanical response in the presence of 1 kV/mm electric field strength. G' with 1 kV/mm of electric field strength is 3.0×10^5 Pa, which is higher than 1.9×10^5 Pa of the G' in the absence of an electric field at 30 °C. This is because an electric field induces dipole moments via the ionic and electronic polarizations within the CelGel, which produce an enhanced shear storage modulus [11]. Moreover, the shear storage modulus (G') is diminished with increasing temperature from 30 °C to 60 °C. Under the 1.0 kV/mm electric field strength, the chloride anion, acting as a crosslinking agent, leaves out of its crosslinking position and approaches the anode electrode (higher potential electrode), producing a lower G'. For the temperature path from 60 °C to 30 °C, the thermo-electromechanical responses under the presence of 1 kV/mm electric field strength exhibit nearly the same values relative to those of the increasing temperature path due to the fact that it is in the equilibrium state.

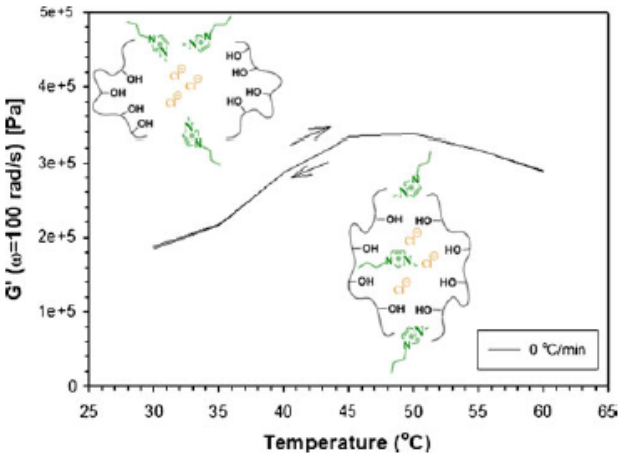

Fig. 1 Shear storage modulus (G') at 100 rad/s vs. temperature of CelGel at 0 °C/min under 0.0 kV/mm

Thermo-chemical characterization at equilibrium

Figure 3 reveals the chemical interactions within and the characteristics of CelGel when temperature increases from 30 °C to 60 °C and then decreases from 60 °C to 30 °C. The

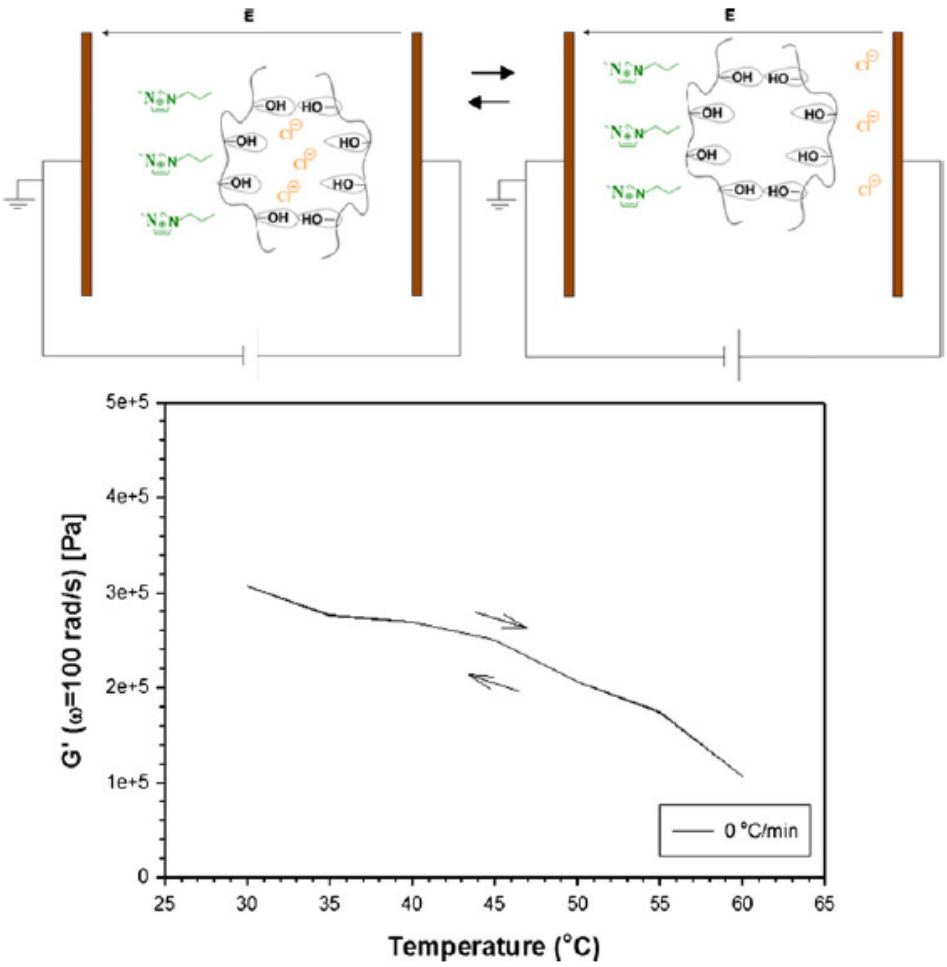

Fig. 2 Shear storage modulus (G′) at 100 rad/s vs. temperature of CelGel at 0 °C/min under 1.0 kV/mm

assignments of all FTIR interactions and characteristics are tabulated in Table 2 [19, 22–27]. The 3402 cm^{-1} absorbance peak is reduced as temperature is increased from 30 °C to 60 °C. This implies a stronger interaction between the cellulosic hydroxyl group and the chloride anion [19, 26]. In other words, a temperature increment produces a stronger crosslinking interaction and a higher G′. In addition, the 3402 cm^{-1} peak shows a stronger absorbance peak and a lower crosslinking interaction when temperature is decreased from 60 °C to 30 °C. This suggests that CelGel exhibits a reversible

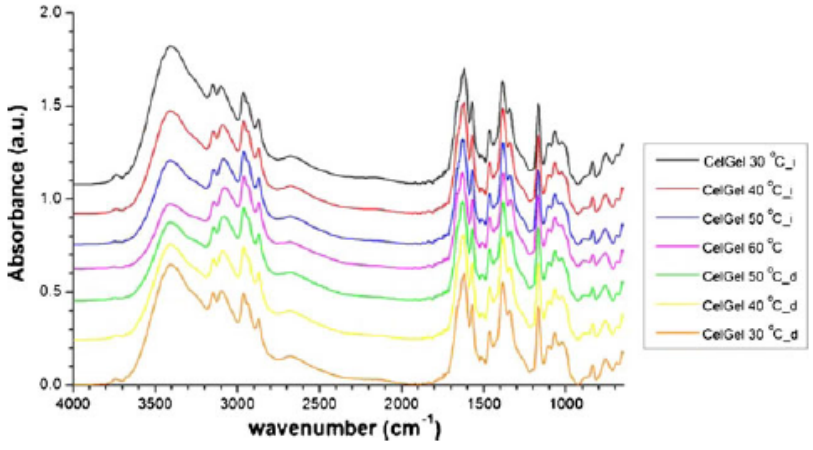

Fig. 3 Fourier transform infrared (FTIR) spectra in the range of 4000 to 650 of wavenumber of CelGel between 30 and 60 °C; i=increasing step, d=decreasing step

Table 2 FT-IR absorption spectrum of CelGel [19, 22–27]

Wavenumbers (cm^{-1})	Assignments	References
1430	CH_2 scissoring of cellulose	[22]
897	C-O-C stretching at β-(1→4)-glycosidic linkage of cellulose	
1160	Anti-symmetric bridge stretching of C-O-C groups of cellulose	[23, 24]
1318	CH_2 wagging vibration of cellulose	[25]
1635-1640	Absorbed water bending vibration of cellulose	
3402	Interaction between cellulosic hydroxyl group and chloride anion	[19, 26]
2876, 2940, and 2964	C-H stretching modes of the methyl and butyl groups of $BMIM^+Cl^-$	[27]
3094	Coupled imidazolium C-H stretching vibrations of $BMIM^+Cl^-$	

thermo-stiffening effect within the temperature range of 30 °C to 50 °C. Moreover, the reversible thermo-stiffening effect does not exist when the temperature is close to 60 °C, the melting temperature of $BMIM^+Cl^-$ [20].

Thermo-electromechanical responses in the absence and presence of electric field at non-equilibrium

Figure 4 shows the thermo-electromechanical response in the absence of an electric field at 0.5 °C/min. In the increment step from 30 °C to 60 °C, G′ increases from 1.7×10^5 to 3.1×10^5 Pa because of a stronger cellulosic hydroxyl group and chloride anion interaction [19]. In the holding step at 60 °C and the temperature-decreasing step from 60 °C to 43 °C, G′ is higher than that of the increasing step. This is due to the strong residual crosslinking interaction. However, from 43 °C to 30 °C in the decreasing step, G′ is lower than that of the increasing step because a recrystallization of $BMIM^+Cl^-$ gradually occurs during the cooling, as confirmed by DSC curves. The ionic liquid molecules may reorder to crystallize themselves to produce lesser chloride anion crosslinking species, and thus a lower G′. In the holding step at 30 °C, G′ increases to obtain nearly the same initial G′, as CelGel needs a certain time period for molecular rearrangement, thus providing a reversible thermomechanical effect.

Figure 5 shows the thermo-electromechanical response under the presence of 1.0 kV/mm electric field at 0.5 °C/min. G′ at 30 °C and 1.0 kV/mm is 3.5×10^5 Pa, which is higher than G′ at 30 °C and 0 kV/mm by about two times. This is due to the $BMIM^+$ and cellulosic hydroxyl group polarizations under an electric field inducing dipole moments and higher G′ [11]. As temperature is increased to 35 °C, G′ approaches its maximum value of 3.6×10^5 Pa, as temperature also promotes these polarizations. Nevertheless, G′ declines as temperature is increased to 60 °C. This is because temperature promotes chloride anion movement towards the anodic electrode under an electric field, producing fewer chloride anion crosslinking species and thus a lower G′ [11, 28, 29]. In the temperature-decreasing step, G′ decreases via the recrystallization of $BMIM^+Cl^-$ with a lower rate of G′ depletion compared to that under absence of an electric field. This suggests that an electric field directly affects the recrystallization $BMIM^+Cl^-$ at 0.5 °C/min. The electric field induces the ionic polarization of $BMIM^+Cl^-$ which produces a smaller $BMIM^+Cl^-$ concentration in the middle of the sample, and induces a faster recrystallization at higher temperature. In

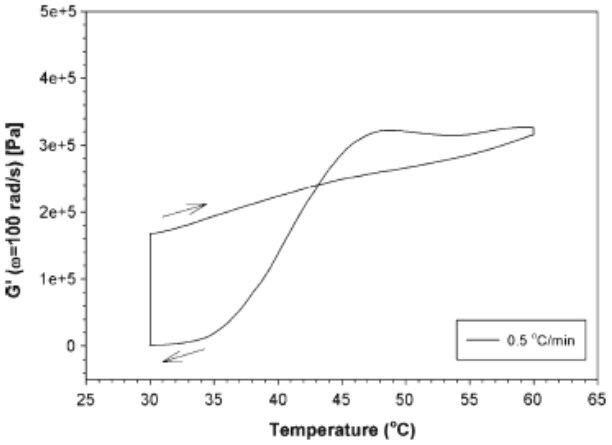

Fig. 4 Shear storage modulus (G′) at 100 rad/s vs. temperature of CelGel at 0.5 °C/min under 0.0 kV/mm

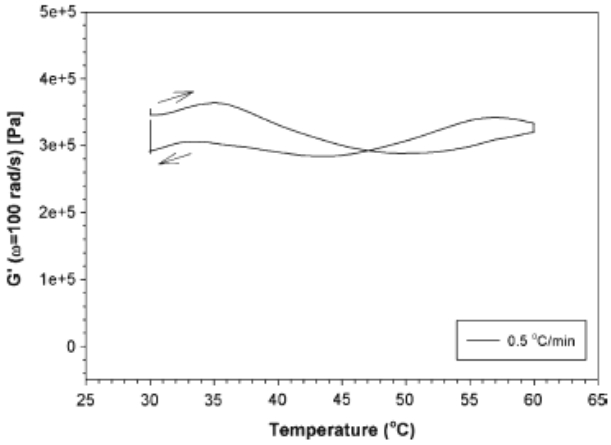

Fig. 5 Shear storage modulus (G′) at 100 rad/s vs. temperature of CelGel at 0.5 °C/min under 1.0 kV/mm

other words, a higher $BMIM^+Cl^-$ concentration provides a sluggish recrystallization [17]. In addition, during the holding step at 60 °C and the decreasing step from 60 °C to 47 °C, G′ is higher than that in the increasing step. This results from increases in the cellulosic hydroxyl-chloride anion interaction and the dipole moments generated from the ionic and electronic polarizations under an applied electric field. Between 47 °C to 30 °C, G′ is quite constant at around 3.0×10^5 Pa, then recovers a value close to the initial G′ value in the holding step at 30 °C.

Figure 6 shows the thermo-electromechanical response in the absence of electric field at 20.0 °C/min. In the temperature-increasing step from 30 °C to 60 °C, the data can be divided to two regimes. The first regime is between 30 °C to 53 °C, where G′ abruptly increases from 1.5×10^5 to 6.5×10^5 Pa because the cellulosic hydroxyl-chloride anion interaction, the $BMIM^+$ polarization, the cellulosic hydroxyl polarization, and the cellulose chain expansion [16] are strongly enhanced at the heating rate of 20.0 °C/min. The second regime is between 53 °C to 60 °C; G′ is steady around 6.6×10^5 Pa, which may result from the saturation of those interactions, the polarizations, and the expansion. In the holding step at 60 °C, G′ slightly decreases because of the relaxation of those interactions, the polarizations, and the expansion at the high heating rate. In the temperature-decreasing step from 60 °C to 30 °C, G′ slightly increases to 6.4×10^5 Pa. This results from the cellulose chain entanglement in which it has little time to disentangle until the holding step at 30 °C [16].

Figure 7 shows the thermo-electromechanical response under the presence of 1.0 kV/mm of electric field strength at 20.0 °C/min. G′ data can also be separated into two regimes: temperature-increasing regime (30 °C to 42.5 °C) and the saturating regime (42.5 °C to 60 °C). The increasing temperature regime occurs due to the stronger cellulosic hydroxyl-chloride anion interaction, the $BMIM^+$ polarization, the cellulosic hydroxyl polarization, and the cellulose chain expansion.

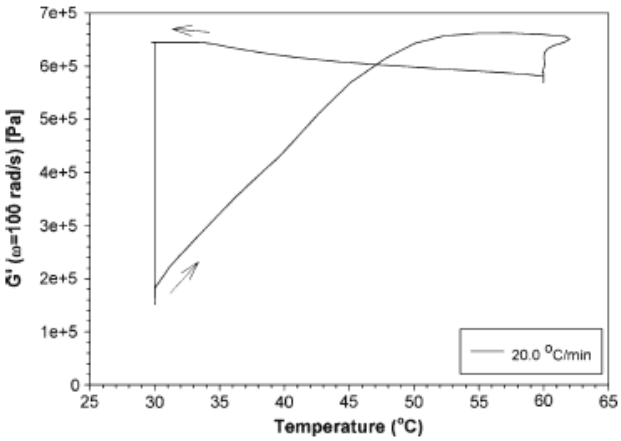

Fig. 6 Shear storage modulus (G′) at 100 rad/s vs. temperature of CelGel at 20.0 °C/min under 0.0 kV/mm

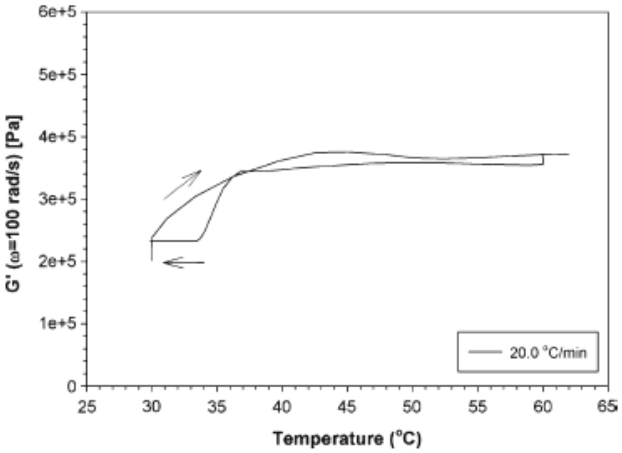

Fig. 7 Shear storage modulus (G′) at 100 rad/s vs. temperature of CelGel at 20.0 °C/min under 1.0 kV/mm

However, the increase in G′ between 30 °C to 43 °C at 20.0 °C/min under 1.0 kV/mm is lesser than that of 0.0 kV/mm. This occurs as the chloride anion leaves out of its crosslinking position to become polarized under 1.0 kV/mm, thus inducing a lower G′. In addition, G′ between 42.5 °C to 60 °C becomes saturated around 3.6×10^5 Pa and stays constant. At the heating rate of 20.0 °C/min, it provides a shorter time scale than that of 0.5 °C/min, so there is less time to allow chloride anions to leave out of the crosslinking position. In the holding step (at 60 °C) and in the decreasing step (60 °C to 37 °C), G′ shows a slightly lower value than that in the increasing step, because these steps provide a period of time for chloride anion movement. G′ decreases when temperature is decreased from 37 °C to 34 °C due to the $BMIM^+Cl^-$ crystallization, then becomes saturated and recovers nearly its initial G′. In summary, an electric field causes the ionic polarization of $BMIM^+Cl^-$ and a faster recrystallization at higher temperature [17].

Thermal properties under absence of electric field at non-equilibrium

The thermal properties of CelGel, BMIMCl, and cellulose were investigated via DSC as shown in Fig. 8. In the case of 0.5 °C/min, CelGel exhibits an endothermic peak as temperature is increased from 30 °C to 60 °C, which can be related to the melting temperature of $BMIM^+Cl^-$ and hydroxyl group rearrangement of cellulose in the CelGel. In addition, CelGel shows an exothermic peak when temperature is decreased from 60 °C to 30 °C, which can be related to the recrystallization of $BMIM^+Cl^-$ and hydroxyl group repacking of cellulose in CelGel. When the heating rate is increased to 20.0 °C/min, the melting process of $BMIM^+Cl^-$ and hydroxyl group rearrangement of cellulose are promoted in incremental steps, as shown by increasing enthalpy through the integrated

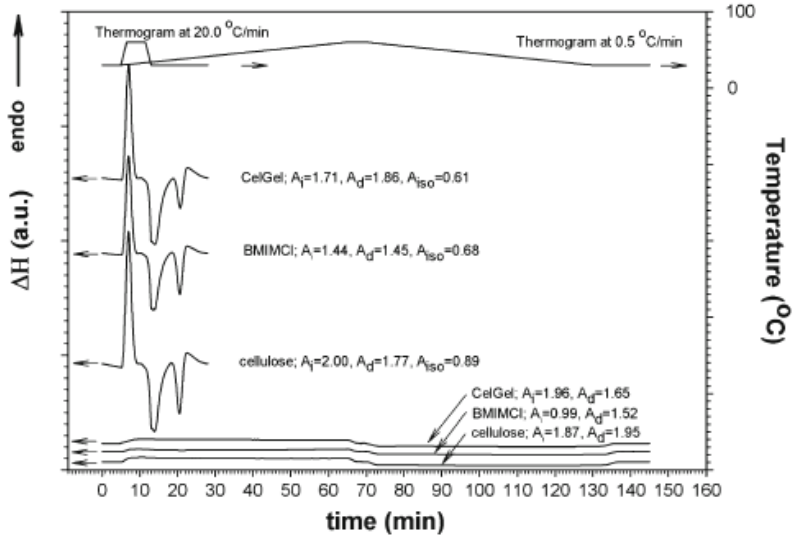

Fig. 8 Differential scanning calorimetric curves and programmed temperature profiles of CelGel, BMIMCl, and cellulose at 0.5 and 20.0 °C/min; A_i=integrated area in temperature increment zone, A_d=integrated area in temperature decrement zone, A_{iso}=integrated area in isothermal zone

area. However, CelGel shows decreasing enthalpy because its heterogeneity obstructs these processes. In other words, the lower enthalpy of CelGel at 20.0 °C/min compared to 0.5 °C/min is related to a lesser softening process and a more solid-like behavior. This is the cause of dramatically increasing G′ of CelGel in increasing temperature from 30 °C to 60 °C as shown in Fig. 6. In the decreasing step of 20.0 °C/min, the recrystallization of $BMIM^+Cl^-$ and hydroxyl group repacking of cellulose in CelGel are promoted by its heterogeneity [30]. Nevertheless, the recrystallization of $BMIM^+Cl^-$ and hydroxyl group repacking of cellulose are reduced due to a shorter time scale. All of the samples (CelGel, $BMIM^+Cl^-$, and cellulose) showed second exothermic peaks, implying that a longer time for the recrystallization of $BMIM^+Cl^-$, the hydroxyl group repacking, and the relaxation process of cellulose [16] is required in the isothermal region [31]. As shown, both $BMIM^+Cl^-$ and cellulose play important roles in the thermal properties of CelGel in the absence of an electric field in non-equilibrium.

Conclusion

The thermo-electromechanical responses of 1-butyl-3-methylimidazolium chloride ($BMIM^+Cl^-$)-cellulose gel, namely CelGel, were investigated via an oscillatory shear experiment. CelGel was subjected to heat under temperatures between 30 °C to 60 °C under equilibrium and non-equilibrium states, satisfying the conditions of $\tau_m << \tau_e >> \tau_r$ and $\tau_m << \tau_e << \tau_r$, respectively. The electromechanical response in terms of G′ in the equilibrium state is temperature history-independent, with equivalent G′ values in both the increasing and decreasing steps at any temperature. At equilibrium state in the absence of an electric field, G′ increases with increasing temperature from 30 °C to 50 °C. This results from the stronger interaction of the cellulosic hydroxyl group and the chloride anion, which is confirmed by the decrease in the 3402 cm^{-1}absorbance peak via FTIR investigation. When temperature is increased from 50 °C to 60 °C, G′ decreases because it is close to the melting temperature of $BMIM^+Cl^-$, inducing lower G′. In equilibrium state in the presence of 1 kV/mm of electric field strength, G′ continuously decreases with increasing temperature from 30 °C to 60 °C, as the chloride anion moves out of its crosslinking position to become polarized under an electric field. The electromechanical response in term of G′ in the non-equilibrium state is significantly temperature history-dependent, with different G′ values in the increasing and decreasing steps at certain temperature. The heating rate effect in the absence of an electric field is investigated between 0.5 and 20.0 °C/min. In the increasing step, G′ increases because of the stronger interaction between the cellulosic hydroxyl group and the chloride anion, including a cellulose chain expansion. In the decreasing step, G′ remains constant at higher level because it needs a longer time to relax. These results can be further investigated by DSC curve. The effect of heating rate is investigated at 0.5 and 20.0 °C/min under 1 kV/mm of electric field strength. In the increasing step, G′ increases with a slower rate because ofthe shorter time scale available for the $BMIM^+$ polarization. In the decreasing step, the recrystallization occurs at lower temperature because a shorter time scale obstructs the recrystallization process. The results suggest that an increase in the heating rate on CelGel retards the melting and promotes recrystallization processes in terms of enthalpy due to its heterogeneity. However, the $BMIM^+Cl^-$ recrystallization and chain relaxation need a longer time, as evidenced by the second DSC peak at 30 °C. The thermo-electromechanical

properties of CelGel have been shown to be drastically different in the equilibrium and non-equilibrium states.

Acknowledgments We wish to express our appreciation for the financial support provided by the Conductive and Electroactive Polymer Research Unit (CEAP) of Chulalongkorn University, the Thailand Research Fund (TRF-RTA), the Royal Thai Government, and the 90th Anniversary of Chulalongkorn University Fund (Ratchadaphiseksomphot Endowment Fund).The materials support from Saint Gobain Sekurit Thailand Co. Ltd is also gratefully acknowledged.

References

1. Klemm D, Heublein B, Fink HP, Bohn A (2005) Cellulose: Fascinating biopolymer and sustainable raw material. Angew Chem Int Ed 44(22):3358–3393
2. Pukada E (2000) History and recent progress in piezoelectric polymers. IEEE Trans Ultrason Ferroelectr Freq Control 47(6):1277–1290
3. Kim J, Yun S, Ounaies Z (2006) Discovery of cellulose as a smart material. Macromolecules 39(12):4202–4206
4. Swatloski RP, Spear SK, Holbrey JD, Rogers RD (2002) Dissolution of cellose with ionic liquids. J Am Chem Soc 124(18):4974–4975
5. Novoselov NP, Sashina ES, Kuz'mina OG, Troshenkova SV (2007) Ionic liquids and their use for the dissolution of natural polymers. Russ J Gen Chem 77(8):1395–1405
6. Lu W, Fadeev AG, Qi B, Smela E, Mattes BR, Ding J, Spinks GM, Mazurkiewicz J, Zhou D, Wallace GG, MacFarlane DR, Forsyth SA, Forsyth M (2002) Use of ionic liquids for π-conjugated polymer electrochemical devices. Science 297(5583):983–987
7. Bennett MD, Leo DJ, Wilkes GL, Beyer FL, Pechar TW (2006) A model of charge transport and electromechanical transduction in ionic liquid-swollen Nafion membranes. Polymer 47(19):6782–6796. doi:10.1016/j.polymer.2006.07.061
8. Bennett MD, Leo DJ (2004) Ionic liquids as stable solvents for ionic polymer transducers. Sensors Actuators A Phys 115(1):79–90. doi:10.1016/j.sna.2004.03.043
9. Ji K, Ma M, Kaneko Y (2008) A facile preparation of gel materials from a solution of cellulose in ionic liquid. Carbohydr Res 343(4):769–772
10. Kunchornsup W, Sirivat A (2010) Effects of crosslinking ratio and aging time on properties of physical and chemical cellulose gels via 1-Butyl-3-methylimidazolium chloride solvent. J Sol-Gel Sci Technol 56(1):19–26
11. Kunchornsup W, Sirivat A (2012) Physically cross-linked cellulosic gel via 1-butyl-3-methylimidazolium chloride ionic liquid and its electromechanical responses. Sensors Actuators A Phys 175(0):155–164. doi:10.1016/j.sna.2011.12.045
12. Pritchard J, Ramesh R, Bowen CR (2004) Time–temperature profiles of multi-layer actuators. Sensors Actuators A Phys 115(1):140–145. doi:10.1016/j.sna.2004.04.019
13. Yoon GH (2012) Topological layout design of electro-fluid-thermal-compliant actuator. Comput Methods Appl Mech Eng 209–212(0):28–44. doi:10.1016/j.cma.2011.11.005
14. Li T, Chen YH, Boey FYC, Ma J (2007) High amplitude vibration of piezoelectric bending actuators. J Electroceram 18(3–4):231–242
15. Putz AMV, Burghelea TI (2009) The solid–fluid transition in a yield stress shear thinning physical gel. Rheol Acta 48(6):673–689
16. Ruan D, Lue A, Zhang L (2008) Gelation behaviors of cellulose solution dissolved in aqueous NaOH/thiourea at low temperature. Polymer 49(4):1027–1036. doi:10.1016/j.polymer.2007.12.044
17. Akbulut O, Taniguchi I, Kumar S, Shao-Horn Y, Mayes AM (2007) Conductivity hysteresis in polymer electrolytes incorporating poly(tetrahydrofuran). Electrochim Acta 52(5):1983–1989. doi:10.1016/j.electacta.2006.08.007
18. Tungkavet T, Sirivat A, Seetapan N, Pattavarakorn D (2013) Stress relaxation behavior of (Ala-Gly-Pro-Arg-Gly-Glu-4Hyp-Gly-Pro-) gelatin hydrogels under electric field: Time-electric field superposition. Polymer (United Kingdom) 54(9):2414–2421
19. Gonjo T, Futami Y, Morisawa Y, Wojcik MJ, Ozaki Y (2011) Hydrogen bonding effects on the wavenumbers and absorption intensities of the OH fundamental and the first, second, and third overtones of phenol and 2,6-dihalogenated phenols studied by visible/near-infrared/infrared spectroscopy. J Phys Chem A 115(35):9845–9853
20. Domańska U, Bogel-Łukasik E (2004) Solid–liquid equilibria for systems containing 1-butyl-3-methylimidazolium chloride. Fluid Phase Equilib 218(1):123–129
21. Iotti M, Gregersen ØW, Moe S, Lenes M (2011) Rheological Studies of Microfibrillar Cellulose Water Dispersions. J Polym Environ 19(1):137–145
22. Nelson ML, O'Connor RT (1964) Relation of certain infrared bands to cellulose crystallinity and crystal lattice type. Part II. A new infrared ratio for estimation of crystallinity in celluloses I and II. J Appl Polym Sci 8(3):1325–1341. doi:10.1002/app.1964.070080323
23. Zhbankov RG, Firsov SP, Korolik EV, Petrov PT, Lapkovski MP, Tsarenkov VM, Marchewka MK, Ratajczak H (2000) Vibrational spectra and the structure of medical biopolymers. J Mol Struct 555:85–96
24. Langkilde FW, Svantesson A (1995) Identification of celluloses with Fourier-transform (FT) mid-infrared, FT-Raman and near-infrared spectrometry. J Pharm Biomed Anal 13(4–5):409–414
25. Spiridon I (2007) Modifications of Asclepias syriaca fibers for paper production. Ind Crop Prod 26(3):265–269. doi:10.1016/j.indcrop.2007.03.015
26. Seo J, Kim J, Koh J, Ahn S, Kim J (2009) Preparation and characterization of crosslinked cellulose/sulfosuccinic acid membranes as proton conducting electrolytes. Ionics 15(5):555–560. doi:10.1007/s11581-009-0314-8
27. Chang HC, Jiang JC, Chang CY, Su JC, Hung CH, Liou YC, Lin SH (2008) Structural organization in aqueous solutions of 1-butyl-3-methylimidazolium halides: A high-pressure infrared spectroscopic study on ionic liquids. J Phys Chem B 112(14):4351–4356
28. Mahadeva SK, Kim J (2009) Electromechanical behavior of room temperature ionic liquid dispersed cellulose. J Phys Chem C 113(28):12523–12529
29. Mahadeva SK, Yi C, Kim J (2009) Effect of room temperature ionic liquids adsorption on electromechanical behavior of cellulose electroactive paper. Macromol Res 17(2):116–120
30. König A, Stepanski M, Kuszlik A, Keil P, Weller C (2008) Ultrapurification of ionic liquids by melt crystallization. Chem Eng Res Des 86(7):775–780. doi:10.1016/j.cherd.2008.04.002
31. Calvar N, Gómez E, Macedo EA, Domínguez A (2013) Thermal analysis and heat capacities of pyridinium and imidazolium ionic liquids. Thermochim Acta 565(0):178–182. doi:10.1016/j.tca.2013.05.007

Journal of Innovative Optical Health Sciences
Vol. 7, No. 6 (2014) 1450016 (7 pages)
© The Authors
DOI: 10.1142/S1793545814500163

World Scientific
www.worldscientific.com

LEAD ZIRCONATE ($PbZrO_3$) EMBEDDED IN NATURAL RUBBER AS ELECTROACTIVE ELASTOMER COMPOSITES

ANUVAT SIRIVAT*, KARAT PETCHAROEN*,
YANEE PORNCHAISIRIARUN†, CHALEOMWUT PHANSA-ARD†
and NUCHNAPA TANGBORIBOON†,‡
*The Petroleum and Petrochemical College
Chulalongkorn University, Bangkok 10330, Thailand

†The Materials Engineering Department and Center for
Advanced Studies in Industrial Technology, Faculty of Engineering
Kasetsart University, Bangkok 10900, Thailand
‡fengnnpt@ku.ac.th

Received 6 August 2013
Accepted 15 November 2013
Published 20 January 2014

Perovskite lead zirconate ($PbZrO_3$) was synthesized in an orthorhombic form at a temperature below the Curie temperature, T_C. The orthorhombic form is a noncentrosymmetric structure which is capable of spontaneous polarization. Fourier transform infrared (FTIR) spectra and X-ray diffraction (XRD) patterns confirm the successful synthesis of the lead zirconate; and scanning electron microscopy (SEM) micrographs indicate that $PbZrO_3$ particles are moderately dispersed in the natural rubber (NR) matrix. Without an electrical field, the particles merely act as a ferroelectric filler, which can absorb and store additional stress. Under an electrical field, particle-induced dipole moments are generated, leading to interparticle interaction and a substantial increase in the storage modulus. At a small amount of lead zirconate particulates present in the natural rubber matrix, at a volume fraction of 0.007306, the electrical conductivity increases dramatically by nearly two orders of magnitude at the electrical frequency of 500 kHz.

Keywords: Natural rubber; perovskite lead zirconate; actuator sensors; smart engineering devices.

J. Innov. Opt. Health Sci. Downloaded from www.worldscientific.com
by CHULALONGKORN UNIVERSITY on 06/09/14. For personal use only.

1. Introduction

Lead zirconate ($PbZrO_3$) is an inorganic and antiferroelectric material containing Pb^{2+}, Zr^{4+}, and O^{2-} ions within the unit cell with the Curie temperature (T_C) approximately at 230°C. The antiferroelectric materials may phase transform to

This is an Open Access article published by World Scientific Publishing Company. It is distributed under the terms of the Creative Commons Attribution 3.0 (CC-BY) License. Further distribution of this work is permitted, provided the original work is properly cited.

J. Innov. Opt. Health Sci. Downloaded from www.worldscientific.com
by CHULALONGKORN UNIVERSITY on 06/09/14. For personal use only.

ferroelectric materials when induced by electrical field. The advantages of lead zirconate are a material for high displacement electromechanical actuator and energy storage applications due to the spontaneous polarizations consisting of: orientation polarization (Debye polarization), and ionic and electronic polarizations (Wagner polarization). Lead zirconate can be prepared by many methods such as sol–gel, conventional process, wet chemical precipitation, and microemulsion.[1,2]

Composite materials are made of a filler or dispersed phase (either particles, flakes, or fibers) embedded in a matrix phase made of polymer, metal, and ceramic materials. Combining a ferroelectric ceramic and a polymer host to form a flexible ferroelectric composite has been the subject of interest in recent years in view of the greater flexibility allowed by these materials to suit particular property requirements such as mechanical, electrical, thermal and/or a coupling between these properties. The characteristics of the ceramic powder depend not only on their composition and their crystal structure but also on the microstructure, including grain size, grain boundary, pore size, crystalline, polarization, and phase transformation which can affect various properties.[3]

The objective in this work was to investigate an uncrosslinked natural rubber (NR) matrix embedded with a dielectric material ($PbZrO_3$) under the effect of volume fraction. The electrical properties, dielectric constant (ε), and electrical conductivity (σ) of the soft composite materials consisting of lead zirconate particles and the NR swollen in a hexane (C_6H_{14}) medium are reported here. It is known that NR containing nonpolar molecules tends to be soluble and swollen in the nonpolar solvents such as carbon tetrachloride, diethyl ether, and benzene, as shown in Scheme 1.[3,4]

Here we have also made detailed investigations by scanning electron microscopy (SEM), Fourier transform infrared spectra (FTIR), and X-ray diffraction (XRD) to confirm the electrical properties and results. Lead zirconate ($PbZrO_3$) and NR (Standard Thai Rubber 5L, STR 5L) composite materials can be used as biomimetic actuators, artificial muscles, and smart engineering devices such as active engine mounts, shock absorbers, clutches, brakes, damping devices, hydraulic valves, and robotic controlling systems.[3–12]

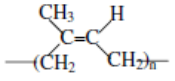

Scheme 1. Polyisoprene structure.

2. Experimental Procedure

2.1. *Materials*

The production process of pure perovskite lead zirconate ($PbZrO_3$) was successfully synthesized via the sol–gel process.[13–15] Lead glycolate and sodium tris (glycozirconate) were used as the starting precursors. The obtained molar ratio (Pb:Zr) of $PbZrO_3$ was 0.9805:1 and in the orthorhombic form when the lead zirconate powder was calcined at 300°C for 1 h, a temperature close to the Curie temperature (T_C). The lead zirconate synthesized possesses high dielectric constant and high electrical conductivity values of 9.248 and 5.84×10^{-7} $(\Omega \cdot m)^{-1}$, respectively, as measured at 27°C and 500 kHz. The density of the calcined lead zirconate powder is 7.50 g/cm^3. The average particle diameter of the $PbZrO_3$ is approximately 16.724 ± 0.026 microns.

The NR (STR5L) was supplied by Union Rubber Product Corporation Co., Ltd., Thailand. The NR is an uncrosslinked rubber type in an extra light color slab suitable for producing rubber bands, cut thread, baby bottle nipples, extruded hoses, footwear, and medical applications. The density, impurity content, Mooney viscosity, initial plasticity, and the plasticity retention of the natural rubber (NR-STR 5L) are 0.92 g/cm^3, 0.004 % by weight, 62.8, 32.0, and 81.3, respectively.

Hexane (High Performance Liquid Chromatography, HPLC grade) medium was obtained from Lab-Scan Co., Ltd., Thailand. It was used for the swelling of the uncrosslinked NR. The dielectric constant and density of acetone are 2.00, and 0.655 g/cm^3, respectively.

2.2. *Instruments*

(1) FTIR were recorded on a Perkin Elmer, model Spectrum One spectrometer with a spectral resolution of 4 cm^{-1}. The samples were measured by single-crystal potassium bromide, KBr.
(2) XRD was taken and analyzed using a Bruker AXS analyzer (D8 Discover) with VANTEC-1

J. Innov. Opt. Health Sci. Downloaded from www.worldscientific.com
by CHULALONGKORN UNIVERSITY on 06/09/14. For personal use only.

Detector. Samples were analyzed using a double-crystal wide-angle goniometer. Peak positions were consistent with those of the International Center for Diffraction Data Standard (JCPDS) patterns to identify crystalline phases and phase transformation via the Bragg equation: $\lambda = 2d\sin\Theta$.

(3) SEM: Micrographs were obtained using a scanning electron microscope (SEM, JEOL-5200).

(4) Electrical properties were measured and obtained using an impedance analyzer (HP, model 16451B) with an LCR meter (HP, model 4284A), in the frequency range of 1 to 1000 kHz. The samples were prepared according to ASTM B263-94 for the electrical properties measurement. Pellet samples were prepared as thin discs having a diameter of 38 mm and a thickness of 0.50 mm. In our experiment, the electrical properties were measured at frequencies from 10^3 to 10^6 Hz with an AC electrical field of 2 A at the volume fraction defined in Eq. (1) as follows:

$$\chi_\beta = \frac{\nu_{\text{disperse}}}{\nu_{\text{total}}}. \tag{1}$$

The electrical resistivity of the composite materials was converted to electrical conductivity using the resistivity-mixture rule, Eqs. (2) and (3), as follows:

$$\rho_{\text{eff}} = \frac{RA}{L} = \frac{1}{\sigma} = \chi_\alpha \rho_\alpha + \chi_\beta \rho_\beta, \tag{2}$$

$$\varepsilon_r = \frac{\varepsilon}{\varepsilon_0}, \tag{3}$$

where ρ_{eff} is the effective resistivity ($\Omega \cdot$ m), R is the resistance (Ω), A is the cross-sectional area of the discs (m^2), L is the total length or thickness (m), χ_α is the volume fraction of the continuous phase, χ_β is the volume fraction of the dispersed phase, ρ_α is the resistivity of the continuous phase, ρ_β is the resistivity of the dispersed phase, ε_r is the relative dielectric constant, ε_0 is the permittivity in a vacuum 8.854×10^{-12} (F/m), σ is the electrical conductivity $(\Omega \cdot \text{m})^{-1}$, and ε is the permittivity of the samples (F/m).

2.3. *Sample preparation of soft composite materials*

Natural rubber (STR5L) samples, consisting of nonpolar molecules, were dissolved and swollen in the 20% V/V hexane medium. The suspensions were homogeneously mixed by using a magnetic stirrer at room temperature for 24 h. Lead zirconate particles were added into the suspensions at the volume fractions of 0.000000 (STR5L/PZ_0), 0.000037 (STR5L/PZ_1), 0.000074 (STR5L/PZ_2), 0.00368 (STR5L/PZ_3), 0.003667 (STR5L/PZ_4), 0.007306 (STR5L/PZ_5), and 0.035494 (STR5L/PZ_6). The suspensions were then poured into petri dishes, covered with glass plates to avoid dust and bubbles, and allowed to dry slowly at room temperature overnight. The dried samples obtained display the colors varying between light yellow to dark yellow, depending on the volume fraction of lead zirconate embedded in NR.

3. Results and Discussion

3.1. *Characterization of natural rubber (NR-STR 5L)/lead zirconate ($PbZrO_3$) composite materials*

The FTIR spectra of lead zirconate ($PbZrO_3$), NR, and NR-STR5L/$PbZrO_3$ composite materials are shown in Fig. 1 and the peaks are tabulated in Table 1. The characteristic peaks of NR-STR5L/$PbZrO_3$ are at: 3459 $cm^{-1}\nu$(O–H); 3036 and 3282 $cm^{-1}\nu$(C–H); 2852, 2915, and 2960 $cm^{-1}\nu$(CH_2); 1663 and 1710 $cm^{-1}\nu$(C=C); 1546 cm^{-1} of CH_3 asymmetry; 1375 and 1448 cm^{-1}(CH_3 of O–CH_2CH_3 and C–O stretching); 1241 and 1287 $cm^{-1}\nu$(C–O–C); 1128 cm^{-1}(R–CO–R); 990 and 1053 $cm^{-1}\nu$(Zr–O–C); 884 cm^{-1}(C–O–Pb and

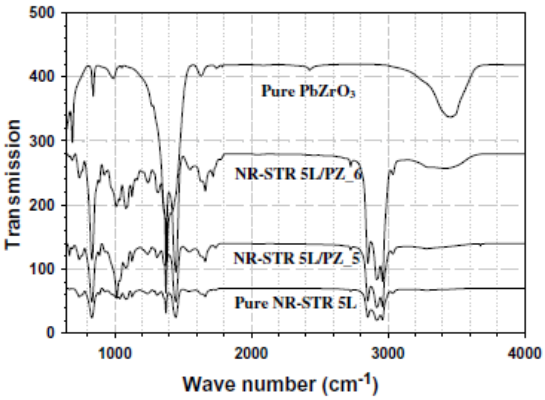

Fig. 1. FTIR spectra of natural rubber (NR-STR 5L), lead zirconate ($PbZrO_3$), NR-STR5L/PZ_5, and NR-STR5L/PZ_6 composite materials.

Table 1. FTIR spectra of natural rubber (NR-STR 5L), lead zirconate ($PbZrO_3$), and NR-STR 5L/$PbZrO_3$ composite materials.

Wave number (cm^{-1})	Functional group
3282, 3459 (CAS7732-18-5); (CAS78-79-5)	OH stretching of $PbZrO_3$ added NR
3036 (CAS78-79-5)	–C–H and =CH stretching vibration of isoprene
2852, 2915, 2960 (CAS78-79-5)	$–CH_2$ stretching vibration of C–CH_2CH_3
1663, 1710 (CAS78-79-4)	>C=C stretching for carbon double bonds
1448 (CAS78-79-5); (CAS110-54-3); (CAS73513-42-5)	$–CH_3$ asymmetric deformation
1375 (CAS78-79-5)	$–CH_3$ deformation of O–CH_2CH_3
1241, 1287 (CAS110-54-3)	Asymmetric C–O–C stretching vibration
1128	R–CO–R symmetric stretching
990, 1053 (CAS110-54-3)	Zr–O–C
884	C–O–Pb and C–O–O–C
691	Pb–O and Pb–O–Zr stretching

J. Innov. Opt. Health Sci. Downloaded from www.worldscientific.com
by CHULALONGKORN UNIVERSITY on 06/09/14. For personal use only.

Table 2. Electrical properties of NR-STR5L/$PbZrO_3$ composites measured at $27 \pm 1°C$, and 500 kHz.

Code	Mass of $PbZrO_3$ (300°C_1 h) (g)	Mass of STR5L (g)	Volume fraction of $PbZrO_3$	Dielectric constant at 500 kHz	Electrical conductivity at 500 kHz $(\Omega \cdot m)^{-1}$	Upper bound of σ $(\Omega \cdot m)^{-1}$	Lower bound of σ $(\Omega \cdot m)^{-1}$
$PbZrO_3$	1.0000	0.00000	1.000000	9.248	5.8400E-07	5.84E-07	2.76E-15
NR-STR5L/PZ_0	0.0000	3.00000	0.000000	0.718	4.7300E-09	4.75E-09	4.73E-09
NR-STR5L/PZ_1	0.0009	3.00000	0.000037	1.062	4.7793E-09	6.14E-09	4.734E-09
NR-STR5L/PZ_2	0.0018	3.00000	0.000074	1.601	5.7783E-09	7.55E-09	4.747E-09
NR-STR5L/PZ_3	0.0090	3.00000	0.000368	1.355	6.6959E-09	1.86E-08	4.752E-09
NR-STR5L/PZ_4	0.0900	3.00000	0.003667	1.243	1.0119E-08	1.19E-07	4.756E-09
NR-STR5L/PZ_5	0.1800	3.00000	0.007306	1.597	4.4283E-08	1.95E-07	4.760E-09
NR-STR5L/PZ_6	0.9000	3.00000	0.035494	1.661	3.0066E-08	4.16E-7	4.900E-09

Note: Density of NR − STR5L = 0.92 g/cm^3, Density of $PbZrO_3$ powder = 7.50 g/cm^3.

C–O–O–C); and 691 cm^{-1} ν(Pb–O) and ν(Pb–O–Zr). The FTIR spectra are consistent with the earlier results obtained by Jha and Bhowmick.[16,17]

A broad XRD characteristic peak of pure natural rubber (NR-STR 5L) shows that it is amorphous. The X-ray characteristic diffraction diagrams of the NR-STR5L/$PbZrO_3$ composites show patterns of the amorphous phase mixed with the crystalline phases, with the peaks at 28.500, 29.305, 30.850, 34.550, and 45.45 (as shown in Fig. 2), indicating the orthorhombic form. These peaks resemble those recorded by the JCPDS numbers 35-739, 77-856, and 75-1607.

The microstructures of pure natural rubber (NR-STR5L), lead zirconate ($PbZrO_3$), NR-STR5L/PZ_5, and NR-STR5L/PZ_6, as obtained by SEM, are shown in Fig. 3. Figure 3(a) is a micrograph of the natural rubber (NR-STR5L). The average particle diameter of $PbZrO_3$ is approximately 16.724 ± 0.026 microns[10–12] as shown in Fig. 3(b); it is

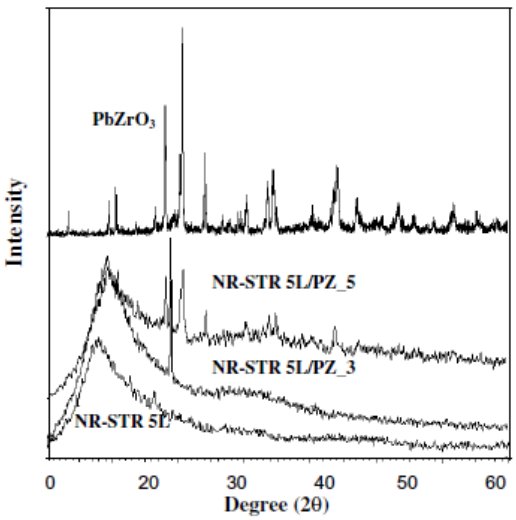

Fig. 2. XRD patterns of natural rubber (NR-STR 5L), lead zirconate ($PbZrO_3$), NR-STR5L/PZ_3, and NR-STR5L/PZ_5 composite materials.

J. Innov. Opt. Health Sci. Downloaded from www.worldscientific.com
by CHULALONGKORN UNIVERSITY on 06/09/14. For personal use only.

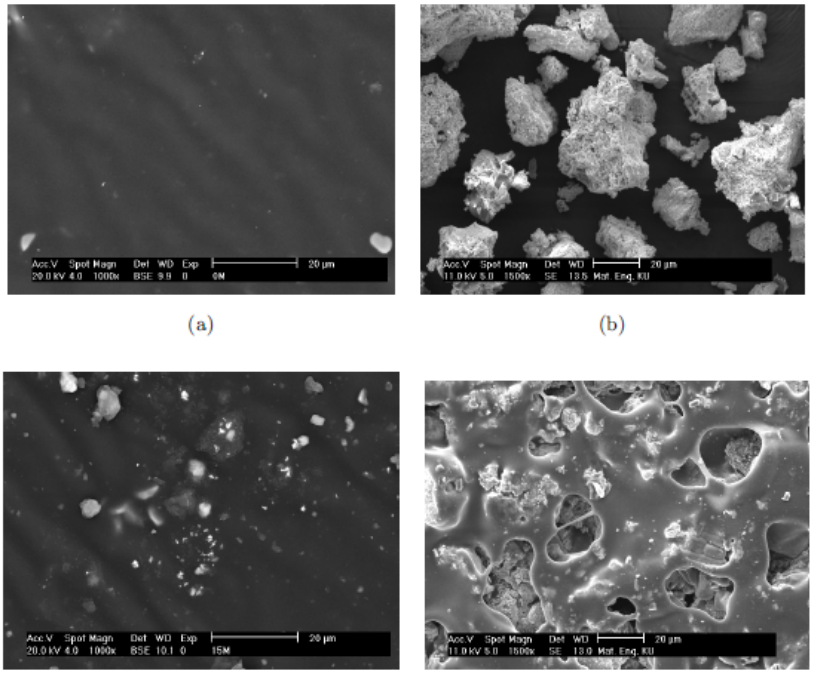

(a) (b)

(c) (d)

Fig. 3. SEM micrographs of: (a) natural rubber (NR-STR 5L), (b) lead zirconate ($PbZrO_3$), (c) NR-STR5L/PZ_5 and (d) NR-STR5L/PZ_6.

irregular in shape. Figure 3(c) shows a uniform dispersion of the doped $PbZrO_3$ particles at a volume fraction of 0.007306 embedded within the natural rubber matrix (NR-STR5L/PZ_5). The NR-STR5L/PZ_6 composite sample suggests a nonuniform dispersion or agglomeration of lead zirconate particles at a high volume fraction of 0.035494, in the NR, as shown in Fig. 3(d).

3.2. *Electrical properties of natural rubber (NR-STR 5L)/lead zirconate ($PbZrO_3$)*

The electrical properties of the NR, dielectric material ($PbZrO_3$), and composite materials (NR-STR5L/$PbZrO_3$) were measured using the impedance analyzer with an AC field at 500 kHz, as tabulated in Table 2. The dielectric constant values are 0.718, 9.248, and 1.597 for NR-STR5L, $PbZrO_3$, and NR-STR5L/PZ_5, respectively. The electrical conductivities of NR-STR5L, $PbZrO_3$, and NR-STR5L/PZ_5 are 4.7300×10^{-9}, 5.8400×10^{-7}, and 4.4283×10^{-8} $(\Omega \cdot m)^{-1}$, respectively. The variation of dielectric constant with frequency from 0.5 to 1000 kHz of the natural rubber (NR-STR5L), $PbZrO_3$, and NR-STR5L/PZ_5 suggests the electronic, ionic, and orientation polarizations of the Pb^{2+}, Zr^{4+}, and O^{2-} ions within the unit cell, as shown in Fig. 4.

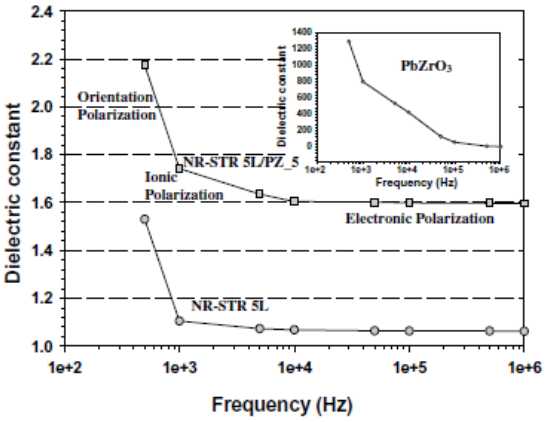

Fig. 4. Dependence of dielectric constant on frequency of NR-STR5L/$PbZrO_3$ composite materials.

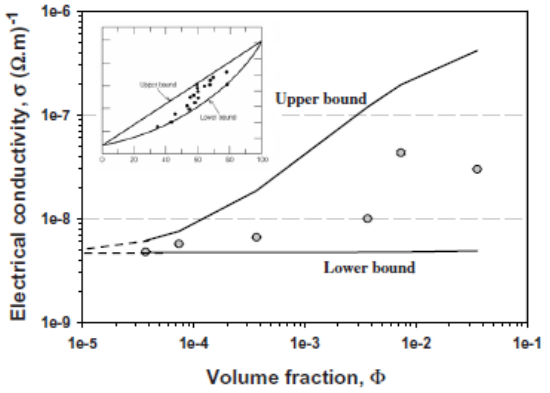

Fig. 5. Electrical conductivity versus volume fraction of NR-STR5L/PZ_5 composite compared to the upper bound and lower bound limitation of the mixture rule.

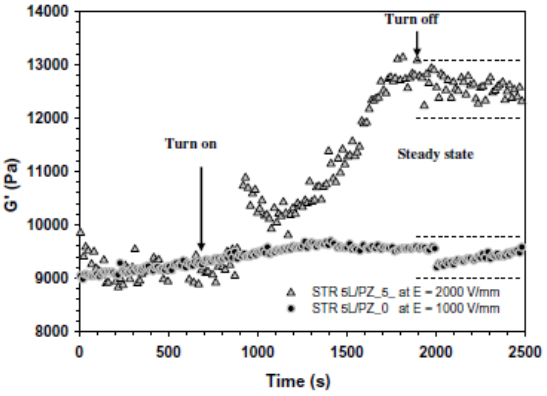

Fig. 6. Temporal response of the storage modulus of NR-STR 5L/PZ_0 and NR-STR 5L/PZ_5 composites at electrical field strength of 1.0 and 2.0 kV/mm, frequency 1.0 rad/s, strain 0.1%, and at 27°C.

J. Innov. Opt. Health Sci. Downloaded from www.worldscientific.com
by CHULALONGKORN UNIVERSITY on 06/09/14. For personal use only.

The electrical conductivity of the composites versus volume fraction is consistent with the mixture rule, as shown in Fig. 5.[8] The mixture rule depends on composition, crystal structure, degrees of crystallization, polarization, and morphology, which includes grain size, grain boundary, and pore size of lead zirconate particles.[3,4]

3.3. *Electrorheological properties of natural rubber (NR-STR5L)/lead zirconate ($PbZrO_3$): Time dependence, effects of particulate volume fraction, and electrical field strength*

The G' temporal characteristics of the samples were recorded in the linear viscoelastic regime at electrical field strengths of 1 and 2 kV/mm, and at the frequency of 1 rad/s. Figure 6 shows the G' temporal characteristics of the dried pure natural rubber (NR-STR 5L/PZ_0) and the composite sample (NR-STR 5L/PZ_5) under the time sweep tests, in which an electrical field is turned on and off. After an initial period with the electrical field on at the electrical field strength 1 kV/mm, the temporal characteristic of the NR-STR 5L/PZ_0 appears to increase from 9.4 kPa and subsequently reach a steady state value of 9.6 kPa. It decreases slightly as the electric field is turned off. While the temporal characteristic of the NR-STR 5L/PZ_5 composite increases abruptly from 9.4 to 12.6 kPa; and then it decreases slowly as the electrical field is turned off; however it does not recover its original value. This behavior indicates that there are some irreversible interactions, possibly due to the dipole bonding between small lead zirconate particles at this volume concentration and some residual dipole moments remaining.

4. Conclusion

Pure perovskite lead zirconate ($PbZrO_3$) of the orthorhombic form can be used as a filler, not only to reinforce the external energy within a NR matrix but also to improve the electrical and electromechanical properties of the composite materials. Lead zirconate ($PbZrO_3$) exhibits a dielectric behavior, which can show spontaneous polarizations (electronic, ionic, and orientation) in the positions of Pb^{2+}, Zr^{4+}, and O^{2-} ions as well as possess the noncentrosymmetric structure. The electrical properties — dielectric constant and electrical conductivity — of the most active sample, NR-STR5L/PZ_5, at a small volume fraction of $PbZrO_3$ (0.007306), are 1.597 and $4.4283 \times 10^{-8}(\Omega \cdot \mathrm{m})^{-1}$, respectively, measured at an AC electrical field at 500 kHz and at 27°C. The NR-STR5L/PZ_5 is demonstrated here as a potential of composite material suitable for use as biomimetic actuators, sensors, artificial muscles, vibration isolators, and smart engineering devices.

Acknowledgments

The authors would like to thank the Faculty of Engineering, Kasetsart University (Thailand) for the financial support, and the Departments of Materials Engineering and Physics, Kasetsart University, for the use of the analytical equipment. We also grateful for the grant support from Center for Advanced Studies in Industrial Technology of the Kasetsart University of the fiscal year 2013. Furthermore, we also would like to acknowledge the financial supports from Conductive and Electroactive Polymers Research Unit of Chulalongkorn University, the Thailand Research Fund (TRF-RTA), and the Royal Thai Government.

J. Innov. Opt. Health Sci. Downloaded from www.worldscientific.com
by CHULALONGKORN UNIVERSITY on 06/09/14. For personal use only.

References

1. L. B. Kong, J. Ma, W. Zhu, O. K. Tan, "Preparation and characterization of lead zirconate ceramics from high-energy ball milled powder," *Mater. Lett.* **49**, 96–101 (2001).
2. T. Ko, D. K. Hwang, "Preparation of nanocrystalline lead zirconate powder by homogeneous precipitation using hydrogen peroxide and urea," *Mater. Lett.* **57**, 2472–2479 (2003).
3. C. J. Dias, D. K. Das-Gupta, "Inorganic ceramic/polymer ferroelectric composite electrets," *IEEE Trans. Dielectr. Electr. Insul.* **5**(3), 706–734 (1996).
4. W. D. Callister, *Materials Science and Engineering: An Introduction*, 7th Edition, John Wiley & Sons, Inc. (2007), 806 pp.
5. T. Shiga, "Deformation and viscoelastic behavior of polymer gels in electric fields," *Adv. Polym. Sci.* **134**, 131–163 (1997).
6. I. Ueda, S. Ikegami, "Piezoelectric properties of modified $PbTiO_3$ ceramics," *IEEE Trans. Electr. Insul.* **7**, 236–254 (1968).
7. Y. Yamashita, K. Yokoyama, H. Honda, T. Takahashi, "Ferroelectric materials and their applications," *J. Appl. Phys.* **20**, 20–24 (1981).
8. B. Jimenez, J. Mendiola, C. Alemany, L. D. Olmo, L. Pardo, E. Maurer, M. L. Calzada, J. D. Frutos, A. M. Gonzalez, M. C. Fandino, "Contributions to the knowledge of calcium-modified lead titanate ceramics," *Ferroelectrics* **87**, 97–108 (1988).
9. M. Tetsu, K. Sugitani, K. Koyama, "Electrorheological response of swollen silicone gels containing barium titanate," *Polymer* **45**, 3811–3817 (2004).
10. N. Tangboriboon, K. Pakdeewanishshsukho, A. Jamieson, A. Sirivat, S. Wogkasemjit, "Electrical properties of a novel lead alkoxide precursor: Lead glycolate," *Mater. Chem. Phys.* **98**, 138–143 (2006).
11. N. Tangboriboon, A. Jamieson, A. Sirivat, S. Wogkasemjit, "A novel route to perovskite lead zirconate from lead glycolate and sodium tris(glycozirconate) via the sol-gel process," *Appl. Org. Chem.* **21**, 849–857 (2007).
12. N. Tangboriboon, A. Jamieson, A. Sirivat, S. Wongkasemjit, "A novel route to perovskite lead zirconate titanate from glycolate precursors via the sol-gel process," *Appl. Org. Chem.* **22**, 104–113 (2008).
13. A. Jha, A. K. Bhowmick, "Thermoplastic elastomeric blends of poly(ethylene terephthalate) and acrylate rubber: 1. Influence of interaction on thermal, dynamic mechanical and tensile properties," *Polymer* **38**, 4337–4344 (1997).
14. N. Tangboriboon, A. Sirivat, S. Wongkasemjit, "Electrorheology and characterization of acrylic rubber and lead titanate composite materials," *Appl. Org. Chem.* **22**, 262–269 (2008).
15. W. Y. Tam, W. Wen, P. Sheng, "Electrorheological fluids using bi-dispersed particles," *Physica B* **279**, 171–173 (2000).
16. C. N. Della, D. Shu, "On the performance of 1–3 piezoelectric composites with a passive and active matrix," *Sens. Actuators A* **140**, 200–206 (2007).
17. M. Wissler, E. Mazza, "Modeling of a pre-strained circular actuator made of dielectric elastomer actuators," *Sens. Actuators A* **120**, 184–192 (2005).

Solid State Ionics 263 (2014) 161–166

Contents lists available at ScienceDirect

Solid State Ionics

journal homepage: www.elsevier.com/locate/ssi

High proton conductivity ZSM-5/sulfonated poly(ether ketone ether sulfone) (S-PEKES) composite proton exchange membrane for using in direct methanol fuel cell

S. Changkhamchom, A. Sirivat *

Conductive and Electroactive Polymers Research Unit, Thailand
The Petroleum and Petrochemical College, Chulalongkorn University, Bangkok 10330, Thailand

ARTICLE INFO

Article history:
Received 5 March 2014
Received in revised form 6 June 2014
Accepted 9 June 2014
Available online xxxx

Keywords:
Sulfonated poly(ether ketone ether sulfone)
ZSM-5
Proton exchange membrane (PEM)
Proton conductivity

ABSTRACT

Composited proton exchange membranes consisting of ZSM-5 embedded in sulfonated poly(ether ketone ether sulfone) (S-PEKES) are fabricated by solvent casting technique in a dispensed zeolite polymer solution. Composite membranes with ZSM-5 content up to 10% v/v exhibit good mechanical properties. The influences of Si/Al and amount of the ZSM-5 on the proton conductivity, methanol permeability, physical properties, and thermal stability of the membranes are investigated. The composite membranes are characterized by FTIR, TGA, LCR meter, and GC techniques. The important properties of the composite membrane are compared with the pristine S-PEKES and Nafion 117 membranes. CBV 2314/S-PEKES composite membrane with 2% v/v ZSM-5 content shows the highest selectivity ~2.12×10^{-5} s·S·cm^{-3}.

© 2014 Elsevier B.V. All rights reserved.

1. Introduction

Direct methanol fuel cell (DMFC) generally has distinct advantages over other proton exchange membrane fuel cells (PEMFCs) due to its low cost, and ease of handling and storage. Moreover, it does not require re-charging, the methanol can be fed directly to the anode and DMFC can produce electricity immediately. DMFC also possesses the advantage of a higher energy density per unit volume in comparison to other hydrogen-fed units [1]. It has attracted substantial interest as an alternative energy source for applications in various portable devices such as mobile phone, and laptop [2].

A polymer electrolyte membrane (PEM) is a solid polymer electrolyte membrane used in both PEMFC and DMFC. However, PEM requires some specific properties; it has to be an electrical insulator which allows only protons to pass through and acts as a barrier against the fuel crossover. Currently used PEM is Nafion produced by Dupont; it is a sulfonated tetrafluoroethylene ionomer carrying the sulfonic acid group along the polymer backbone. Nafion has excellent proton conductivity in the fully hydrated state However, it still has high methanol permeability and cannot be used at high temperature between 80 and 100 °C. Furthermore, it is very expensive [2]. The challenges for further development of PEM are high proton conductivity and thermal stability, low cost and low methanol permeability.

In recent years, there are many types of PEM developed: polybenzimidazoles, polyphenylquinozalines, poly(phenylene oxide), poly(phenylene sulfide), poly(aryl ether sulfone)s, poly(aryl ether ketone)s, polyphosphazenes, etc. There have been many routes to increase proton conductivity such as grafting functional groups that can conduct protons, direct polymerization of sulfonated monomer, polymer blends, and composite membranes [3]. Many research works focus on fabricating composite membrane with high proton conductivity by modifying the membrane composition through adding fillers. Adding an inorganic into the polymer matrix is expected to reduce methanol permeability, to increase proton conductivity, to maintain water at high temperatures, and to increase mechanical properties [4]. In this context, the incorporation of inorganic fillers such as zeolites, into the sulfonated polymer matrix, is one of many routes to form composite proton exchange membranes. The incorporation of a zeolite, in a suitable polymer matrix, can offer several advantages: proper mixing of fillers and polymer at a molecular level provides higher mechanical stability than a pristine polymer membrane; the proton conductor particles can provide pathway on the surface for proton transport. A high surface area of the filler also help to increase the proton conductivity [5].

In the previous work, the proton conductivity of the composite membranes based on zeolite fillers embedded in Nafion was fabricated. Two natural zeolites were selected as inorganic fillers: chabazite and clinoptilolite. The presence of these zeolites affected proton

* Corresponding author at: The Petroleum and Petrochemical College, Chulalongkorn University, Bangkok 10330, Thailand. Tel.: +66 2 218 4131; fax: +66 2 611 7221.
E-mail address: anuvat.s@chula.ac.th (A. Sirivat).

http://dx.doi.org/10.1016/j.ssi.2014.06.008
0167-2738/© 2014 Elsevier B.V. All rights reserved.

conductivity, methanol permeability, and selectivity of the membranes [6]. The self-humidifying polymer electrolyte membrane was fabricated by incorporating zeolite HY-supported Pt particles into Nafion, which was able to maintain the water level inside the membrane due to the zeolite hygroscopic property [7]. Furthermore, the series of zeolite A/Nafion 117 membranes were studied, for DMFC toward decreasing methanol permeability as much as 86% [8]. The systems of zeolites 3A, 4A, 5A, 13X, modenite, and HZSM-5 incorporated into chitosan matrix were also studied; the hydrophobic zeolites prevented the methanol diffusion, whereas the hydrophilic zeolites increase the methanol permeability [9]. Sulfonated poly(ether ether ketone) is one of the candidates for PEM, and the addition of zeolite beta has been shown to improve the proton conductivity of this system. The highest conductivity belonged to the zeolite beta/SPEEK composite membrane having a SiO_2/Al_2O_3 ratio of 50 at 10 wt.% loading [10].

The motivation of this work is to develop the novel proton exchange membrane which can compete with the commercial Nafion membrane by having higher proton conductivity, lower methanol permeability, high chemical and thermal stability, and lower cost than Nafion. In this work, the objective is to exploit the molecular sieving properties of the ZSM-5 zeolite to increase the proton conductivity. The effects of SiO_2/Al_2O_3 ratio and zeolite content were investigated. The S-PEKES was used as the polymer matrix, where the synthesized process has been established elsewhere [11]. The S-PEKES with a sulfonation degree of 0.66 was chosen to prepare the composite membranes. The ZSM-5 zeolites with different Si/Al ratios were used as the inorganic fillers at various volume percentages. All composite membranes were fabricated by solvent casting. The influence of the molecular sieves on the water uptake (%), thermal and mechanical properties, proton conductivity, and methanol permeability of the membranes was characterized and compared with those of the pristine S-PEKES and Nafion 117 membranes.

2. Experimental

2.1. Materials

Nafion 117 was purchased from ElectroChem, Inc. Bisphenol S or 4,4′-dichlorobenzophenone and 4,4′-sulfonyldiphenol (98–99%, Aldrich) were used as the monomers. Concentrated sulfuric acid (Univar, 98 wt.%), sodium chloride (Univar, 99.9%), and sodium hydroxide (Univar, 97%) were used as received. Toluene (Fisher-Scientific 99.99%), potassium carbonate (Riedel-de-Haen, 98–100%) and dimethyl sulfoxide (Riedel-de-Haen, 99.5%) were used as received. Dimethyl sulfoxide was purchased from RCI Labscan Limited. ZSM-5 zeolites: CBV 2314, CBV 5524G, CBV 8014, and CBV 28014 which have Si/Al of 23, 50, 80, and 180, respectively, as the inorganic fillers were purchased from Zeolyst International. All of ZSM-5 zeolites are in the ammonium ion form, and the specific surface areas (ssa) of ZSM-5 zeolites are listed here: C 2314 ssa is 425 m^2/g, CVB 5524G ssa is 425 m^2/g, CVB 8014 ssa is 425 m^2/g, and CVB 28014 ssa is 400 m^2/g.

2.2. Synthesis of poly(ether ketone ether sulfone) (PEKES) and sulfonated poly(ether ketone ether sulfone) (S-PEKES)

Both PEKES and S-PEKES at the degree of sulfonation of 0.66 were synthesized following the previously reported work [11]. S-PEKES was synthesized by using two starting monomers: 4,4′-dichlorobenzophenone and bisphenol S via the nucleophilic aromatic substitution reaction.

The sulfonation process was carried out to attach the sulfonic acid group into the PEKES backbone. Five grams of the PEKES powder was vigorously stirred in 50 ml concentrated H_2SO_4 (98%), at 25 ± 2 °C for 84 h. Then, the polymer solution was precipitated on crushed ice. The white rubber-like solid was obtained. The suspension was left for 12 h at room temperature. Then, the precipitate was filtered and washed several times with de-ionized water until a neutral pH was obtained, The obtained S-PEKES was dried under vacuum at 60 °C for 24 h.

2.3. Membrane preparation

One gram of mixture was dissolved in 30 ml dimethyl sulfoxide (DMSO) with vigorous stirring for 12–18 h until the polymer solutions were homogeneous and the molecular sieve was dispersed evenly. Composite proton exchange membranes were prepared by solvent casting via the incorporation of 4% v/v of different Si/Al ZSM-5zeolites: CBV 2314, CBV 5524G, CBV 8014, and CBV 28014 with the Si/Al ratios of 23, 50, 80, and 180, respectively, into the solution of the sulfonated poly(ether ketone ether sulfone) (S-PEKES) with the sulfonation degree of 0.66. Each solution was cast on a petri dish and kept at room temperature for 12 h, followed by drying at 80 °C for 2 days under a vacuum. The composite membrane with the most suitable properties was selected to further study the effect of zeolite content varying from 2 to 10% v/v.

2.4. Polymer characterization

2.4.1. Fourier transform infrared spectroscopy (FTIR)

The FTIR spectra of the pristine S-PEKES, 4% v/v of CBV 2314, CBV 5524G, CBV 8014, and CBV 28014/S-PEKES composite membranes were taken, using a Thermo Nicolet/Nexus 670 FTIR spectrometer, and the background material was spectronic-grade KBr. The operation condition covered the wavenumber range of 4000–400 cm^{-1} under the absorption mode with 32 scans at a resolution of ±4 cm^{-1} [11].

2.4.2. Thermal behavior

A thermogravimetric analyzer (TGA) (Perkin Elmer/TGA7) was used to investigate the degradation temperature of all composite proton exchange membranes: Nafion 117, pristine S-PEKES; 4% v/v of CBV 2314, CBV 5524G, CBV 8014, and CBV 28014/S-PEKES composite membranes. Between 5.0 and 10.0 mg samples were heated from 50 to 800 °C at a rate of 10 °C/min under N_2 atmosphere [12].

2.4.3. Water uptake (%)

The 4% v/v of ZSM-5/S-PEKES composite membranes with various Si/Al ratios were dried in an oven at 80 °C for 24 h. Then, the membranes were soaked in de-ionized water at room temperature for 24 h, removed from the water, quickly dry-wiped by an absorbent paper to remove any surface moisture, and immediately weighed to determine their wet masses (M_{wet}). The polymer membranes were then dried at 100 °C for 24 h and weighed again to determine their dry masses (M_{dry}). The water uptakes were measured in triplicate and calculated by using the following equation [13]

$$\text{water uptake}\,(\%) = \frac{\left(M_{wet} - M_{dry}\right)}{M_{dry}} \times 100\%. \quad (1)$$

Then, the composite membrane with the highest water uptake (%) was selected to further study the effect of zeolite content (% v/v).

2.4.4. Proton conductivity (σ)

The proton conductivity, one of the most important properties of PEM, the proton conductivity values of the pristine S-PEKES, Nafion 117 and all composite proton exchange membranes were measured by an Agilent E4980A LCR meter at a AC potential of 1 V and in the frequency range between 20 Hz and 2 MHz, at 27 ± 1 °C and 50% RH. The impedances of all membranes were measured by a Dielectric Test Fixture (Agilent, 16451B); a two electrode probe. First, the membranes were soaked in water for 24 h, then wiped off the excess water with tissue paper and impedance measured at room temperature at 50% RH.

The direction of the two electrodes is along the membrane length. The water uptake (%) of the membranes was calculated from the method previously reported [14]. The conductivity values (σ) of all samples were calculated from the impedance data, using this equation

$$\sigma = d/RS, \tag{2}$$

where σ is the proton conductivity (S/cm), d is the membrane thickness (cm), S is the membrane surface area in contact with electrode (cm^2), and R is the resistance which can be derived from the low intersect of the high frequency semi-circle on a complex impedance plane with the Re(Z) or Z′ axis [15]. The impedance of each sample was measured for 3 times to ensure data reproducibility. The proton conductivities of the 4% v/v of ZSM-5/S-PEKES composite membranes with various Si/Al ratios were compared with the pristine S-PEKES and Nafion 117 membrane. And the composite membrane with the highest proton conductivity was selected to further study the effect of zeolite content (% v/v).

2.4.5. Methanol permeability (P)

The composite membrane methanol permeabilities were determined by using the two compartment diffusion cells as previously reported [16]. The compartment A (V_A = 250 ml) was filled with a solution of methanol (2.5 mol/L). The compartment B (V_B = 250 ml) was filled with de-ionized water. The membrane was clamped between the two compartments. The solutions in the two compartments were mechanically stirred during the permeation periods. The solutions in compartments A and B were sampled during these times where the methanol diffused passing through the membrane due to the methanol concentration difference between the compartment A and the compartment B [17]. The methanol permeation in the receiving compartment as a function of time was calculated by:

$$P\left(\mathrm{cm}^2/\mathrm{s}\right) = \frac{k_B \times V_B \times L}{A \times (C_A - C_B)}, \tag{3}$$

where P is the methanol permeability, C_A and C_B are the methanol concentrations in the compartments A and B respectively, k_B is the slope of the methanol concentration gradient in the compartment B, V_B is the volume of the solution in the compartment B, L and A are the thickness and the area of a membrane respectively. The methanol concentrations were measured by using a gas chromatography (Pr2100) fitted with a thermal conductivity detector (TCD); ethanol solution (1 mol/L) was used as an internal standard.

2.4.6. Mechanical properties

Tensile strength, elongation at break, and Young's modulus were measured (Lloyd, UTM) for all composite membranes: the composite membranes between pristine S-PEKES with CBV 2314, CBV 5524G, CBV 8014, and CBV 28014. All membranes were previously equilibrated in water for 24 h and at room temperature as strips (60 mm × 10 mm × 0.2 mm). The gauge length was 30 mm and a crosshead speed of 100 mm/min was used. The measurements were run at room temperature and at 50% RH. For each reported data point, three samples were measured, and the average value was calculated and reported.

3. Results and discussion

3.1. Fourier transform infrared spectroscopy (FTIR)

FTIR spectra of the composite proton exchange membranes, consisting of 4% v/v of ZSM-5 with various Si/Al ratios (CBV 2314, CBV 5524G, CBV 8014, and CBV 28014 with the Si/Al ratios of 23, 50, 80, and 280, respectively) and the highest sulfonated S-PEKES (DS = 0.66) are shown in Fig. 1 and compared with that of the pristine S-PEKES. The FTIR spectra confirm the existence of the hydrogen bonds formed between the S-PEKES molecules and ZSM-5 zeolites. The broad band of all composite membranes appears in the wavenumber range of 3700–3200 cm^{-1} due to the stretching of the hydroxyl group. The other FTIR spectra peaks, appearing in the wavenumber range of 1800–400 cm^{-1}, indicate various characteristic peaks of S-PEKES functional groups as reported in our previous work [11].

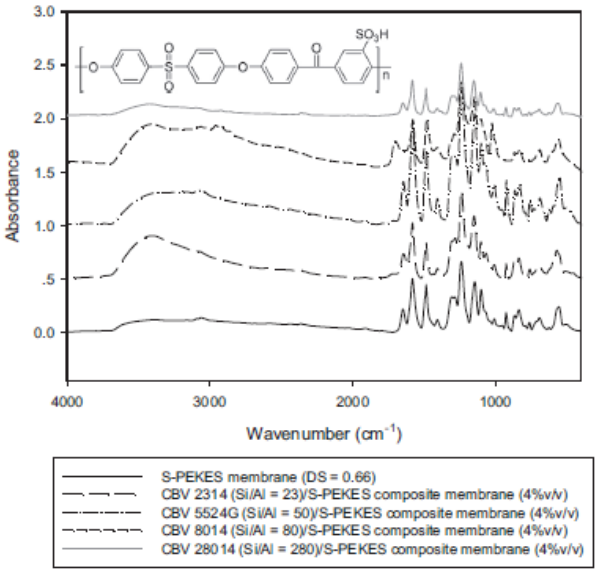

Fig. 1. FTIR spectra of composite proton exchange membrane incorporated with 4% v/v ZSM-5 zeolites (various Si/Al ratios) with the highest degree of sulfonation S-PEKES (DS = 0.66).

The intensity values of the hydroxyl characteristic peaks are in the order of CBV 2314/S-PEKES > CBV 8014/S-PEKES > CBV 5524G/S-PEKES > pristine S-PEKES > CBV 28014/S-PEKES which correspond to the Si/Al ratios of 23, 80, 50, 0, and 280, respectively. The incorporation of ZSM-5 zeolite into the S-PEKES matrix increases the hydrogen-bonding interactions between the hydroxyl groups on the surface of zeolite and the sulfonic acid group of the S-PEKES. Thus, all the composite membranes possess a higher intensity of the hydroxyl stretching peak relative to the pristine S-PEKES, with the exception of the CBV 28014/S-PEKES composite membrane due to the presence of silica-alumina in zeolite. The highest Si/Al ratio belongs to CBV 28014 (Si/Al = 280). This ZSM-5 shows the highest hydrophobicity as well. Thus, hydrogen-bonding interaction between the hydroxyl groups on the surface of zeolite and the sulfonic acid groups of the S-PEKES is decreased.

The acid intensity of the zeolite surface increases with the increment of Si/Al ratio, indicating the stronger hydrogen-bonding interaction [9]. Therefore, the hydroxyl group intensity of the composite membranes is higher than that of the S-PEKES membrane.

3.2. Thermogravimetric analysis (TGA)

The thermograms of Nafion 117 and S-PEKES, the composite proton exchange membranes, consisting of 4% v/v of ZSM-5 with various Si/Al ratios (CBV 2314, CBV 5524G, CBV 8014, and CBV 28014 with the Si/Al ratios of 23, 50, 80, and 280, respectively) and the highest sulfonated S-PEKES (DS = 0.66) are shown in Fig. 2. The thermal stability of Nafion 117 membrane possesses the most inferior degradation temperature, its first degradation step occurs around 250–280 °C and the second step weight loss is at 400 °C. Whereas, the first step weight loss of the pristine S-PEKES membrane starts above 300 °C, representing the sulfonic acid group splitting-off. The second step weight loss occurs at 420–450 °C, representing the degradation temperatures of S-

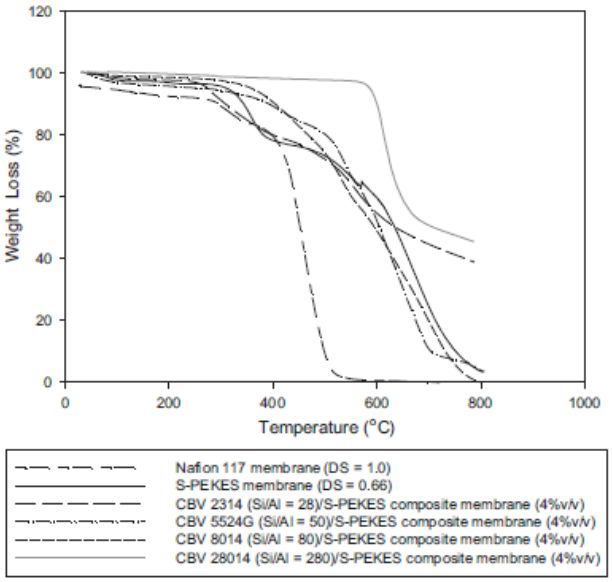

Fig. 2. Thermograms of Nafion 117, pristine S-PEKES, and 4% v/v ZSM-5/S-PEKES composite membranes (various Si/Al ratios).

PEKES backbone which are related with our previous work [16]. All ZSM-5/S-PEKES composite membranes show higher thermal stability than both Nafion 117 and pristine S-PEKES, the major weight loss stage of all composite membranes start over 400 °C which corresponds to the S-PEKES main chain degradation. Especially, the CBV 28014/S-PEKES composite membrane, with the highest Si/Al ratio, has an extremely high degradation temperature around 600 °C. The remaining 40 wt.% of CBV 2314/S-PEKES and CBV 28014/S-PEKES composite membranes are the char formation of the sulfonated polymer membrane itself. It is not the zeolite. In summary, all ZSM-5/S-PEKES composite membranes have high thermal stability over a temperature range of 25–120 °C, and thus are applicable for use in the DMFC application. This result is consistent with previous work which showed that the thermal stability can be enhanced by the intermolecular and intramolecular hydrogen-bondings [18].

3.3. Water uptake (%)

The water uptake (%) values of the pristine S-PEKES (DS = 0.66) and the 4% v/v of composite membranes consisting of S-PEKES (DS = 0.66) and CBV 2314 (Si/Al = 23), CBV 5524G (Si/Al = 50), CBV 8014 (Si/Al = 80), and CBV 28014 (Si/Al = 280) at room temperature (27 °C) are shown in Fig. 3. The water uptake (%) value of the pristine S-PEKES membranes at 0.66 DS is 20.44 ± 1.90%. Whereas the ZSM-5/S-PEKES composite membranes possess the water uptake (%) values of 43.28 ± 2.31%, 36.80 ± 3.43%, 31.28 ± 2.91%, and 17.38 ± 1.62%, corresponding to the systems of CBV 2314, CBV 5524G, CBV 8014, and CBV 28014, respectively. The effect of zeolite on water uptake depends on the hydrophilicity of zeolite, in which a lower Si/Al ratio induces higher hydrophilicity. The addition of ZSM-5 with a low Si/Al ratio (23) facilitates the membrane to adsorb more water than the pristine S-PEKES, where the water cluster can be easily trapped in the zeolite pores. The higher Si/Al ratio in the composite membrane leads to a decrease in water uptake (%) because the membranes become more hydrophobic and do not preferentially adsorb water molecules.

Fig. 4 shows the effect of zeolite content (% v/v) on the water uptake (%) of the composite membranes. The composite membrane consisting of S-PEKES (DS = 0.66) and CBV 2314 (Si/Al = 23) is selected here for further study due to its highest water uptake (%)

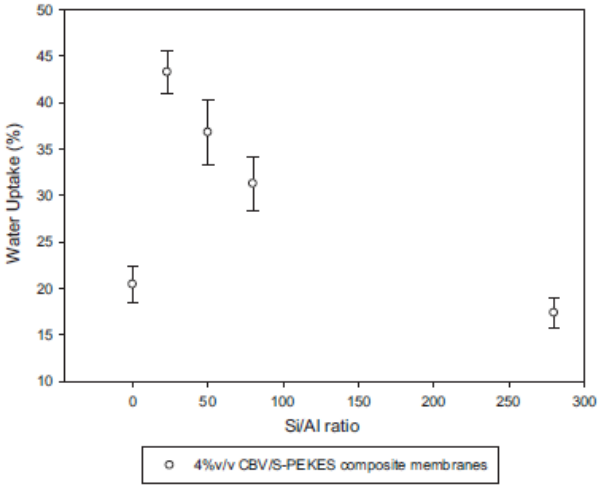

Fig. 3. The water uptake (%) of the pristine S-PEKES (DS = 0.66), and 4% v/v of composite membranes based on S-PEKES (DS = 0.66) with CBV 2314 (Si/Al = 23), CBV 5524G (Si/Al = 50), CBV 8014 (Si/Al = 80), and CBV 28014 (Si/Al = 280) at room temperature (27 °C).

among the composite membranes. At various ZSM-5 contents, the 2, 4, 6, 8, and 10% v/v CBV 2314/S-PEKES composite membranes possess the water uptake (%) values of 49.77 ± 1.86%, 43.27 ± 2.31%, 34.54 ± 0.95%, 21.96 ± 1.73%, and 17.45 ± 1.22%, respectively. Thus, the addition of ZSM-5 weakens the affinity toward water due to its hydrophobic properties.

3.4. Proton conductivity (σ)

Fig. 5 represents the proton conductivities of the pristine S-PEKES (DS = 0.66), the 4% v/v of composite membranes consisting of S-PEKES (DS = 0.66) and CBV 2314 (Si/Al = 23), CBV 5524G (Si/Al = 50), CBV 8014 (Si/Al = 80), and CBV 28014 (Si/Al = 280) at room temperature, they possess the values of $8.45 \times 10^{-3} \pm 5.75 \times 10^{-4}$, $1.35 \times 10^{-2} \pm 1.53 \times 10^{-4}$, $1.31 \times 10^{-2} \pm 4.00 \times 10^{-4}$, $1.07 \times 10^{-2} \pm 4.73 \times 10^{-4}$, and $7.81 \times 10^{-3} \pm 2.93 \times 10^{-4}$ S·cm^{-1}, respectively. The CBV 2314/S-PEKES composite membrane possesses the

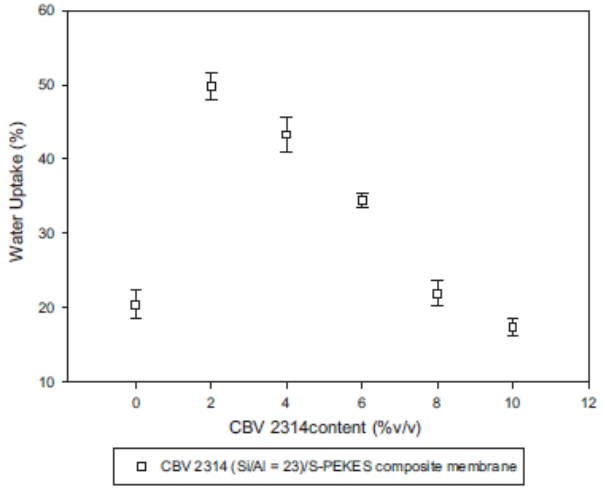

Fig. 4. The water uptake (%) of the pristine S-PEKES (DS = 0.66), and composite membranes based on S-PEKES (DS = 0.66) with CBV 2314 (Si/Al = 23) included at various zeolite contents: 2, 4, 6, 8, and 10% v/v, respectively, at room temperature (27 °C).

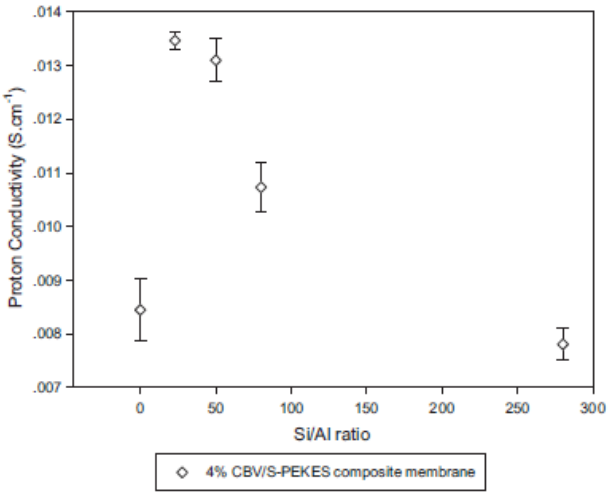

Fig. 5. The proton conductivities of the pristine S-PEKES (DS = 0.66), and 4% v/v of composite membranes based on S-PEKES (DS = 0.66) with CBV 2314 (Si/Al = 23), CBV 5524G (Si/Al = 50), CBV 8014 (Si/Al = 80), and CBV 28014 (Si/Al = 280) at room temperature (27 °C).

highest proton conductivity value which is 1.24 and 1.60 times higher than those of Nafion 117 and S-PEKES, respectively. The low Si/Al ratio ZSM-5 facilitates in increasing the proton conductivity. At a higher Si/Al ratio, a lower in proton conductivity is expected to be obtained due to the increment in hydrophobicity. This result is directly dependent on the water uptake (%) of the composite membranes; the membrane that can hold more water molecules will provide the better proton transport capability via the vehicle mechanism in the form of hydronium ion. Moreover, the proton can generally move via the hopping mechanism along the sulfonic groups of S-PEKES.

The effect of ZSM-5 amount (% v/v) within the composite proton exchange membranes on the proton conductivity is investigated next. Fig. 6 shows the proton conductivities of Nafion 117 and the pristine S-PEKES (DS = 0.66) which possess the values of $1.09 \times 10^{-2} \pm 1.39 \times 10^{-3}$, $8.45 \times 10^{-3} \pm 5.75 \times 10^{-4}$ S·cm^{-1}, respectively. For the composite membranes consisting of S-PEKES (DS = 0.66) and CBV 2314 (Si/Al = 23) at the ZSM-5 contents of 2, 4, 6, 8, and 10% v/v at room temperature, they possess the values of $1.76 \times 10^{-2} \pm 3.61 \times 10^{-4}$, $1.35 \times 10^{-2} \pm 1.52 \times 10^{-4}$, $1.10 \times 10^{-2} \pm 2.52 \times 10^{-4}$, $9.47 \times 10^{-3} \pm 3.06 \times 10^{-4}$, and $7.30 \times 10^{-3} \pm 5.15 \times 10^{-4}$, respectively. The CBV 2314/S-PEKES composite membrane with 2% v/v zeolite content possesses the highest proton conductivity values which are 1.61 and 2.08 times higher than those Nafion 117 and S-PEKES, respectively. However, the proton conductivity decreases with a higher ZSM-5 content. This is consistent with the fact that the water uptake (%) of the composite membrane decreases with the increment of Si/Al ratio, as the membranes cannot hold much water due to their hydrophobicity. The proton transport preferably takes place within the S-PEKES bulk phase instead of the ZSM-5 phase and this phenomenon produces the reduction in the proton conductivity.

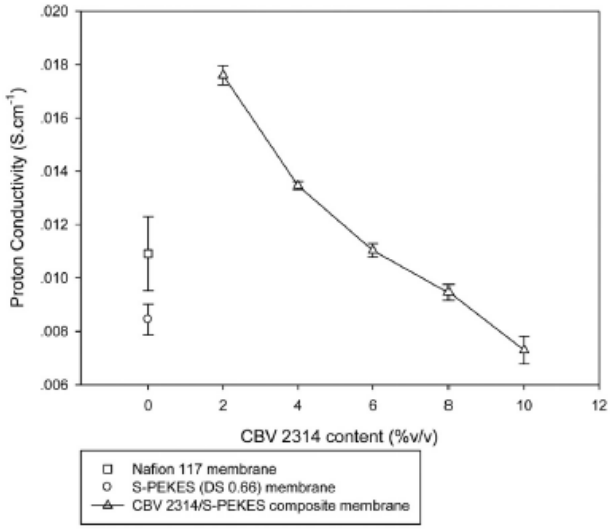

Fig. 6. The proton conductivities of Nafion 117, pristine S-PEKES (DS = 0.66), and composite membranes based on S-PEKES (DS = 0.66) with CBV 2314 (Si/Al = 23) included at various zeolite contents: 2, 4, 6, 8, and 10% v/v, respectively, at room temperature.

3.5. Methanol permeability

Methanol crossover is the major problem in the DMFC applications; methanol permeates easily through the electrolyte membrane from the anode and passes through the polymer electrolyte membrane to the cathode side of the DMFC. As a consequence, excessive methanol crossover of any PEM not only wastes the methanol fuel but also decrease the efficiency in fuel cell performance [2]. Table 1 shows the methanol permeabilities (P) of all proton exchange membranes at the temperatures of 27 °C. The methanol permeabilities of Nafion 117, pristine S-PEKES (DS = 0.66), and the 4% v/v composite membranes consisting of S-PEKES (DS = 0.66) and CBV 2314 (Si/Al = 23), CBV 5524G (Si/Al = 50), CBV 8014 (Si/Al = 80), and CBV 28014 (Si/Al = 280) at room temperature possess the values of 1.41×10^{-6}, 1.03×10^{-7}, 7.85×10^{-8}, 7.73×10^{-8}, 7.52×10^{-8}, 6.34×10^{-8} cm^2·s^{-1}, respectively. All composite membranes show lower methanol permeabilities than the pristine S-PEKES and they are extremely lower than that of the Nafion 117 membrane. The lowest methanol permeability belongs to CBV 2314/S-PEKES composite membrane whose value is 1.32 times lower than that of S-PEKES and 18 times lower than that of Nafion 117. In summary, the methanol permeability monotonically decreases with increasing Si/Al ratio.

The effect of zeolite content (% v/v) within the composite proton exchange membranes on the methanol permeability is investigated next. The CBV 2314/S-PEKES composite membrane is selected to fabricate the membranes at the zeolite contents of 2, 4, 6, 8, and 10% v/v. They possess the methanol permeability values of 8.32×10^{-8}, 7.86×10^{-8}, 7.27×10^{-8}, 6.45×10^{-8}, and 5.26×10^{-8} cm^2·s^{-1}, respectively. Therefore, the methanol permeability decreases with the addition of ZSM-5 zeolite. The transport process of methanol is mainly based the methanol diffusivity. The methanol molecules are preferentially adsorbed and trapped within the zeolites during the diffusion through the membrane. The trapped molecules induce the delay in the methanol diffusion [9].

The membrane selectivity is the ratio between the proton conductivity and the methanol permeability, as shown in Table 1. The highest membrane selectivity belongs to the 2% v/v CBV 2314/S-PEKES composite membrane which has the value of 2.12×10^5 s·S·cm^{-3}. This composite membrane is thus the most suitable for using in the actual DMFC applications due to its optimized fuel efficiency.

3.6. Mechanical properties

All mechanical properties of all composite membranes at room temperature (27 °C) and 50% RH are shown in Table 1. The tensile strength, elongation at break, and Young's modulus of all membranes were evaluated by means of the standard test in the same method with the previous work [16]. The tensile strengths, of the composite membranes at 2, 4, 6, 8, and 10% v/v, for CBV 2314/S-PEKES composite membranes, are

Table 1
Methanol permeabilities (P), proton conductivity (σ), methanol selectivity, tensile strength, Young's modulus, and elongation at break of all proton exchange membranes at the temperature of 27 °C

PEM composite	Si/Al	Zeolite (% v/v)	Thickness (cm)	Methanol permeability ($cm^2 \cdot s^{-1}$)	Proton conductivity ($S \cdot cm^{-1}$)	Membrane selectivity ($s \cdot S \cdot cm^{-3}$)	Tensile strength (MPa)	Young's modulus (MPa)	Elongation at break (%)
Nafion 117 membrane (DS = 1.0)	0	0	0.0200	1.41E−06	1.09E−02	7.72E+03	28.4	100	329.2
S-PEKES membrane (DS = 0.66)	0	0	0.0278	1.03E−07	8.45E−03	8.16E+04	7.94 ± 0.25	16266.87 ± 75.54	6.91 ± 0.46
CBV 2314/S-PEKES composite membrane	23	2	0.0286	8.32E−08	1.76E−02	2.12E+05	17.24 ± 0.73	21378.65 ± 162.95	5.31 ± 0.22
CBV 2314/S-PEKES composite membrane	23	4	0.0314	7.86E−08	1.35E−02	1.71E+05	31.78 ± 0.15	28557.35 ± 237	4.87 ± 1.10
CBV 2314/S-PEKES composite membrane	23	6	0.0327	7.27E−08	1.10E−02	1.52E+05	53.52 ± 1.71	36324.91 ± 116	4.73 ± 0.48
CBV 2314/S-PEKES composite membrane	23	8	0.0329	6.45E−08	9.47E−03	1.47E+05	76.88 ± 0.90	41857 ± 224	3.87 ± 0.22
CBV 2314/S-PEKES composite membrane	23	10	0.0330	5.27E−08	7.30E−03	1.39E+05	82.66 ± 0.50	47644 ± 288	3.55 ± 0.74
CBV 5524G/S-PEKES composite membrane	50	4	0.0327	7.74E−08	1.31E−02	1.69E+05	29.44 ± 0.38	27311 ± 265	4.32 ± 0.11
CBV 8014/S-PEKES composite membrane	80	4	0.0328	7.52E−08	1.07E−02	1.43E+05	30.21 ± 0.59	26548 ± 319	3.95 ± 0.57
CBV 28014/S-PEKES composite membrane	280	4	0.0347	6.34E−08	7.81E−03	1.23E+05	32.22 ± 0.39	30884 ± 169	4.55 ± 0.17

17.24, 31.78 53.52, 76.88, and 82.66 MPa, respectively. They are higher than the value of the pristine S-PEKES membrane by factors of 2, 4, 7, 9.5, and 10 times, respectively. All CBV 2314/S-PEKES composite membranes show much higher tensile strengths and Young's modulus, with the lower elongations at break than those of the pristine S-PEKES and Nafion 117 membranes. The composite membranes in all systems: CBV 214, CBV 5524G, CBV 014, and CBV 28014/S-PEKES with 4% v/v of ZSM-5 show the comparable mechanical properties, thus the Si/Al ratio does not affect the mechanical properties. All composite membranes are thus strong and of high strength; they flexible enough to be used as PEM in a DMFC. Thus, the addition of the ZSM-5 zeolite significantly improves the mechanical strength of the PEM. In the present work, all composite proton exchange membranes (PEEKS/Zeolite) show high tensile strengths in the range of 17.24–82.66 MPa and the Young's modulus in the range of 20,000–48,000 MPa, which are extremely higher than those of the sulfonated poly(ether ether ketone) and poly(ether ether ketone-alt-benzimidazole) that Wang et al. reported in 2012 [19] that their membranes possessed the tensile strength of 21.5–34.6 MPa, and the Young's modulus of 624–753 MPa.

4. Conclusions

The ZSM-5/S-PEKES composite membranes show high thermal stability, because the degradation temperature starts at above 400 °C. The water uptake (%) of the composite membrane first increases and then decreases with the increment of Si/Al ratio and the amount of zeolite due to its hydrophobicity. The ZSM-5 zeolite helps to increase the proton conductivity relative to the pristine S-PEKES and Nafion 117 membranes. For the effects of the Si/Al ratio and zeolite content on the proton conductivity, the same tendency occurs as with the water uptake (%). Moreover, the methanol permeabilities of all composite membranes investigated are much lower than the S-PEKES and Nafion 117 membrane, due to the hindered methanol diffusion. The 2% v/v CBV 2314/S-PEKES composite membrane is selected to be the proton exchange membrane candidate due to its membrane selectivity and is the highest among all the composite membranes investigated.

Acknowledgments

The authors would like to acknowledge the financial supports from the Conductive and Electroactive Research Unit of Chulalongkorn University, the Thailand Research Fund (TRF, TRF-RTA, PHD/0081/2549), and the Royal Thai Government.

References

[1] P.L. Antonucci, A.S. Arico, P. Creti, E. Ramunni, V. Antonucci, Solid State Ionics 125 (1999) 431–437.
[2] L. Carrette, K.A. Friedrich, U. Stimming, Fuel Cells 1 (2001) 5–39.
[3] J. Rozi'ere, D.J. Jones, Annu. Rev. Mater. Res. 33 (2003) 503–555.
[4] J. Ramírez-Salgado, Electrochim. Acta 52 (2007) 3766–3778.
[5] B. Smitha, S. Sridhar, A.A. Khan, J. Membr. Sci. 259 (2005) 10–26.
[6] V. Tricoli, F. Nannetti, Electrochim. Acta 48 (2003) 2625–2633.
[7] D.H. Son, R.K. Sharma, Y.G. Shul, H. Kim, J. Power Sources 165 (2007) 733–738.
[8] X. Li, E.P.L. Roberts, S.M. Holmes, V. Zholobenko, Solid State Ionics 178 (2007) 1248–1255.
[9] J. Wang, X. Zheng, Z. Wu, B. Zheng, Z. Jiang, X. Hao, B. Wang, J. Power Sources 178 (2008) 9–19.
[10] E. Sengul, H. Erdener, R.G. Akay, H. Yucel, N. Bac, I. Eroglu, Int. J. Hydrog. Energy 34 (2009) 4645–4652.
[11] S. Changkhamchom, A. Sirivat, Polym. Bull. 65 (2010) 265–281.
[12] Z. Wang, H. Ni, C. Zhao, X. Li, T. Fu, H. Na, J. Polym. Sci. B Polym. Phys. 44 (2006) 1967–1978.
[13] S. Vetter, B. Ruffmann, I. Buder, S.P. Nunes, J. Membr. Sci. 260 (2005) 181–186.
[14] L. Unnikrishnan, S.K. Nayak, S. Mohanty, G. Sarkhel, Polymer Plast. Technol. Eng. 49 (2010) 1419–1427.
[15] S.D. Mikhailenko, K. Wang, S. Kaliaguine, P. Xing, G.P. Robertson, M.D. Guiver, J. Membr. Sci. 223 (2004) 93–99.
[16] S. Changkhamchom, A. Sirivat, Polymer Plast. Technol. Eng. 52 (2013) 70–79.
[17] P. Mukoma, B.R. Jooste, H.C.M. Vosl, J. Membr. Sci. 243 (2004) 293–299.
[18] Y. Wan, K.A.M. Creber, B. Peppley, V.T. Bui, J. Membr. Sci. 280 (2006) 666–674.
[19] J. Wang, J. Liao, L. Yang, S. Zhang, X. Huang, J. Li, J. Membr. Sci. 415–416 (2012) 644–653.

THE JOURNAL OF PHYSICAL CHEMISTRY B

Article

pubs.acs.org/JPCB

Electrically Controlled Release of Benzoic Acid from Poly(3,4-ethylenedioxythiophene)/Alginate Matrix: Effect of Conductive Poly(3,4-ethylenedioxythiophene) Morphology

Nophawan Paradee and Anuvat Sirivat*

Conductivity and Electroactive Polymer Research Unit, The Petroleum and Petrochemical College, Chulalongkorn University, Bangkok 10330, Thailand

ABSTRACT: A drug-loaded conductive polymer/hydrogel blend, benzoic acid-loaded poly(3,4-ethylenedioxythiophene/alginate (BA-loaded PEDOT/Alg) hydrogel, was used as a carrier/matrix for an electrical stimuli transdermal drug delivery system (TDDS). The effects of cross-linking ratio, PEDOT particle size, and electric field strength on the release mechanism and the diffusion coefficient (D) of BA were examined by using a modified Franz-diffusion cell. The diffusion scaling exponent value of BA is close to 0.5 which refers to the diffusion controlled mechanism, or the Fickian diffusion as the BA release mechanism. The D increased when there was a decrease in the cross-linking ratio due to the mesh size-hindering effect. When increasing electric field strength, the D of BA-loaded PEDOT/Alg hydrogel increased because the cathode−BA^- electro-repulsion, electroinduced alginate expansion, and PEDOT electroneutralization simultaneously occurred. The highest D belonged to a blend with the smallest PEDOT particle and highest electrical conductivity. The D of BA was a function of the matrix mesh size except when drug size/mesh size was lower than 2.38×10^{-3}, where D of BA became mesh size independent as the matrix mesh size was extremely large. Thus, the fabricated conductive polymer hydrogel blends have a great potential to be used in TDDS under electrical stimulation.

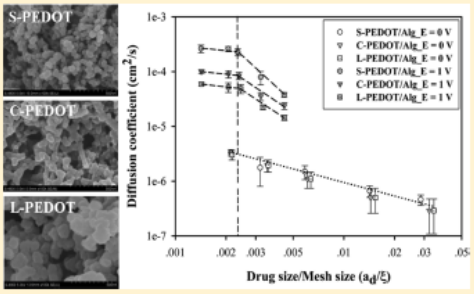

INTRODUCTION

Transdermal drug delivery system (TDDS) is a route for transporting drugs through the skin and into the circulatory system. There are many advantages for using TDDS such as by passing the first pass metabolism, decreasing in concentrations of drug in blood, decreasing side effects, as well as reducing fluctuations of drug in blood. However, the delivery of drugs via the skin is restricted due to lipophilic nature of skin and molecular drug size.[1−6] Iontophoresis is one of the methods used to enhance drug penetration across the skin by applying an electrical potential. This is especially true for both ionized and un-ionized drugs, including high molecular weight such as peptides, proteins, and oligonucleotides.[4−6]

Hydrogel is one class of polymer-based controlled drug release matrices. The physical and chemical cross-linking process can produce a hydrophilic polymer as hydrogel by converting the soluble polymer chains into an insoluble polymer networks.[7,8] Besides exhibiting swelling behavior in water, other environmental conditions may still affect hydrogel volume change: temperature, pH, ionic concentration, solvent composition, and external electrical stimuli.[9,10] However, hydrogel is not an excellent material for response under electrical stimuli due to the relatively low electrical conductivity of the polymer matrix.[11]

Stimulus-responsive hydrogels or smart hydrogels can potentially be used for the development of controlled drug release under applied electric field because the change in the structure of the polymer can change the drug release ability in response to the electrical potential. Electrochemically controlled drug release, using a conductive polymer, has been used in drug release systems.[12] A conducting polymer is composed of a conjugated polymer chain, which can promote π-electron delocalizing along the polymer backbone and contributes to electrical conductivity. Conductive polymers combined with drugs are prepared with ease on conductive substrates to form various patterns and shapes, and drug release is precisely controlled under applied electrical current or potential stimuli.[12] Ge et al.[13] prepared a stimuli-responsive material for electrical drug delivery. Poly[(D,L-lactic acid)-*co*-(glycolic acid)]-*b*-poly(ethylene oxide)-*b*-poly[D,L-lactic acid)-*co*-(glycolic acid)] was used as the hydrogel matrix combined with polypyrrole (PPy) nanoparticles loaded with fluoroescein or daunorubicin as the model drugs. The chemical synthesis produced negatively charged fluoroescein or positively charged daunorubicin incorporated into the PPy nanoparticles. The drugs in PPy nanoparticles were able to prevent the unwanted release from the hydrogel without an applied electric field. Under applied electric field, the fluoroescein was released upon

Received: December 24, 2013
Revised: June 19, 2014
Published: July 16, 2014

ACS Publications © 2014 American Chemical Society

reduction, while the oxidation reaction could promote the release of daunorubicin. The amount of drug released increased with increasing electrical potential.[13]

In this work, poly(3,4-ethylenedioxythiophene) (PEDOT) was selected as the conductive polymer for a drug substrate and blended with a hydrogel because of high conductivity in the doped state.[14] Alginate (Alg), which has biocompatibility, nontoxicity, and transparency, was used as the hydrogel matrix.[15] The objective of this work was to study the release mechanism of a combined conductive polymer/hydrogel system as PEDOT/alginate (PEDOT/Alg) hydrogel for controlled release of benzoic acid under applied electric field. The release profile and release kinetics of benzoic acid from blend films were investigated based on the effects of the matrix mesh size, PEDOT particle size, and electric field strength.

EXPERIMENTAL SECTION

Materials. Alginic acid sodium salt (Na-Alg) from brown algae, 3,4-ethylenedioxythiophene (EDOT), benzoic acid (BA), and 2-(*N*-morpholino) ethanesulfonic acid (MES) monohydrate were purchased from Sigma-Aldrich to act as a matrix, monomer, model drug, and buffer solution, respectively. Calcium chloride dihydrate ($CaCl_2{\cdot}H_2O$) was used as a cross-linking agent and purchased from Ajax Finechem. Ammonium peroxydisulfate (APS) was purchased from Qrec and used as an oxidizing initiator. Acetone, methanol, and dimethyl sulfoxide (DMSO) were purchased from Labscan.

Synthesis of Benzoic Acid-Loaded Poly(3,4-ethylenedioxythiophene) (BA-Loaded PEDOT). BA-loaded PEDOT was prepared by dropping EDOT monomers into a solution that consisted of APS and BA dissolved in distilled water, then it was stirred for 72 h. The preparation of PEDOT particles without BA was similar to the preparation of BA-loaded PEDOT except that the solution before doping EDOT monomer only consisted of APS. The color of solution transformed from yellow to green, then blue to dark blue during that time. The product was separated from the solution by using centrifugal separation and washed with methanol and acetone solution (methanol:acetone = 20:3). Lastly, the product was dried in a vacuum oven at 60 °C for 24 h. The BA-loaded PEDOT particles, at various doping levels (molar of EDOT:molar of APS), were synthesized by various amounts of APS as noted in Table 1.

Table 1. Condition of Synthesis BA-Loaded PEDOT at 0.15 M of EDOT and 0.45 M of BA

doping level (molar of EDOT: molar of APS)	APS (M)
1:1	0.15
1:2	0.30
1:3	0.45

Preparation of Benzoic Acid-Loaded Poly(3,4-ethylenedioxythiophene)/Alginate Hydrogel (BA-Loaded PEDOT/Alg). Na-Alg solution with 0.4% w/v was prepared by dissolving Na-Alg powder in distilled water. Then BA-loaded PEDOT powder (25 mg) was added to the Na-Alg solution under constant stirring. In order to cross-link, $CaCl_2$ was added to the solution under constant stirring at various cross-linking ratios (moles of cross-linking agent/mol of uronic acid monomer unit): 0.3, 0.5, 0.7, 1.0, and 1.3. Each solution was cast onto a mold and dried at 40 °C for 72 h to obtain the homogeneous BA-loaded PEDOT/Alghydrogel films of various cross-linking ratios with a film thickness of ∼0.3 mm.[16]

BA-Loaded PEDOT Characterization. The functional groups of the BA-loaded PEDOT particle were identified using a Fourier-transform infrared spectroscopy (FTIR; Thermo Nicolet, Nexus670). The spectrometer was set up in absorption mode using KBr as the background material with 64 scans, a resolution of ±4 cm^{-1}, and covering the wavenumber range of 400−4000 cm^{-1}.

The thermal behavior of BA-loaded PEDOT particles was examined using a thermogravimatric analyzer (TGA; PerkinElmer, TGA7). An aluminum pan was loaded with samples (5−10 mg). The change of mass was investigated under nitrogen atmosphere from 30 to 900 °C at a heating rate of 10 °C/min.

The morphology of BA-loaded PEDOT was studied using a scanning electron microscopy (SEM; Hitachi, S4800) which was operated in an acceleration voltage of 5 kV and a magnification of 100 k.

Electrical conductivity of the BA-loaded PEDOT was measured by using a custom-built two-point probe connected with an electrometer (Keithley, Model 6517A), which supplied the voltage and recorded the current. The Van der Pauw method was used to estimate the current to find the linear Ohmic regime. The linear Ohmic regime, which consisted of applied voltage and resultant current, was transformed to the electrical conductivity of BA-loaded PEDOT using eq 1:

$$\sigma = \frac{1}{\rho} = \frac{1}{R_s \times t} = \frac{I}{K \times V \times t} \tag{1}$$

where σ is the specific conductivity (S/cm), ρ is the specific resistivity (Ω cm), R_s is the sheet resistivity (Ω), I is the measured current (A), K is the geometric correction factor (3.53×10^{-3}), V is the applied voltage (V), and t is the pellet thickness (cm).

PEDOT/Alginate Hydrogel (PEDOT/Alg Hydrogel) Characterization. The molecular weight between cross-links ($\bar{M}_c$) and the mesh size (ξ) correlates to the release behavior of the drug and the physical properties of hydrogel were determined. A hydrogel sample was immersed in MES buffer solution (pH 5.5) after it was weighed in air and heptane. After the hydrogel sample was swollen to equilibrium for 5 day, it was weighed in air and heptanes again. Lastly, the sample was dried at 40 °C in vacuum oven for 5 days, then weighed in air and heptanes one more time. Various weights were used to determine the polymer volume fraction.[17]

The $\bar{M}_c$ was calculated by the Flory−Rehner equation as follows in eq 2:[17,18]

$$\frac{1}{\bar{M}_c} = \frac{2}{\bar{M}_n} - \frac{\left(\frac{\bar{v}}{V_1}\right)[\ln(1 - v_{2,s}) + v_{2,s} + \chi_1 (v_{2,s})^2]}{v_{2,r}[(v_{2,s}/v_{2,r})^{1/3} - 0.5(v_{2,s}/v_{2,r})]} \tag{2}$$

where $\bar{M}_n$ is the number-averaged molecular weight of the polymer before cross-linking ($\bar{M}_n$ = 450 000 g/mol), $\bar{v}$ is the specific volume of Alg ($\bar{v}$ = 0.60 cm^3/g of Alg),[18] V_1 is the molar volume of the water (V_1 = 18 mol/cm^3),[18] $v_{2,r}$ is the volume fraction of the polymer in a relaxed state, $v_{2,s}$ is the volume fraction of the polymer in a swollen state, and the Flory polymer−solvent interaction parameter (χ_1) for Alg is 0.473.[18]

The ξ was determined using eq 3:[19,20]

dx.doi.org/10.1021/jp502674f | J. Phys. Chem. B 2014, 118, 9263−9271

$$\xi = \upsilon_{2,s}^{-1/3}\left[C_n\left(\frac{2\bar{M}_c}{M_r}\right)\right]^{1/2} l \quad (3)$$

where C_n is the Flory characteristic ratio (C_n = 27.33),[19] l is the carbon−carbon bond length of the monomer unit (l = 5.15 Å),[20] M_r is monomer molecular weight (M_r = 198 g/mol),[20] and $\bar{M}_c$ is the molecular weight between cross-links.

Preparation of MES Buffer pH 5.5. A MES buffer solution was selected to simulate human skin. MES solution 0.1 M (at pH 5.5) was prepared and poured into the receptor chamber of a modified Franz-Diffusion cell.

Spectrophotometric Analysis of Drug. The maximum absorption wavelength of BA was investigated using a UV/Visible spectrophotometer (UV-TECAN infinite M200). The absorbance value at the peak wavelength of BA corresponded to the BA concentration, thus BA calibration curves were created.

Actual Drug Content. The actual amount of BA in the BA-loaded PEDOT was determined by dissolving the BA-loaded PEDOT (0.6 g) in 4 mL of DMSO. Next, the solution (0.5 mL) of BA-loaded PEDOT in DMSO was added to the MES buffer solution (0.8 mL). The amount of BA in the solution was determined by the UV/Visible spectrum peaks (at the wavelengths of 232 nm), which were associated with the calibration curves in order to determine the actual drug content.

Drug Release Studies. Modified Franz-diffusion cells were used to study the diffusion of BA from BA-loaded PEDOT/Alg hydrogels as shown in Figure 1. A diffusion cell is composed of

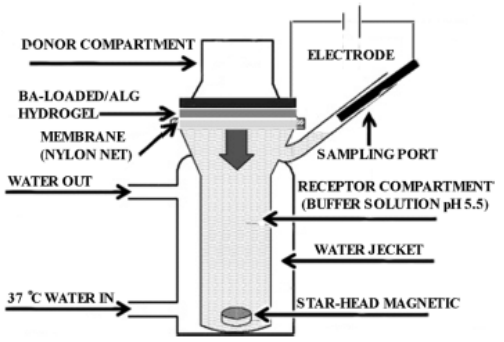

Figure 1. Modified Franz-Diffusion cell experiment set up.

two component chambers as receptor and donor chambers. The receptor chamber was filled with MES buffer solution (pH 5.5) and kept at 37 ± 2 °C via a circulating water bath. The donor component was exposed to ambient conditions. The BA-loaded PEDOT/Alg hydrogel sample was placed over a nylon net (mesh size = 2.25 mm^2), which was on top of the receptor chamber. The area available for BA diffusion was 2.51 cm^2. The MES buffer solution was stirred throughout the experiment for 48 h and came into contact in the receptor chamber. An electric field (various electrical voltages of 0, 0.01, 0.05, 0.5, 0.8, and 1.0 V) was applied on the surface of the hydrogel, nylon net, and buffer solution via an aluminum cathode electrode that was connected to a power supply (KEITHLEY 1100 V Source Meter). The diffusion of BA occurred when it passed through the polymer matrix and nylon net into the solution. A sample (0.1 mL) was taken out at specific times and replaced with fresh buffer solution at an equal volume. The drug amount was determined by a UV/Visible spectrophotometer.[16]

Release Characteristics of BA from BA-Loaded PEDOT/Alg Hydrogel. The release mechanism of BA was studied by the Korsmeyer−Peppas model, as shown in eq 4,[21,22] which explains the drug release from the polymeric system. The amount of drug released was fitted with the Korsmeyer−Peppas model,[21,22] a power law in time:

$$\frac{M_t}{M_\infty} = kt^n \quad (4)$$

where M_t/M_α is the fraction of the drug released at time t, k is the kinetic constant (unit of T^{-n}), and n is the diffusion scaling exponent for drug release, which is used to characterize different release mechanisms. Furthermore, Higuchi's equation as shown in eq 5[22,23] indicates the fraction of drug release from the matrix and is proportional to the square root of time.

$$\frac{M_t}{M_\infty} = k_H t^{1/2} \quad (5)$$

where M_t and M_α are the masses of drug released at the times equal to t and infinite time, respectively, and k_H is the Higuchi constant (unit of T^{-n}). The Higuchi equation corresponds to a particular case of eq 4 when n is precisely equal to 0.5. If the Higuchi drug release (i.e., Fickian diffusion) is obeyed, then a plot of M_t/M_α versus $t^{1/2}$ will be a straight line with a slope of k_H.

The diffusion coefficient of the BA from the PEDOT/Alg hydrogels was calculated from a slope of plot between drug accumulation and the square root of time according to the Higuchi equation as in eq 6:[2,3,24]

$$M_t = 2C_o A\left(\frac{Dt}{\pi}\right)^{1/2} \quad (6)$$

where M_t is the amount of drug released (g), A is the diffusion area (cm^2), C_o is the initial drug concentration in the hydrogel (g/cm^3), and D is the diffusion coefficient of the drug (cm^2/s).

■ RESULTS AND DISCUSSION

BA-loaded PEDOT Characterization. Figure 2a shows the FTIR spectra of BA, PEDOT, and BA-loaded PEDOT. The peaks of BA at 2835 and 1700 cm^{-1} can be referred to as the O−H and C═O bonds. The benzene ring peak appears at 900−1000 cm^{-1}.[25] For the PEDOT particle synthesized without BA, stretching of quinoidal structure in the thiophene ring and stretching of the thiophene ring are presented as peaks at 1519 and 1356 cm^{-1}, which originated from the C−C or C═C respectively. The peaks at 1206 and 1098 cm^{-1} refer to the stretching vibration of the C−O−C bond in the EDOT. The peaks at 980, 843, and 700 cm^{-1} can be referred to as the C−S bond in the thiophene ring.[26,27] The absorption peaks of BA-loaded PEDOT are similar to those of PEDOT except a peak at 1682 cm^{-1} appears, which indicates benzoate anion loaded PEDOT. This peak is referred to as the carboxylate group (COO^-) of BA, which interacts with PEDOT. Furthermore, the thermal stability of BA-loaded PEDOT was examined using TGA. The thermogram is shown in Figure 2b. The decomposition temperature of BA showed up at 135 °C. The PEDOT showed adecomposition temperature of 210 °C as the dopant degradation of SO_4^{-2} from APS, and in the region between 310 to 420 °C the polymer backbone degradation occurred.[28] The decomposition temperature of

dx.doi.org/10.1021/jp502674f | J. Phys. Chem. B 2014, 118, 9263−9271

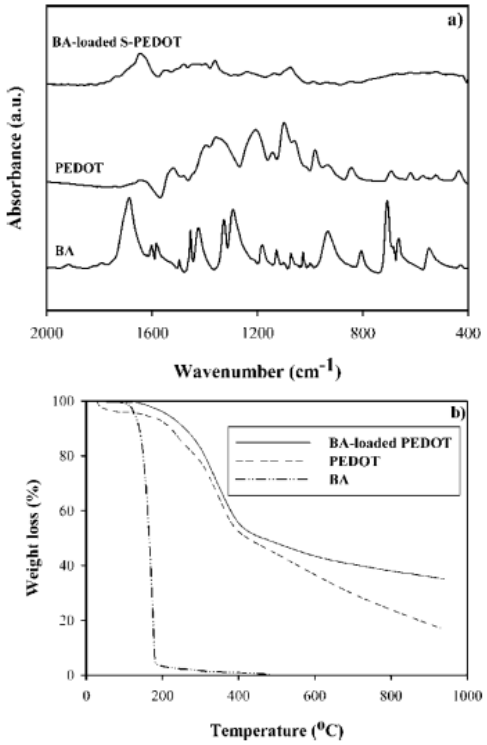

Figure 2. (a) Absoption infrared spectra and (b) thermogravimetric thermograms of BA, PEDOT, and BA-loaded PEDOT.

BA-loaded PEDOT shifted to 215 °C for the dopant and 320–460 for the polymer backbone. Furthermore, the observed changes in thermal stability were accompanied by increasing char residue, showing that existing BA with PEDOT as BA-loaded PEDOT offered higher thermal resistance. This resulted from the electrostatic interaction between the carboxylate group of BA and the positively charged PEDOT sites as shown by FTIR at 1682 cm^{-1}.[29,30]

The BA-loaded PEDOT nanoparticles at various APS concentrations show various particle sizes and shapes, as shown in Figure 3. The particle sizes of BA-loaded PEDOT are 220 nm irregular shape (L-PEDOT), 71 nm raspberry agglomerate shape (S-PEDOT), and 108 nm coralliform shape (C-PEDOT). They were synthesized by 0.15, 0.30, and 0.45 M of APS concentrations, respectively. The BA-loaded PEDOT particle sizes and shapes vary a great deal with APS concentration, in which it acted as an oxidizing initiator affecting the rate of polymerization and PEDOT polymeric cation amount as shown in Figure 4. In the first step, EDOT is

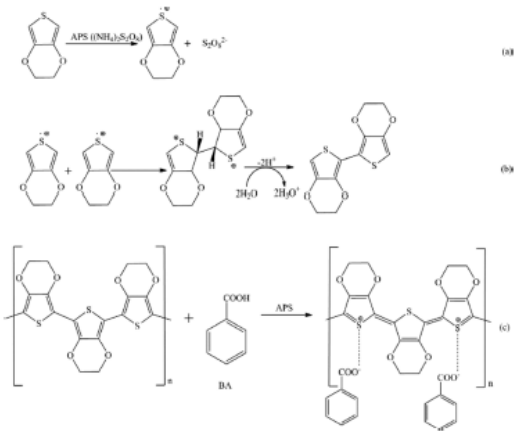

Figure 4. Proposed polymerization mechanism of BA-loaded PEDOT: (a) EDOT as a monomer is oxidized by APS to a cation radical; (b) EDOT cation radicals form dimers that subsequently are deprotonated; and (c) PEDOT polymer is doped by benzoate ion.

oxidized by APS to become EDOT cation radical, which forms EDOT dimers via protonation and deprotonation, respectively. The process is duplicated to polymerize and to obtain PEDOT. Finally, the polymerized PEDOT is doped by the counterions as the benzoate ions.[26,31] The structure was confirmed by FTIR and TGA (Figures 2a,b).

A greater amount of PEDOT polymeric cations is due to a higher APS concentration creating a stronger electrorepulsive

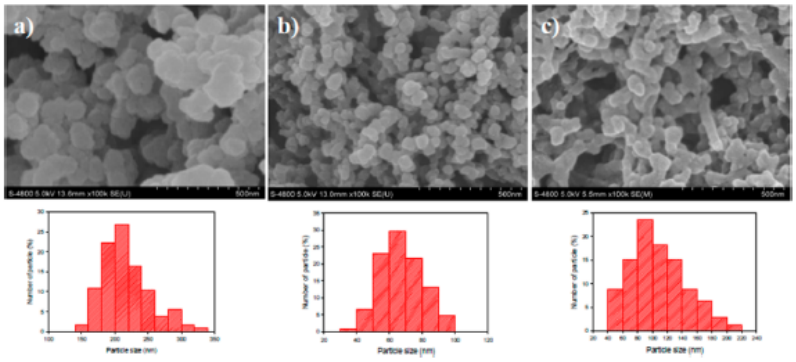

Figure 3. Morphologies and size distributions of BA-loaded PEDOT at various APS concentrations: (a) 0.15 M, (b) 0.30 M, and (c) 0.45 M.

force between PEDOT polymeric cation radicals, leading to a smaller particle size. On the other hand, a higher APS concentration (>0.3 M) enhances the sulfate counteranions of APS, which generates the screening effect of the electrorepulsive reaction. This is the cause of the agglomeration of PEDOT particles resulting in a larger particle size as the coralliform shape.[26]

Table 2 shows the relationship between electrical conductivity and BA-loaded PEDOT particle size. The electrical

Table 2. Particle Size and Electrical Conductivity of BA-Loaded PEDOT and Actual Amount of Benzoic Acid in PEDOT

drug-loaded PEDOT	particle size (nm)	electrical conductivity (S/cm)
BA-loaded S-PEDOT	71 ± 43	95.64 ± 5.52
BA-loaded C-PEDOT	108 ± 43	10.65 ± 3.86
BA-loaded L-PEDOT	220 ± 37	2.78 ± 4.35

conductivity values are 95.64, 10.65, and 2.78 S/cm for BA loaded S-PEDOT, C-PEDOT, and L-PEDOT, respectively. Electrical conductivity increases as the particle size decreases because the smaller particle size has a higher surface area for electron to transfer, and thus higher electrical conductivity.[26,27] Moreover, the electrical conductivity of BA-loaded-C-PEDOT is lower than that of BA-loaded-S-PEDOT because the coralliform shape is a result from PEDOT particles aggregation which possesses a lower surface area and greater free space for electron to transfer, thus reducing electron mobility.[26]

PEDOT/Alg Hydrogel Characterization. The PEDOT/Alg hydrogels were prepared at various cross-linking ratios (0.3, 0.5, 0.7, 1.0, and 1.3) and various PEDOT particle sizes and shapes (S-PEDOT, C-PEDOT, and L-PEDOT). The $\bar{M}_c$ and ξ of the PEDOT/Alg hydrogels were investigated to characterize the porous structure of the hydrogels with and without applied electric field. The $\bar{M}_c$ and ξ are larger at a lower cross-linking ratio because there is a longer Alg strand between cross-links and easier more relaxed swelling behavior, which is produced via a lower cross-linker resulting in larger $\bar{M}_c$ and ξ.[16] The $\bar{M}_c$ and ξ without electric field decrease when PEDOT particles are added to the Alg hydrogel in the preparation of the PEDOT/Alg hydrogel because the PEDOT/Alg hydrogel is more rigid than the Alg hydrogel due to the existing PEDOT particles restricting chain movement and relaxation; thus, the PEDOT/Alg hydrogel exhibits less swelling, and a smaller mesh size results.[32,33] The ξ of the Alg hydrogel varies between 641 and 3313 Å at an electric field strength of 0 V and between 1277 and 3887 Å at an electric field strength of 1 V as shown in Figure 5. The ξ of PEDOT/Alg hydrogel varies between 171 and 2626 Å at an electric field strength of 0 V and between 1282 and 3930 Å at an electric field strength of 1 V. Thus, ξ under applied electric field is larger than that with no electric field applied. The electric field affects Alg chain expansion through the resultant electrorepulsive force between the negatively charged electrode and negatively charged carboxylate group in the Alg structure, so-called "electroinduced Alg expansion".[16] The ξ of the PEDOT/Alg hydrogel increases with decreasing PEDOT particle size, due to more free volume for water adsorption.

Release Characteristics of BA from BA-Loaded PEDOT/Alg Hydrogel. In order to study the release mechanism of BA from the BA-loaded PEDOT/Alg hydrogel, the actual amount of BA within the hydrogel sample was

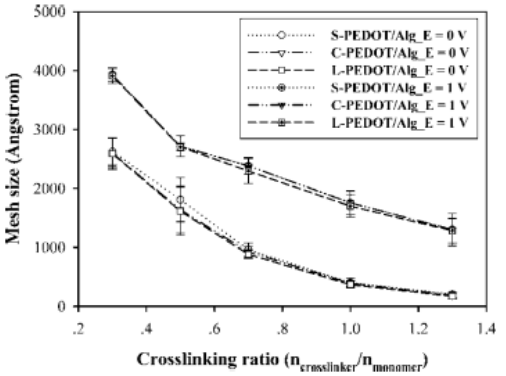

Figure 5. Mesh size of PEDOT/Alg hydrogel at various cross-linking ratios under electric field strength of 0 and 1 V.

determined as a percentage of the BA amount presents relative to the amount actually loaded in the BA-loaded PEDOT/Alg samples. The actual amounts of BA in the samples were 95.4 ± 5.1, 93.8 ± 7.8, and 94.1 ± 6.3% for the BA-loaded S-PEDOT, C-PEDOT, and L-PEDOT/Alg hydrogels, respectively.

Effect of Electric Field Strength. The release mechanism of BA from the BA-loaded PEDOT/Alg hydrogel was analyzed using the diffusion scaling exponent (n) from eq 4. The n value is the slope of the curve of the plot between log (M_t/M_α) and log time, (Figure 6). The n values of the BA-loaded PEDOT/

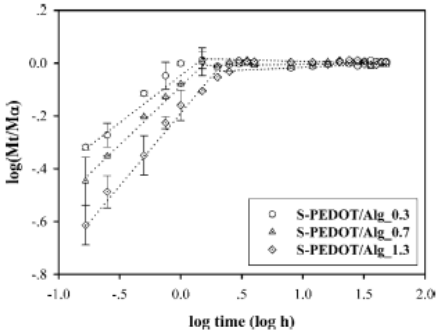

Figure 6. Plot of log M_t/M_α versus log time of benzoic acid released from variously cross-linked S-PEDOT/Alg hydrogels at electric field strength of 1 V.

Alg hydrogels are tabulated in Tables 3 and 4 at electric field strengths of 0 and 1 V, respectively. The n values are between 0.41 and 0.58, which are quite close to 0.5 in both cases, thus the release of BA is the diffusion controlled mechanism or the Fickian diffusion.[22] The PEDOT/Alg hydrogels act as a diffusion barrier, and BA is released mainly by the diffusion mechanism as supported by the swelling behavior.[34,35]

The amount of BA released from the BA-loaded PEDOT/Alg hydrogel increases steadily up to 1 h after that it approaches equilibrium. Plotting the release of BA as a function of the square root of time shows a linear relationship in the first 1 h. In Figure 7a, with the absence of an electric field, the BA molecules are gradually released from the BA-loaded S-PEDOT/Alg hydrogel until the amount of BA released reaches

dx.doi.org/10.1021/jp502674f | J. Phys. Chem. B 2014, 118, 9263−9271

Table 3. Release Kinetic Parameters and the Linear Regression Values Obtained from Fitting the Drug Release Experimental Data

	release kinetics								
	S-PEDOT			C-PEDOT			L-PEDOT		
cross-linking ratio of Ca-Alg	n	$k_H(h^{-n})$	r^2	n	$k_H(h^{-n})$	r^2	n	$k_H(h^{-n})$	r^2
0.3	0.49	0.98	0.9834	0.47	1.09	0.9756	0.48	0.9912	0.9943
0.5	0.48	0.92	0.9922	0.45	1.07	0.9876	0.46	0.9874	0.9874
0.7	0.44	0.86	0.9833	0.42	1.06	0.9833	0.42	0.9718	0.9611
1.0	0.42	0.84	0.9785	0.41	0.98	0.9678	0.41	0.9585	0.9802
1.3	0.42	0.78	0.9876	0.41	0.96	0.9832	0.41	0.9412	0.9798

Table 4. Release Kinetic Parameters and the Linear Regression Values Obtained from Fitting the Drug Release Experimental Data at an Electric Field Strength of 1 V

	release kinetics								
	S-PEDOT			C-PEDOT			L-PEDOT		
cross-linking ratio of Ca-Alg	n	$k_H(h^{-n})$	r^2	n	$k_H(h^{-n})$	r^2	n	$k_H(h^{-n})$	r^2
0.3	0.58	1.00	0.9689	0.59	1.06	0.9698	0.52	0.99	0.9716
0.5	0.56	0.96	0.9461	0.58	1.05	0.9682	0.52	0.98	0.9653
0.7	0.55	0.92	0.9708	0.56	1.02	0.9669	0.52	0.97	0.9527
1.0	0.54	0.88	0.9833	0.55	0.92	0.9947	0.51	0.95	0.9761
1.3	0.50	0.75	0.9288	0.54	0.85	0.9499	0.50	0.82	0.9689

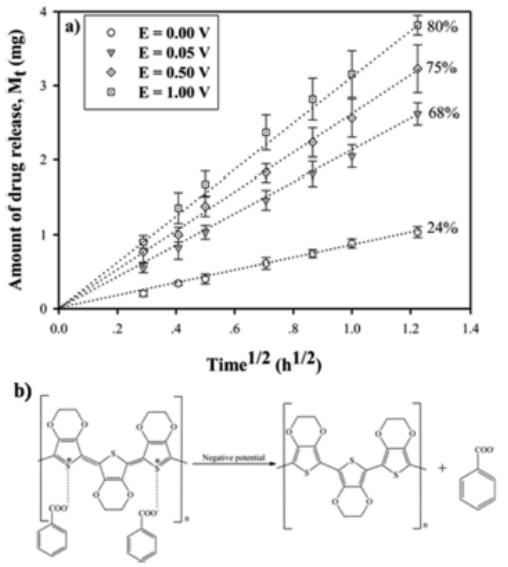

Figure 7. (a) Amount of benzoic acid released from S-PEDOT/Alg_0.7 hydrogels at various electric field strengths. (b) Release reaction of benzoic acid from BA-loaded PEDOT/Alg hydrogel under applied electric field.

equilibrium. Moreover, the amount of BA released from the BA-loaded S-PEDOT/Alg hydrogel is higher with an increase in electric field strength (cathode in a donor part represents a negatively charged electrode). The electric field generates the driving force to enhance the BA diffusion from the electro-repulsive force between the negatively charged BA and the negatively charged electrode, so-called "cathode−BA$^-$ electro-repulsion", as shown in Figure 4b.[36−38] In addition, the electric field also creates electroinduced Alg expansion, which produces the expansion of hydrogel matrix, a larger mesh size, and a corresponding increase in the BA diffusion.[16] Lastly, the electric field strength enhances the release of BA as it provides a stronger reduction reaction of the BA-loaded S-PEDOT as shown in Figure 7b. The PEDOT chain in the reduced form is produced and contracted via electron injection under electric field, this causes squeezing BA$^-$ out of neutralized PEDOT with lesser electrostatic binding interaction, inducing higher drug release, so-called "PEDOT electroneutralization".[36,39]

The D of each system was calculated from the slope of the Higuchi's equation, which is the plot between M_t and $t^{1/2}$. Figure 8 shows the D of BA increases with increasing electric

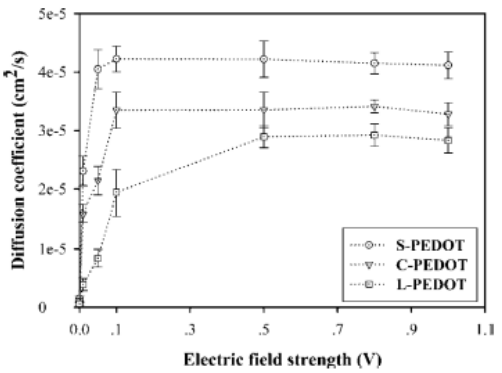

Figure 8. Diffusion coefficient of benzoic acid from PEDOT/Alg_0.7 of various PEDOT particle sizes versus electric field strength.

field strength (E = 0−1 V at the current of 0−0.25 μA) under cathode as an electrode (negative charge) in the donor part. Increasing electric field strength produces greater cathode−BA$^-$ electrorepulsion, facilitating the diffusion of BA from the polymer matrix.[16,40] Furthermore, the particle size of PEDOT affects the D of BA under applied electric field. The D at a given

dx.doi.org/10.1021/jp502674f | J. Phys. Chem. B 2014, 118, 9263−9271

applied electric field strength of BA-loaded S-PEDOT has the highest value, followed by the BA-loaded C-PEDOT, and the BA-loaded L-PEDOT, respectively. The smaller PEDOT particle size exhibits higher electrical conductivity than the larger particle size; this induces electron to transfer more easily as an electric field is applied. Safranin dye was studied for its release characteristics under applied electric field (E = −0.1 V) from a semi-interpenetrating polyaniline-polyacrylamide (PANI−PAAM) network by Lira and Torresi.[41] The safranin release under electric field was greater than without an electric field because the reduced PANI chains created more free volume within the hydrogel, therefore, safranin diffusion increased.[41] Furthermore, heparin was investigated for release from polypyrrole−poly(vinyl alcohol) with applied electric field (E = 1 mA) by Li et al.[42] The amount of heparin released was greater than with no applied electric field. There were several factors in which electric field controls releasing: charged drug electrophoresis reactions, drug doped conductive polymer reduction reactions, mesh size expansion, and increased or decreased pH due to H^+ migration toward the cathode.[42]

Effect of Cross-Linking Ratio. The amount of BA released decreases with increasing cross-linking ratio (as shown in Figure 6) because smaller mesh size at a higher cross-linking ratio results in a smaller pathway for BA to diffuse, the so-called "mesh size-hindering effect".[16]

In Figure 9, the cross-linking ratio and mesh size at the electric field strengths of 0 and 1 V affect the D of BA from the

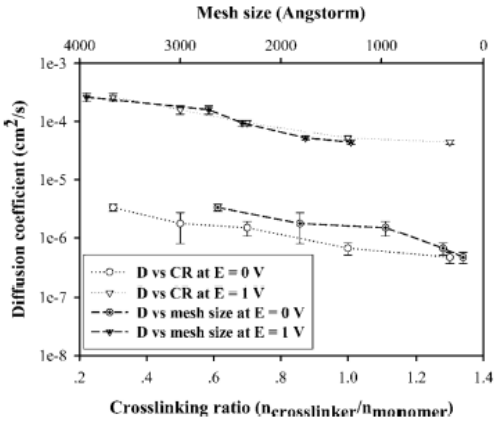

Figure 9. Diffusion coefficient of benzoic acid from S-PEDOT/Alg as a function of cross-linking ratio and mesh size at electric field strength of 0 and 1 V.

BA-loaded S-PEDOT/Alg hydrogels. The D of BA decreases with increasing cross-linking ratio because the mesh size-hindering effect retards BA diffusion. In addition, the D of BA under electric field is higher than that without electric field because the cathode−BA^- electrorepulsion, electroinduced Alg expansion, and PEDOT electroneutralization are created as an electric field is applied.[16,36−40]

Effect of Electrode Polarity. The amount of BA release and the D under cathode are greater than that of no applied electric field, and under anode (positive charge) as electrode in the donor part, as shown in Figure 10. Thus, the electric field under cathode placed on hydrogel generates the cathode−BA^-

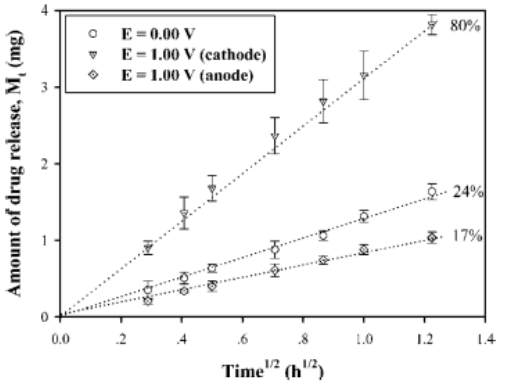

Figure 10. Amounts of benzoic acid released from S-PEDOT/Alg_0.7 hydrogels at electric field strengths of 0 and 1 V with hydrogel samples attached to anode or cathode.

electrorepulsion, which enhances BA diffusion from the BA-loaded PEDOT/Alg hydrogel. On the other hand, the diffusion of BA is retarded when the anode electrode is placed on the hydrogel because it creates an electroattractive force between the positively charged electrode and the negatively charged BA resulting in restricted BA diffusion.[16,40]

The log−log plot of the D as a function of the ratio of drug size over mesh size of hydrogel under the electric field strengths of 0 and 1 V at 37 °C is shown in Figure 11. The scaling exponent, m, can be determined from eq 7:

$$D = D_0(a_d/\xi)^{-m} \quad (7)$$

where D is the diffusion coefficient of the drug; D_0 is the diffusion coefficient at a very small drug size; a_d is the drug size (5.58 Å); ξ is the apparent mesh size of the hydrogel, and m is the scaling exponent.[16,40]

The m values for the BA diffusion through the Alg matrix and the PEDOT/Alg matrix without electric field are 1.06[16] and 1.95, respectively, and the D_0 values are 2.01 × 10^{-7}[16] and 1.02 × 10^{-9} cm^2/s, respectively. The m values under applied electric field (E = 1 V) of Alg, S-PEDOT/Alg, C-PEDOT/Alg, and the L-PEDOT/Alg hydrogel are 1.28,[16] 1.13, 1.05, and 1.31, respectively and the D_0 values are 2.08 × 10^{-6},[16] 1.89 × 10^{-9}, 1.97 × 10^{-8}, 6.57 × 10^{-9} cm^2/s, respectively.

Figure 11a,b shows decreasing diffusion when a_d/ξ increases due to the mesh size-hindering effect. In all cases of applied electric field (cathode in the donor part), the D can be divided onto two regimes, when a_d/ξ is below and above 2.38 × 10^{-3}. Below 2.38 × 10^{-3}, the diffusion is a_d/ξ independent because this a_d/ξ range also provides easy drug penetration. Above 2.38 × 10^{-3}, D decreases monotonically.

Furthermore, Figure 12 shows the comparison of the values of the drug from the Alg, S-PEDOT/Alg, C-PEDOT/Alg, L-PEDOT/Alg, and the polypyrrole/poly(acrylic acid) (PPy/PAA) hydrogels at various conditions. The higher D values of the drugs under these conditions are due to lower cross-linking ratios and smaller drug sizes. In addition, the D increases under applied electric field due to cathode−BA^- electrorepulsion, a larger mesh size, inducing easier drug mobility through the hydrogels. Nevertheless, the D of BA from the Alg hydrogel is higher than that of the BA-loaded PEDOT/Alg hydrogel without electric field because the free volume or pathway for

dx.doi.org/10.1021/jp502674f | J. Phys. Chem. B 2014, 118, 9263−9271

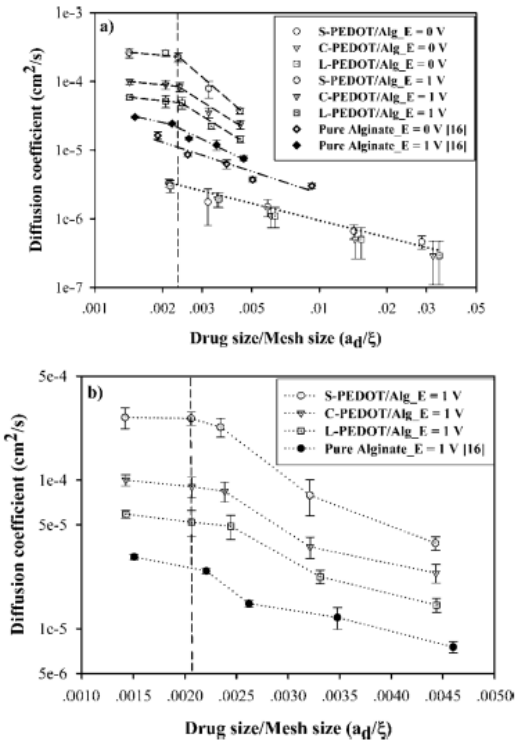

Figure 11. Diffusion coefficient of (a) benzoic acid from alginate and PEDOT/Alg hydrogel at electric field strengths of 0 and 1 V and (b) benzoic acid from PEDOT/Alg hydrogel at electric field strength of 1 V.

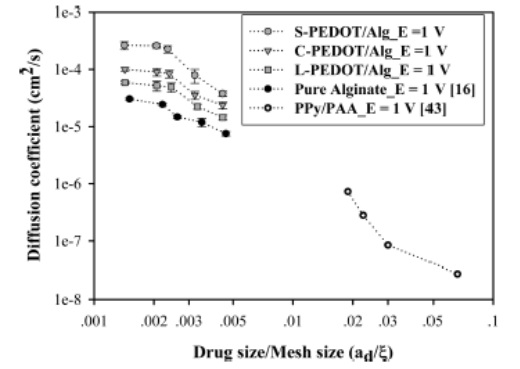

Figure 12. Diffusion coefficient of drug from alginate, PEDOT/Alg, and PPy/PAA hydrogel at electric field strength of 1 V.

drug diffusion is reduced by the presence of PEDOT particles. In addition, the D under applied electric field of the BA-loaded PEDOT is higher than that of BA-loaded Alg hydrogel. The D of the BA-loaded S-PEDOT/Alg hydrogel is the highest because it has the greatest electrical conductivity, resulting in easier electron transfer for the reduction reaction of BA-loaded PEDOT. On the other hand, Chansai et al.[43] studied the D of sulfosalicylic acid (SSA) from the PPy/PAA hydrogel under electric field.[43] SSA was loaded on the PPy structure by chemical oxidation reaction using ammonium persulfate as an initiator. The PPy/PAA blend film was prepared by dispersing SSA-loaded PPy powder in the acrylic solution and cast on mold to obtain the film. In Figure 12, the D of BA from the PEDOT/Alg hydrogel is higher than that of SSA diffusion from PPy/PAA hydrogel because of the larger mesh size of PEDOT/Alg hydrogel, greater electrical conductivity of PEDOT (electrical conductivity of SSA-doped PPy = 51.836 S/cm), and a smaller drug size.

Thus, the diffusion of BA and SSA as anionic drugs through the Alg, PEDOT/Alg, and the PPy/PAA hydrogel occur through the concentration gradient under no applied electric field, and by the electrophoresis of negatively charged drugs under applied electric field. The PEDOT/Alg hydrogel in this study is available for TDDS application because many available PEDOT size critically affect specific controlled release conditions, especially under applied electric field. In addition, the presence of PEDOT allows electrical triggering for drug release to exist in the matrix system.

■ CONCLUSIONS

Polyethylenedioxythiophene/alginate hydrogel acted as a carrier/matrix for the controlled release of benzoic acid. The release behavior and the diffusion coefficient were studied for the effect of cross-linking ratio, PEDOT particle size, electric field strength, and electrode polarity. The release mechanism of BA was the diffusion controlled mechanism or the Fickian diffusion because the diffusion scaling exponent is close to 0.5. The D of BA increased with decreasing cross-linking ratio due to the mesh size-hindering effect. When electric field was applied under cathode placed on the hydrogel, the D was greater than that of no electric field because the electric field induced cathode−BA^- electrorepulsion, electroinduced Alg expansion, and PEDOT electroneutralization. The D of BA-loaded S-PEDOT was the greater under applied electric field at the PEDOT particle size was smallest resulting in the highest electrical conductivity. The D of BA depended on the electrode polarity, under cathode placed on the hydrogel, the D of BA was higher than that of no electric field and anode placed on the hydrogel because cathode−BA^- electrorepulsion was generated. Thus, the D of BA was critically dependent on the mesh size except when the drug size/mesh size was lower than 2.38×10^{-3}; the mesh size had no effect toward BA diffusion because the matrix provided a too large pathway relative to the drug size. Hence, the fabricated conductive polymer hydrogel blends is potentially applicable in TDDS under electrical stimulation.

■ AUTHOR INFORMATION

Corresponding Author

*Tel: 662 218 4131, Fax: 662 611 7221, E-mail: anuvat.s@chula.ac.th.

Notes

The authors declare no competing financial interest.

■ ACKNOWLEDGMENTS

The authors would like to acknowledge the financial support provided by the Thailand Research Fund (TRF-RTA, RGJ PHD/0285/2551); the Royal Thai Government; the Conductive and Electroactive Polymer Research Unit; the

Petroleum and Petrochemical College, Chulalongkorn University; and the Ratchadaphiseksomphot Endownment Fund of Chulalongkorn University.

REFERENCES

(1) Keleb, E.; Sharma, R. K.; B Mosa, E.; Z Aljahwi, A.-A. *Int. J. Adv. Pharm. Sci.* **2010**, *1*, 201−211.
(2) Shingade, G. M.; Quazi, A.; Sabale, P. M.; Grampurohit, N. D.; Gadhave, M. V.; Jashav, S. L.; Gaikwad, D. D. *J. Drug Delivery Ther.* **2012**, *2*, 66−75.
(3) Latheeshjlal, L.; Phanitejaswini, P.; Soujanya, Y.; Swapna, U.; Sarika, V.; Moulika, G. *Int. J. PharmTech Res.* **2011**, *3*, 2140−2148.
(4) Dixit, N.; Bali, V.; Baboota, S.; Ahuja, A.; Ali, J. *Curr. Drug Delivery* **2007**, *4*, 1−10.
(5) Zorec, B.; Preat, V.; Miklavcic, D.; Pavselj, N. *Pregledni Clanek* **2013**, *82*, 339−359.
(6) Khan, A.; Yasir, M.; Asif, M.; Chauhan, I.; Singh, A. P.; Sharma, R.; Singh, P.; Rai, S. *J. Appl. Pharm. Sci.* **2011**, *01*, 11−24.
(7) Green, R. A.; Baek, S.; Poole-Warren, L. A.; Martens, P. J. *Sci. Technol. Adv. Mater.* **2010**, *11*, 1−13.
(8) Gupta, P.; Vermani, K.; Grag, S. *Drug Discovery Today* **2002**, *7*, 569−579.
(9) Kim, S.-J.; Yoon, S.-G.; Lee, S.-M.; Lee, J.-H.; Kim, S. I. *Sens. Actuators, B* **2003**, *96*, 1−5.
(10) Qiu, Y.; Park, K. *Adv. Drug Deliver. Rev.* **2001**, *53*, 321−339.
(11) Kim, D.-H.; Abidian, M.; Martin, D. C. *J. Biomed. Mater. Res., Part A* **2004**, *71*, 577−585.
(12) Luo, X.; Cui, X.-T. *Electrochem. Commun.* **2009**, *11*, 402−404.
(13) Ge, J.; Neofytou, E.; Cahill, T. J.; Beygui, R. E.; Zare, R. N. *ACS Nano* **2012**, *6*, 227−233.
(14) Oh, S.-G.; Im, S.-S. *Curr. Appl. Phys.* **2002**, *2*, 273−277.
(15) Pasparakis, G.; Bouropoulos, N. *Int. J. Pharm.* **2006**, *323*, 34−42.
(16) Paradee, N.; Sirivat, A.; Niamlang, S.; Prissanaroon-Ouajai, W. *J. Mater. Sci.: Mater. Med.* **2012**, *23*, 999−1010.
(17) Peppas, N. A.; Wright, S. I. *Eur. J. Pharm. Biopharm.* **1998**, *1*, 15−29.
(18) Wells, L. A.; Sheardown, H. *Eur. J. Pharm. Biopharm.* **2011**, *79*, 304−313.
(19) Canal, T.; Peppas, N. A. *J. Biomed. Mater. Res.* **1989**, *23*, 1183−1193.
(20) Chan, A. W.; Neufeld, R. J. *Biomaterials* **2009**, *30*, 6119−6129.
(21) Korsmeyer, R. W.; Gurny, R.; Doelker, E.; Buri, P.; Peppas, N. A. *Int. J. Pharm.* **1983**, *15*, 25−35.
(22) Pradhan, R.; Budhathoki, U.; Thapa, P. *Kathmandu Univ. J. Sci., Eng. Technol.* **2008**, *1*, 55−67.
(23) Higuchi, T. *J. Pharm. Sci.* **1963**, *52*, 1145−1149.
(24) Reichling, J.; Landvatter, U.; Wagner, H.; Kostka, K.-H.; Schaefer, U. F. *Eur. J. Pharm. Biopharm.* **2006**, *64*, 222−228.
(25) Hayashi, S.; Kimura, N. *Bull. Inst. Chem. Res., Kyoto Univ.* **1966**, 335−340.
(26) Paradee, N.; Sirivat, A. *Polym. Int.* **2014**, *63*, 106−113.
(27) Yang, Y.; Jiang, Y.; Xu, J.; Yu, J. *Polymer* **2007**, *48*, 4459−4465.
(28) Choi, J. W.; Han, M. G.; Kim, S. Y.; Oh, S. G.; Im, S. S. *Synthetic Metal* **2004**, *141*, 293−299.
(29) Xiao-hong, G.; Guang-hao, C.; Chii, S. *J. Environ. Sci.* **2007**, *19*, 438−443.
(30) Kowalewska, B.; Miecznikowski, K.; Makowski, O.; Palys, B.; Adamczyk, L.; Kulesza, P. J. *J. Solid State Electrochem.* **2007**, 1023−1030.
(31) Mueller, M.; Fabretto, M.; Evans, D.; Hojati-Talemi, P.; Gruber, C.; Murphy, P. *Polymer* **2012**, *53*, 2146−2151.
(32) Dispenza, C.; Presti, C. L.; Belfiore, C.; Spadaro, G.; Piazza, S. *Polymer* **2006**, *47*, 961−971.
(33) Hezaveh, H.; Muhamad, I.-I. *Carbohydr. Polym.* **2012**, *89*, 138−145.
(34) Thakur, A.; Wanchoo, R. K.; Singh, P. *Chem. Biochem. Eng. Q.* **2011**, *25*, 471−482.
(35) Huang, Y.; Zhang, B.; Xu, G.; Hao, W. *Compos. Sci. Technol.* **2013**, *84*, 15−22.
(36) Niamlang, S.; Sirivat, A. *Int. J. Pharm.* **2009**, *371*, 126−133.
(37) Murdan, S. *J. Controlled Release* **2003**, *92*, 1−7.
(38) Kantaria, S.; Rees, G. D.; Lawrence, M. J. *J. Controlled Release* **1999**, *60*, 355−365.
(39) Gordon, G. W.; Geoffrey, M. S.; Leon, A.P. K.; Peter, R. T. *Conductive Electroactive Polymers: Intelligent Polymer Systems*, 3rd ed.; CRC Press: Boca Raton, FL, 2009; p 220.
(40) Juntanon, K.; Niamlang, S.; Rujiravanit, R.; Sirivat, A. *Int. J. Pharm.* **2008**, *356*, 1−11.
(41) Lira, L. M.; Cordoba de Torresi, S. I. *Electrochem. Commun.* **2005**, *7*, 717−723.
(42) Li, Y.; Neoh, K. G.; Kang, E. T. *J. Biomed. Mater. Res., Part A* **2005**, *73*, 171−181.
(43) Chansai, P.; Sirivat, A.; Niamlang, S.; Chotpattananont, D.; Viravaidya-Pasuwat, K. *Int. J. Pharm.* **2009**, *381*, 25−33.

dx.doi.org/10.1021/jp502674f | *J. Phys. Chem. B* 2014, 118, 9263−9271

Bull. Mater. Sci., Vol. 37, No. 5, August 2014, pp. 975–982. © Indian Academy of Sciences.

Effect of electrolytes on electrochromic properties and morphology of poly(2,5-dimethoxy aniline) films

BUREERAT SUEPHATTHIMA[1], NOPHAWAN PARADEE[1], ANUVAT SIRIVAT[1,*] and DATCHANEE PATTAVARAKORN[2]

[1]The Petroleum and Petrochemical College, Chulalongkorn University, Bangkok 10330, Thailand
[2]Department of Industrial Chemistry, Faculty of Science, Chiang Mai University, Chiangmai 50200, Thailand

MS received 21 August 2013; revised 17 October 2013

Abstract. **Poly(2,5-dimethoxyaniline) (PDMA) was electrochemically synthesized in oxalic ($H_2C_2O_4$) nitric (HNO_3) and hydrochloric (HCl) acids and deposited onto flexible indium tin oxide at various synthesis times and deposition potentials as electrochromic materials. The PDMA films were characterized by FT–IR-spectrometry, scanning electron microscopy, UV–Vis spectrophotometry and cyclic voltammetry. All PDMA films show reversible colour changes from yellow to green corresponding to the transition from the fully reduced state to the fully oxidized state under potential switching. The surface morphology and thickness of PDMA films depend critically on the type of acids used in the electrochemical polymerization process. The morphology of PDMA are highly porous microfibres ($H_2C_2O_4$ and HNO_3), tiny granular aggregate (HCl) and particle agglomerate depending on the polymerization time. The fastest response time observed via colour changing of 3·7 s is obtained from the HCl–PDMA film at 3·5 volt and at the synthesis time of 6 min, as primarily due to the thickness of the film. The flexible PDMA film is demonstrated here as a potential candidate to be used in electrochromic devices.**

Keywords. **Electrochromic polymer; poly(2,5-dimethoxyaniline); electrochemical polymerization; response time.**

1. Introduction

Conductive polymers continue to gain growing interest, because they are widely used in many applications: optical displays, rechargeable batteries, electrochromic devices and light emitting diodes (Ramakrishnan 1997). Among organic molecules, conductive polymers have attracted significant interest in the field of electrochromism.

Electrochromism is defined as a reversible and visible change in its transmittance and/or reflectance of electrochromic materials as a result of an oxidation–reduction reaction. The applications for such materials are mirrors of vehicles (Sonmez 2005), smart windows (Kim *et al* 2009), electrochromic displays (Bange 1999), earth-tone chameleon materials (Brotherson *et al* 1999), ink-jet printers and most recently E-paper (Peters and Freeman 1991).

Earlier reports (Sonmez 2005) indicated that the use of inorganic compounds or the metal oxides, iridium dioxide (IrO_2) and tungsten trioxide (WO_3), which were mixed-valence metal complexes. However, these transition metal oxides electrochromically exhibited a slow response time (tens of seconds) and a high processing cost. Compared with electrochromic polymers, they have several merits: low processing cost, low power requirement during switching, low operating voltage, repeatability, high colouration efficiency, good UV stability, fast switching ability and fine-tuning ability of the band gap via modification of chemical structure of the polymer. Additionally, there is no dependence on the angle of vision (Sonmez 2005).

Potential conducting polymers are comprised of a number of functionalized groups such as polypyrroles, polythiophenes, polyanilines, etc. (Sapp *et al* 1998). They have been recognized as an interesting class of electrochromic materials. An important issue of electrochromic polymers has been that of controlling their colours by main-chain and pendant-group structural modifications.

Polyaniline (PANI) is one of the most promising conducting polymers due to an easy polymerization process and excellent chemical stability, combined with relatively high levels of conductivity (Khan *et al* 2003). Poly(2,5-dimethoxyaniline), or PDMA, is the derivative of PANI which shows higher solubility and faster response time than PANI. PDMA film can make reversible colour changes from yellow to green representing a switch between the reduced state to the oxidized state through an application of electrical potential faster than that of PANI (Sun *et al* 2013). Cyclic voltammetry results have also

*Author for correspondence (anuvat.s@chula.ac.th)

confirmed that PDMA can be easily switched from the leucoemeraldine state to the emeraldine state. PDMA also shows a shorter response time (9 s) than the electrochemically prepared PANI (22 s) (Huang *et al* 2002).

Normally, the electrochromic materials are produced in the form of thin film. They can be produced by many methods including electron beam deposition, chemical vapour deposition, the Langmuir–Blodgett technique and the layer-by-layer self-assembly technique (Sarkar *et al* 2000). In the case of electronically functional thin films, thinner films are generally preferred due to the shorter electron and ion transport path length (Montazami *et al* 2010).

The purpose of this work was to polymerize 2,5-dimethoxyaniline (DMA) via electrochemical polymerization on indium tin oxide (ITO) plastic submerged in oxalic, nitric and hydrochloric acids at various synthesis times (3, 6 and 10 min) and applied potentials (1 and 1·5 V). This study was also intended to investigate the effect of various electrolytes on the electrochromic properties of PDMA film due to different doping characteristics. The PDMA films were characterized for the electrochromic properties using a UV–Visible spectroelectrometer. Fourier-transform infrared spectrometer and thermogravimetric analyser were also utilized to investigate the chemical and thermal properties of PDMA film, respectively. The morphology and thickness of the PDMA coated ITO surface were studied by scanning electron microscope. Cyclic voltammetry was used to study the oxidation–reduction properties of the PDMA/ITO plastic.

2. Experimental

2.1 *Materials*

The starting monomer, 2,5-dimethoxy aniline (DMA), was purchased from Sigma Aldrich (AR grade, 98%). Oxalic acid (Ajax Finechem, AR grade), hydrochloric acid (Lab Scan, AR grade, 37%), sulfuric acid (Lab Scan, AR grade, 98%), nitric acid (Lab Scan) and acetic acid (Lab Scan) were used for the synthesis without further purification. An ITO-coated PET substrate (60 Ω) was purchased from Sigma Aldrich.

2.2 *Electrochemical polymerization of PDMA on ITO plastic*

PDMA was electrodeposited onto the ITO plastic using potentials of 1 V and 1·5 V, in either 25 mL of 0·1 M DMA in 0·1 M oxalic acid, hydrochloric acid, or nitric acid, and at various deposition times of 3, 6 and 10 min. Stainless steel and ITO plastic were used as the counter and the working electrodes, respectively.

2.3 *Characterization of PDMA/ITO film*

Infrared absorption spectra of PDMA were taken to study the chemical structure of PDMA. A Fourier transform infrared spectrometer (FT–IR; Thermo Nicolet, Nexus 670) was used in the absorption mode with 64 scans, covering a wavenumber range of 4000–400 cm^{-1}. Optical grade KBr was used as the background material.

A thermogravimetric analyser (TGA; Perkin Elmer, TGA7) was used to study the thermal stability and to determine the decomposition temperature of PDMA. The experiment was carried out by electrochemical polymerization of the DMA monomer in each acid solution on a stainless steel electrode for 20 min. Then, the PDMA coated stainless steel electrodes were dried and PDMA was scrapped into a powder, kept at 105 °C overnight, and later used for TGA measurements. The sample (2–3 mg) was weighed and then placed it in an alumina pan and heated under nitrogen atmosphere with a heating rate of 10 °C/min from 50 to 900 °C.

The synthesized PDMA/ITO films were characterized for redox properties with a cyclic voltammetry using a multi-channel potentiostat (VMP, Bio Logic Science Instrument). Measurements were carried out in 200 mL of 0·01 M H_2SO_4 solution as the background electrolyte, assembled with a three-electrode cells consisting of a saturated calomel electrode (SCE) as the reference electrode, a stainless-steel wire as the counter electrode, with a 2 cm^2 PDMA/ITO plastic stub used as the working electrode. The cyclic voltammogram (CV) of the PDMA/ITO electrodes was measured in the potential range of –1 to + 1·5 V and vs SCE. The parameters and cell characteristics were setup as follows: a scan rate (dE/dt) of 10 mV/s, dE_R = 1 mV, with an electrode surface area of 2 cm^2. A field-emission scanning electron microscopy (FE-SEM; Hitachi S4800) was used to determine morphological structure and thickness (Kang *et al* 2009) of each PDMA-coated ITO.

2.4 *Electrochromic study of PDMA-coated ITO plastics*

Optical absorption spectra as well as optical kinetic responses of the PDMA/ITO electrode polymerized with various acids, were recorded on a spectrometer (Shimadzu, UV-1800). Measurements were carried out in a cuvette cell of 1 cm path length, assembled as an electrochemical cell with PDMA film-coated ITO plastic as the working electrode and stainless-steel wire as the counter electrode, in 0·01 M H_2SO_4 electrolyte solution. The scanned wavelength range was 400–800 nm (Neves *et al* 2004). To study the effect of the applied potential on the response time, the potentials applied to the PDMA/ITO were 0·5, 1, 1·5, 2, 2·5, 3, 3·5, 4, 5 and 10 V in the 0·01 M H_2SO_4 electrolyte solution. The effect of the electrolyte concentration on the response time was studied at the applied

potential 3·5 V in various concentrations of H_2SO_4 (10^{-6}, 10^{-5}, 10^{-4}, 10^{-3}, 10^{-2} and 10^{-1} M).

3. Results and discussion

3.1 *FT–IR spectra of PDMA/ITO film*

The spectra of PDMA synthesized in oxalic ($H_2C_2O_4$–PDMA), nitric (HNO_3–PDMA) and hydrochloric (HCl–PDMA) acids are shown in figure 1. The peak at ~3400 cm^{-1} can be attributed to the secondary N–H stretching mode for the amine functional group. The band at 1570 cm^{-1} belongs to the C=N and C=C stretching modes of the benzenoid ring. The quinoid and benzenoid peaks of PDMA at ~1490 and 1580 cm^{-1} cannot be clearly observed. This may be due to the overlapping with the aromatic C=C stretching bands ranging from 1400 to 1600 cm^{-1} (Neelgund *et al* 2008). The weak band at ~1647 cm^{-1} is indicative of the presence of the carbonyl group C=O contained in the oxalate ion (Patil *et al* 2004). The FT–IR spectrum of HNO_3–PDMA includes an additional peak at 1384 cm^{-1} corresponding to the nitrate group acting as a counter ion with the protonated amine (Blinova *et al* 2009). The FT–IR results suggest that the acid-doped PDMA films are in the emeraldine and pernigraniline forms. In addition, the quinoid and benzenoid peaks appear in the spectra and the dark-green synthesized PDMA films suggest the dominance of the emeraldine and pernigraniline forms of the acid-doped PDMA films.

3.2 *Thermogravimetric analysis*

Decomposition temperatures of TGA curves indicate that all PDMA samples decompose in the same three steps (Sapp *et al* 1998). The initial weight loss at ~130 °C is due to the loss of water bound molecules or moisture. The next weight loss for PDMA at the temperature ~300 °C can be attributed to the removal of the dopant anions (Neelgund *et al* 2008). The third weight loss at ~450 °C indicates structural decomposition of the polymer chain.

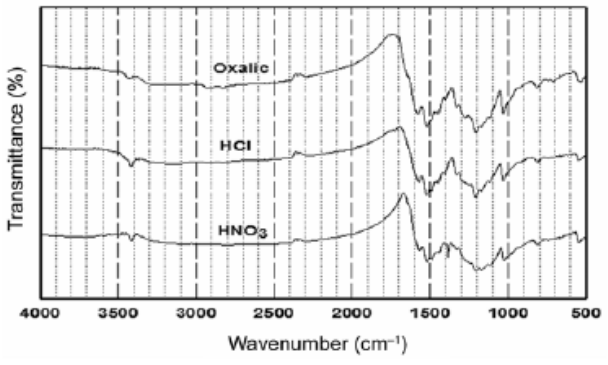

Figure 1. FT–IR spectra of PDMA film synthesized in oxalic acid, HCl and HNO_3 as electrolyte solutions.

3.3 *Morphology of PDMA surface*

Morphology of PDMA is different depending on the acids used (figure 2); the type of acid plays an important role in directing the morphology or in aligning the synthesized polymer. $H_2C_2O_4$–PDMA shows a highly porous microfibre structure (Roy *et al* 2001), while the structure of HNO_3–PDMA becomes a more disordered microfibre. The morphology of HCl–PDMA appears as an ordered tiny-granular aggregate. This is due to the smaller doping acid size ($Cl^- < NO_3^- < C_2O_4^{2-}$); it can occupy more accessible spaces within the chain, leading to a more compact morphology, consistent with previous work (Melato *et al* 2009; Kiani *et al* 2012). Melato *et al* (2009) studied the electro-polymerization condition of poly(3,4-ethylenedioxythiophene) under different supporting electrolytes ($LiClO_4$, $TBAClO_4$ and $TBAPF_6$). The morphology of the film using $LiClO_4$ was more compact than those of the other electrolytes, because the smaller cation size (Li^+) was more accessible to the polymer structure. The slightly higher size of PF_6^-, occupied a larger space than ClO_4^- leading to a less compact structure (Melato *et al* 2009). In all acids, as the polymerization continued, the surface morphology became more disordered and accompanied by particle aggregation. The polymerization time changed the morphology of the polymer film and induced particle fusion (Hernandez-Perez *et al* 2001). On the other hand, Hernandez-Perez *et al* (2001) investigated the morphology of polypyrrole (PPy) film which was prepared by potentiostatic and voltammetric methods on a platinum electrode at various electropolymerization times (50 ms, 200 ms and 5 s). The fusion of PPy cluster formed a smooth compact film (Hernandez-Perez *et al* 2001).

3.4 *Thickness of PDMA on ITO substrate*

Thickness of the PDMA films was analysed by cross-sectional FE–SEM monographs. At a longer polymerization time, the PDMA film is thicker (Kang *et al* 2009). PDMA was synthesized during the polymerization times of 3, 6 and 10 min. The thicknesses of $H_2C_2O_4$–PDMA film are 109 ± 5, 144 ± 5 and 164 ± 8 nm, respectively. The thicknesses of HNO_3–PDMA films are 140 ± 5, 166 ± 9, 188 ± 8 nm, respectively. The thicknesses of the HCl–PDMA films are 78 ± 3 nm and 104 ± 2 nm at 6 and 10 min deposition time, respectively. The HCl–PDMA film produces the thinnest film at the same polymerization time because of the slow polymerization rate. The slow polymerization rate is due to the lack of oxygen atoms in the acid molecules causing no oxygen linkage

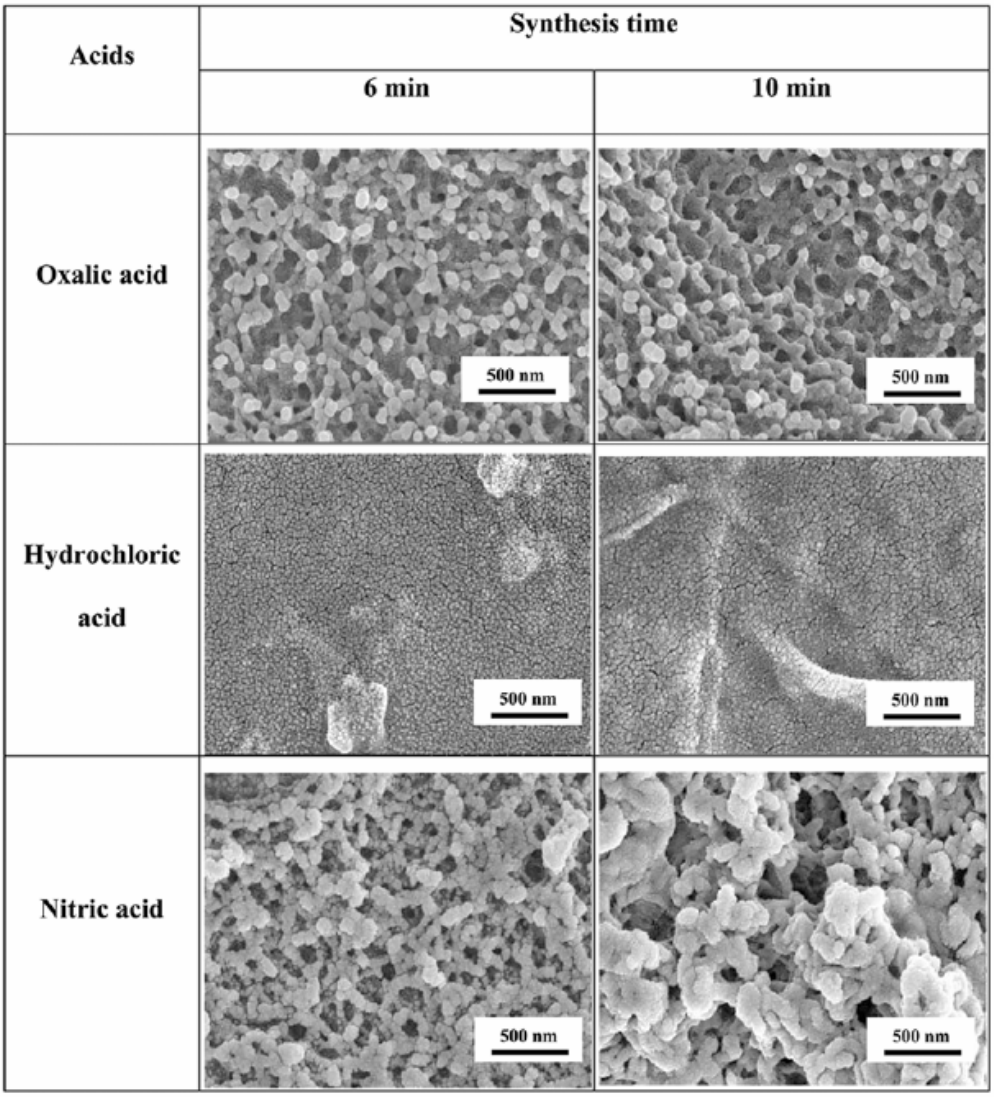

Figure 2. Surface morphology of PDMA film synthesized in oxalic acid, HCl and HNO_3 as electrolyte solutions at 6 and 10 min deposition times.

between the ITO surface and the DMA monomer (Camalet *et al* 1998; Patil *et al* 2004).

3.5 *UV absorption spectrum of PDMA*

UV absorption spectra of the synthesized PDMA films, exhibit a band at λ_{max} ~ 750 nm corresponding to the pernigraniline form. At −1 V, the spectrum shows an absorption band at λ_{max} = 480 nm corresponding to the reduced state (leucoemeraldine) which disappears upon oxidation (Neves *et al* 2004; Huang *et al* 2006).

3.6 *Colouration kinetics of PDMA*

3.6a *Response and reversibility of poly(2,5-dimethoxyaniline) film*: The absorption spectra of $H_2C_2O_4$–PDMA, HNO_3–PDMA and HCl–PDMA films recorded at 1 V with 2 min interval in 0·01 M H_2SO_4 show two absorption bands at λ_{max} ~ 480 and ~ 750 nm. Figure 3(a and b) show the absorption spectra of $H_2C_2O_4$–PDMA film obtained from the oxidation and reduction reactions, respectively. The band at λ_{max} ~ 480 nm corresponds to the reduced state (leucoemeraldine). This band disappears upon an oxidation reaction, while the band appearing at λ_{max} ~ 750 nm corresponds to the oxidation state of PDMA or the pernigraniline form (figure 3a). For the reduction process, under applied potential of −1 V as shown in figure 3(b), the band at λ_{max} ~ 750 nm disappears, while the band at λ_{max} ~ 480 nm is observed, because the transformation of the oxidized pernigraniline form to the reduced leucoemeraldine form. Thus, the PDMA film can be switched from yellow (leucoemeraldine form) to blue

(pernigraniline form) and blue to yellow via the redox switching process under applied negative and positive potentials. The electrolyte type is not critical to the absorption spectra, where the absorption spectra of HNO_3–PDMA and HCl–PDMA are similar to that of $H_2C_2O_4$–PDMA, but it affects the response time.

3.6b *Effect of testing potentials on response time:* The study of the kinetic colouration of the PDMA-coated ITO electrode was carried out via the kinetic mode of a UV–Visible spectrometer. The wavelength 750 nm, representing the oxidized state, was used to identify the response time and the optical contrast between the redox states.

The effect of the testing potentials (1–3·5 V) in 0·01 M H_2SO_4 electrolyte on the reduction time, oxidation time and response time of $H_2C_2O_4$–PDMA, HNO_3–PDMA and HCl–PDMA films at various synthesis times are shown in figure 4. The reduction time, oxidation time and response time decrease with increase in the electrical potential for all PDMA samples as the increase in electrical potential induces electrical conductivity and promote the redox process colour changing mechanism (Abd-Elwahed and Holze 2002). At 6 min synthesis time, the response time of PDMA decreases from 290 to 21 s for $H_2C_2O_4$–PDMA film (figure 4a), 515 to 38 s for HNO_3–PDMA film (figure 4b) and 182 to 3·7 s for HCl–PDMA film (figure 4c) as the applied potential increases from 1 to 3·5 V. At the

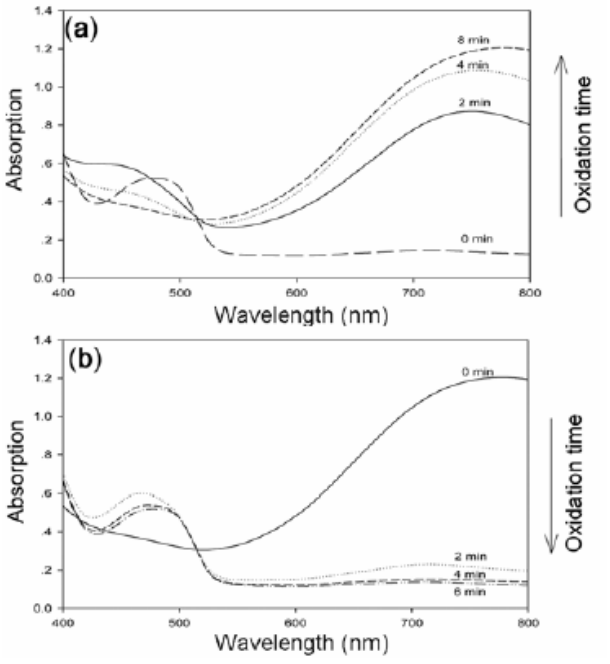

Figure 3. The absorption spectra of $H_2C_2O_4$–PDMA synthesized at 3 min deposition time in 0·01 M H_2SO_4: (**a**) oxidized state at the applied potential of +1 V and (**b**) reduced state at the applied potential of –1 V.

10 min synthesis time, the response time of PDMA decrease from 385 to 25·5 s, 1310 to 35 s and 350 to 15 s for $H_2C_2O_4$–PDMA, HNO_3–PDMA and HCl–PDMA films, respectively (figure 4), when the applied potential increases from 1 to 3·5 V. The fastest response time of $H_2C_2O_4$–PDMA and HNO_3–PDMA films are 12·8 and 20 s, respectively, for 3 min synthesis and at the testing potential of 3·5 V (figure 4(a and b)). The faster response time for HCl–PDMA film is 3·7 s of 6 min and at the testing potential shown in figure 4(c).

The results of the response time of PDMA from various acids indicate that the increase in the polymerization time contributes to the increase in the thickness of the PDMA films and a more compact structure, resulting in slower response time. Moreover, the HCl–PDMA film shows the fastest response time (3·7 s) relative to other acids at the same synthesis time, because it produces the thinnest film and the smallest doping acid size resulting in a faster doping process (Palaniappan *et al* 2012). Furthermore, it is found that the 3·7 s response time of the HCl–PDMA is faster than the ITO/PDMA||$LiClO_4$–PC–PEO (400,000)||WO_3/ITO device (Huang *et al* 2002), since liquid electrolyte has greater ion mobility than gel electrolyte.

3.6c *Effect of electrolyte concentration on response time*: Since, the fastest response time for all acids was obtained at 3·5 V, this potential was used to study the effect of electrolyte concentration on response time of PDMA. In addition, the $H_2C_2O_4$–PDMA and HNO_3–PDMA films for 3 min and HCl–PDMA synthesized for 6 min showed the fastest response times, hence, these films were further used to study the effect of electrolyte concentration.

The PDMA-coated ITO plastics were tested at 3·5 V in various concentrations of H_2SO_4. Figure 5 shows that the increase in the electrolyte concentration from 10^{-6} to 10^{-2} M results in a reduction of the response time from 460 to 13·5 s, 760 to 36 s and 160 to 3·7 s for $H_2C_2O_4$–PDMA, HNO_3–PDMA and HCl–PDMA films, respectively. The HCl–PDMA film is the thinnest, consequently, it has the fastest response time. In addition, the response time decreases with increasing H_2SO_4 concentration as a higher electrolyte concentration has more protons and higher mobility, resulting in a faster response time (Zhu and Mu 2001). Ram and co-workers (1997) studied the switching response time of poly(aniline-co-*o*-anisidine) film based on the effect of HCl concentration. They showed the decrease in response time with increase in HCl concentration. Furthermore, Habib and Glueck (1989) reported that the response time of tungsten oxide film decreased with increase in $LiClO_4$ concentration. In both the cases, they explained that a higher acid concentration produced a higher amount of H^+ ion (from HCl) or Li^+ (from $LiClO_4$). The diffusion rate of H^+ or Li^+ insertion into the film played a major role in the electrochromic process.

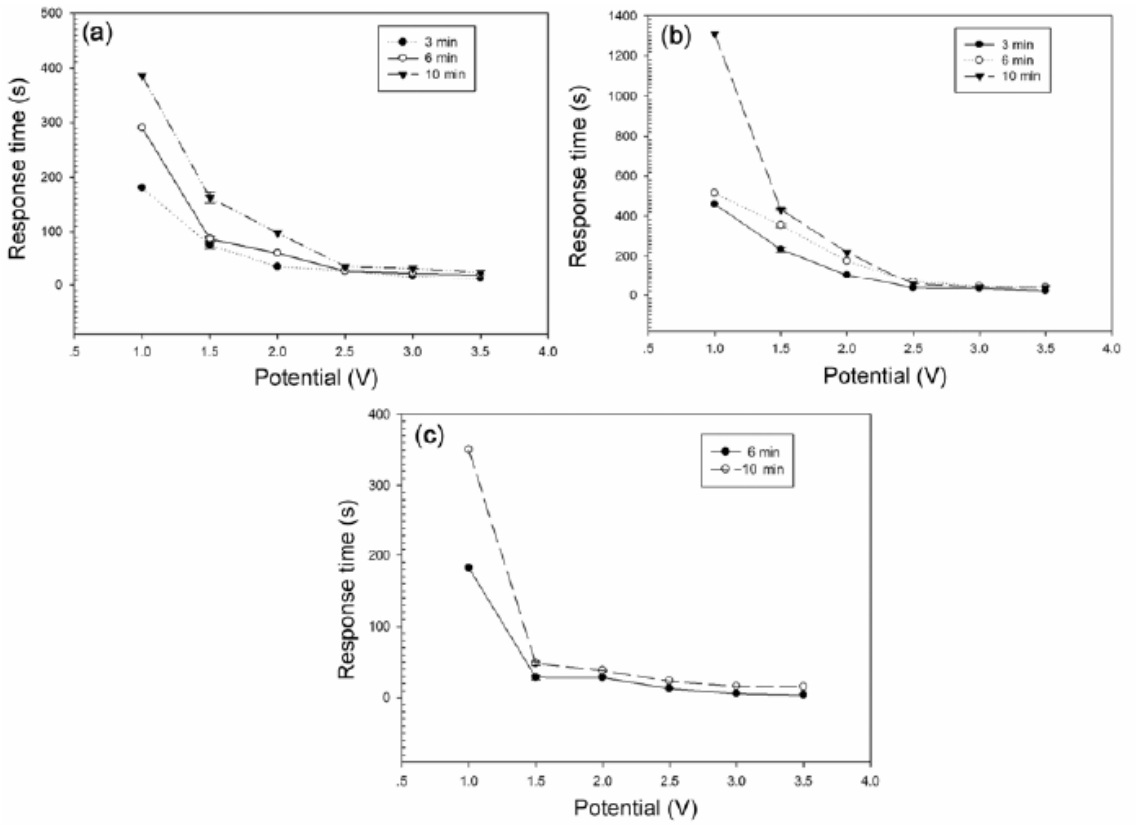

Figure 4. Effect of testing potential on response time at various synthesis times (a) $H_2C_2O_4$–PDMA; (b) HNO_3–PDMA and (c) HCl–PDMA.

3.6d *Effect of the type of acids and synthesis time on the optical contrast*: High optical contrast is an important property of an efficient electrochromic polymer. In this study, the optical contrast (ΔAbs) of PDMA/ITO was determined as the absorbance difference between the steady state values of the reduction and oxidation states. The optical contrasts of $H_2C_2O_4$–PDMA, HNO_3–PDMA and HCl–PDMA film at the 6 min deposition time are 0·372 ± 0·097, 1·770 ± 0·240 and 2·260 ± 0·360, respectively. At the polymerization time of 10 min, the optical contrasts of $H_2C_2O_4$–PDMA, HNO_3–PDMA and HCl–PDMA films are 1·170 ± 0·440, 2·010 ± 0·140 and 2·330 ± 0·300, respectively. The optical contrasts of the PDMA films slightly increase, when the polymerization time increases from 6 to 10 min due to increase in film thickness (Camalet *et al* 1998). PDMA synthesized at the same synthesis time shows optical contrasts in the order of nitric acid > oxalic acid > hydrochloric acid. It is evident that the optical contrast depends on the thickness of PDMA film (Camalet *et al* 1998; Holt *et al* 2005). The highest contrast between the bleached and the coloured forms is observed at $\lambda = 750$ nm ($\Delta T = 73\%$), which is higher than that of an ITO/PDMA electrode ($\Delta T = 23\%$) (Huang *et al* 2002). Kang *et al* (2009) studied the optical properties of PEDOT–PANI hybrid film based on the effect of polymerization time. The result showed that the optical contrast increased with increase in polymerization time. They explained that the polymerization time affected the film thickness and thus, the film optical contrast (Kang *et al* 2009). Holt *et al* (2005) reported the optical contrast of poly(phenylene vinylene) and PPV, based on the effects of applied voltage and salt type. The optical contrast of PPV increased with increase in applied voltage as the higher applied voltage created a greater film thickness, resulting in higher optical contrast. Furthermore, the type of anionic salt (TBA and triflate) affected the optical contrast, because it acted as a dopant (Holt *et al* 2005).

3.7 *Cyclic voltammetry (CV) of PDMA*

All PDMA films deposited on ITO show two main redox processes in which the first peak indicates the oxidation as related to the leucoemeraldine/emeraldine (yellow to green) transformation, and the second sharp peak corresponds to the emeraldine/pernigraniline (green to blue) transformation, consistent with previous studies (Gazotti *et al* 1997; Klink *et al* 2011).

Cyclic voltammograms (CV) of $H_2C_2O_4$–PDMA at various times are shown in figure 6. The $H_2C_2O_4$–PDMA film synthesized at 10 min shows two redox peaks at –0·35/–0·85 and 0·95/1·00 V (E_{pa}/E_{pc}). There are two reduction peaks which appear at 0·80 and 0·85 V for $H_2C_2O_4$–PDMA film synthesized at 6 min and 0·65 and 0·90 V for $H_2C_2O_4$–PDMA film synthesized at 3 min. The oxidation peaks appear at –0·55 and –0·40 V for the 6 and 3 min deposition times, respectively. In this work, it is difficult to observe two oxidation peaks because of the anionic effect (Palys *et al* 2000) hindering the polymer oxidation by the large anion ($C_2O_4^{2-}$) resulting in the board peak as previously shown by Palys *et al* (2000). Furthermore, they reported the shapes of PDMA cyclic voltammograms strongly depended on the anion type (ClO_4^-, SO_4^-, Cl^- and CCl_3COO^-). The oxidation peak current increases, while the reduction peak current decreases with increasing polymerization time, resulting in the expansion of the current–potential curve area due to the increase in film thickness or a higher specific capacitance (Chiu *et al* 1992; Sun *et al* 2013). As the polymerization time increases, the oxidation–reduction potentials of PDMA of all acids shift to being more positive and negative, due to the greater diffusion times of the counter ion for the redox reaction through the thicker films. Chui *et al* (1992) studied the effect of polypyrrole film thickness on cyclic voltammograms. The current–potential curve expanded and the potential difference ($\Delta E_p = E_{pa}–E_{pc}$) increased with the increase in film thickness as the amount of dopant increased. However, they obstructed further anions permeation, thus, higher potential was required for anion movement on the film.

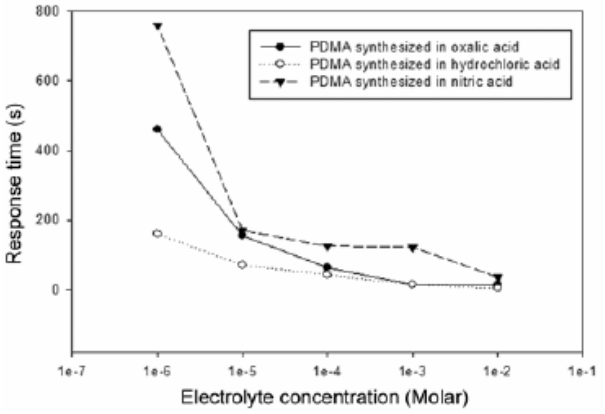

Figure 5. Effect of H_2SO_4 concentration on response time at 3·5 V of PDMA coated electrochemically polymerized ITO.

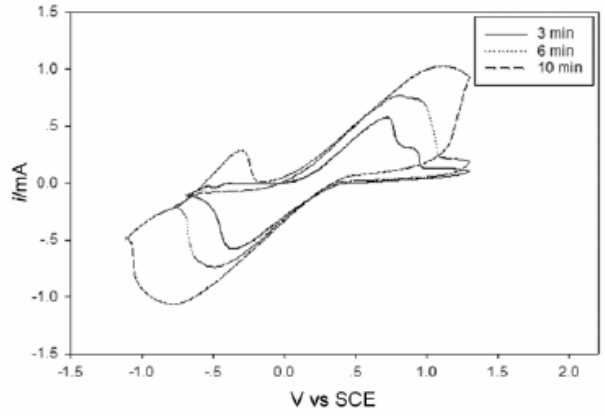

Figure 6. Cyclic voltammograms of $H_2C_2O_4$–PDMA film at 3, 6 and 10 min deposition times within the potential range of –1 to 1·5 V; a scan rate of 10 mV/s and a 0·01 M of H_2SO_4 electrolyte solution background.

On the other hand, Elmansouri *et al* (2007, 2009) showed that the oxidation potentials and currents of different supporting electrolytes depended on the nature and size of the anion present in the solution. The oxidation current was proportional to the speed of the electropolymerization reaction, this suggested faster growth kinetics. The oxidation current increased with increase in film thickness, as a function of the growth kinetics (Elmansouri *et al* 2007, 2009).

4. Conclusions

The synthesized PDMA films show reversible colour change from yellow to green representing the transition between the leucoemeraldine (reduced) state and emeraldine (oxidized) state which depend on the switching potentials. The PDMA/ITO electrochemically polymerized samples have mostly the same structural properties; the only difference is that the FT–IR bands show different counter ions of the oxalate and nitrate groups acting as counter ions with the protonated amine. The important differences of the PDMA synthesized in various acids at the same polymerization time are morphology and thickness of PDMA films, both factors lead to variations in the response time and the optical contrast. The increase of applied potential (1–3·5 V) and the H_2SO_4 electrolyte concentration (10^{-6}–10^{-1} M) contributed significantly to the decrease in the response time. With the increase of the polymerization time, the cyclic voltammetry showed a shift of the oxidation–reduction potentials of PDMA from all acids to being more positive and negative due to the greater diffusion time of the counter ion for the redox reaction through the thicker films.

Acknowledgements

The authors would like to acknowledge financial support from the Conductive and Electroactive Polymers Research Unit, the Petroleum and Petrochemical College, Chulalongkorn University, the Thailand Research Fund (TRF–RTA), and the Royal Thai Government.

References

Abd-Elwahed A and Holze R 2002 *Synth. Met.* **131** 61

Bange K 1999 *Sol. Energy Mater. Sol. Cells* **58** 1

Blinova N V, Stejskal J, Trchova M, Sapurina I and Marjanovic G C 2009 *Polym.* **50** 50

Brotherson I D, Mudigonda D S K, Ocborn J M, Belk J, Chen J, Loveday D C, Boehme J L and Ferraris J P 1999 *Electrochim. Acta* **44** 2993

Camalet J L, Lacroix J C, Aeiyach S, Ching K C and Lacaze P C 1998 *Synth. Met.* **93** 133

Chiu H-T, Lin J-S and Shiau J-N 1992 *J. Appl. Electrochem.* **22** 522

Elmansouri A, Outzourhot A, Lachkar A, Hadik N, Achour M E, Abouelaoualim A, Berrada K and Ameziane E L 2007 *Act. Pass. Electron. Comp.* **7** 1

Elmansouri A, Outzourhot A, Lachkar A, Hadik N, Achour M E, Abouelaoualim A, Berrada K and Ameziane E L 2009 *Synth. Met.* **159** 292

Gazotti W A J, Jannini M J D M, Torres S I C D and Paoli M A D 1997 *J. Electroanal. Chem.* **440** 193

Habib M A and Glueck D 1989 *Sol. Energy Mat.* **18** 127

Hernandez-Perez T, Morales M, Batina N and Salmon M 2001 *J. Electrochem. Soc.* **148** C369

Holt A L, Leger J M and Carter S A 2005 *Appl. Phys. Lett.* **86** 1

Huang L M, Huang G C and Wen T C 2006 *J. Polym. Sci.: Part A: Polym. Chem.* **44** 6624

Huang L M, Wen T C and Gopalan A 2002 *Mater. Chem. Phys.* **77** 726

Kang J H, Jioha Y, Minpaek S, Juhwang S and Hochoy J 2009 *Sol. Energy Mater. Sol. Cells* **93** 2040

Khan A A, Alam M M and Mohammad F 2003 *Electrochim. Acta* **48** 2463

Kiani F, Rostami A A, Omrani A, Sharifirad M, Koohyar F and Moradi A 2012 *Eur. Online J. Nat. Soc. Sci.* **1** 55

Kim Y, Do J, Kim E, Clavier G, Galmiche L and Audebert P 2009 *J. Electroanal. Chem.* **632** 201

Klink M J, Iwuoha E I and Ebenso E E 2011 *Int. J. Electrochem. Sci.* **6** 2429

Mavundla S E, Malgas G F, Baker P and Iwuohab E I 2008 *Electroanalysis* **20** 2347

Melato A L, Mendonca M H and Abrantes L M 2009 *J. Solid State Electrochem.* **13** 417

Montazami R, Jain V and Heflin R J 2010 *Electrochim. Acta* **56** 990

Neelgund G M, Hrehorova E, Joyce M and Bliznyuk V 2008 *Polym. Int.* **57** 1083

Neves S, Santos R F, Gazotti W A and Fonseca C P 2004 *Thin Solid Films* **460** 300

Palaniappan S, Chang Y-T, Liu C-M and Manisankar P 2012 *J. Appl. Polym. Sci.* **124** 4281

Patil V, Sainkar S R and Patil P P 2004 *Synth. Met.* **140** 57

Palys B, Kudelski A, Stankiewicz A and Jackowska K 2000 *Synth. Met.* **108** 111

Peters A T and Freeman H S 1991 *Colour chemistry: The design and synthesis of organic dyes and pigments* (Baraking Essex, UK: Elsevier Applied Science Publishing) p. 193

Ram M K, Maccioni E and Nicolini C 1997 *Thin Solid Films* **303** 27

Ramakrishnan S 1997 *Resonance* **2** 48

Roy C B, Gupta D M, Bhowmik L and Ray K J 2001 *Bull. Mater. Sci.* **24** 389

Sapp S A, Sotzing G A and Reynolds J R 1998 *Chem. Mater.* **10** 2101

Sarkar N, Ram M, Sarkar A, Narizzano R, Paddeu S and Nicolini C 2000 *Nanotechnol.* **11** 30

Sonmez G 2005 *Chem. Commun.* **42** 5251

Sun M, Wang W, He B, Sun M, Liu W, Ge H, Zhang Q and Sun F 2013 *J. Appl. Polym. Sci.* 4672

Zhu H and Mu S 2001 *Synth. Met.* **123** 293

Research Article

Received: 16 January 2014 Revised: 23 March 2014 Accepted article published: 9 April 2014 Published online in Wiley Online Library: 12 May 2014

(wileyonlinelibrary.com) DOI 10.1002/pi.4745

Synthesis of polydiphenylamine with tunable size and shape via emulsion polymerization

Tharaporn Permpool,[a] Anuvat Sirivat[a*] and Darunee Aussawasathien[b]

Abstract

The emulsion polymerization process was used in the synthesis of polydiphenylamine (PDPA) to obtain new morphologies, and the effects of surfactant types – anionic, cationic, non-ionic – and surfactant concentrations were investigated with the roles of a template and a dopant. Scanning electron microscopy images indicated different PDPA morphologies depending on the surfactant type. The new morphological structures of the obtained PDPA were leaf-like, coral-reef-like and red-blood-cell-like, which have not been synthesized or seen before. The agglomeration of each nanoparticle is in the range of 50 nm to 500 nm depending on the surfactant type. The structure characterizations carried out by Fourier transform infrared spectroscopy, X-ray diffractometry and UV–visible spectroscopy confirm the incorporation of surfactant in the PDPA. The electrical conductivity values of the PDPA with surfactants are higher than that without a surfactant by four orders of magnitude and are consistent with the resultant smaller particle sizes and narrower optical band gap as calculated from UV–visible data. To induce higher electrical conductivity of PDPA, various dopants were used. However, the thermal stability of the PDPA is lower than that of conventional microscopic PDPA (cPDPA) due to the larger surface area of PDPA which can decompose more easily.
© 2014 Society of Chemical Industry

Supporting information may be found in the online version of this article.

Keywords: conducting polymer; polydiphenylamine; emulsion polymerization; surfactant; nanostructure

INTRODUCTION

Nanoscience and nanotechnology are of interest among many investigators because the properties of nanomaterials and bulk materials are quite different. Nanomaterials have large effective surface area, low density, and distinct optical, physical, chemical, electronic and magnetic properties.[1,2] Control over the size and shape of the nanomaterials plays an important role in tuning their unique properties.[1] Various synthesis strategies, such as hard/soft template,[1–4] rapid mixing,[5] emulsion,[6] chemical, electrochemical,[7] mechanochemical[8] and interfacial[9,10] polymerization, have been widely employed to control the shape and size. These approaches are of growing interest in the conductive polymer field[1] because conductive polymers on a nano scale are known to exhibit several advantages over micro scale polymers for various applications: sensors, actuators, electrochromic materials, drug delivery systems.[11–14] Nanostructure conductive polymers have been synthesized and reported: polyaniline,[15–17] polypyrrole,[17] polythiophene[18] and poly(3,4-ethylenedioxythiophene).[1,19] Polydiphenylamine (PDPA) has better solubility and processibility than polyaniline. Several investigators have tried to synthesize nanostructure polydiphenylamine (nPDPA) by several techniques such as electrochemical,[20,21] chemical oxidative[7] and mechanochemical[8] polymerization.

To date, there has been no report about synthesizing nPDPA by the emulsion polymerization technique. In this work, emulsion polymerization was used to synthesize and to control the size and shape of nPDPA by incorporating different surfactants – anionic, cationic and non-ionic. The surfactant concentration, morphology, particle size, crystallinity, electrical conductivity, optical band gap and thermal stability of nPDPA are investigated and compared with conventional micro scale nPDPA (cPDPA).

EXPERIMENTAL

Materials

Diphenylamine (Sigma Aldrich, Missouri, USA) was used as a monomer, ammonium persulfate (Riedel-de Haën, Missouri, USA) was used as an oxidant, and hydrochloric acid (37% v/v; J.T. Baker, New Jersey, USA) was used as a protonic acid. Sodium dodecyl sulfate (SDS) (Lobachemie, India), cetyltrimethylammonium bromide (CTAB) (Sigma Aldrich, Missouri, USA) and polyoxyethylene (20) sorbitan monooleate (TW80) (ICI Americas Inc., England) were used as substrate surfactants and dopants. Perchloric acid (70% v/v; RANKEM, India), sulfuric acid (98% v/v; UNIVAR, Australia) and nitric acid (70% v/v; Sigma Aldrich, Missouri, USA) were used as doping agents with a doping mole ratio ($N_{HCl}/N_{monomer}$) of 100:1.[22] Methanol (AR grade, Lab Scan, Thailand) was used as a solvent without additional purification.

* *Correspondence to:* Anuvat Sirivat, Petroleum and Petrochemical College, Chulalongkorn University, Bangkok 10330, Thailand.
E-mail: *anuvat.s@chula.ac.th*

a *Petroleum and Petrochemical College, Chulalongkorn University, Bangkok 10330, Thailand*

b *National Metal and Materials Technology Center, National Science and Technology Development Agency, Ministry of Science and Technology, Pathumthani 12120, Thailand*

Preparation of nPDPA by emulsion polymerization

A pure surfactant (SDS, CTAB or TW80) was dissolved in distilled water at various concentrations from 0.001 mol to 1 mol and stirred continuously for 1 h at room temperature. Next, diphenylamine monomers (0.55 mol L^{-1}) and hydrochloric acid solution (0.55 mol L^{-1}) were added to the surfactant solution, and then continuously stirred for 1 h at room temperature. Ammonium persulfate (0.55 mol L^{-1}) was gradually added to the diphenylamine solution at 0 °C and stirred continuously for 15 h at 0 °C. The green nPDPA product was washed with methanol, centrifuged at least three times until the supernatant solution became colorless[6] and dried at 80 °C for 24 h to get rid of residual water and surfactants. The mole ratios of the monomer to surfactant were 1:0.001, 1:0.01, 1:0.1, 1:0.5 and 1:1.

Characterization

The critical micelle concentration (CMC) of the three surfactants was determined by measuring the surface tension of the pure surfactant with a tensiometer (Kruss/Easydyne tensiometer, K20) using the plate method.[23,24] The three surfactants were dissolved in distilled water at various concentrations (0.001% v/v to 1% v/v) at 25 °C. Surface tension was recorded eight times and averaged for each sample.

The Fourier transform infrared (FTIR) spectra of the nPDPA samples were investigated with an FTIR spectrometer (Thermo Nicolet, Nexus 670). All the samples were pelletized with KBr in the wavenumber range 4000–400 cm^{-1}.

The morphology of the nPDPA samples was investigated with a scanning electron microscope (Hitachi, S-4800 FESEM) operating at 10 kV and with a magnification of 30k. The particle sizes of the nPDPA samples were measured with SEMAFORE 5.21 software.

The conductivity of all nPDPA samples was investigated by a custom-built two-point probe. A conductivity meter (Keithley 6517A) was connected to the probe and the current was measured in response to the applied voltage.[25–28] The sample was compressed in a circular disk form with a diameter of 1.30 cm. The electrical conductivity of the samples was calculated using the equation

$$\sigma = I/KVt \tag{1}$$

where I is the measured current (A), V is the applied voltage (V), t is the sample thickness (cm) and K is the geometric correction factor which is equal to the ratio w/l, where w and l are the probe width and length, respectively (2.15×10^{-3}). The measurement of K is described in the supporting information.

The absorption spectra of all nPDPA samples were investigated by UV–visible spectroscopy (Shimadzu, UV 1800) over wavelength numbers from 200 nm to 500 nm in the absorption mode at room temperature. The Tauc relation was used to calculate the energy band gap from the absorption spectra:[29–32]

$$ah\nu = A\left(h\nu - E_g\right)^n \tag{2}$$

where α is the absorption coefficient, $h\nu$ is the photon energy, h is Planck's constant, A is a constant and E_g is the optical energy gap, for direct transition $n = 1/2$.[31] The absorption coefficient α is calculated using Beer–Lambert's relation:[29]

$$a = (2.303\mathrm{Ab})/l \tag{3}$$

where Ab is the absorbance and l is the sample path length. The extrapolation of the straight line to the $(\alpha h\nu)^2 = 0$ axis from the plot between $(\alpha h\nu)^2$ and $h\nu$ gives E_g.

The thermal degradation of nPDPA was performed with a thermogravimetric analyzer (Perkin–Elmer TGA 7). The sample powder, ~ 5–10 mg, was placed in an alumina pan and then heated at a heating rate of 10 °C min^{-1} from 30 °C to 900 °C under a nitrogen flow.[8]

The XRD patterns of all nPDPA samples were recorded on an X-ray diffractometer (Rigaku/smartlab) operated at a scan range of 5°–60°, scan step 0.01°, scan speed 5° min^{-1}, 30 mA and 40 kV.[22] The percentage of crystallinity of each nPDPA sample was determined using the equation

$$\%\ \text{crystallinity} = \left[A_c/\left(A_c + A_b\right)\right] \times 100 \tag{4}$$

where A_c is the total area of the crystalline portions and A_b is the total area of the amorphous portions.

RESULTS AND DISCUSSION

Morphology

nPDPA was prepared by the emulsion polymerization method using three surfactants (anionic, SDS; cationic, CTAB; non-ionic, TW80) as a template in order to control the size and shape of the particles (Fig. 1). Table 1 compares the nPDPA particle size, shape and electrical conductivity. Figures 2–4 display the SEM images of nPDPA synthesized with SDS, CTAB and TW80, respectively. For nPDPA-SDS, the SEM images show that the particle shape changes from cylindrical, with a particle size of ~ 550 nm (Fig. 2(a)), to leaf-like with a smaller particle size of ~ 66 nm (Figs 2(b)–2(d)) with increasing monomer to SDS mole ratio. The nPDPA-CTAB are seen to be of cylindrical shape with a particle size of ~ 214 nm (Fig. 3(a)) and change to a coral reef shape with a particle size of about 56 nm (Figs 3(b)–3(d)) with increasing monomer to CTAB mole ratio. The nPDPA-TW80 are spherical with a particle size of ~ 343 nm (Fig. 4(a)) and change to a red blood cell shape with a particle size of ~ 64 nm with increasing monomer to TW80 mole ratio. The differences in the morphological structures of nPDPA can be traced to the micelle shape of each surfactant, which depends on the packing parameter.[33,34] The packing parameters of SDS, CTAB and TW80 are 0.5, 0.5 and 1, respectively. Consequently, this results in a cylindrical shape for SDS and CTAB and a vesicle shape for TW80. The CMC concentrations of SDS, CTAB and TW80 are 3.5×10^{-5} mol L^{-1}, 4.12×10^{-4} mol L^{-1} and 8.092×10^{-3} mol L^{-1}, respectively. At a surfactant concentration below the CMC point (0.001 × CMC), polymerization occurs without micelle formation. The resultant nPDPA has large particle sizes. At a surfactant concentration above the CMC point (5–10 × CMC), micelles are formed. The resultant nPDPA is polymerized within the micelles. The size and shape of the nPDPA are controlled by the micelle shape. Therefore, nPDPA with SDS and CTAB appears cylindrical while nPDPA with TW80 has a vesicle shape. However, a cluster of particles can be seen in the SEM images due to physical adsorption on the surface of the nPDPA (Figs 2–4).[20] Hence, particles of nPDPA aggregate and form a leaf shape (SDS), coral reef shape (CTAB) and a red blood cell shape (TW80). In comparison with other research work on nPDPA synthesis with different polymerization methods, the morphology of the present nPDPA is different (Table 2). Zhao *et al.*[20] synthesized nPDPA nanofibrils by electrochemical polymerization using porous anodic aluminum oxide as a template. The morphology of nPDPA was nanofibrils with a diameter of ~ 80 nm. Santhosh *et al.*[21] successfully prepared hollow spherical nPDPA, with an inner diameter in the range 40–90 nm and an outer diameter of about 60–110 nm, by performing *in situ* polymerization using

 © 2014 Society of Chemical Industry

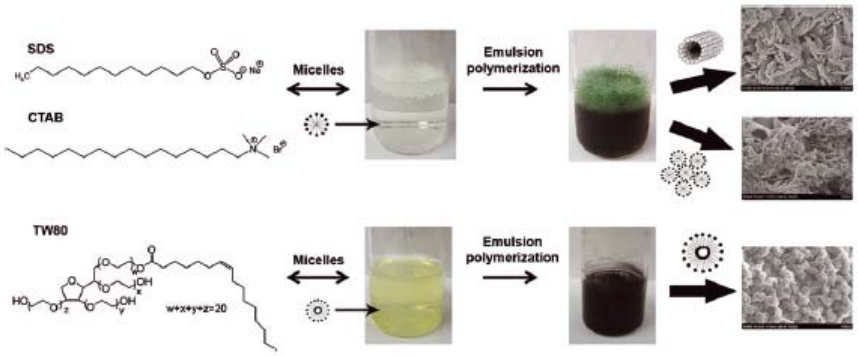

Figure 1. Synthesis of nPDPA via emulsion polymerization using anionic (SDS), cationic (CTAB) and non-ionic (TW80) surfactants.

Table 1. Electrical conductivity and particle size of synthesized nPDPA under different synthesis conditions

Polymer	Monomer:surfactant mole ratio	Shape	Particle size (nm)	Conductivity (S cm^{-1})	Remark
cPDPA	1:0	Irregular	1715.56 ± 249.76	(1.72 ± 0.19) × 10^{-7}	APS as an oxidant 1.1 × 10^{-4} mol HCl as a protonic acid 1.1 × 10^{-2} mol Stir continuously at 5 °C for 15 h
nPDPA-SDS	1:0.001	Cylindrical	549.30 ± 13.56	(5.29 ± 0.01) × 10^{-7}	APS as an oxidant 1.1 × 10^{-4} mol HCl as a protonic acid 1.1 × 10^{-2} mol Stir continuously at 5 °C for 15 h
	1:0.01	leaf	476.90 ± 21.25	(6.47 ± 0.87) × 10^{-7}	
	1:0.05	leaf	147.33 ± 21.23	(2.64 ± 0.06) × 10^{-6}	
	1:0.5	leaf	107.22 ± 33.80	(6.55 ± 2.08) × 10^{-4}	
	1:1	leaf	66.33 ± 13.86	(6.50 ± 1.30) × 10^{-4}	
nPDPA-CTAB	1:0.001	Cylindrical	214.12 ± 38.20	(5.16 ± 2.08) × 10^{-7}	APS as an oxidant 1.1 × 10^{-4} mol HCl as a protonic acid 1.1 × 10^{-2} mol Stir continuously at 5 °C for 15 h
	1:0.01	coral reef	197.13 ± 37.03	(1.76 ± 0.72) × 10^{-6}	
	1:0.05	coral reef	102.78 ± 9.55	(2.35 ± 0.39) × 10^{-5}	
	1:0.5	coral reef	75.33 ± 12.63	(1.74 ± 0.72) × 10^{-3}	
	1:1	coral reef	56.00 ± 14.66	(1.64 ± 0.30) × 10^{-3}	
nPDPA-TW80	1:0.001	Spherical	342.50 ± 42.29	(7.95 ± 0.05) × 10^{-6}	APS as an oxidant 1.1 × 10^{-4} mol HCl as a protonic acid 1.1 × 10^{-2} mol Stir continuously at 5 °C for 15 h
	1:0.01	Red blood cell	112.46 ± 19.92	(2.71 ± 2.20) × 10^{-5}	
	1:0.05	Red blood cell	86.30 ± 15.71	(1.48 ± 0.35) × 10^{-3}	
	1:0.5	Red blood cell	71.49 ± 12.75	(8.00 ± 0.38) × 10^{-3}	
	1:1	Red blood cell	64.18 ± 16.12	(7.80 ± 1.04) × 10^{-3}	

β-naphthalene sulfonic acid as a soft template. Palaniappan and Manisankar[8] synthesized nPDPA by mechanochemical polymerization at room temperature. The morphology of nPDPA was lamellar (~ 100 nm), granular (~ 80 nm) and non-uniform (~ 1 μm) with hydrochloric acid, sulfuric acid and phosphoric acid respectively as doping agents.

Structure characterization

FTIR study

The FTIR absorption spectra and the assignment of FTIR bands of cPDPA and nPDPA prepared in the presence of SDS, CTAB and TW80 are shown in Fig. 5 and Table 3, respectively. The absorption bands at 3388 and 3053 cm^{-1} represent the N–H stretching and C–H stretching in the aromatic rings, respectively.[35] The bands at 1594, 1505 and 1318 cm^{-1} correspond to quinoid ring stretching,[36] phenyl hydrogen[37] and benzenoid ring stretching,[38] respectively. The bands at 1173, 821 and 748 cm^{-1} are due to the vibration band of the nitrogen atom in the quinoid ring stretching,[39,40] C–H out of plane aromatic and 1,4 substituted on aromatic rings, respectively.[38] However, there are new additional bands appearing in the FTIR spectra of nPDPA. Absorption bands in the range 3000–2800 cm^{-1} are detected in the spectra of nPDPA with SDS and CTAB, which can be assigned to aliphatic C–H stretching in the long alkyl chain of the surfactants.[18,41] An absorption band at 1735 cm^{-1} is detected in the spectrum of nPDPA with TW80. This indicates the presence of a hydroxyl group in the TW80 structure.[18,41] The presence of absorption bands indicates the presence of surfactants in the polymer. Moreover, a few FTIR peak shifts are noticed, suggesting an interaction between the surfactant and the polymer.[18] For nPDPA-SDS, the bands at 1220 cm^{-1} and 1083 cm^{-1} belonging to S–O stretching on the covalent sulfate of neat SDS[41] shift to 1230 cm^{-1} and 1037 cm^{-1}, respectively. For nPDPA-CTAB, the band at 1403 cm^{-1}, which can be assigned to C–N stretching in the CTAB structure,[41] shifts to 1401 cm^{-1}. For nPDPA-TW80, the band at 1396 cm^{-1}, which can be assigned to the –O– in the TW80 structure, shifts to 1351 cm^{-1}. It can be concluded that nPDPA was successfully synthesized by emulsion polymerization with different surfactants (anionic, cationic, non-ionic) and that some residual surfactant molecules still interact with the conductive polymer.

© 2014 Society of Chemical Industry

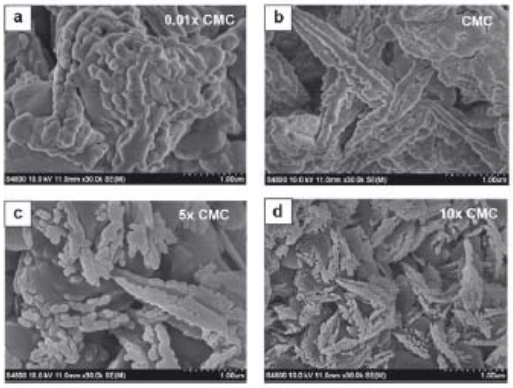

Figure 2. SEM micrographs of nPDPA-SDS at mole ratios of (a) 1:0.001, (b) 1:0.01, (c) 1:0.5 and (d) 1:1.

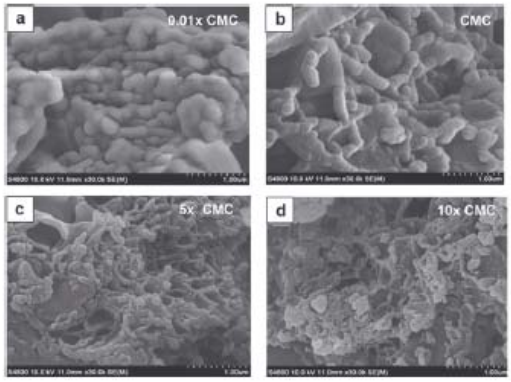

Figure 3. SEM micrographs of nPDPA-TW80 at mole ratios of (a) 1:0.001, (b) 1:0.01, (c) 1:0.5 and (d) 1:1.

XRD study

All of the XRD peaks shown in Fig. 6, nPDPA-SDS_1-0.5 (Fig 6(a)), nPDPA-CTAB_1-0.5 (Fig 6(b)), nPDPA-TW80_1-0.5 (Fig 6(c)), correspond to cPDPA (Fig. 6(d)). In addition, the amounts of crystallinity in nPDPA in the presence of SDS, CTAB and TW80 are 6.85%, 7.69% and 13.58%, respectively. The difference in the crystallinity of nPDPA is due to the difference in interaction between nPDPA and the surfactants. The degrees of crystallinity of nPDPA-SDS and nPDPA-CTAB are less than cPDPA because electrostatic interactions between the head groups of SDS and CTAB and a positive charge of the polaron on the nPDPA chain exist. For SDS, the attractive force between the anionic head group of SDS and the positive charge on the nPDPA chain induces the aggregation of nPDPA particles resulting in low crystallinity. For CTAB, the repulsive force between the cationic head group of CTAB and the positive charge on the nPDPA chain creates interfaces between nPDPA molecules, resulting in lower crystallinity of nPDPA-CTAB relative to cPDPA. The crystallinity of nPDPA-TW80 is also lower than cPDPA because of the dipole–dipole interaction between TW80 molecules, a non-ionic surfactant, which creates interfaces between nPDPA molecules.[42] From these data and results, it can be expected that the electrical conductivity of nPDPA will increase with increasing crystallinity.[43,44]

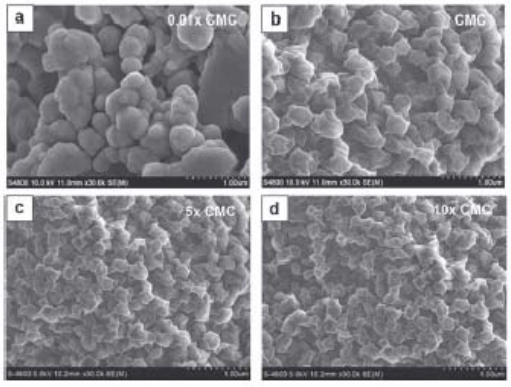

Figure 4. SEM micrographs of nPDPA-TW80 at mole ratios of (a) 1:0.001, (b) 1:0.01, (c) 1:0.5 and (d) 1:1.

UV–visible study

UV–visible spectra of nPDPA-SDS are shown in Fig. 7(a). The cPDPA spectrum shows an absorption band at 340 nm, which is assigned to the $\pi-\pi^*$ transition at $-N^+=$ on the cPDPA backbone.[20,45] In the presence of the surfactants, the absorption band of nPDPA is observed at ~ 290 nm and shifts to a longer wavelength with increasing surfactant concentration, as shown in Table 4. The incorporation of surfactant within the nPDPA structure causes the electron density along the nPDPA backbone to increase, resulting in a shorter conjugate length of polymer molecule.[46] The shift is attributed to a narrower $\pi-\pi^*$ transition of nPDPA (Fig. 7(a)).[47]

Furthermore, the optical band gap of nPDPA was calculated from the absorption spectra using the Tauc relation. The extrapolation of the straight line from the plot between $(\alpha h\nu)^2$ and $h\nu$ produces an energy band gap value (Fig. 7(b)).[29–32] The optical band gaps of nPDPA in the presence of the surfactants are tabulated in Table 4. The optical band gap value of nPDPA (2.95 eV) is less than that of cPDPA (3.83 eV). The nPDPA-TW80 sample shows the narrowest optical band gap value (1.65 eV), followed by nPDPA-CTAB (2.53 eV) and nPDPA-SDS (3.69 eV), respectively, because the surfactants may act as dopant molecules. Thus, the shifting of electrons on the nPDPA backbone occurs from the new excitation band of the benzenoid to quinoid rings ($\pi-\pi^*$ transition).[32] As the surfactant concentration increases, the band gap value decreases because there are more surfactant molecules, or more electron density on the imine nitrogen, leading to narrowing of the excitation transition ($\pi-\pi^*$ transition),[32] which is consistent with the UV–visible results.

TW80 is a non-ionic surfactant and has a hydroxyl group in the molecule. An interaction between the imine nitrogen of nPDPA and oxygen at the hydroxyl group of TW80 can occur. This interaction stabilizes the π^* orbital and reduces the energy gap between the π and π^* orbitals.[32,48] Thus, as the energy required for the $\pi-\pi^*$ transition decreases, nPDPA-TW80 possesses a rather narrow band gap.

For an ionic surfactant, the dominance of the dipole–dipole interaction also plays an important role in the $\pi-\pi^*$ transition, which is known as the inductive effect. The cationic surfactant CTAB will pull an electron from the imine nitrogen. As the electron density on the imine nitrogen increases, the dipole moment increases and vice versa.[32] Stabilization of the π^* orbital occurs leading to a lower energy requirement for the $\pi-\pi^*$ transition. An anionic surfactant such as SDS will give an electron to the

 © 2014 Society of Chemical Industry

Table 2. Comparison of synthesis methods with various nPDPA

Synthesis method	Doping agent	Shape	Average particle size (nm)	Electrical conductivity (S cm^{-1})	Reference
Electrochemical polymerization	–	Nano fibril	80	Not studied	*Materials Chemistry and Physics*, Zhao *et al.*, 2005[20]
Electrochemical polymerization	β-NSA	Hollow spherical	40–90	Not studied	*Biosensors and Bioelectronics*, Santhosh *et al.*, 2009[21]
Chemical oxidative polymerization	CH_3SO_3H	Nano rod	150–200	0.307	*Polymer Science Series B*, Massoumi *et al.*, 2010[7]
	H_2SO_4	Nano particle	150–200	2.9×10^{-3}	
Mechanochemical polymerization	HCl	Lamellar	100	0.55	*Electrochimica Acta*, Palaniappan and Manisankar, 2011[8]
	H_2SO_4	Granular	80	0.90	
	H_3PO_4	Non-uniform	>1000	0.22	

β-NSA, β-naphthalene sulfonic acid.

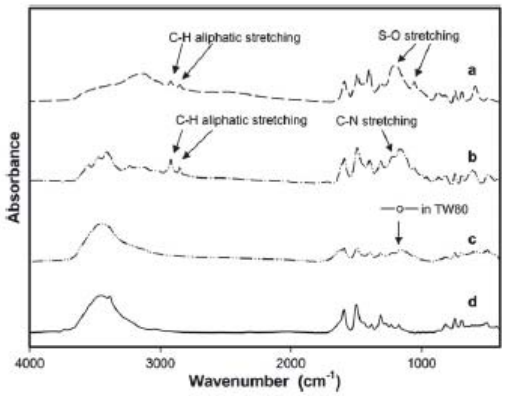

Figure 5. FTIR absorption spectra of (a) nPDPA-SDS_1-0.5, (b) nPDPA-CTAB_1-0.5, (c) nPDPA-TW80_1-0.5 and (d) cPDPA.

imine nitrogen. This will reduce the dipole moment on the nPDPA backbone leading to a higher energy band gap relative to that of nPDPA-CTAB.

Nevertheless, the interaction between the imine nitrogen and the oxygen atom of a non-ionic surfactant is more critical to the $\pi-\pi^*$ transition compared with the change of the dipole moment of the polymer backbone of an ionic surfactant. These results are consistent with previous theoretical principles.[49] Therefore the energy band gap of nPDPA-TW80 is narrower than that of nPDPA-CTAB and nPDPA-SDS.

Electrical conductivity

The conductivity of nPDPA in the presence of surfactants is higher than that of cPDPA. The highest conductivity is obtained with nPDPA-TW80, $(7.80 \pm 1.04) \times 10^{-3}$ S cm^{-1}, followed by nPDPA-CTAB, $(1.64 \pm 0.30) \times 10^{-3}$ S cm^{-1}, and nPDPA-SDS, $(6.50 \pm 1.30) \times 10^{-4}$ S cm^{-1}, compared with that of cPDPA (1.72×10^{-7} S cm^{-1}). A difference of four orders of magnitude in electrical conductivity can be observed here. Furthermore, the conductivity of nPDPA increases with increasing surfactant concentrations from 0.001 mol (0.01 × CMC) to 0.5 mol (5 × CMC), but it becomes constant as the surfactant concentration is increased to 1 mol (10 × CMC), as shown in Fig. 8. There are two reasons for the increasing electrical conductivity: (1) a surfactant molecule that remains attached to the nPDPA backbone acts as a dopant molecule and electrical conductivity increases,[50,51] a process known as counter-ion-induced doping;[52] (2) the smaller the particle size of nPDPA, the higher the surface area for electron

Table 3. Assignment of FTIR bands of nPDPA

Assignments	Wavenumber (cm^{-1})			
	cPDPA	nPDPA-SDS	nPDPA-CTAB	PDPA-TW80
N–H stretching	3388	3388	3389	3388
C–H stretching, aromatic rings	3053	3052	3053	3052
Quinoid ring stretching	1594	1592	1590	1594
Phenyl hydrogen	1505	1490	1493	1505
Benzenoid ring stretching	1318	1311	1318	1312
Vibration band of nitrogen in quinoid ring stretching	1173	1171	1173	1180
C–H out of plane aromatic	821	821	821	821
1,4 substituted on aromatic rings	748	748	748	748
C–H stretching, aliphatic	–	2917, 2849	2920, 2850	–
hydroxyl group	–	–	–	1735
S–O stretches on covalent sulfate	–	1230, 1037	–	–
C–N stretches			1401	
TW80	–	–	–	1351

© 2014 Society of Chemical Industry

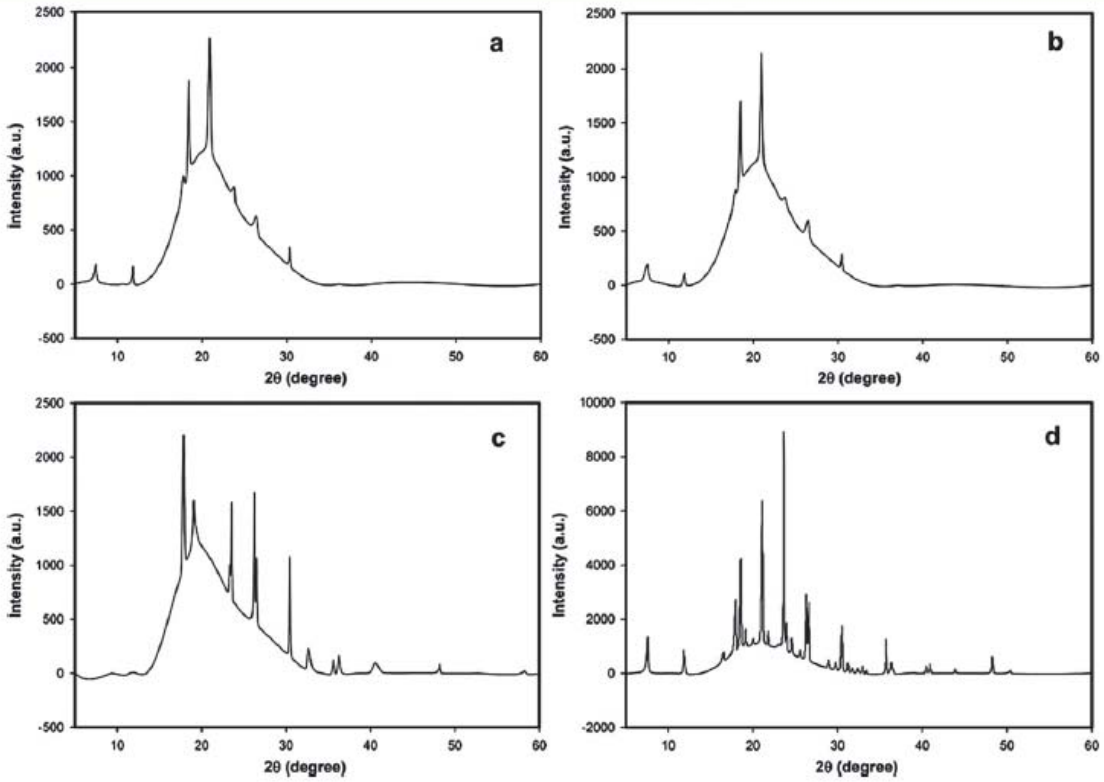

Figure 6. XRD patterns of (a) nPDPA-SDS_1-0.5, (b) nPDPA-CTAB_1-0.5 (c) nPDPA-TW80_1-0.5 and (d) cPDPA.

transfer, and thus electrical conductivity is increased.[19] The electrical conductivity of nPDPA is quite different as each surfactant acts as a doping agent. As nPDPA interacts with each surfactant, it induces a change in conductivity.[50–53] For TW80, there is a hydroxyl group in the molecule that acts as an electron withdrawing group; it pulls an electron out of the nPDPA backbone. Then the nPDPA backbone has a hole and an electron from a neighboring bond jumps to fill the hole. Thus, electrical conductivity of nPDPA occurs. CTAB pulls an electron from the nPDPA backbone. The electrical conductivity of nPDPA occurs because of the hopping of an electron from a neighboring bond to fill the hole in the nPDPA backbone. SDS produces an electron to fill the hole in the polymer backbone. This extra electron jumps to a neighboring bond. Hence there is a charge carrier on the polymer backbone. Thus, electrical conductivity of nPDPA is induced. However, the conductivity of nPDPA-SDS is lower than the other two. This is because the electron mobility on the nPDPA backbone without a hole is lower than those of the nPDPA backbone with a hole. This result is consistent with FTIR, XRD, UV–visible and optical band gap data. Furthermore, to improve the electrical conductivity of nPDPA, the doping agent was varied – perchloric acid ($HClO_4$), nitric acid (HNO_3) and sulfuric acid (H_2SO_4). nPDPA-SDS_1-0.5, nPDPA-CTAB_1-0.5 and nPDPA-TW80_1-0.5 were used to dope nPDPA. The electrical conductivity values of the doped nPDPA are tabulated in Table 5. The conductivity of nPDPA-TW80 doped with $HClO_4$ (30.74 ± 10.81 S cm^{-1}) is the highest, followed by H_2SO_4 (2.88 ± 1.55 S cm^{-1}) and HNO_3 (0.104 ± 0.01 S cm^{-1}). The strength of the acid thus affects the electrical conductivity of nPDPA. Perchloric acid is a stronger acid than H_2SO_4 and HNO_3. So, nPDPA doped with $HClO_4$ will have more holes in the nPDPA backbone than nPDPA doped with H_2SO_4 and HNO_3. The electron mobility on the nPDPA backbone is thus faster. Thus the electrical conductivity of nPDPA doped with $HClO_4$ is higher than nPDPA doped with H_2SO_4 and HNO_3.

In related work, nPDPA was synthesized via electrochemical polymerization[7,20,21] and mechanochemical polymerization,[8] as shown in Table 2. But emulsion polymerization has never been attempted for nPDPA. Palaniappan and Manisankar[8] prepared nano-size nPDPA (80–100 nm) with different shapes: lamellar, granule and non-uniform. The nPDPA was then doped with hydrochloric acid, sulfuric acid and phosphoric acid: conductivity values of 0.55, 0.9 and 0.22 S cm^{-1}, respectively, were obtained. Massoumi *et al.*[7] synthesized nPDPA via electrochemical polymerization. The resultant nPDPA, as nano rods and nano particles, was in the range 150–200 nm when doped with sulfuric acid. The conductivity of the PDPA was $\sim 10^{-1}$–10^{-3} S cm^{-1}. Compared with other work, the emulsion polymerization method is the one method that can be used to tune the size and shape of nPDPA which has not been previously reported. However, a doping process is required to improve its conductivity.

Thermal stability of nPDPA

The thermal stability of the nPDPA particles was investigated by using TGA. Onset decomposition temperatures ($T_{d,onset}$) are shown in Fig. 9. The data show that $T_{d,onset}$ of nPDPA with a surfactant is lower than that of cPDPA because the $T_{d,onset}$ of the surfactant is lower than that of nPDPA. The $T_{d,onset}$ of nPDPA decreases as

 © 2014 Society of Chemical Industry

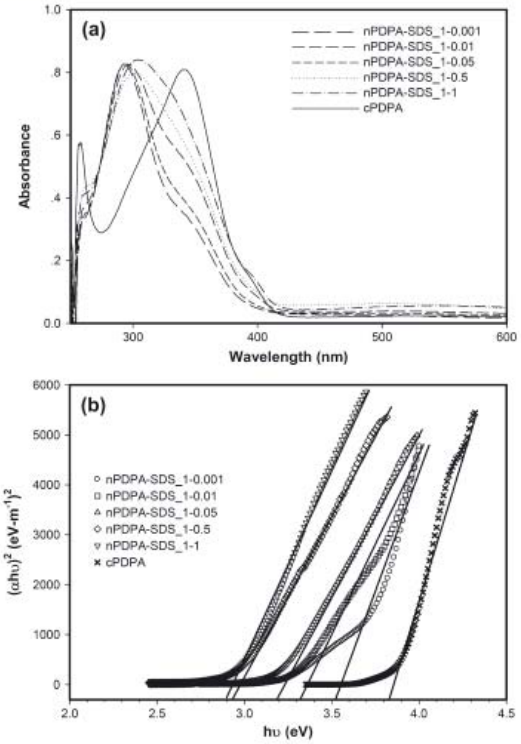

Figure 7. (a) UV–visible spectra of nPDPA-SDS and (b) Tauc plots for the determination of the optical band gap for nPDPA-SDS of various concentrations.

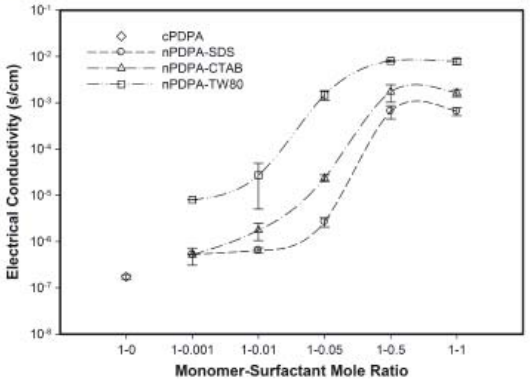

Figure 8. Electrical conductivity of nPDPA in relation to the monomer:surfactant mole ratio of various surfactant types.

Table 5. Conductivity of doped nPDPA with various doping agents

Polymer	Doping agent	Conductivity (S cm^{-1})
nPDPA-SDS_1-0.5	$HClO_4$	0.186 ± 0.078
	H_2SO_4	0.160 ± 0.067
	HNO_3	0.002 ± 0.001
nPDPA-CTAB_1-0.5	$HClO_4$	3.219 ± 2.671
	H_2SO_4	1.650 ± 0.127
	HNO_3	0.058 ± 0.006
nPDPA-TW80_1-0.5	$HClO_4$	30.744 ± 10.807
	H_2SO_4	2.876 ± 1.550
	HNO_3	0.104 ± 0.007

nPDPA-TW80 > nPDPA-CTAB > nPDPA-SDS, because the lengths of the hydrophobic component in the surfactant molecules directly affect the thermal stability of the polymers.[49] The carbon chain length in the TW80 molecule is longer than that of CTAB and SDS, respectively. A higher temperature is required to decompose these surfactant molecules. Moreover, $T_{d,onset}$ decreases with decreasing particle size of nPDPA because a smaller sized nPDPA exhibits a larger surface area. So, it is easier to decompose.[19,54]

CONCLUSION

nPDPA has been successfully synthesized by emulsion polymerization in the presence of three surfactants. The size and shape of the nPDPA depended on the surfactant type, micelle shape and surfactant concentration. The nPDPA particle size varied between 50 nm and 500 nm and new morphologies were obtained – leaf, coral reef, red blood cell shapes – in the presence of SDS, CTAB and TW80, respectively. FTIR and XRD studies of nPDPA revealed the incorporation of surfactants in the nPDPA. The electrical conductivity of nPDPA increased by four orders of magnitude in the presence of surfactants relative to cPDPA. The electrical conductivity of nPDPA was of the order of nPDPA-TW80 > nPDPA-CTAB > nPDPA-SDS. nPDPA was doped with various acids; however, nPDPA doped with perchloric acid showed the highest conductivity (~ 30.74 S cm^{-1}). In addition, the optical band gap of nPDPA calculated from UV–visible spectra confirms the increase in electrical conductivity. One drawback of nPDPA is that its thermal stability is lower than that of cPDPA.

Table 4. UV–visible data of nPDPA with different monomer:surfactant mole ratios

	Monomer:surfactant mole ratio									
	1:0.001		1:0.01		1:0.05		1:0.5		1:1	
Polymer	λ_{max}	E (eV)	λ_{max}	E (eV)	λ_{max}	E (eV)	λ_{max}	E (eV)	λ_{max}	E (eV)
nPDPA-SDS	293	3.52	294	3.33	296	3.20	300	2.93	304	2.89
nPDPA-CTAB	296	3.45	295	3.12	302	2.73	304	2.60	296	2.53
nPDPA-TW80	291	2.99	291	2.89	296	2.37	302	1.74	307	1.65
cPDPA	340	3.83	340	3.83	340	3.83	340	3.83	340	3.83

© 2014 Society of Chemical Industry

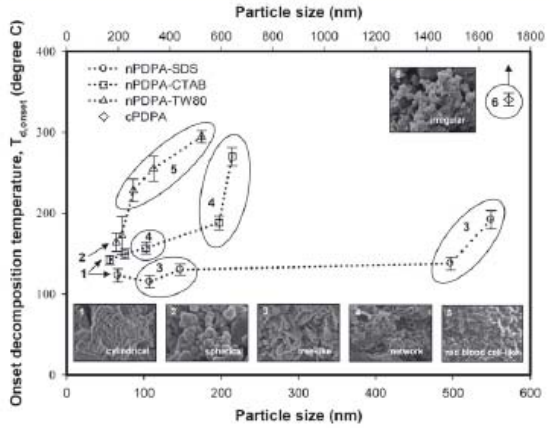

Figure 9. The onset decomposition temperatures ($T_{d,onset}$) of cPDPA and nPDPA with three surfactants, SDS, CTAB and TW80, as functions of particle size.

ACKNOWLEDGEMENTS

This work received financial support from the Conductive and Electroactive Polymers Research Unit of Chulalongkorn University; the Thailand Research Fund (TRF); the Royal Thai Government Budget; the Thailand Graduate Institute of Science and Technology (TGIST) (TGIST-01-54-011); and the 90th Anniversary of Chulalongkorn University Fund (Ratchadaphiseksomphot Endowment Fund).

SUPPORTING INFORMATION

Supporting information may be found in the online version of this article.

REFERENCES

1 Jing S, PhD, School of Chemical Sciences, The University of Auckland, New Zealand (2010).
2 Wang J, Wang J, Yang Z, Wang Z, Zhang F and Wang S, *React Funct Polym* **68**:1435–1440 (2008).
3 Pang S, Li G and Zhang Z, *Macromol Rapid Comm* **26**:1262–1265 (2005).
4 Vito SD and Martin CR, *Chem Mater* **10**:1738–1741 (1998).
5 Huang J and Kaner RB, *J Am Chem Soc* **126**:851–855 (2003).
6 Anilkumar P and Jayakanan M, *Macromol* **40**:7311–7319 (2007).
7 Massoumi B, Najafian S and Entezami AA, *Polym Sci B* **52**:270–276 (2010).
8 Palaniappan SP and Manisankar P, *Electrochim Acta* **56**:6123–6130 (2011).
9 Huang J, Virji S, Weiller BH and Kaner RB, *J Am Chem Soc* **125**:314–315 (2002).
10 Sawall DD, Villahermosa RM, Lipeles RA and Hopkins AR, *Chem Mater* **16**:1606–1608 (2004).
11 Wan M, *Adv Mater* **20**:2926–2932 (2008).
12 Arici E, Meissner D, Schaffler F and Sariciftci NS, *Int J Photoenergy* **5**:199–208 (2003).
13 Jang J, Conducting polymer nanomaterials and their applications, in *Emissive Materials Nanomaterials*, ed by Abe A and Dusek K. Springer publisher, Berlin, pp. 192–246 (2006).
14 Yoon H and Jang J, *Adv Funct Mater* **19**:1567–1576 (2009).
15 King RCY and Roussel F, *Synth Met* **159**:2512–2518 (2009).
16 Srinivas CH, Srinivasu D, Kavitha B, Narsimlu N and Kumer KS, *IOSR J Appl Phys* **1**:12–15 (2012).
17 Wang J, Bunimovich YL, Sui G, Savvas S, Wang J, Guo Y *et al.*, *Chem Commun* **29**:3075–3077 (2006).
18 Gök A, Omastová M and Yavuz AG, *Synth Met* **157**:23–29 (2007).
19 Paradee N and Sirivat A, *Polym Int* **63**:106–113 (2013).
20 Zhao Y, Chen M, Liu X, Xu T and Liu W, *Mater Chem Phys* **91**:518–523 (2005).
21 Santhosh P, Manesh KM, Uthayakumar S, Gopalan AI and Lee KP, *Biosens Bioelectron* **24**:2008–2014 (2009).
22 Permpool T, Supaphol P, Sirivat A and Wannatong L, *Adv Polym Technol* **31**:401–413 (2012).
23 Baquerizo I, Ruiz HJA and Cabrerizo GV, *IL Farmaco* **55**:583–589 (2000).
24 Petrenko VI, Avdeev MV, Garamus VM, Bulavin LA, Aksenov VL and Rosta L, *Colloids Surf A Physicochem Eng Aspects* **369**:160–164 (2010).
25 Chanthaanont P and Sirivat A, *Adv Polym Technol* **32**:1–6 (2013).
26 Konkayan S, Chanthaanont P, Prissanaroon W, Hormnirun P and Sirivat A, *Mater Technol: Adv Perform Mater* **28**:332–338 (2013).
27 Kamonsawas J, Sirivat A, Niamlang S, Hormnirun P and Prissanaroon-Ouajai W, *Sensors* **10**:5590–5603 (2010).
28 Chanthaanont P and Sirivat A, *e-Polym* **12**:106–116 (2012).
29 Gopalakrishnan K, Elango M and Thamilselvan M, *Arch Phys Res* **2**:315–319 (2012).
30 Mehta SK, Kumar S, Chaudhary S and Bhasin KK, *Nanoscale* **2**:145–152 (2010).
31 Tauc J, Grigorovici R and Vancu A, *Phys Status Solidi (B)* **15**:627–637 (1966).
32 Sharma S and Kumar D, *Indian J Eng Sci* **17**:231–237 (2010).
33 Butt HJ, Graf K and Kappl M, Surfactants, micelles, emulsions, and foams, in *Physics and Chemistry of Interfaces*, ed by Butt HJ, Graf K and Kappl M. Wiley-VCH Verlag Gmbh & Co. KGaA, Weinheim, pp. 246–279 (2004).
34 Esumi K and Ueno M, *Structure–Performance Relationships in Surfactants*, ed by Esumi K and Ueno M. Marcel Dekker, New York, pp. 1–110 (2003).
35 Santana H and Temperini M, *J Braz Chem Soc* **7**:485–490 (1996).
36 Athawale AA and Kulkarni MV, *Sens Actuator B Chem* **67**:173–177 (2000).
37 Hua F and Ruckenstein E, *Macromol* **36**:9971–9978 (2003).
38 Sathiyanarayanan S, Muthukrishnan S and Venkatachari G, *Synth Met* **156**:1208–1212 (2006).
39 Athawale AA, Deore BA and Chabukswar VV, *Mater Chem Phys* **58**:94–100 (1999).
40 Orlov AV, Ozkan SZh and Karpacheva GP, *Polym Sci B* **48**:11–17 (2006).
41 Lambert JB, Gronert S, Shurvell HF and Lightner D, *Organic Structural Spectroscopy*, 2nd edn, Prentice HAll PTR, New Jersey, pp. 1–552 (2010).
42 Lee DU, Jang SR, Vittal R, Lee J and Kim KJ, *Sol Energy* **82**:1042–1048 (2008).
43 Angelopoulos M, Manor C, Liao YH and Saraf RF, *Chemical and Biomolecular Engineering Research and Publications*, University of Nebraska-Lincoln, New York. (2003).
44 Clingerman ML, King JA, Schulz KH and Meyers JD, *J Appl Polym Sci* **83**:1341–1356 (2002).
45 Permpool T, Sirivat A, Aussawasathien D and Wannatong L, *Polym Plast Technol Eng* **52**:907–920 (2013).
46 Udum YA, Pekmez K and Yıldız A, *Synth Met* **142**:7–12 (2004).
47 Saini D and Basu T, *Appl Nanosci* **2**:467–479 (2012).
48 Xu JC, Liu WM and Li HL, *Mater Sci Eng C* **25**:444–447 (2005).
49 Kumar S, Spectroscopy of organic compounds, in *Organic Chemistry*, Guru Nanak Dev University, Amritsar, pp. 1–36 (2006).
50 Dai CA, Chang CJ, Chi, HY, Chien HT, Su WF and Chiu WY, *J Polm Sci A Polym Chem* **46**:2536–2548 (2008).
51 Lefebvre M, Qi Z, Rana D and Pickup PG, *Chem Mater* **111**:262–268 (1999).
52 Shreepathi S, Dissertation, Technical University, India (2006).
53 Janata J and Josowicz M, *Nat Mater* **2**:19–24 (2003).
54 Lyon RE, *Polym Degrad Stab* **61**:201–210 (1998).

 © 2014 Society of Chemical Industry

Sensors and Actuators A 220 (2014) 249–261

Contents lists available at ScienceDirect

Sensors and Actuators A: Physical

journal homepage: www.elsevier.com/locate/sna

Electromechanical properties study of 1-butyl-3-methylimidazolium chloride/cellulosic gel blended with polydiphenylamine

Wissawin Kunchornsup, Anuvat Sirivat*

The Petroleum and Petrochemical College, Chulalongkorn University, Bangkok 10330, Thailand

ARTICLE INFO

Article history:
Received 30 December 2013
Received in revised form 13 October 2014
Accepted 16 October 2014
Available online 27 October 2014

Keywords:
Electromechanical responses
Cellulose
1-Butyl-3-methylimidazolium chloride (BMIMCl)
Ionic liquids
Polydiphenylamine (PDPA)
Actuator

ABSTRACT

1-Butyl-3-methylimidazolium chloride (BMIMCl) is an ionic liquid utilized as an effective cellulose gelling agent for the fabrication of electro-responsive cellulose. The cellulose electromechanical properties are primarily dependent on the ionic polarization of $BMIM^+$ and its mobility. This work focuses on the synergism between the ionic contribution of ionic liquid/cellulosic gel (CelGel) and the electronic contribution of a conductive polymer, polydiphenylamine (PDPA) of various doping levels and concentrations (%v/v) under electrical actuation. Initially, CelGel is blended with doped PDPA of various doping levels. At 2.50%v/v, the CelGel blend exhibits the highest electrical conductivity of 21 S/cm at a 10:1 PDPA doping level. This results from proton conduction and electron delocalization which are intrinsically present within the doped PDPA embedded in the blends. Higher PDPA doping level in the blends produces lower storage modulus sensitivity. This suggests that the higher doping levels of PDPA create a higher degree of short-range ionic polarization, thus retarding $BMIM^+$ mobility and lowering storage modulus sensitivity. The %v/v of undoped PDPA (uPDPA) in the blends is further investigated with a %v/v variation between 0.01%v/v and 7.50%v/v. A larger amount of uPDPA in the blend provides a larger electrostatic binding interaction between $BMIM^+$ and Cl^- counterion, and this diminishes the storage modulus sensitivity as well. With a higher amount of uPDPA added, the bending angle also diminishes due to the electrostatic binding interaction. However, the optimal %v/v of uPDPA is 0.01%v/v, the ionic-electronic synergism produces the highest non-symmetric swinging angle of 77° accompanied with dielectrophoresis and electrophoresis force of 8.25 mN. This condition allows a number of polarizable domains on uPDPA with less rigidity on the CelGel relative to the pristine CelGel. The results suggest that uPDPA is a potential conductive polymer candidate for producing tailor-made electromechanical responses at optimal %v/v in the categories of ionic gels and dielectric elastomers.

© 2014 Published by Elsevier B.V.

1. Introduction

Cellulose consists of β-(1→4)-linked glucose repeating units [1], whose piezoelectric properties are attributed to the internal rotation of the polar atomic groups associated with asymmetric carbon atoms based on non-centro symmetry that are required for actuation [2]. However, this limits the dissolution of cellulose via the strong inter- and intra-molecular hydrogen bonding of the cellulosic hydroxyl groups.

Ionic liquids (ILs) are salts composed of organic nitrogen, inorganic cations, and inorganic anions. Swatloski et al. [3] pioneered the dissolution of a cellulose in 1-butyl-3-methylimidazolium chloride (BMIMCl). This dissolution system provided processing advantages, namely high solubility at a suitable temperature, 10 wt% solubility at 100 °C without derivatization, and less chain degradation [4]. When the amount of hydroxyl groups in the gel is attained with highest dissolution without degradation, the gel will exhibit effective actuation via electronic polarization. In addition, certain members of the IL family possess the requirements for electrochemical devices—high ionic conductivity ($>10^{-4}$ S cm^{-1}); large electrochemical windows (>1 V), in which the electrolyte is neither reduced nor oxidized at an electrode; fast ion mobility during redox events ($>10^{-14}$ m^2 V^{-1} s^{-1}); low volatility; and environmental stability [5]. Nafion swollen in 1-ethyl-3-methylimidazolium bis(trifluoromethylsulfonyl)imide (EMI-IM) was studied and shown that the actuation speed and the ionic conductivity increased with increasing counterion size and increasing IL content, due to the counterions of the polymer acting as the primary charge carriers [6]. The use of 1-ethyl-3-methylimidazoliumtrifluoromethanesulfonylimide IL was then

* Corresponding author. Tel.: +66 2 218 4131; fax: +66 2 611 7221.
E-mail address: anuvat.s@chula.ac.th (A. Sirivat).

http://dx.doi.org/10.1016/j.sna.2014.10.019
0924-4247/© 2014 Published by Elsevier B.V.

demonstrated as a viable solvent for Nafion™ polymer actuators and sensors. Experimental results also indicated that the Nafion™ polymer actuators solvated with this ionic liquid possessed the improved stability when operated in air as compared to the same materials solvated with water, although the magnitude of the response decreased at high frequencies relative to that of the materials solvated with water [7].

1-Butyl-3-methylimidazolium bis(trifluoromethylsulfonyl)-imide, BMITFSI, was blended with cellulose to increase bending displacement and AC conductivity by eight times and three times, respectively when compared to the pristine CelGel. The BMITFSI-loaded cellulose has been shown to be thermodynamically compatible and with high miscibility [8]. The actuation performance of the BMITFSI-loaded cellulose was also largely dependent on humidity [9]. 1-Butyl-3-methylimidazolium chloride was used to prepare cellulose gel with a regeneration process. The cellulose gel provided high thermal stability with high ratio of water content. The resonance frequency shifted to a lower range as the amount of residual ionic liquids increased due to higher hygroscopicity of the ionic liquid [10]. The actuation driving force of ionic liquid immersed hydrogel was demonstrated by Osada's works; the mechanism was based on an electrokinetic molecular assembly reaction of ionic liquids on the hydrogel caused by both electrostatic and hydrophobic interactions [11–14].

Conductive polymers (CPs) belong to a type of electroactive polymers with conjugated structures that could be used as potential actuators. Actuation in the conjugated polymers is based on electrochemical switching resulting in volume change as a result of insertion and extraction of counter ions into the polymer matrix. The actuation performance is determined by the monomer of CPs, the dopant ions trapped in the polymer structure, and synthesis conditions [15]. Although most conjugated polymers are electrochemically active, only a few of them have been used as actuators. For example, polypyrrole [16–18], polyaniline [19–21] and derivative polythiophenes [16,22] are popular due to the ease of fabrication and actuation. Polypyrrole was used to improve bending performance with blending with 1-methyl-3-buthylimidazolium tetrafluoroborate (BMIBF4), called cellulose-polypyrrole-ionic liquid (CPIL) nanocomposite. The bending displacement of the CPIL nanocomposite actuator was enhanced with increasing anion size, ionic liquid concentration, and humidity level [23]. Polydiphenylamine (PDPA) is an interesting conductive polymer as it has a molecular structure similar to polyaniline. It can be easily synthesized by oxidative polymerization and is easily doped in an acid solution [24].

In the present work, the electromechanical properties of $BMIM^+Cl^-$ ionic liquid/cellulosic gel (CelGel) blended with polydiphenylamine, PDPA, at various doping levels and %v/v were investigated for actuation performance. In addition, the CelGel and blends were characterized for chemical, electrical, dielectric, and bending properties and shall be reported here.

2. Experimental

2.1. Materials

Cellulose microcrystalline powder (AR grade, Sigma–Aldrich), 1-butyl-3-methylimidazolium chloride (BMIMCl; HPLC grade, Sigma–Aldrich), and N,N-dimethylacetamide (DMAc) were used as received without further purification. Diphenylamine, DPA (ACS reagent; Sigma Aldrich) was used as the monomer. Ammonium persulfate, $(NH_4)_2S_2O_8$ (AR grade, Riedel-de Haën), was used as the oxidant and 36.5–38.0% hydrochloric acid, HCl (ACS reagent, J.T. Baker), was used as the catalyst to accelerate polymerization and as the dopant. Toluene (AR grade, Panreac), isopropyl alcohol (AR grade, Burdick & Jackson), and ethanol (AR grade, Lab Scan) were used without further purification.

Table 1
Sample names and blending conditions.

Sample name	%v/v of PDPA	Doping level of PDPA
CelGel	0	–
2.50% v/v_0:1 uPDPA/CelGel blend	2.50	0
2.50% v/v_1:1 dPDPA/CelGel blend	2.50	1
2.50% v/v_10:1 dPDPA/CelGel blend	2.50	10
2.50% v/v_100:1 dPDPA/CelGel blend	2.50	100
2.50% v/v_200:1 dPDPA/CelGel blend	2.50	200
2.50% v/v_300:1 dPDPA/CelGel blend	2.50	300
0.01% v/v_0:1 uPDPA/CelGel blend	0.01	0
0.05% v/v_0:1 uPDPA/CelGel blend	0.05	0
0.10% v/v_0:1 uPDPA/CelGel blend	0.10	0
0.50% v/v_0:1 uPDPA/CelGel blend	0.50	0
1.00% v/v_0:1 uPDPA/CelGel blend	1.00	0
5.00% v/v_0:1 uPDPA/CelGel blend	5.00	0
7.50% v/v_0:1 uPDPA/CelGel blend	7.50	0

2.2. Preparation of various doped level PDPA

Polydiphenylamine was synthesized via chemical oxidative polymerization [24,25]. Diphenylamine monomer (3.42 g) and $(NH_4)_2S_2O_8$ (5.70 g) were dissolved in 100 mL of toluene and distilled water, respectively. A 1 M solution of HCl was prepared in 100 mL of distilled water. The DPA and HCl solutions were first cooled to a temperature of between 0 and 5 °C with constant stirring for 15 min. After that, the $(NH_4)_2S_2O_8$ solution was added dropwise in the HCl solution. The reaction was carried out under continuous vigorous stirring at 0–5 °C for 4 h, after which the mixture was precipitated into green slurry, then filtered and washed with distilled water three times until the reaction was neutral (colorless).

HCl-doped PDPA (dPDPA; 1.8 g), ethanol (5 mL), and a 27%v/v NH_4OH solution in distilled water (20 mL) were mixed by vigorous stirring at 27 °C for 24 h. The dark purple neutralized PDPA (0:1 uPDPA) was washed three times with an ethanol–water mixture (3:1, v/v) and dried under vacuum at room temperature for 24 h. The doped PDPA (dPDPA) at each doping ratio was prepared by immersing uPDPA (0:1 uPDPA) in a 5 M HCl solution and stirring for 24 h, at room temperature (27 °C). The doping ratios ($Mole_{HCl}/Mole_{DPA\ monomer}$) were at 1:1 (1:1 dPDPA), 10:1 (10:1 dPDPA), 100:1 (100:1 dPDPA), 200:1 (200:1 dPDPA), and 300:1 (300:1 dPDPA). The resultant dPDPA samples were distilled to remove excess HCl, and then dried in a vacuum oven for 24 h at room temperature [24,25].

2.3. Preparation of CelGel, 2.50% v/v_doped PDPA/CelGel blends, and various %v/v_0:1 uPDPA/CelGel blends

BMIMCl and dried cellulose were mixed at a composition of 87% (w/w) of BMIMCl (2.15 g) and 13% (w/w) of cellulose (0.323 g), equivalent to a 6.19:1 molar ratio of BMIMCl:glucose [26]. This molar ratio allowed for the maximum dissolution of the cellulose in BMIMCl at 100 °C under N_2 purge. The cellulose was dissolved in BMIMCl at 100 °C for 15 min. The obtained viscous solution was filled with 1.5 mL of N,N-dimethylacetamide (DMAc) as a plasticizer and a co-solvent, and stirred for 60 min. The solution was degassed and cast into a mold 25 mm diameter with a 1 mm thickness, and kept under a vacuum atmosphere for 12 h. The physically cross-linked cellulosic gel (CelGel) was obtained after curing at ambient conditions for 24 h [27,28]. To fabricate the blends, different amounts of doped PDPA were added to the solution with certain %v/v as shown in Table 1. It was then continuously stirred for 1 h until obtaining a well-distribution, then cast for 12 h under vacuum atmosphere, and kept in a dessicator. CelGel and blends

were then characterized for chemical, electrical, dielectric, and electromechanical properties, including bending characteristics.

2.4. Characterization of various doped level PDPA, CelGel, and blends

To investigate the functional groups and doping level of the synthesized PDPA, Fourier transform infrared spectroscopy (FTIR) was utilized (Thermo Nicolet, Nexus 670), using KBr powder, at a resolution of 4.0 cm^{-1}, a scan number of 64, and a wavenumber range of 400–4000 cm^{-1}. To investigate the functional groups and doping level of the CelGel and blends, Fourier transform infrared spectroscopy-attenuated total reflectance (FTIR-ATR) was used with a 45°-incident angle, using a ZnSe (zinc selenide) crystal, a resolution of 4.0 cm^{-1}, a scan number of 64, and a wavenumber range of 750–4000 cm^{-1}. The thickness of the gels was ~1 mm.

To determine the electrical conductivity, CelGel and blends (25 mm in diameter and ~1 mm thick) were prepared by casting. Electrical conductivity was measured using a custom-built two-point probe. Specific conductivity, σ (S/cm), was obtained by measuring the resistance (R) and using the following equation:

$$\sigma = \left(\frac{1}{Rt}\right)\left(\frac{1}{K}\right), \quad (1)$$

where t is the film thickness and K is the geometric correction factor. A geometric correlation factor was calibrated by using standard silicon wafer sheets with known specific resistivity values. The measurements were performed in the linear Ohmic regime, i.e. the specific conductivity values were independent of the applied DC current. The measurements were carried out at 300 K.

The relative dielectric permittivity values were measured with an LCR meter (HP, model 4284A) connected to a rheometer (Rheometric Scientific, ARES) with a 25-mm parallel plate fixture. The thickness of the specimens was typically 1 mm and the diameter was about 25 mm. The top and bottom sides of the specimens were coated with a silver adhesive to improve the electrical contacts between the specimens and the electrodes. The measurements were carried at 30 °C. The AC voltage applied was 10 V. The dielectric permittivity, at a frequency of 20 Hz, was divided by 8.85 pF/m of free space to obtain the relative dielectric permittivty (ε'_r) or the dielectric constant.

The electromechanical properties were also measured with the rheometer (Rheometric Scientific, ARES). DC voltage was applied with a DC power supply (Instek, GFG 8216A), which can deliver an electric field up to 4 kV. A digital multimeter (Tektronix, CDM 250) was used to monitor the voltage input. The samples were prepared in the configuration of Polyimide/sample/Polyimide sandwich to prevent shorting of the circuit. The insulating Polyimide (PI) film, ®Kapton TH-012 (12 μm), was produced by Saint Gobain Performance Plastic Corporation. It is an excellent insulator with up to 7 kV/mm for the breakdown voltage, a dielectric constant value of 3.3, and volume resistivity >10^{16} Ω-cm. In these experiments, an oscillatory shear strain was applied and the dynamic modulus (G') was measured as a function of frequency and electric field strength. Strain sweep tests were first carried out to determine a suitable strain to measure G' in the linear viscoelastic regime. The appropriate strain was determined to be 0.25% for the CelGel and blends studied. The temporal response experiments of CelGel and the blends were carried out at 1 kV/mm at T = 303 K. Then, the frequency sweep tests were carried out to measure G' of each sample as a function of frequency and electric field strength. The deformation frequency was varied from 0.1 to 100 rad/s. For each measurement, the sample was pre-sheared at a low frequency and then an electric field was applied for 30 min to ensure a steady state condition before taking the G' measurements. The storage modulus sensitivity ($\Delta G'/G'_0$) is defined as a ratio of storage modulus difference at certain electric field strength over storage modulus with absence of an electric field.

The electrophoresis forces were determined by measuring the deflection distances of the gels in a vertical cantilever fixture under electric field. The specimens were vertically immersed in insulating silicone oil (viscosity = 100 cSt) between parallel copper electrode plates (68 mm length, 40 mm width, and 2 mm thickness). The gap between the pair of electrodes was 30 mm. DC voltage was applied with a DC power supply (Goldsun, GPS 3003B) connected to a high voltage power supply (Gamma High Voltage, model UC5-30P and UC5-30 N) which could deliver an electric field up to 25 kV. The output voltage from the high voltage power supply was calibrated using a Fluke 40 kV high voltage probe. A video camera was used to record movement during the experiment. Still pictures were captured from the video and the deflection distances in x (d) and y axes (l) at the ends of the specimen were determined using Scion Image software (version 4.0.3). The electric field strength was varied between 0 and 550 V/mm at a room temperature of 303 ± 1 K. The resisting elastic force of the specimen was calculated under electric field using the non-linear deflection theory of a cantilever [29–34], which can be obtained from the standard curve between $(F_e l_0^2)/(EI)$ and d/l_0 (l_0 = initial length of specimens) [33]; F_e is the elastic force, d is the deflection distance on the horizontal axis, l is the deflection distance on the vertical axis, E is the Young's modulus, which is equal to $2G'(1+\nu)$, where G' is the shear storage modulus taken to be G' (ω = 1 rad/s) at various electric field strengths, and ν is the Poisson's ratio (0.5 for an incompressible sample), and I is the moment of inertia $1/12t^3w$, where t is the thickness and w is the width of the sample. The dielectrophoresis and electrophoresis force can be calculated from the static horizontal force balance consisting of the elastic force and the corrective gravity force term ($mg\sin\theta$), as shown in Eq. (2):

$$F_D \text{ and } F_E \text{ (N)} = F_e + mg\sin\theta, \quad (2)$$

where g = 9.8 m s^{-2}, m is the mass of the specimen, and θ is the deflection angle.

To investigate the materials as potential actuators, energy density and force density are important factors for comparison. These factors were calculated using Eqs. (3) and (4), respectively [29–39]:

$$\text{Energy density (J)} = \frac{1}{2}E\theta^2, \quad (3)$$

$$\text{Force density (N cm}^{-3}) = \frac{F_E}{\text{volume}}, \quad (4)$$

where E is the Young's Modulus, θ is the bending angle, and volume is the sample volume.

3. Results and discussion

3.1. Chemical properties

FTIR spectra of variously doped PDPA, which were synthesized by oxidative polymerization, are shown in Fig. 1. The characteristic band at 3387–3391 cm^{-1} is a result of the N—H stretching mode of the secondary amine, exhibiting higher absorbance at higher doping levels. However, the absorbance at 3387–3391 cm^{-1} decreases when PDPA is doped at more than 10:1; this is because PDPA particles become agglomerated and the surface area is diminished, which in turn, reduces the transfer of electrical current. The strong peak at 1595–1598 cm^{-1} is assigned to the different bending modes of the aromatic secondary amine [40–42]. The band at 1502–1508 cm^{-1} is due to the C—C multiple bond stretching mode of the benzene ring [43]. The C—N stretching mode of the aromatic secondary amine is evidenced by the band at 1316–1319 cm^{-1}. The peak at 1172–1176 cm^{-1} can be assigned to the C—H bending vibration of diphenoquinone [44]. The bands at 746–750 and

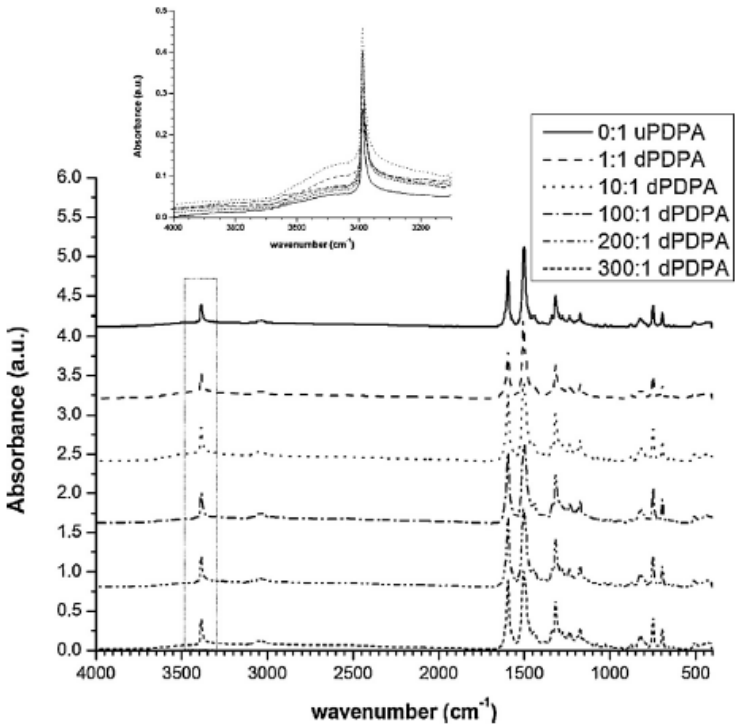

Fig. 1. FT-IR spectra of polydiphenylamine at various doping levels in the range of 4000–400 cm^{-1} (4000–3100 cm^{-1} for the inset).

690–695 cm^{-1} are assigned to the terminal phenyl groups and C—H out-of-plane phase bending vibration of mono-substituted benzene rings at the ends of the polymer chains, respectively.

FTIR spectra of CelGel and the 2.50% v/v_doped PDPA/CelGel blends (Fig. 2) show the characteristic peaks of $BMIM^+$ cations; they are at 2876, 2940, and 2964 cm^{-1}. These peaks can be assigned to the C—H stretching modes of the methyl and butyl groups. The 3122 and 3163 cm^{-1} bands can be attributed to the coupled imidazolium C—H stretching vibrations [45]. The absorption band at 1430 cm^{-1} is assigned to the CH_2 scissoring motion in the cellulose. The absorption band at 897 cm^{-1} is assigned as C—O—C stretching at the β-(1→4)-glycosidic linkage in the cellulose [46]. The absorption band at 3387 cm^{-1} is associated with the interaction between the bound water molecules and the cellulosic hydroxyl group [47], it is superimposed on the characteristic peak of N—H stretching mode of the secondary amine of PDPA. The absorption peak at 3387 cm^{-1} is enhanced with increasing PDPA doping level, when it is blended with CelGel at 2.50%v/v at a 10:1 doping level. The proton conductivity of PDPA is promoted via the hydrophilic channel between the bound water and the cellulosic hydroxyl group clusters, corresponding to the increase in electrical conductivity (Fig. 3). Nevertheless, the absorption at 3387 cm^{-1} and electrical conductivity decrease with overdoping dopant:monomer >10:1 due to particle agglomeration.

3.2. Electrical properties

The effect of PDPA doping level on electrical conductivity is shown in Fig. 3. Electrical conductivity increases with increasing doping level and obtains a maximum value of 4.79×10^{-5} S/cm. The electrical conductivity of dPDPA is a result of the electronic and ionic contributions. The acid protons from the doping process react with the imine nitrogens and the resulting positive charges on the nitrogen atoms are balanced by negatively charged counter-ions. The electrons in the protonated PDPA structure may become delocalized and produce polarons, which are the charge carriers responsible for the electronic conductivity of PDPA. Simultaneously, the chemical structure of a protonated imine site in PDPA represents a typical proton-conducting unit [48]. However, electrical conductivity decreases when it is overdoped at acid:monomer >10:1 as PDPA particles become agglomerated and diminish the available surface area needed to transfer electrons. There is a synergism between ionic conductivity of CelGel (long-range movement of $BMIM^+$ cations [49] and protons) and the electronic-ionic mixed conductivity of dPDPA (polarons and acid protons) [48], whose maximum electrical conductivity is 20.81 S/cm at the 10:1 doping level. High electrical conductivity may also be attributed to the promotion of proton conductivity via the N—H bonding of the dPDPA secondary amine as previously mentioned. There is an increase in electrical conductivity when uPDPA is blended with CelGel; however it is concentration independent. This result suggests that blending of uPDPA in CelGel produces an in situ doping on uPDPA under a cationic-rich environment and creates more protons that transfer electrical current.

3.3. Time dependence of electromechanical response

The temporal characteristics of the CelGel and 0.01% v/v_0:1 uPDPA/CelGel blend at 303 K under 1 kV/mm electric field strength were investigated. The temporal characteristic of each sample was recorded in a linear viscoelastic regime at a strain of 0.25%, and a frequency of 1 rad/s. The change in G' of the CelGel and 0.01% v/v_0:1 uPDPA/CelGel blend at 303 K under the 1 kV/mm electric field strength during a time sweep test, in which an electric field is alternately turned on and off is shown in Fig. 4. In the case of CelGel, G' immediately increases and rapidly reaches a steady-state value. The G' increase under applied voltage results from three dominant mechanisms: primarily dominant $BMIM^+$-cation

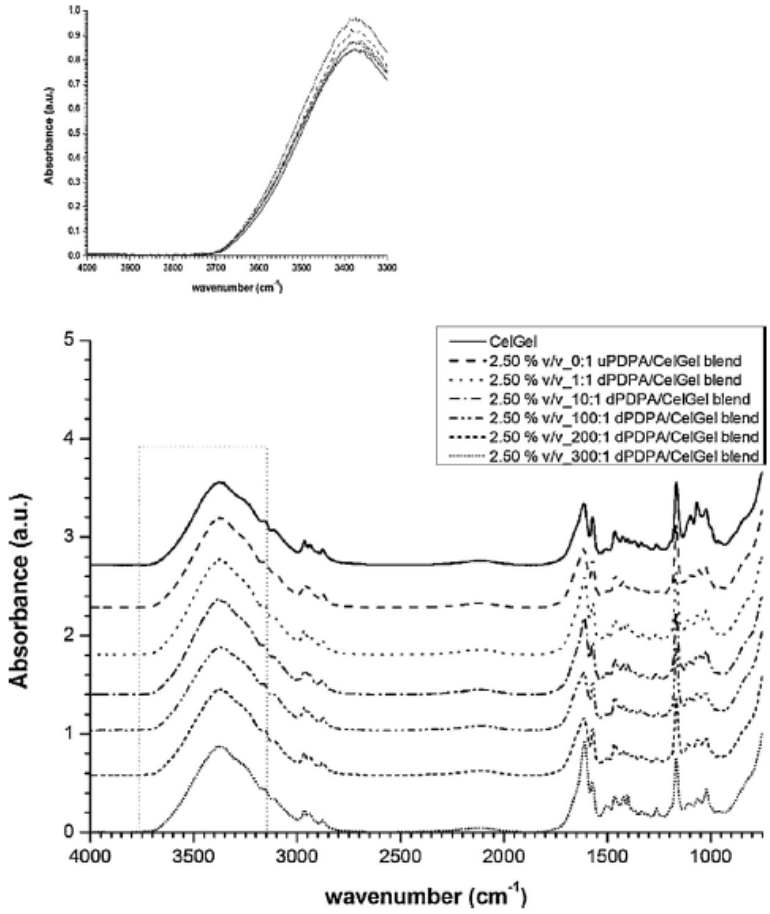

Fig. 2. FT-IR spectra of CelGel and 2.50% v/v_doped PDPA/CelGel blends in the range of 4000–400 cm^{-1} (4000–3300 cm^{-1} for the inset).

polarization (the ionic polarization) [50–52], cellulosic hydroxyl group polarization (the dipolar polarization) [31,32], and shear induced cellulose chain alignment [53]. When the electric field is turned off, G' decreases but does not recover its original value due to some residual polarization and chain alignment. Subsequent on and off electric fields only produce steady state responses after a duration of ~1800 s. The response of G' can be divided into two regimes: the initial regime in which G' rapidly overshoots to a large value in the first cycle, followed by an irreversible decay with the electric field off; and the steady state regime in which G' subsequently exhibits a reversible cyclic response. The steady G' of CelGel is close to steady G' of the 0.01%v/v uPDPA/CelGel blend under the absence of electric field, which is $\sim 1.45 \times 10^5$ Pa. However, steady G' of CelGel under the presence of electric field is higher than steady G' of 0.01%v/v uPDPA/CelGel blend, by a difference of 47.00×10^3 Pa in G'. This suggests that the ionic and electronic polarizations of the 0.01%v/v uPDPA/CelGel blend becomes less pronounced in terms of electro-induced stiffness with more heterogeneous uPDPA particles.

3.4. Relative dielectric permittivity

The relative dielectric permittivity or the dielectric constants of the CelGel and 2.50% v/v_doped PDPA/CelGel blends at 303 K as functions of frequency are shown in Fig. 5 with two regimes: relatively low (10^1–10^3 Hz) and high (10^3–10^6 Hz) responses. The dependence on doping level of PDPA is also shown in the inset. In the low frequency regime, the ionic liquid acts as a good conductor with low frequency or DC measurement as shown in Fig. 3, in which the long-range motions are dominant for conduction mechanism [49]. In the high frequency regime, the relative dielectric permittivity of CelGel increases significantly with increasing frequency when $f > 10^3$ Hz. The rise in relative dielectric permittivity with increasing frequency can be attributed to the resonance response of ionic polarization contribution that comes from the displacement of charged ions with respect to their counterions and $BMIM^+$ transport [49,54]. Although the dipolar polarization exists which tends to decrease the dielectric permittivity with increasing frequency, the ionic polarization is presumably the dominant contributor since the CelGel is an ionic-rich gel. Nevertheless, the relaxation of $BMIM^+$ cation may be investigated in the range of THz, it was not observable in our measuring frequency range [55]. The relative dielectric permittivity also increases with increasing doping levels of PDPA until it reaches the reproducible maximum value of 67.46 at the doping level of 10:1 due to generated dipole moments [56,57] from the more polarizable domains in the blends via polarons, bipolarons, doped imine nitrogens, chloride counterions, and protons. However, 10:1 dPDPA does not show promising electromechanical properties over CelGel in terms of temporal response and storage modulus sensitivity. This may be attributed to the short-range polarization of several moieties as it is not efficient as the long range polarization in CelGel. The overdoping of PDPA at >10:1 diminishes the relative dielectric permittivity, consistent with electrical conductivity of PDPA at different doping levels. The overdoping of

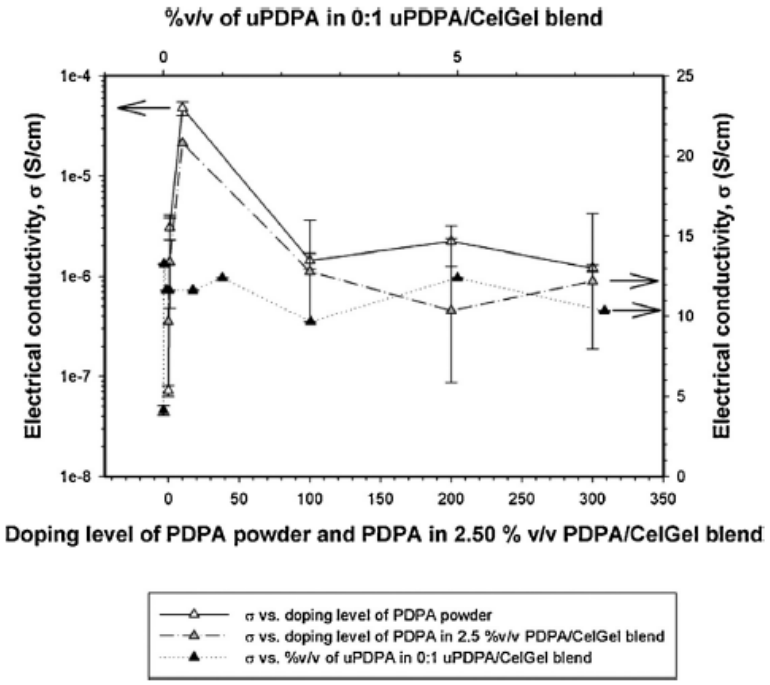

Fig. 3. Electrical conductivity vs. doping levels of PDPA powder, PDPA in 2.50%v/v PDPA/CelGel blend, and electrical conductivity vs. %v/v of uPDPA in 0:1 uPDPA/CelGel blend.

PDPA also shows lower frequency dependence suggesting lesser ionic contribution than electronic contribution.

Fig. 6 shows the relative dielectric permittivity values of the CelGel and various %v/v_0:1 uPDPA/CelGel blends at 303 K as functions of frequency. The dependence on %v/v of uPDPA is also shown in the inset. The relative dielectric permittivity values with frequency dependence of CelGel and the blends decrease with increasing %v/v of uPDPA. This is caused by the electrostatic binding interaction between $BMIM^+$ and Cl^- counterion occurring with increasing amounts of uPDPA. Interestingly, the relative dielectric permittivity of the 0.01% v/v_0:1 uPDPA/CelGel blend at $f > 2 \times 10^3$ Hz is reproducibly greater than that of CelGel. This may be attributed to the creation of more protons, which originate from the in situ doping of uPDPA in the cationic-rich environment.

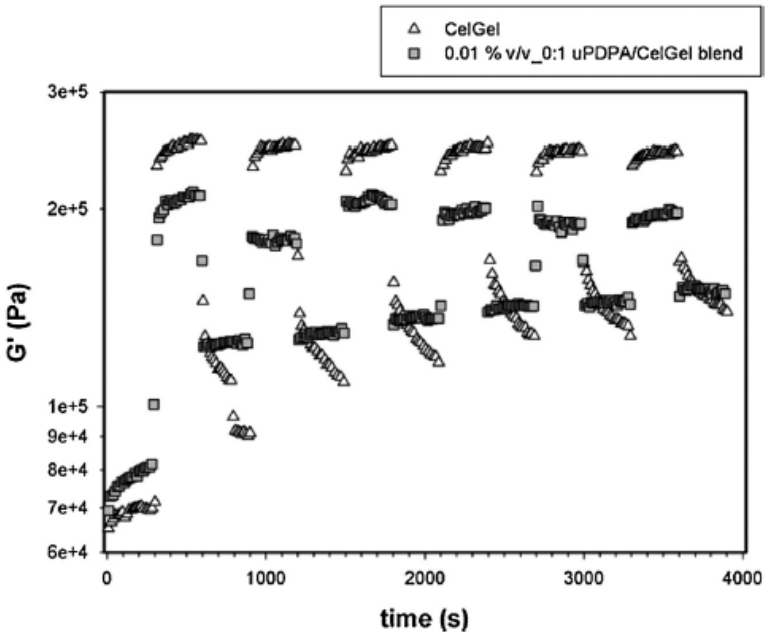

Fig. 4. Temporal responses of CelGel and 0.01% v/v_0:1 uPDPA/CelGel blend.

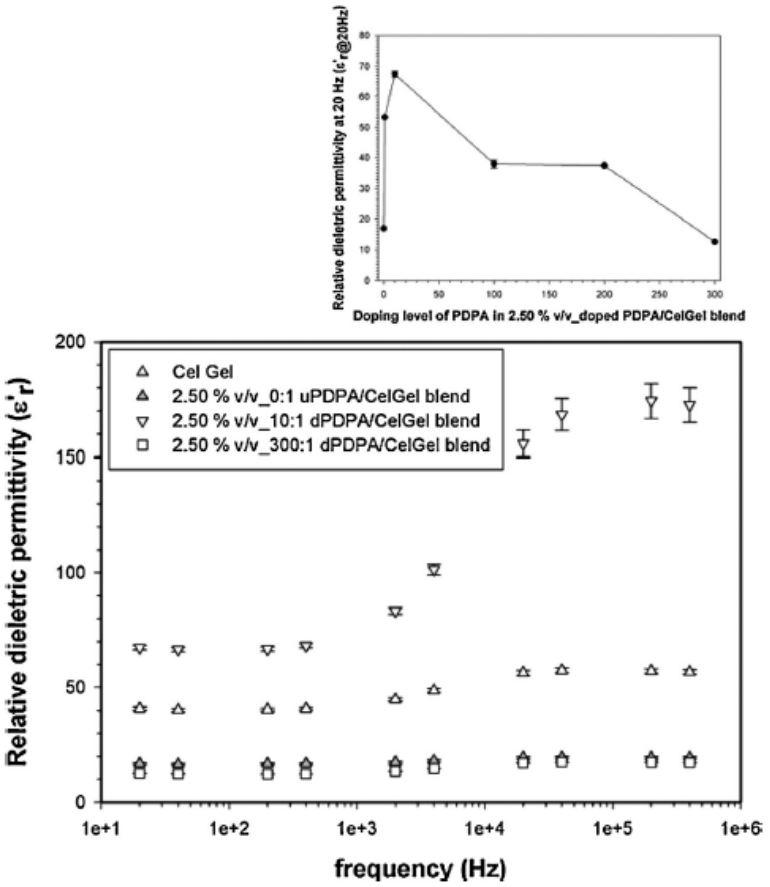

Fig. 5. Relative dielectric permittivity of CelGel and 2.50% v/v_doped PDPA/CelGel blends vs. frequency; inset shows relative dielectric permittivity at 20 Hz vs. doping level of PDPA in 2.50%v/v_doped PDPA/CelGel blend.

3.5. Effect of electric field strength on electromechanical properties

Fig. 7 shows $\Delta G'/G'_0$ at 1 rad/s in relation to electric field strength of CelGel and the 2.50% v/v_doped PDPA/CelGel blends. $\Delta G'/G'_0$ of CelGel increases with increasing electric field strength due to the ionic and electronic polarizations, and the chain alignment under electric field as previously mentioned [50,58]. Introducing of differently doped PDPA at 2.50%v/v into the blends, $\Delta G'/G'_0$ is diminished as the existing dPDPA particles in the blends participates in the electrostatic binding interaction between $BMIM^+$ and Cl^- anion of the HCl dopant. In addition, there is a possibility that $BMIM^+$ may have been trapped with Cl^- dopant counterions. The highest $\Delta G'/G'_0$ is observed with the 2.50% v/v_0:1 uPDPA/CelGel blend. Therefore, the uPDPA particle was selected for further investigation at various %v/v of the uPDPA blends. The decrease in G' may also be attributed to the viscous transition response via electric field strength over 600 V/mm [59]. As shown in Fig. 8, this confirms that more uPDPA particles provide a higher degree of electrostatic binding interaction and a suppression on $\Delta G'$ under electric field.

3.6. Effect of electric field strength on deflection angle and dielectrophoresis and electrophoresis forces

The bending angle of CelGel and blends were investigated under applied electric field (Fig. 9). The effect of electric field strength on the deflection angle was investigated under the electric field strengths between 0 and 550 V/mm at the temperature of 300 ± 1 K. The samples were gripped between copper plates and immersed in a poly(dimethylsiloxane), as shown in Table 2. A video recorder was used to record the displacement of the film. The deflection distance along the x axis and the deflection length were measured through the Scion Image software (version 4.0.3), which is an analysis program. Under externally applied electric field strength, the free end samples bend toward to the positive side, or the anode side. The $BMIM^+$ cations move toward the neutral side due to the cation–anode repulsive force, whereas Cl^- counter ions are immobilized and act as physical crosslinkers. The migration of the cations toward the neutral electrode creates the ionic polarization, the side-by-side volume difference, causing the CelGel to bend toward the anode electrode [50] due to the resultant dielectrophoresis force. The chemical structures of the micro-crystalline cellulose consist of many hydroxyl groups on the polymer chains. Under applied electric field, the hydroxyl groups pull electrons from the carbon atoms on the backbone. Thus, polarity of the hydroxyl group becomes negative. This leads to the apparent deflection toward the anode (positive) side [60] from the electrophoresis force. It is known that the actuation principle of cellulose is a combination of the piezoelectric effect and the ion migration effect, while at the same time it is associated with the dipole moment of the cellulose components. The still pictures of the experiments at 550 V/mm show the bending as shown in Table 2: CelGel, 0.01% v/v_0:1 uPDPA/CelGel blend, and 2.50% v/v_0:1 uPDPA/CelGel blend. When

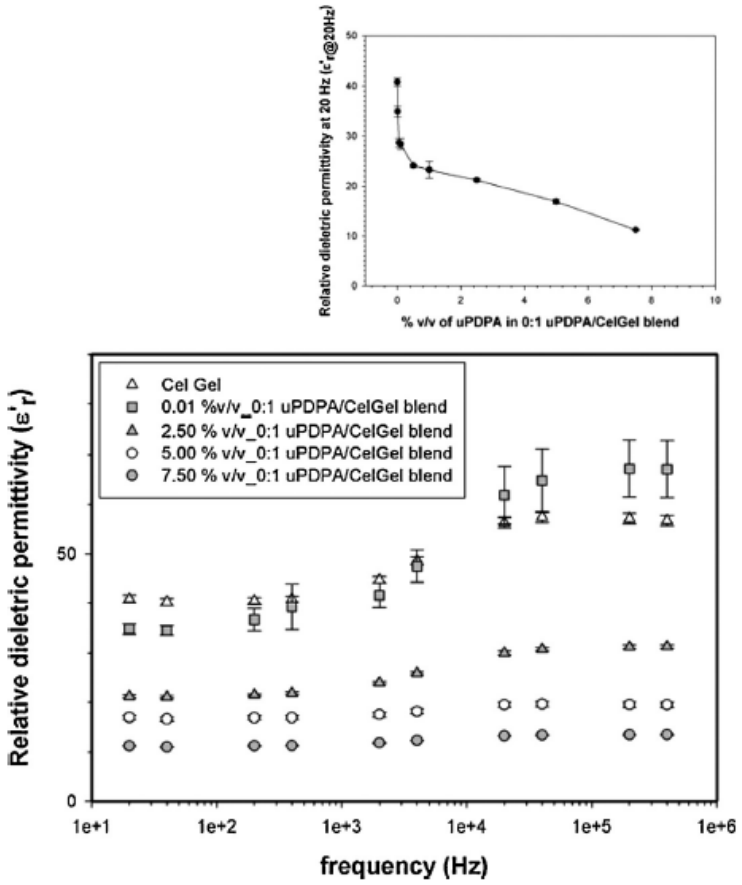

Fig. 6. Relative dielectric permittivity of CelGel and various %v/v_0:1 uPDPA/CelGel blends vs. frequency; inset shows relative dielectric permittivity at 20 Hz vs. %v/v of uPDPA of 0:1 uPDPA/CelGel blend.

Table 2
Bending experiment images and bending mechanisms of CelGel and various %v/v of the 0:1 uPDPA/CelGel blends at the electric field strength of 550 V/mm.

CelGel	0.01 %v/v_0:1uPDPA/CelGel blend	2.50 %v/v_0:1uPDPA/CelGel blend
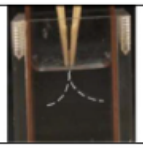		
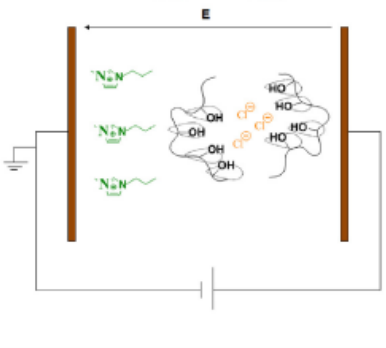	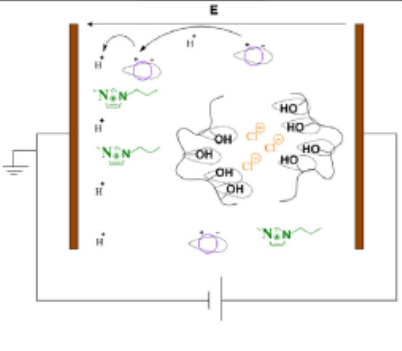	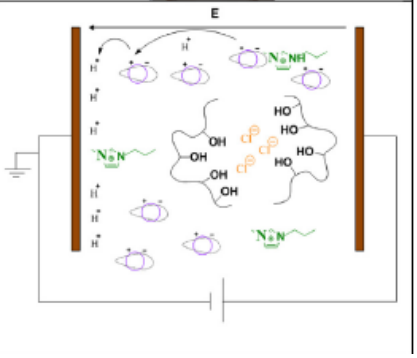

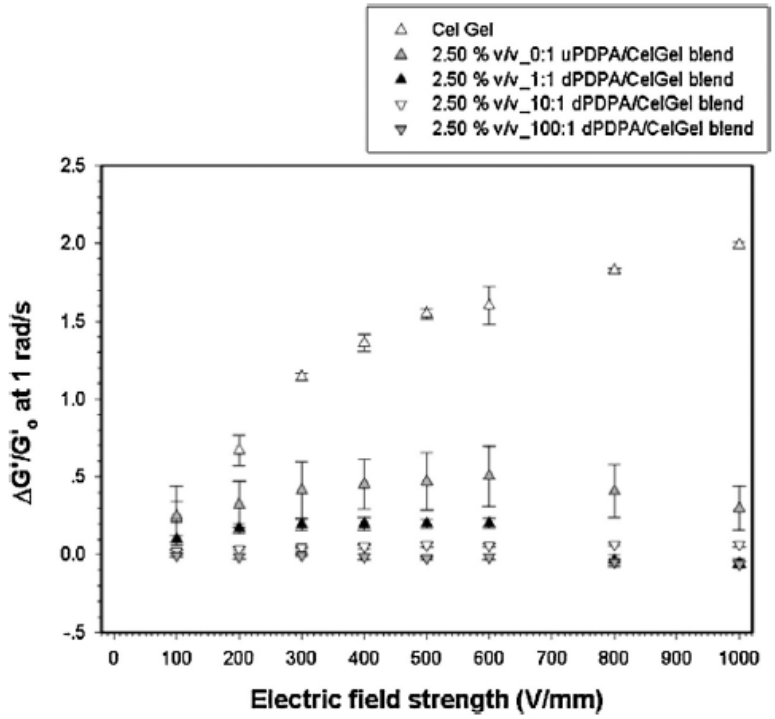

Fig. 7. Storage modulus sensitivity at 1 rad/s vs. electric field strength of CelGel and 2.50% v/v_doped PDPA/CelGel blends.

electric field was applied, all of specimens deflected toward the anode electrode (higher electrical potential) in the direction of right hand side of the images. On the other hand, the back and forth swinging occurred under the electric field strength between 425 and 550 V/mm for CelGel and 350–550 V/mm for the 0.01% v/v_0:1 uPDPA/CelGel blend. The swinging frequencies of CelGel and the 0.01% v/v_0:1 uPDPA/CelGel blend at 550 V/mm were 0.36 s^{-1} and 0.31 s^{-1}, respectively. This swinging is due to the competition

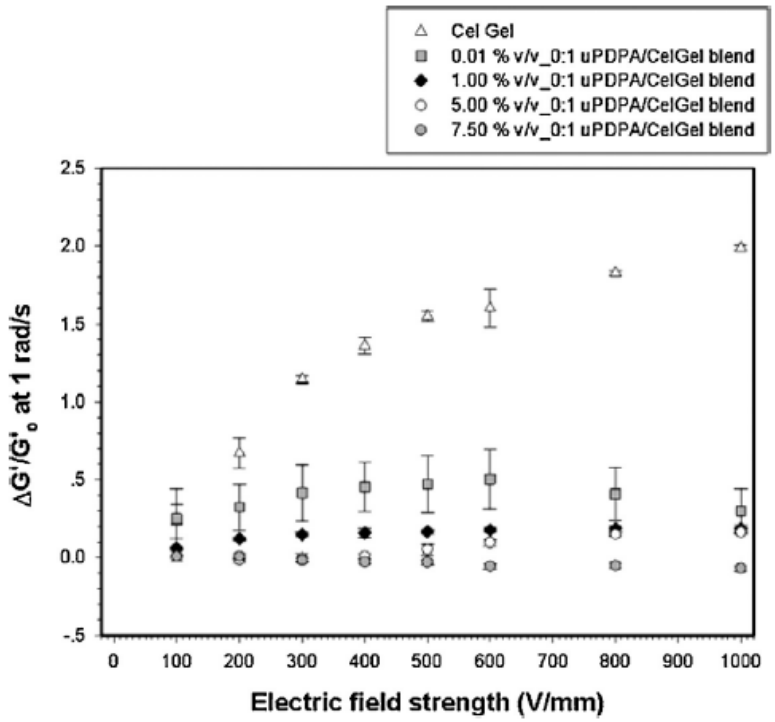

Fig. 8. Storage modulus sensitivity at 1 rad/s vs. electric field strength of CelGel and various %v/v_0:1 uPDPA/CelGel blends.

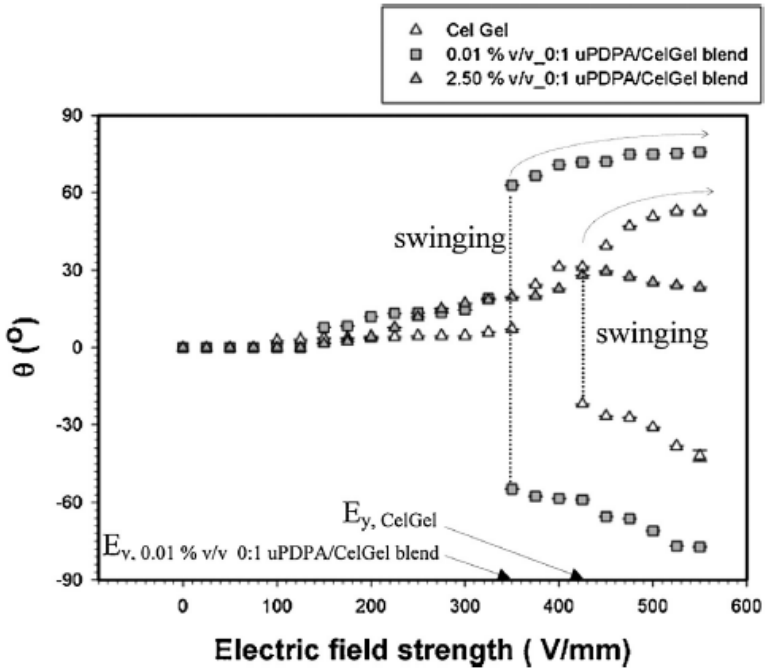

Fig. 9. Bending angle vs. electric field strength of CelGel and various %v/v_0:1 uPDPA/CelGel blends. The yield electric field strength (E_y) for swinging of CelGel and 0.01% v/v_0:1 uPDPA/CelGel blend are 425 V/mm and 350 V/mm, respectively.

between the anion and cation rotary movements within the ionic liquid. The back and forth swing can also be attributed to the difference between the positive and negative charges (cations and anions may form clusters rather than bare ions in the processes of ion transport), and thus a non-symmetric swinging was observed here [61].

The reproducible highest bending angle (77°) and forces (8.25 mN) at specific electric field strengths belonged to the 0.01% v/v_0:1 uPDPA/CelGel blend (Figs. 9 and 10). This may be caused by a relatively lower rigidity or lower electric field induced storage modulus under the presence of uPDPA. It is easier to overcome rigidity and thus easier to bend via increasing polarizable domains

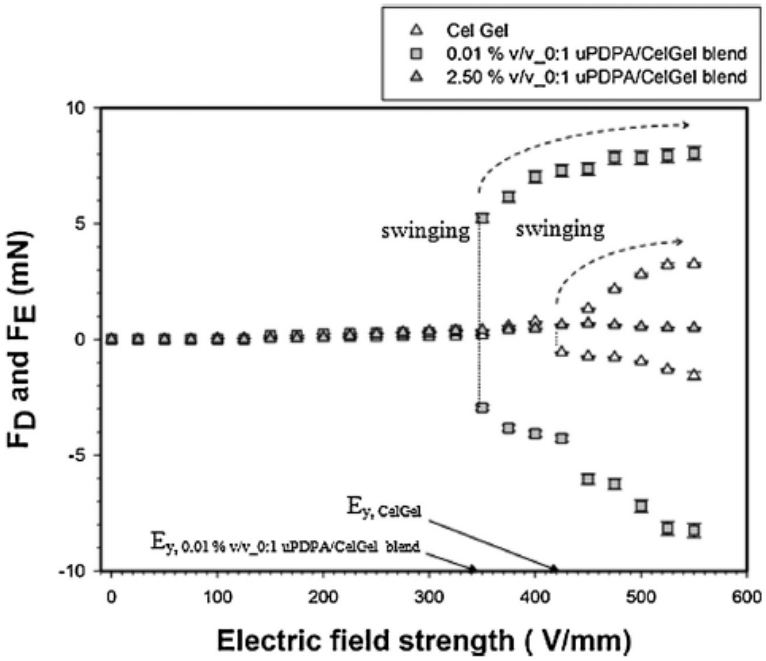

Fig. 10. Dielectrophoresis and electrophoresis force vs. electric field strength of CelGel and various %v/v_0:1 uPDPA/CelGel blends. The yield electric field strength for swinging of CelGel and 0.01% v/v_0:1 uPDPA/CelGel blend are 425 V/mm and 350 V/mm, respectively.

Table 3
Comparison of electromechanical responses of CelGel, various %v/v_0:1 uPDPA/CelGel blends, various %v/v_0:1 uPDPA/D1114P blends, and other dielectric elastomers (AR70, AR71, AR72, SAR, SIS, SBR, SAR negative polarity, SIS negative polarity).

Sample	Electrical yield strength (kV/mm)	θ (°)	F_E (μN)	Energy density (J/m^3)	Force density (N/m^3)	$\varepsilon'_{r,20Hz}$	G' at 1 rad/s (Pa)	Temperature (K)	References
CelGel	0.10	52.8	3250	1.39E+09	4.52E+04	40.83	3.81E+05		
0.01% v/v_0:1 uPDPA/CelGel blend	0.15	77.2	8250	2.19E+09	1.15E+05	34.89	2.13E+05	303	–
2.50% v/v_0:1 uPDPA/CelGel blend	0.15	23.3	493	1.99E+08	6.85E+03	16.93	2.14E+05		
SIS; 19 wt% of PS (D1114P)	0.20	9.9	34	1.51E+03	1.68E+03	2.65	~3.50E+04	300	[63]
10.00% v/v_0:1 uPDPA/D1114P blend	0.20	–	47	–	–	–	~4.00E+04	300	
30.00% v/v_0:1 uPDPA/D1114P blend	0.05	–	15	–	–	–	~2.20E+05	300	
AR70	0.23	64.7	367	6.21E+04	2.47E+04	6.21	3.25E+04	300	
AR71	0.08	70.4	412	4.90E+04	2.80E+04	6.33	2.16E+04	300	
AR72	0.08	57.2	318	1.59E+04	1.70E+04	4.14	1.06E+04	300	
SAR	0.25	33.4	275	3.10E+04	2.05E+04	3.95	6.07E+04	300	[58]
SIS	0.40	11.0	71	1.43E+03	3.39E+03	2.74	2.58E+04	300	
SBR	0.38	8.6	157	7.85E+02	6.91E+03	2.87	2.34E+04	300	
SAR negative polarity	0.28	11.7	47	3.80E+03	3.25E+03	3.95	6.07E+04	300	
SIS negative polarity	0.38	10.7	118	1.43E+03	6.61E+03	2.74	2.58E+04	300	

on uPDPA. This reveals the synergism of bending characteristics between the ionic and electronic polarizations (Table 2). Ionic polarization is composed of suitable amounts of $BMIM^+$ and protons from the in situ doping of uPDPA. Electronic polarization occurs because of the cellulosic hydroxyl groups and polaronic domains on the PDPA particle. The electrostatic binding interaction between $BMIM^+$ and Cl^- counterions within the 0.01% v/v_0:1 uPDPA/CelGel blend is dominant over the effect of electronic polarization. This result is consistent with Fig. 6 which describes the dominant ionic contribution when compared with the case of the pristine CelGel. In other word, the synergism effect in the 0.01% v/v_0:1 uPDPA/CelGel blend provides the highest dielectrophoresis and electrophoresis forces and the highest bending angle response via increasing H^+-ionic polarization and polaron-electronic polarizations (Table 2). With concentration over 0.01%v/v, the dielectrophoresis and electrophoresis force decrease with further additions of more uPDPA particles because $BMIM^+$ cations bind electrostatically with Cl^- counterion and the synergistic effect diminishes. The 2.50% v/v_0:1 uPDPA/CelGel blend exhibits only the right hand bending without swinging because the presence of a larger amount of uPDPA particles produced the electrostatic binding interaction which obstructed free $BMIM^+$ and Cl^- movements. When uPDPA was introduced into CelGel at 2.50%v/v, the bending angle, between 0 and 350 V/mm, was greater than that of the pristine CelGel because there were more generated polaronic domains and protons via the in situ dPDPA particles. However, the bending angle of 2.50% v/v_0:1 uPDPA/CelGel blend was less than that of the pristine CelGel when electric field strength was greater than 350 V/mm. This was because the 2.50% v/v_0:1 uPDPA/CelGel blend possessed a greater electrostatic binding interaction between $BMIM^+$ and Cl^- counterion and hence a smaller bending angle.

Table 3 summarizes bending characteristics of CelGel, various %v/v_0:1 uPDPA/CelGel blends, various %v/v_0:1 uPDPA/D1114P blends, and dielectric elastomers. The data suggest that uPDPA could enhance the bending characteristics of CelGel relative to other dielectric elastomers in terms of bending angle, electrophoresis force, energy density, force density, and dielectric permittivity. The optimal %v/v blend is 0.01%v/v uPDPA. Likewise, uPDPA particles could enhance the resultant dielectrophoresis and electrophoresis forces of D1114P at the optimal concentration at 10.00%v/v uPDPA [62,63]. Therefore, uPDPA has been shown to be a suitable conductive polymer for developing electroactive polymers in the categories of dielectric elastomer and ionic gel.

4. Conclusion

This work investigated the electromechanical properties of $BMIM^+Cl^-$ ionic liquid/cellulosic gel (CelGel) blended with a conductive polymer, polydiphenylamine (PDPA), at various doping levels and concentrations for actuation applications. The optimal doping level of PDPA particles was 10:1, which provided the highest electrical conductivity of 4×10^{-5} S/cm. This corresponded to the highest FTIR absorption at 3387 cm^{-1} which can be assigned to the N—H stretching mode of the secondary amine. The CelGel blended with dPDPA at 2.50%v/v exhibited the highest electrical conductivity at 21 S/cm at a 10:1 doping level. This resulted from the proton conduction and the electron delocalization produced via the dPDPA within the blend. The temporal response of CelGel showed a periodic behavior and an irreversible decay with the on and off electric field which was primarily related to the $BMIM^+$ movement. When uPDPA was introduced into CelGel at 0.01%v/v, it exhibited a lower temporal response due to the electrostatic binding interaction between $BMIM^+$ and Cl^- counterions of uPDPA particles. The 2.50% v/v_10:1 dPDPA/CelGel blend showed the highest dielectric permittivity with the highest frequency dependence, which can be related to the number of existing ions in the blends via dPDPA. However, the blends with variously doped PDPA at 2.50%v/v showed smaller storage modulus sensitivity values ($\Delta G'/G'_0$) when compared to the pristine CelGel because the higher doped PDPA created a short-range ionic polarization which electrostatically restricted the $BMIM^+$ movement. The %v/v of uPDPA in the blends was further investigated with concentrations between 0.01%v/v and 7.50%v/v. The higher concentration of uPDPA in the blends provided a higher degree of electrostatic binding interaction between $BMIM^+$ and Cl^- counterions and thus diminished $\Delta G'/G'_0$. The bending angle of CelGel exhibited a non-symmetric back and forth swinging with

competitive contributions between the $BMIM^+$ cation and chloride anion movements. As more uPDPA was introduced into the blend, the bending angle was diminished due to the electrostatic binding interaction between $BMIM^+$ and Cl^- counterion obstructing the ion movements. However, the optimal concentration was at 0.01%v/v with the ionic-electronic contribution synergism that produced the highest swinging bending angle (77°) and the dielectrophoresis and electrophoresis forces (8.25 mN). At this condition, the blend possessed a number of polarizable domains on uPDPA with a lower electric field induced rigidity relative to CelGel. Thus it has been demonstrated that uPDPA is a suitable conductive particle for development of tailor-made electromechanical responses with optimal %v/v in the categories of ionic gel and dielectric elastomer.

Acknowledgements

We wish to express our appreciation for the financial support provided by the Conductive and Electroactive Polymer Research Unit (CEAP) of Chulalongkorn University, the Thailand Research Fund (TRF-RTA), the Royal Thai Government, and the 90th Anniversary of Chulalongkorn University Fund (Ratchadaphiseksomphot Endowment Fund).

References

[1] D. Klemm, B. Heublein, H.P. Fink, A. Bohn, Cellulose: fascinating biopolymer and sustainable raw material, Angew. Chem. Int. Ed. 44 (2005) 3358–3393.
[2] E. Pukada, History and recent progress in piezoelectric polymers, IEEE Trans. Ultrason. Ferroelectr. Freq. Control 47 (2000) 1277–1290.
[3] R.P. Swatloski, S.K. Spear, J.D. Holbrey, R.D. Rogers, Dissolution of cellose with ionic liquids, J. Am. Chem. Soc. 124 (2002) 4974–4975.
[4] N.P. Novoselov, E.S. Sashina, O.G. Kuz'mina, S.V. Troshenkova, Ionic liquids and their use for the dissolution of natural polymers, Russ. J. Gen. Chem. 77 (2007) 1395–1405.
[5] W. Lu, A.G. Fadeev, B. Qi, E. Smela, B.R. Mattes, J. Ding, et al., Use of ionic liquids for π-conjugated polymer electrochemical devices, Science 297 (2002) 983–987.
[6] M.D. Bennett, D.J. Leo, G.L. Wilkes, F.L. Beyer, T.W. Pechar, A model of charge transport and electromechanical transduction in ionic liquid-swollen Nafion membranes, Polymer 47 (2006) 6782–6796.
[7] M.D. Bennett, D.J. Leo, Ionic liquids as stable solvents for ionic polymer transducers, Sens. Actuators A: Phys. 115 (2004) 79–90.
[8] S.K. Mahadeva, J. Nayak, J. Kim, Structure, tensile and electromechanical properties of 1-butyl-3-methylimidazolium bis(trifluoromethylsulfonyl)imide incorporated cellulose, J. New Mater. Electrochem. Syst. 13 (2010) 113–117.
[9] S. Mahadeva, C. Yi, J. Kim, Electrical and electromechanical properties of 1-butyl-3-methylimidazolium bis(trifluoromethylsulfonyl)imide-blended cellulose, Ionics 17 (2011) 41–47.
[10] S.K. Mahadeva, K.S. Kang, J. Kim, S.H. Ha, Y.M. Koo, The effect of residual ionic liquid for cellulose based electro-active paper actuator, Soft Mater. 8 (2010) 254–262.
[11] Y. Osada, Y. Ueoka, J.P. Gong, Polymer gel: soft and wet intelligent material, Proc. SPIE 2779 (1996) 344–348.
[12] Y. Osada, J.P. Gong, T. Narita, Intelligent gels, Mater. Res. Soc. Symp. Proc. 604 (2000) 149–159.
[13] H. Okuzaki, Y. Osada, Electro-driven chemomechanical polymer gel as an intelligent soft material, J. Biomater. Sci. Polym. Ed. 5 (1994) 485–496.
[14] T. Narita, J. Gong, Y. Osada, Chemomechanical behaviors of polymer gels by surfactant binding, Proc. SPIE 3669 (1999) 264–271.
[15] I. Leger, M. Berggren, S. Carter, Ionic Carriers in Organic Electronic Materials and Devices, CRC Press, Boca Raton, 2011.
[16] Q. Pei, O. Inganäs, Conjugated polymers and the bending cantilever method: electrical muscles and smart devices, Adv. Mater. 4 (1992) 277–278.
[17] M.R. Gandhi, P. Murray, G.M. Spinks, G.G. Wallace, Mechanism of electromechanical actuation in polypyrrole, Synth. Met. 73 (1995) 247–256.
[18] A. Della Santa, D. De Rossi, A. Mazzoldi, Characterization and modelling of a conducting polymer muscle-like linear actuator, Smart Mater. Struct. 6 (1997) 23–34.
[19] K. Kaneto, M. Kaneko, Y. Min, A.G. MacDiarmid, "Artificial muscle": electromechanical actuators using polyaniline films, Synth. Met. 71 (1995) 2211–2212.
[20] J.W.L. Zhou, H.Y. Chan, T.K.H. To, K.W.C. Lai, W.J. Li, Polymer MEMS actuators for underwater micromanipulation, IEEE/ASME Trans. Mechatron. 9 (2004) 334–342.
[21] Q. Pei, O. Inganas, I. Lundstrom, Bending bilayer strips built from polyaniline for artificial electrochemical muscles, Smart Mater. Struct. 2 (1993) 1–6.
[22] F. Vidal, J.F. Popp, C. Plesse, C. Chevrot, D. Teyssié, Feasibility of conducting semi-interpenetrating networks based on a poly(ethylene oxide) network and poly(3,4-ethylenedioxythiophene) in actuator design, J. Appl. Polym. Sci. 90 (2003) 3569–3577.
[23] S.K. Mahadeva, J. Kim, An electro-active paper actuator made with cellulose-polypyrrole-ionic liquid nanocomposite: influence of ionic liquid concentration, type of anion and humidity, Smart Mater. Struct. 19 (2010) 105014–105020.
[24] A. Sirivat, T. Permpool, P. Supaphol, L. Wannatong, Polydiphenylamine–polyethylene oxide blends as methanol sensing materials, Adv. Polym. Technol. 31 (2011) 401–413.
[25] F. Hua, E. Ruckenstein, Water-soluble conducting poly(ethylene oxide)-grafted polydiphenylamine synthesis through a graft onto process, Macromolecules 36 (2003) 9971–9978.
[26] J.i. Kadokawa, M.a. Murakami, Y. Kaneko, A facile preparation of gel materials from a solution of cellulose in ionic liquid, Carbohydr. Res. 343 (2008) 769–772.
[27] W. Kunchornsup, A. Sirivat, Effects of crosslinking ratio and aging time on properties of physical and chemical cellulose gels via 1-butyl-3-methylimidazolium chloride solvent, J. Sol-Gel Sci. Technol. 56 (2010) 19–26.
[28] W. Kunchornsup, A. Sirivat, Physically cross-linked cellulosic gel via 1-butyl-3-methylimidazolium chloride ionic liquid and its electromechanical responses, Sens. Actuators A: Phys. 175 (2012) 155–164.
[29] S. Niamlang, A. Sirivat, Electromechanical responses of a crosslinked polydimethylsiloxane, Macromol. Symp. 264 (2008) 176–183.
[30] S. Niamlang, A. Sirivat, Dielectrophoresis force and deflection of electroactive poly(p-phenylene vinylene)/polydimethylsiloxane blends, Smart Mater. Struct. 17 (2008).
[31] J. Kim, Y. Kang, S. Yun, Blocked force measurement of electro-active paper actuator by micro-balance, Sens. Actuators A: Phys. 133 (2007) 401–406.
[32] J. Kim, W. Jung, H.S. Kim, In-plane strain of electro-active paper under electric fields, Sens. Actuators A: Phys. 140 (2007) 225–231.
[33] J.M. Gere, S.P. Timoshenko, Mechanics of Materials, Chapman & Hall, New York, USA, 1991.
[34] S.T. Smith, R.M. Seugling, Sensor and actuator considerations for precision, small machines, Precis. Eng. 30 (2006) 245–264.
[35] Y.d. Jung, H.s. Park, N.j. Jo, H.d. Jeong, Fabrication and performance evaluation of diaphragm-type polymer actuators using segmented polyurethane according to chemical-hard-segment content, Sens. Actuators A: Phys. 136 (2007) 367–373.
[36] R.E. Pelrine, R.D. Kornbluh, J.P. Joseph, Electrostriction of polymer dielectrics with compliant electrodes as a means of actuation, Sens. Actuators A: Phys. 64 (1998) 77–85.
[37] I. Diaconu, D.O. Dorohoi, F. Topoliceanu, Electrostriction of a polyurethane elastomer-based polyester, IEEE Sens. J. 6 (2006) 876–880.
[38] M. Watanabe, T. Hirai, Space charge distribution in bending-electrostrictive polyurethane films doped with salts, J. Polym. Sci. Part B: Polym. Phys. 42 (2004) 523–531.
[39] P. Hiamtup, A. Sirivat, A.M. Jamieson, Electromechanical response of a soft and flexible actuator based on polyaniline particles embedded in a cross-linked poly(dimethyl siloxane) network, Mater. Sci. Eng. C 28 (2008) 1044–1051.
[40] J. Tang, X. Jing, B. Wang, F. Wang, Infrared spectra of soluble polyaniline, Synth. Met. 24 (1988) 231–238.
[41] T. Ohsaka, Y. Ohnuki, N. Oyama, G. Katagiri, K. Kamisako, Ir absorption spectroscopic identification of electroactive and electroinactive polyaniline films prepared by the electrochemical polymerization of aniline, J. Electroanal. Chem. 161 (1984) 399–406.
[42] Y. Furukawa, F. Ueda, Y. Hyodo, I. Harada, T. Nakajima, T. Kawagoe, Vibrational spectra and structure of polyaniline, Macromolecules 21 (1988) 1297–1305.
[43] D. Pavia, G. Lampman, G.S. Kriz, Introduction to Spectroscopy, W.B. Sanders Co., London, 1979.
[44] H. De Santana, J.D.R. Matos, M.L.A. Temperini, Characterization of polydiphenylamine electrochemically synthesized by spectroscopic and thermal techniques, Polym. J. 30 (1998) 315–321.
[45] H.C. Chang, J.C. Jiang, C.Y. Chang, J.C. Su, C.H. Hung, Y.C. Liou, et al., Structural organization in aqueous solutions of 1-butyl-3-methylimidazolium halides: a high-pressure infrared spectroscopic study on ionic liquids, J. Phys. Chem. B 112 (2008) 4351–4356.
[46] M.L. Nelson, R.T. O'Connor, Relation of certain infrared bands to cellulose crystallinity and crystal lattice type. Part II. A new infrared ratio for estimation of crystallinity in celluloses I and II, J. Appl. Polym. Sci. 8 (1964) 1325–1341.
[47] J. Seo, J. Kim, J. Koh, S. Ahn, J. Kim, Preparation and characterization of crosslinked cellulose/sulfosuccinic acid membranes as proton conducting electrolytes, Ionics 15 (2009) 555–560.
[48] J. Stejskal, O.E. Bogomolova, N.V. Blinova, M. Trchová, I. Šeděnková, J. Prokeš, et al., Mixed electron and proton conductivity of polyaniline films in aqueous solutions of acids: beyond the 1000 S cm^{-1} limit, Polym. Int. 58 (2009) 872–879.
[49] E.I. Izgorodina, M. Forsyth, D.R. MacFarlane, On the components of the dielectric constants of ionic liquids: ionic polarization? Phys. Chem. Chem. Phys. 11 (2009) 2452–2458.

[50] K. Mukai, K. Asaka, K. Kiyohara, T. Sugino, I. Takeuchi, T. Fukushima, et al., High performance fully plastic actuator based on ionic-liquid-based bucky gel, Electrochim. Acta 53 (2008) 5555–5562.
[51] N. Terasawa, I. Takeuchi, H. Matsumoto, Electrochemical properties and actuation mechanisms of actuators using carbon nanotube-ionic liquid gel, Sens. Actuators B: Chem. 139 (2009) 624–630.
[52] N. Terasawa, I. Takeuchi, H. Matsumoto, K. Mukai, K. Asaka, High performance polymer actuator based on carbon nanotube-ionic liquid gel: effect of ionic liquid, Sens. Actuators B: Chem. 156 (2011) 539–545.
[53] G.Y. Yun, H.S. Kim, J. Kim, K. Kim, C. Yang, Effect of aligned cellulose film to the performance of electro-active paper actuator, Sens. Actuators A: Phys. 141 (2008) 530–535.
[54] C. Kittel, Introduction to Solid State Physics, 8th ed., John Wiley & Sons, Inc., Hoboken, New Jersey, 2005.
[55] M. Koeberg, C.-C. Wu, D. Kim, M. Bonn, THz dielectric relaxation of ionic liquid:water mixtures, Chem. Phys. Lett. 439 (2007) 60–64.
[56] G.G. Raju, Dielectrics in Electric Fields, Marcel Dekker, New York, 2003.
[57] A.S. Riad, M.T. Korayem, T.G. Abdel-Malik, AC conductivity and dielectric measurements of metal-free phthalocyanine thin films dispersed in polycarbonate, Physica B: Condens. Matter 270 (1999) 140–147.
[58] R. Kunanuruksapong, A. Sirivat, Effect of dielectric constant and electric field strength on dielectrophoresis force of acrylic elastomers and styrene copolymers, Curr. Appl. Phys. 11 (2011) 393–401.
[59] T. Sato, H. Watanabe, K. Osaki, Rheological and dielectric behavior of a styrene–isoprene–styrene triblock copolymer in n-tetradecane. 1. Rubbery–plastic–viscous transition, Macromolecules 29 (1996) 6231–6239.
[60] V.A. Bazhenov, Piezoelectric Properties of Wood, Consultants Bureau, New York, 1961.
[61] Y. Liu, S. Liu, J. Lin, D. Wang, V. Jain, R. Montazami, et al., Ion transport and storage of ionic liquids in ionic polymer conductor network composites, Appl. Phys. Lett. 96 (2010) 223503.
[62] K. Thongsak, R. Kunanuruksapong, A. Sirivat, W. Lerdwijitjarud, Electroactive styrene–isoprene–styrene triblock copolymer: effects of morphology and electric field, Mater. Sci. Eng. A 527 (2010) 2504–2509.
[63] K. Thongsak, R. Kunanuruksapong, A. Sirivat, W. Lerdwijitjarud, Electroactive polydiphenylamine/poly(styrene-block-isoprene-block-styrene) (SIS) blends: effects of particle concentration and electric field, Mater. Sci. Eng. C 31 (2011) 206–214.

Biographies

Wissawin Kunchornsup obtained B.E. in Polymer Engineering in 2006 and a Ph.D. degree in Polymer Science in 2013 at the Petroleum and Petrochemical College, Chulalongkorn University, Bangkok, whose fields of interests are conductive and electroactive polymers, actuators, electromechanical properties, viscoelastic properties, dielectric properties, ionic liquids, and atomic force spectroscopy. Wissawin Kunchornsup worked as a Research Assistant at the Natural Fibre Composites, School of Polymer Engineering, Institute of Engineering, Suranaree University of Technology, Nakhon Ratchasima during 2005–2006 and also worked as a Research Assistant, the Application of Chitosan for Drug Delivery System (DDS), National Nanotechnology Center (NANOTEC), in 2006; he worked as a Teaching Assistant, Polymer Physics in 2010 at the Petroleum and Petrochemical College, Chulalongkorn University, Bangkok. Since October 2013–2015, Wissawin Kunchornsup is working on Postdoctoral researcher in Istituto Italiano di Tecnologia (IIT), Italy, to fabricate devices for visually impaired people, based on magnetoactive materials. This project is under supervision of Dr. Luca Brayda, affiliated in Department of Robotics, Brain & Cognitive Sciences (RBCS), IIT.

Anuvat Sirivat obtained B.S. in 1977 and M.E. in 1978 followed by Ph.D. in 1983 all in Mechanical Engineering, from Cornell University, USA, and later completed a Post Doctoral study in Chemical Engineering in 1985 from Johns Hopkins University. Anuvat Sirivat is a Professor of Polymer Engineering, Petroleum and Petrochemical College, Chulalongkorn University, Bangkok, whose fields of interests are conductive and electroactive polymers; rheology, stability, transition, and turbulence of complex fluids; and light scattering.

Materials Science and Engineering C 46 (2015) 281–289

Contents lists available at ScienceDirect

Materials Science and Engineering C

journal homepage: www.elsevier.com/locate/msec

Electromechanical properties of multi-walled carbon nanotube/gelatin hydrogel composites: Effects of aspect ratios, electric field, and temperature

Thawatchai Tungkavet [a], Nispa Seetapan [b], Datchanee Pattavarakorn [c], Anuvat Sirivat [a,*]

[a] The Petroleum and Petrochemical College, Chulalongkorn University, Bangkok 10330, Thailand
[b] National Metal and Materials Technology Center, Pathum Thani 12120, Thailand
[c] Department of Industrial Chemistry, Faculty of Science, Chiang Mai University, Chiangmai 50200, Thailand

ARTICLE INFO

Article history:
Received 6 January 2014
Received in revised form 15 September 2014
Accepted 23 October 2014
Available online 24 October 2014

Keywords:
Electromechanical properties
Actuator
Biopolymer
Gelatin
Hydrogels
Multi-walled carbon nanotubes

ABSTRACT

The effects of multi-walled carbon nanotube (MWNT) aspect ratio, electric field strength and temperature on the electromechanical properties of MWNT/gelatin hydrogel composites were investigated. The highest aspect ratio of MWNT provides the composites with the highest dynamic moduli under electric field. The MWNT/gelatin hydrogel composites of 0.01, 0.1, 0.5, and 1 vol.% and the pure gelatin hydrogel possess the storage modulus sensitivity values of 0.69, 1.23, 0.94, 0.81 and 0.47, respectively, at 800 V/mm. The results can be interpreted in terms of the enhanced polarizability between the carboxyl groups of gelatin under the presence of MWNT. The effect of temperature on the electromechanical properties of MWNT/gelatin hydrogel composites investigated between 30 °C and 90 °C shows three distinct regimes of temperature-dependent storage modulus behavior. In the deflection testing, the effects of electric field on the deflection distance and the dielectrophoresis force of the MWNT/gelatin hydrogel composites were also investigated. MWNT/gelatin hydrogel composites suspended in the silicone oil between electrodes, respond rapidly with a deflection toward the anode site, indicating the attractive force between anode and the polarized carboxyl group as the gelatin structure possesses negative charges.

© 2014 Elsevier B.V. All rights reserved.

1. Introduction

Electroactive polymers (EAPs) have been continuously utilized and developed for several applications such as muscle-like actuator, compliant electrode, robotics and drug release. Hydrogel is a promising material structure for the development of EAPs since it possesses a reversible response subject to external stimuli such as temperature [1,2], pH [3], ionic strength [4,5], and electric fields [6–8]. Gelatin is one type of hydrogels or EAPs; it is a biopolymeric-protein derived from animal collagen by thermal and hydrolyzing processes with either acid or bases. It is stable as a film, a hydrogel, or a composite [9]. Because gelatin possesses non-immunogenicity, biodegradability, biocompatibility, bioactivity and commercial availability at relatively low cost, it has been widely used in the medical fields such as drug delivery, wound dressings, and artificial muscles [10]. Usually, gelatin is produced by denaturing a naturally derived collagen in a solution through either an acidic or base process at high temperature in which the triple-helix structure is split to random coil structure. During the gel forming process at the temperature around 40 °C, the gelatin random chain in a warm aqueous solution undergoes a disorder–order transition into the coil–helix structure when cooled [11]. However, gelatin exhibits poor water resistance and low mechanical properties when compared with synthetic polymers, these limit its possible application as an EAP [12]. Therefore gelatin needs to be reinforced either through chemical crosslinking or using some filler materials. Chemical crosslinking enhances thermal and mechanical properties through covalent bonds between the reactive side groups in gelatin molecules. However, this process presents the residual crosslinking agents that lead to toxic side effects. MWNTs are chosen to enhance the mechanical and electromechanical properties in the gelatin hydrogel because they can provide the biocompatibility and great mechanical properties. In the previous works, Fraczek et al. [13] reported that MWNTs induced rapid tissue regeneration process. Nevertheless, the biocompatibility of MWNTs depended on their size, shape, length, and chemical surface. Chlopek et al. [14] reported that MWNTs possessed good biocompatibility to the cells studied (fibroblasts and osteoblasts). The use of multiwall carbon-nanotube (MWNT) as a reinforcement in gelatin has been studied by Li et al. [15]. They studied gelatin with MWNTs that can be embedded as an additive to enhance the mechanical properties of the gelatin hydrogel. Haider et al. [16] investigated the swelling of MWNT/gelatin hydrogel composites. MWNT could maintain the stability

* Corresponding author at: Conductive and Electroactive Polymers Research Unit, The Petroleum and Petrochemical College, Chulalongkorn University, Soi Chula 12, Phayathai Rd., Bangkok 10330, Thailand. Tel: +662 218 4131; fax: +662 611 7221.
E-mail address: anuvat.s@chula.ac.th (A. Sirivat).
URL: http://www.cepruresearch.ac.th (A. Sirivat).

http://dx.doi.org/10.1016/j.msec.2014.10.068
0928-4931/© 2014 Elsevier B.V. All rights reserved.

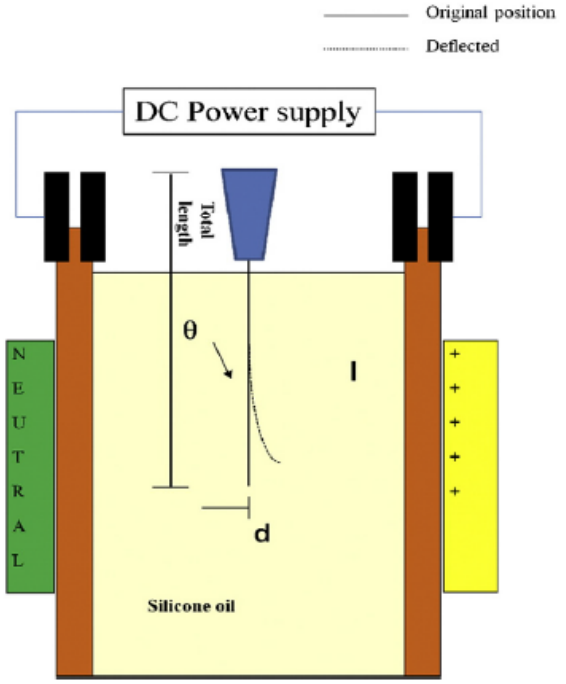

Fig. 1. Schematic diagram of the apparatus used to observe the dielectrophoresis force on the hydrogel samples.

of the composites without crosslinking agent due to the hydrophobic effect of the MWNT. Carbon nanotubes (CNTs) are an attractive form of carbon, consisting of concentric cylinders of graphite layer to graphene cylinders. CNT diameters are smaller than conventional carbon or glass fibers about 1000 times. Usually, nanotube aspect ratios are over 1000. The structural characteristics of CNTs are high aspect ratio, high surface area, and excellent mechanical, electrical and thermal properties. The MWNTs, used to enhance the mechanical properties of other hydrogels, have been previously investigated [17,18]. Chatterjee et al. [17] studied the mechanical strength of chitosan hydrogels with carbon nanotubes (CS/CNT). The 0.01 wt.% CS/CNT provided the greater mechanical strength than the crosslinked CS hydrogel. Tong et al. [18] investigated carbon nanotube/poly(vinyl alcohol) hydrogel to enhance the mechanical properties of the hydrogel and found that the 0.5 wt.% CNT/PVA hydrogel exhibited the improved tensile modulus, tensile strength and strain at break by 78.2%, 94.3% and 12.7%, respectively. Therefore MWNTs are excellent-promising-reinforcing materials for biopolymers that have been developed to several applications such as biosensor [19], and bioelectronic materials [20].

The objective of our investigation is to determine the electromechanical properties of multi-walled carbon nanotube/gelatin hydrogel composites containing an anionic surfactant (i.e., sodium dodecylsulfate) as candidate materials for actuator in robots or micro-devices. The electrical properties, thermal properties, and electrorheological properties were investigated in terms of MWNT concentration and aspect ratio, electric field strength, and temperature.

Table 1
Determination of density, diameter, and conductivity of multi-walled carbon nanotubes (MWNTs).

Samples	Quoted diameter of tube (nm)	Measured diameter of tube (nm)	Aspect ratios	Density (g/cm^3)	Average conductivity (S/cm)
MWNTs	3–10	9.47 ± 1.59	2100	2.103 ± 0.10	3237 ± 240
	10–20	18.38 ± 0.43	1200	2.170 ± 0.13	2161 ± 328
	20–30	27.09 ± 2.39	740	2.140 ± 0.10	1977 ± 195
	30–50	42.63 ± 3.85	470	2.143 ± 0.15	1693 ± 142

2. Experimental

2.1. Materials

Gelatin (Type B, bovine skin) and sodium dodecyl sulfate (SDS) were purchased from Sigma-Aldrich (Singapore) and Loba Chemie (India), respectively. Various multi-walled carbon nanotubes (MWNTs, >95 wt.% purity), as purchased from Alphanano Technology Co., Ltd., China, have specified diameters of 3–10, 10–20, 20–30, and 30–50 nm.

2.2. Preparation of MWNT/gelatin hydrogel composites

The final volume fractions of MWNTs were 0.01, 0.1, 0.5, and 1 vol.% in which MWNT volumes were compared with the volume of gelatin. The MWNTs (0.00063; 0.0063; 0.032; 0.063 g) were dispersed in 10 ml aqueous medium filled with SDS (~0.03 g) by a transonicator (Elma, S 70H, D 78224) at 30 °C, 50/60 Hz, 150 W, and 15 min. Then gelatin (~2.94 g) was dissolved in distilled water (20 ml; pH = 6.40) at 40 °C 2 h by magnetic stirring. Finally, two solutions were well-mixed at 40 °C overnight through magnetic stirring to obtain mixtures with various MWNT/gelatin volume fractions of 0.01, 0.1, 0.5, and 1 vol.%. Then the solutions were poured into Petri dishes to obtain the MWNT/gelatin hydrogel composites through solvent casting. The hydrogel composites were allowed to settle in as a sheet at 25 °C. The thickness of hydrogel composites was about 1.64 mm.

2.3. Characterization and testing of MWNT/gelatin hydrogel composites

True density of each multi-walled carbon nanotubes (MWNT) was measured by a gas pycnometer (Thermo Nicolet, Nexus 670) which was operated in He gas atmosphere (20 psi) at 25 °C with a purging gas time of 1 min. The true density of MWNT was measured repeatedly 20 times to obtain the average value and the standard deviation.

The electrical conductivity measurement (Keithley, Model 8009A) of the MWNT film samples was measured at 25 °C, and the fixture consisted of two probes that made contact with the surface of the MWNT film samples. The test fixture was connected to the power source (Keithley, Model 6517A) to supply a constant voltage source and for reading the resultant current. The applied voltage and the resultant current were used to determine electrical conductivity of the MWNT film samples by the following Eq. (1):

$$\sigma = \frac{I}{\rho} = \frac{I}{R_s t} = \frac{I}{KVt} \tag{1}$$

where σ is the specific conductivity (S/cm), ρ is the specific resistivity (Ω cm), t is the specimen thickness (cm), R_s is the sheet resistivity (Ω), I is the measured current (A), K is the geometric correction factor, and V is the applied voltage (V).

Scanning electron micrographs were taken with a scanning electron microscope (SEM; S-4800, Hitachi, Tokyo, Japan) to determine the morphology and sizes of the MWNT in a powder form, pristine gelatin, and MWNT/gelatin composites at various MWNT concentrations. The cross-section micrographs of gelatin and MWNT/gelatin composites were obtained by using an acceleration voltage of 10 kV with magnifications of 60 000 times. SEM imaging software (SEMAFORE 5.21) was used to provide tube diameter.

The topology and phase images of specimens were obtained from the atomic force microscopy (AFM, Park System, XE-100) where images were taken in the non-contact mode with the cantilever (NSC-14-CrAu) tapping at a scan rate of 0.25 Hz. The electrostatic force microscope (EFM) was determined at signal amplitude of 5 V, and a scan size of 1.25 × 1.25 μm^2. Each sample was scanned at two height levels above

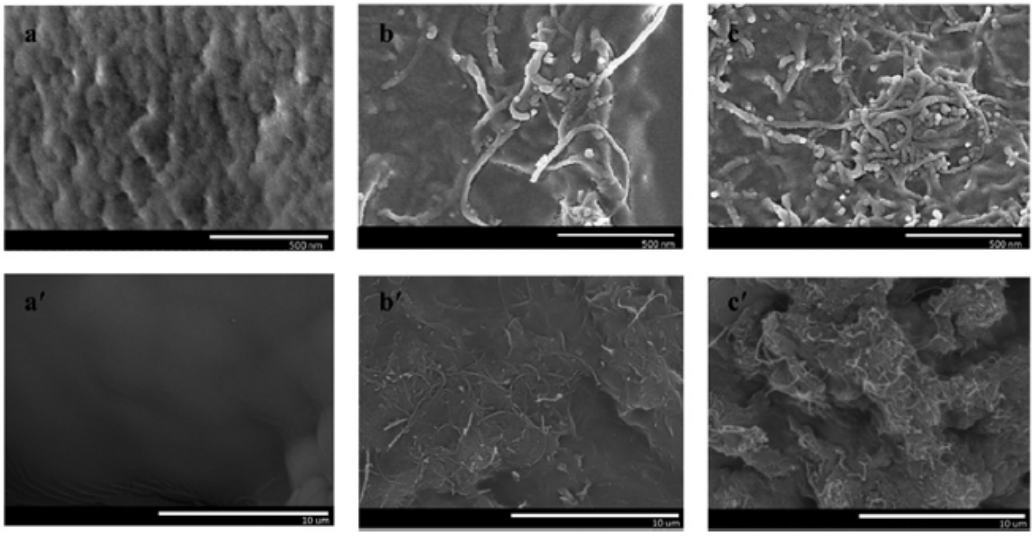

Fig 2. SEM micrograph of cross-sections of the pure gelatin and MWNT/gelatin hydrogels (magnification of 60 K and 10 K): (a) cross-sections of the pure gelatin of 60 K; (b) cross-section of the 0.1 vol.% MWNT/gelatin hydrogel of 60 K; (c) cross-section of the 1 vol.% MWNT/gelatin hydrogel of 60 K; (a′) cross-sections of the pure gelatin of 10 K; (b) cross-section of the 0.1 vol.% MWNT/gelatin hydrogel of 10 K; and (c) cross-section of the 1 vol.% MWNT/gelatin hydrogel of 10 K.

the surface. In the first level, tip scanned the surface to obtain the topology images in the non-contact AFM mode in response to the van der Waals forces. The second scan was carried out by measuring the tip-surface distance as a result of the electrostatic force. The charge distribution and the degree of charge generated were obtained from the EFM technique.

A melt rheometer (Rheometric Scientific, ARES) was used to study the electromechanical properties of the MWNT/gelatin hydrogel composites. They were fitted with a custom-built copper parallel plate fixture of 30-mm diameter. A DC voltage was applied at the electric field strength of 800 V/mm using a DC power supply (Instek, GFG8216A). First, a strain sweep test was operated to determine the suitable strain for measuring storage modulus (G') in the linear viscoelastic regime. The appropriate strain was determined to be 0.10% for both pure gelatin hydrogel and the MWNT/gelatin hydrogel composites. Prior to the temporal sweep and the frequency sweep test, samples were presheared at a low frequency (0.039811 rad/s) and a low strain (0.10%) with the application of electric field (800 V/mm) for 15 min to ensure the formation of equilibrium polarization. In both experiments, the specimens were measured as functions of electric field strength (0–800 V/mm) and temperature (30–80 °C). The bending behavior and the dielectrophoresis force were investigated under applied electric field strengths between 0 and 600 V/mm. Samples were gripped between copper plates and immersed in a transparent chamber containing polydimethylsiloxane (PDMS, viscosity 100 cSt) (as shown in Fig. 1). The input electric field strength was provided by a DC power supply (Gold Sun 3000, GPS 3003D) connected to a high voltage power supply (Gamma High Voltage, UC5-30P), which can deliver various electric field strengths from 25 to 600 V/mm. The amount of deflection of the pure gelatin and MWNT/gelatin hydrogel composites at the specific electric field strength is described by the parameters (d, l, and θ). A video recorder (Sony, Handicam HR1) was used to record the displacement of the pure gelatin and MWNT/gelatin hydrogel composites. The bending distances of the composites were measured from a Scion Image (Beta 4.0.3) program.

The dielectrophoretic force (F_d) on the samples was calculated through the static horizontal force balance consisting of the elastic force (F_e), the gravity force, and the buoyancy force as shown in Eq. (2)

$$F_d = F_e + mg(\sin\theta) - \rho V g(\sin\theta) \quad (2)$$

where m is the mass of sample (kg), g is the gravity constant (9.8 m/s^2), θ is the deflection angle, ρ is the density of fluid, V is the volume of the displaced fluid, and F_e is the resisting elastic force (N). In our experiment, the elastic force can be calculated by the following Eq. (3) [21,22]:

$$F_e = \frac{dEI}{l^3} \quad (3)$$

where E is the Young's modulus which is equal to $2G'(1+\nu)$ in which G' is the shear modulus (taken to be $G'(\omega = 1$ rad/s)) and ν is the Poisson's ratio, which is equal to 1/2 for an incompressible sample, I is the moment of inertia $t^3w/12$, t is the thickness of specimen, w is the width of specimen, d is the deflection distance, and l is the length of specimen.

3. Results and discussion

3.1. Characterization of multi-walled carbon nanotubes (MWNTs)

Characteristics of MWNTs are summarized in Table 1. True densities of four MWNTs are 2.143 ± 0.15, 2.140 ± 0.10, 2.170 ± 0.13, and 2.103 ± 0.10 g/cm^3, independent of different aspect ratio values. Our measured true density values are similar to the value (~2.1 g/cm^3) as reported by Lehman et al. [23].

The average diameters of the tubes at various aspect ratios as measured by SEM are 9.47 ± 1.59, 18.38 ± 0.43, 27.09 ± 0.10, and 42.63 ± 3.85 nm, which are consistent with the supplier material specification.

The specific conductivity values of MWNTs are approximately 3237, 2161, 1977, and 1693 S/cm (with standard deviations of 240, 328, 195, and 142 S/cm), respectively as shown in Table 1. Thus, the electrical conductivity of the lowest aspect ratio possesses the smallest value because electrons cannot transfer well in the spacing between MWNTs [24,25]. The smaller diameter nanotube promotes better packing and enhances the electrical conductivity [26]. For typical single-walled carbon nanotubes, the specific electrical conductivity is of the order of 10^3–10^4S/cm [27]. Dai et al. [28] reported that the electrical conductivity of MWNTs at ambient temperature is between 1250 and 8333 S/cm.

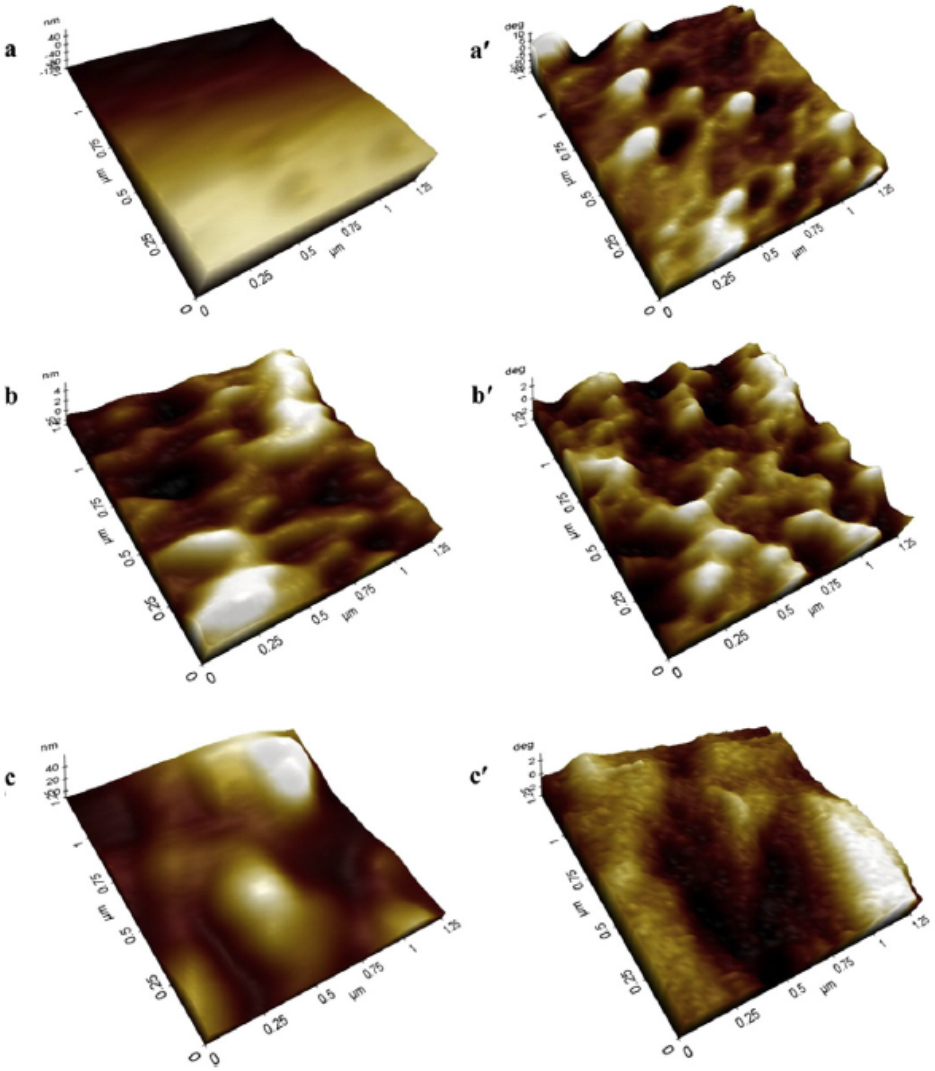

Fig. 3. (a) Topology image of pure gelatin hydrogel; (a′) EFM image under 5 V of sample voltage bias of pure gelatin hydrogel; (b) topology image of 0.1 vol.% MWNT/gelatin hydrogel; (b′) EFM image under 5 V of tip voltage bias of 0.1 vol.% MWNT/gelatin hydrogel; (c) Topology image of 1 vol.% MWNT/gelatin hydrogel; (c′) EFM image under 5 V of tip voltage bias of 1 vol.% MWNT/gelatin hydrogel.

3.2. Morphology of gelatin hydrogel and MWNT/gelatin hydrogel composites

The representative MWNT used was MWNT (3–10 nm), providing the aspect ratio of 2100 for observing its dispersion in a gelatin hydrogel. The MWNT has the highest aspect ratio which can induce the highest entanglement and bundling through strong van der Waals [29]. Cross-sectioned scanning electron micrographs of the gelatin hydrogel and composites are shown in Fig. 2 at 0.1 and 1 vol.% MWNT at the magnifications of 60 K and 10 K. It can be seen that the MWNT shows a moderately uniform dispersion in the gelatin hydrogel at low MWNT concentration (0.1 vol.%) with the aid of the surfactant, owing to the attraction of hydrophobic chain of SDS molecule around the surface of MWNTs [30]. In Fig. 2c and c′, the dispersion of MWNT at high concentration (1 vol.%) is relatively poor because of the difficulty in obtaining homogeneous dispersion of 1 vol.% MWNT in gelatin solution due to the large van der Waals attraction forces between MWNT molecules.

The topology and the phase charged surface of the MWNT/gelatin hydrogel composites were also investigated by the EFM phase measurement as shown in Fig. 3. The topology of the pure gelatin hydrogel and the 0.1 and 1 vol.% MWNT/gelatin hydrogel composites without electrical charge are shown in Fig. 3a–c. Fig. 3a shows the smooth surface of the pure gelatin hydrogel at a nanoscale. A micrograph of the 0.1 vol.% MWNT/gelatin hydrogel composite shows a well-distributed and randomly-aligned MWNT by the mechanical stirring force as shown in Fig. 3b. On the contrary, Fig. 3c demonstrates the agglomerated topology of 1 vol.% MWNT/gelatin hydrogel composites. Fig. 3a′–c′ shows the phase charged image of the pure gelatin hydrogel and the MWNT/gelatin hydrogel composites. The images exhibit the charge distributions within the materials where the light areas indicate the presence of the attractive charge generated between the probe tip and the materials. The degree of attractive charge generated on the pure gelatin hydrogel and the MWNT/gelatin hydrogel composites is shown in Fig. 4. Both of 0.1 and 1 vol.% MWNT/gelatin hydrogel composites possess the degrees of attractive charge generated of 101 and 106% respectively, values which are greater than that of the pure gelatin hydrogel.

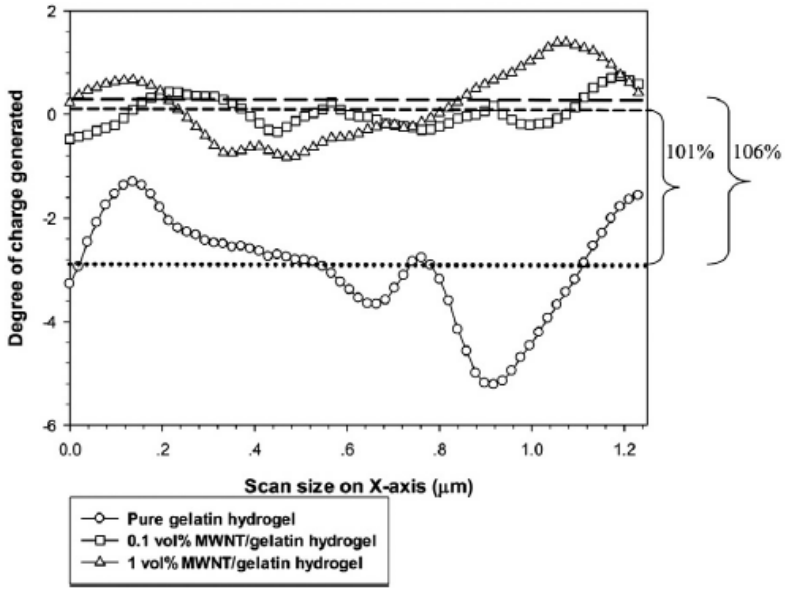

Fig. 4. Degree of charge generated on MWNT/gelatin hydrogel under 5 V of tip bias at whole region.

3.3. Electromechanical properties

3.3.1. Time dependence of the electrorheological response

The temporal response of the pure gelatin and the MWNT/gelatin hydrogel composites (0.1 vol.% and 1 vol.% MWNT) was investigated under the applied electric field strength of 800 V/mm as the electric field was switched on and off alternately. The temporal characteristics of materials were measured in the linear viscoelastic regime at a strain of 0.10%, and frequency of 100 rad/s. Fig. 5 shows the storage modulus (G') of the pure gelatin and of the MWNT/gelatin hydrogel composites during the time sweep tests under the electric field. For the pure gelatin hydrogel, when the electric field is switched on at 800 V/mm, G' immediately increases and rapidly reaches a steady-state value as the dipole moment within the materials are induced. As the electric field is switched off, G' decreases instantaneously close to its original value which can be referred to a reversible material. In contrast, for both MWNT/gelatin hydrogel composites (0.1 vol.% and 1 vol.% MWNT), G' decreases after switching off the electric field but it does not recover to their original values. These characteristics indicate that there are some residue dipole moments due to the agglomerations of the MWNT.

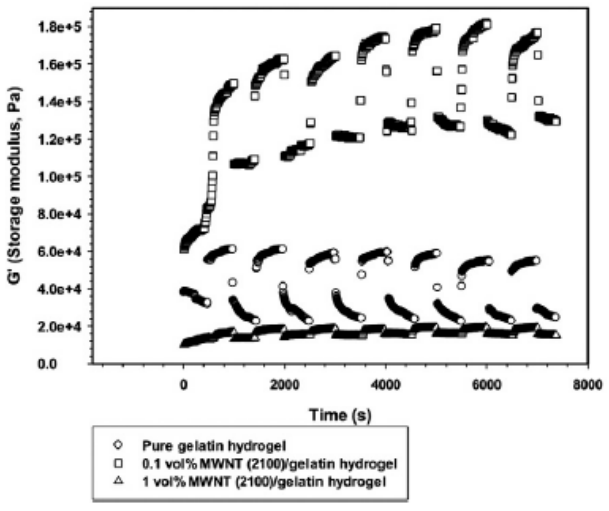

Fig. 5. Temporal responses of the storage modulus (G') of the pure gelatin hydrogel and the MWNT/gelatin hydrogels (sample diameter 30 mm, gel thickness 1.540 mm, 0.10% strain, frequency of 100 rad/s, 800 V/mm, 30 °C): pure gelatin hydrogel (○); 0.1 vol.% MWNT/gelatin hydrogel (□); 1 vol.% MWNT/gelatin hydrogel (Δ).

3.3.2. Effects of electric field strength and aspect ratio on electromechanical properties of MWNT/gelatin hydrogel composites

Effect of MWNT aspect ratios (470, 740, 1200, and 2100) on the electromechanical properties of 0.1 vol.% MWNT/gelatin hydrogel composites was first investigated in the range of 0 to 800 V/mm. Fig. 6 shows the storage modulus response ($\Delta G'$) and the storage modulus sensitivity ($\Delta G'/G'_o$) of the composites vs. electric field strength at a

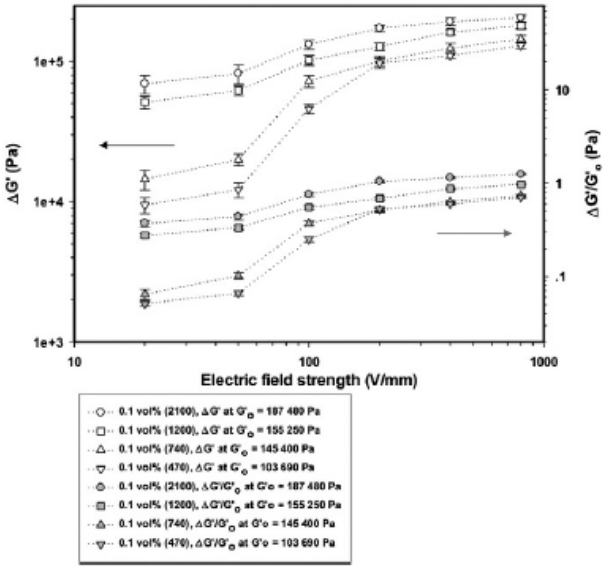

Fig. 6. Effect of aspect ratios of MWNT on the storage modulus response ($\Delta G'$) and storage modulus sensitivity ($\Delta G'/G'_o$) at various electric field strengths (sample diameter 30 mm, gel thickness 1.640 mm, 0.10% strain, frequency of 100 rad/s, 30 °C).

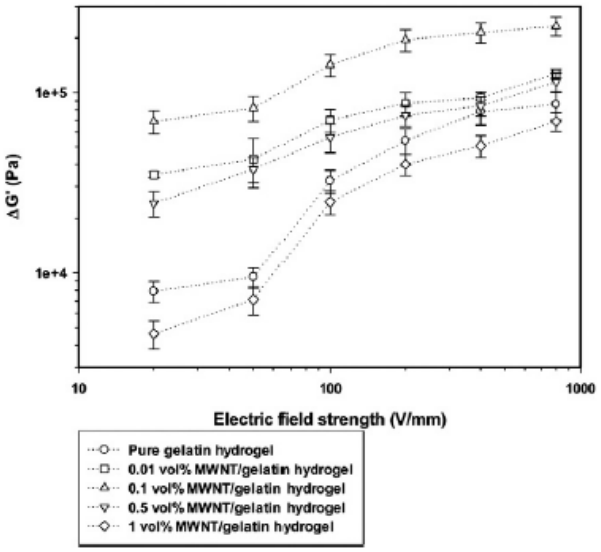

Fig. 7. Effect of concentration of MWNT (2100) on the storage modulus response ($\Delta G'$) at various electric field strengths (sample diameter 30 mm, gel thickness 1.640 mm, 0.10% strain, frequency of 100 rad/s, 30 °C).

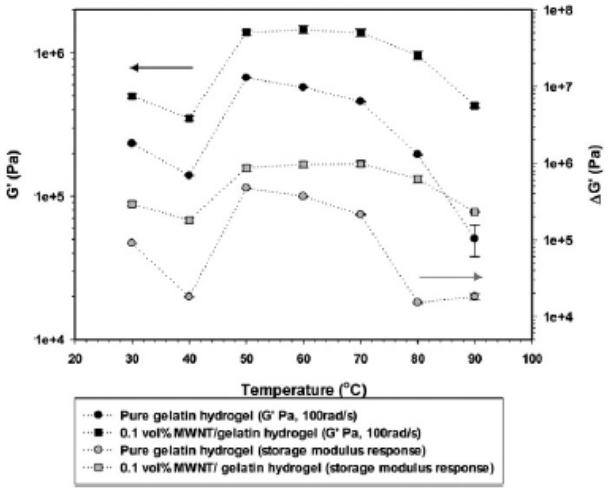

Fig. 8. Effect of concentration of MWNT (2100) on the storage modulus (G') and storage modulus response ($\Delta G'$) at various temperature (sample diameter 30 mm, gel thickness 1.640 mm, 0.10% strain, frequency of 100 rad/s, 800 V/mm).

frequency of 100 rad/s, a strain of 0.10%, and at a temperature of 30 °C. It can be seen that $\Delta G'$ and $\Delta G'/G'_o$ of 0.1 vol.% MWNT/gelatin hydrogel composites increase with increasing aspect ratio of MWNT and with increasing of electric field strength as the polarization is generated on carboxyl groups on the gelatin side chain, the dipole moment, leading to intermolecular interactions [12]. The main reason is the higher response with increase of MWNT aspect ratio is be due to the stronger interfacial force between the nanotube and the matrix due to a higher surface area [31], or the nanotube-matrix interaction [32].

Ayatollahi et al. [31] reported the mechanical properties of epoxy/0.5 wt.% MWNT at various aspect ratios (455, 555, 715, and 1000). Both of the modulus of elasticity and the tensile strength of the samples increased with increasing of aspect ratio. Manoharan et al. [32] reported that MWNT with a smaller diameter enhanced a stronger interface with the polymer matrix due to the higher surface area of the nanotube. Boo et al. [33] studied the effect of nanoplatelet structure on mechanical properties of epoxy nanocomposites. They found that the larger surface area increased the modulus of epoxy/ZrP-1000 relative to than that of epoxy/ZrP-100.

3.3.3. *Effect of concentration on electromechanical properties of MWNT/gelatin hydrogel composites*

The effect of MWNT concentration on the electromechanical properties of MWNT/gelatin hydrogel composites was studied at 30 °C with the electric field strength varying between 0 and 800 V/mm. Fig. 7 shows the storage modulus response ($\Delta G'$, $\omega = 100$ rad/s) of the gelatins at various MWNT contents of 0, 0.01, 0.1, 0.5 and 1 vol.%. $\Delta G'$ increases nonlinearly with increasing electric field strength. With increasing MWNT concentration from 0 to 0.1 vol.%, $\Delta G'$ increases from 82 507 to 223 600 Pa at an applied electric field strength of 800 V/mm. Further increase in the MWNT concentration (at 0.5 and 1 vol.%) leads to a reduction of $\Delta G'$. Interestingly, $\Delta G'$ of the 1 vol.% MWNT/gelatin hydrogel composite is inferior when compared to the pure gelatin hydrogel. Table 2 lists the storage modulus sensitivity ($\Delta G'/G'_o$) values of these materials at various MWNT contents. As MWNT concentration increases, the induced dipole moment increases under the applied electric field strength [34] due to the enhanced polarizability of the carboxyl groups of gelatin chains under the presence of MWNT. The maximum $\Delta G'$ and $\Delta G'/G'_o$ are found in the 0.1 vol.% MWNT/gelatin hydrogel composite. However, as the MWNT content is higher than 0.1 vol.%, $\Delta G'$ decreases. As the highest MWNT concentration of 1 vol.%, $\Delta G'$ under the applied electric field diminishes since the material presumably consists of the phase separation between the hydrogel and the MWNT agglomeration as previously observed in the SEM image and topology surface (see Figs. 2c and 3c).

Ayatollahi et al. [31] found the similar behavior in that the Young's modulus and the tensile strength of epoxy/MWNT composites increased with increasing of MWNT. However at the higher MWNT concentration of 0.5 wt.%, the mechanical properties decreased due to the effect of agglomeration. Prashantha et al. [35] reported the optimum mechanical properties of multi-walled carbon nanotube filled polypropylene nanocomposite, 2 wt.% MWNT was the optimum concentration to enhance the modulus of the composite due to the dispersion and the distribution of individual nanotubes in the matrix. Evingur and Pekcan [36] studied the elasticity modulus of polyacrylamide (PAAm)/multi-walled carbon nanotube (MWNT). The elastic modulus of PAAm/MWNT increased with increasing of MWNT concentration. Kunanuruksapong and Sirivat [37] reported a similar effect for poly(*p*-phenylene)/acrylic elastomer blended. The storage modulus response ($\Delta G'$) of poly(*p*-phenylene)/acrylic elastomer blended increased with increasing poly(*p*-phenylene) concentration.

Table 2
Sensitivity of storage modulus of the pure gelatin hydrogel and the MWNT (2100)/gelatin hydrogels (0.10% strain, electric field strength 800 V/mm, frequency 100 rad/s, 30 °C).

Materials (MWNT diameter 3–10 nm)	Storage modulus (G') (Pa)	Initial storage modulus (G'_o) (Pa)	Sensitivity of storage modulus ($\Delta G'/G'_o$)
Pure gelatin hydrogel	2.60×10^5	1.78×10^5	0.47
0.01 vol.% MWNT (2100)/gelatin hydrogel	3.08×10^5	1.81×10^5	0.70
0.1 vol.% MWNT (2100)/gelatin hydrogel	4.21×10^5	1.87×10^5	1.25
0.5 vol.% MWNT (2100)/gelatin hydrogel	2.34×10^5	1.20×10^5	0.94
1 vol.% MWNT (2100)/gelatin hydrogel	1.53×10^5	8.50×10^4	0.81

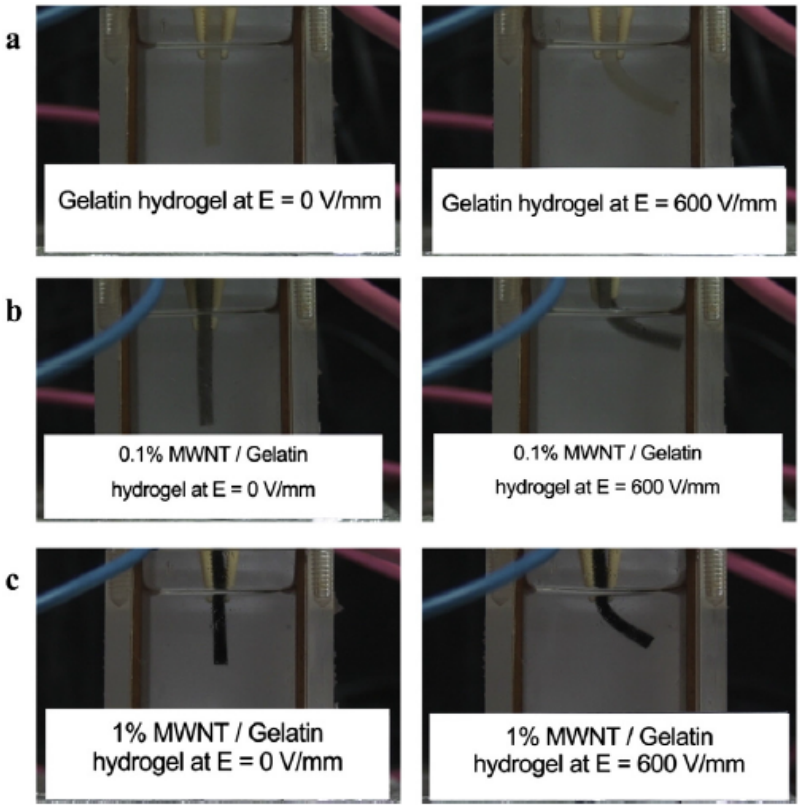

Fig. 9. Deflection of the gelatin hydrogels at E = 0 and 600 V/mm: (a) pure gelatin hydrogel; (b) 0.1 vol.% MWNT/gelatin hydrogel; (c) 1 vol.% MWNT/gelatin hydrogel. (Note that the polarity of the electrode on the right-hand side is positive.)

3.3.4. Effect of the operating temperature

The electromechanical properties of the pure gelatin and the MWNT/gelatin hydrogel composites were investigated at the temperature range between 30 and 90 °C. The result shows that storage modulus at 800 V/mm (G') and storage modulus response ($\Delta G'$) of the composites exhibit three response regimes as shown in Fig. 8. With increasing temperature from 30 to 40 °C, G' of the pure gelatin hydrogel decreases because the triple-helix structure is split to the random coil structure [38]. At the temperature range of 40–50 °C, G' increases again with temperature. According to the classical network theory [22], as temperature increases, the entropy of gel increases that leading to more retractive force. However further increase in temperature (from 60 to 90 °C) leads to a decrease in G' since α-amino acid block of the gelatin chain is isolated at a temperature close to the low-temperature glass transition of 120 °C [39]. Similar electromechanical properties are observed during the same temperature range for the 0.1 vol.% MWNT/gelatin hydrogel composite, the level of triple-helix structure denaturation (30–40 °C) and the lower temperature glass transition temperature (~60–80 °C) of the composite could be retarded due to the enhanced polarizability of the carboxyl groups in the gelatin chains. The obtained result indicates that the electromechanical responses of the MWNT/gelatin hydrogel composites are largely improved in term of $\Delta G'$ due to the presence of MWNT. At any temperatures studied, $G'_{800v/mm}$ and $\Delta G'$ are higher than those of the pure gelatin hydrogel because MWNT acts as reinforced particles and enhances the polarizability in the gelatin chains under the electric field.

Table 3
Induction time of MWNT/gelatin hydrogel at various electric field strengths from deflection measurement: (a) pure gelatin hydrogel; (b) 0.1 vol.% MWNT/gelatin hydrogel; (c) 1 vol.% MWNT/gelatin hydrogel.

Materials	Induction time (s) at various electric field strength (V/mm)							
	25	50	100	200	300	400	500	600
Pure gelatin hydrogels	–	–	10	8	7	7	6	4
0.1 vol.% MWNT (3–10 nm)/gelatin hydrogel	–	–	6	6	4	3	2	1
1 vol.% MWNT (3–10 nm)/gelatin hydrogel	–	–	7	6	6	4	3	2

3.4. Deflection of MWNT/gelatin hydrogel composites

The bending behavior of the pure gelatin and all MWNT/gelatin hydrogel composites is shown in Fig. 9a–c. Results show that all of the samples bend toward the anode side (positive charge) under the influence of the electric field strength of 600 V/mm due to the attractive force between the polarized carbonyl group of hydrogel and the anode side. The polarization of the carbonyl groups can be referred to as the electrophilic behavior which generates the negative charges on their groups. As higher electric field strength is applied, stronger dipole moments are generated leading to a higher degree of deflection. The pure gelatin, 0.1 vol.% MWNT/gelatin, and 1 vol.% MWNT/gelatin hydrogels start to deflect at lower critical electric field strengths of 100 V/mm, 100 V/mm, and 250 V/mm, respectively. The 0.1 vol.% MWNT/gelatin hydrogel composite exhibits the greatest deflection values relative to other samples. The degree of deflection (θ) of 0.1 vol.% MWNT/gelatin hydrogel composite is higher than the pure gelatin hydrogel due to the higher amount of polarizability from MWNT. In contrast, the 1 vol.% MWNT/gelatin hydrogel composite shows a lesser deflection

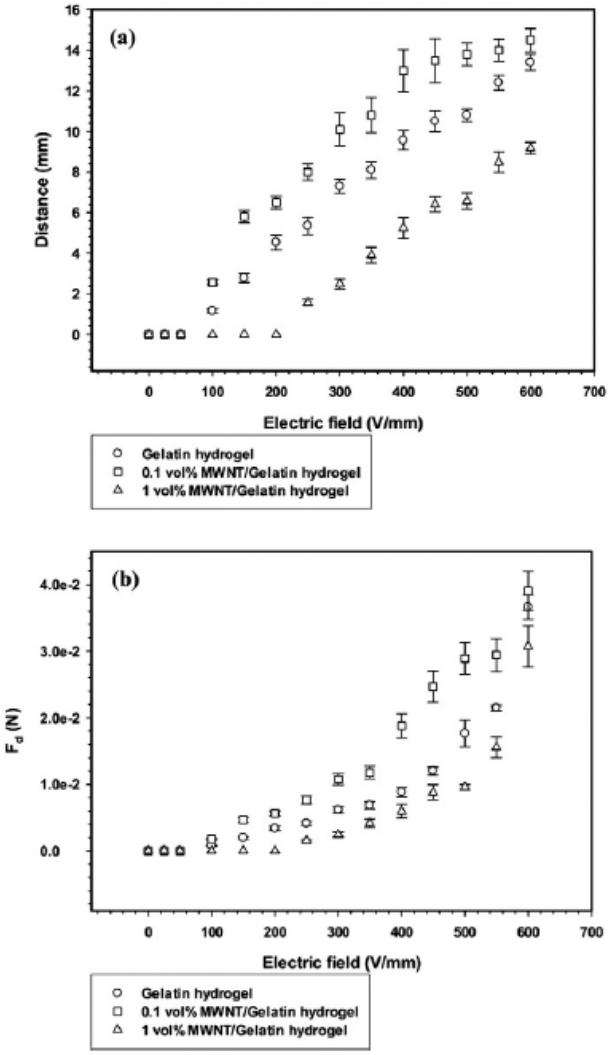

Fig. 10. Deflection distance of the pure gelatin hydrogel, the 0.1 vol.% MWNT/gelatin hydrogel, and the 1 vol.% MWNT/gelatin hydrogel at various electric field strengths. (b) Dielectrophoresis force calculated through the linear deflection theory.

response than the other two samples due to too high particle contents [40]. The induction times of these samples of deflection response are tabulated in Table 3. The induction time is the time which is required for the sample to deflect toward the maximum distance in the influence of applied electric field strength. All of the samples studied exhibit fast deflection response which is one of the important factors for actuator application. Fig. 10a–b shows the deflection distances and the dielectrophoresis forces (F_d) of the pure gelatin and the MWNT/gelatin hydrogel composites under electric field strength. The deflection distances and the dielectrophoresis forces of these materials become larger with increasing electric field strength. At electric field strength of 600 V/mm, F_d of the pure gelatin hydrogel, 0.1 vol.% MWNT/gelatin, and 1.0 vol.% MWNT/gelatin hydrogel composites are 0.036, 0.039, and 0.031 N, respectively. The F_d of 0.1 vol.% MWNT/gelatin hydrogel composites is the highest since such a composite has a higher amount of polarized nanotube content that creates a stronger attractive with the anode side. However, the 1 vol.% MWNT/gelatin hydrogel composite shows a lower F_d than the pure gelatin and 0.1 vol.% MWNT/gelatin hydrogel composite due to the particle steric hindrance [41].

In the previous works, Niamlang and Sirivat [42] investigated dielectrophoresis force and deflection of poly(p-phenylenevinylene)/polydimethylsiloxane blends (PPV/PDMS). The dielectrophoresis force and the degree of deflection of the PPV/PDMS films increased with increasing electric field strength. Kunchornsup and Sirivat [43] reported the dielectrophoresis force of cellulose gel under the electric field strength between 0 and 550 V/mm. At 500 V/mm, the cellulose gel showed the dielectrophoresis force of 4.6 N and deflection angle at 44°, respectively. Tungkavet et al. [8] reported the dielectrophoresis forces at E = 600 V/mm of 0.1 vol.% and 1 vol.% nanowire-Ppy gelatin hydrogels to be 6.60 and 1.60 mN, respectively since the 1 vol.% nanowire-Ppy has strong positive charges that counteract those of negative charges in gelatin structure and the effect of steric hindrance. Petcharoen and Sirivat [44] studied the dielectrophoresis force of thermoplastic polyurethane elastomer (TPE-PU). TPE-PU generated the highest dielectrophoresis force (43 μN) and deflection distance (10 mm) at electric field strength of 500 V/mm. In this work, 0.1 vol.% MWNT/gelatin hydrogel composite provide the greatest deflection distance at 14.50 mm and the maximum dielectrophoresis force of 0.039 N.

4. Conclusions

This work presents the electromechanical properties, the dynamic storage moduli (G') and the bending measurement of pure gelatin and MWNT/gelatin hydrogel composites as functions of electric field strength and temperature. When the electric field was applied, the polarization generated in gelatin chain was further enhanced by the presence of MWNT and induced greater electrostatic interaction. Both of the storage modulus response ($\Delta G'$) and the storage modulus sensitivity ($\Delta G'/G_o$) increased with increasing electric field strength up to 800 V/mm. The maximum $\Delta G'$ and $\Delta G'/G_o$ were 2.34×10^5 Pa and 1.25, respectively, for the 0.1 vol.% MWNT/gelatin hydrogel composite. For the effect of temperature, both G' and $\Delta G'$ exhibited three behaviors between 30 and 90 °C. From the deflection measurement, the deflection distance and the dielectrophoresis force (F_d) of the pure gelatin and 0.1 vol.% and 1 vol.% MWNT/gelatin hydrogel composites increased with increasing electric field strength. The 0.1 vol.% MWNT/gelatin hydrogel composite exhibited the greatest deflection response; whereas the 1 vol.% MWNT/gelatin hydrogel composite showed the lowest deflection distance and F_d due to the particle steric hindrance.

Acknowledgments

The authors would like to acknowledge the financial supports from the Conductive and Electroactive Polymers Research Unit of Chulalongkorn University; the Thailand Research Fund (TRF); the Royal Thai Government; the 90th Anniversary of Chulalongkorn University Fund (Ratchadaphiseksomphot Endowment Fund); The Petroleum and Petrochemical College (PPC); Chulalongkorn University; and the Doctoral Scholarship from the Thailand Graduate Institute of Science and Technology (TGIST) (TG-33-09-53-003D).

References

[1] T. Okano, Y.H. Bae, H. Jacobs, S.W. Kim, Thermally on-off switching polymers for drug permeation and release, J. Control. Release 11 (1990) 255–265.
[2] H.M. Zareie, E.V. Bulmus, A.P. Gunning, A.S. Hoffman, E. Piskin, V.J. Morris, Investigation of stimuli-responsive copolymer by atomic force microscopy, Polymer 41 (2000) 6723–6727.
[3] T.G. Park, A.S. Hoffman, Synthesis and characterization of pH- and/or temperature-sensitive hydrogels, J. Appl. Polym. Sci. 46 (1992) 659–671.
[4] S.Y. Kim, H.S. Shin, Y.M. Lee, C.N. Jeong, Properties of electroresponsive poly(vinyl alcohol)/poly(acrylic acid) IPN hydrogels under an electric stimulus, J. Appl. Polym. Sci. 73 (1999) 1675–1683.
[5] S.J. Kim, K.J. Lee, S.I. Kim, Y.M. Lee, T.D. Chung, S.H. Lee, Electrochemical behavior of an interpenetrating polymer network hydrogel composed of poly(propylene glycol) and poly(acrylic acid), J. Appl. Polym. Sci. 89 (2002) 2301–2305.

[6] S. Kaewpirom, S. Boonsang, Electrical response characterization of poly(ethylene glycol) macromer (PEGM)/chitosan hydrogels in NaCl solution, Eur. Polym. J. 42 (2006) 1609–1616.
[7] S.J. Kim, S.J. Park, I.Y. Kim, M.S. Shin, S.I. Kim, Electric stimuli response to poly(vinyl alcohol)/chitosan interpenetrating polymer network hydrogel in NaCl solutions, J. Appl. Polym. Sci. 86 (2002) 2285–2289.
[8] T. Tungkavet, N. Seetapan, D. Pattavarakorn, A. Sirivat, Improvements of electromechanical properties of gelatin hydrogels by blending with nanowire polypyrrole: effects of electric field and temperature, Polym. Int. 61 (2012) 825–833.
[9] X.J. Yang, P.J. Zheng, Z.D. Cui, N.Q. Zhao, Y.F. Wang, K.D. Yao, Swelling behavior of elastic properties of gelatin gels, Polym. Int. 44 (1997) 448–452.
[10] T.H. Nguyen, B.T. Lee, Fabrication and characterization of cross-linked gelatin electro-spun nano-fibers, J. Biomed. Sci. Eng. 3 (2010) 1117–1124.
[11] S.B. Ross-Murphy, Structure and rheology of gelatin gels: recent progress, Polymer 33 (1992) 2622–2627.
[12] T. Tungkavet, D. Pattavarakorn, A. Sirivat, Bio-compatible gelatins (Ala-Gly-Pro-Arg-Gly-Glu-4Hyp-Gly-Pro-), J. Polym. Res. 19 (2012) 9759-3.
[13] A. Fraczek, E. Menaszek, C. Paluszkiewicz, M. Blazewicz, Comparative in vivo biocompatibility study of single- and multi-wall carbon nanotubes, Acta Biomater. 4 (2008) 1593–1602.
[14] J. Chlopek, B. Czajkowska, B. Szaraniec, E. Frackowiak, K. Szostak, F. Beguin, In vitro studies of carbon nanotubes biocompatibility, Carbon 44 (2006) 1106–1111.
[15] H. Li, D.Q. Wang, H.L. Chen, B.L. Liu, L.Z. Gao, A novel gelatin–carbon nanotubes hybrid hydrogel, Macromol. Biosci. 3 (2003) 720–724.
[16] S. Haider, S.Y. Park, K. Saeed, B.L. Farmer, Swelling and electroresponsive characteristics of gelatin immobilized onto multi-walled carbon nanotubes, Sensors Actuators B Chem. 124 (2007) 517–528.
[17] S. Chatterjee, M.W. Lee, S.H. Woo, Enhanced mechanical strength of chitosan hydrogel beads by impregnation with carbon nanotubes, Carbon 47 (2009) 2933–2939.
[18] X. Tong, J. Zheng, Y. Lu, Z. Zhang, H. Cheng, Swelling and mechanical behaviors of carbon nanotube/poly(vinyl alcohol) hybrid hydrogels, Mater. Lett. 61 (2007) 1704–1706.
[19] Z. Guo, P.J. Sadler, S.C. Tsang, Immobilization and visualization of DNA and protein on carbon nanotubes, Adv. Mater. 10 (1998) 701–703.
[20] R.A. Macdonald, B.F. Laurenzi, G. Viswanathan, P.M. Ajayan, J.P. Steqemann, Collagen–carbon nanotube composite materials as scaffolds in tissue engineering, J. Biomed. Mater. Res. A 74 (2005) 489–496.
[21] T. Sato, H. Watanabe, K. Osaki, Rheological and dielectric behavior of a styrene–isoprene–styrene triblock copolymer in n-tetradecane. 1. Rubbery-Plastic-Viscous transition, Macromolecules 29 (1996) 6231–6239.
[22] S.P. Timoshenko, J.N. Goodier, Theory of Elasticity, McGraw-Hill, Auckland, 1970.
[23] J.H. Lehman, M. Terrones, E. Mansfield, K.E. Hurst, V. Meunier, Evaluating the characteristics of multiwall carbon nanotubes, Carbon 49 (2011) 2581–2602.
[24] Q. Li, Y. Li, X. Zhang, S.B. Chikkannanavar, Y. Zhao, A.M. Dangelewicz, L. Zheng, S.K. Doorn, Q. Jia, D.E. Peterson, P.N. Arendt, Y. Zhu, Structure-dependent electrical properties of carbon nanotube fibers, Adv. Mater. 19 (2007) 3358–3363.
[25] C. Du, N. Pan, Carbon nanotube-based supercapacitors, NLB 4 (2007) 569–576.
[26] D. Chattopadhyay, I. Galeska, F. Papadimitrakopoulos, A route for bulk separation of semiconducting from metallic single-wall carbon nanotubes, J. Am. Chem. Soc. 125 (2003) 3370–3375.
[27] P.R. Bandaru, Electrical properties and applications of carbon nanotube structures, J. Nanosci. Nanotechnol. 7 (2007) 1–29.
[28] H. Dai, W. Wong, C.M. Lieber, Probing electrical transport in nanomaterials: conductivity of individual carbon nanotubes, Science 272 (1996) 523–526.
[29] R. Rastogi, R. Kaushal, S.K. Tripathi, A.L. Sharma, I. Kaur, L.M. Bharadwaj, Comparative study of carbon nanotube dispersion using surfactants, J. Colloid Interface Sci. 328 (2008) 421–428.
[30] C. Richard, F. Balavoine, P. Schultz, T.W. Ebbesen, C. Mioskowski, Supramolecular self-assembly of lipid derivatives on carbon nanotubes, Science 300 (2003) 775–778.
[31] M.R. Ayatollahi, S. Shadlou, M.M. Shokrieh, M. Chitsazzadeh, Effect of multi-walled carbon nanotube aspect ratio on mechanical and electrical properties of epoxy-based nanocomposites, Polym. Test. 30 (2011) 548–556.
[32] M.P. Manoharan, A. Sharma, A.V. Desai, M.A. Haque, C.E. Bakis, K.W. Wang, The interfacial strength of carbon nanofiber epoxy composite using single fiber pullout experiments, Nanotechnology 20 (2009) 1–5.
[33] W.J. Boo, L. Sun, G.L. Warren, E. Moghbelli, H. Pham, A. Clearfield, H.J. Sue, Effect of nanoplatelet aspect ratio on mechanical properties of epoxy nanocomposites, Polymer 48 (2007) 1075–1082.
[34] T. Shiga, Deformation and viscoelastic behavior of polymer gels in electric fields, Advances in Polymer Science, Springer-Verlag, Berlin, 1997. 134.
[35] K. Prashantha, J. Soulestin, M.F. Lacrampe, P. Krawczak, G. Dupin, M. Claes, Masterbatch-based multi-walled carbon nanotube filled polypropylene nanocomposites: assessment of rheological and mechanical properties, Compos. Sci. Technol. 69 (2009) 1756–1763.
[36] G.A. Evingur, O. Pekcan, Temperature effect on elasticity of swollen composite formed from polyacrylamide (PAAm)-multiwall carbon nanotubes (MWNTs), Engineering 4 (2012) 619–624.
[37] R. Kunanuruksapong, A. Sirivat, Poly(p-phenylene) and acrylic elastomer blends for electroactive application, Mater. Sci. Eng. A 454–455 (2007) 453–460.
[38] A. Bigi, S. Panzavolta, K. Rubini, Relationship between triple-helix content and mechanical properties of gelatin films, Biomaterials 25 (2004) 5675–5680.
[39] A.N. Fraga, R.J.J. Williams, Thermal properties of gelatin films, Polymer 26 (1985) 113–118.
[40] S. Krause, K. Bohon, Electromechanical response of electrorheological fluids and poly(dimethylsiloxane) networks, Macromolecules 34 (2001) 7179–7189.
[41] B. Liu, T.M. Shaw, Electrorheology of filled silicone elastomers, J. Rheol. 45 (2001) 641–657.
[42] S. Niamlang, A. Sirivat, Dielectrophoresis force and deflection of electroactive poly(p-phenylenevinylene)/polydimethylsiloxane blends, Smart Mater. Struct. 17 (2008) 1–8.
[43] W. Kunchornsup, A. Sirivat, Physically cross-linked cellulosic gel via 1-butyl-3-methylimidazolium chloride ionic liquid and its electromechanical responses, Sensors Actuators A 175 (2012) 155–164.
[44] K. Petcharoen, A. Sirivat, Electrostrictive properties of thermoplastic polyurethane elastomer: effects of urethane type and soft–hard segment composition, Curr. Appl. Phys. 13 (2013) 1119–1127.

Polym. Bull. (2015) 72:281–294
DOI 10.1007/s00289-014-1272-5

ORIGINAL PAPER

Synthesis and characterization of sulfonated poly(aromatic imide-*co*-aliphatic imide) (S-coPI) membrane for direct methanol fuel cells

N. Taweekarn · S. Changkhamchom · A. Sirivat

Received: 9 September 2013 / Accepted: 4 November 2014 / Published online: 12 November 2014
© Springer-Verlag Berlin Heidelberg 2014

Abstract A novel polymer electrolyte membrane (PEM) based on sulfonated poly(aromatic imide-*co*-aliphatic imide) (S-coPI) is synthesized by the polycondensation of 3,3′,4,4′-benzophenonetetracarboxylic dianhydride (BPTDA) with 4,4′-diaminodiphenylmethane (DDM), 4,4′-diaminodiphenylmethane-3,3′-disulfonic acid disodium salt (S-DDM), and adipic acid dihydrazide (ADH). The ADH is utilized to increase the flexibility of the backbone structure due to its aliphatic structure. The sulfonation degree of S-coPI is controlled by varying the mole ratio of DDM, S-DDM, and ADH. The S-DDM containing two sulfonated groups is confirmed by ^{1}H-NMR. S-coPI membranes are characterized by FT-IR to identify the characteristic peaks of the sulfonated group at 1,298, 1,159, 1,098, and 1,065 cm^{-1}. Thermogravimetric analysis is used to investigate the thermal stability of S-coPI; it undergoes 2 steps in the degradation process, one at 320 °C which represents the decomposition of the sulfonated group and one at 560 °C which represents the polymer backbone degradation. The S-coPI-3, with the highest sulfonation degree, possesses proton conductivity value of about 1.16×10^{-2} S cm^{-1}. The methanol permeability of the S-coPI films are in the range of 3.864×10^{-8}–6.521×10^{-8} cm^2 s^{-1}, about 26–40 times lower than that of Nafion 117.

Keywords Sulfonated poly(aromatic imide-*co*-aliphatic imide) · Sulfonated group · Proton conductivity · Methanol permeability

N. Taweekarn · S. Changkhamchom · A. Sirivat (✉)
Conductive and Electroactive Polymers Research Unit, The Petroleum and Petrochemical College, Chulalongkorn University, Bangkok 10330, Thailand
e-mail: anuvat.s@chula.ac.th

Introduction

Fuel cells are alternative energy sources which can replace traditional fossil energy in the future. Furthermore, they are environmental friendly, available in a wide-size range, and suitable for portable electronic device to large electric vehicle. One of the most popular fuel cells is the direct methanol fuel cell (DMFC) because of its high energy efficiency and its simple operating system design. The polymer electrolyte membrane should have the following properties: high proton conductivity, high chemical and thermal stabilities, high mechanical strength, and low cost. The DMFC consists of an anode where methanol is fed and catalyzed to protons and electrons and a cathode in which oxygen (usually air) is fed and combined with protons which is then passed through the polymer membrane from the anode and an electron which passes through an external circuit that generates electricity to a connected device [1].

The main problematic issues of DMFCs are: (1) the crossover of methanol over the membrane from the anode to the cathode, which leads to the poisoning of the catalyst (reduce electrical efficiency of fuel cell) [2]; and (2) the drying of the polymer electrolyte at a high temperature, which results in the loss of proton conductivity from the evaporation of water. Furthermore, an electrolyte membrane may degrade at a high temperature. The degradation has been investigated by some researchers; however, a problem still remains in the film-casting step as polymers cannot dissolve in common organic solvents.

Several techniques such as blending with other polymers and particles loading into the membrane have been developed to solve these problems. One method for dealing with the degradation and the processing is to modify the polymer structure used as the electrolyte membrane. Several monomers and polymers have been selected, modified, and synthesized with different functional groups within the main chains and/or existing as pendant groups. Aromatic polymers are already well-known for their high thermal stability. Polyimide has been commercially available possessing good mechanical, thermal, and oxidative stabilities [3]. A problem occurs in the processing, namely the insolubility [4] of common organic solvents due to the rigidity of their backbone, the strong hydrogen bonding in aromatic polyimide, and the charge transfer complex formation in aromatic polyimides [5]. One way to improve solubility of the polymer membrane is to introduce a sulfonated group to the polymer structure; a sulfonated group not only improves solubility but also increases the proton conductivity as the presence of the sulfonated groups increases the proton hopping area [6].

The objective of this work is synthesize and characterize a sulfonated poly(aromatic imide-*co*-aliphatic imide) (S-coPI) membrane which contains a flexible backbone structure, and to study proton conductivity, thermal and mechanical properties, and methanol permeability of three different S-coPI cast films.

Experimental

Materials

3,3′,4,4′-Benzophenonetetracarboxylic dianhydride (BPTDA; Aldrich, 96 %), 4,4′-diaminodiphenylmethane (DDM; Aldrich, 97 %), and adipic acid dihydrazide (ADH; Fluka, 97 %) were used as the starting monomers. Fuming sulfuric acid (SO_3; Merck, 65 %), concentration sulfuric acid (H_2SO_4; Univar, 98 %), and sodium hydroxide (NaOH; Univar, pellet 97 %) were used in the sulfonation process. Hydrochloric acid (HCl; Univar, 37 %), sodium chloride (NaCl; Lab-Scan, 99 %), and 1 M sodium hydroxide (Fisher Scientific) were used to determine the sulfonation degree and the ion exchange capacity. Methanol (Lab-Scan, 99.9 %) and ethanol (Lab-Scan, 99.9 %) were used in the determination of the methanol permeability. Dimethylsulfoxide (DMSO; RCI Labscan, 99.9 %) and dimethylformamide (DMF; RCI Labscan, 99.8 %) were used as solvents. Benzoic acid (Univar, 99.9 %) and triethylamine (Et_3N; Fluka, 98 %) were used in the synthesis step. Acetone (Burdick & Jackson, 99.9 %) was used to precipitate the polymer powder.

Sulfonation of 4,4′-diaminodiphenylmethane-2,2′-disulfonic acid disodium salt (S-DDM)

Ten grams (50.45 mmol) of 4,4′-diaminodiphenylmethane was dissolved in 20 ml of 98 % sulfuric acid using three-necked round-bottom flask, with a mechanical stirring device. The solution was submerged in an ice bath until completely dissolved. A 10 ml of 65 % fuming sulfuric acid was added and the solution was stirred for 2 h, then it was heated to 80 °C and stirred for another 2 h. The solution was slowly poured into the ice bath and the polymer powder was precipitated by adding a sodium hydroxide solution until obtaining a basic solution. The precipitate was filtered, washed with deionized water, and dried at room temperature in a vacuum oven for 24 h [7]. The scheme of the sulfonation is shown in Fig. 1.

Preparation of sulfonated poly(aromatic imide-*co*-aliphatic imide)

S-DDM, DDM, and ADH at various mole ratios were dissolved in dimethylsulfoxide; the degree of sulfonation was controlled by changing the molar ratio of S-DDM and DDM. For the synthesis, the S-coPI-1 with the molar ratio of 1:3:6, the following took place: 0.374 g (0.931 mmol) of S-DDM and 0.554 g (2.793 mmol) of DDM were dissolved in DMSO and then 0.26 ml (1.86 mmol) of triethylamine

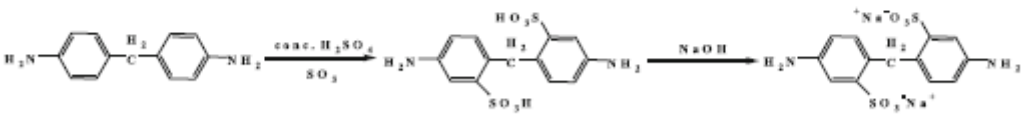

Fig. 1 The scheme for sulfonation of 4,4′-diaminodiphenylmethane (DDM)

was added. After that, 0.973 g (5.586 mmol) of ADH was added to the solution. Next, 3.00 g (9.31 mmol) of BPTDA in dimethylsulfoxide solution was added, and lastly 0.25 g (2.05 mmol) of benzoic acid was added. The reactions were carried out under a nitrogen atmosphere for 24 h to obtain sulfonated polyamic acid. Then, the solution was heated to 90 °C for 4 h. After the solution was cooled, the precipitate in acetone was vigorously stirred to produce a yellow powder. The precipitate was dried at room temperature under vacuum for 24 h. The powder was dissolved in DMF and casted onto a glass plate, then dried at 80 °C under vacuum for 24 h, and then at 160 °C under vacuum for 24 h to get a S-coPI membrane [8]. The scheme of the synthesis is shown in the Fig. 2.

Characterizations and testing

FT-IR and ^{1}H-NMR spectroscopy

The S-DDM and S-coPI powders were first characterized for the functional groups with a FT-IR spectrometer (Thermo Nicolet, Nexus 670), in the absorption mode with 64 scans and a resolution of 4 cm^{-1}, and in a wavenumber range of 4,000–400 cm^{-1}. Optical grade KBr was used as the background material and the powder was mixed with the dried KBr before measurement. The ^{1}H-NMR spectra of S-DDM in deuterated dimethylsulfoxide (DMSO-d_6) were recorded on a Varian mercury 400 MHz instrument to confirm the positions and the number of the sulfonated groups on the monomer.

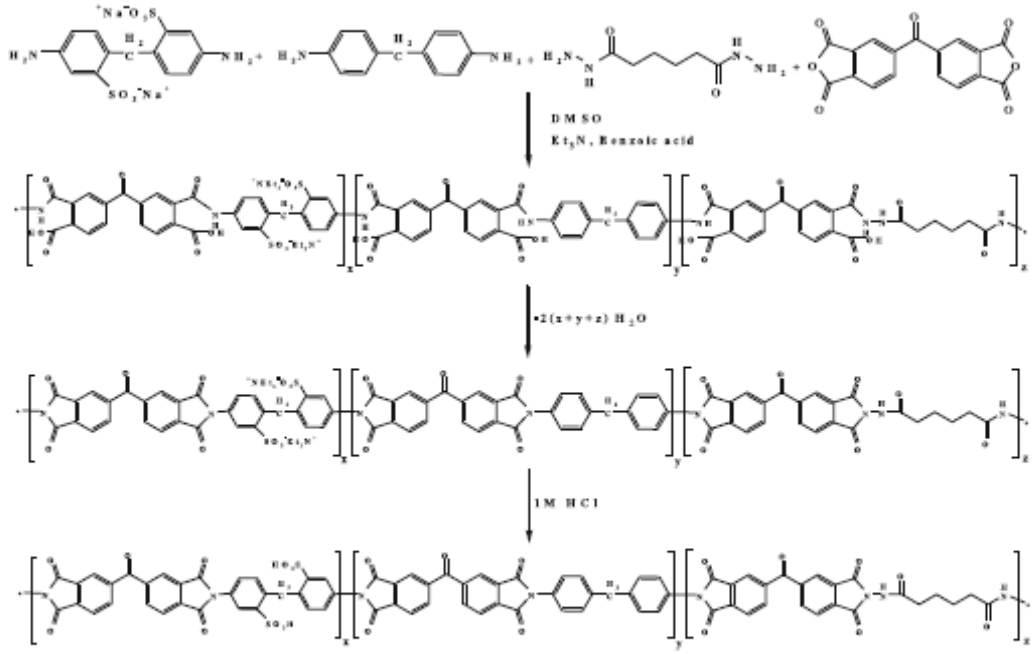

Fig. 2 The scheme for sulfonated poly(aromatic imide-*co*-aliphatic imide) (S-coPI) synthesis

Thermogravimetric analysis (TGA)

Thermogravimetric analysis (PerkinElmer, Pyris Diamond TG/DTA) was performed to determine the thermal stability of the polymer membrane [4]. The experiment was carried out by placing 2–4 mg film samples in an alumina pan, and then heated under nitrogen atmosphere with a heating rate of 10 °C min^{-1} in the temperature range of 50–800 °C. All the samples were dried at 100 °C for 24 h before measurement.

Tensile test

The mechanical properties of the polymer films were measured using a universal testing machine (Lloyd, model SMT2-500N) at a gage length of 30.0 mm, a speed of 10 mm min^{-1}, and at room temperature. Five measurements were taken for each polymer sample. The membranes, about 160–200 μm in thickness, were cut into 1 × 5 cm pieces and soaked in a deionized water bath for 2 days before testing.

X-Ray diffraction (XRD)

A wide-angle X-ray diffraction microscope (Rigaku D/MAX 2200) was used to study the crystallinity of Non-S-coPI and S-coPI. The S-coPI-3 was used as a sample of S-coPI. A Cu K-alpha radiation source was operated at 40 kV/30 mA. A K-beta filter was used to eliminate the interference peak. A divergence slit and scattering slit of 0.5° together with a 0.3 mm of receiving slit were set on the instrument. The film was placed into a sample holder and the measurement was continuously run. The data were recorded by monitoring the diffraction angles at the 2θ range from 5 to 90, with a scan speed of 5° min^{-1}, and a scan step of 0.02°.

Water uptake and moisture absorption

The polymer membranes were dried in an oven at 100 °C for 24 h. The dried membranes were weighed (W_d). Then the polymers were soaked in deionized water at room temperature for 2 days. They were removed from the water, quickly dry-wiped with an absorbent paper to remove any surface moisture, and then weighed immediately to determine their wet mass (W_w). The measurements were repeated three times to obtain an average water uptake value. The water uptake was calculated with the following formula [9]:

$$\text{Water uptake}\,(\%) = \frac{(W_w - W_d) \times 100}{W_d} \quad (1)$$

The moisture absorption was determined with the same method of water uptake but after the membranes were dried, the membranes were placed at room at room temperature for 2 days before being weighted (W_m) again. The moisture absorption was calculated with the following formula:

$$\text{Moisture absorption}\,(\%) = \frac{(W_m - W_d) \times 100}{W_d}, \tag{2}$$

Degree of sulfonation (DS)

The polymer membranes were acidified with an excess 0.1 M HCl solution at room temperature for 24 h. Then, they were washed and dried at 80 °C for 24 h. The membranes were immersed in 50 ml of 1 M NaCl for 24 h. The solution was titrated with 0.01 M NaOH using phenolphthalein as an indicator. The titrations were repeated two times and the DS value was obtained with the formula:

$$\text{DS}\,(\%) = \frac{(V_{\text{NaOH}} \times M_{\text{NaOH}})/1{,}000}{\text{Mole of polymer membrane}} \times 100 \tag{3}$$

where V_{NaOH} is the volume of sodium hydroxide solution, N_{NaOH} is the concentration of sodium hydroxide solution, and W_d is the weight of the dried membrane.

Ion exchange capacity (IEC)

The membrane samples (0.25–0.30 g) in acid form were immersed in 50 ml of 1 M NaCl solution at room temperature for 24 h to allow the H^+ ions to be replaced by Na^+ ions. Then, the H^+ ions were titrated with 0.01 M NaOH solution using phenolphthalein as an indicator. The titrations were repeated two times for an average IEC value. The IEC was calculated from the titration result using the equation:

$$\text{IEC}\ \ (\text{meq. g}^{-1}) = \frac{V_{\text{NaOH}} \times M_{\text{NaOH}}}{W_d} \tag{4}$$

where V_{NaOH} is the volume of sodium hydroxide solution, N_{NaOH} is the concentration of sodium hydroxide solution, and W_d is the weight of the dried membrane.

Proton conductivity

Proton conductivities of the films were measured by an Agilent E4980A LCR meter in terms of the impedance data. The fully hydrated film samples were cut into 0.5 × 0.5 cm and painted with silver paints on both side of the film [10]. The film samples were measured at a potential of 1 V and with an alternating current in the frequency range of 20 Hz–2 MHz. The plot between the radian and the impedance data was used to determine the conductivity values (σ) of the samples from the following equation:

$$\sigma\ (\text{S cm}^{-1}) = \frac{d}{SR} \tag{5}$$

where σ is the proton conductivity, d is the thickness of the membrane, S is the area of the interface between the membrane and the electrode, and R is the resistance which can be derived from the low intersect of the high-frequency semi-circle on a complex impedance plane with the Re(Z) or Z' axis.

Methanol permeability

The methanol permeabilities of the membranes were determined using the two compartment diffusion cell technique. One compartment ($V_A = 250$ ml) was filled with a solution of 2.5 M methanol. The other compartment ($V_B = 250$ ml) was filled with deionized water. The membrane was clamped between the two compartments. The solutions in the two compartments were magnetically stirred during the permeation experiments. Methanol passed through the membrane due to the methanol concentration difference between compartment A and compartment B. The methanol permeation in compartment B as a function of time is given by equation [11]:

$$P\,(\mathrm{cm}^2/\mathrm{s}) = \frac{k_B \times V_B \times L}{A \times (C_A - C_B)} \tag{6}$$

where P is the methanol permeability, C_A is the methanol concentration in compartment A, C_B is the methanol concentration in compartment B, A is the area of the membrane which is in contact with the solutions, L is the thickness of the membrane, V_B is the volume of the solution in compartment B, and k_B is the slope of methanol concentration profile in compartment B. The methanol concentrations were measured using a PR2100 gas chromatography (GC) fitted with a thermal conductivity detector (TCD); 2.5 M ethanol was used as the internal standard. Selectivity (Φ) was also calculated by the equation:

$$\Phi = \sigma / P \tag{7}$$

Selectivity is an effective parameter for evaluating membrane performance in a DMFC system. The higher the selectivity, the higher performance of the proton exchange membrane can be expected [12].

Results and discussion

Sulfonated monomer

The ^{1}H-NMR of S-DDM peak is shown in Fig. 3. The signal at 5.55 ppm (singlet) is assigned to the primary anime proton, which is correlated with H_1. The signal at 7.16 ppm (doublet), 7.12 ppm (doublet of singlet), and 6.71 ppm (doublet of doublet) is attributed to the aromatic protons H_3, H_5 and H_2, respectively. The signal at 3.82 ppm (singlet) is assigned to the methylene proton H_4 between the phenyl groups.

Fourier transform infrared (FT-IR)

The FT-IR peak of S-coPI is shown in Fig. 4, the bands at 1,740 and 1,665 cm^{-1} can be attributed to the C=O asymmetric and the symmetric stretching of the carbonyl group of the imido ring, respectively. The band at 1,386 cm^{-1} is attributed

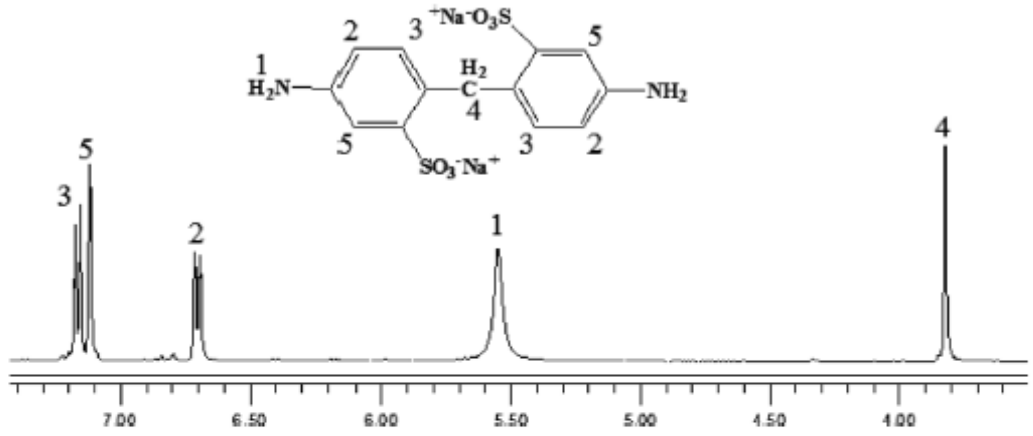

Fig. 3 The ^{1}H-NMR spectrum of sulfonation of 4,4′-diaminodiphenylmethane-3,3′-disulfonic acid disodium salt (S-DDM)

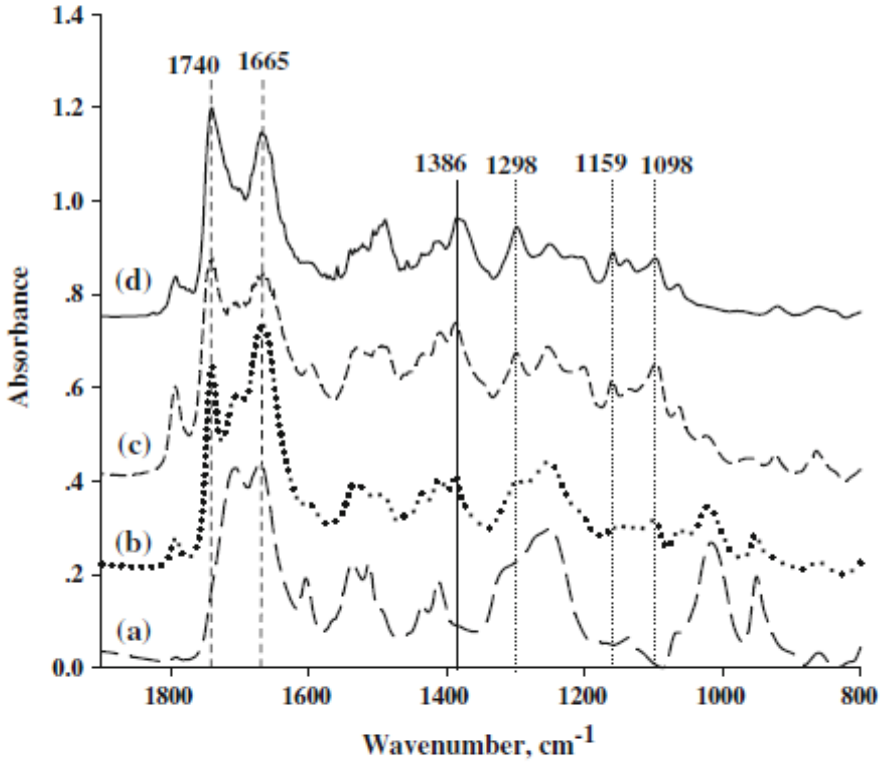

Fig. 4 FT-IR spectra of: *a* Non-S-coPI; *b* S-coPI-1; *c* S-coPI-2; *d* S-coPI-3

to the C–N–C stretching of the imide ring [13]. The S=O bond of the sulfonic group can be observed at around 1,298 and 1,159 cm^{-1}. The bands at 1,098 and 1,065 cm^{-1} are assigned to the S–O of sulfonated group [14]. The peak intensity at 1,298 cm^{-1} increases with increasing DS.

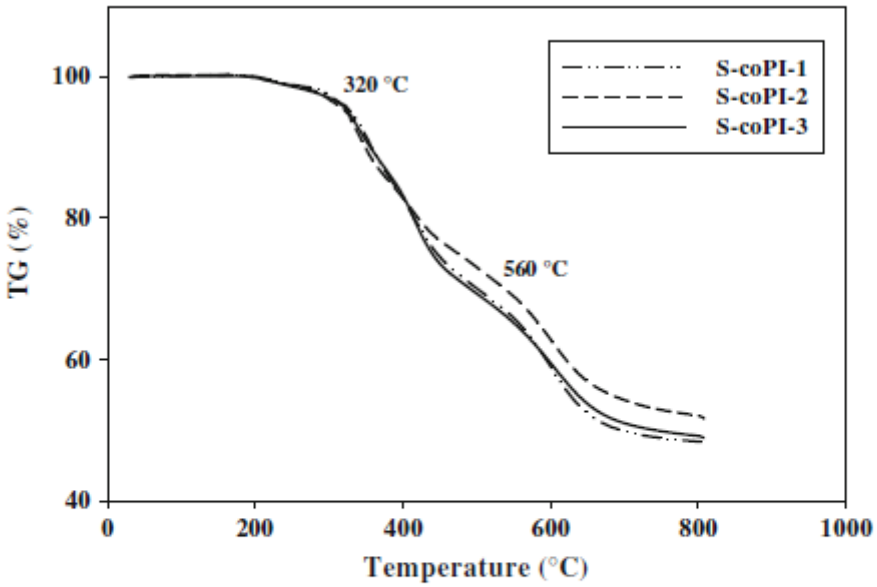

Fig. 5 The thermogravimetric analysis curves of S-coPI membranes

Thermogravimetric analysis (TGA)

The thermal property of the S-coPI membranes was investigated by TGA and is shown in Fig. 5. The weight loss at ~320 °C is assigned to the decomposition of the sulfonated group, and the weight loss due to degradation of backbone structure appears at ~560 °C.

Tensile test

Young's modulus of the membrane increases with increasing DS; Non-S-coPI, S-coPI-1, S-coPI-2, and S-coPI-3 have a Young's modulus ~651.00 ± 53.84, 829.58 ± 27.84, 980.01 ± 68.88, and 1,065 ± 47.86 MPa, respectively. In the hydrous or wet state, the water acts as the plasticizer which can increase the elongation at break.

X-Ray diffraction (XRD)

The crystalline structure of Non-S-coPI and S-coPI was characterized by wide-angle X-ray diffractions as shown in Fig. 6. The five main peaks of Non-S-coPI are found at 2θ of 26.64°, 20.84°, 50.14°, 59.94°, and 68.14°. For the S-coPI, the diffraction data represent an amorphous structure with only broad peaks at 2θ about 24.7° and 43.5° since the sulfonated group obstructs the chain packing of the polymer chain, which reduces the crystallinity.

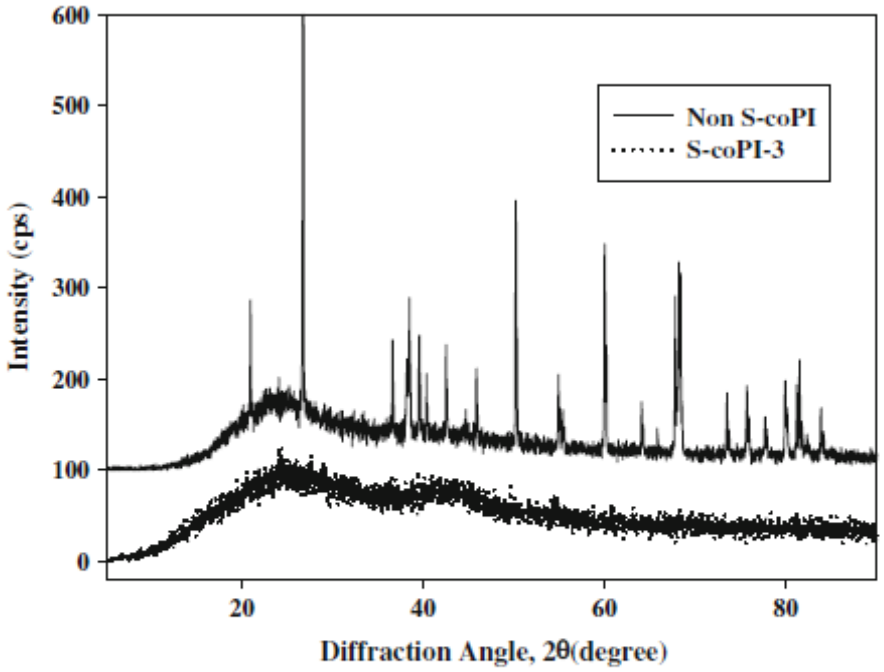

Fig. 6 XRD diffraction patterns of the Non-S-coPI and S-coPI-3 films

Table 1 The degree of sulfonation with difference monomer feed ratio by titration method

Sample	Monomer feed ratio (mol) S-DDM: DDM:ADH	Expected DS (%)	Actual DS (%) from titration	IEC (meq. g^{-1})
Non-S-coPI	0:4:6	0	0	0
S-coPI-1	1:3:6	20	18.450 ± 1.287	0.380 ± 0.026
S-coPI-2	2:2:6	40	34.530 ± 0.042	0.689 ± 0.001
S-coPI-3	4:0:6	80	65.585 ± 0.417	1.230 ± 0.008

Degree of sulfonation (DS) and ion exchange capacity (IEC)

The DS of the polymer membranes is controlled by varying the feed ratio of the monomers, but the actual DS is lower than expected value by about 10–15 %, because some of the monomers did not react. The ion exchange capacity of each S-coPI membrane is tabulated in the Table 1.

Water uptake and moisture absorption

The water uptake of the S-coPI membranes can be seen in Fig. 7, where the water uptake decreases with increasing DS because the sulfonated group induces higher rigidity. A low chain expansion occurs and forms agglomerate ionic water clusters [8] for two main reasons. First, the main chain structure of the S-coPI is composed of a rigid aromatic group, whereas Nafion117 is composed of a linear fluorinated chain and contains a long grafted ionic group which enhances the plasticity of the

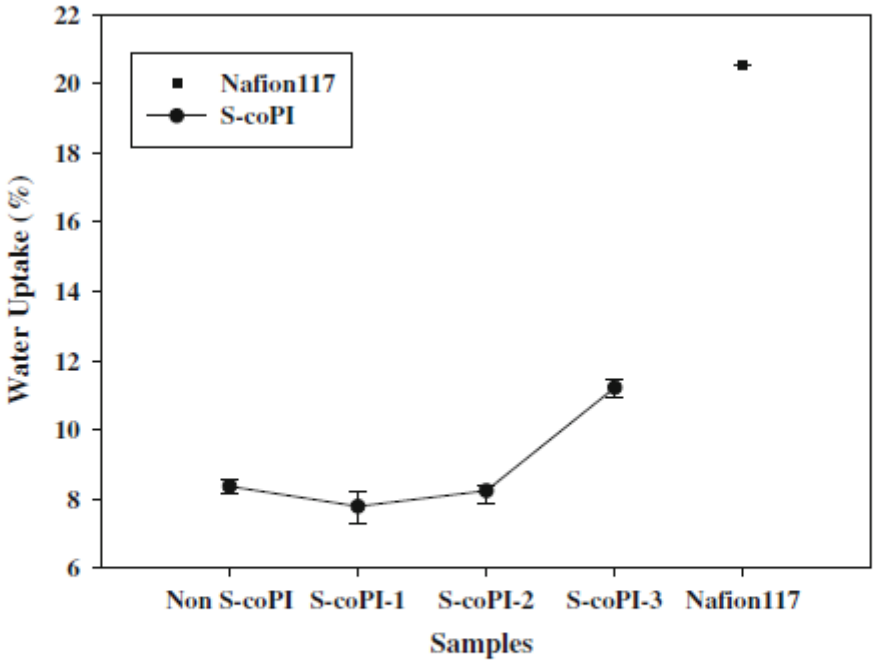

Fig. 7 Water uptake of S-coPI and Nafion117 films

membrane [8, 15]. Second, the crosslinking bonds between chains generate a built-in network structure, thus the water uptake is much lower than that of Nafion 117 [8]. However, the moisture absorption of the membrane did not occur at the same rate as the water uptake because no chain expansion occured in the moisture absorption test.

Proton conductivity

The proton conductivity of S-coPI membranes is shown in Fig. 8 and Table 2. The proton conductivity increases with increasing DS from 5.07×10^{-10} S cm^{-1} for Non-S-coPI to 1.16×10^{-2} S cm^{-1} for S-coPI-3, because an increase in the number of the sulfonated groups increases the proton hopping area. The proton conductivity of Nafion was reported in the work of Li et al. [17]. In the previous work reported by Sung et al., at the room temperature (30 °C), the proton conductivities in the fully hydrated state of the pristine sPI membrane and the coated sPI membrane were 0.65×10^{-1} and 0.62×10^{-1} S cm^{-1}, respectively [3], which are comparable to ours of the present work. The other work as reported by Li et al. [18], the NPI(1)/SPP(70) membrane attained the proton conductivity value of 0.207 S cm^{-1} at 30 °C which was higher than our membrane.

Methanol permeability

Table 2 lists the methanol permeability and the membrane selectivity [16] of the S-coPI membranes. The proton conductivity data of Nafion117 reported in literature

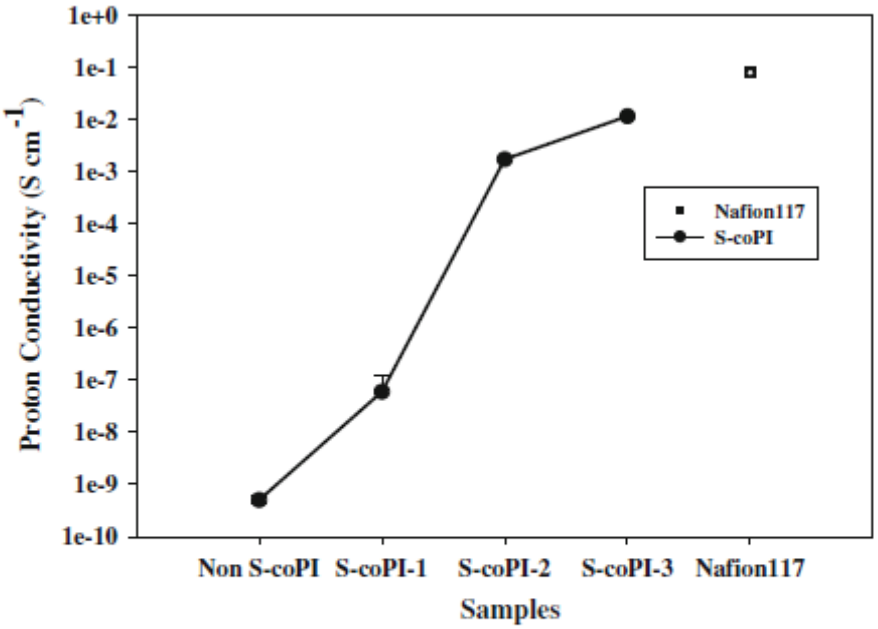

Fig. 8 The proton conductivity of and the S-coPI and Nafion117 films

Table 2 Proton conductivity, methanol permeability, and selectivity of S-coPI membranes and Nafion117

Sample	Proton conductivity, σ (S cm^{-1})	MeOH permeability, P (cm^2 s^{-1})	Selectivity, $(\Phi) = \sigma/P$ (S s cm^{-3})
Non-S-coPI	5.07×10^{-10}	3.86×10^{-8}	1.31×10^{-2}
S-coPI-1	6.01×10^{-8}	5.85×10^{-8}	1.03
S-coPI-2	1.73×10^{-3}	6.52×10^{-8}	2.65×10^{4}
S-coPI-3	1.16×10^{-2}	4.02×10^{-8}	2.89×10^{5}
Nafion117	8.00×10^{-2}[a]	1.74×10^{-6}	4.59×10^{4}

[a] Ref. [17]

are also listed in this table. All of the S-coPI membranes are of lower methanol permeability than that of Nafion117 and the selectivity of S-coPI-3 is six times higher than Nafion117 consequently, so the S-coPI-3 is of higher performance than Nafion117 with respect to the DMFC membrane. The methanol permeabilities of Non-S-coPI, S-coPI-1, S-coPI-2, and S-coPI-3, are 3.86×10^{-8}, 5.85×10^{-8}, 6.52×10^{-8}, and 4.02×10^{-8} cm^2 s^{-1}, respectively, which are much lower than that of Nafion 117 membrane (1.74×10^{-6} cm^2 s^{-1}). The previous work as reported by Li et al. [18], all of NPI/SPP membrane systems attained the methanol permeability values in the range of 1.3–6.2 $\times 10^{-7}$ cm^2 s^{-1}, which is about 10 times higher than ours. So, the S-coPI membrane in the present work is a suitable candidate for using as the proton exchange membrane.

Conclusions

In this study, S-DDM was successfully sulfonated using 98 % sulfuric acid and 65 % fuming sulfuric acid. Two sulfonated groups were contained in the S-DDM monomers, the positions of the sulfonated groups were confirmed by ^{1}H-NMR. The S-coPI membrane was synthesized by the polycondensation method using thermal imidization to obtain an imide structure; the four monomers at various mole ratios of S-DDm were used to control the amount of the sulfonated group. The characteristic peaks of the sulfonated group were at 1,298, 1,159, 1,098, and 1,065 cm^{-1} as confirmed by FT-IR. TGA showed the thermal stability of S-coPI; it had two structure decompositions at 320 and 560 °C. The DS of the membranes from titration was about 10–15 % lower than the expected. The crystallinity of the S-coPI membrane decreased with increasing DS due to the effect of the sulfonated group, which disrupted the polymer chain packing. The proton conductivity of the membranes increases with increasing sulfonated groups in the polymer chain; the highest proton conductivity was 1.16×10^{-2} S cm^{-1} for S-coPI-3 at the highest S-DDM feed ratio. The S-coPI membranes were of lower methanol permeability than that of Nafion 117 and the membrane selectivity of S-coPI-3 is 2.89×10^{5}, which was about 6 times higher value than that of Nafion117. Thus, the S-coPI membrane is a suitable candidate for using as the proton exchange membrane in DMFC.

Acknowledgments This work was supported by the Petroleum and Petrochemical College, the Conductive and Electroactive Polymers Research Unit of Chulalongkorn University, the Thailand Research Fund (TRF), and the Royal Thai Government.

References

1. Andújar JM, Segura F (2009) Fuel cells: history and updating. A walk along two countries. Renew Sustain Energy Rev 13:2309–2322
2. Kirubakaran A, Jain S, Nema RK (2009) A review on fuel cell technologies and power electronic interface. Renew Sustain Energy Rev 13:2430–2440
3. Sung KA, Cho KY, Kim WK, Park JK (2010) Sulfonated polyimide membrane coated with cross-slinkable layer for direct methanol fuel cell. Electrochim Acta 55:995–1000
4. Kausar A, Zulfiqar S, Ahmad Z, Sarwar MI (2010) Novel processable and heat resistant poly(phenylthiourea azomethine imide)s: synthesis and characterization. Polym Degrad Stab 95:1826–1833
5. Cheng L, Jian X (2004) Synthesis of new aromatic poly(amide imide)s from unsymmetrical extended diamine containing a phthalazinone moiety. Chin J Polym Sci 22(4):389–393
6. Peighambardoust SJ, Rowshanzamir S, Amjadi M (2010) Review of the proton exchange membranes for fuel cell applications. Int J Hydrogen Energy 35:9349–9384
7. Somboonsub B, Srisuwan S, Invernale MA, Thongyai S, Praserthdam P, Scola DA, Sotzing CA (2010) Comparison of the thermally stable conducting polymers PEDOT, PANi, and PPy using sulfonated poly(imide) templates. Polym 51:4472–4476
8. Woo Y, Oh SY, Kang YS, Jung B (2003) Synthesis and characterization of sulfonated polyimide membranes for direct methanol fuel cell. J Membr Sci 220:31–45
9. Xue S, Yin G, Cai K, Shao Y (2007) Permeabilities of methanol, ethanol and dimethyl ether in new composite membranes: a comparison with Nafion membranes. J Membr Sci 289:51–57
10. Ahmad MI, Zaidi SMJ, Rahman SU (2006) Proton conductivity and characterization of novel composite membranes for medium-temperature fuel cells. Desalin 193:387–397

11. Feng S, Shang Y, Wang Y, Liu G, Xie X, Dong W, Xu J, Mathur VK (2010) Synthesis and crosslinking of hydroxyl-functionalized sulfonated poly(ether ether ketone) copolymer as candidates for proton exchange membranes. J Membr Sci 352:14–21
12. Li W, Cui Z, Zhou X, Zhang S, Dai L, Xing W (2008) Sulfonated poly(arylene-*co*-imide)s as water stable proton exchange membrane materials for fuel cells. J Membr Sci 315:172–179
13. Vora RH, Goh SH (2006) Designed poly(ether-imide)s and fluoro-copoly(ether-imide)s: synthesis, characterization and their film properties. Mater Sci Eng B 132:24–33
14. Zhu X, Pan H, Liang Y, Jian X (2008) Synthesis and properties of novel sulfonated polyimides containing phthalazinone moieties for PEMFC. Eur Polym J 44:3782–3789
15. Guo Q, Pintauro PN, Tang H, O'Connor S (1999) Sulfonated and crosslinked polyphosphazene-based proton-exchange membranes. J Membr Sci 154:175–181
16. Shabani I, Hasani-Sadrabadi MM, Haddadi-Asl V, Soleimani M (2011) Nanofiber-based polyelectrolytes as novel membranes for fuel cell applications. J Membr Sci 368:233–240
17. Li T, Zhong G, Fu R, Yang Y (2010) Synthesis and characterization of Nafion/cross-linked PVP semi-interpenetrating polymer network membrane for direct methanol fuel cell. J Membr Sci 354:189–197
18. Li W, Cui Z, Zhou X, Zhanga, Dai L, Xing W (2008) Sulfonated poly(arylene-*co*-imide)s as water stable proton exchange membrane materials for fuel cells. J Membr Sci 315:172–179

Effect of Transition Metals on the Electrical Conductivity Response of dPPV/Zeolite Y Composites toward Ketone Vapors

JIRARAT KAMONSAWAS, ANUVAT SIRIVAT

The Petroleum and Petrochemical College, Chulalongkorn University, Bangkok, Thailand

Correspondence to: A. Sirivat, e-mail: anuvat.s@chula.ac.th.

Received: May 27, 2014
Accepted: August 1, 2014

ABSTRACT: Doped poly(*p*-phenylene vinylene) (dPPV) is mixed with modified zeolite Y to improve the selective and sensitive response of zeolite Y toward three different ketone vapors (acetone, methyl ethyl ketone, and methyl iso-butyl ketone), which are known as the toxic components. Zeolite Y (Si/Al 5.1, Na^+) or NaY is ion exchanged with transition cations, Cu^{2+}, Ni^{2+}, and Fe^{2+}, at 80% cation exchanged to prepare 80CuNaY, 80NiNaY, and 80FeNaY. In this work, the effects of transition cations, ketone vapor type, and ketone vapor concentration are systematically investigated. The highest electrical conductivity response and sensitivity toward acetone vapor at the vapor concentration of 30,000 ppm is obtained with 80CuNaY, whereas 80FeNaY shows the lowest values due to the electrostatic interaction between the zeolite framework and the cation. dPPV is mixed with 80CuNaY and exposed to the three ketone vapors. The electrical conductivity response and sensitivity of the composites toward acetone exhibits the highest values, whereas with MIBK they show the lowest value. After mixing of 80CuNaY with dPPV, the minimum vapor concentration toward acetone vapor decreases from 9 to 5 ppm. The response of the composite is irreversible as evidenced by Fourier transform infrared and atomic force microscopy techniques. © 2014 Wiley Periodicals, Inc. Adv Polym Technol 2015, 34, 21473; View this article online at wileyonlinelibrary.com. DOI 10.1002/adv.21473

KEY WORDS: Conducting Materials, Ketones, Sensors, Zeolites

Introduction

Air pollution mainly results from the usage of petroleum and petrochemical products. The concerned processes generate toxic gases and chemical vapors. Therefore, the development of toxic gas and vapor detection materials is always needed, which possess high response, good selectivity, fast recovery, and low cost. Many types of material have been explored and used as gas sensors: conducting polymers,[1–4] porous materials,[5–8] and metal oxides.[9–13]

Zeolite is one porous material, which is widely used as sensor materials such as faujasite (zeolite X and zeolite Y), ZSM-5, and mordernite because of its adsorption and separation properties. The structure of zeolite is the framework of hydrated aluminosilicates consisting of group I and II elements. The zeolite framework contains channels and interconnected voids, which are occupied by water and cations. Zeolites are known to provide high chemical stability, high porosity, high surface area, high selectivity, and adsorption properties. Nevertheless, zeolites still possess low electrical conductivity. The processes for improving the electrical conductivity of a zeolite are through adjusting the Si/Al ratio of zeolite, the ion-exchange process, and blending with conductive polymers (CPs).[5–8,14] The ion-exchange processes with alkaline, alkaline earth, and transition metals are expected to change the response and selectivity properties of zeolites. The ion-exchange process combined with blending a CP into the zeolite matrix has been shown to effectively improve the electrical conductivity of the zeolite for detecting toxic gases and chemical vapors.[5–8,14–24]

CPs are the other type of materials, which can be used as gas-sensing materials as they show the high electrical conductivity, magnetic, and optical properties. One of the CPs, which has been widely used in the gas-sensing application, is poly(*p*-phenlene vinylene) (PPV) because it has a high electrical conductivity, good mechanical properties, good chemical stability, and ease in synthesizing.[25,26] A positive or negative response of doped PPV or dPPV depends on the electrophilic or nucleophilic nature of the gases or chemical vapors. Although dPPV exhibits a high electrical conductivity, its selectivity and adsorption properties

Contract grant sponsor: Conductive and Electroactive Polymers Research Unit of Chulalongkorn University.
Contract grant sponsor: Thailand Research Fund.
Contract grant number: TRF-RTA, TRF-RGJ-PhD/0026/2553.
Contract grant sponsor: Royal Thai Government.

© 2014 Wiley Periodicals, Inc.

are still poor toward a particular chemical vapor. Previous work has combined the best characteristics of zeolites and the high electrical properties of the CPs to improve the selective, adsorptive, and electronic properties toward gases and vapors.[18,27]

In this work, zeolite Y was an ion-exchanged process with the transition cations (Cu^{2+}, Ni^{2+}, and Fe^{2+}) to improve the electrical conductivity response of zeolite Y (Si/Al 5.1) toward acetone vapor under the effects of transition metal and vapor concentration. The electrical conductivity responses of the composites between zeolite Y and dPPV toward three different types of ketone vapors (acetone, methyl ethyl ketone (MEK), methyl iso-butyl ketone (MIBK)) were also investigated. The interaction between the active site of the sensing materials and the chemical vapors was investigated by Fourier transform infrared (FTIR) and atomic force microscopy (AFM) techniques and will be reported here.

Experimental

MATERIALS PREPARATION

Synthesis of PPV and Doping Process

The synthesis of PPV was prepared via the Wessling route.[25] The α,α'-dichloro-*p*-xylene (Aldrich, Steinheim, German) and tetrahydrothiophene (Aldrich) were used as raw materials to synthesize the *p*-xylene-bis(tetrahydrothio-phenium chloride) monomer. The polymerization step was induced by the base to form a precursor polymer. PPV was obtained by heating the precursor polymer in the vacuum oven at 180°C for 6 h. [25] Adding the solution of 18 M sulfuric acid at the mole ratio of 1:100 (PPV repeating units and sulfuric acid to the polymer powder and the change in the polymer color from bright yellow to black brown was observed, which indicated the complete doping process.[26]

The Cation-Exchange Process

The ion-exchange process was carried out by using the zeolite Y (Si/Al = 5.1, Na^+) or NaY purchased from Zeolyst. The preparations of the zeolite Y (Si/Al = 5.1, 20% mol of Na^+ and 80% mol of Cu^{2+}) or 80CuNaY, the zeolite Y (Si/Al = 5.1, 20% mol of Na^+ and 80% mol of Ni^{2+}) or 80NiNaY, and the zeolite Y (Si/Al = 5.1, 20% mol of Na^+ and 80% mol of Fe^{2+}) or 80FeNaY were carried out by adding the 0. 1 M solution of $CuCl_2$, $NiCl_2$, and $FeSO_4$ into 5 g of NaY and stirred at 25°C for 24 h. Then, the zeolite samples were filtered and washed with deionized water for five times.[24,27]

Preparation of dPPV_Zeolilte Y Pellet

dPPV was mixed with the zeolite Y matrix (80CuNaY, 80NiNaY, 80FeNaY, and NaY). The composites between zeolite Y and dPPV were prepared by physical blending at the percentage volume of dPPV of 10% v/v. The hydraulic press was used to form composite pellets at the pressure of 6 kN.

CHARACTERIZATION OF PPV, dPPV, AND COMPOSITE

The surface area analysis (Sorptomatic-1990) was used to determine the median pore sizes and the surface areas of the zeolite Y. The percentage of ion exchange was measured by an atomic adsorption spectrophotometer (Spectra A300; Varian). A FTIR spectrometer (Inclolet; model FRA 106/S) was used to characterize functional groups of PPV and dPPV and the interaction between the chemical vapors and the active site of gas-sensing materials. The morphology of PPV, dPPV, zeolite Y, the 10% v/v of dPPV on the composites or dPPV_[90]80CuNaY, and the dispersion of the CP particles in the zeolite Y were investigated using a scanning electron microscope (Hitachi, SU1510) at the magnifications of 1000× and 5000× and at 10 kV. The specific electrical conductivity was measured by a custom-made two-point probe with a linear geometric array connected to a voltage supplier (Keithley, 6517A). An atomic force microscope (Park Systems; XE-100) was used to characterize the phase changes during the acetone exposure.

ELECTRICAL CONDUCTIVITY AND THE FLOW GAS DETECTION SYSTEM

A voltage supplier (Keithley, 6517A) was connected to a custom-made two-point probe to measure the electrical conductivity of the gas-sensing materials under the condition of air, N_2, and chemical vapors where the voltage was varied, and the current was measured. The electrical conductivity was calculated using given below:

$$\sigma = (I/KVt) \tag{1}$$

where I is the measured current (A), V is the applied voltage (V), t is the thickness, and K is the geometric correction factor of the two-point probe, which was determined by calibrating the probe with a silicon wafer possessing a known resistivity value.

The flow system of a gas detection unit was connected to the custom-made two-point probe, and the voltage supplier (Keithley, 6517A) was used to monitor the change in the electrical conductivity during the chemical vapor exposure. The chemical vapors in this work used were acetone (dimethyl ketone or propan-2-one), MEK (methyl ethyl ketone or butan-2-one), and MIBK (methyl iso-butyl ketone or 4-methylpentan-2-one). All of chemicals were purchased from Labscan (AR grade). The chemical vapors were generated by the flow system at the vapor concentrations of 30,000 ppm (3% v/v), 3000 ppm (0.3% v/v), 300 ppm (0.03% v/v), 30 ppm (0.003% v/v), and 10 ppm (0.001% v/v) in N_2 gas. The surface cleaning gas, which vaporized the chemical solvents, was nitrogen (N_2; TIG). All chemicals were used without further purifications. Air and moisture were evacuated from the chemical chamber until the steady state was obtained, and nitrogen was injected as into the chemical chamber. When the electrical conductivity in N_2 gas reached the steady state, the electrical conductivity was recorded as $\sigma_{N2,\text{ before exposure}}$. Before injecting the chemical vapor into the chemical chamber, nitrogen gas was evacuated first and chemical vapor was later injected into the chamber. At the steady state, the electrical conductivity was recorded as $\sigma_{\text{chemical vapor}}$. The chemical vapor was removed by the vacuum pump, then N_2 was injected into

TABLE I
Analytical Data and Electrical Conductivity of Modified Zeolite Y

Sample	Sample Code	Percent Mole of Cation	EN	Cationic Radii (Å)	Median Pore Width (Å)	Surface Area (m^2/g)	σ_{air} (S/cm)
Zeolite Y (Si/Al = 5.1, Na^+)	NaY	100% Na^+	0.93 (Na^+)	1.16(Na^+)	7.4875 ± 0.34	617.0 ± 7.0	$2.50 \times 10^{-3} \pm 2.51 \times 10^{-5}$
Zeolite Y (Si/Al = 5.1, Na^+, Cu^{2+})	80CuNaY	79% Cu^2, 21% Na^+	0.93 (Na^+), 1.372 (Cu^{2+})	1.16(Na^+), 0.87(Cu^{2+})	7.092 ± 0.04	526.0 ± 2.0	$5.67 \times 10^{-3} \pm 7.08 \times 10^{-5}$
Zeolite Y (Si/Al = 5.1, Na^+, Ni^{2+})	80NiNaY	84% Ni^{2+}, 16% Na^+	0.93 (Na^+), 1.367 (Ni^{2+})	1.16(Na^+), 0.83(Ni^{2+})	7.656 ± 0.03	506.0 ± 6.0	$3.51 \times 10^{-3} \pm 1.15 \times 10^{-6}$
Zeolite Y (Si/Al = 5.1, Na^+, Fe^{2+})	80FeNaY	90% Fe^{2+}, 10% Na^+	0.93 (Na^+), 1.292 (Fe^{2+})	1.16(Na^+), 0.75(Fe^{2+})	7.326 ± 0.39	535.0 ± 4.0	$2.44 \times 10^{-3} \pm 1.66 \times 10^{-5}$

the chamber, and the electrical conductivity was measured as $\sigma_{N2,\ after\ exposure}$. The electrical conductivity response and sensitivity of the composites were calculated by the following equations:

$$\Delta\sigma = \sigma_{chemicalvapor} - \sigma_{N_2,beforeexposure} \quad (2)$$

$$\text{Sensitivity} = \Delta\sigma/\sigma_{N_2\ \text{before exposure}} \quad (3)$$

where $\Delta\sigma$ is the difference in the specific electrical conductivity (S/cm), $\sigma_{N2,\ before\ exposure}$ is the specific electrical conductivity in N_2 before exposure (S/cm), and $\sigma_{chemical\ vapor}$ is the specific electrical conductivity under chemical vapor exposure (S/cm).[16,27]

Results and Discussion

CHARACTERIZATION OF dPPV, MODIFIED ZEOLITE Y, AND ITS COMPOSITE

Table I shows the analytical data and the electrical conductivity of the modified zeolite Y, which was ion exchanged with three different transition cations. Zeolite Y (Si/Al 5.1, Na^+) or NaY was ion exchanged with Cu^{2+}, Ni^{2+}, and Fe^{2+}. The amount of cation exchange was determined by an atomic adsorption spectrophotometer in terms of the cation mole percentage. From the previous work.[27–29] the cation mole percentage is defined as the ratio of Cu^{2+}, Ni^{2+}, and Fe^{2+} divided by the sum of moles of individual cations and multiplied by 100. The cation mole percentage of Cu^{2+}, Ni^{2+}, and Fe^{2+} is 79, 84, and 90, respectively, for the exchange time of 24 h as presented in Table I.[14,27–29]

Figure 1 shows the morphology of dPPV, 80CuNaY, and the composites. The morphology of dPPV and 80CuNaY is shown in Figs. 1a and 1b at the magnification of 5000× and 10 kV, respectively. Figure 1c shows the morphology of the composites between 10% v/v of dPPV and 80CuNaY or dPPV_[90]80CuNaY at a magnification of 5000×. After mixing 10% v/v of dPPV with the 80CuNaY matrix, the morphology of the composite appears as a nearly homogeneous mixture.

The values of electrical conductivity of 80CuNaY, 80NiNaY, NaY, and 80FeNaY under ambient conditions are $5.67 \times 10^{-3} \pm 7.08 \times 10^{-5}$, $3.51 \times 10^{-3} \pm 1.15 \times 10^{-6}$, $2.50 \times 10^{-3} \pm 2.51 \times 10^{-5}$, and $2.44 \times 10^{-3} \pm 1.66 \times 10^{-5}$ S cm^{-1}, respectively, as presented in I The electrical conductivity of the zeolite depends on the cationic radii. 80CuNaY shows a higher value of the electrical conductivity than 80NiNaY and 80FeNaY, respectively, because of the charge-balanced ion size. The size of Cu^{2+} (0.87 Å) is larger than those of Ni^{2+} (0.83 Å) and Fe^{2+} (0.75 Å), respectively. The large cation size leads to a reduction in the electrostatic force of the zeolite framework and the increase in the proton mobility along the zeolite structure.[27,30–33] In addition, the electron orbitals of the cation in the zeolite framework are other factors affecting the electrical conductivity. Figure 2 shows the electron orbitals of Cu^{2+}, Ni^{2+}, and Fe^{2+}. The electron orbital of Cu^{2+}, Ni^{2+}, and Fe^{2+} is in the unfilled state in the 3d orbitals, and the unfilled electron state of Cu^{2+}, Ni^{2+}, and Fe^{2+} is 1, 2, and 4, respectively, as shown in Fig. 2. Therefore, Cu^{2+} is capable of rapidly accepting electrons and induces the highest electrical conductivity. In the case of Na^+, which is an alkaline cation, the electrical conductivity of NaY is lower than those of 80CuNaY and 80 NiNaY due to the void size within the zeolite. Typically, two Na^+ ions are replaced with one Cu^{2+} ion where the ionic radius of Na^+ and Cu^{2+} is 1.16 and 0.87 Å, respectively. After replacing Na^+ with Cu^{2+}, this results in increasing the void within the zeolite framework and leads to the increase in the proton mobility along the zeolite framework.[17,22] The electrical conductivity sensitivity of dPPV, zeolite Y, and composites toward three different ketone vapors is presented and discussed next.

THE TEMPORAL RESPONSE OF ZEOLITE Y AND COMPOSITES

Table II presents the inductions time (T_i) and recovery time (T_r) of zeolite Y and the composites. The induction time of 80CuNaY, 80NiNaY, NaY, and 80FeNaY when exposed to acetone vapor at the vapor concentration of 30,000 ppm, 25ºC, and 1 atm is 38 ± 1, 40 ± 1, 42 ± 2, and 45 ± 1 min, respectively. The recovery time is 31 ± 2, 32 ± 1, 27 ± 2, and 38 ± 1 min, respectively. Generally, the induction time is dependent on the cation type, which possesses different electronegativity (EN) values, cationic radii, and electron configuration properties.[20–22] Cu^{2+} in the zeolite framework has the electron configuration that remains one electron unfilled state in the 3d orbital, resulting in an increase in the adsorption property, as shown in Fig. 2.[20–22] Therefore, 80CuNaY shows the shortest induction time. In the case of Na^+, it is an alkaline cation, which has a lower EN value (0.93) than Cu^{2+} (1.372) and Ni^{2+} (1.367). Therefore, Na^+ also

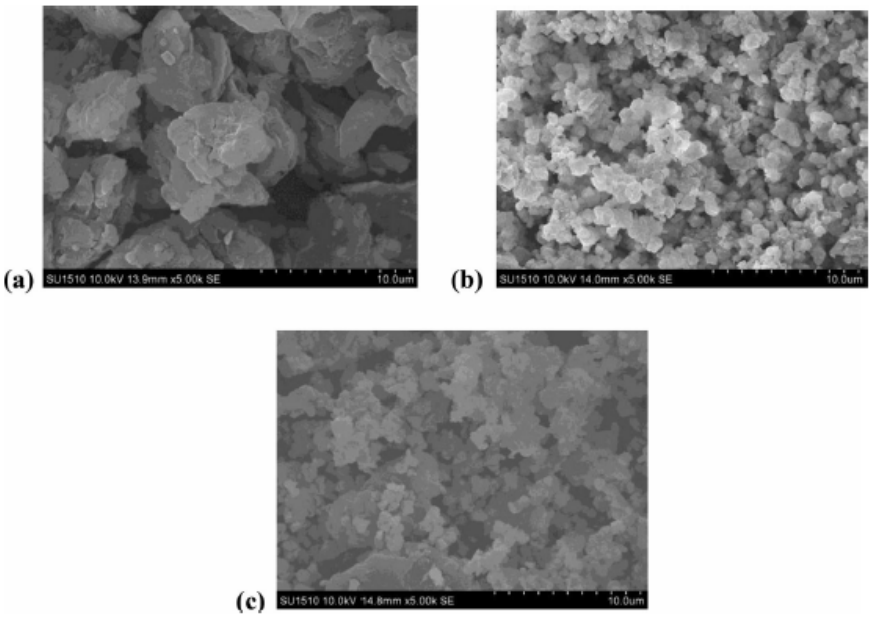

FIGURE 1. Morphology of dPPV, 80CuNaY powders, and dPPV_[90]80CuNaY composites with 10% v/v of dPPV: (a) dPPV at a magnification of 5000× (b) 80CuNaY at a magnification 5000×, and (c) dPPV_[90]80CuNaY at a magnification of 5000×.

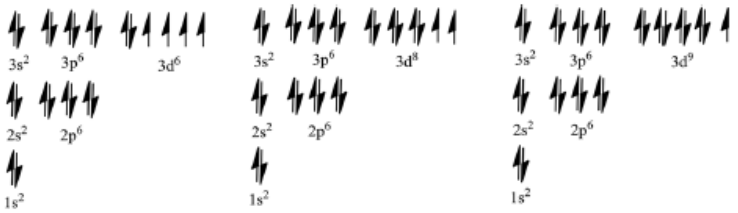

Cation	Fe^{2+}	Ni^{2+}	Cu^{2+}
EN	1.292	1.367	1.372
Cationic radii (Å)	0.75	0.83	0.87

FIGURE 2. Electronic orbitals of Fe^{2+}, Ni^{2+}, and Cu^{2+}.

shows the longer induction time than Cu^{2+} and Ni^{2+}. For the recovery time, NaY takes the shortest time due to its EN value. The EN value of Na^{+} (0.93) is considerably lower than Cu^{2+} (1.372), Ni^{2+} (1.367), and Fe^{2+} (1.292), respectively. The low EN value suggests a weaker interaction between the active site and the chemical vapor. Therefore, 80CuNaY is chosen for the further study under the effects of ketone type and dPPV. The induction and recovery times of 80CuNaY are investigated under the effect of ketone type. The induction time of 80CuNaY is 38 ± 1,35 ± 2, and 18 ± 2 min, respectively, and the recovery time of this sample is 31 ± 2, 13 ± 1, and 12 ± 2 min, respectively, under the exposure of acetone, MEK, and MIBK at the vapor concentration of 30,000 ppm. The induction and recovery times depend on the ketone molecular size. A solvent molecule with a smaller size can easily penetrate into the zeolite framework and takes a longer time. The size of acetone is smaller than those of MEK and MIBK molecules. Hence, the 80CuNaY sample when exposed to acetone vapor takes the longer time to reach a steady state than MEK.[22,31]

dPPV is mixed with 80CuNaY at the ratio of 10% PPV and exposed to acetone vapor at the vapor concentration of 30,000 ppm, 25°C, and 1 atm. The induction time of dPPV_[90]80CuNaY is 36 ± 1, and the recovery time is 26 ± 1. After mixing of dPPV with the 80CuNaY matrix, the induction and the recovery time decrease due to the available active site property change in the composite system. Other ketone types show similar results.[17,18,27–31]

TABLE II
Induction and Recovery Times of Modified Zeolite Y, dPPV, and Composites

Sample	Sample Code	Ketone Type	Induction Time, T_i (min) at the Vapor Concentration of					Recovery Time, T_r (min) at the Vapor Concentration of				
			10 ppm	30 ppm	300 ppm	3000 ppm	30,000 ppm	10 ppm	30 ppm	300 ppm	3000 ppm	30,000 ppm
Doped PPV	dPPV	Acetone	15 ± 0.3	15 ± 0.6	18 ± 0.8	20 ± 0.5	35 ± 0.2	11 ± 0.1	11 ± 0.2	13 ± 0.5	13 ± 0.2	20 ± 1.0
Zeolite Y (Si/Al 5.1, Na^+)	NaY		–	22 ± 0.5	27 ± 1.0	34 ± 0.8	42 ± 2.0	–	10 ± 3.0	12 ± 2.0	20 ± 0.3	27 ± 2.0
Zeolite Y (Si/Al 5.1, Na^+, Cu^{2+})	80CuNaY		19 ± 1.0	20 ± 1.0	21 ± 3.0	23 ± 2.0	38 ± 1.0	10 ± 4.0	15 ± 1.0	18 ± 2.0	23 ± 4.0	31 ± 2.0
Zeolite Y (Si/Al 5.1, Na^+, Ni^{2+})	80NiNaY		–	21 ± 1.0	23 ± 1.0	29 ± 2.0	40 ± 1.0	–	16 ± 1.0	16 ± 2.0	23 ± 1.0	32 ± 1.0
Zeolite Y (Si/Al 5.1, Na^+, Fe^{2+})	80FeNaY		–	24 ± 2.0	29 ± 2.0	36 ± 2.0	45 ± 1.0	–	19 ± 2.0	21 ± 1.0	25 ± 2.0	38 ± 1.0
10%v/v of dPPV_Zeolite Y (Si/Al 5.1, Na^+, Cu^{2+})	dPPV_[90] 80CuNaY		15 ± 2.0	16 ± 1.0	18 ± 0.8	18 ± 2.0	36 ± 1.0	10 ± 0.5	12 ± 1.0	12 ± 2.0	25 ± 1.0	26 ± 2.0
Doped PPV	dPPV	MEK	–	12 ± 1.0	13 ± 2.0	18 ± 1.0	32 ± 2.0	–	9 ± 1.0	9 ± 2.0	10 ± 1.0	11 ± 2.0
Zeolite Y (Si/Al 5.1, Na^+, Cu^{2+})	80CuNaY		–	16 ± 1.0	17 ± 2.0	20 ± 1.0	35 ± 2.0	–	11 ± 1.0	11 ± 3.0	11 ± 1.0	13 ± 1.0
10%v/v of dPPV Zeolite Y (Si/Al 5.1, Na^+, Cu^{2+})	dPPV_[90] 80CuNaY		–	13 ± 1.0	15 ± 2.0	18 ± 1.0	31 ± 1.0	–	9 ± 1.0	10 ± 0.5	10 ± 1.0	12 ± 2.0
Doped PPV	dPPV	MIBK	–	9 ± 1.0	10 ± 1.0	10 ± 2.0	12 ± 0.5	–	6 ± 2.0	6 ± 1.0	9 ± 1.0	10 ± 1.0
Zeolite Y (Si/Al 5.1, Na^+, Cu^{2+})	80CuNaY		–	16 ± 1.0	16 ± 2.0	17 ± 1.0	18 ± 2.0	–	9 ± 2.0	10 ± 1.0	12 ± 1.0	12 ± 1.0
10%v/v of dPPV_Zeolite Y (Si/Al 5.1, Na^+, Cu^{2+})	dPPV_[90] 80CuNaY		–	15 ± 0.5	15 ± 2.0	16 ± 2.0	17 ± 2.0	–	6 ± 0.7	9 ± 2.0	11 ± 1.0	11 ± 2.0

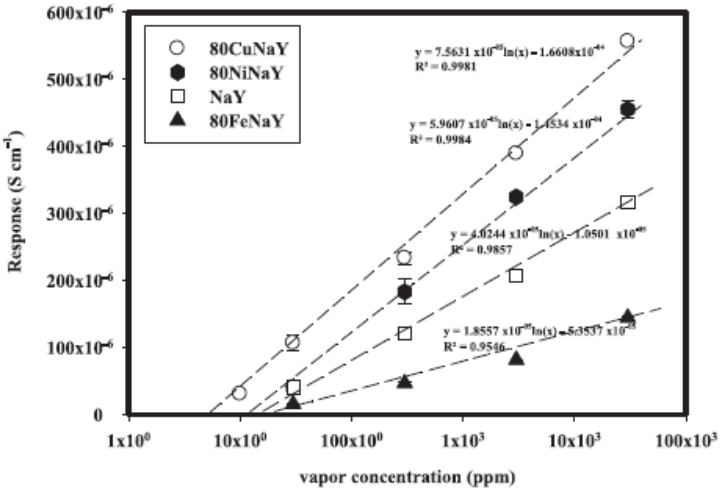

FIGURE 3. Electrical conductivity response of the NaY, 80CuNaY, 80NiNaY, and 80FeNaY under acetone exposure at 25°C, 1 atm, at vapor concentrations of 30,000, 3000, 300, 30, and 10 ppm.

TABLE III
Response and Sensitivity of Modified Zeolite Y, dPPV, and Composites

Sample	Chemical Vapor	Response (S/cm)[a]	Sensitivity[a]	Minimum vapor Concentration (ppm)
80FeNaY	Acetone	$1.49 \times 10^{-04} \pm 2.16 \times 10^{-06}$	$2.38 \times 10^{-01} \pm 1.66 \times 10^{-02}$	18
NaY	Acetone	$3.23 \times 10^{-04} \pm 9.95 \times 10^{-05}$	$2.64 \times 10^{-01} \pm 2.05 \times 10^{-02}$	14
80NiNaY	Acetone	$4.62 \times 10^{-04} \pm 8.06 \times 10^{-06}$	$3.53 \times 10^{-01} \pm 1.93 \times 10^{-02}$	12
80CuNaY	Acetone	$6.74 \times 10^{-04} \pm 2.04 \times 10^{-05}$	$5.00 \times 10^{-01} \pm 2.20 \times 10^{-02}$	9
80CuNaY	MEK	$1.56 \times 10^{-04} \pm 1.88 \times 10^{-03}$	$2.64 \times 10^{-01} \pm 5.25 \times 10^{-02}$	18
80CuNaY	MIBK	$1.07 \times 10^{-04} \pm 2.75 \times 10^{-06}$	$1.88 \times 10^{-01} \pm 5.59 \times 10^{-04}$	20
dPPV	Acetone	$9.76 \times 10^{-02} \pm 2.05 \times 10^{-02}$	$4.41 \pm 8.02 \times 10^{-01}$	5
dPPV	MEK	$3.17 \times 10^{-02} \pm 8.68 \times 10^{-03}$	$1.96 \pm 1.83 \times 10^{-01}$	7
dPPV	MIBK	$1.66 \times 10^{-02} \pm 1.47 \times 10^{-04}$	$1.00 \pm 9.95 \times 10^{-03}$	9
dPPV_[90]80CuNaY	Acetone	$1.16 \times 10^{-01} \pm 4.74 \times 10^{-03}$	$4.98 \pm 1.53 \times 10^{-02}$	5
dPPV_[90]80CuNaY	MEK	$4.97 \times 10^{-02} \pm 5.30 \times 10^{-03}$	$2.51 \pm 5.72 \times 10^{-02}$	7
dPPV_[90]80CuNaY	MIBK	$2.41 \times 10^{-02} \pm 2.07 \times 10^{-04}$	$1.70 \pm 1.03 \times 10^{-02}$	10

[a]The response and sensitivity of gas sensing materials at vapor concentration of 30000 ppm

THE RESPONSE OF ZEOLITE Y, dPPV, AND COMPOSITES

Effect of Transition Cations

The electrical conductivity response and the sensitivity values of 80CuNaY, 80NiNaY, NaY, and 80FeNaY are shown in Fig. 3 and presented in Table III Zeolite Y (Si/Al ratio 5.1, Na^+) or NaY was ion exchanged with Cu^{2+}, Ni^{2+}, and Fe^{2+} at 80% mol to investigate the effect of transition metals toward acetone vapor at the vapor concentrations of 30,000, 3000, 300, 30, and 10 ppm.

The electrical conductivity response of 80FeNaY, NaY, 80NiNaY, and 80CuNaY in acetone exposure at the vapor concentration of 30,000 ppm is $1.49 \times 10^{-04} \pm 2.16 \times 10^{-06}$, $3.23 \times 10^{-04} \pm 9.95 \times 10^{-05}$, $4.62 \times 10^{-04} \pm 8.06 \times 10^{-06}$, and $6.74 \times 10^{-04} \pm 2.04 \times 10^{-05}$ S cm^{-1}, respectively. The electrical conductivity sensitivities are $2.38 \times 10^{-01} \pm 1.66 \times 10^{-02}$, $2.64 \times 10^{-01} \pm 2.05 \times 10^{-02}$, $3.53 \times 10^{-01} \pm 1.93 \times 10^{-02}$, and $5.00 \times 10^{-01} \pm 2.20 \times 10^{-02}$, respectively. The electrical conductivity response increases with increasing cationic radii. The larger cation size decreases the electrostatic interaction between the cation and the zeolite framework and thus increases the proton mobility along the zeolite structure.[27,30–33] The cation radii of Fe^{2+}, Ni^{2+}, and Cu^{2+} are 0.75, 0.83, and 0.87 Å, respectively.[34] Thus, 80CuNaY exhibits the highest response value toward the acetone vapor whereas 80FeNaY shows the lowest value. Moreover, another factor is the electron configuration of cation. Cu^{2+}, Ni^{2+}, and Fe^{2+} remain in the unfilled electron state in the 3d orbital; only Cu^{2+} contains one unfilled electron state in the 3d orbital as shown in Fig. 2. Therefore, Cu^{2+} is capable of rapidly accepting electrons, which results in the increase in the proton mobility along the zeolite structure. Therefore, 80CuNaY exhibits the highest response to acetone vapor at the concentration of 30,000 ppm relative to those of 80NiNaY and 80FeNaY, respectively. In the case of NaY, the electrical conductivity response and sensitivity of NaY are lower than those of 80CuNaY and 80NiNaY due to the coordination number. Generally, the ion-exchange process between the

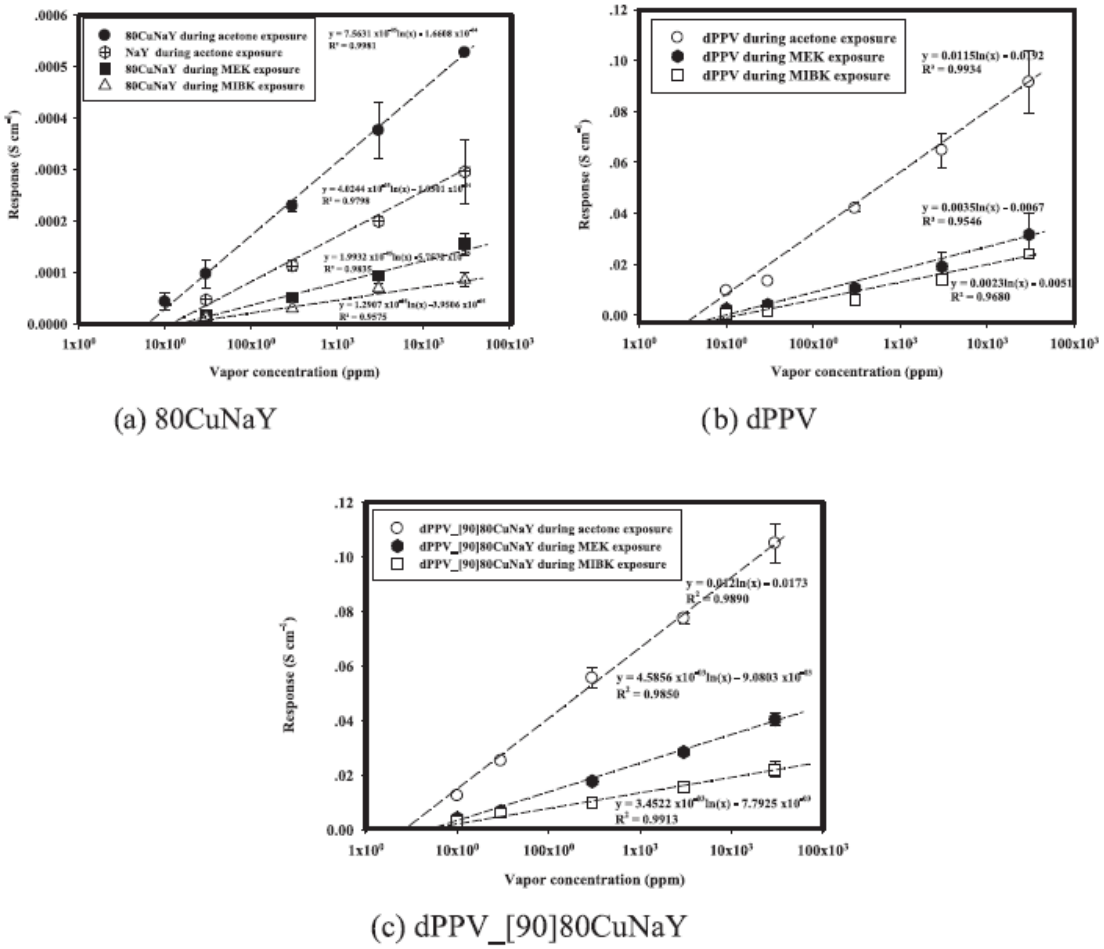

FIGURE 4. Electrical conductivity response of (a) 80CuNaY, (b) dPPV, and (c) dPPV_[90] 80CuNaY under acetone, MEK, and MIBK exposures at 25°C, 1 atm, at vapor concentrations of 30,000, 3000, 300, 30, and 10 ppm.

monovalent and divalent electrons is that two units of monovalent cation are replaced with one unit of divalent cation. Hence, two units of Na^+ are replaced with one unit of Cu^{2+} leading to the increase in the void size within 80CuNaY and the increase in the proton mobility.[22–24,30–33] In this work, 80CuNaY is used to further investigate the effects of dPPV and the ketone vapor concentration and will be discussed next.

The Effect of Ketone Type

Figure 4 shows the plot between response and vapor concentration (ppm) of 80CuNaY (Fig. 4a), dPPV (Fig. 4b), and dPPV_[90]80CuNaY (Fig. 4c) under acetone, MEK, and MIBK at 25°C, 1 atm, and at the vapor concentrations of 30,000, 3000, 300, 30, and 10 ppm.

The electrical conductivity response of 80CuNaY under acetone, MEK, and MIBK exposure at the vapor concentration of 30,000 ppm is $6.74 \times 10^{-04} \pm 2.04 \times 10^{-05}$, $1.56 \times 10^{-04} \pm 1.88 \times 10^{-05}$, and $1.07 \times 10^{-04} \pm 2.75 \times 10^{-06}$, respectively. The electrical conductivity sensitivity of 80CuNaY in acetone, MEK, and MIBK exposures at the vapor concentration of 30,000 ppm is $5.00 \times 10^{-01} \pm 2.20 \times 10^{-02}$, $2.64 \times 10^{-01} \pm 5.25 \times 10^{-02}$, and $1.88 \times 10^{-01} \pm 5.95 \times 10^{-04}$, respectively as shown in Fig. 4a and presented in III The electrical conductivity response and sensitivity of 80CuNaY depend on the solvent molecular size. For a large solvent molecular size, it is more difficult to penetrate into the zeolite framework. The size of acetone molecule is 0.524 nm, which is smaller than the molecular sizes of MEK (0.667 nm) and MIBK (0.828 nm). Thus, the electrical conductivity response and sensitivity of 80CuNaY show the highest values during the acetone exposure whereas during the MIBK exposure they show the lowest values.[23,30,31]

Figure 4b shows the plot of dPPV versus vapor concentration (ppm). The electrical conductivity response of dPPV toward acetone, MEK, and MIBK vapors at the vapor concentration of 30,000 ppm is $9.76 \times 10^{-02} \pm 2.05 \times 10^{-02}$, $3.17 \times 10^{-02} \pm 8.68 \times 10^{-03}$, and $1.66 \times 10^{-02} \pm 1.47 \times 10^{-04}$, respectively. The values of electrical conductivity sensitivity of dPPV toward acetone,

MEK, and MIBK vapors are $4.41 \pm 8.02 \times 10^{-01}$, $1.96 \pm 1.83 \times 10^{-01}$, and $1.00 \pm 9.95 \times 10^{-03}$, respectively, as presented in Table II All values of the electrical conductivity response and sensitivity depend on the solvent molecular size, the same as 80CuNaY sample. When the dPPV sample is exposed to acetone vapor, it shows high electrical conductivity response and sensitivity when compared to those of MEK and MIBK vapors, respectively.[23,30,31]

Figure 4c shows the plot of the electrical conductivity response of dPPV_[90]80CuNaY versus vapor concentration (ppm). The electrical conductivity response of composite under acetone, MEK, and MIBK vapors at the vapor concentration of 30,000 ppm is $1.16 \times 10^{-01} \pm 4.74 \times 10^{-03}$, $4.97 \times 10^{-02} \pm 5.30 \times 10^{-}03$, and $2.41 \times 10^{-02} \pm 2.07 \times 10^{-04}$, respectively. The values of electrical conductivity sensitivity of the composite during acetone, MEK, and MIBK exposures at the vapor concentration of 30,000 ppm are $4.98 \pm 1.53 \times 10^{-02}$, $2.51 \pm 5.72 \times 10^{-02}$, and $1.70 \pm 1.03 \times 10^{-02}$, respectively. The electrical conductivity response and sensitivity also depend on the solvent molecular size, the same as the 80CuNaY and dPPV samples. The electrical conductivity response and sensitivity depend on the proton transfer along the zeolite framework; however, dPPV has the conjugated double bond along the polymer chain, leading to more electrons to transfer along the polymer chain, resulting in the higher values of the electrical conductivity response and sensitivity than those of the pristine 80CuNaY. Thus, after mixing of dPPV with 80CuNaY matrix, the electrical conductivity response and sensitivity increase by an order magnitude as shown in Table III and Fig. 4c.[16–22,30,31]

The Effect of Vapor Concentration

NaY, 80FeNaY, 80NiNaY, and 80CuNaY samples were investigated for the effect of the vapor concentration. Figure 3 shows the plot between electrical conductivity response versus vapor concentration (ppm) of zeolite Y with four different transition cations in the zeolite framework. When the vapor concentration decreases, the electrical conductivity response and sensitivity of all samples also decrease. The minimum vapor concentration of 80CuNaY during acetone vapor exposure is 9 ppm. 80NiNaY, NaY, and 80FeNaY can respond to the minimum vapor concentrations of 12, 14, and 18 ppm, respectively, as shown in III This is because both the cationic radii and the electron configuration combine to have an effect on the ability of the zeolite to respond to acetone vapor.[20,23,24]

Figure 4a is the plot between the response versus vapor concentration of 80CuNaY and under the effect of ketone solvent type. The minimum vapor concentrations of acetone, MEK, and MIBK in which 80CuNaY is able to respond are 9, 18, and 20 ppm, respectively. This is because of the solvent molecular size. Figure 4b shows the response of dPPV versus vapor concentration. dPPV can respond to the acetone, MEK, and MIBK minimum vapor concentrations of 5, 7, and 9 ppm, respectively. This is again due to the solvent molecular size effect, same as the 80CuNaY sample.[17,20,22,23,29,30]

dPPV is mixed with the 80CuNaY matrix at the ratio of 10% v/v of dPPV; dPPV has been shown to enhance the response of 80CuNaY. The minimum vapor concentrations in which composites can respond are further reduced to 5 ppm (acetone), 7 ppm (MEK), and 10 ppm (MIBK) as shown in Fig. 4c and shown in Table II. [16–20,27–31]

TABLE IV
Comparison with Other Materials

Materials	Method	Vapor type	Minimum Vapor Concentration (ppm)	References
NaY	LCR meter	DMMP	20	Li and Dutta (2010)
CsNaY	TCL	*n*-Hexane	0.43	23
Cu-ZSM-5	QCM	DMMP	0.1	24
Co-BEA	LCR meter	Ethanol	66	35
Polyaniline	QCM	Methanol	9	11
dPPV_[90] 80CuNaY	2-Point probe	Acetone	5	This recent work

For comparing with other materials, NaY or zeolite Y (Na^+, Si/Al 2.5) was exposed to dimethyl methanephosphonate (DMMP) vapor.[24] The minimum vapor concentration was 20 ppm. For the process of the ion-exchange process in zeolite such as Cs-NaY and Cu-ZSM-5, they showed the lower minimum vapor concentration than NaY.[23,35] Moreover, a CP such as polyaniline, as shown in Table IV, shows the high electrical conductivity response and a low vapor concentration toward methanol.[11] It can be concluded that the ion-exchange process and the effect of CP can have dramatic effects on the response toward chemical vapors.

INVESTIGATING THE REACTIONS OF ADSORBED ACETONE VAPOR

Investigating the Interaction by FTIR

The interaction of zeolite Y and acetone vapor is investigated by the FTIR technique. The FTIR spectra of 80CuNaY (Fig. 5) and dPPV_90[80]CuNaY (Fig. 6) were taken in the 650-4000 cm^{-1} region. The spectra were collected before, during exposure, and after the acetone exposure.

Figure 5 shows the FTIR spectrum of 80CuNaY sample before, during, and after the acetone exposure. Before the acetone exposure, the adsorption peak of the Si–OH group (ν = 3640 cm^{-1}) appears as one of the zeolite characteristics.[14,24,30–32] The characteristics of the tetrahedral unit are identified at 790, 1010, 1150 cm^{-1}.[14,31] The OH stretching, which suggests the possibility of water in the zeolite structure, is identified with the peak of 1600 cm^{-1}.[14,24,30–32] During the acetone exposure, the new peaks at 3420, 1734, and 1210 cm^{-1} can be assigned to the interaction between the carbonyl group of acetone molecule with 80CuNaY and the cation in the zeolite framework, as shown in Fig. 7a (see later). [14,24,30–32,35–42] After the acetone exposure, the IR spectrum peaks at 3420 and 1210 cm^{-1} evidently decrease; this confirms that the interaction between 80CuNaY and acetone vapor is not reversible.

Figure 6 shows the FTIR spectrum of dPPV_[90]80CuNaY. Before the acetone exposure, the adsorption peak appears at 1150 cm^{-1} suggesting the quinoid structure, a characteristic of dPPV. The characteristics of the phenylene group appear as the peaks at 1514 and 3012 cm^{-1}.[26,27,30,31] The characteristic of the Si–OH

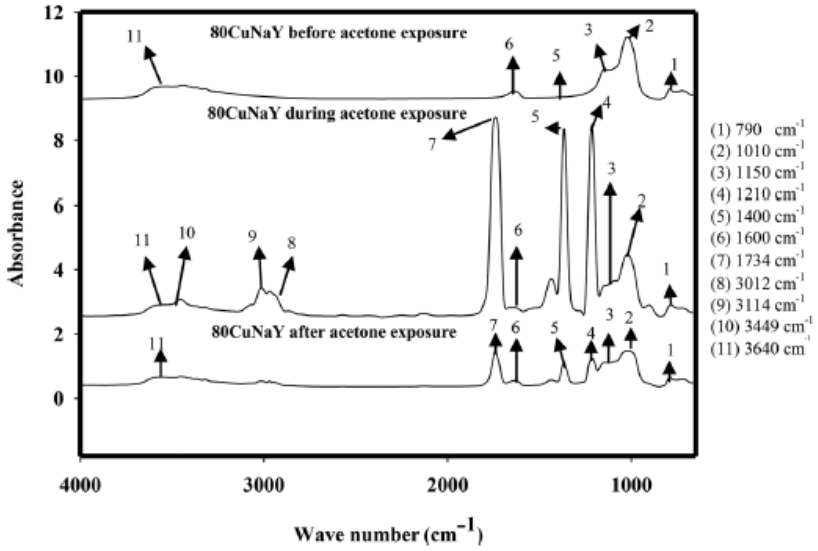

FIGURE 5. FTIR spectra of 80CuNaY exposed to acetone at the vapor concentration of 30,000 ppm (at the pressure of 1 atm and at $T = 25$°C).

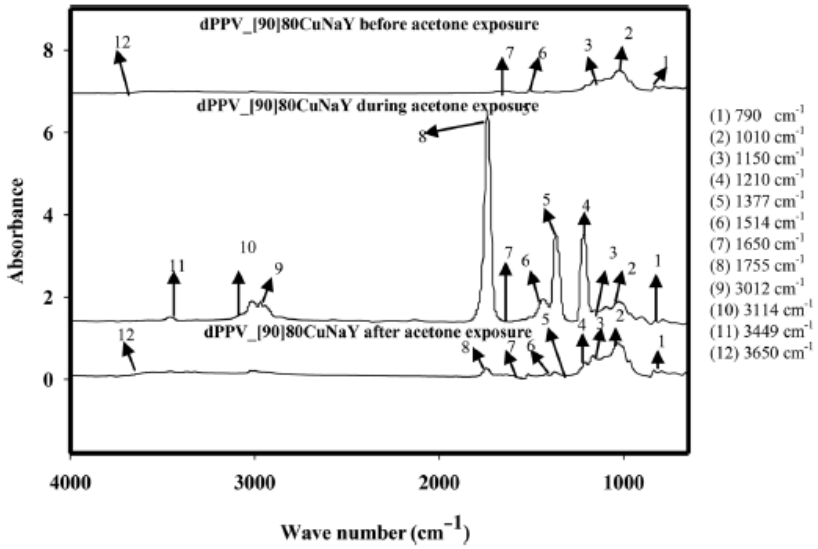

FIGURE 6. FTIR spectra of dPPV_[90]80CuNaY exposed to acetone at the vapor concentration of 30,000 ppm (at the pressure of 1 atm and $T = 25$°C).

group appears at 3650 cm^{-1}.[14,24,30-32] During the acetone exposure, the new peaks at 3449 and 1377 cm^{-1} appear as the characteristic of Si–O–C, suggesting an interaction between acetone and 80CuNaY.[14,24,30-32,35-42] The new peak at 1210 cm^{-1} indicates the characteristic of C–O; this also suggests an interaction between acetone and dPPV, as shown in Fig. 7b. During the acetone exposure, the intensity at 1140 cm^{-1} increases due to the increase in the number of the quinoid structures of dPPV.[26,27,30,31] After the acetone exposure, the intensities at 3012 and 1514 cm^{-1} decrease, suggesting that the acetone molecule acts as a secondary dopant leading to an increase in the number of the quinoid structures in the dPPV chain.[26,27,30-32] The interaction is clearly irreversible.

The interaction of 80CuNaY with acetone vapor is shown in Fig. 7a. The electron-donating acetone molecule stabilizes the copper cation in the 80CuNaY. Thus, during the acetone exposure an electron on the acetone molecule can move along the 80CuNaY structure and increases the electrical conductivity.[14,24,30-32] When dPPV is mixed with the 80CuNaY matrix at the ratio of dPPV 10% v/v, acetone acts as an electron-donating species for the 80CuNaY and dPPV structures during the acetone exposure as shown in Fig. 7b. The lone pair

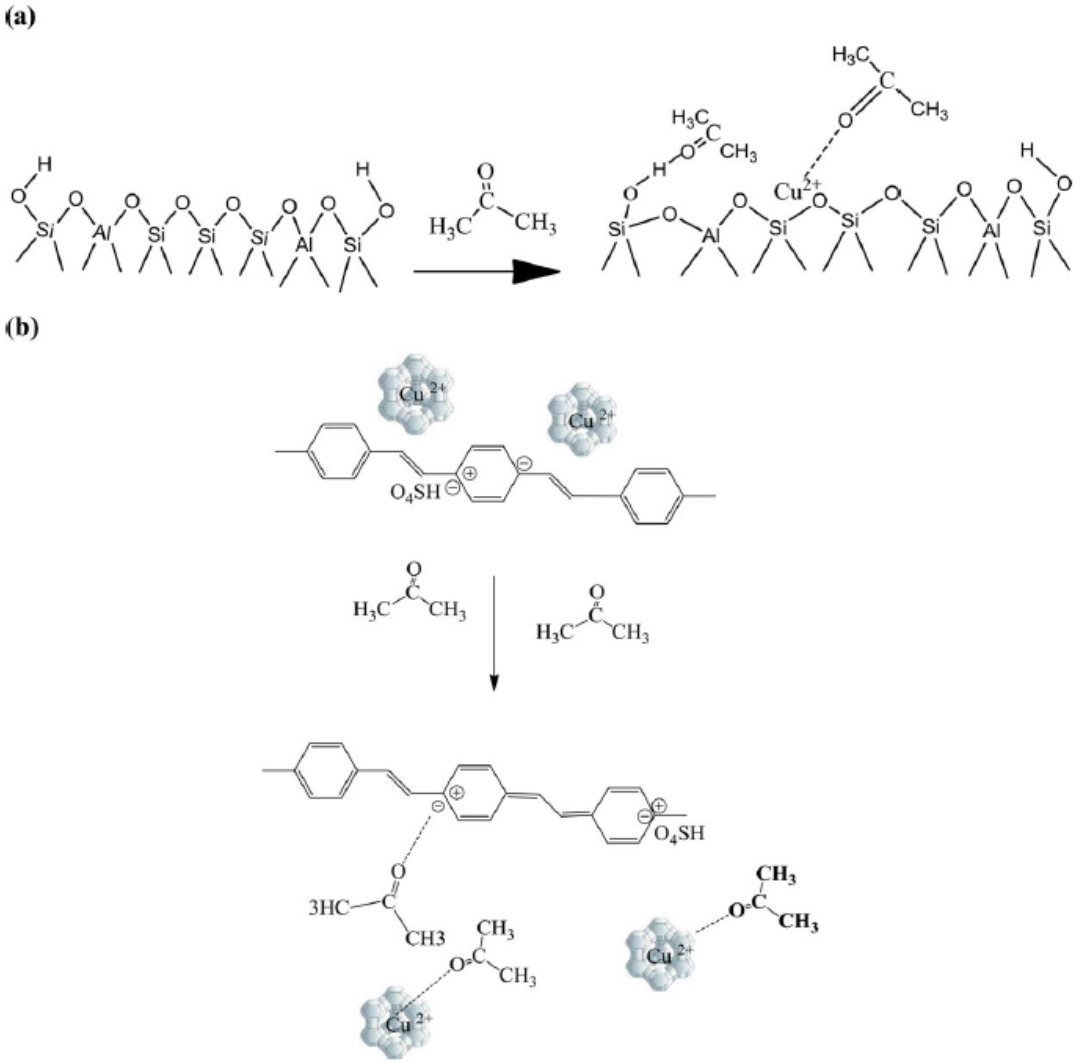

FIGURE 7. Interactions between acetone vapor and (a) 80CuNaY and (b) dPPV_[90]80CuNaY.

electron of the carbonyl group of the acetone molecule stabilizes the cation along the dPPV structure, resulting in greater negative charges corresponding to higher electrical conductivity when exposed to the acetone vapor.[26,27,30–32]

Investigating the Interaction by AFM

The interaction between dPPV[90]80CuNaY and acetone vapor is investigated by the phase changed by electrostatic force microscope (EFM) mode under applied voltage at −8 V. When applying a negative voltage at the tip, the material has a positive charge and the bright area appears as shown because of the attractive force between the tip and the material. If the material has a negative charge, then it will show the dark area due to the repulsive force between the tip and the material. Before the acetone exposure, the phase image shows the bright area, which suggests as the positive charge area as shown in Fig. 8a. Figure 8c shows the plot between the degree of charge generated versus distance. The attractive force between the tip and the dPPV_[90] 80CuNaY sample before acetone exposure indicates that the sample has a lot of positive charges from the cation in zeolite frameworks.

After the acetone exposure, the phase image is changed to the dark area and the degree of charge generated decreases due to the repulsive force between dPPV_[90]80CuNaY and the tip because the active sites or positive charges react with the acetone vapor, as shown in Figs. 8b and 8c. Before and after the acetone exposure, it is shown here that the phase image changes from bright area to dark area and the degree of charges generated changes by 20.77%.

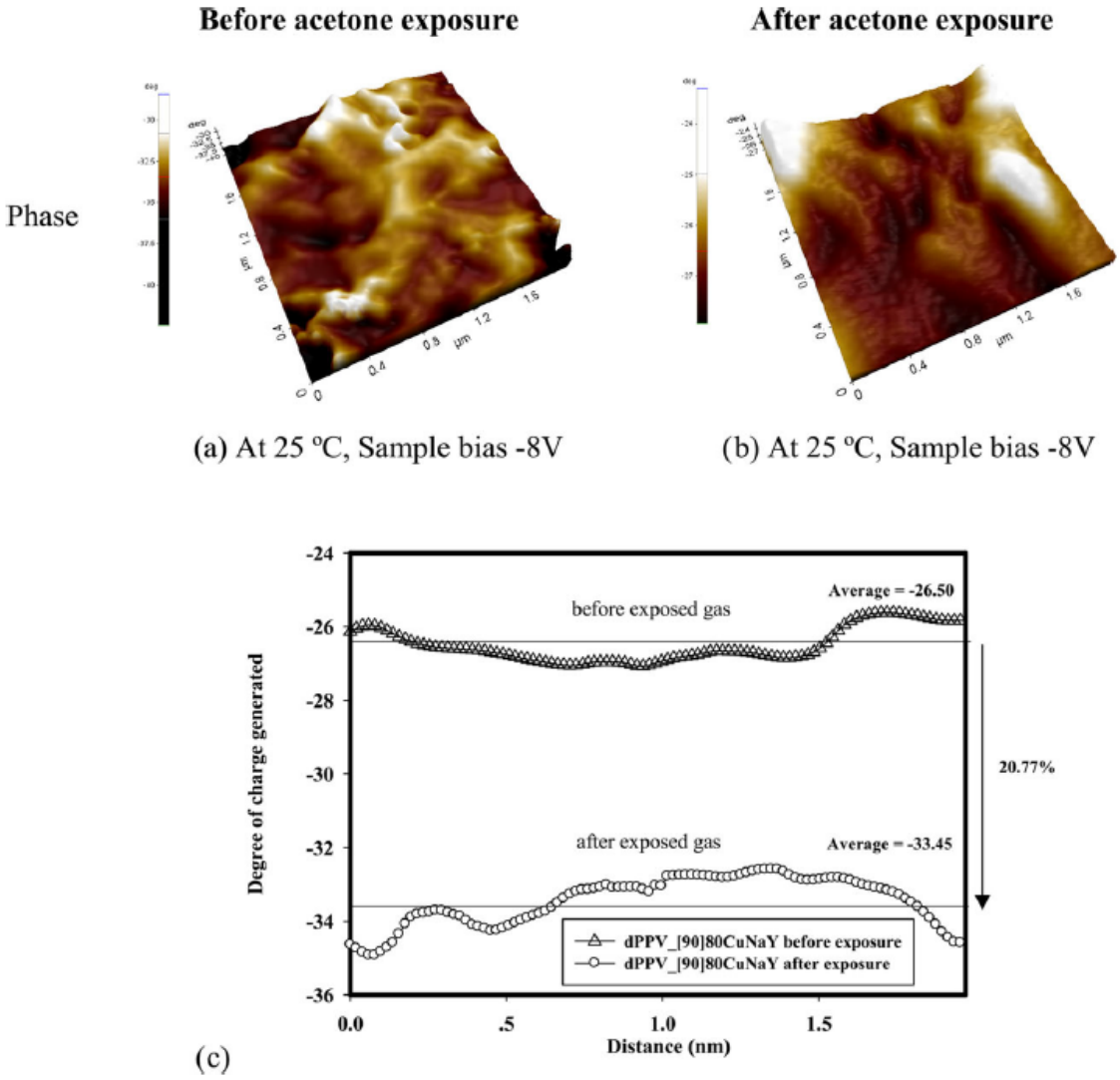

FIGURE 8. EFM phase images of (a)dPPV_[90]80CuNaY before exposure, (b) during acetone exposure, and (c) degree of charges generated on dPPV_[90]80CuNaY under –8 V of tip bias across the whole region.

Conclusions

The $CuCl_2$, $NiCl_2$, and $FeCl_2$ solutions are used for the ion-exchange NaY to prepare 80CuNaY, 80NiNaY, and 80FeNaY at 80% mol of cation. The highest electrical conductivity response and sensitivity when exposed to acetone vapor at the vapor concentration of 30,000 ppm belong to 80CuNaY in comparison to 80NiNaY, NaY, and 80FeNaY because of the proton mobility and electron configuration of cation in the zeolite structure. The large size of cation in the framework of zeolite leads to a reduction in the electrostatic force between the framework and the cation, and the ease in which a proton can move. For the effect of the vapor concentration, 80CuNaY can adsorb and respond to acetone vapor at the minimum vapor concentration of 9 ppm. When dPPV is mixed with the 80CuNaY matrix, the ability to adsorb and response decreases the minimum value to 5 ppm. For the effect of ketone vapor types, dPPV_[90]80CuNaY exposed to three different ketone vapors (acetone, MEK, and MIBK) at 3% v/v in N_2, the highest value of electrical conductivity response and sensitivity is obtained in the acetone exposure, whereas MIBK shows the lowest values due to the ability of the acetone molecule to penetrate into the zeolite framework. Thus, dPPV has been shown that it can enhance the electrical conductivity response and sensitivity of the 80CuNaY matrix. Moreover, under the acetone exposure the composite can respond to the acetone vapor at the lowest vapor concentration of 5 ppm whereas in the MIBK exposure the lowest vapor concentration is

10 ppm. The irreversible interaction between the active site and the acetone vapors is evidenced by the FTIR spectrum and AFM technique.

Acknowledgments

The authors would like to acknowledge the financial supports from the Conductive and Electroactive Polymers Research Unit of Chulalongkorn University, the Thailand Research Fund (TRF-RTA, TRF-RGJ-PhD/0026/2553), and the Royal Thai Government.

References

1. Heeger, A.; Diaz-Gracia, M.A. Solid-State Mater Sci 1998, 3, 16.
2. Pirsa, S.; Alizadeh, N. Sens Actuator, B 2012, 168, 303.
3. Benvenho, A. R. V.; Li, R. W. C.; Gruber, J. Sens Actuators, B 2008, 136, 173.
4. Yung, Y. S.; Jung, W.; Tuller, H. L.; Ross, C. A. Nano Lett. 2008, 8, 3777.
5. Vijaya, J. J.; Kenedy, L. J.; Sekaran, G.; Bayhan, M.; William, M. Sens Actuator, B 2008, 134, 604.
6. Urbiztondo, M. A.; Peralta, A.; Pellejero, I.; Sese, J.; Pina, M. P.; Dufour, I.; Santamaria, J. Sens Actuator, B 2012, 171–172, 822.
7. Satsuma, A.; Yang, D.; Shimizu, K. I. Microporous Mesoporous Mater 2011, 141, 20.
8. Varsani, P.; Afonia, A.; Williams, D. E.; Parkin, I.; Binions, R. Sens Actuator, B 2011, 168, 475.
9. Tang, L.; Li, Y.; Xu, K.; Hou, X.; Lv, Y. Sens Actuator, B 2008, 132, 243.
10. Gao, J. F.; Yan, D. X.; Huang, H. D.; Zeng, X. B.; Zhang, W. Q.; Li, Z. M. J Polym Res 2011, 18, 2239.
11. Ayad, M. M.; Hefnawey, G. E.; Torad, N. L. J Hazard Mater 2009, 168, 85.
12. Chang, C. J.; Lin, C. K.; Chen, C. C.; Chen, Y. C.; Kuo, E. H. Thin Solid Films 2011, 520, 1546.
13. Hung, S. T.; Chang, C. J.; Hsu, C. H.; Chu, B. H.; Lo, C. F.; Hsu, C. C.; Pearton, S. J.; Holzworth, M. R. Int J Hydrogen Energy 2012, 37, 13783.
14. Auerbach, S. M.; Carrado, K. A.; Dutta, P. K. Hand Book of Zeolite Science and Technology; CRC Press: Boca Raton, FL/Marcel Dekker: New York, 2003.
15. Ruangchuay, L.; Srivat, A.; Schwank, J. React Funct Polym 2004, 61, 11.
16. Ruangchuay, L.; Srivat, A. Schwank React Funct Polym 2008, 68, 1646.
17. Thongchai, N.; Kunanuruksapong, K.; Niamlang, S.; Wannatong, L.; Srivat, A. Wongkasemjit, S. Materials 2009, 2, 2259.
18. Chanthaanont, P.; Sirivat, A. e-Polymers 2012, 19, 1.
19. Arvand, M.; Ansari, R.; Heydari, L. Mater Sci Eng, C 2011, 31, 1398.
20. Shannon, R. D. Acta Crystallogr, Sect A: Cryst Phys, Diffr, Theor Gen Crystallogr 1976, 32, 751.
21. Li, K.; Xue, D. J. Phys Chem A 2006, 110, 11332.
22. Ji, X.; Yao, W.; Peng, J.; Ren, N.; Zhou, J.; Huang, Y Sens Actuator, B 2012, 166–167, 50.
23. Yang, P.; Ye, X.; Lau, C.; Liu, X.; Lu, J. Anal Chem 2007, 79, 1425.
24. Li, X.; Dutta, P. K. J Phys Chem C. 2012, 114, 7986.
25. Wessling, R. A.; Zimmerman, R. G. U. S. Patent 1968, 3, 401.
26. Ahlskog, M.; Reghu, M.; Noguchi, T.; Ohnishi, T. Synth Met 1997, 89, 11.
27. Kamonsawas, J.; Sirivat, A.; Niamlang, S.; Hormnirun, P.; Prissanaroon-Ouijai, W. Sensors 2010, 10, 5590.
28. Thuwachaosoan, K.; Chottananont, D.; Sirivat, A.; Rujiravanit, R.; Schwank, J. W. Mater Sci Eng B 2007, 140, 23.
29. Soontornworajit, B.; Wannatong, L.; Hiamtup, P.; Niamlang, S.; Chotpattananont, D.; Sirivat, A.; Schwank, J. Mater Sci Eng B, 2007, 15, 78.
30. Kamonsawas, J.; Sirivat, A.; Hormnirun, P. Int J Polym Mater Polym Bio Mater 2013, 62, 583.
31. Kamonsawas, J.; Sirivat, A.; Hormnirun, P. J Polym Res 2012, 19, 1.
32. Yimlamai, I.; Niamlang, S.; Chanthaanont, P.; Kunanuruksapong, R.; Changkhamchom, S.; Sirivat, A. Ionics 2011, 17, 607.
33. McKeen, J. C.; Davis, M. E. J Phys Chem C 2009, 113, 9870.
34. Wasastjerna, J. A. Acta Soc Sci Fenn 1923, 1(38), 1.
35. Urbiztondo, M. A.; Pellejero, I.; Villarroya, M.; Sese, J.; Pina, M. P.; Dufour, I.; Santamaria, J. Sens Actuator, B 2009, 137, 608.
36. Florian, J.; Kubelkova, L. J. Phys Chem 1994, 98, 8734.
37. Panov, A. G.; Fripiat, J. J. Langmuir 1998, 14, 3788.
38. Biaglow, A. I.; Gorte, R. J.; David, W. J. Phys Chem 1993, 97, 7135.
39. Martins, A. V. G.; Berlier, G.; Bisio, C.; Coluccia, S.; Pastore, H. O.; Marchese, L. J. Phys Chem C. 2008, 112, 7139.
40. Fameth, W. E.; Gorte, R. J. Chem Rev 1995, 95, 615.
41. Boekfa, B.; Pantu, P.; Prosbt, M.; Limtrakul, J. J Phys Chem, C 2012, 114, 15061.
42. Hoost, T. E.; Laframboise, K. A.; Otto, K. Catal Lett 1996, 37, 153.

REGULAR CONTRIBUTED ARTICLES

*N. Tangboriboon[1], H. Deechaiyapum[1], K. Petcharoen[2], A. Sirivat[2]**

[1] *Materials Engineering Department, Faculty of Engineering, Kasetsart University, Bangkok, Thailand*
[2] *Petroleum and Petrochemical College, Chulalongkorn University, Bangkok, Thailand*

Effect of Alumina Particles Embedded in Natural Rubber Foams on Cell Morphology and Thermo-Mechanical Properties

International Polymer Processing downloaded from www.hanser-elibrary.com by Hanser Verlag (Office) on March 30, 2015
For personal use only.

Alumina particles is a ceramic powder used as a dispersed phase or filler to reinforce the mechanical properties and improve thermal properties of natural rubber foams via the vulcanization process at curing temperature 150 °C with a two-roll mill. The amount of alumina added in natural rubber foams were varied from 0 to 60 phr on 100 phr of natural rubber in a sulfur curing system. The sodium bicarbonate ($NaHCO_3$) and N,N'-dinitrosopentamethylenetetramine (DNPT) were used as foaming agents. The sponge rubber composite foams were characterized for the microstructure, phase formation, thermal property, particle size distribution, and mechanical property by scanning electron microscope (SEM), X-ray diffraction (XRD), thermogravimetric analyzer (TGA), particle size analyzer,and compression set testing. The fabricated sponge rubber composite foams have distinctive characteristics such as light weight and good mechanical and thermal properties suitable for energy absorption such as thermal, noise, and vibration.

1 Introduction

Natural rubber, or cis-1,4-polyisoprene, can be applied in a wide range of applications such as gaskets, tires, LEDs, FETs, and solar cells due to its flexibility, ease of process-ability, and high mechanical performance (Najidha, 2005; Al-Homoud, 2005; Nam, 2003). However, natural rubber (NR), which is different from other polymers, is highly sensitive to degradation because there are unsaturated double bonds within the polymer main chain. Humidity, heat, ozone, light, and radiation contribute to the accelerated degradation of NR. Vinod reported that alumina, which acts as a filler in NR, can increase mechanical properties (tensile strength, elongation, and cross-linking in the composite) after thermal aging (Vinod, 2002). Another major application of NR is in the form of rubber foam, generally known as sponge, cellular, or expanded rubber (Najib, 2011). Rubber foam can be produced from both of NR latex, which is in liquid form, and dry NR, which is in solid form. Rubber foam processing, from a dry rubber, is derived from compounding the rubber with foaming agents or blowing agents, and vulcanizing agents (Najib, 2011). NR foams make excellent thermal and acoustic insulation, are light weight, and can be used for impact damping, cushioning, buoyancy, as well as production being cost effective. Sponge rubber is used for pipe insulation, gaskets, automotive weather-stripping, building construction materials, i.e. roof, wall, and decorative building construction.

Blowing agents are chemical substances that provide production and physical improvements, and increase economic advantages when processed a wide range of rubbers. The rubber blowing agents are used to increase the volume of product per unit rubber mass, rigidity per unit rubber mass, thermal insulation, sound absorption with a reduction of density and operating costs. There are eight key agents that are widely used as blowing materials: azodicarbonamide, 4,4-oxybis benzene sulfonylhydrazide, 5-phynyltetrazole, p-toluene sulfonylhydrazide, p-toluene sulfonylsemicarbazide, dinitrosopentamethylenetetramine, sodium bicarbonate, and zinc carbonate. Rubber blowing agents generate inert gases when heated effect to produce cellular structure formation. Typically, the blowing agent used for foaming production depends on the type of gases released during vulcanization process. Both temperature and time are important processing parameters of rubber vulcanization that produce different rubber foam properties from rubber blowing agents (Najib, 2011; Ariff, 2008; Pugh, 1996).

The cellular structures are reinforced by adding short glass fibers or rigid fillers (carbon black, silica, alumina, clay, and zeolite etc.) to the polymer resin before it is prepared into composite foams (Datta, 2002). Alumina is an inorganic and ceramic substance which can enhance mechanical property, thermal conductivity, thermal stability, flame resistance, and cost effectiveness. It is widely applied in a large number of applications: high temperature protective coatings, microelectronic packaging, infrared transmitting materials, microwave dielectrics, catalysts, and automotive devices due to its low thermal expansion coefficient, good thermal and chemical stability, high creep resistance, good thermal shock resistance, high

* Mail address: Anuvat Sirivat, Petroleum and Petrochemical College, Chulalongkorn University, Bangkok, 10330, Thailand
E-mail: anuvat.s@chula.ac.th

 © Carl Hanser Verlag, Munich

International Polymer Processing downloaded from www.hanser-elibrary.com by Hanser Verlag (Office) on March 30, 2015
For personal use only.

melting point, and superior toughness and strength (Lee and Choi, 2007; Kansal and Laine, 1997; Rozenberg and Tenne, 2008; Ansarifar, 2006).

The objective of the present work was to prepare sponge composite materials consisting of alumina (Al_2O_3) and natural rubber (STR 5 L) and sodium bicarbonate ($NaHCO_3$) and N,N′-dinitrosopentamethylenetetramine (DNPT; $C_5H_{10}N_6O_2$) as the foaming agents. The optimal foaming agent and feeding ratio of alumina for these products were selected with respect to density, physical, mechanical, and thermal properties. The present work evaluated the characterizations of physical-, thermal-, and mechanical properties, and microstructures of sponge natural rubber (STR 5 L) and alumina (Al_2O_3) composites with a sulfur curing system at 150 °C.

2 Experimental

2.1 Materials

Natural rubber was provided by Venus Technology Co., Ltd (VTEC), Thailand. The Standard Thai Rubber type 5 L, or encoded STR 5 L, was in the form of dry rubber with an extra light color slab and low dirt content (< 0.04 % wt). The Mooney viscosity (ML 1′ + 4′) at 100 °C, specific gravity, plasticity retention, initial plasticity, and impurity content of STR 5 L were 62.8, 0.92 g/cm^3, 81.3, 32.0, and 0.02 % wt, respectively. The characteristics of STR 5 L were good hot tensile properties, high compounded gum tensile strength, and low levels of non-polymer constituents.

Aluminum oxide or alumina (Al_2O_3) was supplied from Sigma-Aldrich Chemical Co., Ltd, USA. The purity, specific gravity, water solubility, average particle size, thermal conductivity, heat capacity, color of the alumina powder were 99 % wt, 3.34 g/cm^3, insoluble in water, 9.873 ± 0.034 microns, 18 W/m K, 79.04 J/mol K, and white color, respectively. Furthermore, alumina particles were quite uniform in shape.

The vulcanizing agents for the rubber compounds were sulfur (S), stearic acid, zinc oxide (ZnO), benzothiazyl-2-cyclohexyl-sulfenamide (CBS), and tetramethylthiuram disulfide (TMTD) furnished by the Rubber Research Institute of Thailand, Department of Agriculture of the Ministry of Agriculture, Bangkok, Thailand.

Titanium dioxide (TiO_2), in the form of brilliant white powder with high opacity acting as a pigment, was provided by the Rubber Research Institute of Thailand, Department of Agriculture, the Ministry of Agriculture, Bangkok, Thailand.

Sodium bicarbonate ($NaHCO_3$) was used as a foaming agent and was contributed by Ajax Finechem Pty. Ltd., Australia. The $NaHCO_3$ had high purity (> 99.7 % wt), with low impurity elements such as chloride, PO_4, S, Ca, Mg, Fe, K, NH_4, Cu, and Pb.

N,N′-dinitrosopentamethylenetetramine (DNPT) as a foaming agent was purchased from Nippon Zeon Co., Ltd., USA. The molecular weight, density, temperature of decomposition in air, and temperature of resin and additive decoposition of DNPT were186.18 g/mol, 1.45 to 1.51 g/cm^3, 190 to 205 °C, and 130 to 190 °C, respectively.

2.2 Instruments for Characterizations

X-ray diffraction (XRD) data were examined by an analyzer (Bruker, D8 Discover) connected with a double-crystal wide-angle goniometer and VANTEC-1 detector. Analytical method was scan from 10° to 80° 2θ with0.05° or 0.03° 2θ increments and a scan speed of 5° 2θ/min using CuKα radiation (λ = 0.154 nm). Matching of peak positions was determined from the standard JCPDS files for crystalline phase identification.

Fourier transform infrared spectra (FTIR) were measured to analyze chemical functional groups in the samples (Perkin Elmer, model Spectrum One) with a spectra resolution of 4 cm^{-1}. Samples were mixed with potassium bromide, as the material background, and then compressed to form thin film specimens.

Cumulative and fractional distribution was evaluated by a particle size analyzer (Mastersizer S long bed, model Polydisperse 2.19). The sample powders were dispersed in water, as the dispersing medium, and then vibrated in the ultrasonic vibration for 20 min.

The true density of the samples was measured by a gas pycnometer (Quantachrome, Ultra pycnometer 1000) using Eq. 1:

$$\rho = \frac{\text{Weight (D)}}{\text{True volume}}, \tag{1}$$

where ρ is the true density without porosity; D is the weight of the dry sample (g); and true volume is the volume of the solid component only. It was determined by crushing the specimen into a powder so that all pores were destroyed before analysis.

The bulk density of the samples was measured and calculated according to Eq. 2:

$$\rho = \frac{\text{Weight (D)}}{\text{Apparent volume}}, \tag{2}$$

where ρ is the bulk density with porosity (closed and open pores); D is the weight of dry sample (g); and apparent volume is the volume of the sample including open pores and closed pores.

The relative foam density of the sampleswas measured and calculated according to ASTM D3575 and ASTM D1056 using Eq. 3:

$$\frac{\text{Foam density}(\text{g/cm}^3)}{\text{Solid density } (\text{g/cm}^3)} = \text{Relative foam density}. \tag{3}$$

Scanning electron micrographs (SEM) were taken by a scanning electron microscope (SEM, JEOL-5200). The STR 5 L, sponge rubber foam added with alumina, and alumina particles were fixed onto stubs and sputter-coated with gold (~ 0.1 μm thick) to improve conductivity. Acceleration voltage of 15–20 kV with magnifications of 100 times was used for the experiments.

The curing behavior studied for the vulcanization temperature and vulcanization time of natural rubber compounds with a moving die rheometer (Techpro-Rheo Tech, MDR121105) at the Rubber Research Center, Kasetsart University, Thailand.

The crosslink density measurement was taken to determine bridge bonding and elasticity of samples by the toluene-swelling method described in ASTM D-6814-02. The dimension of samples was 1 cm^2 in a square shape and 3 to 5 mm in thickness. The samples were weighed before and after swelling in toluene for 72 h to reach complete swelling. The crosslink den-

International Polymer Processing downlooded from www.hanser-elibrary.com by Hanser Verlag (Office) on March 30, 2015
For personal use only.

sity test was performed at room temperature and calculated by the Flory-Rehner equation:

$$\nu_e = \frac{-\left[\ln(1-V_r) + V_r + \chi_1 V_r^2\right]}{\left[V_1\left(V_r^{1/3} - (V_r)/2\right)\right]}, \quad (4)$$

$$V_r = \frac{W_{Dryrubber}/density_{Dryrubber}}{\frac{W_{Dryrubber}}{D_{Dryrubber}} + \frac{W_{Absorbed\ solvent}}{D_{Solvent}}}, \quad (5)$$

where V_e is the effective number of chains in the real network per unit volume (mol/cm^3), V_r is the volume fraction of polymer in a swollen network at equilibrium with pure solvent; the dimensionless χ_1 is the Flory-Huggins interaction parameter – polymer-solvent interaction parameter – at 25 °C (for toluene in cis-polyisoprene 0.391), and V_1 is the molecular volume of solvent (toluene 106.3 cm^3/mol).

The compression set was tested following the ASTM D 395-03 (Method B) by using a compression set fixture (Hampden, APH40). It measured the ability of rubber compounds to retain elasticity after the extended action of compressive stresses. The actual stressing service is the speedy repeated deformation and recovery from intermittent compressive forces, the preservation of a definite deflection, or the constant application of a known force. The compression set comes from a latter dynamic stressing, but its whole effects are similar to the hysteresis tests or compression flexing. The samples were prepared in the cylindrical shape with a diameter of 2.9 cm and 1.3 cm in height. The compression strain employed was approximately 25%. The suitable test conditions for the compression set were 22 h and 70 ± 2 °C (158 ± 3.6 °F). The minimum force required to close the spring and steel plate to make contact with the rubber specimens was 2.4 kN (530 lbf). The result of the compression set is described as a percentage of deflection with the following equation:

$$C_B = [(t_o - t_i)/(t_o - t_n)] \times 100, \quad (6)$$

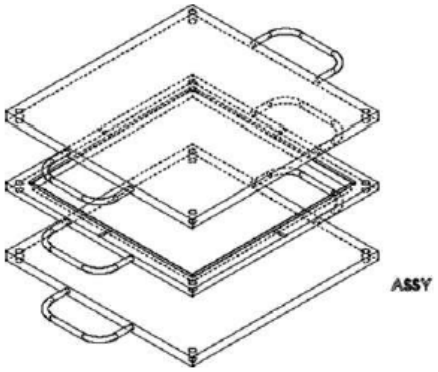

Scheme 1. Stainless Steel 304 mold for rubber foamspreparation as designed by our group

where C_B is the compression set (method B testing), t_o is the original thickness of the specimen, t_i is the final thickness of the specimen, and t_n is the spacer bar thickness.

The thermal conductivity of sponge rubber was measured with samples in a square sheet, 30 cm^2 and 1.5 cm thickness, using SS 304 hard-chrome plating according to Scheme 1. Thermal conductivity was measured according to ASTM C 518.

2.3 Sponge Rubber Composites Preparation

The sponge rubber composites composed of the natural rubber, zinc oxide, stearic acid, tetramethylthiuram disulfide (TMTD), sodium bicarbonate ($NaHCO_3$), N,N′-dinitrosopentamethylenetetramine (DNPT), benzothiazyl-2-cyclohexyl-sulfenamide (CBS), sulfur (S), titanium dioxide (TiO_2), and alumina (Al_2O_3) were prepared in parts per hundred rubber (phr) as tabulated in Table 1. The step of mixing is important to obtain

Raw materials	Formula 1 phr*	Formula 2 phr	Formula 3 phr	Formula 4 phr	Formula 5 phr	Formula 6 phr	Formula 7 phr	Formula 8 phr
NR STR 5L	100	100	100	100	100	100	100	100
Stearic acid	2	2	2	2	2	2	2	2
Zinc oxide	4	4	4	4	4	4	4	4
Tetramethylthiuram disulfide (TMTD)	0.2	0.2	0.2	0.2	0.2	0.2	0.2	0.2
Sodium bicarbonate ($NaHCO_3$)	5	5	5	5	–	–	–	–
N,N′-dinitrosopenta methylenetetramine (DNPT)	–	–	–	–	5	5	5	5
Benzothiazyl-2-cyclohexyl-sulfenamide (CBS)	1.8	1.8	1.8	1.8	1.8	1.8	1.8	1.8
Sulfur (S)	2	2	2	2	2	2	2	2
Alumina (Al_2O_3)	0	20	40	60	0	20	40	60
Titanium dioxide (TiO_2)	5	5	5	5	5	5	5	5

*phr = parts per hundred of rubber

Table 1. Compositions of raw materials for sponge rubber preparation

International Polymer Processing downloaded from www.hanser-elibrary.com by Hanser Verlag (Office) on March 30, 2015
For personal use only.

good sponge rubber samples. In the first step, the natural rubber (STR 5 L) was compounded in order to reduce molecular chain length of the natural rubber, to reduce viscosity, and to be able to mix easily with other chemical substances at 50 to 60 °C by a two roll mill. In the next step, the order of adding chemical substances is stearic acid, ZnO, TMTD, CBS, TiO_2, Al_2O_3 within 20 min. Then, we added sulfur and a foaming agent either $NaHCO_3$ or DNPT into rubber compounds for 5 min. After that, the mixed rubber compounds were formed by the compressing molding at 150 °C.

The sponge rubber samples prepared can be divided into two groups depending on the type of foaming agents: four formulations for sodium bicarbonate as a foaming agent and the other four formulations for DNPT as a foaming agent in order to study the effect of foaming agents and amount of alumina filler added on thermo-mechanical properties and microstructures. The sponge rubber samples were studied for the optimum curing temperature and curing time in order to achieve a 90% cured reaction (t_{90}), as evaluated from the rheometer cure curves. After that, the compounded rubber was formed by compressing molding at 150 °C.

3 Results and Discussion

3.1 Physical Properties of Natural Rubber and Alumina Particles

The qualities of the STR 5 L natural rubber, namely dirt content, volatile matter content, ash content, nitrogen content, initial plasticity, plasticity retention index, Mooney viscosity, and color value weremeasured according to SMR: Bulletin No. 7-1992 equal to 0.03 %wt, 0.24 %wt, 0.19 %wt, 0.32 %wt, 27.0, 51.9, 75.2, and 4.5, respectively, as described in Table 2. The STR 5 L is high purity suitable for using as a starting material to prepare the sponge rubber. Alumina particles have white color, uniform shape, and 99 %wt high purity. The particle size distributions (d_{90}, d_{50}, d_{10}, d_{avg}) of alumina particles are 142.72, 87.30, 9.05, and 82.82 µm, respectively, as shown in Fig. 1.

3.2 Characterization of Sponge Rubber Composites

Natural rubber (STR 5 L) and alumina particles have true density values equal to 0.92 and 3.34 g/cm^3, respectively. The sponge composite rubber, formulae 1–4, are composed of 100 g of NR and sodium bicarbonate as the foaming agent mixed with alumina particles added as a filler (0, 20, 40, and 60 g), whereas the sponge composite rubber, encoded formulae 5–8, are composed of 100 g of NR with DNPT as the foaming agent and alumina particles added as a filler (0, 20, 40, and 60 g). The bulk density and relative foam density values are tabulated in Table 3. As the amount of alumina particles increases, the bulk density and relative foam density values increase. Both the bulk density and relative foam density values of the sponge rubber with sodium bicarbonate are lower than those of the sponge rubber with DNPT, at the same amount of alumina particle as filler. The molecular weight of sodium bicarbonate is 105.99 whereas the molecular weight of DNPT is 186.17 g/mol, affect cell morphology, cell size, and cell shape. Furthermore, the gas outlet during the vulcanization by each foaming agent is different. The gas outlet from $NaHCO_3$ is the CO_2 and CO whereas the gas outlet from DNPT is N_2. Both CO and CO_2 have molecular weights (28 and 44 g/mol) more than the molecular weight of N_2 (28 g/mol). Therefore, the type and amount of gas decomposition affect cell morphology namely both open and closed cells including bulk density and relative foam density values.

The crosslink density values of the sponge rubbers are tabulated in Table 4. The crosslink density values of sponge rubbers with sodium bicarbonate formulae 1–4 decrease as the amount of alumina particles increases. The crosslink density values of sponge rubbers with DNPT formulae 5–8 tend increase as the amount of alumina particles increases. The crosslink density values of the sponge rubbers with added alumina mixed with $NaHCO_3$tend to decrease because the strong inter-atomic bonding and the ion exchange between the filler and the blowing agent. Ionic charges (Na^+, HCO_3^-, Al^{3+}, and O^{2-}) induce strong attractive force with the natural rubber matrix. The crosslink density values of the sponge rubbers with alumina particles added as the filler mixed with DNPT as the blowing agent tend to increase with the filler content because of the inter-atomic bonding within the microstructure due to Al^{3+} and O^{2-} DNPT ($C_5H_{10}N_6O_2$) is an organic compound composed of the covalent bonds. $NaHCO_3$ possesses ionic bonds.

Characteristics	Results	Testing
Dirt content (% w/w)	0.03	Part B.4
Volatile matter content (% w/w)	0.24	Part B.5
Ash content (% w/w)	0.19	Part B.6
Nitrogen content (% w/w)	0.32	Part B.7
Initial plasticity (P_0)	27.0	Part B.8
Plasticity Retention Index (PRI)	51.9	Part B.8
Mooney viscosity ML (1′ + 4′) 100 °C	75.2	Part B.9
Color	4.5	Part B.10

Table 2. Quality of raw natural rubber (STR 5 L)

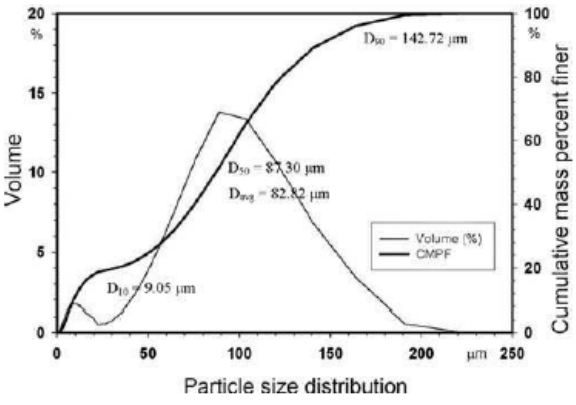

Fig. 1. Particle size distribution and cumulative mass percent finer (CMPF) of alumina particles

International Polymer Processing downlooded from www.hanser-elibrary.com by Hanser Verlag (Office) on March 30, 2015
For personal use only.

Therefore, the sponge rubber samples with DNPT have high crosslink density values due to a lower ionic charge content and high covalent bonding from DNPT reacting with the natural rubber.

XRD peak patterns of the NR, the alumina particle, the sponge rubber samples with sodium bicarbonate mixed with/without alumina particles, and the sponge rubber samples with DNPT cooperated with/without alumina particles are shown in Fig. 2. The XRD peak pattern of STR 5 L shows an amorphous phase whereas the XRD peak pattern of alumina particles indicates crystalline phase formation in terms of rhombohedral or corundum, consistent with the JCPDS Nos. 00-001-1243, 00-001-1296, and 00-001-1304 at 2θ: 43.473 (113), 57.955 (116), 25.652 (012), 35.165 (104), and 66.763 (214). The XRD peak patterns of the sponge rubber samples with sodium bicarbonate or DNPT as the blowing agents without alumina particles show a semi-crystalline phase between the amorphous and monoclinic phase formations, consistent with the JCPDS No. 00-003-0653 and 00-021-1119 at 2θ: 25.577, 28.967, and 30.378. Furthermore, the XRD peak patterns of the sponge rubber samples with sodium bicarbonate or DNPT added as the blowing agents and alumina particles as the filler show a crystalline phase due to the rhombohedral phase formation of aluminum oxide or corundum, and the monoclinic phase formation of the blowing agent. Thus, the XRD peak patterns of the sponge rubber with filler particles indicate a mixed phase formation between the matrix and the dispersed phase, consistent with the crosslink density results due to the interatomic bonding within the microstructures.

Figure 3 shows the FTIR spectra of STR 5 L, alumina particles (Al_2O_3), and the composite (STR5L-Al_2O_3) in the wave number range of 400 to 4000 cm^{-1}. The characteristic peaks

Samples/properties	True density g/cm³	Bulk density g/cm³	Relative foam density
Natural rubber (STR 5 L)	0.92	–	–
Alumina	3.34	–	–
Formula 1 STR 5L_Al_2O_3 0 phr_$NaHCO_3$	–	0.32 ± 0.02	0.3543
Formula 2 STR 5L_Al_2O_3 20 phr_$NaHCO_3$	–	0.37 ± 0.02	0.4051
Formula 3 STR 5L_Al_2O_3 40 phr_$NaHCO_3$	–	0.41 ± 0.01	0.4658
Formula 4 STR 5L_Al_2O_3 60 phr_$NaHCO_3$	–	**0.44 ± 0.01**	**0.4810**
Formula 5 STR 5L_Al_2O_3 0 phr_DNPT	–	0.34 ± 0.02	0.3798
Formula 6 STR 5L_Al_2O_3 20 phr_DNPT	–	0.41 ± 0.01	0.4557
Formula 7 STR 5L_Al_2O_3 40 phr_DNPT	–	0.44 ± 0.00	0.4810
Formula 8 STR 5L_Al_2O_3 60 phr_DNPT	–	**0.46 ± 0.01**	**0.5063**

Table 3. Density values of sponge rubber samples

Samples	Crosslink density[a] mol/cm³	Swelling ratio[b]	Molecular weight[c] M_c g/mol	Volume fraction of swollen polymer in solvent[d] (V_r)
Formula 1	7.63×10^{-5}	5.45	12590	0.1487
Formula 2	7.39×10^{-5}	5.44	12437	0.1475
Formula 3	7.23×10^{-5}	5.51	12729	0.1460
Formula 4	$\mathbf{6.38 \times 10^{-5}}$	**5.90**	**14414**	**0.1377**
Formula 5	4.03×10^{-5}	7.58	22802	0.1105
Formula 6	6.39×10^{-5}	5.90	14403	0.1375
Formula 7	7.72×10^{-5}	5.32	11937	0.1505
Formula 8	$\mathbf{8.59 \times 10^{-5}}$	**5.01**	**10703**	**0.1581**

[a] Crosslink density or effective number of chains in a real network per unit volume is calculated using the Flory-Rehner equation.
[b] Swelling ratio calculation: Swelling ratio = $(w_2 - w_1)/w_1$, where w_1 and w_2 are the weights of swollen rubber and dry rubber, respectively.
[c] Average molecular weight between the network crosslinks
[d] Volume fraction of rubber in a swollen network at equilibrium with pure solvent (toluene)

Table 4. Crosslink density values of sponge rubber samples

International Polymer Processing downloaded from www.hanser-elibrary.com by Hanser Verlag (Office) on March 30, 2015
For personal use only.

of the STR 5L/Al_2O_3 composites are at 3400 to 3000 cm^{-1} ν(O–H); 3000 to 2800 cm^{-1} ν(C–H) and (=CH); 2900 to 2800 cm^{-1} ν(CH_2); 1700 to 1600 cm^{-1} ν(C=C); 1500 to 1300 cm^{-1}(CH_3 asymmetric deformation); 1300 to 1100 cm^{-1} ν(C–O–C); 1100 to 740 cm^{-1} (=CH bending) and $(CH_2)_n$, $n \geq 5$; and 640 to 580 cm^{-1} ν(Al–O). The FTIR peak positions of STR 5 L and alumina (Al_2O_3) are consistent with the FTIR results reported by Vinod (2002); Tangboriboon (2011); Ismail (2008) and Kansal (1997). The obtained FTIR results confirm that the samples are composite materials having the alumina particles as a dispersed phase to enhance the thermal-mechanical-physical properties of the STR 5 L matrix phase.

SEM micrographs of the sponge rubber samples (formulae 1, 4, 5, and 8), at the cross-sectional areas with magnification of 100×, are shown in Fig. 4. The SEM micrographs of the sponge rubber samples with blowing agents (sodium bicarbonate or DNPT) without adding the filler of formula 1 (Fig. 4A) and formula 5 (Fig. 4C), respectively, indicate different cell sizes and cell distributions due to different types of blowing agents. The cell size of the sponge rubber samples with sodium bicarbonate added as the blowing agent (Fig. 4A) is bigger than that of the cell size of the sponge rubber samples with DNPT added as the blowing agent (Fig. 4C) due to different gas outlets and their molecular weights during the vulcanization process. The CO and CO_2 are gas outlets from $NaHCO_3$ whereas the N_2 is the gas outlet from the DNPT producing a stench during the vulcanization process. The SEM micrographs of both sponge rubber composite samples with 60 phr alumina added as the filler mixed with two kinds of blowing agents, sodium bicarbonate encoded formula 4 (Fig. 4B) and DNPT encoded formula 8 (Fig. 4D), show different cell morphologies and cell distributions due to the types, amounts, and molecular weights of the gas outlet during the vulcanization process. Furthermore, adding alumina particles as a filler in the natural rubber can reduce cell size of samples as shown in Fig. 4B and D. The gas outlet during the vulcanization process also affect the physical- (bulk density, relative foam density, and color), thermal-, and mechanical properties.

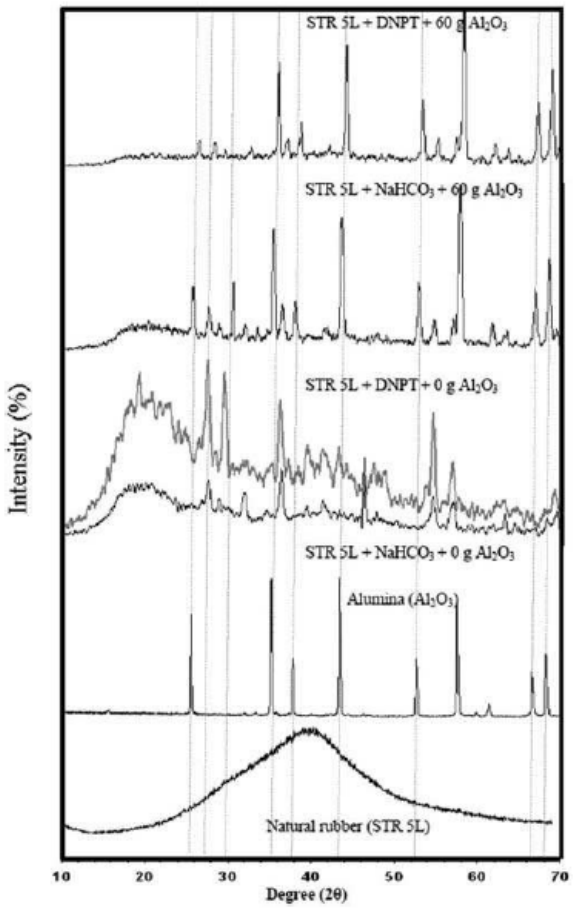

Fig. 2. XRD patterns of pure natural rubber (STR 5 L), alumina (Al_2O_3), natural rubber foams added sodium bicarbonate with and without Al_2O_3, and natural rubber foams added DNPT with and without Al_2O_3

3.3 Mechanical and Thermal Properties of Sponge Rubber Composites

All data of the sponge rubber composite samples from the Mooney viscosity test, curing time, and compression set measurements, are tabulated in Table 5. The sponge rubber sample

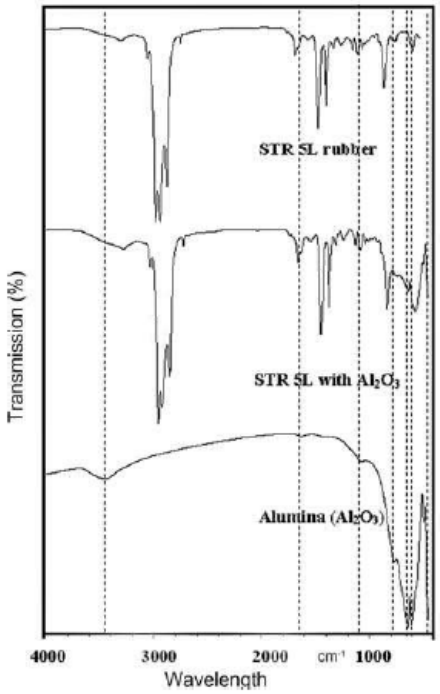

Fig. 3. FTIR patterns of pure natural rubber (STR 5 L), alumina (Al_2O_3), and natural rubber (STR 5 L) added with alumina

with sodium bicarbonate added as the blowing agent possesses lower Mooney viscosity and has a longer curing time than the sponge rubber sample with DNPT added as the blowing agent. The sponge rubber sample with sodium bicarbonate also offers better compression set resistance than the sponge rubber sample with DNPT. However, as the amount of alumina particles in the sponge rubber samples with both types of blowing agents (sodium bicarbonate and DNPT) increases, the compression set values tend to decrease. The result suggests that the alumina particles can be used to reinforce the mechanical properties of the sponge rubber consistent with the mixture rules (Callister, 2007).

The heat capacity values of sodium bicarbonate and DNPT, acting as the foaming agents, were studied by plotting the relation between the heat flow and temperature, starting from room temperature (25 °C) to 500 °C,as shown in Fig. 5A and B. The heat capacity values of sodium bicarbonate and DNPT are 25.19 kJ/kg °C and 5.77 kJ/kg °C, respectively. The endothermic reactions of sodium bicarbonate ($NaHCO_3$) occur at 162.71 °C whereas the DNPT occur at 206.14 °C, respectively, due to the gas decomposition out of their microstructures.

The specific heat values of the sponge rubber composites were calculated from the amount of alumina particles added as the filler according to the mixture rules (Callister, 2007) as

International Polymer Processing downloaded from www.hanser-elibrary.com by Hanser Verlag (Office) on March 30, 2015
For personal use only.

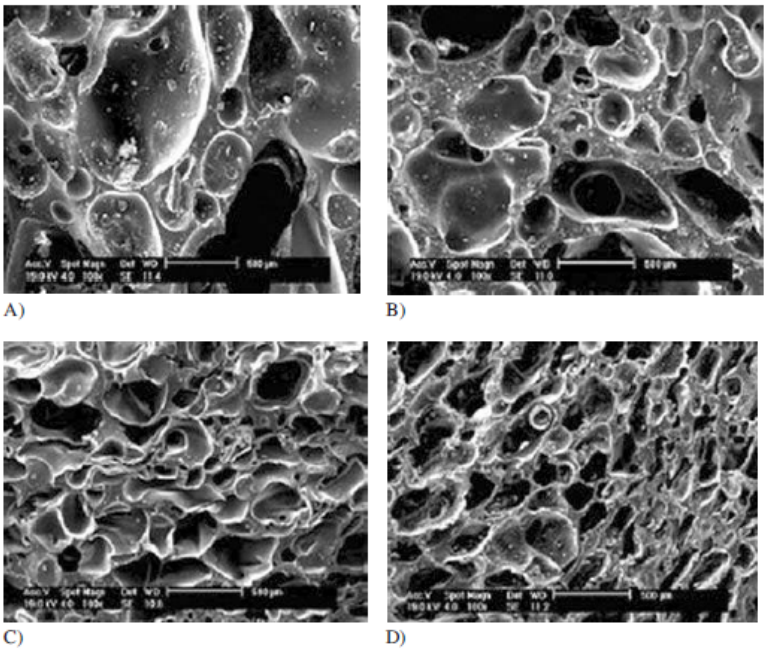

Fig. 4. SEM micrographs at the position of cross sectional areas with the magnification of 100X, A) formula 1 (natural rubber STR 5 L with $NaHCO_3$ without adding Al_2O_3), B) formula 4 (natural rubber STR 5 L with $NaHCO_3$ added 60 phr Al_2O_3), C) formula 5 (natural rubber STR 5 L with DNPT without adding Al_2O_3), D) formula 8 (natural rubber STR 5 L with DNPT added 60 phr Al_2O_3)

Properties	Formula 1	Formula 2	Formula 3	Formula 4	Formula 5	Formula 6	Formula 7	Formula 8
Mooney Viscosity (ML 1′ + 4) 100 °CISO 289-1	17.40	22.40	23.50	**25.30**	28.90	30.20	31.70	**35.70**
t_{90} (min) Curing time (MDR Type, TECH PRO) Arc 0.5°, 150 °C, ASTM D 5289	5.05	5.25	4.88	**3.94**	1.90	2.54	2.45	**2.34**
Compression set (%) at 70 °C, 22 hr. ASTM D 395-03 (Method B)	64.00	51.90	50.20	**46.40**	69.70	61.40	58.70	**54.10**

Table 5. Mechanical properties of sponge rubber samples

International Polymer Processing downloaded from www.hanser-elibrary.com by Hanser Verlag (Office) on March 30, 2015
For personal use only.

shown in Fig. 6. The experimental specific heat values of sponge rubber with 60 phr of alumina particles added as a filler of both blowing agents (sodium bicarbonate and DNPT) are in the range of upper-lower bound region. The sponge rubber samples added $NaHCO_3$ has a specific heat value close to the upper bound region consistent with the mixture rules. This result suggests that adding alumina (Al_2O_3) particles into the sponge rubber can increase thermal property.

Finally, the thermal conductivity values of the sponge rubber composites were measured according to ASTM C518 as tabulated in Table 6. The thermal conductivity values of formulae 1, 4, 5, and 8 are 0.068, 0.077, 0.049, and 0.061 W/m K, respectively. All data show low thermal conductivity values, which are lower than that of concrete (0.77 to 0.79 W/m K), plywood (0.12 W/m K), and particle board (0.14 W/m K) (Callister, 2007) measured at room temperature (24 °C). The results suggest that the fabricated sponge rubber samples have potential to be used as thermal insulation.

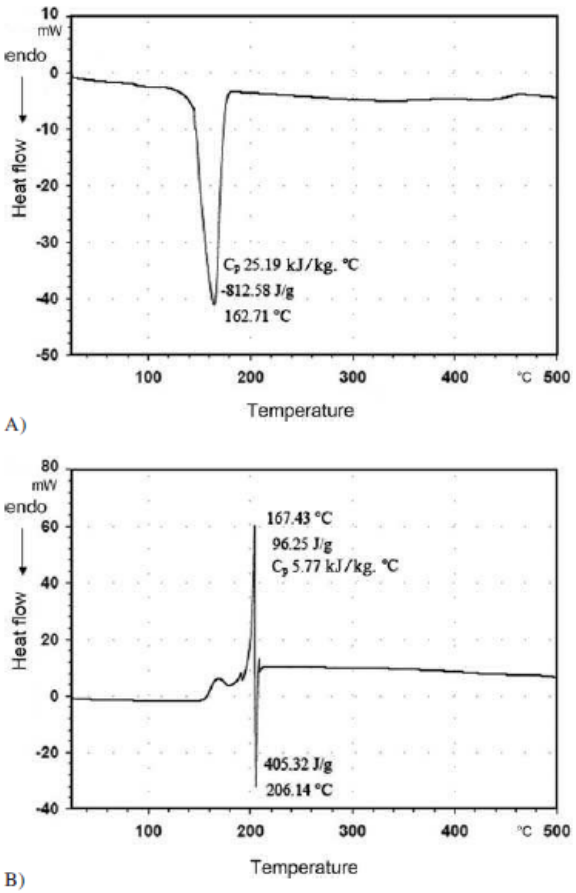

Fig. 5. DSC profiles of foaming agents,
A) sodium bicarbonate ($NaHCO_3$),
B) N,N'-dinitrosopentamethylenetetramine (DNPT, $C_5H_{10}N_6O_2$)

4 Conclusions

Sponge rubber is a kind of composite material, consistent with the FTIR and XRD results, which is composed of natural rubber (STR 5 L) as a matrix phase and alumina particles acting as a dispersed phase consistent with the mixture rules. Sodium bicarbonate or DNPT were employed as the blowing agents. Both foaming agents and the filler have been shown here to be important substances in controlling mechanical, thermal, and physical properties of the fabricated sponge rubber. The obtained sponge rubber samples encoded formulae 4 and 8 are of light weight, possessing good compression set, and high thermal resistance which are desirable properties for thermal insulation and energy absorption. The obtained sponge rubber composite foams with sodium bicarbonate and 60 phr alumina particles encoded formula 4 have crosslink density, bulk density, relative foam density, compression set, and thermal conductivity equal to 6.38×10^{-5} mol/cm^3, 0.44 ± 0.01, 0.4810, 46.40 %, 0.077 W/m K, respectively. The sponge rubber composite foams with DNPT and 60 phr alumina particles encoded formula 8 have crosslink density, bulk density, relative foam density, compression set, and thermal conductivity equal to 8.5986×10^{-5} mol/cm^3, 0.46 ± 0.01, 0.5063, 54.10 %, 0.061 W/m K, respectively. Both samples have good thermo-mechanical properties and light weight suitable for using as thermal and energy absorption. Furthermore, the curing (t_{90}) times of the sponge rubber composites with 60 phr alumina particles and with $NaHCO_3$ (formula 4) and DNPT (formula 8) are short and equal to 3.94 and 2.34 min, respectively. The short curing

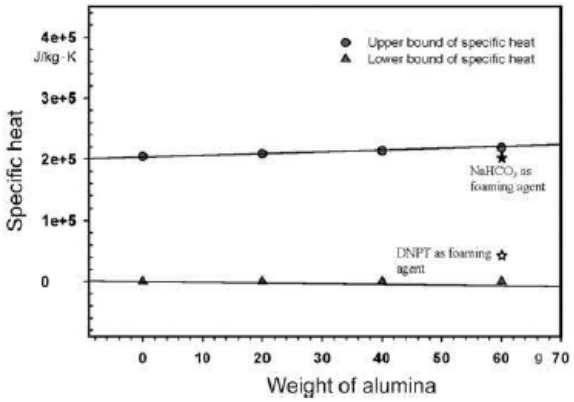

Fig. 6. The relationship between upper bound and lower bound of specific heat values versus weight of alumina

Sample codes	Thermal conductivity at 24 °C W/m K
Formula 1	0.068
Formula 4	**0.077**
Formula 5	0.049
Formula 8	**0.061**

Table 6. Thermal conductivity values of sponge rubber samples

time is an advantage for sponge rubber preparation to obtain high productivity and energy saving. Both samples (formulae 4 and 8) possessed different cell morphologies as caused by the blowing agents which generated gas during the vulcanization process namely N_2 (M_w 28 g/mol) from DNPT and CO and CO_2 from $NaHCO_3$ (M_w 28 and 44 g/mol). The generated gases affected the cell size and morphology. The sample with a larger cell size corresponded with lower bulk density and relative foam density values which are suitable for insulation and construction applications. In addition, the release of N_2 gas from DNPT produced a stench during the vulcanization process causing anodor pollution. In summary, various parameters are important in controlling the properties and characteristics of the sponge rubber composite foams namely the amount and type of fillers and blowing agents, curing temperature and time.

References

Al-Homoud, M. S., "Performance Characteristic and Practical Applications of Common Building Thermal Insulation Material", Build. Environ., **40**, 353–366 (2005), DOI:10.1016/j.buildenv.2004.05.013

Ansarifar, A., Shiah, S. F. and Bennett, M., "Optimising the Chemical Bonding between Silanised Silica Nanofiller and Natural Rubber and Assessing its Effects on the Properties of the Rubber", Int. J. Adhes. Adhes., **26**, 454–463 (2006), DOI:10.1016/j.ijadhadh.2005.06.008

Ariff, Z. M., Zakaria, Z., Tay, L. H. and Lee, S. Y., "Effect of Foaming Temperature and Rubber Grades on Properties of Natural Rubber Foams", J. Appl. Polym. Sci., **107**, 2531–2538 (2008), DOI:10.1002/app.27375

Callister, W. D.: Materials Science and Engineering: An Introduction, 7th Edition, John Wiley & Sons, Hoboken (2007)

Datta, D., Kirchhoff, J., Mewes, D., Herrmann, W. and Galinsky, G., "An Ultrasonic Technique to Monitor the Blowing Process in Sponge Rubbers", Polym. Test., **21**, 209–216 (2002), DOI:10.1016/S0142-9418(01)00072-1

Ismail, Y. A., Shin, S. R., Shin, K. M., Yoon, S. G., Shon, K. and Kim, S. L., "Electrochemical Actuation in Chitosan/Polyaniline Microfibers for Artificial Muscles Fabricated Using an in situ Polymerization", Sen. Act. B.,**129**, 834–840 (2008), DOI:10.1016/j.snb.2007.09.083

Kansal, P., Laine, R. M., "Processable Mullite Precursor Prepared by Reacting Silica and Aluminum Hydroxide with Triethanolamine in Ethylene Glycol: Structural Evolution on Pyrolysis", J. Am. Ceram. Soc., **80**, 2597–2606 (1997), DOI:10.1111/j.1151-2916.1997.tb03162.x

Lee, E. K., Choi, S. Y., "Preparation and Characterization of Natural Rubber Foams: Effects of Foaming Temperature and Carbon Black Content", Korean J. Chem. Eng., **24**, 1070–1075 (2007), DOI:10.1007/s11814-007-0123-6

Najib, N. N., Ariff, Z. M., Bakar, A. A. and Sipaut, C. S., "Correlation between the Acoustic and Dynamic Mechanical Properties of Natural Rubber Foam: Effect of Foaming Temperature", Mater. Des., **32**, 505–511 (2011), DOI:10.1016/j.matdes.2010.08.030

Najidha, S., Saxena, N. S., Sreeja, R., Unnithan, C. H. and Predeep, P., "Optical and Electrical Characterization of $SbCl_5$ Doped cis-1, 4-Polyisoprene", Mater. Lett., **59**, 3431–3436 (2005), DOI:10.1016/j.matlet.2005.06.021

Nam, J. D., Choi, H. R., Tak, Y. S. and Kim, K. J., "Novel Electroactive, Silicate Nanocomposites Prepared to Be Used as Actuators and Artificial Muscles", Sens. Act. A., **105**, 83–90 (2003), DOI:10.1016/S0924-4247(03)00066-9

Pugh, R. J., "Foaming, Foam Films, Antifoaming and Defoaming", Adv. Coll. Interf. Sci., **64**, 67–142 (1996), DOI:10.1016/0001-8686(95)00280-4

Rozenberg, B. A., Tenne, R., "Polymer-Assisted Fabrication of Nanoparticles and Nanocomposites", Prog. Polym. Sci., **33**, 40–112 (2008), DOI:10.1016/j.progpolymsci.2007.07.004

Tangboriboon, N., Chaisakrenon, S., Banchong, A., Kunanuraksapong, R. and Sirivat, A., "Mechanical and Electrical Properties of Alumina/Natural Rubber Composites", J. Elast. Plast., **44**, 21–41 (2012), DOI:10.1177/0095244311416579

Tangboriboon, N., Wongpinthong, P., Sirivat, A. and Kunanuraksapong, R., "Electroactive Alumina Particles Embedded in an Acrylic Elastomer", Polym. Compos., **32**, 44–51 (2011), DOI:10.1002/pc.21014

Vinod, V. S., Varghese, S. and Kuriakose, B., "Degradation Behavior of Natural Rubber-Aluminium Powder Composites: Effect of Heat, Ozone and High Energy Radiation", Polym. Degrad. Stab., **75**, 405–412 (2002), DOI:10.1016/S0141-3910(01)00228-2

Acknowledgements

The authors would like to acknowledge the following: the Petroleum and Petrochemical College, and the Scientific and Technological Research Equipment Centre, at Chulalongkorn University, Thailand, and the Department of Materials Engineering, at Kasetsart University for the use of analytical equipment. We are also appreciative for grant support from the Small Projects on Rubber (SPR 54) no. RDG5450056, the Thailand Research Fund, and the Kasetsart University Fund for fiscal year 2011. We also would like to acknowledge financial supports from Conductive and Electroactive Polymers Research Unit of Chulalongkorn University, the Thailand Research Fund (TRF), and the Royal Thai Government.

Date received: April 24, 2014
Date accepted: September 22, 2014

Bibliography
DOI 10.3139/217.2966
Intern. Polymer Processing
XXX (2015) 1; page 82–90
© Carl Hanser Verlag GmbH & Co. KG
ISSN 0930-777X

International Polymer Processing downloaded from www.hanser-elibrary.com by Hanser Verlag (Office) on March 30, 2015
For personal use only.

Effect of alkaline and alkaline earth ion exchanged Y zeolites on electrical conductivity and response of PEDOT-PSS/Y zeolite composites toward SO_2

P. Chanthaanont, T. Permpool and A. Sirivat*

This work reports on the association between a conductive polymer and zeolite framework towards SO_2. Responses and the interaction mechanism of conductive polymer/zeolite composite sensors were investigated. Poly(3,4-ethylenedioxythiophene) (PEDOT)–poly(styrene sulphonic acid) (PSS) complexes were prepared at a 1:1 molar ratio of EDOT/PSS. The adsorption properties of the faujasite zeolite (sodium form), with a Si/Al mole ratio of 5·1, were modified by changing the existing cation with alkaline and alkaline earth metal. The composites were fabricated to investigate the effects of zeolite content (vol.-%) and cation type (univalent cation: H^+, Li^+, Na^+ and K^+; divalent cation: Mg^{2+}, Ca^{2+} and Ba^{2+}) of faujasite zeolite type Y on electrical conductivity response when exposed to SO_2. The highest electrical conductivity response and sensitivity belonged to the PEDOT-PSS/KY zeolite composite. The different cation types in the Y zeolite can fine tune the adsorption–desorption properties, which influenced the electrical sensitivity of the composite. The composites showed reversibility to detect SO_2.

Keywords: Conducting polymers, Poly (3, 4-ethylenedioxythiophene), Faujasite, Y Zeolite, Sulphur dioxide

Introduction

Emissions of sulphur dioxide (SO_2) into the atmosphere are of high concern because SO_2 is the primary toxic gas produced from the use of fossil fuels in the electric power generation industry. Other sources of SO_2 in the air come from heavy industries and heavy vehicles using diesel.[1,2] Exposure to SO_2 by breathing it from the air can cause serious injury to people since it can burn the nose and throat, causing breathing difficulties and obstructing airways.[3,4] Consequently, the appropriate detection of SO_2 is an issue of major interest in the related gas sensing industry.[5,6]

In recent decades, new materials with unique properties for monitoring SO_2 and other toxic gases have been studied. Various kinds of gas sensor devices, such as solid electrolyte, oxide semiconductors, zeolite based gas sensors, mixed sensors, etc., have been investigated.[7–10] Most devices are well suited for use at high temperatures and have some limitations such as high cost, as well as low sensitivity, selectivity and reproducibility. The use of conductive polymers as gas sensing materials has been reported on numerous occasions.[11,12] They can be operated at room temperature, are of low cost and are easy to synthesise.[13,14] Recently, the effective use of zeolite for improving sensor responses has been demonstrated.[15,16] The aluminosilicate framework structure allows gas molecules to diffuse into the channels and pores of the zeolite. The electronegative charge of the framework is compensated by the electropositive ion whose ion size and charge depend on the pore geometry of the framework. Charge compensation allows the ion exchange process with alkaline, alkaline earth or transition metal cations, resulting in a change in gas adsorption behaviour of the zeolite.

The association of a conductive polymer and a zeolite framework is a novel concept. Poly(3,4-ethylenedioxythiophene)–poly(styrene sulphonic acid) (PEDOT-PSS) has been used as a semiconductor, where its electrical conductivity can be altered when exposed to various gases.[17,18] The electrical conductivity response depends on the adsorption properties of a zeolite microporous material.[19,20] A faujasite zeolite type Y with an Si/Al mole ratio of 5·1 was modified by an ion exchange process. The sodium form of Y zeolite was subjected to the ion exchange treatment using a chloride solution of alkaline and alkaline earth to produce univalent cation and divalent cation exchange zeolites.

The present work describes the effect of zeolite content (vol.-%) and cation type (univalent cation: H^+, Li^+, Na^+ and K^+; divalent cation: Mg^{2+}, Ca^{2+} and Ba^{2+}) of faujasite zeolite type Y on the electrical conductivity and sensitivity response of PEDOT-PSS/Y

Conductive and Electroactive Polymer Research Unit, The Petroleum and Petrochemical College, Chulalongkorn University, Bangkok 10330, Thailand

*Corresponding author, email anuvat.s@chula.ac.th

© 2015 W. S. Maney & Son Ltd.
Received 30 June 2014; accepted 26 September 2014
DOI 10.1179/1753555714Y.0000000207

zeolite composites when exposed to SO_2. The sensor response behaviour was investigated including the mechanism involved between the polymer/zeolite composites and SO_2.

Experimental

Materials

The 3,4-ethylenedioxythiophene, EDOT (AR grade, Aldrich), was used as the monomer. Poly(styrene sulphonic acid) was used as the dopant. Sodium persulphate, $Na_2S_2O_8$ (AR grade, Aldrich), was used as the oxidant. Y zeolite samples (HY and NaY with Si/Al=5·1) in powder form were purchased from Zeolyst International. Sulphur dioxide gas (TIG, 1000 ppm in N_2) and nitrogen gas (TIG, 99% purity) were used to investigate the electrical conductivity and sensitivity responses of the composites.

Polymerisation of PEDOT

The chemical polymerisation of PEDOT-PSS followed the procedures reported in prior research.[21] PEDOT-PSS, at a 1 : 1 mole ratio of EDOT/PSS, was prepared by adding EDOT monomers to an aqueous solution of PSS, and $Na_2S_2O_8$. After initial stirring at room temperature for 10 min, $Fe_2(SO_4)_3$ was added, and the mixture was stirred vigorously for 24 h. The dark aqueous PEDOT-PSS mixture was purified by ion exchanging with Lewatit M600 and Lewatit S100, resulting in a dark blue, aqueous PEDOT-PSS solution. A PEDOT-PSS film was obtained by casting the aqueous PEDOT-PSS solution and drying at 100°C for 24 h in a vacuum oven.

Preparation of ion exchange zeolites

The M^{n+} zeolites studied in this work were faujasite type Y zeolites (Zeolyst, Si/Al=5·1) with different compensating cations (H^+, Li^+, Na^+, K^+, Mg^{2+}, Ca^{2+} and Ba^{2+}). The Li^+, K^+, Mg^{2+}, Ca^{2+} and Ba^{2+} exchanged faujasites were processed using conventional ion exchange procedures.[22] NaY zeolite was used as the starting material for the metal exchange. For the metal exchanged zeolites, 1 g of NaY zeolite was added to 25 mL of 0·1M metal chloride solution at room temperature and stirred for 24 h. The modified zeolite was filtered and washed with distilled water to remove the Cl^- ions followed by drying at 373 K in air for 24 h.

Composite preparation

The PEDOT-PSS powder was ground, sieved with a 38 μm sieve and then dried before being mechanically mixed with dried Y zeolite powders at various zeolite concentrations: 0, 10, 20, 30, 40 and 50 vol.-%. The mixtures were obtained by compressing with a hydraulic press at a pressure of 6 kN into a thin disc with a diameter of 10 mm and a nominal thickness of 1 mm.

Characterisation

A Fourier transform infrared spectrometer (FTIR Nicolet, Nexus 670) with a resolution of 4 cm^{-1} and scan number of 32 was used to characterise the functional groups. The thermal stability of PEDOT-PSS was investigated using a thermogravimetric analyser (Dupont 2950) with a heating rate 10°C min^{-1} under O_2 atmosphere. A scanning electron microscope (SEM; JEOL, JSM 5200) was used to observe the morphology of PEDOT-PSS, zeolites and PEDOT-PSS/zeolite composites in powder form. An X-ray diffractometer (XRD; Phillips, Rigaku) was used to examine the degree of crystallinity of PEDOT-PSS and the crystal order of the zeolites. The surface area, pore width and pore volume of the Y zeolite were measured using a surface area analyser (Sorptomatic 1990). The ion exchange (%) was measured for each Y zeolite sample by the inductively coupled plasma technique (Perkin-Elmer/Optima 4300DV). Temperature programmed desorption (TPD; Micromeritics, 2900) was conducted. The Y zeolites were pretreated at 773 K. NH_3 was adsorbed at room temperature and subsequently flushed with He. Temperature programmed desorption was started by increasing the temperature to 873 K with 10 K min^{-1} lamp.

Electrical conductivity measurement and gas detection

The electrical conductivity values of PEDOT-PSS, Y zeolites and the resulting composites under exposure to air, N_2 and SO_2 were measured in a special gas cell. The gas cell consisted of two stainless steel chambers connected in a series. The first chamber and the second chamber were called the mixing and measurement chambers respectively. Temperature controllers, connected to both chambers, were used to monitor and control the temperature within the gas chambers. The second chamber contained two custom built two-point probe meters connected to a voltage supply (Keithley, 6517A) for applying a constant voltage source and recording the resultant current. The specific conductivity σ (S cm^{-1}) values of the pellets were obtained by measuring the bulk pellet resistance R (Ω). The equation $\sigma = \left(1/Rt\right)\left(1/K\right) = \left(I/Vt\right)\left(1/K\right)$ was used to calculate specific conductivity, where t is the pellet thickness (cm), I is the resultant current (A), V is the applied voltage (V) and K is the geometric correction factor, which is equal to the ratio w/l, where w and l are the probe width and the length respectively. The geometrical correction factor K was determined by calibrating the custom built, two-point probe with semiconducting silicon sheets of known resistivity values. Electrical conductivity values of several samples were first measured at various applied DC voltages to identify the linear ohmic regimes. The electrical conductivity response $\Delta\sigma$ and sensitivity S of the composites are defined by $\Delta\sigma = \sigma_{SO_2} - \sigma_{N_2}$ and $S = \Delta\sigma/\sigma_{N_2}$ respectively, where σ_{N_2} and σ_{SO_2} are the electrical conductivity of the composite in N_2 and target gas SO_2 respectively.

Results and discussion

Characterisation of PEDOT-PSS, Y zeolite and composites

PEDOT-PSS was synthesised by the polymerisation of EDOT in an aqueous solution of PSS using $S_2O_8^{2-}$ as the oxidant. The FTIR spectrum of PEDOT-PSS (Fig. 1) shows peaks at 1520 and 1339 cm^{-1}, which are assigned to the C=C and the C–C stretching in the thiophene ring;[23,24] the peaks at 929 and 834 cm^{-1} correspond to the symmetric vibration of C–S bond in the thiophene ring.[23–25] The peaks at 1127 and 1039 cm^{-1} are assigned to the stretching mode of the ethylenedioxy group,[23,24] and the peaks at 1198 and 929 cm^{-1} correspond to the $-SO_3^-$ and the S–OH

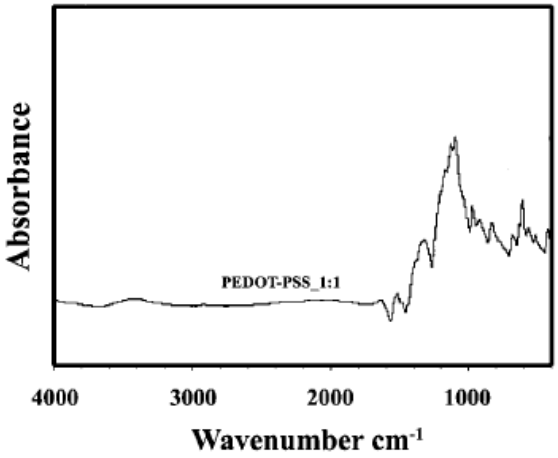

1 Spectra (FTIR) of PEDOT-PSS

stretchings of the PSS molecule.[23,26] The vibration of the bending mode of the C–H bond in the EDOT monomer (~892 cm^{-1}) is not present.[23] This result confirms the formation of PEDOT molecular chains. The absorption peak at 1645 cm^{-1} can be assigned to the oxidation state of the PEDOT, which indicates the successful doping of PEDOT polymer with PSS. In summary, the FTIR spectrum data indicate the successful formation of PEDOT molecular chains doped with PSS counter ion.

Four transitions are observed in the PEDOT-PSS thermograms (Fig. 2): 30–110, 160–380, 380–550 and 560–900°C. They are related to the loss of water, the side chain degradation and the polymer backbone degradations of PSS and PEDOT respectively.[27,28] The XRD patterns of PEDOT-PSS displayed in Fig. 3 show that there is no characteristic peak; the broad scattering background indicates the amorphous nature of the materials.[27,28] The mean particle diameter of PEDOT-PSS_1:1 was determined to be $\sim 34 \pm 0{\cdot}22$ μm. The micrograph, in Fig. 4, of the PEDOT-PSS particles shows rough surfaces and irregular shapes; they are moderately dispersed. The density of PEDOT-PSS_1:1 is $1{\cdot}4750 \pm 0{\cdot}0003$ g cm^{-3}. The electrical conductivities of PEDOT-PSS in air and nitrogen atmosphere are $(1{\cdot}169 \pm 0{\cdot}003) \times 10^1$ and $(1{\cdot}123 \pm 0{\cdot}001) \times 10^1$ S cm^{-1} respectively.

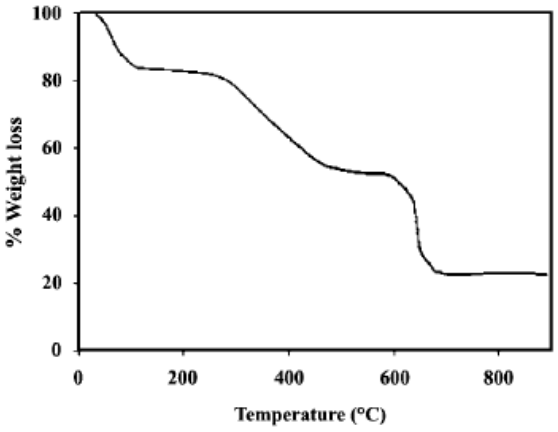

2 Thermogravimetric analysis thermograms of PEDOT-PSS

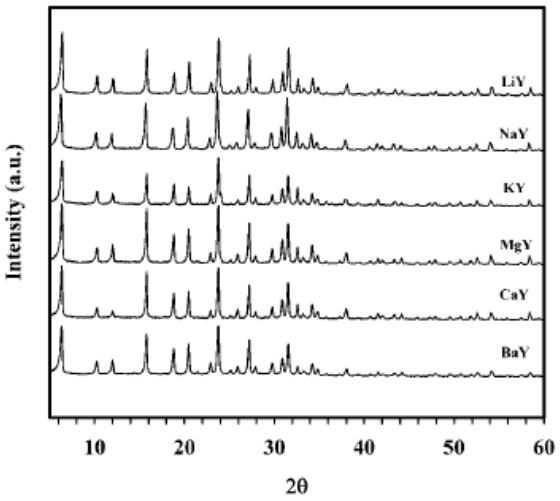

3 X-ray diffraction patterns of LiY, NaY, KY, MgY, CaY and BaY zeolite

NaY zeolite was 90% ion exchanged by various alkali and alkaline earth cations (Li^+, K^+, Mg^{2+}, Ca^{2+} and Ba^{2+}) (Table 1). Comparison of the scanning electron micrographs (SEM) of the starting material NaY zeolite and the zeolite powders obtained by the ion exchange method indicate there was no change of the particle size or morphology after the ion exchange process. Y zeolite particles possess irregular crystal shapes and appear to be inhomogeneously dispersed in the conductive polymer matrix of the composites (Fig. 4). The XRD of all Y zeolite samples, as shown in Fig. 4, shows the characteristic peaks of the faujasite framework, which is highly crystalline in the range of 5–70°. Comparison of the XRD patterns of the metal exchanged zeolite to the NaY starting material shows no significant changes in the crystalline structure of the zeolite during the ion exchange process (Fig. 3). There are no significant diffraction lines of any new phase, and no shift in the peak positions was observed after metal ion exchange due to its low metal content and high dispersion through ion exchange.[30] The mean particle diameters of H^+, Li^+, Na^+, K^+, Mg^{2+}, Ca^{2+} and Ba^{2+} exchanged faujasites (Si/Al mole ratios equal to 5·1) are ~200 nm (Table 1).[29]

The BET surface area and pore volume are consistent with cationic size: Li>Na>K and Mg>Ca>Ba as seen in Table 1. The BET surface area and pore volume increase as cation size decreases, except for the HY zeolite. This result indicates that larger ions occupy more pore space, resulting in less adsorbable sites. In regards the HY zeolite, the amount of cations increases due to the small size of H^+, which leads to lower surface area and pore volume.[30]

The exchangeable cation in the zeolite micropores can alter the acid–base properties, which play an important role in adsorption–desorption properties, thus influencing the electrical sensitivity of the sensor. The NH_3-TPD technique was used to determine the acid strength. The acidity of all ion exchanged zeolites from NH_3-TPD technique is shown in Table 1. For the univalent cation Y zeolite, the acidity increases as cation size in the zeolite micropore decreases (HY>LiY>NaY>KY). The divalent cation Y zeolites show the same result as

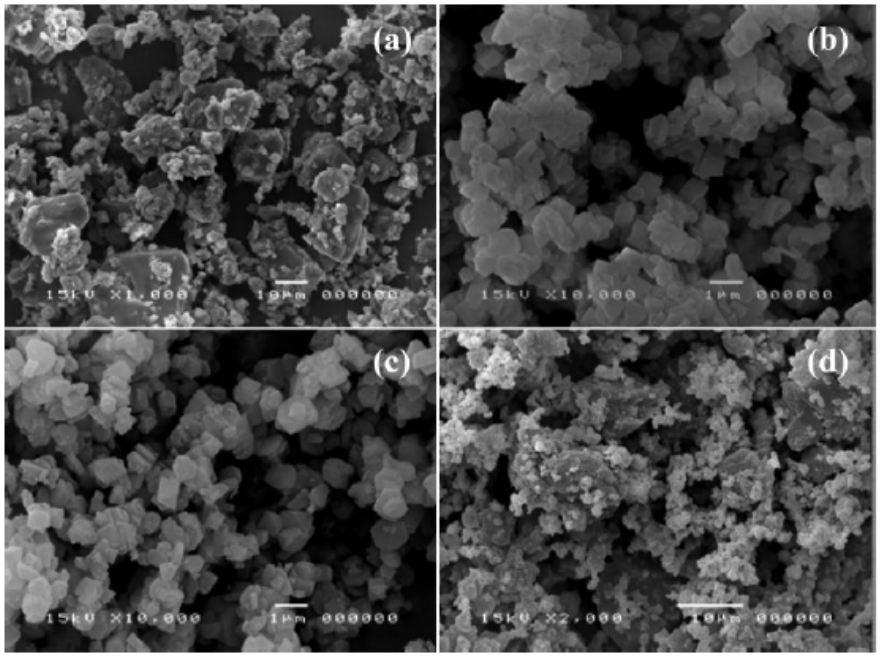

a PEDOT-PSS at 1000×; *b* NaY zeolite at 10000×; *c* LiY zeolite at 10000×; *c* PEDOT-PSS/NaY at 2000×

4 Morphology of PEDOT-PSS particles, Y zeolite powders and PEDOT-PSS/Y zeolite composites

univalent cation zeolite Y (MgY>CaY>BaY). A comparison of the univalent and divalent cation zeolites shows that the divalent cation zeolite Y has higher acidity (lower basic strength) than the univalent cation Y zeolite. The divalent cation Y zeolites have a loss of basicity, which is related to the decreased negative charge on the oxygen framework.[31]

Electrical conductivity data in N_2, for the Y zeolites with different cation types are also tabulated in Table 1. The HY zeolite has the smallest charge balancing cation (0·30 Å), exhibits the lowest electrical conductivity inversely to KY zeolite and has the highest electrical conductivity due to the large cation size (1·38 Å), which leads to a reduced electrostatic interaction with the anionic framework sites and easy cation transfer from one site to another.[32]

Electrical conductivity response to SO_2

Effect of zeolite content

The electrical sensitivity values of PEDOT-PSS_1 : 1 and its composites with zeolite Y when exposed to air, N_2 and SO_2 were measured under a chamber temperature T_c of 27±1°C, at 1 atm. The electrical conductivity sensitivity values of the PEDOT-PSS/NaY zeolite composites in 1000 ppm SO_2/N_2 are shown in Fig. 5. The composites show a negative response to SO_2. The sensitivity value of PEDOT-PSS/NaY increases as NaY zeolite content increases from 0 to 20 vol.-%. Beyond this volume fraction, the sensitivity value decreases as NaY zeolite content increases from 20 to 50 vol.-% respectively. As more Y zeolite content is added, its presence also reduces the direct contact area between SO_2 and PEDOT, hence lowering the sensitivity response.[32] This result suggests that the preparation of the composite with appropriate amount of zeolite could raise the sensitivity of the sensor materials.

Effect of cation type

The electrical sensitivity values of PEDOT-PSS_1 : 1 and its composites with Y zeolites when exposed to air, N_2 and SO_2 were measured under T_c of 27±1°C, at 1 atm. The electrical conductivity sensitivity values of the PEDOT-PSS/M^{n+}Y composites in 1000 ppm SO_2/N_2 are shown in Fig. 6. For the composites of PEDOT-PSS/M^+Y, electrical sensitivity to SO_2 increases as cation size of the zeolite increases. This result corresponds to the electrical sensitivity of SO_2 in the PEDOT-PSS/

Table 1 Physicochemical property of Y zeolites on faujasites with pore size of 0·74×0·74 nm and particle size of 200 nm

	HY	LiY	NaY*	KY	MgY	CaY	BaY
Surface area/$m^2\ g^{-1}$	630	886	800	772	856	834	847
Pore volume/$cm^3\ g^{-1}$	0·2476	0·2435	0·2463	0·2224	0·2421	0·2428	0·2421
% Cation exchange	...	91	...	88	93	92	89
Cation radius/Å	0·30	0·69	1·02	1·38	0·72	1·00	1·35
Electronegativity (Pauling)	2·3	0·98	0·93	0·82	1·31	1·00	0·89
Total acidity/mmol g^{-1}†	2·5000	1·5652	1·3305	0·7903	2·1394	1·8236	1·7349
$\sigma/10^{-3}$ S cm^{-1}‡	1·26±0·035	2·59±0·247	2·69±0·417	2·63±0·035	1·92±0·042	2·11±0·100	1·99±0·035

*Zeolite used for cation exchange process.
†Calculated from NH_3-TPD analysis.
‡DC electrical conductivity σ calculated from 2-point probe measurement.

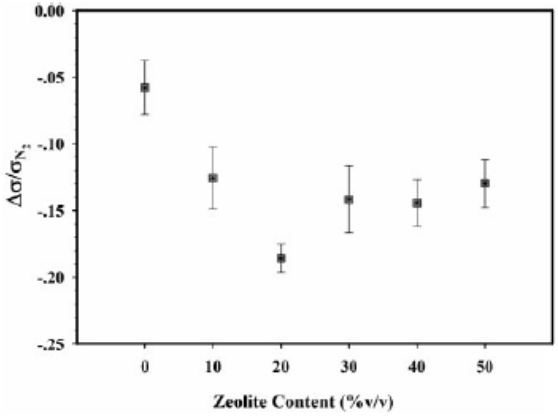

0, 10, 20, 30, 40 and 50 vol.-% when exposed to SO_2 at 27±1°C, 1 atm

5 Electrical conductivity sensitivity of PEDOT-PSS_1 : 1, and PEDOT-PSS_1 : 1/NaY zeolite composites at various contents

$M^{2+}Y$ composites. The PEDOT-PSS/HY composite has the lowest sensitivity. The results show that the Y zeolite acid–base properties affect the sensitivity of the PEDOT-PSS/Y composites toward SO_2. The cation type in the Y zeolite depends on the gas adsorption characteristics of the cation exchanged Y zeolite. This is consistent with the acidity of the ion exchanged Y zeolite from the NH_3-TPD technique (Table 1).

It was observed that the cation type in the Y zeolite could alter the electrical conductivity and sensitivity response of the composites toward SO_2, which influenced the gas adsorption–desorption characteristics of the composites. The composites with alkaline cations (Li^+, Na^+ and K^+) in the Y zeolite provided the higher sensitivity to SO_2 more than the composite with alkaline earth cation (Mg^{2+}, Ca^{2+} and Ba^{2+}) Y zeolite and HY zeolite. This result is related to the acid–base properties of the cation exchanged Y zeolite that was altered by the cation exchanged process. The acid sites were assigned

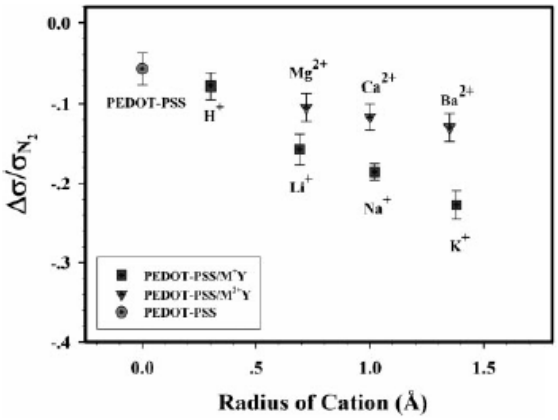

H^+, Li^+, Na^+, K^+ Mg^{2+}, Ca^{2+} and Ba^{2+} (20 vol.-%) when exposed to SO_2 at 27±1°C, 1 atm

6 Electrical conductivity sensitivity of PEDOT-PSS, and PEDOT-PSS/Y zeolite composites with various cation type

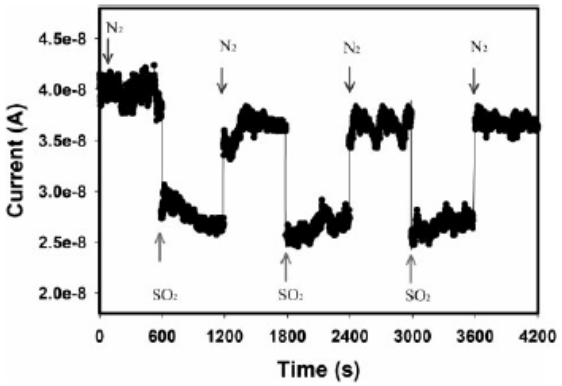

7 Responses of PEDOT-PSS/KY zeolite composite when exposed to N_2 (recovery) and SO_2 (sensing) at 27±1°C, 1 atm

to the compensating cations and the basic sites to the oxygen framework adjacent to the cation. The adjacent cation mainly influenced the framework basic sites. Electrical conductivity sensitivity to SO_2 of the alkaline cation exchanged Y zeolite composites increases with increasing cation size (electronegativity value decreased and basic strength increased) due to a lesser interaction between SO_2 and the zeolite; hence, there was a greater interaction between SO_2 and the active sites on the PEDOT polymer chain. The stronger bonding between the lithium cations and oxygen in the zeolite induced a greater reduction in negative charge on the adjacent oxygen frame work, resulting in the lower basic strength than other alkaline cation exchanged materials. The PEDOT-PSS/KY had the highest electrical sensitivity due to the highest basic strength.

he divalent exchanged or alkaline earth exchanged zeolites had reduced basic activity toward SO_2 due to the greater acid strength, so that the basic sites of the zeolite framework decreased in relation to the negative charge on the oxygen framework, which decreased as a result of the lower electrical conductivity sensitivity than the alkaline cation Y zeolite composite.[31] Furthermore, the PEDOT-PSS/HY zeolite composite showed the lowest sensitivity toward SO_2, which was related to the reduced surface area and basic strength of the HY zeolite, thus resulting in a lesser degree of interaction between acid gas SO_2 molecules and the active sites of the zeolites. In addition, the PEDOT-PSS/HY zeolite had poor electrical conductivity, and it was more hydrophobic,[32] consequently not adsorbing on the polar molecules like SO_2.

The temporal response time is the time required for the electrical conductivity value to rise from its initial value in N_2 towards the equilibrium value when exposed to SO_2. The recovery time is the time required for the electrical conductivity value return to baseline value after step removal of SO_2. By adding the Y zeolite, a longer response time and recovery time were observed, and the response time and recovery time increased with decreasing cation size of the Y zeolite. The response time of the PEDOT-PSS/LiY zeolite was longer than PEDOT-PSS and that of the other composites (12·8 min) due to the higher density of the adsorption sites available for SO_2 molecules and greater ion

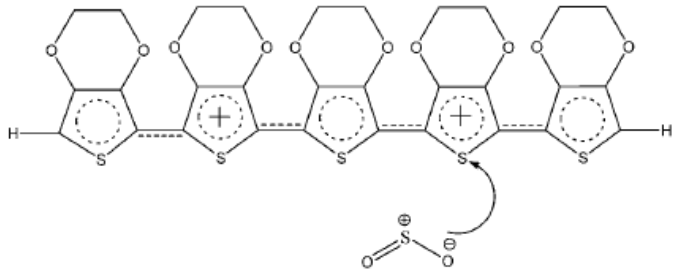

8 Propose mechanism of SO_2-PEDOT interaction

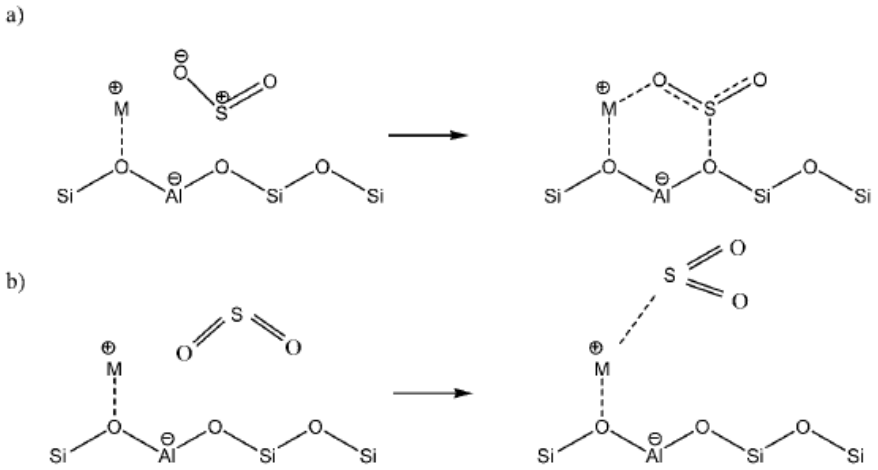

9 Schematic diagram indicates all possibilities of electrostatic interactions between SO_2 and Y zeolite

quadrupole interactions with SO_2. The shortest temporal response and recovery time were obtained from PEDOT-PSS/KY due to weaker interaction between the SO_2 molecules and KY zeolite (9·4 min), which allowed the SO_2 molecules to diffuse from the composites. The addition of Y zeolite enhanced the interaction between PEDOT-PSS and the SO_2 molecules; thus, the zeolites improved the sensitivity of the pristine PEDOT-PSS, but at the expense of a longer response time.

The PEDOT-PSS/KY zeolite composite was tested at three sensing cycles by repeating sensing and recovery to investigate the reversibility and reproducibility of the composites. The conductivity of the PEDOT-PSS/KY zeolite composite, which showed the highest sensitivity for SO_2 gas when exposed to three cycles of a sequence of SO_2 exposure (sensing), evacuation and kept under N_2 atmosphere (recovery), is shown in Fig. 7. During the recovery process, the conductivity of the composites does not have much decay, which proved that the sensing characteristics are repeatable.

Proposed mechanism of SO_2 adsorption in PEDOT-PSS and Y zeolites

Because SO_2 gas is electron donating, the observed decrease in the sensor electrical conductivity could be attributed to the charge transfer. The analysis of the results suggests that upon electron transfer from SO_2 to the partially positive charged sulphur site on the backbone of the p type PEDOT-PSS, the charge carrier concentration on the polymer backbone decreased, resulting in a decrease in electrical conductivity (Fig. 8). After SO_2 was evacuated and replaced by N_2, electrical conductivity of all composites returned almost completely to baseline. Most importantly, the interaction between SO_2 and the Y zeolites occurred through the basic oxygen centres of the Si–O–Al fragment (Lewis basic site). It could be proposed that the basic oxygen framework forms a bond with the sulphur atom of an SO_2 molecule via a donor–acceptor interaction. Beside the negative charges on the oxygen, other zeolite sites interacted with SO_2 bridging the metal centre via an ion–dipole interaction (Fig. 9).

Conclusions

Electrical sensitivity of pristine PEDOT-PSS was improved by adding Y zeolite but provided a longer response time and recovery time. The preparation of the composite with 20 vol.-% of zeolite content gave the highest sensitivity to SO_2. The highest electrical sensitivity response belonged to the PEDOT-PSS/KY zeolite composite. The type of cation in the zeolite pores affected the sensitivity of the composite, consistent with the acidity of ion exchanged Y zeolite. The composite showed nearly complete reversibility at room temperature. The experimental results showed that the zeolite acid–base properties played an important role in the sensitivity response of the composite toward SO_2. With increasing basicity of ion exchanged Y zeolites, the sensitivity of the composites increased.

Acknowledgements

The authors would like to acknowledge financial support from the Conductive and Electroactive

Polymers Research Unit of Chulalongkorn University, Thailand, the Thailand Research Fund and the Royal Thai Government Budget.

References

1. H. Bai and G. Shi: 'Gas sensors based on conducting polymers', *Sensors*, 2007, **7**, 267–307.
2. B. Adhikari and S. Majumdar: 'Polymers in sensor applications', *Prog. Polym. Sci.*, 2004, **29**, 699–766.
3. Rajesh, T. Ahuja and D. Kumar: 'Recent progress in the development of nano-structured conducting polymers/nanocomposites for sensor applications', *Sens. Actuators B*, 2009, **136B**, 275–286.
4. A. Galdikas, Ž. Kancleris, D. Senulien and A. Šetkus: 'Influence of heterogeneous reaction rate on response kinetics of metal oxide gas sensors: application to the recognition of an odour', *Sens. Actuators B*, 2003, **95B**, 244–251.
5. M. K. Ram, Ö. Yavuz, V. Lahsangah and M. Aldissi: 'CO gas sensing from ultrathin nano-composite conducting polymer film', *Sens. Actuators B*, 2005, **106B**, 750–757.
6. Y. Chen, Y. Li, H. Wang and M. Yang: 'Gas sensitivity of a composite of multi-walled carbon nanotubes and polypyrrole prepared by vapor phase polymerization', *Carbon*, 2007, **45**, 357–363.
7. N. Hu, Y. Wang, J. Chai, R. Gao, Z. Yang, E. S. W. Kong and Y. Zhang: 'Gas sensor based on p-phenylenediamine reduced graphene oxide', *Sens. Actuators B*, 2012, **163B**, 107–114.
8. M. Matsuguchi, J. Io, G. Sugiyama and Y. Sakai: 'Effect of NH_3 gas on the electrical conductivity of polyaniline blend films', *Synth. Met.*, 2002, **128**, 15–19.
9. S. Cosnier, S. Da Silva, D. Shan and K. Gorgy: 'Electrochemical nitrate biosensor based on poly(pyrrole–viologen) film–nitrate reductase–clay composite', *Bioelectrochemistry*, 2008, **74**, 47–51.
10. B. Soontornworajit, L. Wannatong, P. Hiamtup, S. Niamlang, D. Chotpattananont, A. Sirivat and J. Schwank: 'Induced interaction between polypyrrole and SO_2 via molecular sieve 13X', *Mater. Sci. Eng. B*, 2007, **B136**, 78–86.
11. K. Thuwachaowsoan, D. Chotpattananont, A. Sirivat, R. Rujiravanit and J Schwank: 'Electrical conductivity responses and interactions of poly(3-thiopheneacetic acid)/zeolites L, mordenite, beta and H_2', *Mater. Sci. Eng. B*, 2007, **B140**, 23–30.
12. C. Chuapradit, L. Wannatong, D. Chotpattananont, P. Hiamtup, A. Sirivat and J. Schwank: 'Polyaniline/zeolite LTA composites and electrical conductivity response towards CO', *Polym.*, 2005, **46**, 947–953.
13. N. Densakulprasert, L. Wannatong, D. Chotpattananont, P. Hiamtup, A. Sirivat and J. Schwank: 'Electrical conductivity of polyaniline/zeolite composites and synergetic interaction with CO', *Mater. Sci. Eng. B*, 2005, **B117**, 276–282.
14. E. Izni and A. Izni: 'Dielectric behavior of the catalyst zeolite NaY', *Turk. J. Chem.*, 2007, **31**, 523–530.
15. M. E. Franke and U. Simon: 'Proton mobility in H-ZSM5 studied by impedance spectroscopy', *Solid State Ionics*, 1999, **118**, 311–316.
16. S. V. Goryainov, R. A. Secco, Y. Huang and H. Liu: 'Pressure dependence of ionic conductivity of hydrated and dehydrated zeolites A', *Physica B*, 2007, **390B**, 356–365.
17. S. V. Goryainov, R. A. Secco, Y. Huang and A. Y. Likhacheva: 'Pressure-induced ionic conductivity of overhydrated zeolite NaA at different water/zeolite ratios', *Microporous Mesoporous Mater.*, 2013, **171**, 125–130.
18. F. Louwet, L. Groenendaal, J. Dhaen, J. Manca, J. Van Luppen, E. Verdonck and L. Leenders: 'PEDOT/PSS: synthesis, characterization, properties and applications', *Synth. Met.*, 2003, **135–136**, 115–117
19. B. Thomas and S. Sugunan: 'Influence of residual cations (Na^+, K^+ and Mg^{2+}) in the alkylation activity of benzene with 1-octene over rare earth metal ion exchanged FAU–Y zeolite', *Microporous Mesoporous Mater.*, 2004, **72**, 227–238.
20. D. Han, G. Yang, J. Song, L. Niu and A. Ivaska: 'Morphology of electrodeposited poly(3,4-ethylenedioxythiophene)/poly(4-styrene sulfonate) films', *J. Electroanal. Chem.*, 2007, **602**, 24–28.
21. S. Garreau, G. Louarn, J. P. Buisson, G. Froyer and S. Lefrant: 'In situ spectroelectrochemical raman studies of poly(3,4-ethylenedioxythiophene) (PEDT)', *Macromol.*, 1999, **32**, 6807–6812.
22. C. Li and T. Imae: 'Electrochemical and optical properties of the poly(3,4-ethylenedioxythiophene) film electropolymerized in an aqueous sodium dodecyl sulfate and lithium tetrafluoroborate medium', *Macromol.*, 2004, **37**, 2411–2416.
23. B. D. Martin, N. Nikolov, S. K. Pollack, A. Saprigin, R. Shashidhar, F. Zhang and P. A. Heiney: 'Hydroxylated secondary dopants for surface resistance enhancement in transparent poly(3,4-ethylenedioxythiophene)–poly(styrenesulfonate) thin films', *Synth. Met.*, 2004, **142**, 187–193.
24. W. Wichiansee and A. Sirivat: 'Electrorheological properties of poly(dimethylsiloxane) and poly(3,4-ethylenedioxy thiophene)/poly(styrene sulfonic acid)/ethylene glycol blends', *Mater. Sci. Eng. C*, 2009, **C29**, 78–84.
25. P. Chanthaanont and A. Sirivat: 'Interaction of carbon monoxide with PEDOT-PSS/zeolite composite: effect of Si/Al ratio of ZSM-5 zeolite', *e-Polymers*, 2012, **10**, 1–11.
26. S. Bendenia, K. Marouf-Khelifa, I. Batonneau-Gener, Z. Derriche and A. Khelifa: 'Adsorptive properties of X zeolites modified by transition metal cation exchange', *Adsorption*, 2011, **17**, 361–370.
27. G. Maurin, P. L. Llewellyn, T. Poyet and B. Kuchta: 'Adsorption of argon and nitrogen in X-faujasites: relationships for understanding the interactions with monovalent and divalent cations', *Microporous Mesoporous Mater.*, 2005, **79**, 53–59.
28. S. S. Nam, H. Kim, G. Kishan, M. J. Choi and K. W. Lee: 'Catalytic conversion of carbon dioxide into hydrocarbons over iron supported on alkali ion-exchanged Y-zeolite catalysts', *Appl. Catal. A*, 1999, **179A**, 155–163.
29. P. Castaldi, L. Santona, S. Enzo and P. Melis: 'Sorption processes and XRD analysis of a natural zeolite exchanged with Pb^{2+}, Cd^{2+} and Zn^{2+} cations', *J. Hazard. Mater.*, 2008, **156**, 428–434.
30. R. Mews, E. Lork, P. G. Watson and B. Görtler: 'Coordination chemistry in and of sulfur dioxide ', *Coordin. Chem. Rev.*, 2000, **197**, 277–320.
31. M. Matsuguchi, K. Tamai and Y. Sakai: 'SO_2 gas sensors using polymers with different amino groups', *Sens. Actuators B*, 2001, **77B**, 363–367.
32. V. A. Nasluzov, A. M. Shor, F. Nörtemann, M. Staufer, I. V. Yudanov and N. Rösch: 'Density functional study of SO_2 adsorption in HY zeolites', *J. Mol. Struc. Theochem.*, 1999, **466**, 235–244.

Materials and Manufacturing Processes, 0: 1–10, 2015
Copyright © Taylor & Francis Group, LLC
ISSN: 1042-6914 print/1532-2475 online
DOI: 10.1080/10426914.2014.994768

Taylor & Francis
Taylor & Francis Group

Processing of Kaolinite and Alumina Loaded in Natural Rubber Composite Foams

NUCHNAPA TANGBORIBOON[1], SURARIT SAMATTAI[1], JIRARAT KAMONSAWAS[2], AND ANUVAT SIRIVAT[2]

[1]*The Materials Engineering Department, Faculty of Engineering, Kasetsart University, Bangkok, Thailand*
[2]*The Petroleum and Petrochemical College, Chulalongkorn University, Bangkok, Thailand*

Composite natural rubber foams were successfully prepared from the vulcanization of natural rubber in a sulfur curing system. The natural rubber matrix phase was added with chlorinated polyethylene, kaolinite, and alumina. The morphology of natural rubber composite foams was altered when a gas was generated at the vulcanization temperature of 150°C to obtain open and closed cell structures. Furthermore, the kaolinite and alumina reinforced the mechanical properties and increased the thermal resistance of the composite foams. The composite foams were light in weight and had good thermal, mechanical, and electrical properties, suitable for energy absorption, thermal insulation, and structural uses.

Keywords Alumina; Chlorinated polyethylene (CPE); Flame retardant; Kaolinite; Natural rubber.

Downloaded by [Chulalongkorn University] at 21:04 16 March 2015

INTRODUCTION

The polyacetal backbone can be developed to polyisoprene, which can be used in several applications: solar cells, FETs, LEDs, and rubber foams [1, 2]. Natural rubber (NR) is an elastomeric material referred to as a crosslinked compound comprising an elastomer and additives. Rubber foam is one kind of NR product and is also known as cellular, expanded rubber, or sponge. They can be divided into three applications: energy absorption, thermal insulation, and structural uses [3]. The characteristics of composite rubber foam depend on the density of foam, microstructure such as size of cell, cell morphology, and shape of cells, and the mechanical properties of the base solid polymer. The cell structure of NR is produced from composite cellular rubber or rubber foam. Generally, composite rubber foam starting materials are synthetic materials such as polyurethane (PU), acrylic, ethylene propylene diene (EPDM) terpolymer, and ethylene vinyl acetate (EVA) copolymer. Generally, manufacturing foams are formed using a liquid called latex or a solid called dry NR [3]. The processing of rubber foam from dry rubber involves compounding rubber with vulcanizing agents, foaming agents, and other additives, namely filler, color, oil, and antioxidant. There are several important factors controlling the characteristics of rubber foam or sponge rubber: (a) the foaming agents or blowing agents; (b) the feeding ratio and fillers: silica, carbon black, silicate fillers, and calcium carbonate, and (c) the vulcanization temperature and time in processing. The applications of foam rubber or sponge rubber are acoustic absorbing materials for noise and vibration control, thermal insulation for building construction, and packaging materials due to its mechanical properties such as flexibility, buoyancy, light weight, and cushioning performance [3–4].

Several kinds of fillers are added to polymers, namely clay, silica, alumina, carbon black, chlorinated polyethylene (CPE), and calcium carbonate, to improve the mechanical, thermal, electrical, and physical properties. The process for producing CPE or CPE elastomer is synthesized from high-density polyethylene (HDPE) through the aqueous slurry process. The properties of polymers are controlled for molecular weight, chlorine content, and crystallinity. Generally, chlorine concentrations are varied from 25% to 42%. The advantages of CPE are very good resistance to oxidation, ozone, and chemicals (such as alcohol, alkalis, and acids). They also have good abrasion resistance and flex cracking properties. One limitation of CPE is moderate resistance to aromatic oxygenated solvents. Kaolinite or clay mineral is an inorganic material composed of a sheet of silica in the form $Al_2Si_2O_5(OH)_4$. The layers of silica clay are suitable candidate for reinforced polymer, swelling capacities, and network stability. Alumina (Al_2O_3) particles which are inorganic material or ceramic powders have good thermal properties, creep resistance, high melting temperature, chemical stability, and excellent hardness and strength. Both alumina and kaolinite particles have been used as rigid fillers or as a dispersed phase to reinforce the mechanical, thermal, and electrical properties of NR foams via the vulcanization process at a curing temperature of 150°C by a two-roll mill [5–10].

The objective of this study was to fabricate NR composite foams from a solid dry NR (STR 5L) as the matrix phase containing a vulcanizing agent, clay,

Received September 23, 2014; Accepted November 5, 2014
Address correspondence to Anuvat Sirivat, The Petroleum and Petrochemical College, Chulalongkorn University, Soi Chula 12, Phyathai Road, Bangkok 10330, Thailand; E-mail: anuvat.s@chula.ac.th

Downloaded by [Chulalongkorn University] at 21:04 16 March 2015

chlorinated polyethylene (CPE), alumina (Al_2O_3) powder as a dispersed phase, and sodium bicarbonate ($NaHCO_3$) as a blowing agent at a fixed processing time and temperature using a two-roll mill. Furthermore, scanning electron microscope (SEM), X-ray diffraction (XRD), thermal conductivity, flame retardant, electrical properties, and physical properties (color, bulk density, and relative foam density) were measured to investigate the microstructure, phase composition, thermal property, dielectric constant, and characteristics of the NR composite.

Materials and methods

Thai Hua Rubber Public Co., Ltd, Thailand, supplied the NR, STR 5L. The STR 5L extra light colored slab dry was changed to rubber slab dry in light yellow color. The specific gravity, the impurity content, the Mooney viscosity (ML 1′+4′) at 100°C, the initial plasticity, and the plasticity retention of the STR 5L were equal to 0.92 g/cm^3, 0.02% by weight, 75.2, 37.0, and 88.8, respectively. The characteristics of STR 5L provided good hot tensile properties, high tensile strength, and low levels of nonpolymer constituents.

Aluminum oxide (Al_2O_3) came from Sigma-Aldrich Chemical Co., Ltd, USA, which had a specific gravity of 3.90 g/cm^3. The weight percentage of purity content of the alumina powder was more than 99.

The chemicals used in the vulcanization process for the NR compound were sulfur (S), zinc oxide (ZnO), steric acid, tetramethyl thiuram disulfide (TMTD), benzothaizyl-2-cyclohexyl sulfonamide (CBS), and titanium dioxide (TiO_2), which were supplied by the Rubber Research Institute of Thailand, the Department of Agriculture of the Ministry of Agriculture, Bangkok, Thailand.

Sodium bicarbonate ($NaHCO_3$) was supplied by Ajax Finechem Pty. Ltd., Australia. It had high purity of more than 99.7 wt%, and low impurity contents, namely chloride, PO_4, S, Ca, Mg, Fe, K, NH_4, Cu, and Pb.

Chlorinated polyethylene (CPE 135A) was supplied by HANGZHOU KELI CHEMICAL Co., Ltd., China. The characteristics of the CPE are white powder, chlorine content of 34–36%, heat fusion ≤2 J/g, volatilization ≤0.40%, shore hardness ≤56, tensile strength ≥8.0 MPa, elongation at break ≥700%, and Mooney viscosity (1′+4′, at 121°C) 95 ± 5.

Kaolinite ($Al_2Si_2O_5(OH)_4$) was supplied by Compound Clay Co., Ltd., Thailand. It appeared as fine particles and was used as filler or an additive in the NR compounds.

Bruker, D8 Discover, was used to analyze XRD data. The scanning rate was 5° 2θ/min in 0.05° or 0.03° 2θ and the angle was varied from 10° to 80° 2θ. The crystalline phase was identified by a comparison between peak positions and JCPDS standard file.

Mastersizer S long bed, model Polydisperse 2.19, was used to determine the cumulative and fractional distributions of samples. The ultrasonic bath was used to improve the dispersion between sample phase and medium phase.

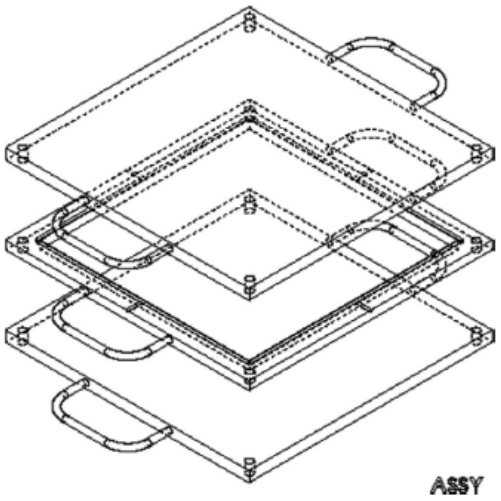

Scheme 1.—Insulation rubber molds.

True density of samples was measured by a gas pycnometer (Quantachrome, Ultra pycnometer 1000) as follows:

$$\rho = \frac{Weight(D)}{True\ volume} \tag{1}$$

where ρ is the bulk density, D is the dry sample weight (g), and *true volume* is the solid component volume.

Bulk density of samples was measured and calculated according to Eq. (2):

$$\rho = \frac{Weight(D)}{Apparent\ volume} \tag{2}$$

where ρ is the bulk density, D is the dry sample weight (g), and *apparent volume* is the volume of sample including open pores and closed pored within sample.

Relative foam density of samples was measured and calculated according to ASTM D3575 and ASTM D1056 using Eq. (3) as follows:

$$\frac{Foam\ density\left(\frac{g}{cm^3}\right)}{Solid\ density\left(\frac{g}{cm^3}\right)} = Relative\ foam\ density \tag{3}$$

Table 1.—Compositions of raw materials for natural rubber composites.

Characteristic	Result	Testing
Dirt content(% w/w)	0.04	Part B.4
Volatile matter content(% w/w)	0.20	Part B.5
Ash content(% w/w)	0.30	Part B.6
Nitrogen content(% w/w)	0.46	Part B.7
Initial Plasticity(P_0)	37.0	Part B.8
Plasticity Retention Index(PRI)	88.8	Part B.8
Mooney viscosityML (1′ + 4′) 100°C	75.2	Part B.9
Color	4.0	Part B.10

Downloaded by [Chulalongkorn University] at 21:04 16 March 2015

TABLE 2.—Quality of natural rubber STR 5 L according to SMR: Bulletin No. 7-1992.

	Encode no.									
Composition (g)	0	1	2	3	4	5	6	7	8	9
NR STR 5 L	100	100	100	100	100	100	100	100	100	100
Stearic acid	2	2	2	2	2	2	2	2	2	2
Zinc oxide	5	5	5	5	5	5	5	5	5	5
Sulfur	1.8	1.8	1.8	1.8	1.8	1.8	1.8	1.8	1.8	1.8
MBTS, Mercaptoben zothaizyl disulphide	1.5	1.5	1.5	1.5	1.5	1.5	1.5	1.5	1.5	1.5
TMTM Tetramethylene thiuram monosulphide	0.15	0.15	0.15	0.15	0.15	0.15	0.15	0.15	0.15	0.15
WingstayL, WSL	1	1	1	1	1	1	1	1	1	1
TiO_2	3	3	3	3	3	3	3	3	3	3
Chlorinated polyethylene, CPE	**0**	**20**	–	–	–	–	–	–	–	–
Sodium bicarbonate	5	5	5	5	5	5	5	5	5	5
Kaolinite, clay	**-**	**-**	**20**	**30**	**40**	**50**	**-**	**-**	**-**	**-**
Alumina, Al_2O_3	**-**	**-**	**-**	**-**	**-**	**-**	**20**	**30**	**40**	**50**

TABLE 3.—Chemical composition of kaolinite.

Composition	%wt
SiO_2	46.70
Al_2O_3	36.70
Fe_2O_3	1.09
MgO	0.05
CaO	0.01
Na_2O	0.05
K_2O	1.25
TiO_2	0.05
P_2O_5	0.01
MnO	0.05
Loss of ignition	14.30

Residual on sieve 200 mesh <5% wt.
Residual on sieve 325 mesh <6%wt.
Total firing shrinkage at 1280°C equals to 7.5–9.5% wt.

The SEM (JEOL-5200) was used to analyze the SEM micrographs. The STR 5 L compound was added with a foaming agent with and without fillers (chlorinated polyethylene (CPE 135A), kaolinite (clay), and alumina (Al_2O_3)) and was plated on a sample stub and coated with gold. An acceleration voltage of 12 kV with a magnification of 100X was used.

The moving die rheometer (Techpro-Rheo Tech, MDR121105) (Rubber Research Center, Kasetsart University, Thailand) was used to investigate the curing behavior.

The crosslink density was measured by the swelling method as described in ASTM D-6814-02. Before being swollen in the toluene, the cured samples were cut into squares shape (1 cm wide and 0.3–0.5 cm thick) and were swollen in toluene for 72 h to reach the equilibrium state. The crosslink density was calculated using the Flory–Rehner equation as follows:

$$\nu_e = \frac{-\left[\ln(1 - V_r) + V_r + \chi_1 V_r^2\right]}{\left[V_1\left(V_r^{1/3} - (V_r)/2\right)\right]} \quad (4)$$

TABLE 4.—Density and relative foam density values of samples.

Samples/Property	True density (g/cm^3)	Bulk density (g/cm^3)	Relative foam density	Crosslink density[a] (mol/cm^3)	Swelling ratio[b]
Natural rubber (STR5 L)	0.92	–	–	–	–
Alumina	3.34	–	–	–	–
Kaolinite, clay	2.33	–	–	–	–
Encode no. 0_no chlorinated polyethylene and no filler	–	0.28 ± 0.07	0.30 ± 0.08	8.64×10^{-3}	4.09
Encode no. 1_20 phr Chlorinated polyethylene-no filler	–	0.27 ± 0.02	0.29 ± 0.02	7.94×10^{-3}	3.68
Encode no. 2_20 phr kaolinite	–	0.31 ± 0.07	0.09 ± 0.02	6.29×10^{-3}	3.49
Encode no. 3_30 phr kaolinite	–	0.35 ± 0.02	0.11 ± 0.01	5.39×10^{-3}	3.05
Encode no. 4_40 phr kaolinite	–	0.38 ± 0.02	0.12 ± 0.01	4.31×10^{-3}	2.74
Encode no. 5_50 phr kaolinite	–	0.42 ± 0.07	0.12 ± 0.02	3.70×10^{-3}	2.62
Encode no. 6_20 phr Al_2O_3	–	0.32 ± 0.065	0.07 ± 0.01	7.22×10^{-3}	3.23
Encode no. 7_30 phr Al_2O_3	–	037 ± 0.02	0.09 ± 0.01	4.52×10^{-3}	3.17
Encode no. 8_40 phr Al_2O_3	–	0.42 ± 0.03	0.09 ± 0.01	3.36×10^{-3}	2.98
Encode no. 9_50 phr Al_2O_3	–	0.58 ± 0.05	0.14 ± 0.01	1.60×10^{-3}	2.85

[a]Crosslink density or effective number of chains in a real network per unit volume is calculated using the Flory–Rehner equation.
[b]Swelling ratio calculation; Swelling ratio $= \frac{(w_2 - w_1)}{w_1}$, where w_1 and w_2 are the weight of swollen rubber and dry rubber, respectively.

Downloaded by [Chulalongkorn University] at 21:04 16 March 2015

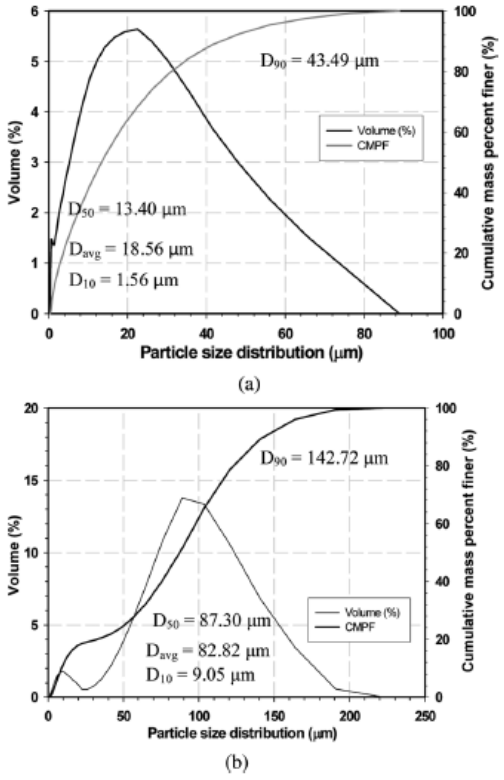

FIGURE 1.—Particle size distribution and cumulative mass percent finer (CMPF) of samples: (a) kaolinite particles and (b) alumina particles.

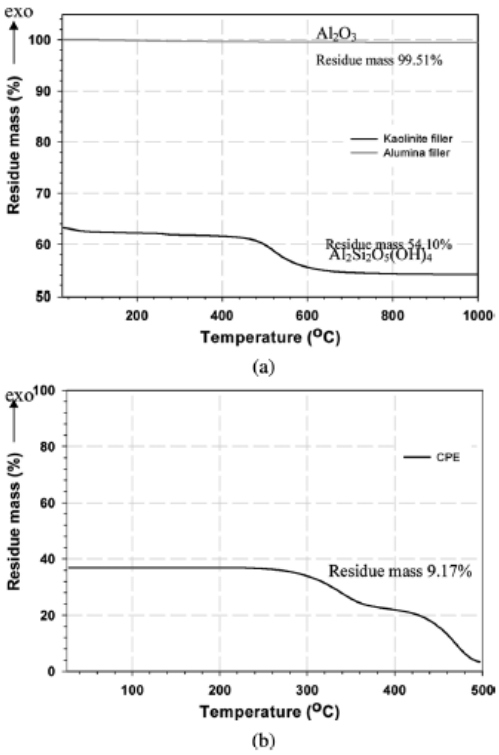

FIGURE 2.—TGA of raw materials: (a) alumina and kaolinite fillers and (b) chlorinated polyethylene.

$$V_r = \frac{W_{Dryrubber}/density_{Dryrubber}}{\frac{W_{Dryrubber}}{D_{Dryrubber}} + \frac{W_{Absorbedsolvent}}{D_{Solvent}}} \quad (5)$$

where ν_e is the effective chain number in real network per unit volume; mol/cm^3, V_r is the polymer volume fraction in a swollen network at equilibrium state, χ_1 is the Flory–Huggins interaction parameter (toluene in cis-polyisoprene 0.391 at 25°C), and V_1 is the molecular volume of solvent (toluene), $\frac{Mw}{Density}$ or 106.3; cm^3/mol.

The compression set (Hamden, APH40) was used to test the rubber as followed for ASTM D395-03 (Method B). Compression set testing was used to measure the retained elastic properties of the rubber compounds after being stretched under the compressive stresses. The actual stressing service may involve the maintenance of a definite deflection, the constant application of a known force, or the rapidly repeated deformation and recovery resulting from intermittent compressive forces. The set of compression was produced from dynamic stressing. Thus, compression set testing is mainly used to service conditions involving static stresses at elevated temperatures. The compression set was transformed into an original deflection percentage as follows:

$$C_B = [(t_o - t_i)/(t_o - t_n)] \times 100 \quad (6)$$

where C_B is the set of compression (Test Method B), t_o is the original thickness of the specimen, t_i is the final thickness of the specimen, and t_n is the thickness of the spacer bar used.

Thermal properties (thermal conductivity and flame retardant) of insulation rubber samples were prepared with a 1.5 cm-thick, 30 cm^2 SS400 hard-chrome plated sheet according to scheme I. The samples were measured using thermal conductivity values according to ASTM C518-10.

Flame retardancy of the rubber samples was prepared and tested according to UL 94, vertical burning test, the limiting oxygen index (LOI) test, and cone calorimetry. The results were recorded in terms of the weight loss and the residue mass percentage.

An impedance analyzer (HP, model 16451B), connected with an inductance capacitance resistance (LCR) meter (HP, model 4284A), was used to measure the dielectric constant of the sample. The ASTM B263-94 was used to prepare the sample. Composite foam

Downloaded by [Chulalongkorn University] at 21:04 16 March 2015

samples were prepared into discs shape, which had a 25 mm diameter and 0.50 mm thickness. The electrical properties were measured at frequencies from 500 to 600 Hz and at an AC current of 2 A.

The raw materials for NR composite foams are composed of NR, stearic acid, ZnO, mercaptobenzothaizyl disulphide (MBTS), tetramethylenethiuram monosulphide (TMTM), $NaHCO_3$, S, TiO_2, with/without fillers: Al_2O_3, CPE 135A, or kaolinite (clay). The weights having the unit of parts per hundred NR (phr) are shown in Table 1. The formulae of composite foams are encoded 0–9, with a fixed weight of 5 phr $NaHCO_3$ acting as a foaming agent, and three fillers. A roll mill (Mitsubishi, model R11-3FF) was used to prepare the composite foams. The foaming agent or blowing agent ($NaHCO_3$) and the crosslink agent were loaded into the composite. The rheometer was used to determine the curing percentage at 90% or t_{90}.

Results and discussion

Quality of STR 5L was characterized according to SMR, bulletin No. 7-1992, as shown in Table 2. The dirt content, volatile matter content, ash content, nitrogen content, initial plasticity, plasticity retention index, Mooney viscosity ML($1'+4'$) at 100°C, and color are 0.04% w/w, 0.24% w/w, 0.19%w/w, 0.32% w/w, 27.0, 51.9, 75.2, and 4.5, respectively.

The chemical composition of kaolinite is composed of SiO_2, Al_2O_3, Fe_2O_3, MgO, CaO, Na_2O, K_2O, TiO_2, P_2O_5, and MnO, and loss of ignition is 46.70, 36.70, 1.09, 0.05, 0.01, 0.05, 1.25, 0.05, 0.01, 0.05, and 14.30, respectively; data are shown in Table 3. The weight percentages of residue mass on 200- and 325-meshed sieve sizes are equal to 5% and 6%, respectively. The main compositions of kaolinite are silicon dioxide or silica (SiO_2) and aluminum oxide or alumina (Al_2O_3) at approximately 83.40%w/w. Both silica and alumina are inorganic materials having high melting temperatures and good heat resistance, and can be used as insulation materials.

True density values at 27°C of STR 5L, Al_2O_3, and kaolinite are 0.92, 3.34, and 2.33 g/cm^3, respectively, and data are shown in Table 4.

The particle size distributions of kaolinite and Al_2O_3 particles are shown in Fig. 1(a) and (b), respectively. The particle sizes at 10% w/w (d_{10}), at 50%w/w (d_{50}), at 90%w/w (d_{90}), and at average (d_{avg}) of kaolinite are 1.56, 13.40, 43.49, and 18.56 µm, respectively. The particle sizes at 10%w/w (d_{10}), at 50%w/w (d_{50}), at 90% w/w (d_{90}), and at average (d_{avg}) of Al_2O_3 are 9.05, 87.30, 142.72, and 82.82 µm, respectively. The particle sizes of kaolinite particles are smaller than those of Al_2O_3 particles.

The thermogravimetric analysis (TGA) results of fillers (Al_2O_3, kaolinite, and CPE 135A) were carried out from 25°C to 1000°C with 10°C/min of heating rate as shown in Fig. 2(a) and (b). The weight percentages of residue mass contents of Al_2O_3, kaolinite, and CPE 135A are 99.51%, 54.10%, and 9.17%, respectively. The obtained TGA results of Al_2O_3, kaolinite, and CPE 135A suggest that Al_2O_3 particles have high thermal resistance better than those of kaolinite and CPE 135A. Furthermore, the obtained TGA results indicated the degradation temperatures of the three fillers: CPE 135A at approximately 300°C, kaolinite at about 500°C, and Al_2O_3 at nearly 1000°C.

The patterns of XRD peak of STR 5L, CPE 135A, kaolinite, Al_2O_3, and NR compound without filler are shown in Fig. 3. The XRD pattern of NR shows an amorphous or noncrystalline phase due to the main organic compositions of carbon and hydrogen. The XRD peak pattern of CPE 135A shows a semicrystalline phase because CPE 135A as produced from HDPE contained 25–42% chlorine, a small amount of lead acting as a stabilizer, and organic as a plasticizer. The XRD peak pattern of kaolinite is consistent with JCPDS file No. 01-089-6538 (anorthic, aluminum

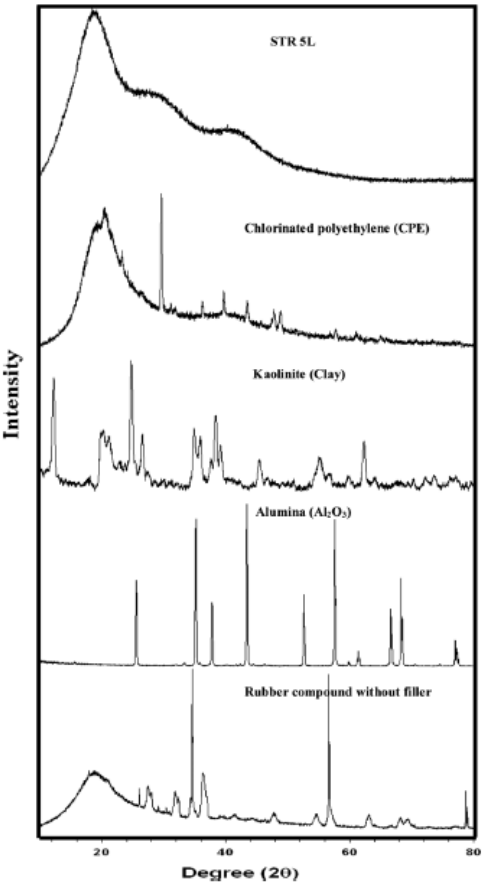

Figure 3.—XRD peak patterns of raw materials: STR 5L, chlorinated polyethylene (CPE), kaolinite (clay), alumina (Al_2O_3), and NR compound without filler.

Downloaded by [Chulalongkorn University] at 21:04 16 March 2015

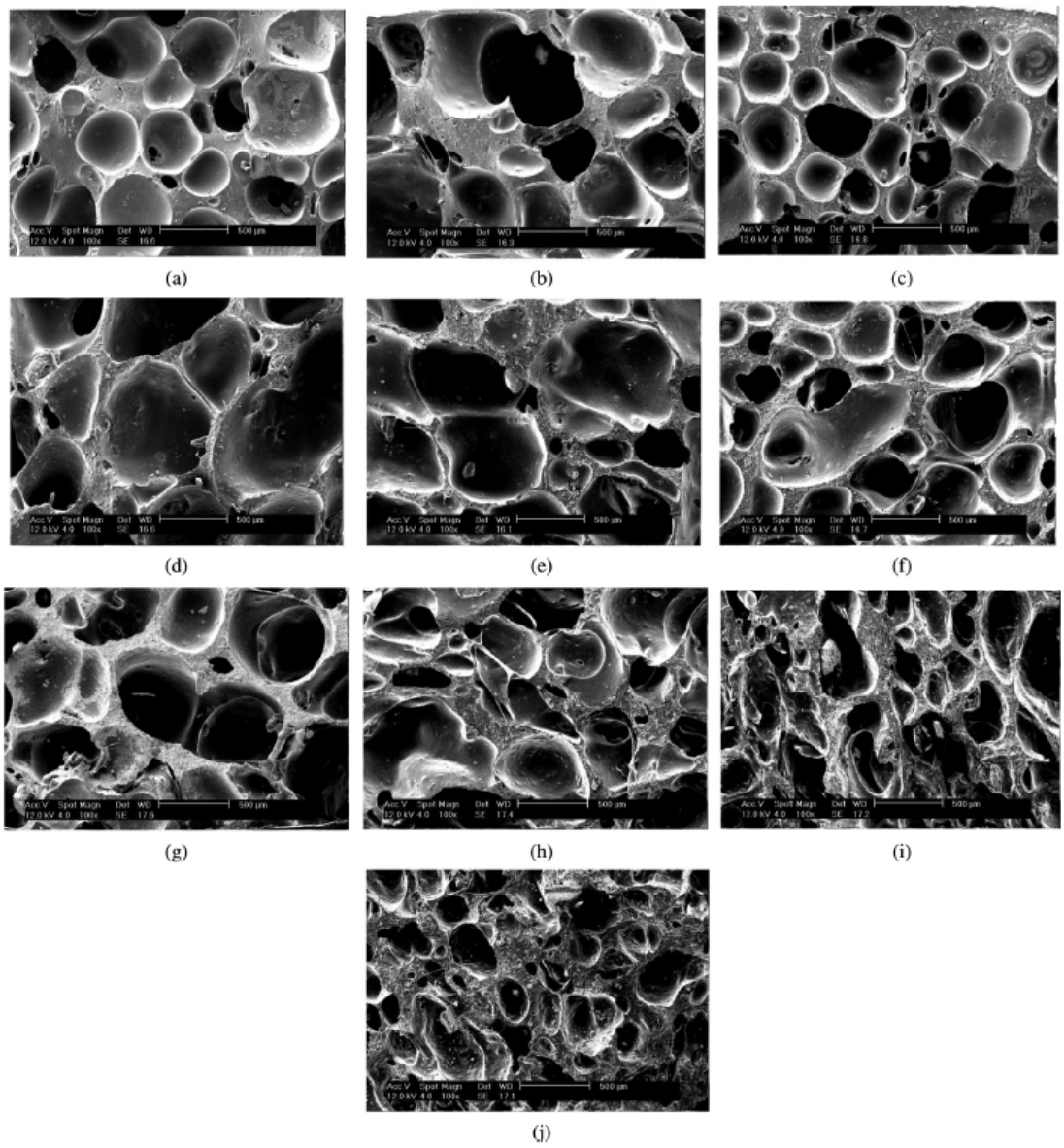

FIGURE 4.—SEM cross-sectional area micrographs of rubber composite samples with a magnification of 100X: (a) without adding filler or reference encoded No. 0; (b) with 20 phr chlorinated polyethylene encoded as No. 1; (c) with 20 phr kaolinite encoded as No. 2; (d) with 30 phr kaolinite encoded as No. 3; (e) with 40 phr kaolinite encoded as No. 4; (f) with 50 phr kaolinite encoded as No. 5; (g) with 20 phr alumina encoded as No. 6; (h) with 30 phr alumina encoded as No. 7; (i) with 40 phr alumina encoded as No. 8; and (j) with 50 phr alumina encoded as No. 9.

silicate hydroxide, $Al_2(Si_2O_5)(OH)_4$). The XRD peak pattern of Al_2O_3 is consistent with the JCPDS file Nos. 00-048-0.367 (aluminum oxide) and 01-089-7717 (corundum or rhombohedral structure). The XRD peak pattern of the NR compound without a filler shows a semicrystalline phase between the phase of amorphous NR and the phase of crystalline $NaHCO_3$ acting as a foaming agent, consistent with JCPDS file Nos. 00-021-1119 and 00-003-0653.

Bulk density, relative foam density, and crosslink density values of NR composite foams are tabulated in Table 4. The NR compound without a filler encoded

Downloaded by [Chulalongkorn University] at 21:04 16 March 2015

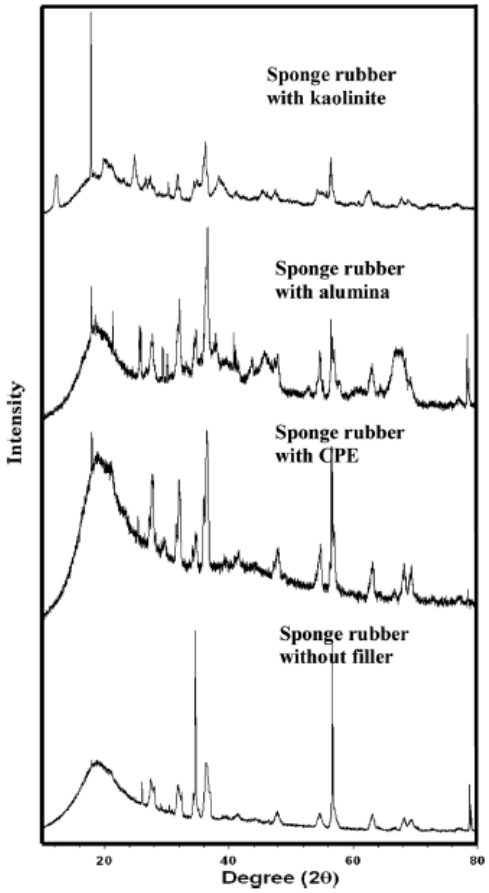

FIGURE 5.—XRD peak patterns of samples: sponge rubber with kaolinite, sponge rubber with alumina, sponge rubber with CPE, and sponge rubber without filler.

as No.0 has the bulk density, relative foam density, and crosslink density values equal to $0.2802 \pm 0.0713\,g/cm^3$, 0.306 ± 0.0775, and $8.642 \times 10^{-3}\,mol/cm^3$, respectively. The NR compound with 20 phr CPE 135A as a filler encoded as No.1 has the bulk density, relative foam density, and crosslink density values equal to $0.2754 \pm 0.0155\,g/cm^3$, 0.2993 ± 0.0168, and $7.937 \times 10^{-3}\,mol/cm^3$, respectively. The NR compounds with 5 phr $NaHCO_3$ as a foaming agent, and with 20, 30, 40, and 50 phr kaolinite ($Al_2Si_2O_5(OH)_4$) as a filler are encoded as No. 2, 3, 4, and 5, respectively. The NR compounds with 5 phr $NaHCO_3$ as a foaming agent, and with 20, 30, 40, and 50 phr Al_2O_3 as filler are encoded No. 6, 7, 8, and 9, respectively. Both groups of NR composite foams with the two fillers (kaolinite and Al_2O_3) have the same trend for the bulk density and relative foam density: the higher the amount of filler content added in NR compounds, the higher the bulk density and relative foam density values are. However, the NR composite foams with kaolinite and Al_2O_3 as fillers possessed decreasing crosslink density values, when the amount of filler added in the NR compound increased due to the interaction, exfoliation, and/or phase separation within the NR compound matrix. Furthermore, the bulk density values of the NR composite foams with alumina are higher than those of the NR composite foams with kaolinite because the true density value of alumina is $3.34\,g/cm^3$ higher than that of the true density value of kaolinite, which is $2.33\,g/cm^3$. The obtained results suggest that the chemical composition, quantity, physical properties (shape, size, and true density), crystal structure, and charge carrier of fillers critically affect the physical properties of the NR composite foams namely the bulk density, crosslink density, relative foam density, and swelling ratio.

SEM micrographs of the NR composite foams with and without fillers (CPE 135A, kaolinite, and Al_2O_3) are shown in Fig. 4. The NR compounds with sodium bicarbonate ($NaHCO_3$) as a blowing agent or foaming agent vulcanized at 150°C. The NR composites vulcanized at 150°C produced carbon dioxide (CO_2) and carbon monoxide (CO) from the decomposition of $NaHCO_3$ to obtain open and closed cell morphology. The SEM micrographs of the NR composite foams with fillers (CPE 135A, kaolinite, and Al_2O_3) show different cell morphologies and cell sizes due to particle size distribution and true density. The SEM micrographs of the NR composite foams with kaolinite have uniform cell morphology and spherical shape relative to those of the NR composite foams with Al_2O_3. The obtained micrographs clearly suggest that the amount and type of fillers are important factors to control cell morphology and physical properties (bulk density, relative foam density, and crosslink density), including the mechanical and thermal properties of NR composite foams.

XRD peak patterns of NR composite foams with/without fillers (CPE 135A, kaolinite, and alumina) are shown in Fig. 5. The NR composite foams without fillers show semicrystalline phases consisting of the NR amorphous phase and the crystalline phase of curing agents (S, ZnO, and TiO_2). The NR composite foams with $NaHCO_3$ as a foaming agent and alumina as a filler are consistent with JCPDS file Nos. 01-089-7717 and 00-048-0367 of corundum (Al_2O_3), and consistent with JCPDS file Nos. 00-021-1119 and 00-003-0653 of monoclinic ($NaHCO_3$). The XRD patterns of the NR composite foams with kaolinite as a filler are consistent with JCPDS file No. 01-089-6538 of anorthic structure ($Al_2Si_2O_5(OH)_4$) and the JCPDS file Nos. 00-021-1119 and 00-003-0653 of monoclinic ($NaHCO_3$).

Mechanical properties (Mooney viscosity, curing time, and compression set) of NR composite foams were measured according to ISO 289-1, ASTM D5289, and ASTM D395 (method B), respectively, as tabulated in Table 5. The NR composite foams with the fillers (CPE 135A, kaolinite, and clay) have short scorch times and curing times. The Mooney viscosity values of the natural

Downloaded by [Chulalongkorn University] at 21:04 16 March 2015

TABLE 5.—Mechanical properties of natural rubber composite foams.

Properties	Reference	Encode no. 0	1	2	3	4	5	6	7	8	9
Mooney viscosity (ML 1′ + 4) 100°C	ISO 289-1	19.8	21.2	25.5	26.8	27.4	31.5	19.4	25.0	25.8	35.4
Curing time (MDR Type, TECH PRO) Arc 0.5°, 150°C, t_{90} (min)	ASTM D 5289	7.15	9.06	7.81	9.24	8.96	8.32	4.99	3.91	3.64	2.69
Compression set 70°C, 22 h.(%)	ASTM D 395 (Method B)	24.1	28.3	31.9	31.6	30.2	26.3	47.3	28.6	35.6	48.1
$Ts_1^{(a*)}$	–	4.76	6.06	5.09	5.60	5.09	4.59	3.13	2.44	1.96	1.42
$Ts_2^{(b*)}$	–	5.22	6.84	5.46	6.24	5.68	5.05	3.45	2.65	2.19	1.56
$Tc_{10}^{(c*)}$	–	4.43	5.35	4.77	5.11	4.67	4.33	2.95	2.35	1.81	1.37
$Tc_{50}^{(d*)}$	–	5.56	7.08	5.88	6.63	6.13	5.53	3.76	2.94	2.47	1.82
$Tc_{90}^{(e*)}$	–	7.15	9.06	7.81	9.24	8.96	8.32	4.99	3.91	3.64	2.69
$Tc_{95}^{(f*)}$	–	7.72	9.75	8.46	10.1	10.1	9.53	5.43	4.25	4.07	3.02

Mooney viscosity (ML 1′ + 4) 100°C of pure STR 5L is 28.4.
[a*] means scorch time: time required for the increase of point 1 (T_{s1}) from minimum torque or in order to indicate time required for the beginning of the crosslink process [6, 10].
[b*] means scorch time: time required for the increase of point 2 (T_{s2}) from minimum torque or in order to indicate time required for the beginning of the crosslink process [6, 10].
[c*] means time corresponding to 10% curing.
[d*] means time corresponding to 50% curing.
[e*] means time corresponding to 90% curing or optimum vulcanization time.
[f*] means time corresponding to 95% curing or optimum vulcanization time.
– means N/A.

composite foams increase when the amount of filler added into the NR increases. The NR composite foams with 50 phr kaolinite possess a good compression set value equal to 26.3%, whereas the NR composite foams with 50 phr Al_2O_3 have a compression set value equal to 48.1%.

Thermal conductivity values of NR composite foams with/without fillers were measured as followed for ASTM C518-10. The value of thermal conductivity of samples encoded as Nos. 0, 5, and 9 are 0.1107 ± 0.0002, 0.1362 ± 0.0005, and 0.1377 ± 0.0005 W/m.K, respectively. The thermal conductivity values of other materials such as concrete (1.25–1.75 W/m.K), glass (1.70 W/m.K), , elastomer (0.25 W/m.K), wood (0.14–0.18 W/m.K), steel (51.90 W/m.K), polycarbonate (0.20 W/m.K), and polyvinyl chloride or PVC (0.15–0.21 W/m.K) are relatively higher than NR composite foams. Therefore, the obtained NR composite foams have a potential to be used as insulation materials.

Flame retardancy testing of samples was measured according to UL-94 as the data tabulated in Table 7. The NR composite foams with fillers (20 phr CPE 135A, 50 phr kaolinite, and 50 phr Al_2O_3) have weight loss percentages equal to 72.4317, 49.0270, and 56.9001, respectively. Both kaolinite and Al_2O_3 as fillers produced good thermal resistance because both are ceramic or inorganic materials; thus, they helped the NR foams retard the flame suitable for insulation.

Dielectric constant values versus frequency measured at room temperature (25°C) from 500 to 10^6 Hz are shown in Fig. 6(a) and (b). Both groups of samples with kaolinite and alumina fillers have dielectric constant values higher than those of NR composite foams without a filler and NR composite foams with CPE 135A. This is because both kaolinite and Al_2O_3 particles are composed of Al^{3+}, Si^{4+}, and O^{2-} ions affecting the

TABLE 6.—Thermal conductivity values of natural rubber composite foams.

Samples	Thermal conductivity (W/m.K)	Thermal diffusivity (mm^2/s)	Specific heat ($MJ/m^3.K$)
Encode no.0			
No chlorinated polyethylene and no filler	0.11 ± 0.01	0.10 ± 0.01	1.07 ± 0.01
Encode no.5			
50 wt% kaolinite	0.14 ± 0.01	0.19 ± 0.01	0.69 ± 0.01
Encode no.9			
50 wt% Al_2O_3	0.14 ± 0.01	0.12 ± 0.01	1.11 ± 0.01

References: Thermal conductivity values of concrete; glass; elastomer; wood; steel; polycarbonate; and polyvinylchloride (PVC) are 1.25–1.75, 1.70, 0.25, 0.14–0.18, 51.90, 0.20, 0.15–0.21 W/m.K [11].

TABLE 7.—Flame retardant of natural rubber composite foams according to UL-94.

Samples	% Weight loss	% Residue mass
Encode no.1		
20 wt% chlorinated polyethylene and no filler	72.4	27.6
Encode no.5		
50 wt% kaolinite	49.1	50.9
Encode no.9		
50 wt% Al_2O_3	56.9	49.1

Downloaded by [Chulalongkorn University] at 21:04 16 March 2015

interfacial, ionic, and electronic polarization under an electrical field. Furthermore, as the amount of filler particles of both Al_2O_3 and kaolinite increases, the dielectric constant values increase from 500 to 10^6 Hz as shown in Fig. 6(a). The dielectric constant values of NR composite foams with 20 phr CPE are 388.15 at 500 Hz, 149.19 at 1000 Hz, 24.42 at 5000 Hz, and 1.61 at 1 MHz. The dielectric constant values of NR composite foams with 50 phr kaolinite are 483.11 at 500 Hz, 293.05 at 1000 Hz, 28.50 at 5000 Hz, and 1.87 at 1 MHz. The dielectric constant values of NR composite foams with 50 phr alumina are 390.73 at 500 Hz, 203.07 at 1000 Hz, 25.47 at 5000 Hz, and 1.76 at 1 MHz. The dielectric constant values of NR composite foams without filler are 348.45 at 500 Hz, 129.49 at 1000 Hz, 22.98 at 5000 Hz, and 1.41 at 1 MHz.

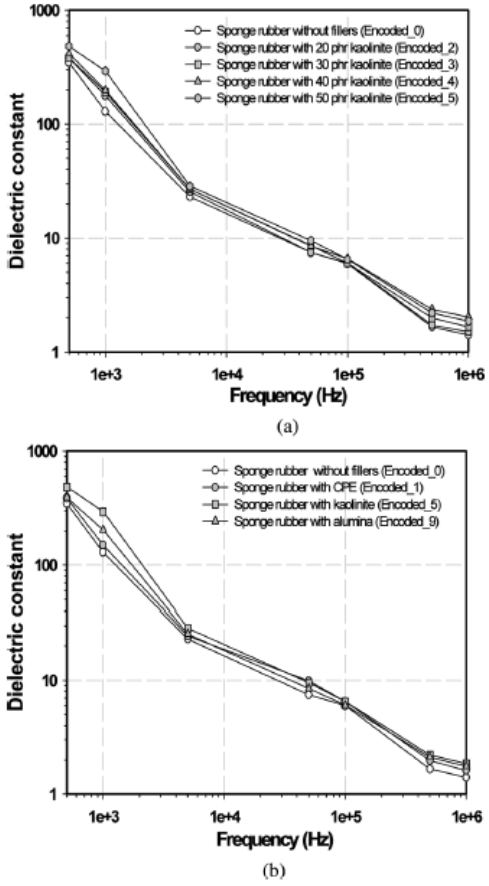

FIGURE 6.—Dielectric constant values of samples versus frequency from 500 Hz to 1 MHz measured at 27°C of: (a) the natural rubber composite foams with 0, 20, 30, 40, and 50 phr kaolinite; and (b) the comparison of effect of fillers (CPE, kaolinite, and alumina) on dielectric constant of natural rubber composite foams.

CONCLUSIONS

Foaming agent namely sodium bicarbonate ($NaHCO_3$) released CO_2 and CO, during the vulcanization process at 150°C, to produce the closed and open cell morphology in NR composite foams or sponge rubbers or cured expanded rubbers. The type and amount of gas outlet from the foaming agent affected the size and cell morphology, mechanical properties, thermal properties, and physical properties such as odor of the sponge rubbers. Furthermore, adding CPE 135A, kaolinite, and alumina (Al_2O_3) as fillers into the NR composite foams also affected the following: mechanical properties, namely curing time, Mooney viscosity, and compression set; thermal properties, namely thermal conductivity, thermal diffusivity, and heat capacity; electrical properties, namely dielectric constant; and physical properties, namely bulk density, crosslink density, and relative foam density. The composite sponge rubber samples with 50 phr kaolinite and with 5 phr $NaHCO_3$ as the foaming agent possessed bulk density, relative foam density, crosslink density, compression set, thermal conductivity, the percentage of residue mass obtained from flame retardant testing, and dielectric constant at 500 Hz of 0.4171 ± 0.0746 g/cm^3, 0.1284 ± 0.0230, 3.702×10^{-3} mol/cm^3, 26.30%, 0.1362 ± 0.0005 W/m.K, 50.9730%w/w, and 433.27, respectively. The composite sponge rubber samples with 50 phr Al_2O_3 and with $NaHCO_3$ as the foaming agent possessed bulk density, relative foam density, crosslink density, compression set, thermal conductivity, the percentage of residue mass obtained from flame retardant testing, and dielectric constant of 0.5860 ± 0.0498 g/cm^3, 0.1376 ± 0.0117, 1.601×10^{-3} mol/cm^3, 48.10%, 0.1377 ± 0.0005 W/m.K, 49.0993% w/w, and 319.94, respectively. The NR composite foams with kaolinite were better than those of the NR composite foams with Al_2O_3 due to the smaller average particle size (d_{avg} 18.56 μm) and shape, smaller true density (2.33 g/cm^3), and a variety of ionic polarization contents (Al^{3+}, Si^{4+}, and O^{2-}) combining to produce uniformly spherical open and closed cell morphology. The fabricated composite NR foam samples have a potential to be used as the insulation materials: noise and vibration control of acoustic absorbing material and thermal insulation for building construction. The advantages of the composite NR foam samples are flexibility, light weight, buoyancy, cushioning performance, and effective packaging.

ACKNOWLEDGMENTS

The authors would like to acknowledge the following: The Petroleum and Petrochemical College, and the Scientific and Technological Research Equipment Centre, at Chulalongkorn University, Thailand; the Department of Materials Engineering, at Kasetsart University, for the use of their analytical equipment.

FUNDING

We are thankful for the grant support from the Center for Advanced Studies in Industrial Technology, the

Kasetsart University Research and Development of the fiscal year 2013, the Conductive and Electroactive Polymers Research Unit of Chulalongkorn University, the Thailand Research Fund (TRF), and the Royal Thai Government.

References

1. Najidha, S.; Saxena, N.S., Sreeja, R.; Unnithan, C.H.; Predeep, P. Optical and electrical characterization of $SbCl_5$ doped *cis*-1, 4-polyisoprene. *Materials Letter* **2005**, *59*, 3431–3436.
2. Al-Homoud, M.S. Performance characteristic and practical applications of common building thermal insulation materials. *Building and Environment* **2005**, *40*, 353–366.
3. Nam, J.D.; Choi, H.R.; Tak, Y.S.; Kim, K.J. Novel electroactive, silicate nanocomposites prepared to be used as actuators and artificial muscles. *Sensor and Actuators A* **2003**, *105*, 83–90.
4. Lin, G.; Zhang, X.J.; Liu, L.; Zhang, J.C.; Chen, Q.M.; Zhang, L.Q. Study on microstructure and mechanical properties relationship of short fibers/rubber foam composites. *European Polymer Journal* **2004**, *40*, 1733–1742.
5. Hwang, H.Y.; Kim, D.J.; Kim, H.J.; Hong, Y.T.; Nam, S.Y. Effect of nanoclay on properties of porous PVdF membranes. *The Transactions of Nonferrous Metals Society of China* **2011**, *21*, 141–147.
6. Kaneko, M.L.Q.A., Bonzanini, R.B.; Gonçalves, M.d.C., Yoshida, I.V.P. High molar mass silicone rubber reinforced with montmorillonite clay masterbatches: Morphology and mechanical properties. *European Polymer Journal* **2010**, *40*, 881–890.
7. Kiliaris, P.; Papaspyrides, C.D. Polymer/layered silicate (clay) nanocomposites: an overview of flame retardancy. *Progress in Polymer Science* **2010**, *35*, 902–958.
8. Pavlidou, S.; Papaspyrides, C.D. A review on polymer-l ayered silicate nanocomposites. *Progress in Polymer Science* **2008**, *33*, 1119–1198.
9. Najib, N.N.; Ariff, Z.M.; Bakar, A.A.; Sipaut, C.S. Correlation between the acoustic and dynamic mechanical properties of natural rubber foam: Effect of foaming temperature. *Materials & Design* **2011**, *32*, 505–511.
10. Ariff, Z.M.; Zakaria, Z.; Tay, L.H.; Lee, S.Y. Effect of foaming temperature and rubber grades on properties of natural rubber foams. *Journal of Applied Polymer Science* **2008**, *107*, 2531–2538.
11. Tetelman, A.S. *Engineering Materials Handbooks*; The McGraw-Hill Companies Engineering Materials Handbooks: New York, NY, 1957.

Downloaded by [Chulalongkorn University] at 21:04 16 March 2015

Outputs of TRF- RTA 5580003

Project Duration: 24 August 2012– 23 August 2015

Refereed Journals:

(Impact Factor Source: 2013 ISI Impact Factor Report)

1) Tangboriboon, N., Chaisakrenon, S., Banchong, A., Kunanuruksapong, R., Sirivat*, A. (2012) Mechanical and electrical properties of alumina/natural rubber composites. Journal of Elastomers & Plastics Volume 44 Issue 1, 21-41. (ISI Impact Factor: 0.714)

2) Kamonsawas, J., Sirivat*, A., Hormnirun, P. (2012)
Poly(p-phenylene vilnylene)/zeolite Y composite as a ketone vapors sensor: effect of alkaline cation. Journal of Polymer Research, Volume 19, Issue 12, Article Number 20, 1-12. (ISI Impact Factor: 1.897)

3) Tangboriboon, N., Kunanuruksapong, R., Sirivat*, A. (2012)
Preparation and properties of calcium oxide from eggshells via calcinations. Materials Science-Poland, Volume 30, Issue 4, 313-322. (ISI Impact Factor: 0.327)

4) Changkhamchom, S., Sirivat*, A. (2013)
Polymer electrolyte membrane based on sulfonated poly(ether ketone ether sulfone) (S-PEKES) with low methanol permeability for direct methanol fuel cell application. Polymer-Plastics Technology and Engineering, Volume 52, 70–79. (ISI Impact Factor: 1.481)

5) Kunanuruksapong, R., Sirivat*, A. (2013)
Highly electroresponsive polymer blends of polyaniline nanoparticles and chloroprene Rubbers. Advances in Polymer Technology, Volume 32, 556-571. (ISI Impact Factor: 2.147)

6) Tungkavet, T., Sirivat*, A., Seetapan, N., Pattavarakorn, D. (2013)
Stress relaxation behavior of (Ala-Gly-Pro-Arg-Gly-Glu-4Hyp-Gly-Pro-) gelatin hydrogels under electric eld: Time-electric eld superposition. Polymer, Volume 54, 2414-2421. (ISI Impact Factor: 3.766)

7) Kamonsawas, J., Sirivat*, A., Hormnirun, P. (2013)
Sensitive and selective responses of poly(para-phenylene vinylene)/zeolite Y-based sensors toward ketone vapors. International Journal of Polymeric Materials and Polymeric Biomaterials, Volume 62, Issue 11, 583-589. (ISI Impact Factor: 2.784)

8) Petcharoen, K., Sirivat*, A.(2013)
Electrostrictive properties of thermoplastic polyurethane elastomer: Effects of urethane type and soft-hard segment composition. Current Applied Physics, Volume 13, Issue 6, 1119-1127. (ISI Impact Factor: 2.026)

9) Tangboriboon, N., Phudkrachang, P., Mulsow, L.-O., Kunchornsup, W., Sirivat*, A. (2013) Removal of water extractable proteins from concentrated natural rubber latex by eggshells. Journal of Elastomers and Plastics, Volume 45, Issue 3, 253-269. (ISI Impact Factor: 0.714)

10) Permpool, T., Sirivat*, A., Aussawasathien, D., Wannatong, L. (2013)
Development of polydiphenylamine/zeolite Y composite by dealumination process as a sensing material for halogenated solvents. Polymer-Plastics Technology and Engineering, Volume 52, Issue 9, 907-920. (ISI Impact Factor: 1.481)

11) Supattarasakda, K., Petcharoen, K., Permpool, T., Sirivat*, A., Lerdwijitjarud, W. (2013)
Control of hematite nanoparticle size and shape by the chemical precipitation method. Powder Technology, Volume 249, 353–359. (ISI Impact Factor: 2.269)

12) Konkayan, S., Chanthaanont, P., Prissanaroon, W., Hormnirun, P., Sirivat*, A (2013) Ammonia sensing and electrical properties based on composite of poly(3-thiopheneacetic acid) and zeolite Y. Materials Technology: Advanced Performance Materials, Volume 28, 332-338. (ISI Impact Factor: 0.746)

13) Chanthaanont, P., Sirivat, A. (2013)
Effect of transition metal ion-exchanged into the zeolite Y on electrical conductivity and response of PEDOT-PSS/MY composites toward SO2. Advances in Polymer Technology Volume 32, Issue 4, 21367(1-6). (ISI Impact Factor: 2.147)

14) Permpool, T., Sirivat*, A., Aussawasathien, D., Wannatong, L. (2013)
Polydiphenylamine/zeolite Yc and electrical conductivity responses toward halogenated hydrocarbons. Materials Research-IBERO-American Journal of Materials, Volume 16, Issue 5, 1020-1029. (ISI Impact Factor: 0.483)

15) Tangboriboon, N., Mulsow, L., Kunchornsup, W., Sirivat*, A. (2013)
Ceramic granules forming from calcium sodium aluminosilicate and carboxymethyl cellulose. Journal of Ceramic Processing Research, Volume 14, No. 6, 658-666. (ISI Impact Factor: 0.349)

16) Paradee, N., Sirivat*, A., (2014)
Synthesis of poly(3,4-ethylenedioxythiophene) nanoparticles via chemical oxidation polymerization. Polymer International, Volume 63, Issue 1, 106-113. (ISI Impact Factor: 2.247)

17) Changkhamchom, S., Sirivat*, A. (2014)
Composite proton exchange membranes of sulfonated poly(ether ketone ether sulfone) (S-PEKES) and molecular sieve with high mechanical strength for direct methanol fuel cell. International Journal of Polymeric Materials and Polymeric Biomaterials, Volume 63, Issue 6, 315-322. (ISI Impact Factor: 2.784)

18) Kunchornsup, W., Sirivat*, A. (2014)
Thermo-electromechanical responses of 1-butyl-3-methylimidazolium chloride ionic liquid-cellulose gel. Journal of Polymer Research, Volume 21:369, 1-9. (ISI Impact Factor: 1.897)

19) Sirivat, A., Petcharoen, K., Pornchaisiriarun, Y., Phansa-Ard, C., Tangboriboon*, N. (2014)

Lead zirconate (pbzro3) embedded in natural rubber as electroactive elastomer composites. Journal of Innovative Optical Health Sciences, Volume 7, No. 6, 1450016(1-7), (ISI Impact Factor: 0.933)

20) Changkhamchom, S., Sirivat*, A. (2014)
High proton conductivity ZSM-5/sulfonated poly(ether ketone ether sulfone) (S-PEKES) composite proton exchange membrane for using in direct methanol fuel cell. Solid State Ionics, Volume 263, 161–166. (ISI Impact Factor: 1.836)

21) Paradee, N., Sirivat*, A. (2014)
Electrically controlled release of benzoic acid from poly(3,4 ethylenedioxythiophene)/ alginate matrix: Effect of conductive poly(3,4-ethylenedioxythiophene) morphology. Journal of Physical Chemistry B, Volume 118, 9263–9271. (ISI Impact Factor: 3.377)

22) Suephatthima, B., Paradee, N., Sirivat*, A., Pattavarakorn, D. (2014)
Effect of electrolytes on electrochromic properties and morphology of poly(2,5-dimethoxy aniline) films. Bulletin of Materials Science, Volume 37, 975–982. (ISI Impact Factor: 0.870)

23) Permpool, T., Sirivat*, A., Aussawasathien, D. (2014)
Synthesis of polydiphenylamine with tunable size and shape via emulsion polymerization. Polymer International, Volume 63, 2076–2083. (ISI Impact Factor: 2.247)

24) Kunchornsup, W., Sirivat*, A. (2014) Electromechanical properties study of 1-butyl-3-methylimidazolium chloride/cellulosic gel blended with polydiphenylamine. Sensors and Actuators A: Physical, Volume 220, 249–261. (ISI Impact Factor: 1.943)

25) Tungkavet, T., Seetapan, N., Pattavarakorn, D., Sirivat*, A. (2015) Electromechanical properties of multi-walled carbon nanotube/gelatin hydrogel composites: Effects of aspect ratios, electric field, and temperature. Materials Science and Engineering: C, Volume 46, 281–289. (ISI Impact Factor: 2.763)

26) Taweekarn, N., Changkhamchom, S., Sirivat*, A. (2015)
Synthesis and characterization of sulfonated poly(aromatic imide-co-aliphatic imide) (S-coPI) membrane for direct methanol fuel cells. Polymer Bulletin, Volume 72, Issue 2, 281-294. (ISI Impact Factor: 1.491)

27) Kamonsawas, J., Sirivat*, A. (2015)
Effect of transition metals on the electrical conductivity response of dPPV/zeolite Y composites toward ketone vapors. Advances in Polymer Technology, Volume 34, Issue 1, number 21473(1-12). (ISI Impact Factor: 2.147)

28) Tangboriboon, N., Deechaiyapum, H., Petcharoen K., Sirivat*, A. (2015)
Effect of alumina particles embedded in natural rubber foams on cell morphology and thermo-mechanical properties. International Polymer Processing, Volume 30, Issue 1, 82-90. (ISI Impact Factor: 0.682)

29) Chanthaanont, P., Permpool, T., Sirivat*, A. (2015)

Effect of alkaline and alkaline earth ion exchanged Y zeolites on electrical conductivity and response of PEDOT-PSS/Y zeolite composites toward SO2. Materials Technology. Volume 30, Issue 4, 193-199. (ISI Impact Factor: 0.746)

30) Tangboriboon, N., Samattai, S., Kamonsawas, J., Sirivat*, A (2015)
Processing of kaolinite and alumina loaded in natural rubber composite foams. Materials and Manufacturing Processes, Volume 30, Issue 5, 595-604. (ISI Impact Factor: 1.486)

Conference Proceedings:

1) Pinit, J., Sirivat, A. (2013)
Electrochromic properties of poly(o-toluidine) coated on indium tin oxide (ITO) plastic. PETROMAT and PPC SYM 2013, Bangkok, Thailand, 23 April 2013

2) Charoonrak, N., Sirivat, A. (2013)
Development of poly(p-phenylene)/crosslinked poly(ε-caprolactone) as electroactive shape memory composite. PETROMAT and PPC SYM 2013, Bangkok, Thailand, 23 April 2013

3) Kotaphan, P., Sirivat, A., Schwank, J. (2013)
Composite membrane of sulfonated poly(2,6-dimethyl-1,4-phenylene oxide) and zeolite for direct methanol fuel cell applications. PETROMAT and PPC SYM 2013, Bangkok, Thailand, 23 April 2013

4) Pairatwachapun S., Sirivat, A. (2013)
Electrically-controlled release of acetylsalicylic acid from carrageenan hydrogel. PETROMAT and PPC SYM 2013, Bangkok, Thailand, 23 April 2013

5) Srisawasdi, T., Sirivat, A., Jamieson A.M. (2013)
Silk fibroin/polycarbazole composite as artificial muscle. PETROMAT and PPC SYM 2013, Bangkok, Thailand, 23 April 2013

6) Watpathomsub, S., Jitkanka, S., Sirivat, A. (2014)
Modified poly(ether ether ketone) and poly(phenylene ether ether sulfone) as proton exchange membrane for vanadium redox flow battery. PETROMAT and PPC SYM 2014, Bangkok, Thailand, 22 April 2014.

7) Korattanawittaya, S., Sirivat, A. (2014)
Preparation of graphenen/natural rubber composite for compliant electrode applications. PETROMAT and PPC SYM 2014, Bangkok, Thailand, 22 April 2014.

8) Khamngoen, K., Sirivat, A. (2014)
Chemical oxidation polymerization and characterization of poly o-anisdine nanoparticles. PETROMAT and PPC SYM 2014, Bangkok, Thailand, 22 April 2014.

9) Thomgkham, P., Sirivat, A. (2014)

Permeation study of indomethacin from polycarbazole/natural rubber blend film under electric field. PETROMAT and PPC SYM 2014, Bangkok, Thailand, 22 April 2014.

10) Pianmanakij, M., Sirivat, A., Siemanond, K., Changkhamchom, S. (2014)
Improving PEM with sulfonated polysulfone and polyvinylidene fluoride/ZSM-5 composite membranes for direct methanol fuel cells. PETROMAT and PPC SYM 2014, Bangkok, Thailand, 22 April 2014.

11) Sangwan, W., Sirivat, A. (2015)
Electrical responsive material base polycarbazole/alginate biocomposite hydrogel as an actuator. PETROMAT and PPC SYM 2015, Bangkok, Thailand, 21 April 2015.

12) Bunlengsuwan, P., Sirivat, A., Siemanond, K. (2015)
Effect of sulfonated grapheme oxide on sulfonated polysulfone membrane for direct methanol fuel cell. PETROMAT and PPC SYM 2015, Bangkok, Thailand, 21 April 2015.

13) Choowongapichat, S., Sirivat, A. (2015)
Development of natural rubber matrix using in electrical stimuli transdermal drug delivery drug application. PETROMAT and PPC SYM 2015, Bangkok, Thailand, 21 April 2015.

Oral Presentations:

1) Sirivat, A. (2012)
Conductive and Electroactive Polymers: Actuation and Drug Controlled Release.
การประชุมนักวิจัยรุ่นใหม่ พบ เมธีวิจัยอาวุโส สกว. ครั้งที่ 12, เพชรบุรี, 10-12 October 2012. [Invited Speaker]

2) Paradee, N., Sirivat, A. (2013)
Electrically-assisted transdermal delivery of drug from Ca-alginate hydrogel. CEAP 2013, Bangkok, Thailand, 22 April 2013

3) Kamonsawas, J., Sirivat, A., Hormnirun, P. (2013)
Sensitive and selective sensors based on poly(para-phenylene vinylene)/zeolite composites: Influece of alkaline cation. CEAP 2013, Bangkok, Thailand, 22 April 2013

4) Niamlang, S., Buranut, A., Niansiri, A., Sirivat, A. (2013)
Controlled aloin release from crosslinked polyacrylamide hydrogel: Effect of mesh size, electric field strength and conductive polymer. CEAP 2013, Bangkok, Thailand, 22 April 2013

5) Changkhamchom, S., Sirivat, A. (2013)
Sulfonated poly(ether ketone ether sulfone) (S-PEKES)/zeolite proton exchange membranes for direct methanol fuel cell. CEAP 2013, Bangkok, Thailand, 22 April 2013

6) Tungkavet, T., Seetapan, N., Pattavarakornt, D., Sirivat, A. (2013)
Effect of electric field and crosslinking ratios on stress relaxation of gelatin hydrogel. CEAP 2013, Bangkok, Thailand, 22 April 2013

7) Niamlang, S., Srithong, K., Pansuwan, N., Nakthae, S., Sirivat, A. (2014)
Electronic controlled diffusion drug molecule in hydrogel. PETROMAT and PPC SYM 2014, Bangkok, Thailand, 22 April 2014.

8) Takkire, R., Samattai, S., Tangboriboon, N., Sirivat, A. (2014)
Eggshells embedded in natural rubber latex glove to enhance physical and mechanical properties. PETROMAT and PPC SYM 2014, Bangkok, Thailand, 22 April 2014.

9) Wattanakul, K., Boonsitthichoke, P., Wongsuntirad, N., Meejaijaroen, R., Sirivat, A. (2014)
Preparation of eLectroPatch electrode using in-situ silver nanoparticle filled-latex composite. PETROMAT and PPC SYM 2014, Bangkok, Thailand, 22 April 2014.

10) Tungkavet, T., Sirivat, A., Seetapan, N., Pattavarakorn, D. (2014)
A study of electromechanical properties of gelatin for actuator application. PETROMAT and PPC SYM 2014, Bangkok, Thailand, 22 April 2014.

11) Changkhamchom, S., Sirivat, A. (2014)
Methanol permeability and proton conductivity of a novel sulfonated poly(ether ketone ether sulfone) electrolyte membrane. PETROMAT and PPC SYM 2014, Bangkok, Thailand, 22 April 2014.

12) Petcharoen, K., Sirivat, A. (2014)
Bi-functional actuator material made of magnetite and polyurethane composite. PETROMAT and PPC SYM 2014, Bangkok, Thailand, 22 April 2014.

13) Kamonsawas, J., Sirivat, A. (2014)
Electrical conductivity response of dPPV/zeolite Y composite towards ketone vapors: Effect of alkaline cation. PETROMAT and PPC SYM 2014, Bangkok, Thailand, 22 April 2014.

14) Prissanaroon-Ouajai, W., Sirivat, A., Pigram, P., Brack, N. (2015)
Potentiometric urea biosensor based on a urease-immobilized polypyrrole. PETROMAT and PPC SYM 2015, Bangkok, Thailand, 21 April 2015.

15) Tangboriboon, N., Samattai, S., Kamonsawas, J., Sirivat, A. (2015)
Effect of themo-mechanical properties of embedded alumina in natural rubber composite foams. PETROMAT and PPC SYM 2015, Bangkok, Thailand, 21 April 2015.

16) Niamlang, S., Nakthae, S., Sirivat, A. (2015)
Controlled acid drug delivery from polyacrylamide hydrogel by electric field in transdermal drug delivery patch for diarrhea treatment of suckling pigs. PETROMAT and PPC SYM 2015, Bangkok, Thailand, 21 April 2015.

17) Kamonsawas, J., Sirivat, A. (2015)
dPPV/zeolite Y composite response towards ketone vapors. PETROMAT and PPC SYM 2015, Bangkok, Thailand, 21 April 2015.

18) Petcharoen, K., Sirivat, A. (2015)
Solid-state-soft actuator based on electroactive polymer and hybrid filler. PETROMAT and PPC SYM 2015, Bangkok, Thailand, 21 April 2015.

19) Paradee, N., Sirivat, A. (2015)
Effect of poly(3,4-ethylenedioxythiophene) morphology on electrically stimulated drug release from poly(3,4-ethylenedioxythiophene)/Ca-alginate hydrogel. PETROMAT and PPC SYM 2015, Bangkok, Thailand, 21 April 2015.

Poster Presentations:

1) Kunchornsup, W., Sirivat, A. (2013)
Polarizability investigation of 1-butyl-3-methylimidazolium cation in electroactive ionic liquid-cellulose gel actuator. SPIE 2013, San diego, USA, 10-14 March 2013.

2) Paradee, N., Sirivat, A. (2013)
Electrically controlled release of tannic acid from calcium-alginate hydrogel in transdermal drug delivery application. SPIE 2013, San diego, USA, 10-14 March 2013.

3) Macksasitorn, S., Changkhamchom, S., Sirivat, A., Siemanond, K. (2013)
Proton exchange membrane based on sulfonated poly(ether ether ketone and sulfonated poly(1,4-phenylene ether ether sulfone) for vanadium redox flow battery. SPIE 2013, San diego, USA, 10-14 March 2013.

4) Pinit, J., Sirivat, A. (2013)
Study of poly(0-toluidine) as electrochromic properties coated on indium tin oxide (ITO). CEAP 2013, Bangkok, Thailand, 22 April 2013.

5) Petcharoen, K., Sirivat, A. (2013)
Electrostrictive performance of thermoplastic elastomer polyurethanes under the influence of electric field. CEAP 2013, Bangkok, Thailand, 22 April 2013.

6) Charoonrak, N., Sirivat, A. (2013)
Development of poly(E-caprolactone)/poly(P-phenylene) as electroactive shape memory polymer blend. CEAP 2013, Bangkok, Thailand, 22 April 2013.

7) Kotaphan, P., Sirivat, A., Schwank, J. (2013)
Preparation and characterization of sulfonated poly(2,6-dimethyl-1,4-phenylene oxide) composite membrane for direct methanol fuel cell. CEAP 2013, Bangkok, Thailand, 22 April 2013.

8) Chanthaanont, P., Sirivat, A. (2013)
Sensitivity and response of PEDOT-PSS/ion-exchanged zeolite Y composite towards SO2. CEAP 2013, Bangkok, Thailand, 22 April 2013.

9) Pairatwachapun, S., Sirivat, A. (2013)

Controlled transdermal delivery of acetylsalicylic acid from carrageenan hydrogel. CEAP 2013, Bangkok, Thailand, 22 April 2013.

10) Srisawasdi, T., Sirivat, A., Jamieson, A.M. (2013)
Developments of polycarbazole/Silk fibroin hydrogel for artificial muscle. CEAP 2013, Bangkok, Thailand, 22 April 2013.

11) Permpool, T., Sirivat, A., Aussawasathien, D., Wannatong, L. (2013)
Dealuminated polydiphenylamine/zeolite Y composite as a sensine material for halogenated Solvents. CEAP 2013, Bangkok, Thailand, 22 April 2013.

12) Kunchornsup, W., Sirivat, A. (2013)
Electromechanical and dielectric properties of ionic liquid/cellulose gel. CEAP 2013, Bangkok, Thailand, 22 April 2013.

13) Petcharoen, K., Sirivat, A. (2013)
Effect of electric field strength on the dielectrophoresis force and the electrostrictive strain of thermoplastic elastomer polyurethanes. Frontiers in Polymer Science 2013, Spain, 21-23 May 2013.

14) Pinit, J., Sirivat, A. (2013)
Synthesis and characterizations of poly(o-toluidine) as electrochromic material. Frontiers in Polymer Science 2013, Spain, 21-23 May 2013.

15) Pairatwachapun, S., Sirivat, A. (2013)
Polythiophene/carrageenan hydrogel as drug release matrix under electric field. Frontiers in Polymer Science 2013, Spain, 21-23 May 2013.

16) Kotaphan, P., Sirivat, A., Schwank, J. (2013)
Sulfonated poly(2,6-dimethyl-1,4-phenylene oxide) composite membranes filled by zeolite for direct methanoi fuel cell. Frontiers in Polymer Science 2013, Spain, 21-23 May 2013

17) Charoonrak N., Sirivat, A. (2013)
Development of poly(para-phenylene)/poly(ε-caprolactone) as electroactive shape memory composite. Frontiers in Polymer Science 2013, Spain, 21-23 May 2013.

18) Srisawasdi, T., Sirivat, A., Jamieson, A.M. (2013)
Silk fibroin/polycarbazole composite as artificial muscle. Frontiers in Polymer Science 2013, Spain, 21-23 May 2013.

19) Tharaporn P., Sirivat, A., Aussawasathien, D. (2013)
Development of polydiphenylamine/zeolite Y composites and electrical conductivity responses toward halogenated hydrocarbons. EuroEAP 2013, Duebendorf, Switzerland, 25-26 June 2013.

20) Tungkavet T., Seetapan, N., Pattavarakorn, D., Sirivat, A. (2013)

Electromechanical properties of biocompatible gelatin as actuator. EuroEAP 2013, Duebendorf, Switzerland, 25-26 June 2013.

21) Kamonsawas J, Sirivat, A. (2014)
Improvement of sensitive and selective properties of dPPV/zeolite Y composite towards 3 different ketone vapors. BMMP 2014, Takayama, Japan, 24-27 January 2014.

22) Petcharoen, K., Sirivat, A. (2014)
Bending behavior of magnetite nanocomposites under magnetic and electric fields as a bi- functional smart material for biomimetic robots. BMMP 2014, Takayama, Japan, 24-27 January 2014.

23) Paradee, N., Sirivat, A. (2014)
Controlled transdermal Iontophoresis of drug from PEDOT/alginate hydrogel. BMMP 2014, Takayama, Japan, 24-27 January 2014.

24) Permpool, T., Sirivat, A., Ausawasathien, D. (2014)
Synthesis of polydiphenylamine nanoparticle: Effects of surfactant type and concentration. BMMP 2014, Takayama, Japan, 24-27 January 2014.

25) Tungkavet, T., Seetapan, N., Pattavarakorn, D., Sirivat, A. (2014)
Effect of electric field and multi-walled carbon nanotube concentration on the bending distance and dielectrophoresis force of multi-walled carbon nanotube blended with gelatin. BMMP 2014, Takayama, Japan, 24-27 January 2014.

26) Samattai, S., Takkire, R., Tangboriboon, N., Sirivat, A. (2014)
Compliant electrode preparation from embedding eggshells in natural rubber latex films. PETROMAT and PPC SYM 2014, Bangkok, Thailand, 22 April 2014.

27) Boonsitthichoke, P., Wattanakul, K., Wongsuntirad, N., Meejaijaroen, R., Sirivat, A. (2014) Preparation of eLectroPatch electrode from in-situ silver nanoparticle filled-latex composite via reduction. PETROMAT and PPC SYM 2014, Bangkok, Thailand, 22 April 2014.

28) Permpool, T., Aussawasathien, D., Sirivat, A. (2014)
Polydiphenylamine/zeolite Y composites as a sensing material for halogenated solvents. PETROMAT and PPC SYM 2014, Bangkok, Thailand, 22 April 2014.

29) Paradee, N., Sirivat, A. (2014)
Development of electrically triggered release of alginate hydrogel for transdermal drug delivery application. PETROMAT and PPC SYM 2014, Bangkok, Thailand, 22 April 2014.

30) Paradee, N., Sirivat, A. (2014)
Electrically triggering drug release of poly(3,4-ethylenedioxy thiophene)/alginate hydrogel. MRS 2014, San Francisco, California, USA, 21-25 April 2014.

31) Permpool, T., Ausawasathien, D., Sirivat, A. (2014)

Electrical conductivity responses of polydiphenylamine/zeolite Y composites toward halogenated hydrocarbons. MRS 2014, San Francisco, California, USA, 21-25 April 2014.

32) Korattanawittaya, S., Sirivat, A. (2014)
Fabrication of compliant electrode based on natural rubber filled with graphene nanofiller. European Biotechnology Congress 2014, Lecce, Italy, 15-18 May 2014.

33) Khamngoen, K., Sirivat, A. (2014)
Synthesisand characterization of doped form of poly o-anisidine nanoparticles by chemical oxidation polymerization for biosensor and bioactuator. European Biotechnology Congress 2014, Lecce, Italy, 15-18 May 2014.

34) Thorngkham, P., Sirivat, A. (2014)
Electrically controlled release of indomethacin from polycarbazole/ natural rubber blend film. European Biotechnology Congress 2014, Lecce, Italy, 15-18 May 2014.

35) Pianmanakij, M., Sirivat, A., Siemanond (2014)
Sulfonated polysulfone and polyvinylidene fluoride membranes for direct methanol fuel cell. European Biotechnology Congress 2014, Lecce, Italy, 15-18 May 2014.

36) Petcharoen, K., Sirivat, A. (2014)
Electromechanical performance of magnetite nanoparticle and polyurethane composite. IC-MAST 2014, Bilbao, Spain, 8-11 June 2014.

37) Kamonsawas, J., Sirivat, A. (2014)
The selective ketone vapor sensor based on poly(p-phenylene vilnylene)/zeolite Y Composites. IC-MAST 2014, Bilbao, Spain, 8-11 June 2014.

38) Paradee, N., Sirivat, A. (2014)
Electric-field triggered controlled drug release from PEDOT/alginate hydrogel. IC-MAST 2014, Bilbao, Spain, 8-11 June 2014.

39) Petcharoen, K., Sirivat, A. (2014)
Performance of magneto-electro-responsive material in bending actuation. EMSA 2014, Vienna, Austria, 6-9 July 2014.

40) Petcharoen, K., Sirivat, A. (2015)
Electromechanical and electrostrictive behavior of polyurethane: effects of urethane type. SPIE 2015, San Diego, California, United States, 8-12 March 2015.

41) Paradee, N., Sirivat, A. (2015)
Morphological enhancement of poly(3,4-ethylenedioxythiophene) in alginate hydrogel for electrically controlled drug release. SPIE 2015, San Diego, California, United States, 8-12 March 2015.

42) Tungkavet, T., Sirivat, A. (2015)

Stress relaxation behavior in the effect of electric field and degree of crosslinking on gelatin hydrogels: time-electric field superposition. SPIE 2015, San Diego, California, United States, 8-12 March 2015.

43) Permpool, T., Sirivat, A., Aussawasathien, D. (2015)
Synthesis of polydiphenylamine nanoparticles: effect of surfactant type and concentration. SPIE 2015, San Diego, California, United States, 8-12 March 2015.

44) Kamonsawas, J., Sirivat, A. (2015)
Enhanced the interaction of dPPV/zeolite Y composites towards ketone vapors: effect of transition metals. SPIE 2015, San Diego, California, United States, 8-12 March 2015.

45) Phasuksom, K., Sirivat, A. (2015)
Effects of surfactant and oxidant on morphology and conductivity of polyindole synthesized by emulsion polymerization. PETROMAT and PPC SYM 2015, Bangkok, Thailand, 21 April 2015.

46) Thammarungsan, N., Sirivat, A. (2015)
Poly(lactic acid) filled with various plasticizers for using in actuator applications. PETROMAT and PPC SYM 2015, Bangkok, Thailand, 21 April 2015.

47) Choeichom, P., Sirivat, A. (2015)
Synthesis of poly(p-phenylene) nanoparticles via chemical oxidative polymerization. PETROMAT and PPC SYM 2015, Bangkok, Thailand, 21 April 2015.

48) Boonsitthichoke, P., Sirivat, A. (2015)
Preparation of multiwalled carbon nanotubes/natural rubber composite for compliant electrode application. PETROMAT and PPC SYM 2015, Bangkok, Thailand, 21 April 2015.

49) Changkhamchom, S., Sirivat A. (2015)
Molecular sieve 13X mixed with sulfonated poly(ether ketone rther sulfone) (S-PEKES)/ poly(phenylene ether ether sulfone) (PPEES) blended membrane for DMFC. PETROMAT and PPC SYM 2015, Bangkok, Thailand, 21 April 2015.

50) Permpool, T., Sirivat, A., Aussawasathien, D. (2015)
Effects of surfactant type and concentration based on emulsion polymerization of polydiphenylamine nanoparticles. PETROMAT and PPC SYM 2015, Bangkok, Thailand, 21 April 2015.

51) Choowongapichat, S., Sirivat, A. (2015)
Development of natural rubber matrix using in electrical stimuli transdermal drug delivery application. Frontiers in Polymer Science, Riva del Garda, Italy, 20-22 May 2015.

52) Choeichom, P., Sirivat, A. (2015)
Poly(p-phenylene)/ZSM-5 zeolite composites as CO and SO2 sensing materials. Frontiers in Polymer Science, Riva del Garda, Italy, 20-22 May 2015.

53) Bunlengsuwan, P., Pianmanakij, M., Changkhamchom, S., Sirivat, A., Siemanond, K. (2015) Development of sulfonated polysulfone/zeolite Y composite membranes for direct methanol fuel cell. Frontiers in Polymer Science, Riva del Garda, Italy, 20-22 May 2015.

54) Sangwan, W., Sirivat, A. (2015)
Electrical responsive material based polycarbazole and alginate bio-composite hydrogel as an actuator. Frontiers in Polymer Science, Riva del Garda, Italy, 20-22 May 2015.

Organizing Annual Conferences

1) The 1st Annual Symposium of Conductive and Electroactive Polymers (CEAP 2013)
22 April 2013 Sukosol Hotel, Bangkok, Thailand. The participants were 40
2) The 2st Annual Symposium of Conductive and Electroactive Polymers (CEAP 2014)
[The 5th Research Symposium on Petrochemical and Materials Technology and the 20th PPC Symposium on Petroleum, Petrochemical and Polymer (Session 8: Conductive and Electroactive Polymers)] at Ballroom and Meeting Room 3, Queen Sirikit National Convention Center, Tuesday, April 22, 2014. There were 52 participants.
3) The 3st Annual Symposium of Conductive and Electroactive Polymers (CEAP 2015)
[The 6th Research Symposium on Petrochemical and Materials Technology and the 21th PPC Symposium on Petroleum, Petrochemical and Polymer (Session 8: Conductive and Electroactive Polymers), Tuesday, April 21, 2015. There were 27 participants.
4) SPIE 2013, EAPAD Program Committee, San Diego, California, USA, 10-14 March 2013.
5) SPIE 2014, EAPAD Program Committee, San Diego, California, USA, 22-27 June 2014.
6) SPIE 2015, EAPAD Program Committee, San Diego, California, USA, 8-12 March 2015.
7) TRF-RGJ, Session Chairman, 5-7 May 2013.
8) TRF-RGJ, Session Chairman, 28-30 May 2014.
9) TRF-RGJ, Session Chairman, 11-13 June 2015.
10) การประชุมนักวิจัยรุ่นใหม่พบเมธีวิจัยอาวุโส สกว. ครั้งที่ 12 (Invited Speaker)
วันที่ 10 - 12 ตุลาคม 2555 ณ โรงแรมฮอลิเดย์ อินน์ รีสอร์ท รีเจ้นท์ บีช ชะอำ จังหวัดเพชรบุรี
11) การประชุมนักวิจัยรุ่นใหม่พบเมธีวิจัยอาวุโส สกว. ครั้งที่ 13 (ผู้ทรงคุณวุฒิ)
วันที่ 16-18 ตุลาคม 2556 ณ โรงแรมเดอะ รีเจ้นท์ ชะอำ บีช รีสอร์ท จังหวัดเพชรบุรี
12) การประชุมนักวิจัยรุ่นใหม่พบเมธีวิจัยอาวุโส สกว. ครั้งที่ 14 (ผู้ทรงคุณวุฒิ)
วันที่ 23-25 ตุลาคม 2557 ณ โรงแรมแอมบาสเดอร์ ซิตี้ จอมเทียน พัทยา จังหวัดชลบุรี

PhD. Graduates

1) Sairung Changkhamchom (2013)
Development of Sulfonated Poly(ether ketone ether sulfone) (S-PEKES) as Proton Exchange Membrane (PEM) for Using in Direct Methanol Fuel Cell (DMFC)
PhD. Thesis, Polymer Science, the Petroleum and Petrochemical College.

2) Wissawin Kunchornsup (2014)
Development of 1-Butyl-3-Methylimidazolium Chloride (BMIM+Cl-) Ionic Liquid – Cellulose Gel for Actuator Application.

PhD. Thesis, Polymer Science, the Petroleum and Petrochemical College.

3) Tharaporn Permpool (2015)
Polydiphenylamine/zeolite Y composites and electrical conductivity response toward halogenated hydrocarbons.
PhD. Thesis, Polymer Science, the Petroleum and Petrochemical College.

4) Thawatchai Tungkavet (2015)
Development of electromechanical properties of biocompatible gelatin as actuator applications.
PhD. Thesis, Polymer Science, the Petroleum and Petrochemical College.

MS. Graduates

1) Julaluk Pinit (2013)
Electrochromic Properties of Poly(o-toluidine) Coated on Indium Tin Oxide (ITO)
M.S. Thesis, Polymer Science, the Petroleum and Petrochemical College.

2) Sanita Pairatwachapun (2013)
Polythiophene/Carrageenan Hydrogel as Drug Release Matrix under Electric Field.
M.S. Thesis, Polymer Science, the Petroleum and Petrochemical College.

3) Thanida Srisawasdi (2013)
Silk Fibroin/Polycarbazole Composite as Artificial Muscle.
M.S. Thesis, Polymer Science, the Petroleum and Petrochemical College.

4) Napat Charoonrak (2013)
Development of Poly(p-phenylene)/Crosslinked poly(ε-caprolatone) as Electroactive Shape Memory Composite.
M.S. Thesis, Polymer Science, the Petroleum and Petrochemical College.

5) Piyanat Kotaphan (2013)
Sulfonated Poly(2,6-Dimethyl-1,4-Phenylene Oxide) Composite Membrane Filled by Zeolite for Direct Methanol Fuel Cell.
M.S. Thesis, Polymer Science, the Petroleum and Petrochemical College.

6) Pornwalai Thorngkham (2014)
Permeation Study of Indomethacin from Polycarbazole/Natural Rubber Blend Film for Electric Field Controlled Transdermal Delivery.
M.S. Thesis, Polymer Science, the Petroleum and Petrochemical College.

7) Sasithorn Korattanawittaya (2014)
Preparation of Graphene/Natural Rubber Composite for Compliant Electrode plications.
M.S. Thesis, Polymer Science, the Petroleum and Petrochemical College.

8) Kiattipong Khamngoen (2014)
Chemical Oxidation Polymerization and Characterization of Poly Ortho-Anisidine Nanoparticles.
M.S. Thesis, Polymer Science, the Petroleum and Petrochemical College.

9) Monchai Pianmanakij (2014)
Processing of Proton Exchange Membrane for Direct Methanol Fuel Cell.
M.S. Thesis, Petroleum Technology, the Petroleum and Petrochemical College.

10) Somchai Watpathomsub (2014)
Processing of Proton Exchange Membrane for Vanadium Redox Flow Battery.
M.S. Thesis, Petrochemical Technology, the Petroleum and Petrochemical College.

11) Sanchalit Choowongapichat (2015)
Development of Natural Rubber Matrix using in Electrical Stimuli Transdermal Drug Delivery Application.
M.S. Thesis, Polymer Science, the Petroleum and Petrochemical College.

12) Watchara Sangwan (2015)
Electrical Responsive Material based Polycarbazole and Alginate Bio-composite Hydrogel as an Actuator.
M.S. Thesis, Polymer Science, the Petroleum and Petrochemical College.

13) Phuwadon Bunlengsuwan (2015)
Improvement of Sulfonated Polysulfone Membrane for Direct Methanol Fuel Cell: Effect of Zeolite Y and Sulfonated Graphene Oxide.
M.S. Thesis, Petrochemical Technology, the Petroleum and Petrochemical College.

Summary of Outputs

PI: Professor Dr. Anuvat Sirivat

Award: TRF-RTA (24 August 2012- 23 August 2015)

	Publications	Proceedings	Presentations	PhD Grad	MS Grad	Conferences Organized/Committee
Year 1 Period 1	2	-	1	-	-	1 (TRF-Young Researchers)
Year 1 Period 2	4	5	25	1 (Sairung)	5	3 (TRF-RGJ, SPIE 2013, CEAP 2013)
Year 2 Period 1	6	-	5	1 (Wissawin)	-	1 (TRF-Young Researchers)
Year 2 Period 2	6	5	21	-	5	3 (TRF-RGJ, SPIE 2014, CEAP 2014)
Year 3 Period 1	6	-	-	2 (Tharaporn) (Thawatchai)	-	1 (TRF-Young Researchers)
Year 3 Period 2	6	3	21	-	3	3 (TRF-RGJ, SPIE 2105, CEAP 2015)
Total	30	13	73	4	13	12

Other Activities:

Editorial Boards of:

a) Recent Patents on Mechanical Engineering
b) Research and Report on Transdermal Drug Delivery
c) Data Sets in Materials Science
d) Open Journal of Chemical Engineering and Science

Conferences Participation and -Organization:

TRF-RGJ: Royal Golden Jubilee PhD Congress, Thailand Research Fund, Session Chairman
TRF-Young Researchers: Maethee Vijai Meet Young Researchers, Thailand Research Fund, Evaluator
CEAP: Conductive and Electroactive Polymers Symposium, Organizing Committee
SPIE 2013-2015, EAPAD Program Committee